A THESIS
FOR THE DEGREE OF DOCTOR OF PHILOSOPHY

Development of Self-Powered Sensors using Hybrid Piezoelectric Structure Nanogenerators

ALLURI NAGAMALLESWARA RAO

Faculty of Applied Energy Systems (Major: Mechanical Engineering)

GRADUATE SCHOOL
JEJU NATIONAL UNIVERSITY

February 2018

Development of Self-Powered Sensors using Hybrid Piezoelectric Structure Nanogenerators

Alluri Nagamalleswara Rao

(Supervised by Professor Sang-Jae Kim & Professor Ji Hyun Jeong)

A thesis submitted in partial fulfillment of the requirement for the degree of
Doctor of Philosophy
2017.12

The thesis has been examined and approved.

Young Sun Mok

Thesis Director, Professor, Department of Chemical Engineering,
Prof. Young Sun Mok College of Engineering, Jeju National University

Thesis Committee Member, Assistant Professor, Department of Energy Engineering,
Prof. Soo Seok Choi College of Engineering, Jeju National University

Thesis Committee Member, Professor, Department of Mechatronics Engineering,
Prof. Sang-Jae Kim College of Engineering, Jeju National University

Thesis Committee Member, Professor, Department of Mechanical Engineering,
Prof. Ji Hyun Jeong College of Engineering, Jeju National University

Kim Woo Young

Thesis Committee Member, Assistant Professor, Department of Electronics Engineering,
Prof. Woo Young Kim College of Engineering, Jeju National University

December, 2017

Faculty of Applied Energy Systems (Major: Mechanical Engineering)

GRADUATE SCHOOL
JEJU NATIONAL UNIVERSITY
Republic Korea

Acknowledgements

I would like to express my sincere gratitude to all who have supported, contributed to the completion of this doctoral thesis. I experienced and crossed the toughest paths, lots of failures and many significant achievements during this research work. I am so grateful to the people who have stayed all the times, guidance, consistent help to overcome the barriers, and encouragement.

First and foremost, I would like to express my sincere and deep gratitude to my beloved research advisor, **Prof. Sang-Jae Kim,** Jeju National University, for giving me the opportunity to execute the research work, supervision, and invaluable suggestions to extend the research works through simple, cost-effective approaches. His vision towards the practical application, research methodology and motivation much inspired me. The extended discussions, advice and timely support greatly helped to the improve the present thesis work. It was a great honor and privilege to perform the research work under his guidance. I am incredibly grateful for his friendship, and empathy. My heartfelt thanks to my co-research supervisor **Prof. Ji Hyun Jeong**, Jeju National University, for his scholarly advice and consistent help during the whole period of this course. My sincere gratefulness to him for the academic support and encouragement during the research period.

I express my sincere thanks to **Prof. B. S. Murty**, from Indian Institute of Technology Madras, **Prof. S.K.S Parashar**, and **Prof. Kajal Parashar** from KIIT University, who initiated my research career, valuable inputs, and directions to extend my research activities at the higher end. Many thanks and ineffable sense of gratitude to my best friends **Dr. P. Haribabu**, Korea Institute of Materials Science (KIMS), South Korea, and **Dr. B. Suresh Kannan**, Norwegian University of Science and Technology, Norway for his valuable guidance, motivation and research discussions to complete this work successfully.

The nanomaterials and systems group members are immensely helped to my personal and professional life at Jeju Island. This doctoral degree is not at all possible without their help and friendly environment. I sincerely thank my senior **Dr. V. Gunasekaran** for his recommendation to join in this research lab. My heartfelt gratitude to beloved former research group members **Dr. Ananthakumar Ramadoss, Dr. Saravanakumar Balasubramaniam, Dr. Kaliannan Thiyagarajan, Dr. V. Ganesh Kumar** and my

endorsers **Dr. Anil Kumar Khambampati, Dr. Dharaneetharan** for their initial support, nurture to settle down at Jeju National University. I sincerely thanks to my colleagues **Dr. Arunkumar Chandrasekhar**, **Dr. Sophia Selvarajan, Ms. Yuvasree Purusothaman, Mr. Vivekananthan Venkateswaran, Mr. Parthiban Pazhamalai, Ms. Kausalya Ganesan, Mr. Surjit Sahoo, Mr. Gaurav K, Mr. Nirmal Prashanth MJR, Ms. Sinduja, Mr. Vimal, Mr. Eui-Youg Hong, Ms. Shin So Yoon, Mr. Kim Taehyun, Mr. Ko Eunhyung, Ms. Park Minhee and Mr. Seong Mingeon** for their timely help and support.

It's a significant challenge and not so easy to stay away from the family, beloved friends and home country. I am so glad to have great friends at Jeju National University. They created a family environment, lots of unforgettable moments and hardships, which always helps to overcome the homesickness. My sincere thanks to **Mr. Sravan Kumar Konki** for his valuable support, care, and encouragement in research as well as in personal life. My heartfelt thanks to **Dr. Raj Mogre, Mr. Rajveer, Mr. Sachin Kumar Gupta, Mr. Vineet Singh, Mr. Suresh Rai, Ms. Shirjana Saud, Mr. Sudhakaran MSP, Mr. Nilojan, Dr. Radhakrishnan, Dr. Antony Ananth, Dr. Sodhi, Dr. Srikanth**, and **Mr. Kugan** for giving me so many wonderful memories to cherish during my stay in Jeju.

I would like to thank the following Jeju friends, who made homely environment during my stay in Korea "**Dr. Trinh, Mr. Moker, Dr. Adikari, Dr. Kalpa, Dr. Kamran, Dr. Safdar, Dr. Farrukh, Dr. Sohail, Dr. Junaid, Dr. Zahid, Dr. Siddique, Dr. Memoon, Dr. Shahid, Mr. Zubair, Dr. Waqar, Mr. Gul, Mr. Mutee, Mr. Lakmal, Mr. Anushka, Mr. Sachith** and **Mr. Rahman**". My special thanks to **Mr. Kanak, Mr. Phong** for their sacrifice as my room buddies. I also appreciate all the JISO members who have been very co-operative and support during my stay in Jeju. I am very much thankful to Research Instrument Center at JNU for providing the instrumental facilities during my study.

For this dissertation, I would like to thank my thesis evaluation director **Prof. Young Sun Mok**, and thesis committee members, **Prof. Soo Seok Choi** and **Prof. Woo Young Kim** for their time, interest, and insightful questions. I sincerely thank the Brain Korea 21 plus and graduate school of Jeju National University for the full support of research allowances, International conference trip allowances, and a stipend during my research period. My deep gratitude to the **Prof. Kyung-Youn Kim** for selecting me as a BK21^{+} fellow researcher and I

am so glad to the BK office member **Ms. So-Hee Kim** for processing my application forms and timely support.

Last but certainly not least, my earnest gratitude to my parents (**Mr. Alluri Sivarao** & **Mrs. Alluri Sankaramma**), My beloved sister (**Mrs. K. Vijaya Lakshmi**), and brother (**A. Sambasivarao**) for their encouragement and great help at every stage of my personal, academic life and wished to see this achievement come true. I express my sincere thanks to my brother-in-law (**Late Mr. K. Ravindra babu**), my nephews (**K. Lakshman & K. Bhargav**), sister-in-law (**Mrs. A. Varalakshmi**) and my love (**Mrs. B. Srilatha**) for their timely support, and cheering during this journey. My thanks are unbounded for their unconditional love and care. Above all peoples support, encouragement shown paths and strengthen my inherent capability to undertake this research project and enabling me to its completion.

Alluri Nagamalleswara Rao

Thesis Overview-I

Development of Cost-effective Hybrid Piezoelectric Structures

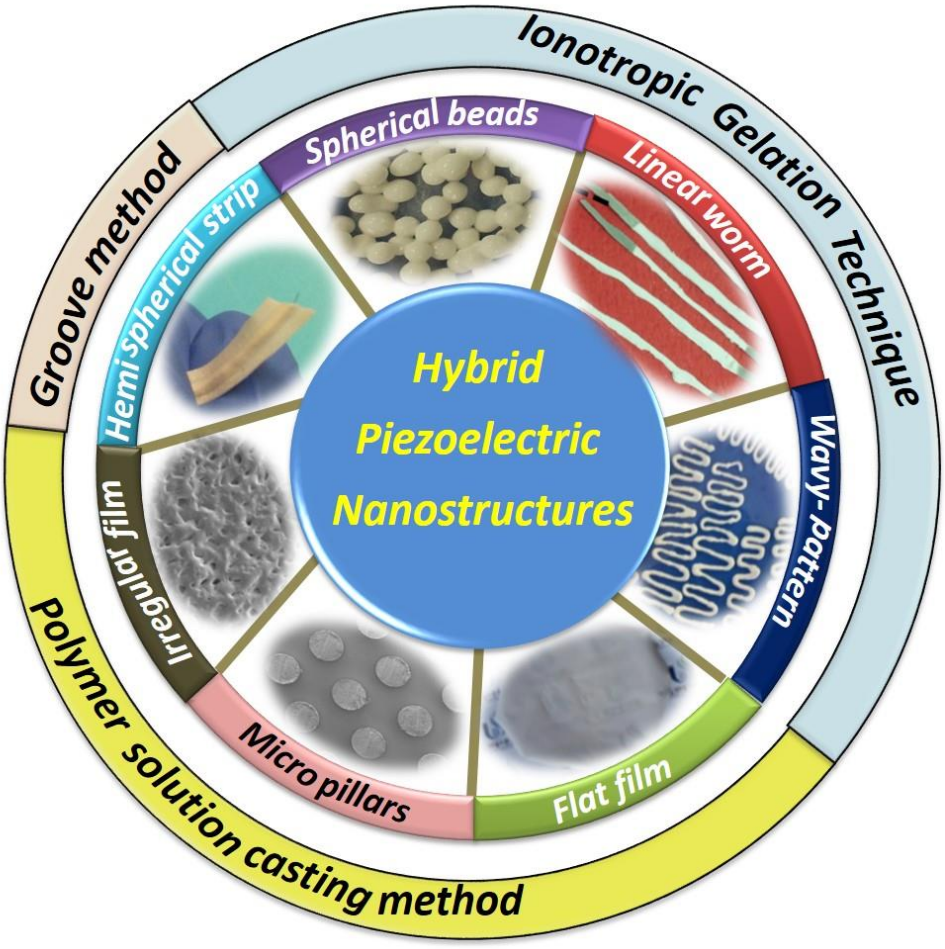

Thesis Overview-II

Design of Multifunctional Nanogenerators, Self-Powered Sensors

and its Performance Evaluation

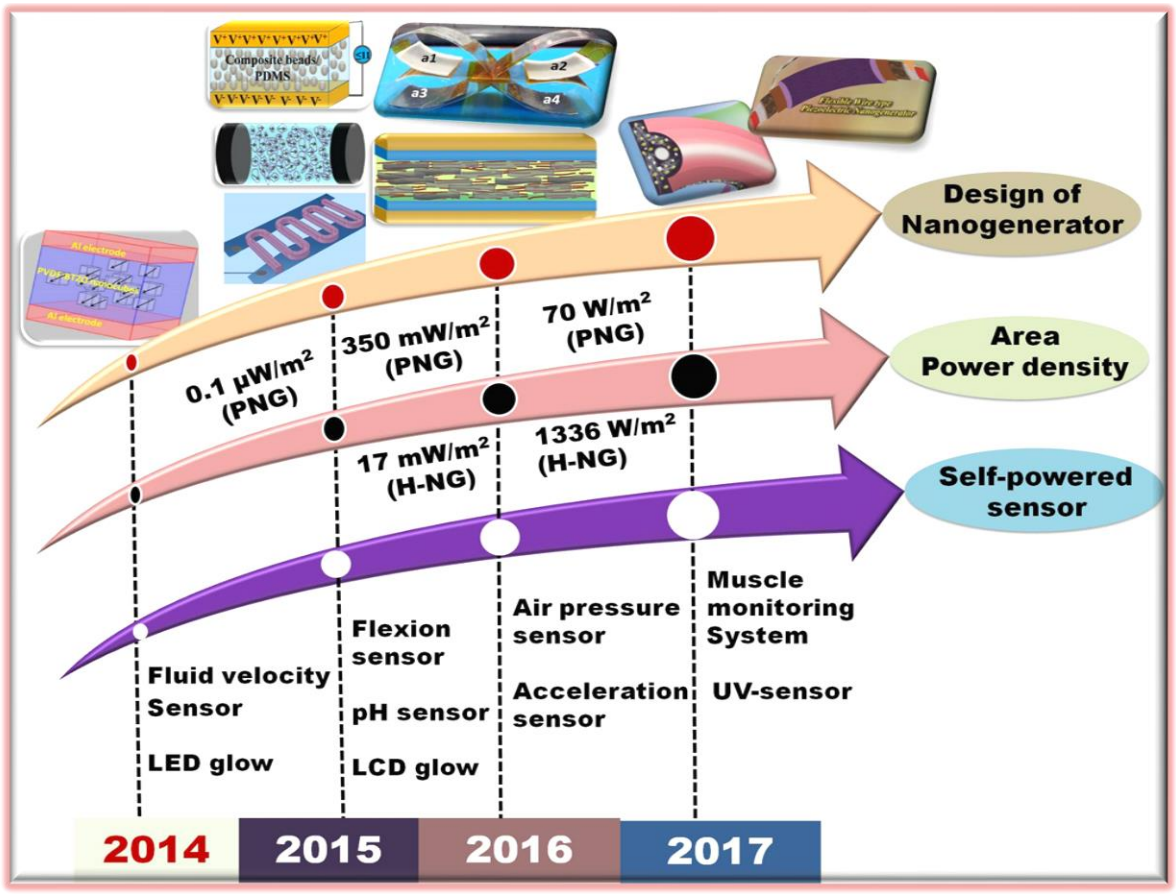

Contents

CHAPTER-I
Introduction

CHAPTER-II
Synthesis, fabrication methods for the piezoelectric nanoparticles, composite films and characterization techniques

CHAPTER-III
Self-powered wire type UV sensor using piezoelectric $BaTiO_3$ and semiconducting TiO_2 nanostructures on Ti-metal wire

CHAPTER-IV
Self-powered fluid velocity sensor-LEDs by polymer/$Ba(Ti,Zr)O_3$ nanocubes hybrid film piezoelectric nanogenerator

4.1 Self-powered fluid velocity sensor based on polyvinylidene/ $BaTi_{(1-x)}Zr_xO_3$ nanocubes hybrid film piezoelectric nanogenerator

CHAPTER-VI
Self-powered acceleration sensor using enhanced electroactive β-phase of PVDF/activated carbon hybrid film nanogenerator

CHAPTER-VII
Self-powered muscle monitoring system/air-pressure sensor based on PDMS/(BaCa)(SnTi)O_3 hybrid film nanogenerators

7.1 Groove technique derived adaptable piezoelectric hemispherical composite strips for self-powered muscle monitoring system

7.2 Self-powered air pressure sensor using high output butterfly wing-structure type multiunit-hybrid nanogenerator

CHAPTER-VIII
Summary and future work

Nomenclature

IEA	International energy agency
PNG	Piezoelectric nanogenerator
ITF	International transport forum
TENG	Triboelectric nanogenerator
LED	Light emitting diode
PVDF	Polyvinylidne fluoride
XRD	X-Ray diffraction
XPS	X-Ray photoelectron spectroscopy
FT-IR	Fourier transform infrared spectroscopy
FE-SEM	Field emission scanning electron microscope
PDMS	Polydimethyl siloxane
EDS	Energy dispersive x-ray spectroscopy
PNG	Piezoelectric nanogenerator
H-NG	Hybrid nanogenerator
SG	Sol-gel
COM	Chemical oxidation modification
TW-UV	Titanium dioxide wire ultraviolet
NSs	Nanostructures
DI	De-ionized
FWHM	Full width half maximum

FW-PNG	Flexible wire type piezoelectric nanogenerator
SPW	Self-powered wire
RT	Room temperature
AC	Activated carbon
C-NG	Composite nanogenerator
S-AS	Self-powered acceleration sensor
HS-CSPNG	Hemispherical composite strip based piezoelectric nanogenerator
SPS	Self-powered sensor or system
TG	Thermoelectric generator
HS-FPCS	Hemispherical shaped flexible piezoelectric composite strip
SP-MMS	Self-powered muscle monitoring system
FEHG	Flexible energy harvesting glove
LCD	Liquid crystal display
ECE	Energy conversion efficiency
BWS	Butterfly wing structure
CLW	Composite linear worm
CWPW	Composite wavy pattern worm
SPR	Surface Plasmon resonance
PVD	Pulsed vapor deposition
CVD	Chemical vapor deposition
WPNG	Worm based piezoelectric nanogenerator

SSR	Solid state reaction
IG	Ionotropic gelation
EH	Energy harvesting
EMG	Electromicrograph
SWF	Self-powered wearable flexion
CBNG	Composite bead based nanogenerator
S-CBNG	Strip-based composite bead nanogenerator
MOCVD	Metal organic chemical vapor deposition

List of Tables

List of Figures

추상

자체 전원 장치 기술은 스마트 기술의 차기 혁명으로 복잡한 배터리 소스, 외부 회로 부품 및 에너지 생성을위한 자연스러운 소스의 사용을 폐지합니다. 일반적으로,보다 우수한 감지 기능은 다양한 자극을 측정 / 모니터하기위한 감지 유닛, 회로 구성 요소를 인터페이싱하는 것, 처리 유닛 및 배터리 소스와 같은 주요 단계를 통해 실현 될 수있다. 현대 사회의 가장 중요한 요소는 자연 자원을 절약하고 환경 친화적 인 운영을보다 쉽게하는 방식으로 물건을 만드는 것이고 핵심 포인트는 주변 환경에서 오는 대체 에너지 원으로 독성이있는 복잡한 배터리 소스를 제거하는 것입니다. 더욱이, 다기능 나노 물질을 이용한 재생 가능 대체 에너지 수확 (AEH) 접근법의 지속적인 진보 또는 발명은 매우 바람직하다. 우리의 일상 생활에서 전기 에너지는 최대 장치를 구동하는 주된 입력 소스이기 때문에 에너지 소비와 세계 에너지 위기는 인구 증가, 라이프 스타일 선택의 급속한 증가로 엄청나게 증가합니다. 전통적인 수확 접근법은 천연 자원의 더 큰 범위를 소모하여 인류와 우주에 잠재적 인 위협 인 지구 온난화, 오염 및 탄소 배출을 증진시킵니다. 많은 AEH 기술 중에서 압전 나노 발전기 (PNG) (또는 에너지 수확기)는 저주파 기계 진동과 같은 사회의 폐기물 기계 에너지 (WME)를 기계, 인체 운동, 해양으로 변환하는 매우 안정적이고 안정적이며 효율적인 접근법입니다 파도 및 바람/ 물 흐름 운동을 유용한 전기 에너지로 변환합니다.

지금까지 광범위한 제조 방법, 플라스틱 기판상의 다양한 1 차원 무기물 압전 나노 구조 (NSs)의 성장, 유연한 압전 폴리머 필름 및 장치 설계가 지속 가능한 독립적 인 전력을 창출하는 탁월한 에너지 활용 방법으로 PNG 기술을 향상시키는 것으로보고되었습니다 소스는 저전력 소비 전자 장치를 구동합니다. 또한 다양한 가혹한 환경에서의 기기 호환성, 전기 출력 성능

(nW/cm^2~μW/cm^2) 및 유연성 문제가 실시간 상용화 PNG 제품에 대해 생각하기에 최적화되었습니다. 다른 한편, 상업용 전자 장치를 구동 할 수있는 웨어러블 / 휴대용 독립 전원과 같은 이중 기능을 가진 PNG는 거의 없으며 다양한 물리적, 화학적, 생물학적 및 광학적 자극을 측정하는 자체 전원 센서로 작동 할 수도 있습니다. 여전히, 취성, 누설 전류 문제, 전기 출력 생성 및 장기 내구성과 같은 다양한 요인으로 고통받는 PNG 기술은 혁신적인 비용 효율적인 제조 방법을 사용하여 다기능 하이브리드 압전 구조를 개발함으로써 제어해야합니다.

3 장에서 화학적 산화법과 저온 수열 기술을 사용하여 유연한 인간의 머리카락 크기의 Ti 금속 선에 반도체 성 TiO_2와 페 로브 스카이 트 압전체 BaTiO3 NSs의 반경 방향 성장을 설명한다. 또한, 와이어 형 나노 발전기와 자외선 센서 사이의 외부 병렬 연결에 의해 자체 구동 와이어 타입 자외선 센서의 개발에 사용되는 가공 와이어. 에너지 레벨 밴드 다이어그램에 의한 상세한 반경 방향 성장 과정과 UV 감지 작업 메커니즘이 탐구되었다. 4 장에서는 유연한 평면형 하이브리드 PNG를 사용하여 출구 파이프를 통해 흐르는 물의 속도를 측정하고 발광 다이오드를 구동하는 자체 구동 식 유체 속도 센서에 대해 설명합니다. 고결 정성 BTO 나노 큐브와 $Ba(ZrTi)O_3$ 나노 큐브는 저비용 솔루션 캐스팅 기술로 평면 복합 필름 (PDMS/BTO, PVDF/$Ba(ZrTi)O_3$)의 대규모 생산을 위해 개발 및 활용되었습니다. 두 평면 PNG 장치의 전기적 응답은 수직의 기계적 힘에 대해 분석하고 특정 힘 조건에서 순간 전력 밀도 값을 평가합니다. 처음으로 ionotropic gelation 방법을 도입하여 제 5 장에서 기술 한 새로운 압전 구형 하이브리드 비드, 선형 웜 및 파형 생성 웜 구조를 제작하여 전기를 발생시켰다. 이들 구조의 형성 메카니즘, 용해도, 유연성 및 다양한 치수 크기가 공정 조건을 변경하여 얻어지고 분석되었다. 일정한 기계적 힘을받는 선형 및 물결 모양 웜 구조 기반 PNG의

길이 의존 압전 전위 반응을 조사했습니다. 물결 모양의 PNG 장치와 선형 웜 pH 센서 사이의 외부 병렬 연결을 통해 자체 구동 식 pH 센서를 입증했습니다. 나중에, BTO/Ca-alginate 구형 비드/PDMS 폴리머를 사용하여 개발 된 스트립 타입 하이브리드 나노 발전기 (H-NG)는 다양한주기 주파수 종속 기계력, 다양한 기계 압력 및 굴곡 각도에서 에너지 포집 능력을 평가했습니다. 스트립 장치는 개인/결합 된 손가락 굴곡/신전 운동을 모니터링하기 위해 비 침습적 자체 구동 굴곡 센서를 시연하는 데 사용되었습니다.

압전 PVDF 폴리머의 자 극 (self-poled)은 초음파 화학 공정을 사용하여 탐구되었고 폴리머 매트릭스에 활성탄 충진제가 포함되어 향상되었습니다 (6 장). 이 프로세스는 영구 전기 분극을 생성하기 위해 압전 재료의 추가 전기 폴링 프로세스를 완전히 제거합니다. 복합 막, 형성 메커니즘 및 평면 PNG 장치 응답의 전기 활성 -β 위상 백분율은 조심스럽게 평가됩니다. 이 유형의 PNG에는 리니어 모터 샤프트 하중 (자체 동력 가속도 센서)의 다양한 가속도를 감지 할뿐만 아니라 에너지를 사용하는 것과 같은 이중 기능이 있습니다. 처음으로 혁신적인 비용 효율적이고 환경 친화적 인 그루브 기술 (Chapter-7)이 고도의 적응성 / 유연성 반구형 복합 스트립 (HCS)을 준비하기 위해 개발되었습니다. 다양한 길이의 HCS, 비틀림 능력, 유연한 에너지 수확 장갑 및 순간 전력 밀도 생성이 신중하게 조사되었습니다. 고도의 생체 적합성 자체 구동 근육 모니터링 시스템은 여러 개의 HCS-PNG를 제작하고 인체 관절에 위치시킴으로써 구현되었습니다. Chapter-7은 단일 하이브리드 필름, 호 모양의 H-NG 및 나비 멀티 유닛 H-NG의 구성에서 압전 및 마찰 전기 기능을 결합하여 나노 발전기의 출력 밀도를 향상시키는 혁신적인 방법을 설명합니다. 여기서, PDMS 매트릭스, 적용된 힘 의존 분석, 다중 나노 발전기 모드 (압전, 마찰 전기 및 하이브리드) 응답, 스위칭 극성

테스트, 표면 형태 의존 출력, 접촉 - 이격 거리 효과 및 많은 디바이스 설계 파라미터에서 $BaCaTiO_3$-$x$$BaSnTiO_3$ 나노 입자의 중량 비율 평가되었습니다. 처음으로, 하이브리드 필름의 유도면 밀도를 향상시킴으로써 H-NG에 대해 엄청난 양의 순시 전력 밀도가 달성되었습니다. 다양한 공기압 범위를 측정하기 위해 나비 식 멀티 유닛 H-NG를 사용하여 자체 구동 식 공기 압력 센서를 시연했습니다.

Abstract

Self-powered device technology is the forthcoming revolution in smart technology and resulting abolish the usage of complex battery sources, external circuit components and natural sources for energy generation. Generally, the better sensing functionality can be realized by the following key steps such as sensing unit to measure/monitor various stimuli, interfacing circuit components, a processing unit and battery source to power up the whole unit. The modern society's foremost parameter is to make the things in an easier manner, saving natural resources, eco-friendly operation and the key point is to remove the toxic, complex battery sources by the alternative energy sources, which is coming from the surrounding environments. Moreover, the continuous progress or invention of renewable, alternative energy harvesting (AEH) approaches using the multifunctional nanomaterials was highly desirable. Because in our daily life the electrical energy is the primary input source to drive the maximum devices, energy consumption and world energy crisis increase tremendously due to rapid growth of population, lifestyle choices. Traditional harvesting approaches consume the greater extent of natural resources leads to enhance the global warming, pollution and carbon emissions, which is a potential threat to the human race and universe. Among many AEH technologies, piezoelectric nanogenerator (PNG) (or energy harvester) is highly reliable, stable and efficient approach to convert the waste mechanical energy (WME) in the society such as low frequency mechanical vibrations from the machines, human body motions, ocean waves and wind/water flow motions into useful electrical energy.

To date, extensive fabrication methods, growth of various one dimensional (1D)/two dimensional (2D) inorganic piezoelectric nanostructures (NSs) on plastic substrates, flexible piezoelectric polymer films and device designs (planar, stretchable, cylindrical or fiber) were developed to improve the PNG technology as a prominent energy harnessing approach for creating the sustainable independent power source to drive the low power consumed electronic devices/sensors. Moreover, the device compatibility, electrical output performance (nW/cm^2 to $\mu W/cm^2$) under various harsh environments and flexibility issues were optimized to think about the real-time commercialized PNG product. On the other side, few PNGs have dual functionality such as wearable/portable independent power source to drive the commercial electronic devices and can also work as a self-powered sensor (or battery-free sensor) to measure/monitor the various physical, chemical, biological and optical stimuli. Still, PNG technology suffering from various factors such as brittleness, leakage current issues, electrical output generation and long-term durability, which needs to be controlled by developing the multifunctional hybrid piezoelectric structures using innovative, cost-effective fabrication approaches.

In **chapter-3** elucidate the radial growth of semiconducting TiO_2 and perovskite piezoelectric $BaTiO_3$ (BTO) NSs on the flexible human hair-sized Ti-metal wire using the chemical oxidation method followed by the low-temperature hydrothermal technique. Further, as-fabricated wires used for the development of self-powered wire type UV sensor by the external parallel connection between the wire type nanogenerator and UV-sensor. The detailed radial growth process and UV-sensing working mechanism by energy level band diagram were explored. **Chapter-4** describes the self-powered fluid velocity sensor

to measure the water velocity flowing through the outlet pipe and light emitting diodes (LEDs) using the flexible planar type hybrid PNG. High crystalline BTO nanocubes and $Ba(ZrTi)O_3$ nanocubes were developed and utilized to fabricate the large-scale production of planar composite films (PDMS/BTO, PVDF/ $Ba(ZrTi)O_3$) by the low-cost solution casting technique. Both the planar PNG devices electrical response analyzed upon the perpendicular mechanical force and evaluated the instantaneous power density values at particular force conditions. For the first time, ionotropic gelation method introduced to fabricate the novel piezoelectric spherical hybrid beads, linear worm and wavy-pattern worm structures for generating electricity described in **Chapter-5**. The formation mechanism of these structures, solubility, flexibility and various dimensional sizes were obtained and analyzed by changing the process conditions. The length-dependent piezoelectric potential response of the linear and wavy-pattern worm structure based PNGs under constant mechanical forces was investigated. Self-powered pH sensor was demonstrated by the external parallel connection between the wavy-pattern PNG device and the linear worm pH sensor. Later, strip type hybrid nanogenerator (H-NG) developed using the BTO/Ca-alginate spherical beads/PDMS polymer and evaluated the energy harvesting capability under different cyclic frequency dependent mechanical forces, various mechanical pressures, and bending angles. The strip device has been used to demonstrate the non-invasive self-powered flexion sensor to monitor the individual/combined finger flexion/extension movements.

Self-polarization of the piezoelectric PVDF polymer were explored using the sonochemical process and enhanced by the substitution of activated carbon fillers in a

polymer matrix (**Chapter-6**). This process completely removes the additional electrical poling process of the piezoelectric materials to create the permanent electric polarization. The electroactive-β phase percentage of the composite film, formation mechanism and its planar PNG device response evaluated carefully. This type of PNG has dual functionality such as harnessing energy as well as sensing the various accelerations of the linear motor shaft load (self-powered acceleration sensor). For the first time, innovative, cost-effective, eco-friendly groove technique (**Chapter-7**) was developed to prepare the highly adaptable/flexible hemispherical composite strip (HCS). Multiple lengths of HCSs, twisting capability, flexible energy harvesting glove and instantaneous power density generation were investigated carefully. The highly biocompatible self-powered muscle monitoring system was implemented by fabricating the multiple HCS-PNGs and placing on the human body joints. **Chapter-7** describes the innovative approach to improve the power density of the nanogenerator by the combining the piezoelectric and triboelectric functional properties in single hybrid film, arc-shaped H-NG and the construction of butterfly multi-unit H-NGs. Here, weight ratio of $BaCaTiO_3$-$x$$BaSnTiO_3$ nanoparticles in PDMS matrix, applied force dependent analysis, multiple nanogenerator mode (piezoelectric, triboelectric and hybrid) responses, switching polarity test, surface morphology dependent output, contact-separation distance effects, and many device design parameters were evaluated. For the first time, an enormous amount of instantaneous power density was achieved for H-NG by improving the induced surface density of the hybrid film. Self-powered air pressure sensor was demonstrated using the butterfly multi-unit H-NG to measure the various air-pressure ranges.

CHAPTER-I

Introduction

1.1 Energy crisis and effects of traditional energy harvesting technologies

The present society and technology directing towards the digitalization of the world increases the huge consumption of electrical energy. Over the decades, the major percentage amount of electrical energy generated by the consumption of the natural sources like oil, gas, coal, and water as shown in **Figure 1a**. But the natural sources are limited in supply and the continuous energy generation using these sources creates a global warming issues and pollution, which will effect on the lifespan of human race. Moreover, the regeneration or restore of the natural sources take hundreds of the thousand years. In another view, the energy crisis increasing day-by-day due to the lifestyle choices, climate change, industrialization of sectors and typical regulation-policies by power management sectors.

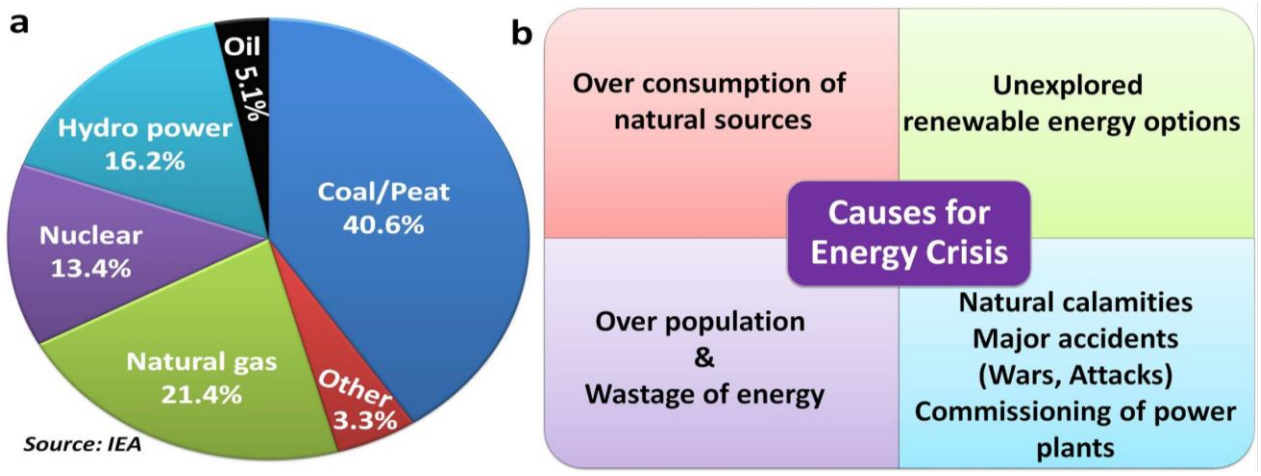

Figure 1 Energy crisis: (a) Overview of traditional energy sources (b) Causes for Energy crisis

The International Energy Agency (IEA) [1] report depicts that the major problem in the world energy sector is the “energy crisis”, which is in two ways 1) the power supply and demand 2) over-consumption of natural sources. This is imminent to the present human generation and

serious issue for the future generation mankind. The causes for the energy crisis can be explained in different ways as shown in **Figure 1b**. To overcome the energy crisis, alternating energy harvesting options and energy policies are introduced across the world. The detailed possible solutions [2] were depicted in **Figure 1.2**. But have not been widely investigated. The development and searching of the renewable energy sources is the prime factor to solve the partial amount of energy crisis. Most of the renewable energy comes from the indirect or direct source of sunlight. The renewable energy comes from the various ways such as solar, wind power, hydroelectric energy, hydrogen and fuel cells, geothermal energy, biomass, and other forms of energy.

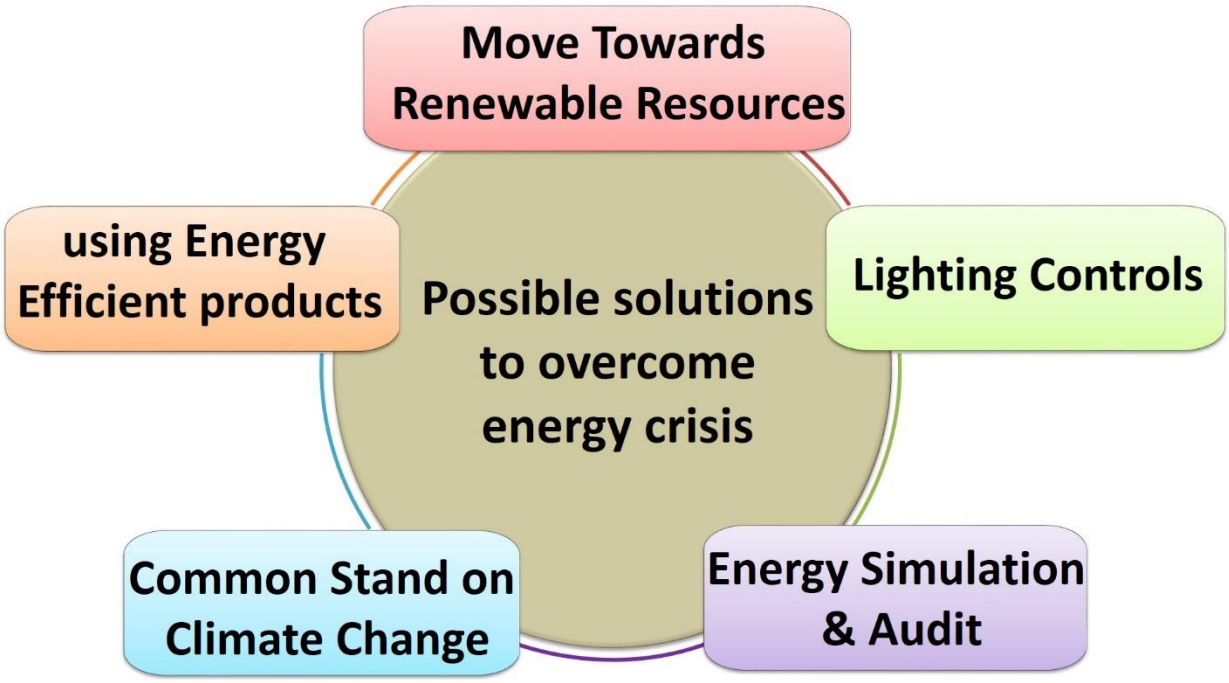

Figure 1.2 Possible solutions to overcome the crisis

1.2 Waste mechanical energy sources and utilization approaches

The waste mechanical energy can be found in everywhere through various forms such as machine vibrations, vehicle motions, vibrations induced by the water/air and ocean waves,

human body movements as shown in **Figure 1.3**. Globally, lots of mechanical energy is wasted in our day-to-day lives. For example the average number of vehicles running per day in South Korea is greater than 22 000, which cover more than 300 000 km (as per a report by the International Transport Forum (ITF), 2016). The wind power capacity in South Korea is 835 MW with an annual wind speed of 4–4.5 ms^{-1}. Further, this is expected to be increased to 2.5GW in the near future. Taking a macroscopic view, worldwide, lots of vehicle/machinery motion and human body movement is generating surplus amounts of mechanical energy. But there is no proper technology to utilize this type of waste mechanical energy [3].

Figure 1.3 Various forms of waste mechanical energy sources

Recently, many scientists and academic researchers believe that the harnessing waste mechanical energy in our regular life (low-frequency mechanical vibrations) using the functional nanomaterials is an innovative direction. Over the last decade, lots of device designs (i.e., Nanogenerators) were demonstrated to utilize these mechanical energies by the piezoelectric and

triboelectric effects of the nanomaterials and devices. The instantaneous power density of these nanogenerators improved from the nW/cm^2 to W/cm^2 suggests that these devices, approaches are the perfect choice to utilize the waste mechanical energy. Moreover, this type of energy generation is clean, eco-friendly, cost-effective and pollution free.

1.3. Piezoelectric/triboelectric nanogenerators and working principles

Nanogenerator is device can detect/harvest the small periodic changes in the mechanical and thermal energies using the specialized functional nanostructures. Both piezoelectric/triboelectric devices generate electricity with respect to the time-dependent mechanical fluctuations. The individual nanogenerator device designs and its working principles were described below:

1.3.1 Piezoelectric nanogenerator

The active layer in piezoelectric nanogenerator is made up of non-centrosymmetric nanostructure materials have a capability to convert the external mechanical energy or strain into useful electric energy. These materials experience a generation of cumulative electric dipole moment per unit volume (i.e., polarization), whenever subjected to mechanical stress. Over the last decade, many researchers showed a great effort to improve the performance of the piezoelectric nanogenerator using various materials, approaches. Figure 1.4 shows the possible types of piezoelectric nanogenerator and its device designs [4, 5] and figure 1.5 shows the improved normalized open circuit voltage (V_{OC}) and short circuit current (I_{SC}) of the piezoelectric nanogenerator upon the periodic bending conditions.

The relationship between the electrical quantities and the mechanical force parameters for the piezoelectric energy harvesting devices:

The open circuit voltage (V_{OC}) and short circuit current (I_{SC}) of piezoelectric nanogenerators are directly related to the mechanical parameters such as force and displacement (Z). The relationship can be written as follows (the macroscopic view) [6-12]:

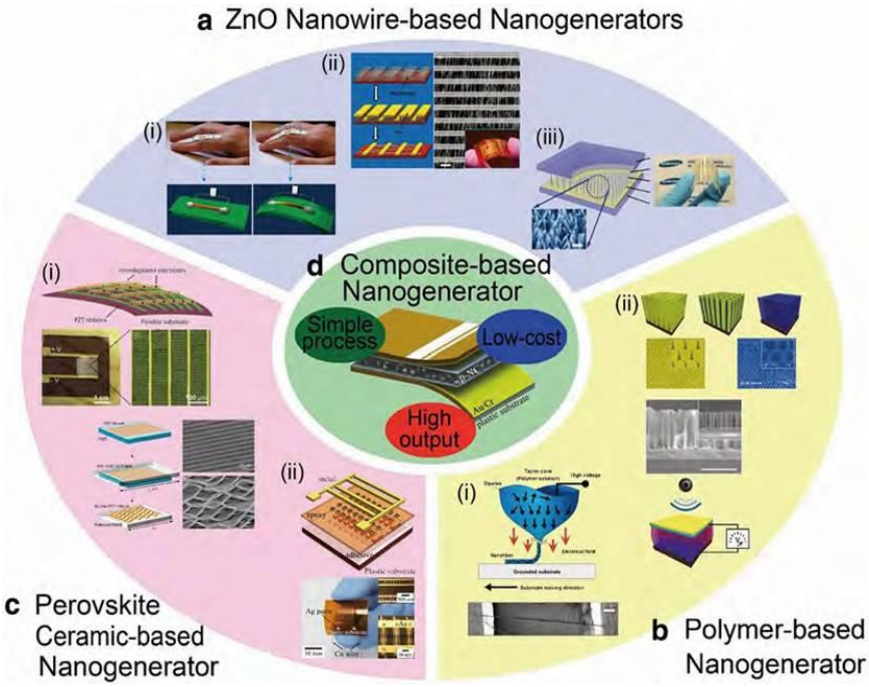

Figure 1.4 Possible types of flexible energy harvesting devices (Park et al. Nano Convergence (2016) 3:12)

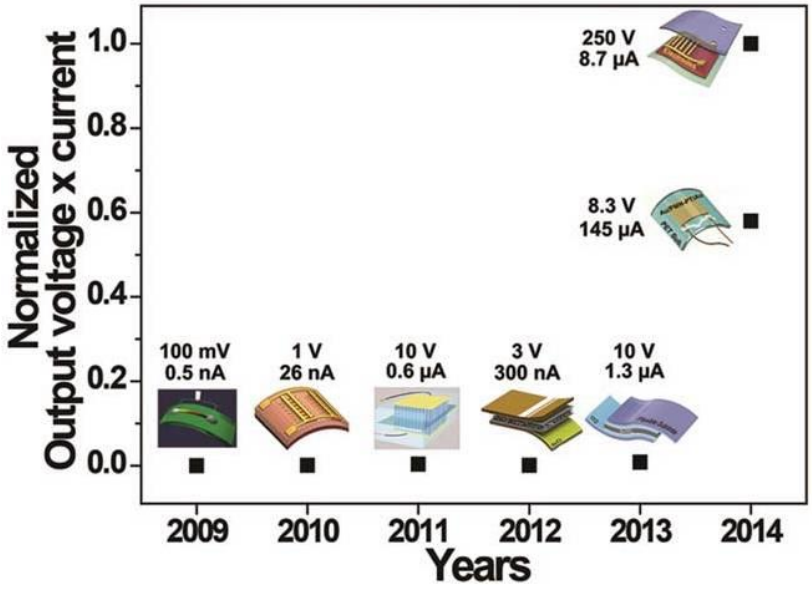

Figure 1.5 A summary of the performance improvement of flexible piezoelectric energy harvesters since 2009. The normalized products of generated open-circuit voltage and short-

circuit current by bending motions were used to compare the performance of flexible piezoelectric NGs.

$$F_P = K_{PE} Z + \alpha V_{OC}$$

and

$$I_{SC} = \alpha \dot{Z} - C_P \frac{dV_{OC}}{dt} \quad \text{(E1.1)}$$

where α represents the force factor, F_P is the restoring force of the piezoelectric material, C_P is the clamped capacitance and K_{PE} is the stiffness of the piezoelectric material. The variables C_P, K_{PE}, and α defined as follows:

$$K_{PE} = \frac{C_{33}^E A}{L}, C_P = \frac{\varepsilon_{33}^S A}{L}, \alpha = \frac{e_{33} A}{L} \quad \text{(E1.2)}$$

The electromechanical quantities of stress (*T*), strain (*S*), the electric field (*E*) and electrical induction (*D*) are obtained by the tensor and electric induction tensor matrices and can be written as follows:

$$E = -\frac{V}{L}, S = \frac{Z}{L}, I = A\frac{dD}{dt}, F_P = AT \quad \text{(E1.3)}$$

where *A* and *L* represent the sectional area and thickness of the active working zone of the piezoelectric nanogenerator, respectively. By solving Equation (E1.1), the open circuit voltage for the piezoelectric nanogenerator as a function of the piezoelectric coefficient (d_{33}) and relative permittivity can be computed as follows:

$$V_{OC} = g_{33} \sigma Y t \quad \text{(E1.4)}$$

where $g_{33}$is the piezoelectric voltage constant ($d_{33} = g_{33} \epsilon_O K$), *Y* and *t* are the Young's modulus of the composite and the thickness of the device, and σ is the strain in the perpendicular direction. The short circuit current can be evaluated by using the equation:

$$I_{SC} = d_{ii} Y A \varepsilon \quad \text{(E1.5)}$$

where d_{ii} is the piezoelectric coefficient, A is the cross-sectional area, and ε is the applied strain.

1.3.2 Triboelectric nanogenerator

The triboelectric effect can be experienced with the two opposite, electrically charged materials come in contact or creating friction between them. In the old days, this effect classified as a negative effect or noise or interference in many electronic devices. The two different materials can be categorized as any dielectric-dielectric, dielectric-conductor, and metal-metal. The triboelectric charge transfer (electrons or ions/molecules) will exist between the two contacted materials by creating/modulating the chemical bonds on the surface of the materials and balances the electrochemical potential. The generation of triboelectric power or response is mainly due to the electrostatic induction and triboelectrification. The charge transfer process between the metal to polymer (or any composite) surface is too slow, and sometimes it follows the multiplication boosting the free electrons generation in short time. Over the last decade, the lots of progress happen on the triboelectric nanogenerator (TENG) device designs and it possible to work under four different modes [13] as shown in **Figure 1.6**. The governing relationship between the voltage (V)-charge (Q)-contact-separation distance (X) provides the first-order lumped equivalent circuit. It is a combination of an ideal power source connected with the variable capacitor. The open circuit voltage and short circuit current for the dielectric-to-conductor type TENG mode (**Figure 1.6a**) can be written as [14]:

$$V = -\frac{Q}{S\varepsilon_o}\left(d_o + X(t)\right) + \frac{\sigma X(t)}{\varepsilon_o} \qquad \text{From electrodynamics theory} \qquad \text{(E1.6)}$$

$$Q_{SC} = \frac{\sigma S}{\left(1+{}^{C_1(X)}/_{C_2(X)}\right)} - \frac{\sigma S}{\left(1+{}^{C_1(X=0)}/_{C_2(X=0)}\right)} \qquad \text{From Kirchhoff's Law} \qquad \text{(E1.7)}$$

$$V_{OC} = \frac{\sigma X(t)}{\varepsilon_o} \;;\; Q_{SC} = \frac{S\sigma X(t)}{(d_o + X(t))} \;;\; C = \frac{\varepsilon_o S}{(d_o + X(t))} \quad \text{(E1.8)}$$

where d_o is sum of the thicknesses of all the dielectrics, V is the induced potential difference between the two plates, $X(t)$ is the distance between the two triboelectric layers with respect to time, S is the areal size of the metal, Q_{SC} is the short circuit charge, C is the capacitance and σ is the static charge density.

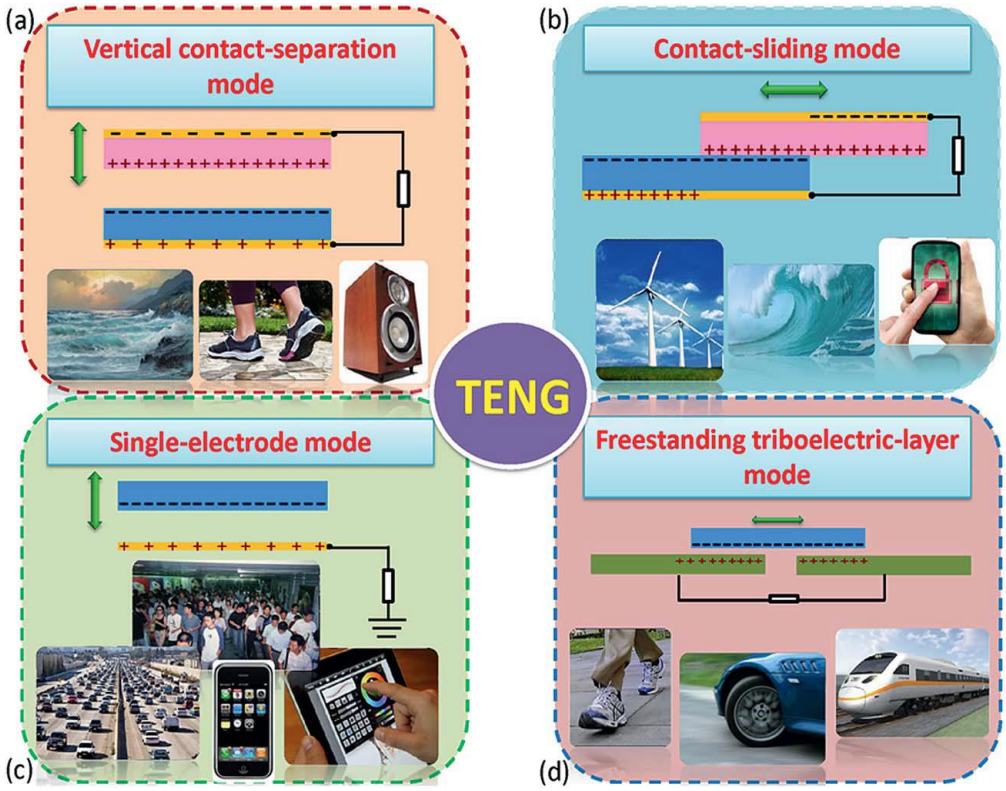

Figure 1.6 The four fundamental modes of triboelectric nanogenerators: (a) vertical contact-separation mode; (b) in-plane contact-sliding mode; (c) single-electrode mode; and (d) freestanding triboelectric-layer mode.

1.4 Types of piezoelectric materials

The piezoelectric materials are commercialized in the year 1945, when the man-made pre-defined shape, size of the mixed oxide compound barium titanate ($BaTiO_3$) was invented and proposed that the material has spontaneous polarization without an external electric field. This is highly stable, non-toxic and better piezoelectric constants than the natural piezoelectric crystals.

Later, many other piezoelectric/ferroelectric perovskite materials are developed and successfully industrialized.

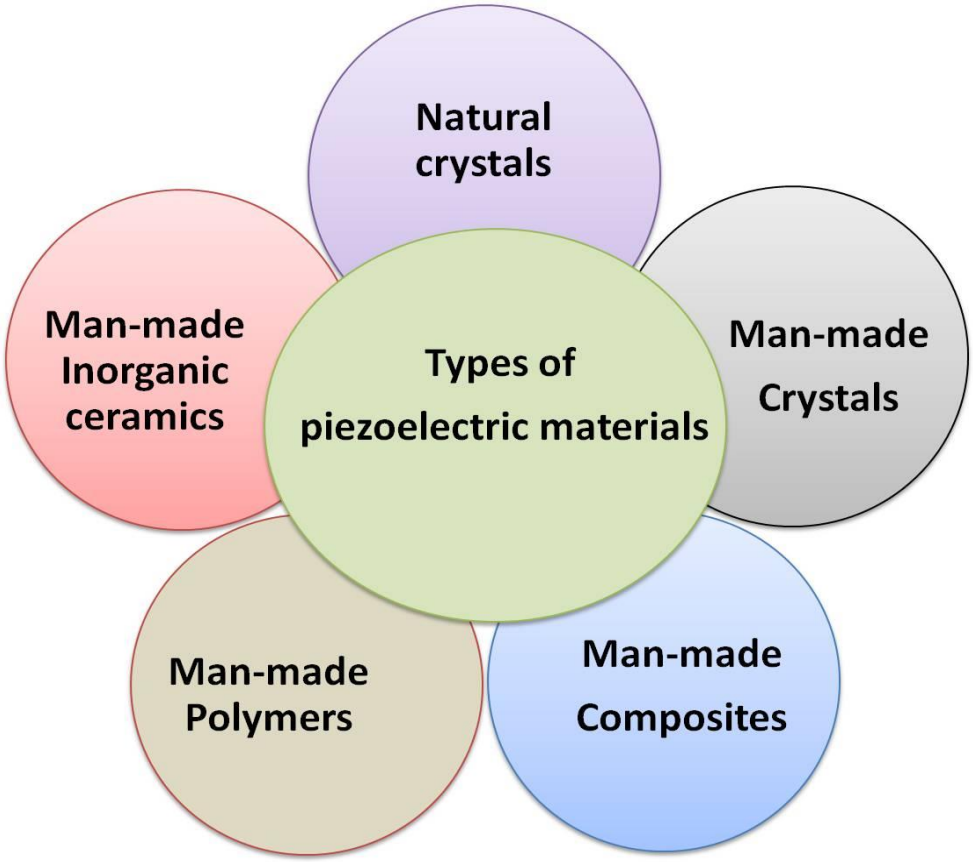

Figure 1.7: Types of piezoelectric materials

The piezoelectric materials are a special type of anisotropic dielectrics, where the electric and elastic fields are coupled together. The change in the position of the atoms due to applied stress leads to the formation of net dipole moments that causes polarization and an electric field, respectively [15]. Generally, the piezoelectric materials can be classified into two types as shown in **Figure 1.7.**

1.4.1 Natural piezoelectric crystals

For example Quartz (SiO_2), Rochelle salt, Topaz, Tourmaline-group minerals and some organic substances as silk, wood, enamel, dentin, bone, hair, rubber, etc.

1.4.2 Man-made piezoelectrics

1.4.2.1 Crystals

For example Gallium orthophosphate ($GaPO_4$) and Langasite ($La_3Ga_5SiO_{14}$)

1.4.2.2 Inorganic perovskite ceramics

The general chemical formulae for piezoelectric perovskite ceramic is ABO_3, where A, B are the larger, smaller metal cations and O is the anion. Generally, the piezoelectric perovskite ceramics can be classified with different families as shown in **Figure 1.8.** The lead-based piezoelectrics have high piezoelectric coefficient and electromechanical coupling coefficient. But these materials are facing global restriction due to the lead toxicity, pollution and the synthesis techniques are not eco-friendly. Over two decades, continuous progress happens on the lead-free piezoelectric ceramics by synthesis wise, co-doping of foreign atoms with parent lattice, the growth of various types of nanostructures to improve the piezoelectric performance as like lead-based piezoelectric.

Particularly, many scientists and researchers were concentrated on the development of $BaTiO_3$ and $KNbO_3$ families and suggesting that the ceramics are potential candidates to replace the lead-based ceramics with the similar functional properties. In the present thesis work, $BaTiO_3$ nanoparticles and it's co-doping with zirconium, tin and calcium atoms were studied and also implemented the various novel composite structures to improve the energy harvesting capability of piezoelectric nanogenerator.

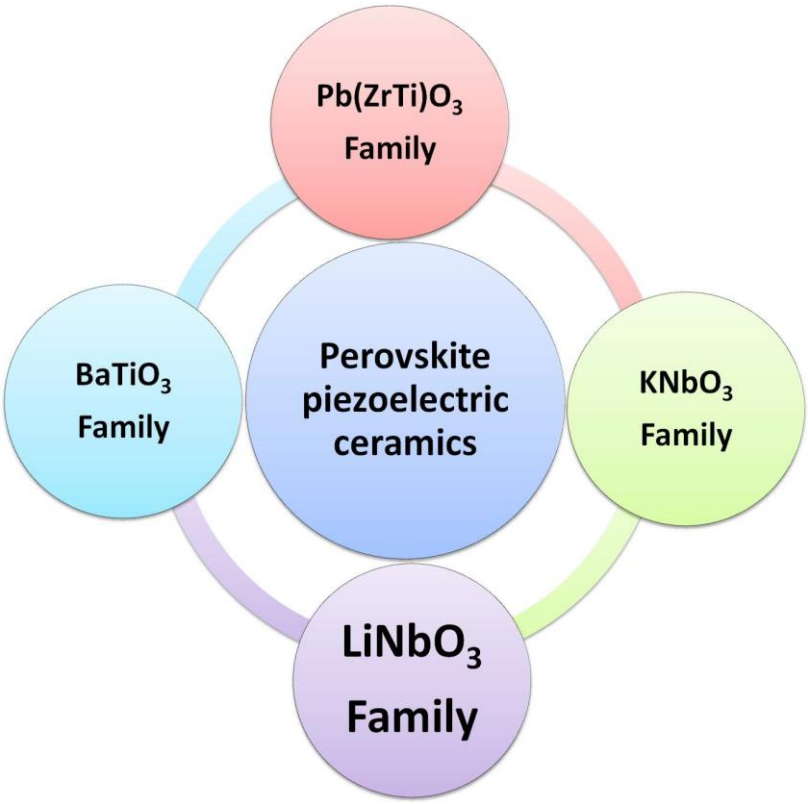

Figure 1.8 Classification of the perovskite piezoelectric ceramics

$BaTiO_3$ crystal structure: A pure $BaTiO_3$ nanoparticle has a moderate piezoelectric coefficient, electromechanical coupling coefficient and insoluble in water. It has different forms of crystalline phases from high temperature to a low temperature such as hexagonal, cubic, tetragonal, orthorhombic and rhombohedral. The cubic phase of BatiO3 does not have active vibrational modes, and it can exhibit ferroelectric property. Among all other, the crystalline phase's, tetragonal phase exhibits high ferroelectric nature and a potential candidate for many applications such as microphones, transducers, energy harvesting devices, sensors, and thermistors. **Figure 1.9** shows the cubic, tetragonal crystalline unit cells of $BaTiO_3$ nanoparticles.

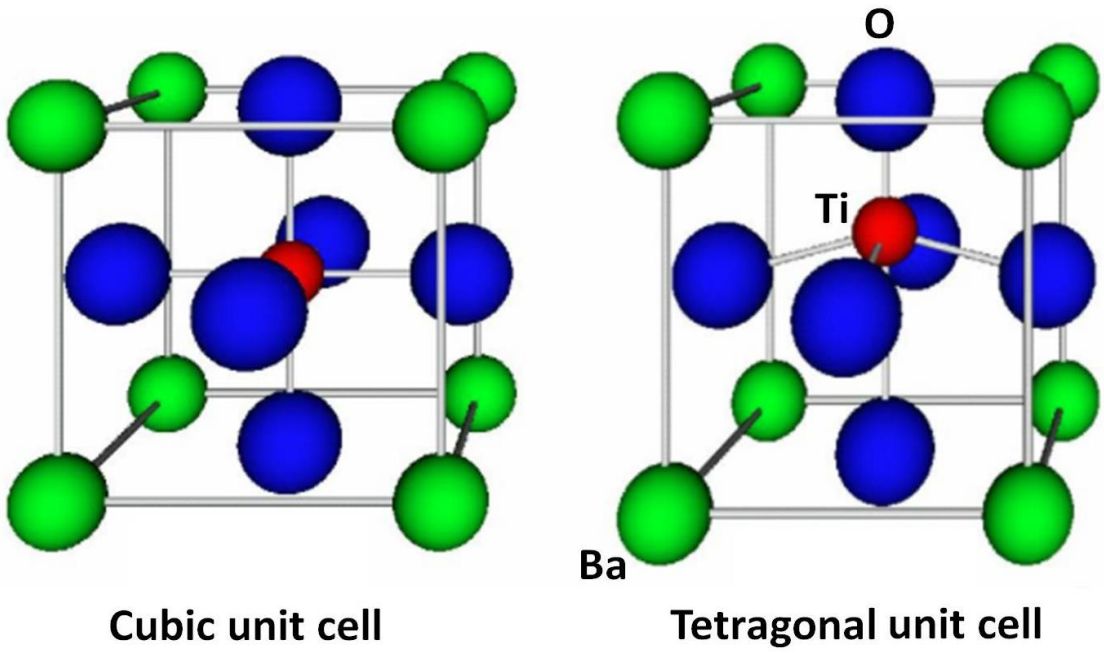

Figure 1.9: $BaTiO_3$ crystalline unit cells. (a) Cubic and (b) Tetragonal

1.4.2.3 Piezoelectric polymers

The piezoelectric polymers are limited such as PVDF and its copolymers, cellulose, collagen, and glycine. These entire polymers have lower piezoelectric coefficient than the inorganic perovskite piezoelectric ceramics, but it has good flexibility and high mechanical stability at larger applied forces.

1.4.2.4 Piezoelectric composites (inorganic nanoparticles/polymer)

The piezoelectric composites with different shapes and thicknesses can be designed by the substitution of piezoelectric ceramic nanoparticles into polymer matrices. It has many advantages than the pure piezoelectric polymers, inorganic perovskite nanoparticles and has a broad range of applications in various industrial sectors as shown in **Figure 1.10**. Moreover, the composite structures reduce the production cost of the functional materials, large-scale synthesis in short time duration and the process is eco-friendly.

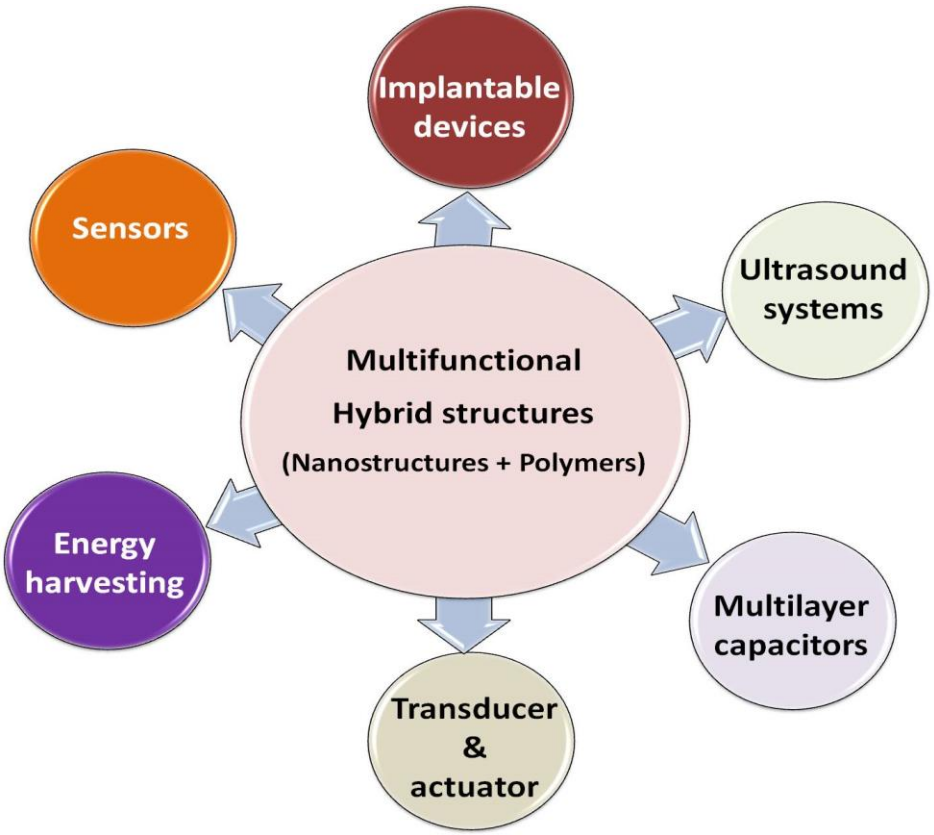

Figure 1.10 Applications of the piezoelectric hybrid structures

1.5 Necessity to develop the Self-powered sensors/systems

Self-powered portable devices and active transducers play key roles at present and will continue to do so in the near future because they can function without any external bias voltage sources or additional processes [16]. Self-powered sensors of pH [17], temperature [18], vibration [19] ethanol [20] micro flow [21], and water motion active transducers [22] have been intensely investigated and successfully implemented. Conventional battery-based sensors have several disadvantages, such as power consumption, large package size, high system cost [23], and risk of environmental pollution resulting in the demand for new, alternative approaches including self-powered technology. The importance of this technology is based on driving a device or sensor by

harvesting energy from piezoelectric [24], triboelectric [25] thermal gradient [26] or solar methods [27].

1.6 Objectives and scope of thesis

The literature reports depict that the energy crisis, consumption of the natural sources for energy generation is an imminent threat to the present and future generation mankind. The existing renewable harvesting technologies contribution is not so high and needs to be improved. Moreover, the present sensor technology and low power consumed electronic devices (LEDs, display devices) depends on the performance of the complex external battery source and few additional circuit components. The conventional battery-based sensors have several disadvantages, such as power consumption, large package size, high system cost, and environmental pollution.

Hence, it is mandatory to investigate the alternating energy harvesting approaches to utilize the abundant waste mechanical energy i.e., biomechanical motions, machine vibrations, ocean waves, fluid/air flow, new techniques for the development of efficient multi-functional nanostructures, synergistic effect of the materials, and innovative device designs to remove the battery use (self-powered sensor technology). In this regard, multiple hybrid structures were developed using the composite-technology by combining the barium titanate (or doped barium titanate) nanostructures into the polymer matrix. For improving the instantaneous power density of the nanogenerators, various piezoelectric nanogenerator models such as planar, wire type, linear worm structure type, wavy-pattern type, spherical beads, hemispherical strip type, butterfly wing structure type designs were tested. The objectives of this thesis work briefly described below:

- To prepare the high crystalline piezoelectric inorganic nanostructures ($BaTiO_3$, $Ba(ZrTi)O_3$, and $(BaCa)TiO_3$-$x$$Ba(SnTi)O_3$) using the molten-salt, solid-state reaction, and hydrothermal techniques.
- To develop the flexible Hybrid piezoelectric structures (PVDF/ $Ba(ZrTi)O_3$, PDMS/ $BaTiO_3$, Ca-alginate/ $BaTiO_3$, PDMS/$(BaCa)TiO_3$-$x$$Ba(SnTi)O_3$ and PVDF/activated carbon) using the ultasonication method followed by solution casting, iontropic gelation approach, and groove techniques.
- To investigate and analyze the crystalline phase analysis, surface morphology and elemental identification of as-prepared samples by the X-ray diffraction (XRD), Raman spectroscopy, Fourier transform Infrared spectroscopy (FT-IR), X-ray photoelectron spectroscopy (XPS), and Field emission scanning electron microscopy (FE-SEM).
- To design the multiple piezoelectric nanogenerators (planar, wire, hemispherical strip, wavy-pattern worm, linear worm structure), hybrid nanogenerators (strip type, arc-shaped, and butterfly multi-unit).
- To observe and analyze the electrical response of the as-fabricated nanogenerator upon the mechanical force (linear motor, electrodynamic shaker, biomechanical hand force) using the electrometers, nanovoltmeter, picoammeter, and low noise-preamplifiers.
- To evaluate nanogenerator performance parameters such as switching polarity test, load resistance analysis, cyclic-frequency dependence, instantaneous power density calculations, charging analysis of capacitors, stability test.
- Finally, to develop and sense/monitor the various self-powered sensors such as UV-sensor, a fluid velocity sensor, pH sensor, flexion sensor, air-pressure sensor, an

acceleration sensor, muscle monitoring and powering the LEDs/electronic display devices.

The results described in this thesis may explore the cost-effective techniques and eco-friendly processes to develop the novel hybrid structure based nanogenerators with high power density. In addition, demonstrate the next-generation self-powered sensors to monitor the physical/optical/chemical stimuli (without using any additional battery source). The arc-shaped hybrid nanogenerator output response explores the synergistic effect and multiplication process of the piezoelectric-triboelectric effects. The described basic approaches for nanogenerators and self-powered sensors in the thesis work can pave the way to develop the flexible/portable smart electronics/sensors in the near future.

1.7 Structure of thesis

The present thesis work mainly describes the three research contents such as

- Cost-effective development of hybrid piezoelectric structures
- Design of effective, flexible nanogenerators to harness the waste mechanical energy (Mechanical vibrations, Biomechanical motions, fluid/air flow)
- Realization and prototype of next-generation self-powered sensors/light emitting diodes/electronic display (removal of external battery source, additional components)

The outline of the thesis classified into eight chapters

Chapter-1 describes the energy crisis, the effect of the traditional energy harvesting technologies on the human life, society and nature, explained about the role renewable or alternative energy approaches, types of nanogenerators, types of piezoelectric materials and its applications in different industrial sectors.

Chapter-2 demonstrates the materials, reagents, and apparatus used in the present thesis work. It gives an insight into the fabrication methods for piezoelectric nanoparticles, hybrid films, and nanogenerators. The structural, surface morphological, elemental identification, spectroscopic studies and polarization measurements were performed and analyzed for the as-prepared samples. Further, it describes the types of piezoelectric nanogenerators, electrical responses analysis of as-fabricated device, and modes of self-powered sensors.

Chapter-3 reports the radial growth of TiO_2, $BaTiO_3$ nanostructures on the flexible human hair-sized metal Ti-wire using the chemical oxidation modification method followed by a hydrothermal technique. The self-powered wire type UV sensor was demonstrated using the parallel connection between the wire type piezoelectric nanogenerator, and wire type UV sensor, respectively.

Chapter-4 describes the two types of planar piezoelectric composites such as PVDF/BTZO-nanocubes, PDMS/BTO-nanocubes using the solution casting technique. The PVDF/BTZO-nanocubes film based nanogenerator electrical response was studied and demonstrated the practical self-powered fluid velocity sensor to monitor the water flow at the tape. The second composite film based nanogenerator was tested under biomechanical force conditions, and the generated electrical output is used to light up the low power consumed light emitting devices.

Chapter-5 emphasizes the ionotropic gelation approach to develop the innovation piezoelectric structures such as spherical beads, linear worms, and wavy-pattern worm structures. All these structures were used to fabricate the nanogenerators such as piezoelectric, triboelectric and hybrid devices to analyze the energy harvesting capability and its usefulness as self-sustaining power sources. Finally, demonstrated the self-powered flexion sensor, electronic display and pH sensor using the beads, linear worm and wavy-pattern worm structure based nanogenerators.

Chapter-6 describes the enhancement of electroactive-β phase of the PVDF polymer by applying the high tip amplitude of the ultrasonicator probe and also the inclusion of the conductive activated carbon particles. The formation mechanism of β-phase PVDF, energy harvesting capability of the composite nanogenerator was investigated and successfully utilized to monitor the various accelerations of the linear motor shaft load.

Chapter-7 reports the innovative, cost-effective groove technique to fabricate the adaptable/flexible hemispherical composite strips. Also developed the flexible energy harvesting glove to harness the biomechanical energy and demonstrated the self-powered muscle monitoring system using the multiple hemispherical composite strip based devices. The second part of this chapter describes the efficient approach to generate the maximum amount of electrical energy by combining the piezoelectric and triboelectric properties in a single composite. Also designed the arc-shaped hybrid nanogenerator and investigated the electrical response by modulating the contact-separation distance between the layers, changing the surface morphology of the composite films. Finally, developed the butterfly wing structure type multi-unit hybrid nanogenerator and tested to monitor the various amounts of air-pressures.

Chapter-8 summarizes the salient features of the present work, suggestions, and directions for the future work.

1.8 References

1. International Energy Outlook 2017 (www.eia.gov/ieo)
2. https://www.conserve-energy-future.com/causes-and-solutions-to-the-global-energy-crisis.php
3. Venkateswaran Vivekananthan, Nagamalleswara Rao Alluri, Yuvasree Purusothaman, Arunkumar Chandrasekhar, and Sang-Jae Kim , Nanoscale, 2017, 9, 15122–15130.
4. Kwi‑Il Park, Chang Kyu Jeong, Na Kyung Kim and Keon Jae Lee, Nano Convergence (2016) 3:12.
5. Geon-Tae Hwang , Myunghwan Byun , Chang Kyu Jeong , and Keon Jae Lee, Adv. Healthcare Mater. 2015, 4, 646–658
6. Caliò, R.; Udaya Bhaskar, R.; Camboni, D.; Milazzo, M.; Stefanini, C.; Petris, G. de.; Maria Oddo, C. *Sensors.* **2014**, 14, 4755-4755.
7. Lefeuvre, E.; Badel, A.; Richard, C.; Petit, L.; Guyomar, D. *Sens Actuators A Phys.* **2006**, 126, 405-416.
8. Weitzel, E. K.; Tasker, R.; Brownell, W. E.; *J. Acoust. Soc. Am.* **2003**, 114, 1462-1466.
9. Lesieutre, G.A.; Ottman, G.K.; Hofmann, H.F. *J. Sound. Vib.* **2004**, 269, 991-1001.
10. Dhakar, L.; Liu, H.; Tay, F.E.H.; Lee, C. *Sens Actuators A Phys.* **2013**, 199, 344-352.
11. Nagamalleswara Rao, A.; Saravanakumar, B.; Kim, S. J. *ACS Appl. Mater. Interfaces*, ***2015***, *7*, 9831-9840.
12. Chen, X.; Xu, S.; Yao, N.; Shi, Y. *Nano Lett*, **2010**, 10, 2133-2137.
13. Zhong Lin Wang, Faraday Discuss, DOI: 10.1039/c4fd00159a
14. Niu, S.; Wang, Z. L. *Nanoenergy*, **2015**, 14, 161-192.

15. P. Dineva et al., Chapter-2, piezoelectric materials, Springer International Publishing Switzerland 2014, DOI: 10.1007/978-3-319-03961-9_2
16. Rui, Z.; Lin, L.; Jing, Q.; Wu, W.; Zhang, Y.; Jiao, Z.; Yan, L.; Han, R. P. S.; Wang, Z. L. Energy Environ. Sci. 2012, 5, 8528−8533.
17. Xu, S.; Qin, Y.; Xu, C.; Wei, Y.; Yang, R.; Wang, Z. L. Nat. Nanotechnol. 2010, 5, 366−373.
18. Yang, Y.; Zhou, Y.; Wu, J. M.; Wang, Z. L. ACS Nano 2012, 6, 8456−8461.
19. Yu, A.; Zhao, Y.; Jiang, P.; Wang, Z. L. Nanotechnology 2013, 24, 055501−055507.
20. Lin, Z. H.; Cheng, G.; Wu, W.; Pradel, K. C.; Wang, Z. L. ACS Nano 2014, 8, 6440−6448.
21. Liu, H.; Zhang, S.; Kathiresan, R.; Kobayashi, T.; Lee, C. Appl. Phys. Lett. 2012, 100, 223905.
22. Kwon, S. H.; Park, J.; Kim, W. K.; Yang, Y. J.; Lee, E.; Han, C. J.; Park, S. Y.; Lee, J.; Kim, Y. S. Energy Environ. Sci. 2014, 7, 3279−3283.
23. St. Clair, D.; Bibo, A.; Sennakesavababu, V. R.; Daqaq, M. F.; Li, G. Appl. Phys. Lett. 2010, 96, 144103.
24. Wang, Z. L.; Song, J. Science 2006, 312, 242−246.
25. Hu, Y.; Yang, J.; Jing, Q.; Niu, S.; Wu, W.; Wang, Z. L. ACS Nano 2013, 7, 10424−10432.
26. Yang, Y.; Guo, W.; Pradel, K. C.; Zhu, G.; Zhou, Y.; Zhang, Y.; Hu, Y.; Lin, L.; Wang, Z. L. NanoLett. 2012, 12, 2833−2838.
27. Yang, J.; You, J.; Chen, C. C.; Hsu, W. C.; Tan, H. R.; Zhang, X. W.; Hong, Z.; Yang, Y. ACS Nano 2011, 5, 6210−6217.

CHAPTER-II

Synthesis, fabrication methods for the piezoelectric nanoparticles, composite films, and characterization techniques

2.1 Reagents and apparatus

The research experiments in the following thesis were conducted using the various chemicals and reagents purchased from the different vendors from South Korea, and Japan. The analytical grades were not changed during the experiments. Below mentioned **Table 2.1** represents the list of chemicals and reagents were used in this research work.

Table 2.1 List of chemicals and reagents were used in this research work

Chemicals	**Formula**	**Purity**	**Vendor**
Titanium wire	Ti	99.5%	The Nilaco Corporation, Japan
Oxalic acid	$C_2H_2O_4$	99.5%	Kanto Chemical Co. Ltd, Japan
Hydrogen peroxide	H_2O_2	30%	Junsei Chemical Co. Ltd, Japan
Titanium (III)chloride	$TiCl_3$	20%	Kanto Chemical Co. Ltd, Japan
Barium hydroxide octahydrate	$Ba(OH)_2.8H_2O$	97%	Daejung Chemicals, Korea
Potassium hydroxide	KOH	85%	Daejung Chemicals, Korea
Barium carbonate	$BaCO_3$	99.95%	High Purity Chemicals, Japan
Titanium dioxide	TiO_2	98%	Daejung Chemicals, Korea
Zirconium oxide	ZrO_2	99%	High Purity Chemicals, Japan
Potassium chloride	KCl	99%	Daejung Chemicals, Korea
Sodium chloride	NaCl	99.5%	Daejung Chemicals, Korea
Sodium sulfate	Na_2SO_4	99%	Daejung Chemicals, Korea

Poly(vinylidene fluoride)	$-(C_2H_2F_2)_n-$	-	Sigma Aldrich, Korea
N, N-Dimethylformamide	C_3H_7NO	99.8%	Daejung Chemicals, Korea
Acetone	C_3H_6O	99.8%	Fisher Scientific Korea Ltd
Ethanol	C_6H_6O	99.5%	Daejung Chemicals, Korea
Alginic acid sodium salt			Sigma Aldrich, Korea
Calcium chloride	$CaCl_2$	93%	Daejung Chemicals, Korea
Polydimethylsiloxane	$(C_6H_6OSi)_n$	-	Dow Corning Corporation
Activated Carbon powder	-	-	Daejung Chemicals, Korea
Tin dioxide	SnO_2	99.99%	Sigma–Aldrich
Calcium carbonate	$CaCO_3$	99.99%	High purity chemicals Ltd. Japan)

The apparatus used to synthesize the piezoelectric nanomaterials, fabrication of hybrid films and the instruments used to characterize the electrical response of nanogenerator were given in Table 2.2.

Table 2.2 List of apparatus and instruments used in this research work

Apparatus	**Specification/model**	**Company**
Spin Coater	SPIN 1200	Midas System
Tubular furnace	-	Korea Furnace Development Co.Ltd.
Ultrasonicator	SONIC VCX 500 model (20 kHz, 500 W)	Sonics & Materials Inc.
Muffle furnace	CRF-M15	Ceber
Balance	AUW220D	Shimadzu
Ultrasonic cleaner	Elmasonic S15H	Elmasonic

Centrifuge	Gyrozen 1580 MG	Gyrozen
Oven	OF-02-GW	JIEO Tech
Autoclave	PTFE container	Latech
Hot plate & magnetic stirrer	MS300HS	M TOPS
Microwave	MW 202BG	LG
Multimeter	73303	Yokogawa, Japan
linear motor system	LinMot-HF01-37	LinMot
Semiconductor parameter analyzer	Agilent-B1500A	Agilent
light sources	365 nm, 405 nm & 535 nm	Prizmatix Ltd.
Electrometers	6514	Keithley
Picoammeter (Keithley)	6584	Keithley
Nanovolmeter	2182A	Keithley
Electrodynamic shaker	ET–126	LabWorks Inc.
Power Amplifier	Pa-138	LabWorks Inc.
Sweep function generator	FG-1880B	ED corporation
Bending Tester	JIBT-200	JUNIL-TECH
Low-noise current preamplifier	SR-570	Stanford Research Systems
Low-noise voltage preamplifier	SR-560	Stanford Research Systems
Hysterisis loop tester	Precision LC-II	Radiant Technologies, Inc.
Mixed Domain	MDO3034	Tektronix

Oscilloscope		
Thermal Evaporator	JEE-4X	JEOL
DC Electrical poling Unit	-	-
Breadboard	EIC-104	EIC
Regulated DC power supply	E49-79	NISTAC

2.2 Synthesis of perovskite piezoelectric nanomaterials

The perovskite (ABO_3) piezoelectric nanostructures such as nanocubes, nanoparticles, and nanorods were synthesized using various simple, cost-effective approaches, which are described below.

2.2.1 Solid state reaction synthesis

The most widely accepted method to prepare the large-scale production of perovskite (ABO_3) polycrystalline nanomaterials is the solid state reaction method. It can also be used to prepare the sulfides, nitrides, and aluminosilicates. This method offers the high elevated temperatures for making the better diffusion and reaction between the reactants, leads to forming the high crystalline product. Kinetic parameters and thermodynamic coefficients play a key role in this process. The process is eco-friendly, non-toxic and the obtained product is highly stable. For example, The solid-state reaction process to synthesize the $BaTiO_3$ nanoparticles (fired at **1200 °C for 2 h**) using the initial raw materials such as barium carbonate and titanium dioxide given below:

$$BaCO_3+TiO_2 \rightarrow BaTiO_3+CO_2$$

2.2.2 Molten salt synthesis

It is a slight modification of the solid-state reaction or powder metallurgical process. Here, the molten salts (chlorides and sulfates) having low melting temperature uses as a medium to synthesize the final ceramic products from the initial precursors such as oxides and carbonates [1, 2]. A typical molten salt-process for the ceramic powder is shown in **Figure 2.1.** The final product powder characteristics such as shape, size depends on the type of salts, amount of quantity, processing temperature, and duration of heat. The use of molten-salts has many advantages such as 1) decreasing the processing temperature and increasing the reaction rate 2) controlling the agglomeration and increasing the degree of homogeneity 3) shape and size control

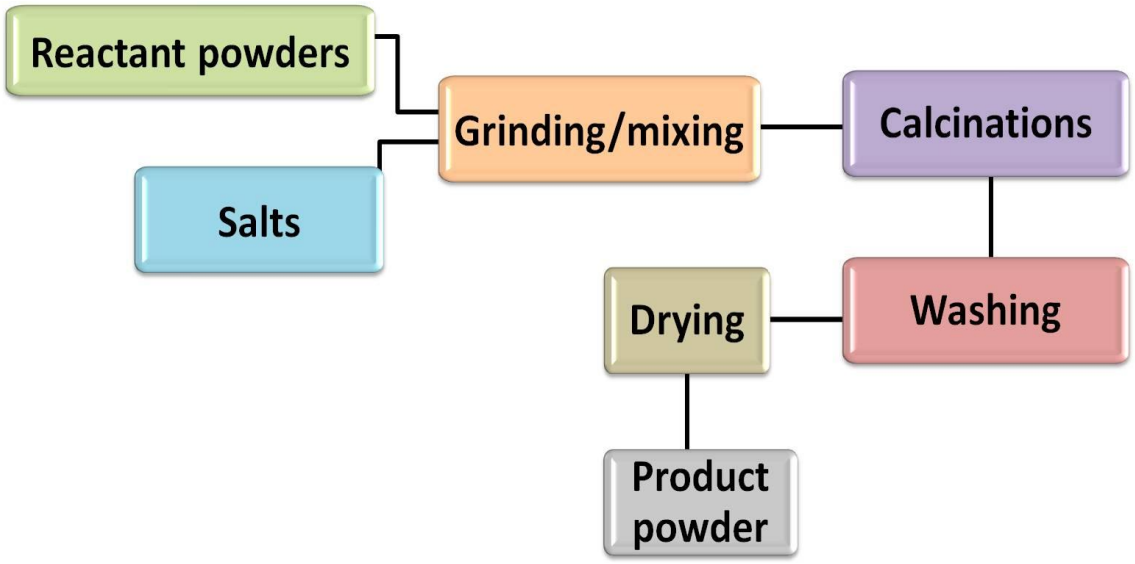

Figure 2.1 Schematic of the molten-salt process to prepare the ceramic powders.

2.2.3 Hydrothermal synthesis

In recent days, the use of the hydrothermal process for developing the single crystal growth, inorganic nanoparticles under the mild conditions (temperature ≤350 °C, pressure≤100 MPa) attracted great attention. The hydrothermal reaction can be possible takes place in combined

mediums such as aqueous and solvent-based mixed systems. It conducted in a closed environment with a controlled pressure of the solution at the specified temperature and composition of the hydrothermal solution [3]. The process offers many advantages over the traditional ceramic methods such as 1) all possible shapes of ceramics [powders, fibers, single crystals, coatings on flexible/non-flexible metals/polymers/ceramics, and monolithic ceramic bodies] 2) homogeneous nucleation, growth and aging possible to control the shape of the product 3) improving the purity of the product compared to the stating purity of the raw materials 4) Highly reproducible 5) low cost and large-scale production.

2.3 Fabrication methods for hybrid (or composite) solutions and films

2.3.1 Ultrasonication method

The ultrasonication process utilizes the sound energy to disperse, polymerize, and to prepare the nanomaterials such as oxides, conductive metals, and chalcogenides [4]. Acoustic cavitation is the key process to attain the required sonochemical effects (reaction speed, efficient use of energy, phase conversion, and activation) in the liquid medium. The micro-tip amplitude, frequency, and applied power, controlling the generated heat during the process by cold bath and reaction time are typical parameters to achieve the better sonochemical process. In the present work, the sonochemical process or ultrasonication method used to polymerize the polyvinylidene fluoride (PVDF) powder (α-phase) using the N, N dimethylformamide (DMF)/acetone medium to achieve the electroactive β-phase of the transparent PVDF solution. Further, homogeneous dispersion of the ABO_3 inorganic nanoparticles into PVDF polymer was obtained by the ultrasonication process.

2.3.2 Polymer solution casting method

The solution casting process has many advantages over the conventional or traditional processes such as cost-effective, large-production of volume, incorporating the broad range of the nanoparticles into the pure polymer solution and thickness/shape control. The polymer solution casting method has three major components such as

1. Homogeneous polymerized solution
2. The mold should be clean and have reasonable surface adhesion capability
3. Proper viscosity of the polymer or composite (solid nanoparticles content should be less) solution

2.3.3 Ionotropic gelation method

Multiple forms of functional composite structures such as hydrogels (or spherical beads), linear worms and wavy pattern worms were possible to fabricate using the cost-effective, eco-friendly ionotropic gelation (IG) method. Generally, this method widely used in pharmaceutical industry to prepare the gel spheres, drug delivery systems. For the first time, we introduced this method to prepare the energy harvesting piezoelectric composite beads, linear worms and wavy pattern worms. This method contains three key steps:

1) Homogeneous polymer solution (particularly alginate, collagen, fibrin, gelatin, etc.)
2) Gelation process using the multivalent cations to prepare the green hydrogels or other forms of structures. The cations diffuse into the polymeric molecular chains, forming a three-dimensional lattice of the ionically crosslinked moiety.
3) Washing/drying at optimized conditions (temperature, humidity, and pressure)

For example, Piezoelectric hybrid beads ($BaTiO_3$ nanoparticles/Ca-alginate) were developed using the IG technique as shown in Figure 2.2.

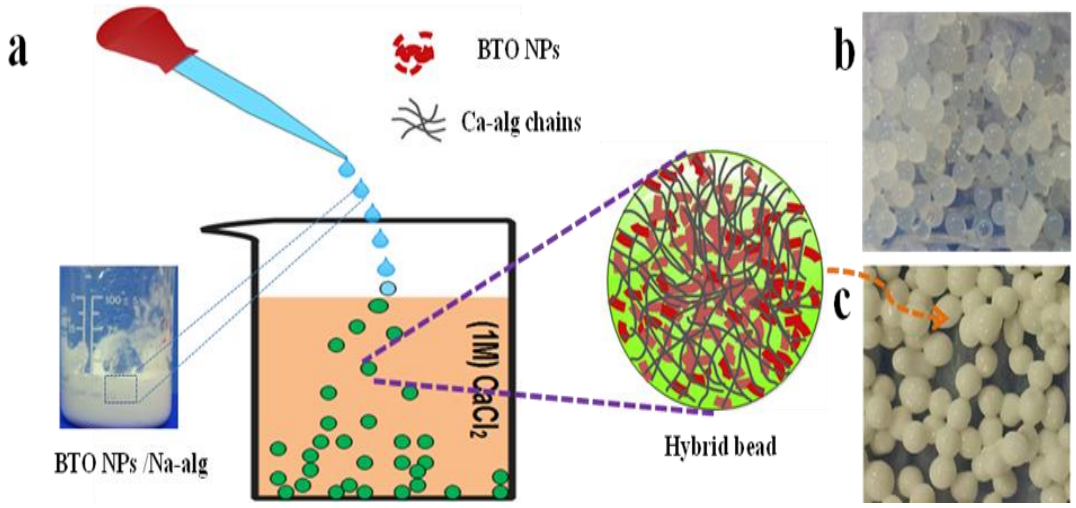

Figure 2.2 Fabrication of pure and piezoelectric hybrid beads using the ionotropic gelation (IG) method. **(a)** Schematic representation of hybrid beads fabricated using a 1 M $CaCl_2$ solution. **(b, c)** Optical photographs of the pure and hybrid beads.

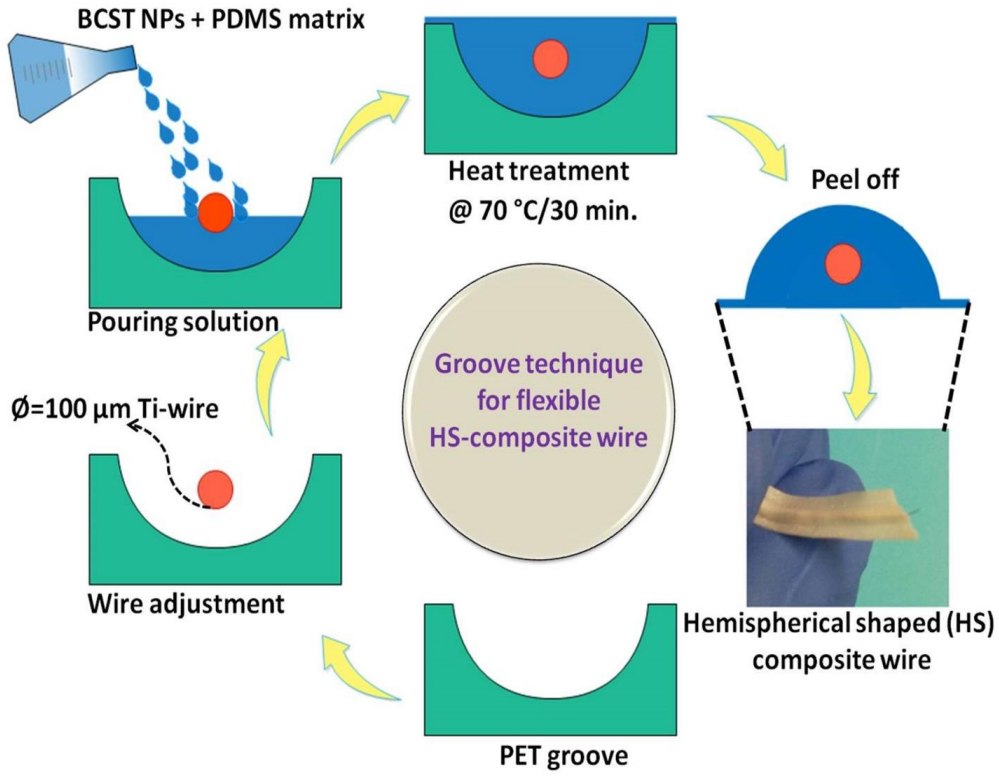

Figure 2.3 Schematic representation of groove technique for the fabrication of hemispherical composite strips and the inset shows a digital photograph of as-fabricated single hemispherical composite strips.

2.3.4 Groove technique

The cost-effective groove technique has been proposed (or invented) for the fabrication of adaptable/flexible composite strips. This method is a slight modification of the simple solution casting technique. The fabrication procedure consists of five major steps:

(1) Generation of pre-defined hemispherical groove shape on flat thick plastic/metal sheet by the removal of required part from the surface

(2) Placing the metal wire or any thread exactly at the center of the groove by the support of rigid stands. This metal wire has a dual purpose, one it will act as an inner electrode and second is supporting wire to retain the formed hemispherical shape without any defects

(3) Pouring the limited amount of as-prepared composite solution into that groove.

(4) Heat treatment of as-poured composite solution along with the groove at certain time duration for achieving good solidification (or solid hemispherical composite solution)

(5) As-obtained product peel off from the surface called as composite strips

For example The fabrication of hemispherical composite strips ($0.3Ba_{0.7}Ca_{0.3}TiO_3$-$0.7BaSn_{0.12}Ti_{0.88}O_3$ nanoparticles/PDMS polymer) using the groove technique as shown in Figure 2.3.

2.4 Materials characterization

The crystalline phase purity, surface morphology, atomic vibration modes, elemental identification, surface states and polarization information of as-prepared nanoparticles were analyzed using the various quantitative measurement instruments. Some of the major instruments and its technical principle were given below.

2.4.1 X-ray diffraction technique

It is the most widely accepted and non-destructive analytical technique for the identification/quantification of various crystalline phases of materials. According to Bragg's law, the x-ray patterns of the crystal are obtained by the reflected X-ray peaks off each atomic plane in the crystal. The phase formation of as-synthesized nanostructures was obtained with an X-ray diffractometer (XRD, Rigaku), operated at 40 kV and current 40 mA patterns recorded using Cu-Kα radiation (2θ range from 20° to 50°) at room temperature as shown in Figure 2.4.

Figure 2.4 Rigaku X-ray diffractometer

2.4.2 Raman spectroscopy

The Raman studies are sensitive towards the crystallization, structural disorders, and defects in nanostructures. Therefore, Raman-scattering studies have been performed for the as-synthesized resultant materials. Further, it is also used to study the bonding nature of various carbon materials such as graphene, graphene oxide, and carbon nanotubes. Raman spectra of the samples were studied using a LabRam HR800 micro Raman spectroscopy (Horiba Jobin-Yvon,

France) as shown Figure . The Raman system was operated at a laser power of 10 mW and an excitation wavelength of 514 nm with an Ar+ ion laser. The data were collected using a 10-s data point acquisition time in the spectral region of 100–3500 cm^{-1}.

Figure 2.5 LabRam HR800 micro Raman spectroscope instrument (Horiba Jobin-Yvon, France).

2.4.3 Fourier transforms infrared spectroscopy

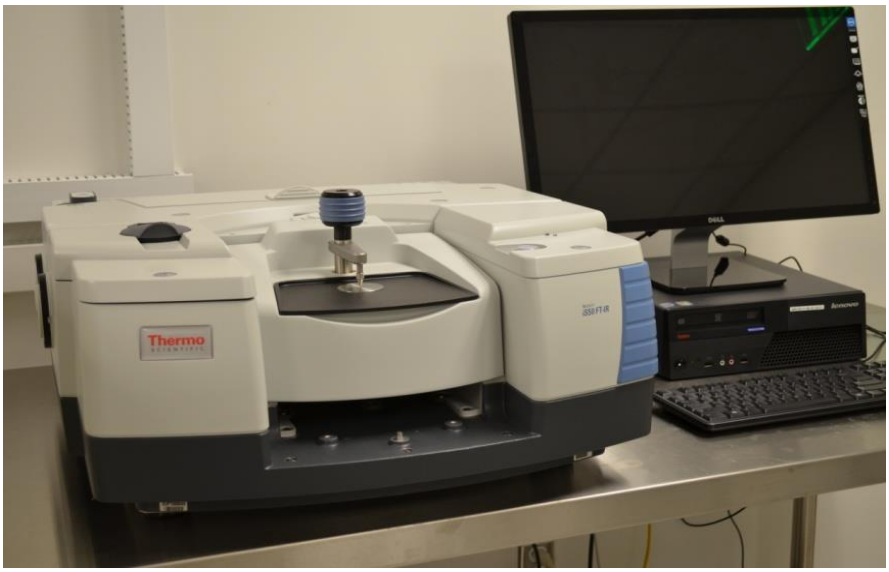

Figure 2.6 FT-IR spectrometer from Thermo Scientific Systems (Nicolet-6700).

FT-IR spectroscopy is an important technique for the direct monitoring of interaction between adsorbed molecules and the material. FT-IR spectra were measured at room temperature with an FT-IR spectrometer (Thermo Scientific Systems, Nicolet-6700) using the KBr pellet technique in the range of 4000 to 400 cm-1 as shown in Figure 2.6.

2.4.4 Field-emission scanning electron microscopy

The surface morphology and particle size of the prepared materials were studied by the field emission scanning electron microscope (FE-SEM, Zeiss Supra-55vp) with an acceleration voltage of 5 kV and a filament current of 10 μA. Before measurement, the as-prepared samples were fixed onto a double-face conducted tape mounted on a metal stud and coated with platinum with a sputter coater (Cressing ton sputter coater -108 auto).

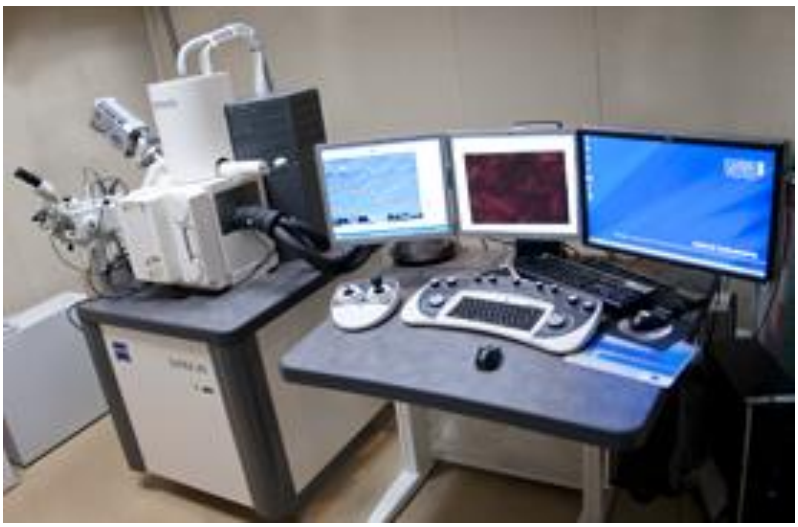

Figure 2.7 Field emission scanning electron microscope (Zeiss Supra-55vp)

2.4.5 Energy dispersive X-ray spectroscopy

The elemental composition of the prepared samples was measured using Energy Dispersive X-ray Spectroscopy (EDS). The EDS analysis was done with the Field Emission Scanning

Electron Microscopy (FE-SEM) instrument (Zeiss ultra FE-SEM instruments) with a separate EDS detector (INCA) connected to that instrument.

2.4.6 X-ray photoelectron spectroscopy

The chemical composition and the state of elements present in the outermost part of samples were obtained by X-ray photoelectron spectroscopy (XPS) techniques using ESCA- 2000, VG Microtech Ltd and Theta Probe AR-XPS system (Thermo Fisher Scientific, U.K). Here a monochromatic X-ray beam source at 1486.6 eV (Aluminum anode) and 14 kV was used to scan the sample surface. A high flux X-ray source with Aluminum anode was used for X-ray generation, and a quartz crystal monochromatic was used to focus and scan the X-ray beam on the sample.

2.4.7 Ferroelectric hysteresis (P-E) loop

Figure 2.8 Ferroelectric hysteresis loop measurement unit (Precision LC-II)

The spontaneous electric polarization, coercive field, remnant polarization of as-prepared piezoelectric samples was measured using the ferroelectric loop tester (Precision LC-II) from the Radiant Technologies, Inc as shown in Figure 2.8. The measurement voltage range of the loop tester with an external amplifier is ±10 KV having internal fatigue frequency is 5 kHz. The hysteresis loop information of the as-prepared sample was obtained using the computer controlled software, i.e., vision data Acquisition and management system.

2.5 Fabrication & measurement unit of nanogenerator

2.5.1 Fabrication piezoelectric nanogenerators

Over the last decade, continuous progress happens to improve the device design and performance valuation of the piezoelectric nanogenerator (PNG) using the various nanostructures, flexible polymers and composite films (inorganic/polymer). The output power density of the PNG improved from the $\mu W/m^2$ to mW/m^2. The most commonly applicable device design is the planar type and later extended to flexible wire/fiber, hemispherical strip type PNGs. The fabrication of any type of PNG consists of four important layers named as: active piezoelectric layer, top/bottom electrodes, and packaging layer. Sometimes, additional protective polymer layer will appear in the devices to prevent the short circuit connection between the top/bottom electrodes and also provide the mechanical stability of the as-grown piezoelectric nanostructures. Here, the packaging layer controls the external interference of the PNG from the environment such as humidity, high temperature and protect from the external physical damage of PNG [5, 6].

The active piezoelectric layer generates the stress-induced charge carriers across the top/bottom surface of the film upon applied mechanical force, and top/bottom electrodes collect the accumulated charge carriers via inductive charge transport process. The fabrication process of the planar and wire/strip type PNG demonstrated in **Figure 2.9**. The active piezoelectric layer

is sand-witched between the top/bottom electrodes using deposition, casting techniques. Two external copper wires were attached to top/bottom of the electrodes to collect the accumulated charge carriers. Finally, the whole device has been covered with a flexible insulating packaging layer (for example PDMS). The packed device has been subjected to the external electrical poling process, to improve the permanent polarization of the piezoelectric material via electrically stress-induced effects.

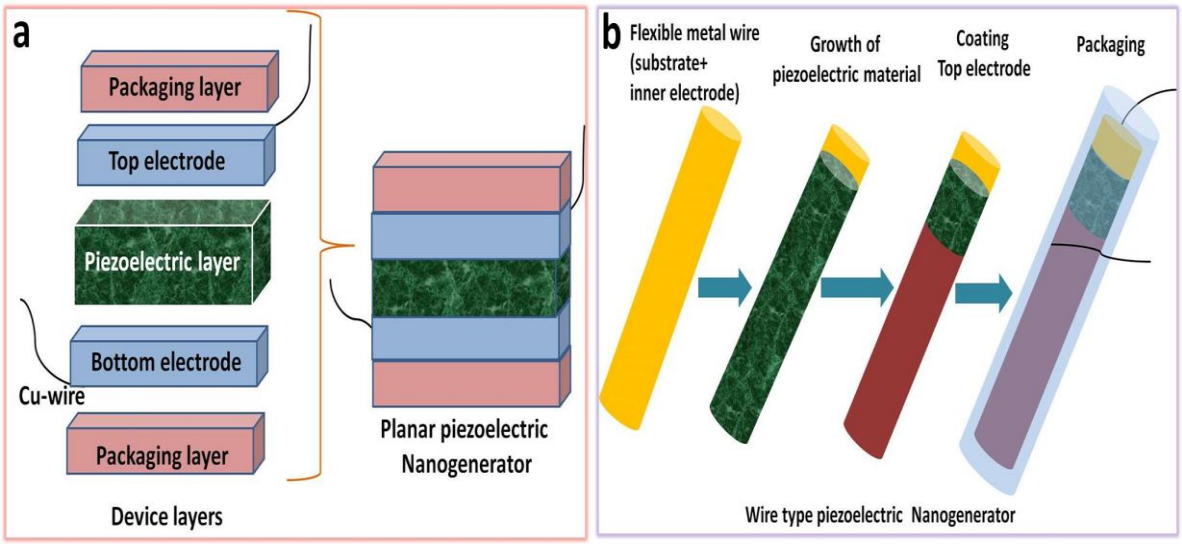

Figure 2.9 Schematic for the fabrication of piezoelectric nanogenerators. **(a)** Planar piezoelectric nanogenerator **(b)** Wire type piezoelectric nanogenerator

2.5.2 Nanogenerator testing and characterization

The cyclic frequency and force-dependent piezoelectric potential response, switching polarity test, stability, load resistance analysis, instantaneous power density calculations of as-fabricated piezoelectric nanogenerator (PNG) were obtained using the nanogenerator workstation as shown in **Figure 2.10.** It consists of the electrometers (or nanovoltmeters) to measure the generated open circuit voltage (V_{OC}), short circuit current (I_{SC}), various mechanical forces generated from the linear motor, electrodynamic shaker, low noise current/voltage preamplifiers to reduce the noise in the PNG output and the display computer to observe the generated output continuously.

The obtained PNG electrical output is used to charge the commercial capacitors and calculated the stored energy. The nanogenerator measurement unit and working bench should be properly grounded while obtaining the electrical response of the nanogenerator. The important electrical output parameters of PNG device upon mechanical load were explained in a detailed manner.

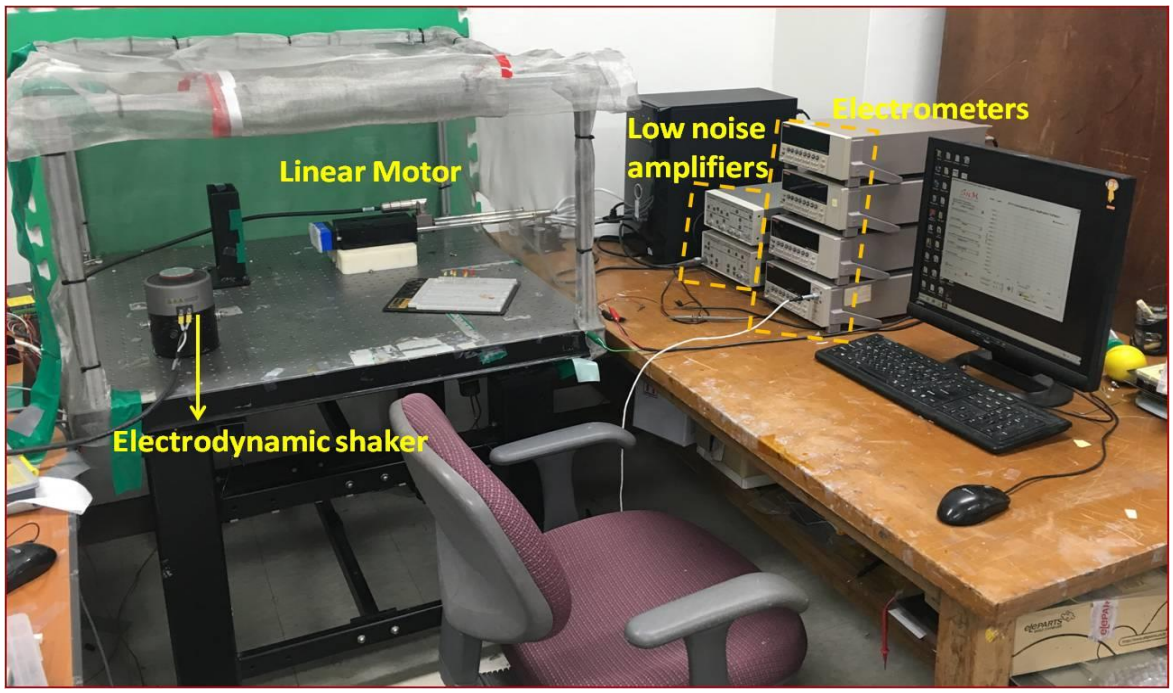

Figure 2.10 Nanogenerator workstation

2.6 Modes of self-powered sensor/systems

2.6.1 External and internal modes

The goal of nanotechnology is to build self-powered nanosystems that exhibit ultrasmall size, super sensitivity, extraordinary multi-functionality and extremely low power consumption. As a result, the energy harvested from the environment may be sufficient to power the system. **Figure 2.11** demonstrates the possible schematic view of the self-powered sensors/systems. The self-powered sensor using the external integration requires the additional charging circuits, active switch network and full wave bridge rectifiers. But in the second mode (Figure 2.11b) does not

require any additional components and harvested energy from the environment directly utilized with respect to the applied input stimuli [7, 8].

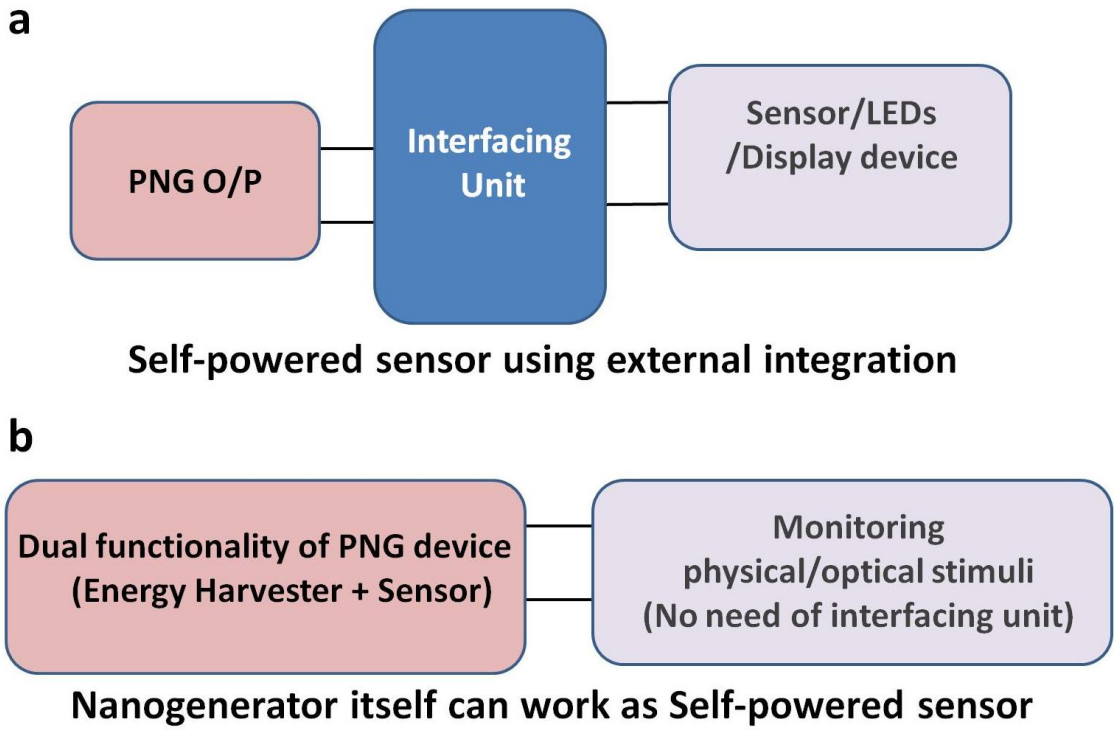

Figure 2.11 Schematic of the self-powered sensor modes **(a)** External integration using the interfacing unit components **(b)** Internal integration (i.e., PNG device itself can work as sensor+ energy harvester)

2.7 References

(1) Toshio Kimura, Molten Salt Synthesis of Ceramic Powders, published by INTECH

(2) Xiaofeng Liu, Nina Fechler and Markus Antonietti, Salt melt synthesis of ceramics, semiconductors and carbon nanostructures, Chem. Soc. Rev., 2013, **42**, 8237.

(3) Wojciech L. Suchanek and Richard E. Riman, Hydrothermal Synthesis of Advanced Ceramic Powders, Advances in Science and Technology Vol. 45 (2006), 184-193.

(4) Suslick, K.S. (1988): Kirk-Othmer Encyclopedia of Chemical Technology; 4th Ed. J. Wiley & sons: New York, 1998, Vol.26, 517-541.

(5) Nagamalleswara Rao, A.; Saravanakumar, B.; Kim, S. J. Flexible, Hybrid Piezoelectric Film ($BaTi_{(1-x)}Zr_xO_3$)/PVDF Nanogenerator as a Self-Powered Fluid Velocity Sensor. *ACS Appl. Mater. Interfaces, **2015**, 7,* 9831-9840.

(6) Chen, X.; Xu, S.; Yao, N.; Shi, Y. 1.6 V Nanogenerator for Mechanical Energy Harvesting Using PZT Nanofibers. Nano Lett, **2010**, 10, 2133-2137.

(7) Wang, Z. L. Self-Powered Nanosensors and Nanosystems. Adv.Mater. 2012, 24, 280−285.

(8) Xu, S.; Qin, Y.; Xu, C.; Wei, Y.; Yang, R.; Wang, Z. L. Self-Powered Nanowire Devices. Nat. Nanotechnol. 2010, 5, 366−373.

Chapter III

Self-powered Wire type UV Sensor using piezoelectric $BaTiO_3$ and Semiconducting TiO_2 Nanostructures on Ti-Metal Wire

Highlights

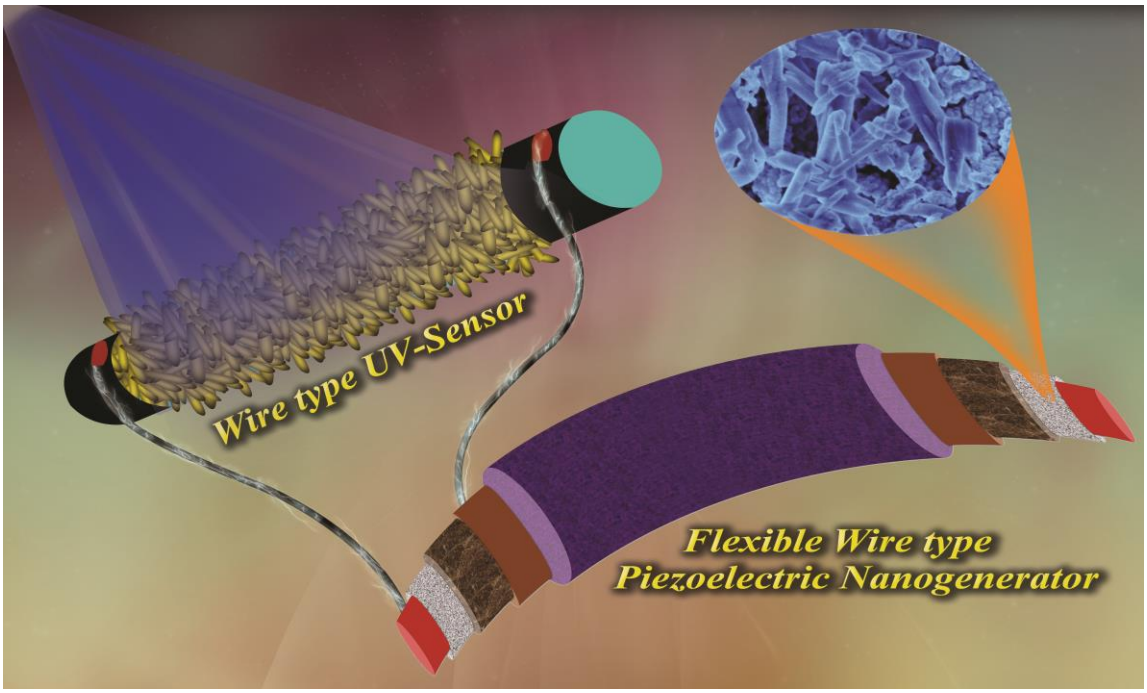

- A flexible human hair sized [(Ø) ≈100 μm, (*L*) ≤6 cm] Ti-wire/$BaTiO_3$ core-shell nanostructures was developed by COM method followed by a hydrothermal technique.
- Photo-responsive performance investigated by fabricating the TiO_2 NSs/Ti wire based UV sensors as a function of fixed bias voltages (±1 V and ±7 V) under various light sources having wavelengths.
- Flexible wire type piezoelectric nanogenerator was fabricated to harness the mechanical energy, biomechanical motions into useful electrical energy.
- Realized self-powered wire type UV sensor by the parallel connection between piezoelectric nanogenerator and TW-UV sensor.

3.1 Introduction

The growth of nano-sized inorganic perovskite and semiconductor materials on various types of substrates (flexible, non-flexible) receiving great attention due to its wide application utility in energy harvesting [1, 2], electronic [3], bio-medical [4], and textile [5-7] industries. Tuning the functional properties of nano-sized materials will depend on the type of growth process conditions, chemical composition, surface morphology, the thickness of film and type of substrates used for the growth. Among these, growth process and type of substrates will play a key role to achieve desirable functionalities like enhanced functional properties, flexibility/wearability and cost-effectiveness for accomplishing real-time device applications such as sensors, energy harvesting devices, and security systems. Numerous techniques reported for the growth of high crystalline perovskite piezoelectric/ferroelectric materials. Pulsed laser deposition (PLD) [2], radio frequency magnetic sputtering (MS) [1], hydrothermal [3], metal-organic chemical vapor deposition (MOCVD) [8], and sol-gel (SG) [9] methods are widely reported. But MOCVD, MS, and SG techniques offer high processing temperature (≥ 650 °C) or high deposition rate for achieving high-quality crystalline materials with desirable functional properties. In contrast, PLD technique generates more stoichiometric perovskite films and quality of films depends on the laser source, gas pressure, the applied frequency of laser pulses and processing temperature [2]. Recently, the hydrothermal process gets more attention and well reported for the growth of piezoelectric/ferroelectric films, because of cost-effectiveness, eco-friendly nature, low processing temperature and nanomaterials shape controlling and suitable to use organically printed circuit boards during the synthesis process. Many researchers investigated the growth and functional properties of nanostructured materials on non-flexible substrates are $SrTiO_3$ [10, 11], MgO [12], glass [3], $LaAlO_3$ [13], and flexible substrates are

Ni/Cr metal foil [14], Ti/Al/Kapton [15], indium tin oxide/polyethylene terephthalate (ITO/PET) [16, 17], silicon [18] and carbon fiber [19], respectively.

Zheng et al. [11] investigated the deposition of $BaTiO_3$ (BTO)-$CoFe_2O_4$ (CFO) thin films on $SrTiO_3$ substrates under various temperature conditions with dynamic pressure ≈100 m Torr using pulsed laser deposition (PLD) method. Aneesh et al. [3] developed BTO nanowires based accelerometer sensor by transferring grown BTO nanowires on to a borosilicate glass substrate along with silver electrodes. Linglong et al. [13] studied the memristive switching behavior of $NaNbO_3$-Nb_2O_5 composite thin films deposited on $LaAlO_3$ substrate [(001) orientation] with $SrRuO_3$ buffer layer by PLD technique. Anuj et al. [2] designed columnar growth of $(PbZrTi)O_3$ (PZT) films having (100) orientation on the nanosheet-buffered glass substrate *via* PLD method and studied the piezoelectric response behavior. Young et al. [14] investigated the growth of flexible PZT film on a flexible Ni-Cr metal foil substrate with a conductive $LaNiO_3$ bottom electrode. They also stated that as-fabricated flexible PZT films have high piezoelectric and pyroelectric coefficients at room temperature. Ru et al. [15] fabricated BTO films on flexible Ti-Al covered Kapton substrate using hydrothermal synthesis and investigated the piezoelectric response by piezoresponse force microscopy. Similarly, Minbaek et al. [19] designed radial growth of ZnO nanowires on a flexible gold-coated carbon fiber using hydrothermal synthesis and energy harvesting performances were studied. The literature reports suggest that growth or deposition of high-performance ABO_3 perovskite nanostructures (NSs) on planar type flexible/non-flexible substrates was investigated and well reported. But it is highly desirable and essential to explore the growth of ABO_3 piezoelectric NSs on flexible non-planar structures (cylindrical surfaces), i.e., human hair-sized single metal wires/carbon fibers. This type of substrates and growth will reduce the active device area with excellent performance, increasing

portability/wearability, and potential to develop the micro/nanoelectronic devices onto contour (non-planar) mechanical structures. Moreover, ABO_3 NSs/cylindrical flexible substrates highly suitable for various fields such as wearable energy harvesters, self-powered sensors, implantable biomedical devices and security systems.

In this section, demonstrated the first time use of human hair-sized flexible metal Ti-wire (*Ø* ≈100 μm, *L* ≤6 cm) as a substrate for the growth of high performance lead-free piezoelectric nanomaterial (i.e., BTO) for alternative energy harvesting applications, i.e., conversion of waste biomechanical energy into useful electrical energy. The radial growth of BTO NSs onto a flexible Ti-wire was realized using the cost-effective chemical oxidation-modification (COM) technique followed by a low-temperature hydrothermal process. Initially, various TiO_2 NSs such as nanoneedles and nanoparticles were grown radially onto Ti-wires having *L* ≈6 cm and different *Ø* ≈800 μm and 100 μm, respectively. As-fabricated metal (Ag)-semiconductor (TiO_2 wires)-metal (Ag) devices tested under various light sources with multiple wavelengths such as 365 nm, 405 nm and 535 nm with different light intensities. Among them, TiO_2 NSs/Ti wire (*Ø* ≈800 μm) based UV sensor (TW-UV sensor) has good responsivity under low bias voltage compared to TW-UV sensor (*Ø* ≈100 μm) based UV sensor. In contrast, the TiO_2 NSs/Ti wire (*Ø* ≈800 μm) has been lost the flexibility and not suitable for flexible electronic applications. It may be due to the permanent loss of tensile strength and other mechanical properties of Ti-wire during the high thermal oxidation temperature. Further, flexible TiO_2 NSs/Ti wire (*Ø* ≈100 μm) used for the radial growth of BTO NSs by the hydrothermal temperature at 180 °C for 24 h. Raman analysis confirms that TiO_2 is in anatase phase, BTO NSs are in tetragonal phase, and XPS analysis proves the existence of Ti2p, Ba3d, Ba4p, Ba4d, and O1s elements. The piezoelectric behavior of BTO wire obtained by the electrical responses from the flexible wire

based piezoelectric nanogenerator (FW-PNG) upon periodic mechanical force. For real-time utility, demonstrated the possibility of self-powered wire based UV sensor (SPW-UV sensor) using the parallel connection between FW-PNG device and TW-UV sensor under various light intensities (18, 40 and 60 mW/cm^2) of the light source (365 nm).

3.2 Experimental Method

3.2.1 Radial growth of TiO_2 and BTO nanostructures on flexible Ti-wire

The growth of BTO NSs on flexible Ti wire contains two crucial processing steps: one is the growth of TiO_2 NSs on the outer surface of Ti-wire using COM method and second is the conversion of TiO_2 NSs into BTO NSs using the low-temperature hydrothermal technique. Commercially purchased flexible Ti-wire substrate (The Nilaco Corporation, Japan) with different diameters (*Ø*) such as 100 μm, 800 μm having multiple lengths was taken and pickled into 5 wt % oxalic acid (Kanto Chemical Co. Ltd, Japan) solution at a temperature of 100 °C for 2 hr. Pickled Ti-wire [(*Ø)* ≈100 μm] was cleaned using the deionized (DI) water for 10 minutes and then dried into air atmosphere. Next, the pickled Ti-wire dipped into 20 wt % hydrogen peroxide (H_2O_2) (Junsei Chemical Co. Ltd, Japan) solution with the closed container and soaked at 80 °C for 24 hr. After that, DI water used to clean the pickled Ti-wire and then dried into air atmosphere. The growth of TiO2 NSs were examined in two approaches such as 1) the direct heat treatment (at 500 ^oC for 2 h) of H_2O_2 treated Ti-wires as shown in **Figure 3.1.1** and 2) Treated Ti-wire has been placed into 0.2 wt % titanium (III) chloride ($TiCl_3$) (Kanto Chemical Co. Ltd, Japan) transparent solution, soaked at temperature 80 °C for two hours and then cleaned using DI water for 10 minutes/dried into air atmosphere. Finally, chemically treated Ti-wire placed into the extended aluminum boat and soaked at 500 °C for two hours under air atmosphere using the open tubular furnace as shown in Figure 31.1.b.

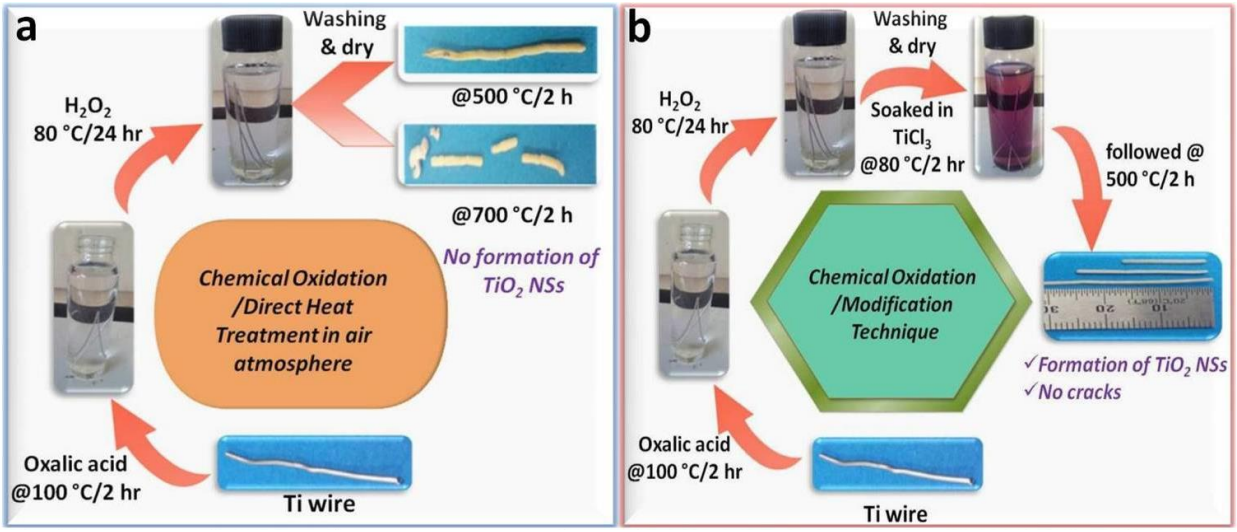

Figure 3.1.1 Radial growth process of TiO_2 NSs on Ti-wire: (a) Digital photographs represent the growth process of TiO_2 NSs on Ti-wire (Ø ≈800 μm) using chemical oxidation method followed by direct heat treatment at 500 °C and 700 °C for two hours. In both cases, no formation of TiO_2 NSs on Ti-wire and the obtained wires have non-conducting in nature with multiple cracks on the top surface of the wire. **(b)** Digital photographs represent the growth process of TiO_2 NSs on Ti-wire (800 μm) using COM technique followed at 500 °C for two hours. In this case, the formation of TiO_2 NSs on Ti-core without any multiple cracks observed.

The as-developed flexible core-shell wire (Ti/TiO_2 NSs) is used for the growth of BTO NSs by the hydrothermal technique and the corresponding schematic shown in **Figure 3.1.2**. The hydrothermal solutions prepared by the 0.1 M of barium hydroxide octahydrate ($Ba(OH)_2.8H_2O$) (Daejung Chemicals, Korea) and 0.6 an M potassium hydroxide (KOH) (Daejung Chemicals, Korea) using boiled DI water under continuous stirring. An as-prepared solution (50 ml) poured into Teflon vessel, and as-grown TiO_2 NSs/Ti flexible wire submersed entirely with the solution. Further, filled Teflon vessel tightly sealed using stainless steel autoclave and kept at a temperature of 180 °C for 24 h. After complete reaction, flexible BTO NSs/Ti wire (Ø ≈100 μm) washed several times using DI water for the removal of unwanted carbonate contents and then dried in an air atmosphere.

Figure 3.1.2 Schematic for the conversion of TiO_2 NSs into BTO NSs on flexible Ti-wire (*Ø* ≈100 µm) using the low-temperature hydrothermal technique.

3.2.2 Fabrication of TiO_2/Ti wire (TW)-UV sensor & Flexible wire BTO piezoelectric nanogenerator (FW-PNG)

TW-UV sensor was fabricated with the as-fabricated TiO_2 NSs/Ti wires having fixed length (≈1 cm) and variable diameters (*Ø* ≈800 μm and 100 μm) on rigid polyethylene terephthalate (PET) substrate. The desired TiO_2 NSs/Ti wires were taken and placed on a PET substrate. Silver (Ag) paste attached both ends of the wire and heat-treated at 70 °C over a period of 30 minutes. The insulating epoxy polymer is used to cover the dried silver to control the external noise/short circuit parameters. The external connections for TW-UV sensor were taken using the flexible copper (Cu) wires, and its top surface was covered using the flexible Kapton tape. Fabricated the flexible wire based BTO piezoelectric nanogenerator (FW-PNG) device by a combination of five layers. It consists of one active piezoelectric layer (BTO NSs), two electrodes (inner Ti electrode and outer Ag electrode) and two insulating layers (Polymethyl

methacrylate (PMMA) for providing the high mechanical stability/controlling BTO NSs cracks and polydimethylsiloxane (PDMS) as a packaging layer), respectively. Here, BTO NSs on flexible Ti electrode (L ≈4 cm, $Ø$≈100 μm) were grown by the low-temperature hydrothermal process and remaining PMMA/PDMS coatings were performed using the dip coating process. The outer Ag electrode coating on PMMA/BTONSs/Ti wire were performed using brush coating technique.

3.3 Results and Discussion

3.3.1 Structural and surface morphology of radially grown TiO_2 NSs

Radially-oriented TiO_2 nanoneedles and nanoparticles with anatase crystalline phase structure were grown on Ti-wire using COM method followed at 500 °C for two hours soaking time. The growth processing conditions for TiO_2 NSs were given in the experimental section. Initially, Ti-wire outer surface was chemically modified using 5 wt % of oxalic acid solution (at 100 °C for 2 h soaking) and 20 wt % H_2O_2 treatment (at 80 °C for 24 h soaking) in a closed vessel, as shown in **Figure 3.1.1**. Here, the use of aqueous oxalic acid treatment of Ti-wire provides necessary etching of Ti-wire outer surface improves the adhesion property or coating. During this treatment, Ti-wire outer surface may possible to change the titanious oxalate and the excess amount of oxalic acid solution on Ti-wire (after sufficient time) can be washed using pure DI water and dried in an air atmosphere. This type of aqueous treatment will be better, easy and cost-effective than hydrochloric acid treatment. Next, H_2O_2 treatment of Ti-wire will improve the surface topography and may possible to increase the oxide thickness layer. Literature reports suggest that soaking time and the weight percentage of the H_2O_2 solution on Ti-substrate will affect the surface roughness from nanometer range (1 to 6 h, 30 wt %) to micrometer range (≥ 24 h, 30 wt %). In present work, 24 h soaking time and 20 wt % of H_2O_2 solution were used to treat

the Ti-wire outer surface (pre-treated oxalic acid Ti-wires) and estimated to achieve the surface roughness greater than 1 μm thickness. Controlled experiments were performed to convert the outer surface of Ti-wire becomes TiO_2 surface using two principle approaches. The first method is the direct heat treatment process of treated (oxalic acid/H_2O_2) flexible Ti-wires at different elevated temperatures under an air atmosphere (**Figure 3.1.1a**).

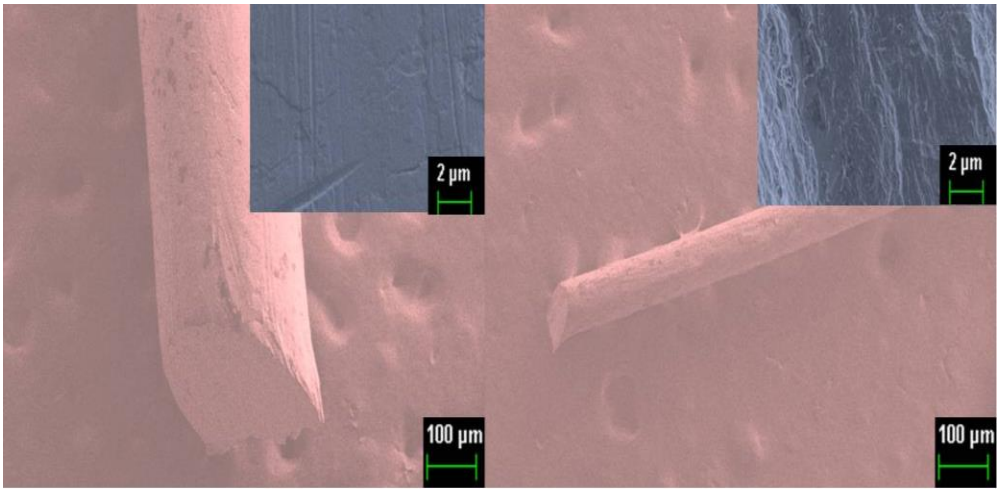

3.1.3 (a, b) FE-SEM images of real Ti-wires (*Ø* ≈800 and 100 μm) top surface at 100 μm scale and the inset shows the magnified portion at 2 μm range represents the smooth morphology.

The conductive flexible Ti-wires become non-conductive after the direct heat treatment at 500, 700 °C with 2 h soaking time. Here, the loss of conductivity, flexibility, and changes in Ti-wire color from shiny grey color to milky white indicates that something has grown on Ti-wire. The Raman spectroscopic pattern of these wires indicates that no active modes of TiO_2 anatase phase are available. The second approach is soaking in chemically treated TiO_2 wires in $TiCl_3$ solution at 80 °C for 2 h and then washing/dried at room temperature. Further, these wires fired at 500 °C for 2 h in open tube furnace at air atmosphere as shown in **Figure 3.1.1b**. Fig. 1(c, d) shows surface morphology of commercially purchased conductive Ti-wires with different diameters (*Ø)* ≈800 μm, 100 μm having multiple lengths at 100 μm scale shown in **Figure 3.1.3(a, b)**. The inset shows magnified images of pure Ti-wires top surface represents the smooth

surface morphology at 2 μm. There is no sign of nanoparticles growth. In contrast, the chemically modified Ti-wires outer surface shows the continuous growth of nanostructure forest throughout the Ti-wires as shown in **Figure 3.1.4(a-d)**. The surface morphology of TiO_2 NSs/Ti-wire (Ø ≈800 μm) at 100 μm scale and the magnified image at 10 μm scale indicate the uniform TiO_2 growth as shown in **Figure 3.1.4a**. The grown thickness of the TiO_2 NSs lies between 1 to 5 μm as shown in **Figure 3.1.5**. Here, two different kinds of TiO_2 NSs were grown on surface of Ti-wire (Ø ≈800 μm) such as nanoneedles and nanoparticles.

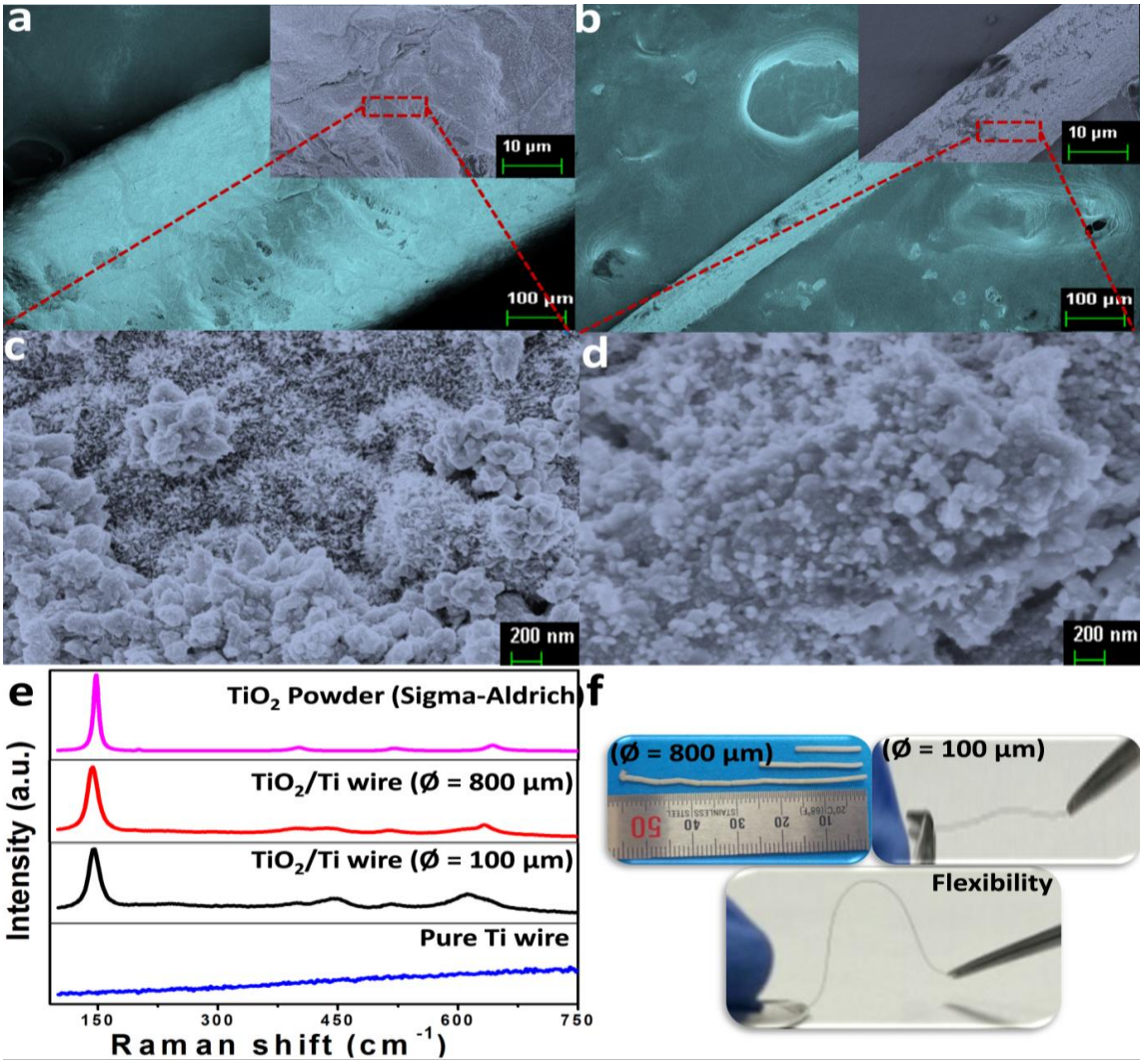

Figure 3.1.4 Surface morphology and structural analysis of Ti/TiO_2 NSs core-shell structure: (a, c) FE-SEM image represents radially grown TiO_2 NSs (nanoneedles and

nanoparticles) on Ti-wire (Ø ≈800 μm) at 100 μm and 200 nm scales. **(b, d)** FE-SEM image represents radially grown TiO_2 nanoparticles on flexible Ti-wire (Ø ≈100 μm) at 100 μm and 200 nm scales. The magnified image at 2 μm scale shows uniform distribution and continuous radial growth of NSs throughout the wires. **(e)** Raman spectra of all samples such as commercial Ti-wire, TiO_2 anatase powder (Sigma-Aldrich), as-grown TiO_2 NSs on Ti-wire (Ø ≈800 μm) and as-grown TiO_2 nanoparticles on Ti-wire (Ø ≈100 μm). **(f)** Optical images of as-grown Ti/TiO_2 NSs core-shell structure based wires (Ø ≈800 μm, 100 μm) and demonstration of flexibility of Ø ≈100 μm wire.

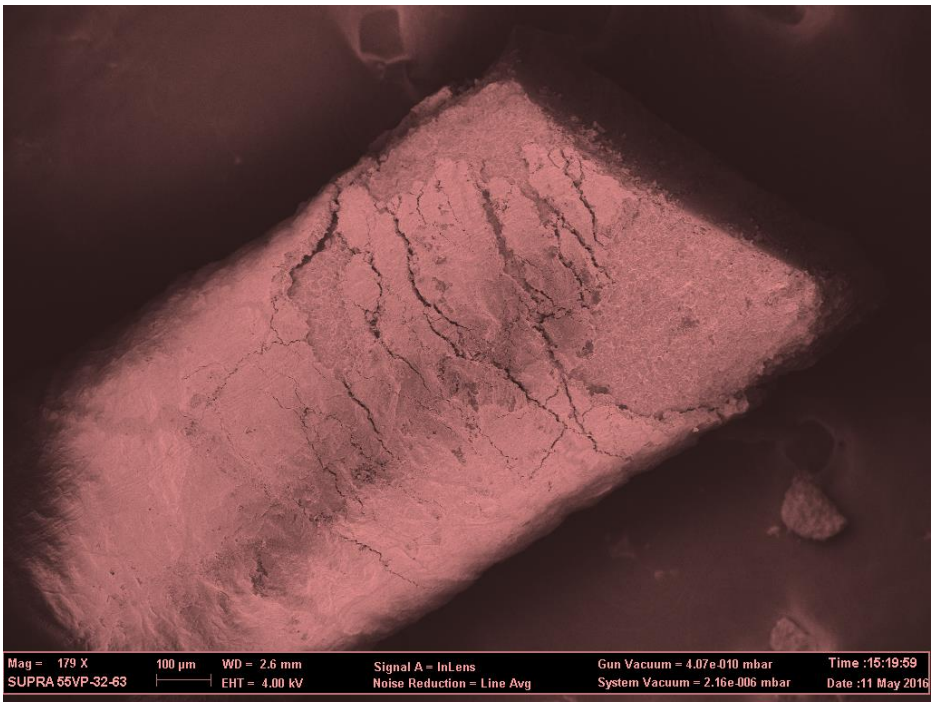

Figure 3.1.5 FE-SEM image of TiO_2 NSs on Ti-wire Ø ≈800 μm at 100 μm scale, and the image capture at one corner of wire for the identification of thickness of TiO_2 NSs growth on Ti-wire.

The FE-SEM images reveal that nanoneedles distributed throughout the outer surface of Ti-wire as the bottom layer and on that nanoparticles were distributed as small islands at particular locations as shown in **Figure 3.1.4c** and well depicted in **Figure 3.1.6 (a-d).** The nanoparticles grain size varies between 50 nm to 200 nm as shown in **Figure 3.1.6b**. Size wise, nanoneedles length is in few micrometers and Ø is less than 20 nm as shown in **Figure 3.1.6d. Figure 3.1.6 (c, d)** shows the TiO_2 nanoneedles facing radially outward direction to the outer surface of Ti-wire. Similarly, TiO_2 growth happens uniformly in all the directions on Ti-wire (Ø

=100 μm), and its surface morphology at 100 μm scale as shown in **Figure 3.1.4b.** The inset figure shows a magnified image of continuous growth of TiO_2 on Ti wire at 10 μm scale. Interestingly, only nanoparticles were grown on surface of Ti-wire (Ø =100 μm) as shown in **Figure 3.1.4b.**

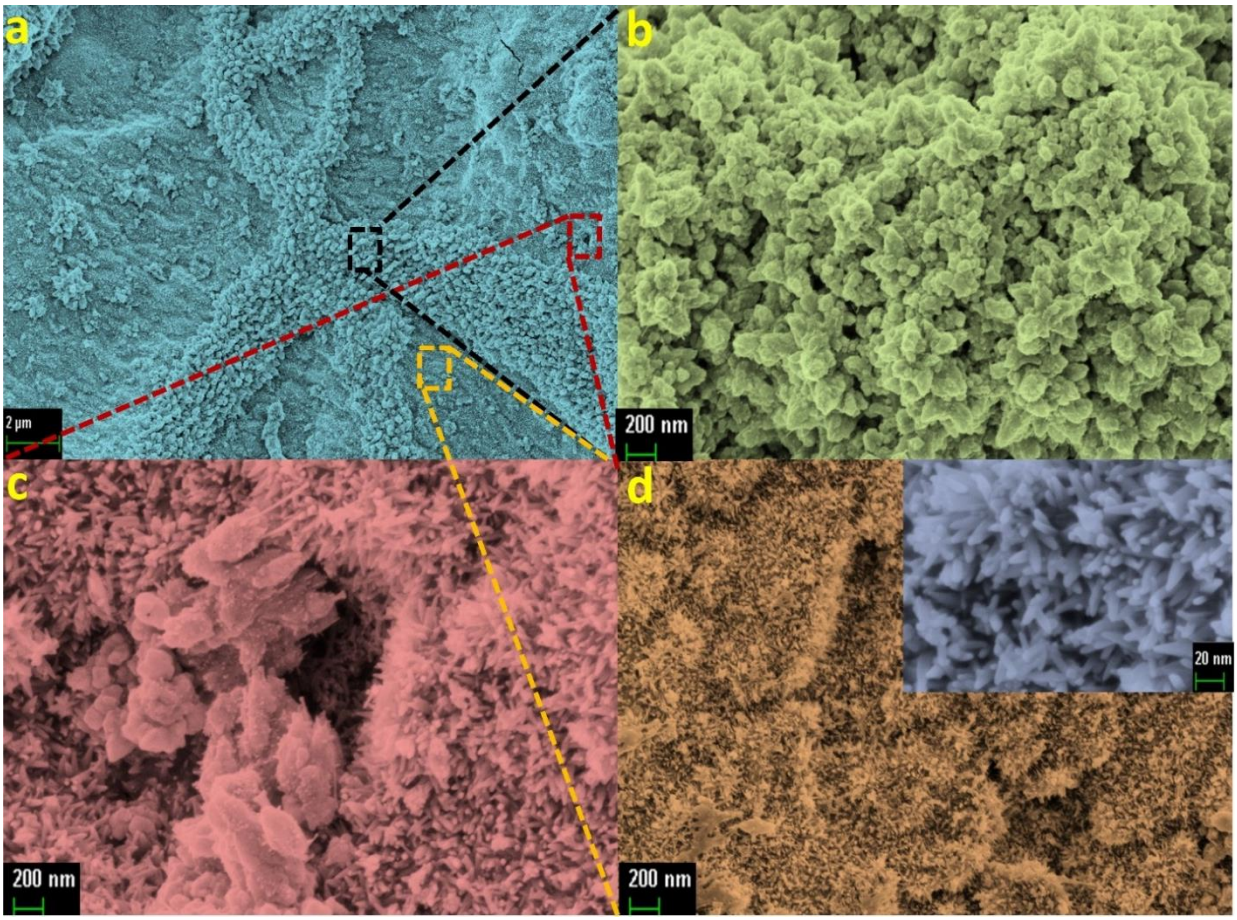

Figure 3.1.6 (a) FE-SEM image represents radially grown TiO_2 NSs on Ti-wire (Ø ≈800 μm) at 2 μm scale shows two different kinds of surface morphology. **(b)** Magnified portion of top layer shows the growth of TiO_2 nanoparticles at 200 nm scale. **(c)** Magnified portion of interfacing layer between nanoneedles and nanoparticles at 200 nm scale. **(d)** Magnified portion of bottom layer shows the uniform distribution and continuous radial growth of TiO_2 nanoneedles on Ti-wire at 200 nm scale.

The phase formation and dynamic symmetry of grown NSs investigated by qualitative Raman spectroscopic technique (λ_{exe} =514 nm, power =20 mW). **Figure 3.1.4e** shows the comparison of various Raman patterns of commercially purchased Ti-wire from Nilaco

Corporation, TiO_2 powder from Daejung chemical Pvt. Ltd and chemically modified Ti-wires (Ø ≈100 μm, 800 μm). The conductive pure Ti-wire shows no Raman active modes. In contrast, commercial TiO_2 crystalline powder shows Raman active modes at various positions such as 147, 200, 400, 519 and 642 cm^{-1} corresponds to the anatase phase structure of TiO_2 nanoparticles [20, 21] as shown in **Figure 3.1.4e.** The changes in full width at half maximum (FWHM), intensity and peak positions corresponds to the size dependency of NSs, phonon confinement behavior, anatase-rutile mixed phase and non-stoichiometry of TiO_2. Moreover, chemically modified Ti-wire (800 μm) shows Raman active modes between the wavelength range from 100 cm^{-1} to 750 cm^{-1} and the corresponding major peaks located at 143, 397, 514 and 633 cm^{-1}, respectively. The major peak position of 143 cm^{-1} assigned to E_g mode has a higher intensity than all other peaks, which is nothing but an external vibration of long-range formed anatase structure of TiO_2. The other peaks such as 397, 514, and 633 cm^{-1} assigned to various modes such as B_{1g}, $A_{1g}+B_{1g}$, and E_g represent the successful growth of TiO_2 NSs on Ti-wire as shown in **Figure 3.1.4e.** All these peaks have a close resemblance and well matched with the Raman pattern of commercial anatase structure of TiO_2 nanopowder [20, 21]. A small shoulder peak at 433 cm^{-1} generates along with the 397 cm^{-1} peak confirms the existence of weak rutile phase. Similarly, Raman pattern of chemically modified Ti-wire (100 μm) shows similar kind of peak behavior for TiO_2 anatase phase structure as shown in **Figure 3.1.4e.** But few peaks such as 517 and 611 cm^{-1} show lower wavelength phase shift and few other peaks 145 and 402 cm^{-1} shows higher wavelength phase shift (≈ ≤3 cm^{-1}) compared to the Raman pattern of commercial TiO_2 nanopowder, it may be due to the size of grown nanoparticles and its formation type. **Figure 3.1.4f** shows the digital photographs of Ti/TiO_2 NSs based wires with different Ø ≈800 and 100 μm. Ti-wire (Ø ≈800 μm) shows the possibility of radial growth (360° view) of TiO_2 NSs (nanoneedles and nanoparticles)

in few centimeters ranging from 1.5 to 5.5 cm, but unfortunately, the wires losses its flexibility due to the permanent loss of tensile strength during the high thermal oxidation temperature. It suggests that Ti/TiO_2 core-shell wire (Ø ≈800 μm) not suitable for smart, flexible harvester applications but suitable for UV sensors. At the same time, Ti-wire (Ø ≈100 μm) has a similar kind of TiO_2 radial growth as like wire (Ø ≈800 μm), but it has a single surface morphology, i.e., TiO_2 nanoparticles as shown in **Figure 3.1.4(b, d)** and good flexibility depicted in **Figure 3.1.4f.** Next, as-fabricated TiO_2 NSs on Ti-wires (800 μm, 100 μm) successfully utilized by fabricating the TW-UV-sensor, i.e., metal (Ag)-semiconductor (TiO_2)–metal (Ag) device structure on flexible PET sheet as shown in **Figure 3.1.7a.**

3.3.2 Photo-response of TiO_2/Ti wire based UV-sensor

The inset shows optical photograph of as-fabricated non-flexible TW-UV sensor (Ø ≈800 μm). Similarly, flexible TW-UV sensor (Ø ≈100 μm) was fabricated (inset shows the optical image of device) and the corresponding electrical performance was estimated under dark environment and in various light sources of wavelengths such as 365 nm, 405 nm and 535 nm as shown in **Figure 3.1.7b**. I-V response of flexible TW-UV sensor under a dark environment with a bias voltage ±7 V shows non-ohmic behavior. It may be due to the establishment of contact between the TiO_2 NSs (for atomic level TiO_2 regulated surface have 4.13 eV) and Ag (4.26 eV) metal surface and also depend on the radial growth of NSs. The flexible TW-UV sensor shows no change in the current response (25 nA at -7 V) under the light sources of wavelengths such as 405 nm (maximum power ≈42 mW/cm^2) and 535nm (maximum power ≈40 mW/cm^2). But the considerable change in current response (approximately fourfold increment) are observed whenever illuminated with the 365 nm source having maximum power ≈60 mW/cm^2 as shown in **Figure 3.1.7b.** The I-V response of non-flexible TW-UV sensor under dark and various light

sources with a bias voltage of ±1 V as shown Figure 3c. This non-flexible TW-UV sensor shows similar kind of response like flexible TW-UV-sensor, but the difference is in the generation of dark current (I_D), photocurrent (I_{Ph}) under 365 nm and lower operating bias voltage (±1 V). Here, the I_D of the non-flexible TW-UV sensor is greater than the I_D of the flexible TW-UV sensor. In both cases, the length between the two Ag electrodes is same and the improved current response may be due to the combined growth of nanoneedle and nanoparticles structures on non-flexible Ti-wire and its synergistic effect, and may also depend on the grown radial thickness of NSs. Further, the I_{Ph} response of non-flexible TW-UV sensor as a function of light intensity with a source wavelength 365 nm was performed and well depicted in **Figure 3.1.7d.** The change in I_{Ph} was observed with the change in light intensity from 0 mW to 18 mW/cm^2 (365 nm source) and increases proportionately by increasing the intensity from 18 mW/cm^2 to 36 mw/cm^2 and 60 mw/cm^2 as shown in **Figure 3.1.7d**. Similar I_{Ph} response was observed for the flexible TW-UV sensor and the corresponding response was shown in **Figure.3.1.8c.** Next, same devices were tested as a function of light intensity (P_L) having source wavelengths 405 nm and 535 nm as shown in **Figure 3.1.8 and Figure 3.1.9**. But no change between the I_D and I_{Ph} was observed i.e. as-fabricated TW-UV sensors are inactive under source wavelengths 405 and 535 nm, respectively. The above results determines that as-grown TiO_2 NSs on flexible/non-flexible Ti-wire have good sensitivity with the function of light intensities of 365 nm source wavelength. In present case, length of the TW-UV sensor and Ti core kept constant, but the non-flexible TW-UV sensor (nanoneedles + nanoparticles growth) is highly sensitive even at low operating bias voltages (≤ 1 V), whereas in flexible TW-UV sensor (nanoparticles) started to work ≥ 1 V. It indicates that, the operating voltage or bias voltage is purely depending on type of growth NSs and its thickness. The I_{Ph}/I_D ratio of non-flexible TW-UV sensor at bias voltage ≈ -1 V is 2.19.

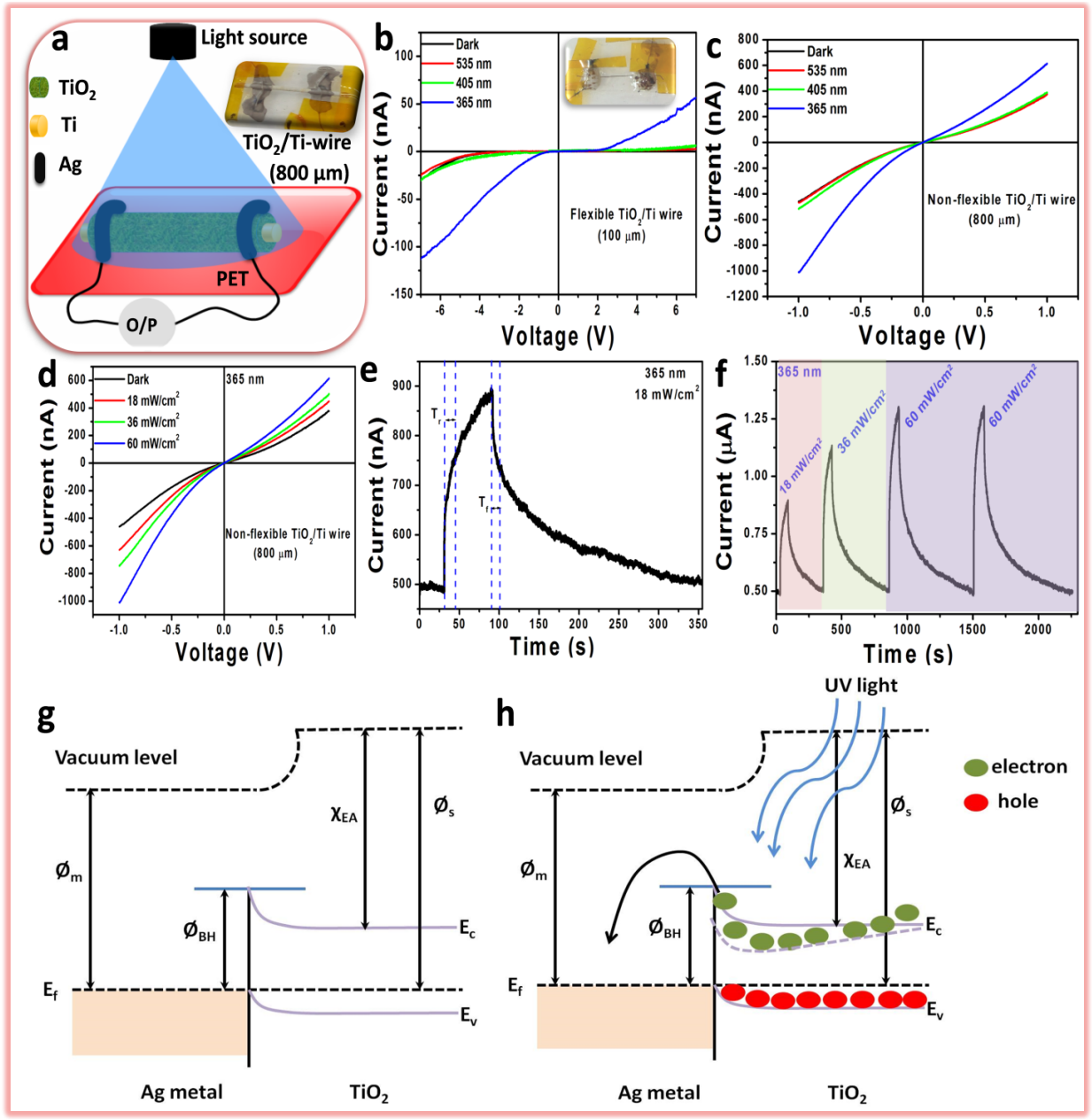

Figure 3.1.7 Fabrication and photo-response analysis of TW-UV sensor: (a) Schematic of TW-UV sensor and inset shows the optical image of as-fabricated TW-UV sensor (Ø ≈800 μm). **(b)** I-V response of TW-UV sensor (Ø ≈100 μm) as a function of fixed input bias voltage ±7 V upon various light sources having wavelengths 365, 405 and 535 nm. The inset shows optical image of as-fabricated TW-UV sensor (Ø ≈100 μm). **(c, d)** I-V response of TW-UV sensor (Ø ≈800 μm) as a function of bias voltage ±1 V, under various light sources having wavelengths 365, 405, and 535 nm, different light intensities (18, 36 and 60 mW/cm^2) of 365 nm source. **(e, f)** I-T response analysis of TW-UV sensor (Ø ≈800 μm) as a function of the light source 365 nm with the light intensity ≈18 mW/cm^2, 40 and 60 mW/cm^2, respectively. **(g, h)** The working

mechanism of TW-UV sensor explained through the estimated energy band diagram under two conditions such as dark and UV light conditions.

Photo-responsivity (R_λ) of both devices with respect to the active surface area (S) has been evaluated with the following equation-E3.1 [17]:

$$R_\lambda = \frac{I_{Ph} - I_D}{P_L \times S} \qquad \text{(E3.1)}$$

The calculated photo-responsivity of non-flexible TW-UV sensor (Ø ≈800 μm) at bias voltage ≈-1 V is 35.024 μA/W. It is higher than the photo-responsivity (1.682 μA/W) of flexible TW-UV sensor (Ø ≈100 μm) at bias voltage ≈-1 V, respectively. The response time (T_r ≈ time required to reach 63% of maximum I_{Ph} from I_D) and recovery time (T_f ≈ time required to recovery of 37% of maximum I_{Ph}) of non-flexible TW-UV sensor with an incident power of 18 mW/cm^2 of 365 nm source is ≈13.9 s and 10.23 s as shown in **Figure 3.1.7e**.

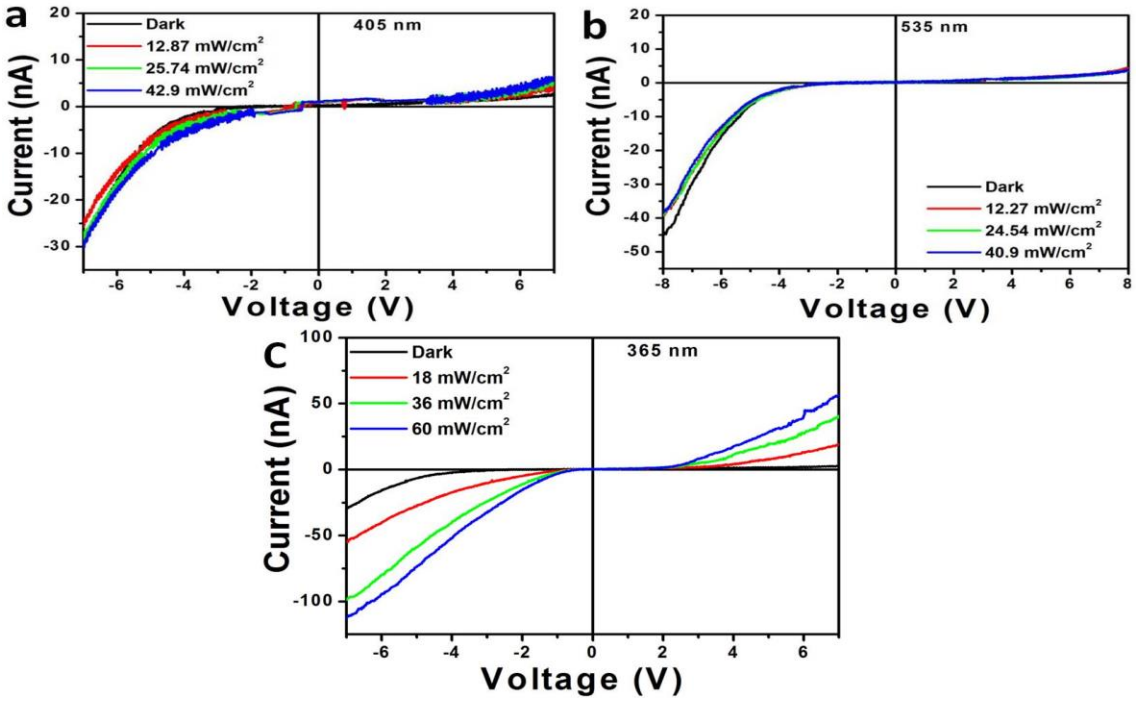

Figure 3.1.8 (a, c) S4 (a) I-V response of TW-UV sensor (Ø ≈100 μm) as a function of bias voltage ±7 V under various light intensities (12.87, 25.74, and 42.9 mW/cm^2) of source wavelength 405 nm. **(b)** I-V response analysis of TW-UV sensor (Ø ≈100 μm) as a function of

bias voltage ±8 V under various light intensities (12.27, 24.54, and 40.9 mW/cm^2) of source wavelength 535 nm. (C) I-V response of TW-UV sensor (Ø ≈100 μm) as a function of bias voltage ±7 V under light intensities (18, 36, and 60 mW/cm^2) of source wavelength 365 nm.

The dark current generated with a bias voltage of 1 V and suddenly raises the current value due to the incident of light power on the device and reached to the maximum value over a period of 60 s. The photo-generated current started to decrease whenever the input incident light power is in OFF condition, and after some time it reached to the dark current value of the device as shown in **Figure 3.1.7e**. The I-T response of non-flexible TW-UV sensor under various light intensities (18, 36 and 60 mW/cm^2) of source wavelength ≈365 nm as shown in **Figure 3.1.7f**. It shows the proportionate photo-generated current behavior with respect light intensity of the source. The working mechanism of the proposed TW-UV sensor demonstrates through the simple energy band diagram as shown in **Figure 3.1.7(g, h).**

Table-3.1: The comparison of proposed TiO_2 NSs wire type-UV sensor photoresponse behavior with the other published reports.

Material /Device type	**A (cm^2)**	**λ (nm)**	**V (V)**	**I_{Ph} (μA)**	**T_r (s)**	**T_f (s)**	**R_λ (A/W)**	**D* (cmHz$^{1/2}$W^{-1})**	**Ref.**
ZnO:Cd /film	0.25	365	10	330	8	10	164 m	1 x 10^{11}	17
TiO_2 /film	0.0038	260	5	2.3	6	15	199	-	23
TiO_2 /film	0.0038	260	5	-	13.34	11.43	899.6	-	24
TiO_2 /film	0.0028	300	50	-	7	3	1.73	-	25
ZnO:Sb /film	-	3	3	28.3	7.3	20.3	-	-	26
ZnO film	100	305	5	-	-	-	0.268	1.19 x 10^{10}	27
TiO_2 /wire type	0.2615	365	-1	1	13.9	10.23	35 μ	0.467 x 10^8	This work

A = Area, λ = Wavelength, V = Bias voltage, I_{Ph} = Photo-current, T_r = Response or Rise time, T_f = Recovery or fall time, R_λ = Photo-responsivity or photosensitivity, D* = Detectivity

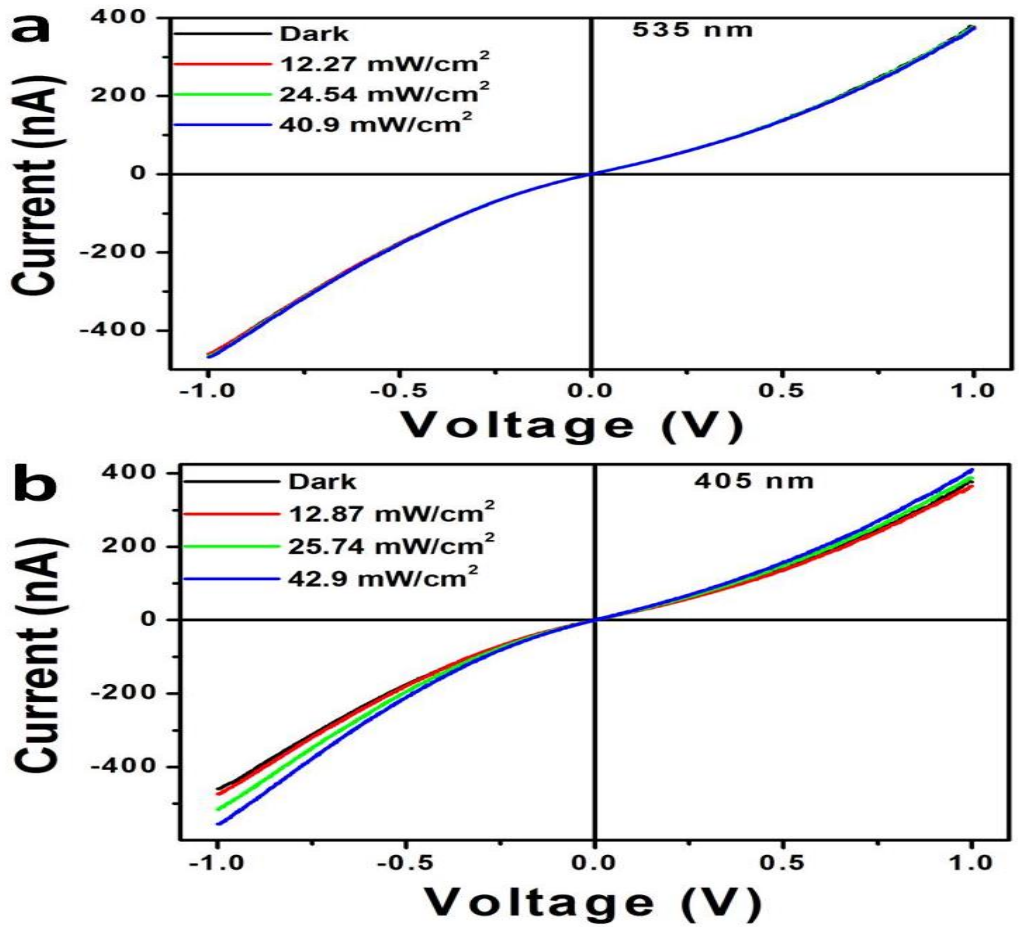

Figure 3.1.9 (a) I-V response analysis of TW-UV sensor (Ø ≈800 μm) as a function of bias voltage ±1 V under various light intensities (12.27, 24.54, and 40.9 mW/cm^2) of source wavelength 535 nm. **(b)** I-V response analysis of TW-UV sensor (Ø ≈800 μm) as a function of bias voltage ±1 V under various light intensities (12.87, 25.74, and 42.9 mW/cm^2) of source wavelength 405 nm.

The energy band levels and interfacing barrier height ($Ø_{BH}$) mainly depending on the work functions of the anatase phase of TiO_2 NSs, is $Ø_s$ ≈5.1 eV [22] and for the silver (Ag) metal is lying in the range of $Ø_m$ ≈4.2 eV to 4.7 eV, respectively. The energy band gap of anatase TiO_2 NSs is lying in the range of 3.2 to 3.35 eV, and electron affinity is 5.1 eV, respectively. The TW-UV sensor generates low current response under the dark environment suggesting that the formed interface barrier height or depletion region between the TiO_2 NSs and silver (Ag) is

somewhat high as shown in **Figure 3.1.7g**. The TW-UV sensor generates many folds increment of current response whenever the UV light is acting on the device. It is due to the generation of more number of electron-hole pairs in the TiO_2 semiconductor material due to the band-to-band excitation. At the same time, the interfacing barrier height between TiO_2/Ag will reduce, and the generated electrons will jump from semiconductor to metal as shown in **Figure 3.1.7h. Table-3.1** demonstrates the comparison of proposed TW-UV sensor (Ø ≈800 μm) performance with the other published reports [17, 23-27]. The calculated photoresponsivity (R_λ) or photo-sensitivity, detectivity (D*), response time (T_r) and recovery time (T_f) of TW-UV sensor (Ø ≈800 μm) are 0.035 mA/W, 0.467×10^8 $cmHz^{1/2}W^{-1}$, 13.9 s, and 10.23 s respectively. It demonstrates that the proposed TW-UV sensor has reasonable photosensitivity and detectivity under a particular wavelength of light source.

3.3.3 Growth mechanism, structural and surface morphology of BTO NSs

The grown TiO_2 NSs on flexible wire (Ø ≈100 μm) converted into perovskite BTO NSs using the low-temperature hydrothermal technique. Similar, approach is possible to turn these TiO2 NSs into other ternary compounds or perovskites such as $ZnTiO_3$, $FeTiO_3$, $PbTiO_3$, and other derivatives (Zn_2TiO_4, $Zn_2Ti_3O_8$, and $FeTiO_{3\pm\delta}$). But these materials have various other functional properties such as semiconducting, photocatalytic [28], antiferromagnetic [29], microwave dielectric nature [30] and photoluminescent nature [31], except the piezoelectric/ferroelectric nature. It suggests that these ternary materials are not potential candidates to convert the mechanical energy into useful electrical energy (alternative energy harvesting approach). The $ZnTiO_3$ [32] have slight piezoelectric coefficient like $PbTiO_3$, which is less compared to the piezoelectric coefficient of BTO NSs. Therefore, the grown TiO_2 NSs converted into efficient BTO NSs. The structural parameters evaluated by the Raman, X-ray

photoelectron spectroscopy analysis and the FE-SEM characterization observed its surface morphology. As-prepared flexible BTO NSs based wire tested for scavenging the mechanical energy by fabricating the flexible wire based piezoelectric nanogenerator (FW-PNG).

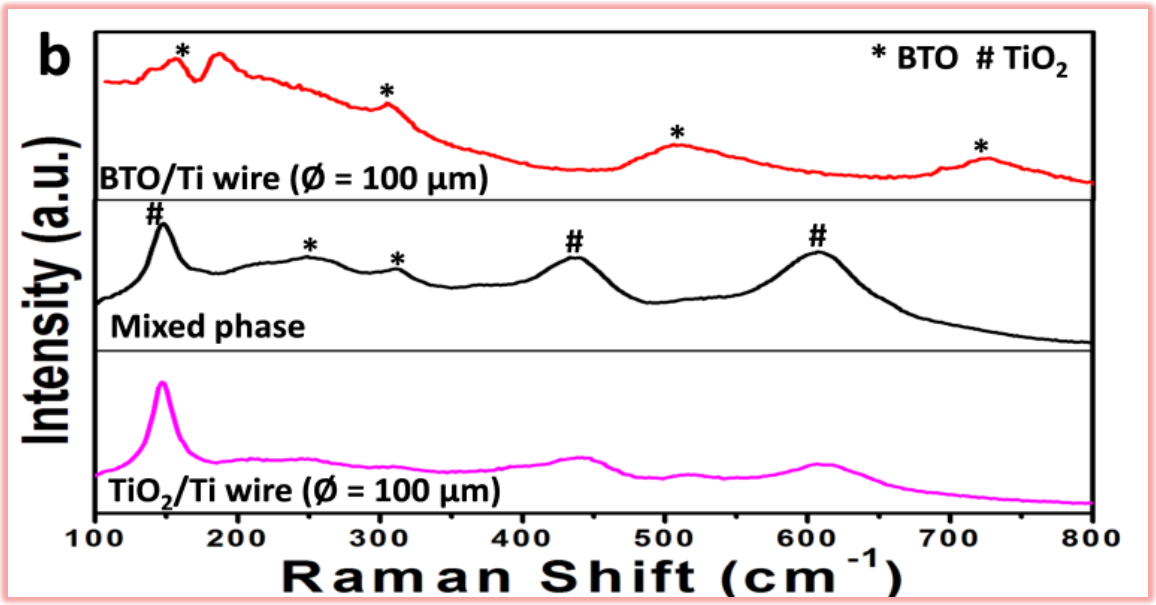

Figure 3.1.10 Raman spectra of all samples such as TiO_2 NSs/Ti wire, a mixed phase of BTO NSs/TiO_2NSs/Ti-wire, and BTO NSs/Ti-wire.

The conversion of TiO_2 nanoparticles to BTO NSs on flexible Ti-core was obtained using the cost-effective hydrothermal technique with an operating temperature 180 °C for 24 hr as schematically shown in **Figure 3.1.2.** Flexible wires have been collected after the termination of chemical reaction and washed several times using DI water and then dried in an air atmosphere. Raman spectroscopic technique was employed to estimate the grown NSs on flexible Ti-wire is related BTO NSs or not, as shown in **Figure 3.1.10**. Raman pattern (black color) of hydrothermally (0.1 M of $Ba(OH)_2.8H_2O$:0.1 M KOH solution) treated flexible wire shows various active vibrational modes describe the mixed phase of anatase TiO_2 nanoparticles and BTO NSs. The broad peaks at 147, 438, and 607 cm^{-1} are related to TiO_2 nanoparticles and peaks at 248 cm^{-1}, and 311.94 cm^{-1} represents the traces of BTO NSs formation. It confirms that

complete hydrothermal reaction was not happening due to the less concentration of KOH. Further, flexible TiO_2 NSs/Ti wires treated with a hydrothermal solution with constant $Ba(OH)_2.8H_2O$ concentration (0.1 M), and increased concentration of KOH (0.6 M) and its corresponding Raman pattern (red color) of obtained wires given in **Figure 3.1.10**. This pattern represents the diminishing of major TiO_2 anatase peaks entirely, and the generation of new peaks at various positions such as 186, 304, 511 and 724 cm^{-1} confirms the complete conversion of TiO_2 nanoparticles into BTO NSs. All these peaks matched with the published reports of BTO NSs [33,34]. The in-situ transformation mechanism or formation of BTO NSs relates to the heterogeneous nucleation, growth and topochemically interaction between the Ba^{2+}, $Ba(OH)^{+}$ ions and the titanium precursors surface. The hydrothermal growth of BTO NSs from the precursors of barium hydroxide octahydrate ($Ba(OH)_2.8H_2O$), anatase phase of TiO_2NSs/Ti, and KOH reaction medium leads to generate two possible ways of chemical reaction for reaching the final product. The following chemical reactions are [35-37]

Reaction-1:

$TiO_2+2KOH+2H_2O \leftrightarrow K_2Ti(OH)_6$

$Ba(OH)_2 \leftrightarrow Ba^{2+}+2OH^-$

$Ba(OH)_2.8H_2O+ K_2Ti(OH)_6 \leftrightarrow BaTiO_3+11H_2O+2KOH$

(Or)

Reaction-2:

$TiO_2+2KOH+H_2O \leftrightarrow K_2TiO_3+2H_2O$

$Ba(OH)_2.8H_2O+ K_2TiO_3 \leftrightarrow BaTiO_3+2KOH+8H_2O$

By assuming the whole process contains the multiple slow reaction steps and the possibility for the formation of intermediate chemical products ($K_2Ti(OH)_6$ or K_2TiO_3) from the reaction

between the solid TiO_2 NSs and liquid KOH solution. Further, this intermediate product interacts with the Ba^{2+} ions forms the small BTO NSs layer. By providing the proper soaking time, temperature and sufficient reaction medium in the hydrothermal process will convert the whole TiO_2 surface into the final BTO NSs product. Here, the morphology of BTO NSs may possible to depend on the surface morphology of the intermediate product ($K_2Ti(OH)_6$ or K_2TiO_3), and it's hard to define in the present case, because of the continuous hydrothermal chemical reaction from TiO_2 to BTO NSs. Here, the TiO_2 nanoparticles successfully converted to the randomly oriented BTO nanoparticles and nanorods. It indicates that the intermediate products may be the combined form of nanoparticles and nanorods.

The major characteristic peaks positioned at 304 cm^{-1} assigned to [B_1(TO+LO), E] mode, 511 cm^{-1} peaks assigned to [A_1 (TO), E] modes confirms the radially grown BTO NSs are in tetragonal crystalline phase. Few minor peaks at 186 cm^{-1} and 724 cm^{-1} assigned to [A_1 (TO), E (LO)] and [A_1 (TO), E (LO)] vibrational modes. The peak at 155 cm^{-1} is may be due to the internal defect of BTO lattice. Here, KOH concentration is a key parameter for the successful conversion of TiO_2 nanoparticles to BTO NSs. Next, the surface morphology of Ti/BTO NSs core-shell wires analyzed by FE-SEM and the images at 100 μm, 20 μm and 200 nm scale shown in **Figure 3.1.11(a-c).** The surface morphological image reveals uniform distribution and continuous radial growth of NSs throughout the flexible wire and magnified image depicts two different kinds of BTO NSs formed on outer surface of Ti wire such as nanorods and nanoparticles. The *Ø* of the nanorod is less than 350 nm, *L* is in several micrometers, and nanoparticles size is less than 200 nm range as shown in **Figure 3.1.11c**. Here, the existence of core-shell structure formation analyzed by the electrical conductivity measurement test. The core material is the Ti-metal wire highly conductive, and the grown shell nanostructures are pure

$BaTiO_3$ is electrically non-conductive. **Figure 3.1.11d** depicts digital photograph of as-developed radial growth of Ti/BTO NSs core-shell structure based flexible wire having $Ø \leq 100$ µm and L is in several centimeters, which is precisely in the range of single human hair dimension ($Ø \approx 17$ to 181 µm and L is in centimeter range). The one-side of the wire scratched with the fine blade and removed the grown BTO NSs as shown in **Figure 3.1.11e**, and the conductivity measurements were performed using the two digital multimeters (Model: 73303, Yokogawa, Japan, and Model: MY68, Mastech) as shown in **Figure 3.1.11(f, g)**. As expected that the scratched region (core) of wire shows high conducting nature (8.3 **Ω**) and unscratched shell region shows non-conductive nature (no detection of a change in resistance) confirms the existence of core-shell structures.

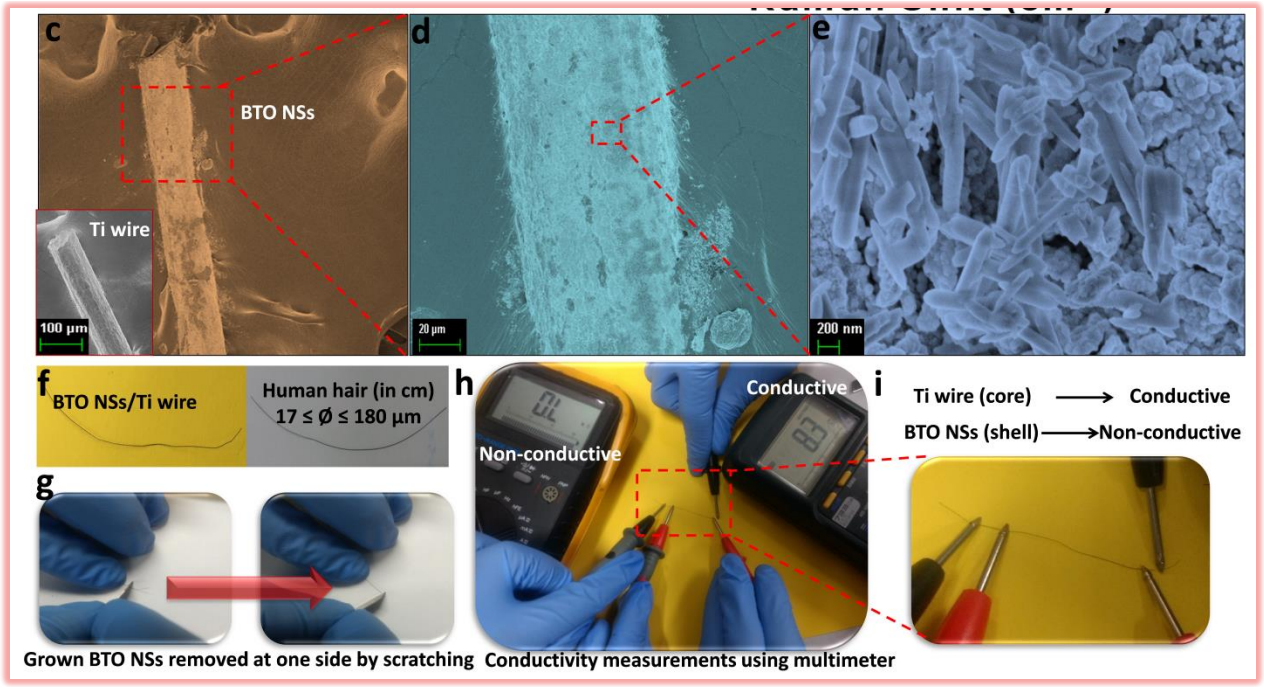

Figure 3.1.11 Surface morphology of In-situ radial growth BTO NSs on flexible Ti-wire (a-b) FE-SEM image of Ti/BTO NSs core-shell wire at 100 µm, 20 µm scale shows uniform distribution and continuous radial growth of NSs throughout the wire. **(c)** Magnified image of Ti/BTO NSs core-shell wire at 200 nm scale presents the random growth of nanorods and nanoparticles. **(d)** The comparison of as-grown Ti/BTO NSs core-shell wire with the human hair dimensions. **(e)** Obtaining the Ti- metal wire (core section) at one-side by scratching the grown

BTO NSs. **(f, g)** electrical conductivity measurement of core-shell structure based wire using the digital multimeters and the magnified portion shows the multimeter probes location on the wire.

X-ray photoelectron spectroscopy (XPS) technique employed to understand the elemental identity and chemical state information from as-grown NSs on flexible Ti wire. **Figure 3.1.12a** represents the XPS survey spectra of TiO_2 NSs on Ti-wire (black color) and shows the existence of Ti, O and C elements [38]. Two strong peaks generate at the binding energies of 458.5 eV and 464.37 eV ascribed to Ti^{+4} $2p_{3/2}$, and Ti^{+4} $2p_{1/2}$ represents the formation of strong Ti^{+4}-O bonds as shown in **Figure 3.1.12b.** The difference in binding energy between two peaks ≈6 eV, which arises from the oxidation state of Ti is 4+. The deconvolution of Ti^{+4} $2p_{3/2}$ and Ti^{+4} $2p_{1/2}$ peaks generates two subpeaks at 459.71 eV, 463.38 eV confirms the existence of the lesser oxidation states of Ti ions and the formation of loosely bound Ti^{+3}-O bonds as shown in **Figure 3.1.12(c, d)** [38, 39]. These two subpeaks assigned to Ti^{+3} $2p_{3/2}$ and Ti^{+3} $2p^{1/2}$ and possible to improve the charge transfer process between the anion and cations, respectively. The peak at a binding energy of 529.5 eV corresponds to O 1s in TiO_2 lattice as shown in **Figure 3.1.12i**. Similarly, XPS survey spectra of BTO NSs grown on Ti-wire as shown in **Figure 3.1.12a** (red color) and represents the presence of Ba, Ti, O and C elements on the surface of Ti-wire. The strongest peak at a binding energy of 780.95 eV corresponds to Ba $3d_{5/2}$ and peak at 796.25 eV corresponds to Ba $3d_{3/2}$. Both these peaks were aroused from the formation of barium atoms in the perovskite phase of $BaTiO_3$ and are from the oxidation state of Ba is 2+. The deconvolution and curve fitting of Ba $3d_{5/2}$ (780.95 eV) and Ba $3d_{3/2}$ (796.25 eV) peaks generates two subpeaks at 778.80 eV, and 794.12 eV corresponds to the barium atoms existing at the surface phase of $BaTiO_3$ [40, 41] as shown in **Figure 3.1.12(e, f)**. Moreover, the two subpeaks create the ion displacements in the tetragonal crystalline phase leading to two types of O^{2-} positions and two

types of Ba^{2+} positions. Additionally, low significance peaks at different binding energies such as Ba 4d (88 eV) and Ba 4p (176.15 eV) represents the existence of various spin states of barium orbital's as shown in **Figure 3.1.12(g, h)**. Ti 2p and O 1s oxidation peak positions in XPS spectra of BTO represent the slight shift, and no huge changes in the broadness of peak represent the internal stresses of TiO_6 octahedron in BTO lattice as shown in **Figure 3.1.12(b, i).**

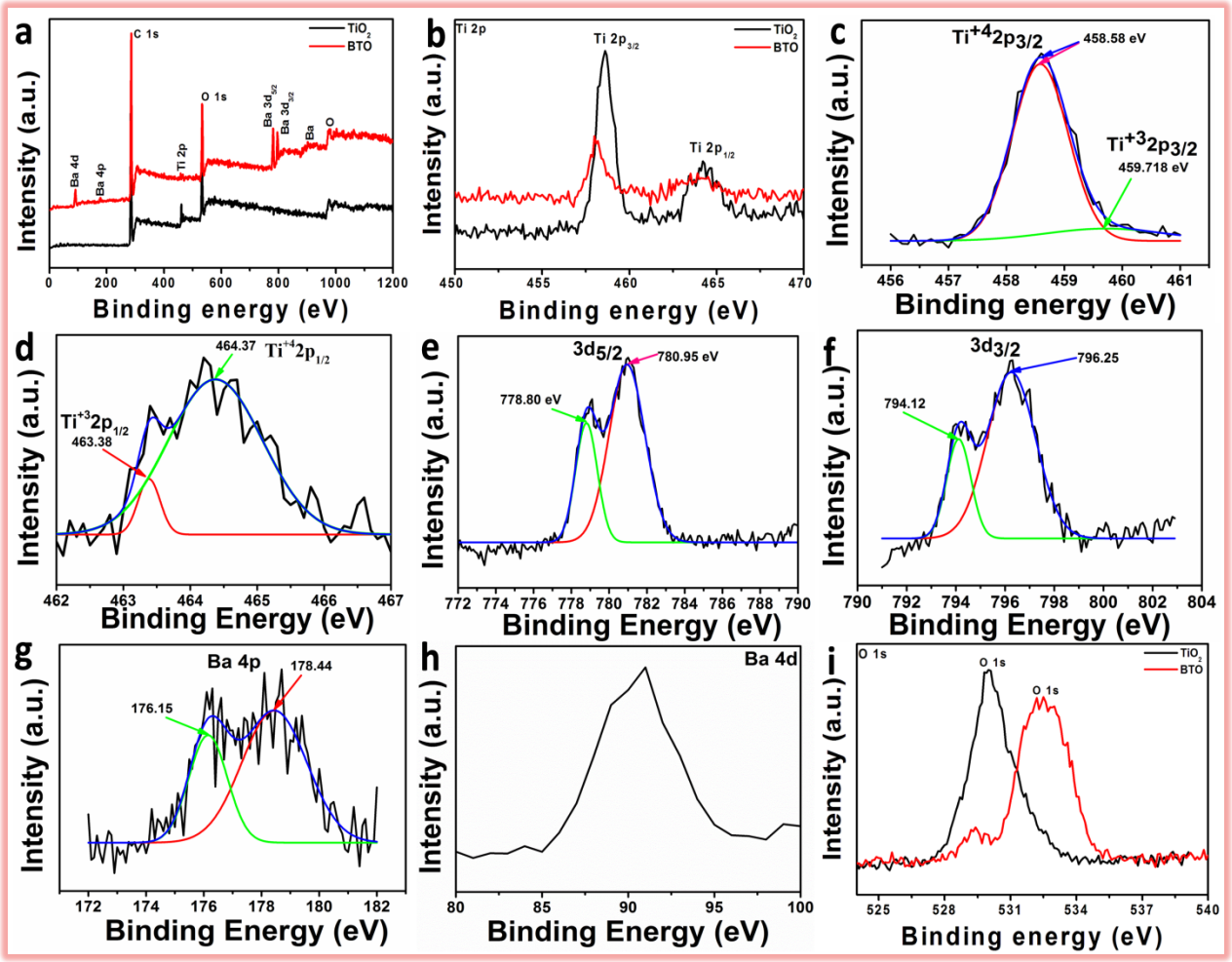

Figure 3.1.12 Elemental composition analysis of TiO_2, BTO NSs on Ti-wire: (a) Survey XPS spectra of Ti/TiO_2 NSs and Ti/BTO NSs core-shell flexible wires. **(b)** Narrow scan spectrum of Ti 2p element ($2p_{3/2}$, $2p_{1/2}$ spin states). **(c, d)** Deconvolution and curve fitting analysis of Ti $2p_{3/2}$ and Ti $2p_{1/2}$ spin states. **(e-g)** Deconvolution and curve fitting analysis of Ba $3d_{5/2}$, Ba $3d_{3/2}$, and Ba 4p spin sates. **(h, i)** Narrow scan spectrums of Ba 4d spin state, and O 1s element respectively.

3.3.4 Self-powered wire type UV-sensor

Flexible wire type piezoelectric nanogenerator (FW-PNG) ($L \approx 4$ cm, $5 \leq Ø \leq 10$ μm of NSs thickness) was fabricated to analyze the piezoelectric effect of as-grown BTO NSs on flexible Ti-wire and the corresponding FW-PNG device structure as shown in **Figure 3.1.13d.** FW-PNG consists of five layers such as one active layer (BTO NS), supporting layer (PMMA), inner electrode (conductive Ti-wire), outer electrode (Ag) and outer packaging layer (PDMS), respectively. **Figure 3.1.13(a, b)** shows the generated short-circuit current (I_{SC}), and open circuit voltage (V_{OC}) of FW-PNG device upon periodic load ≈2 N. The obtained peak-to-peak I_{SC} and V_{OC} of FW-PNG is ≈600 nA and ≈7 V upon 2 N load. Switching polarity test was performed to identify the generated output is coming from the FW-PNG device or not as shown in **Figure 3.1.13a.** In forward connection, FW-PNG device generates positive peak whenever the mechanical load is acting on it and negative peak generated after the removal of the mechanical load. In reverse connection, FW-PNG device generates negative peak whenever the mechanical load is acting on it and positive peak generated after the removal of the mechanical load. There is a clear phase shift was observed between the output signals during forward and reverse connection of FW-PNG device confirms that the generated output is true output and not from any other external sources. Load resistance analysis and instantaneous area power density (P_A) of FW-PNG was evaluated upon the mechanical load ≈2 N, and the corresponding results were shown in **Figure 3.1.13c**. The generated output voltage gradually increases by increasing the load resistance and the obtained maximum P_A of FW-PNG is 22.5 μW/cm^2 at 10 MΩ. It clearly indicates that the optimized load resistance for FW-PNG is 10 MΩ.

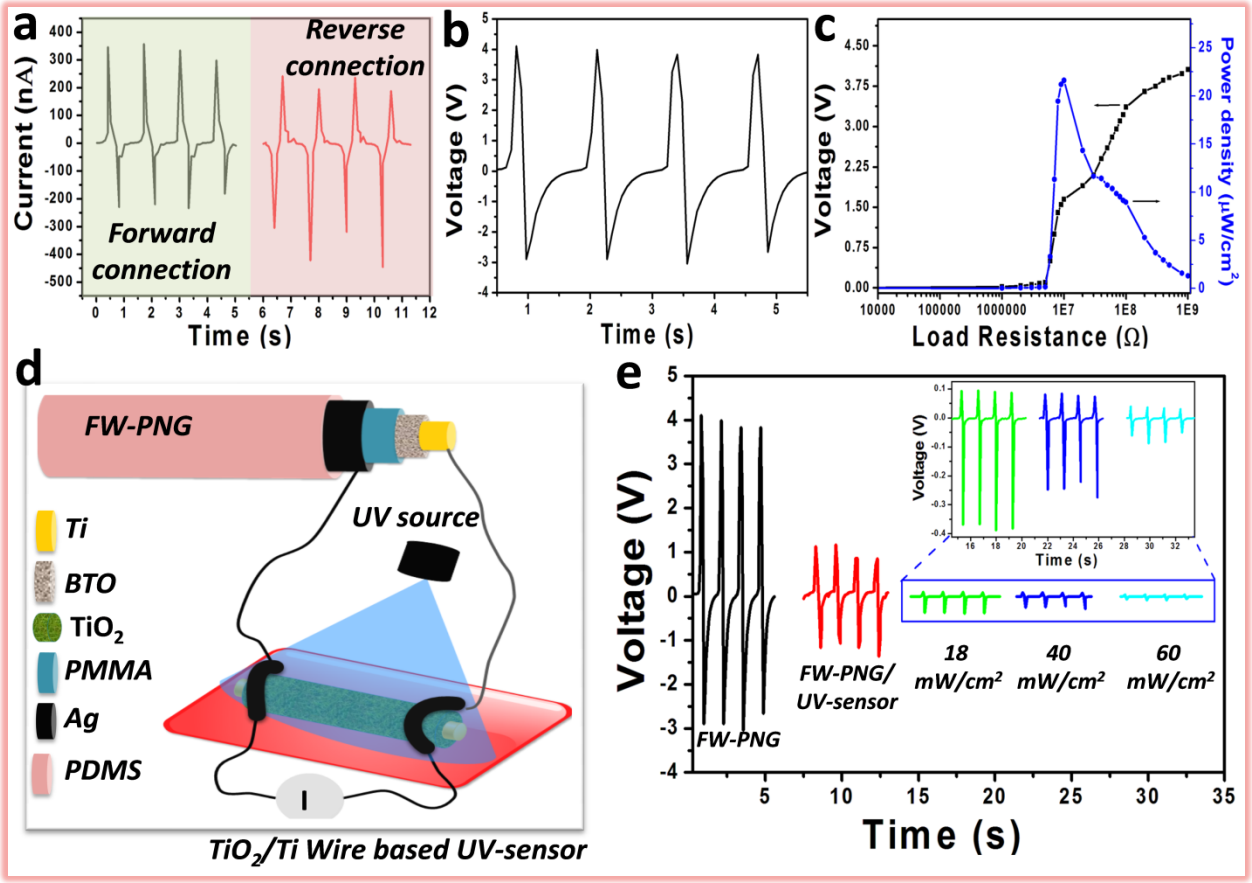

Figure 3.1.13 Energy harvesting analysis of FW-PNG device upon constant mechanical force. (a) Switching-polarity test of I_{SC} for FW-PNG device upon constant mechanical force 2 N. (b, c) The V_{OC}, load resistance and instantaneous power density analysis of FW-PNG device upon force (2 N). (d) Schematic for the demonstration of SPW-UV sensor by the parallel connection between FW-PNG device and TW-UV sensor. (e) The V_{OC} of FW-PNG and SPW-UV sensor upon constant mechanical force (2 N) as a function of various light intensities (18, 40 and 60 mW/cm^2) of the light source 365 nm, respectively.

For real-time analysis, as-prepared FW-PNG and TW-UV sensor were utilized successfully and demonstrated the possibility of self-powered wire (SPW) based UV sensor (SPW-UV sensor) as shown in **Figure 3.1.13d**. In this case, FW-PNG device working as a sustainable independent power source driving the high-performance TW-UV sensor by the parallel connection. Initially, FW-PNG device generates peak-to-peak V_{OC} ≈7 V upon 2 N, and this voltage decreases up to ≈2 V whenever NG output terminals connected to the input of TW-

UV sensor under same load condition. The decrement in output voltage is due to the mismatch of resistance between the FW-PNG device (load matching resistance ≈10 MΩ for maximum power density) and TW-UV sensor (calculated resistance range from I-V graph is around 600 to 800 kΩ). Further, this peak-to-peak voltage output reduced to 460 mV, 330 mV and reached to 90 mV, whenever the UV source (365 nm) irradiated on TW-UV sensor with various light intensities ≈18 mW/cm^2, 40 mW/cm^2 and 60 mW/cm^2 as shown in **Figure 3.1.13e**.

The FW-PNG device was also tested under biomechanical index finger force, and the corresponding peak-to-peak electrical responses were shown in **Figure 3.1.14(a, b).** The FW-PNG device generates peak-to-peak V_{OC} and I_{SC} are 3 V and 120 nA upon index finger force. The asymmetric nature of electrical response may be due to asymmetric nature of input finger force. In the present case, a single FW-PNG device with small device area generates reasonable area power density ≈22.5 μW/cm^2 upon 2 N, which is comparable/higher to the many published reports on traditional PNGs. Still, the generated output energy can be possible to enhance by assembling or stack of flexible BTO NSs/Ti-wires. The above-demonstrated results describe that the as-grown radial TiO_2 NSs (nanoneedles + nanoparticles) based wires were potential candidates for optical electronics [23-25, 42-44] applications. The tetragonal crystalline phase of grown piezoelectric BTO NSs based flexible wires are suitable candidates to convert the generated mechanical energy from the linear motor shaft load, human hand index force into useful electrical energy [1, 35, 36, 45]. This kind of in-situ radial growth based low dimensional semiconductor/piezoelectric wires can pave the way for a generation of smart wire based optoelectronic devices, sustainable power sources, solar cells, memristors and also suitable to work as portable/flexible self-powered sensors.

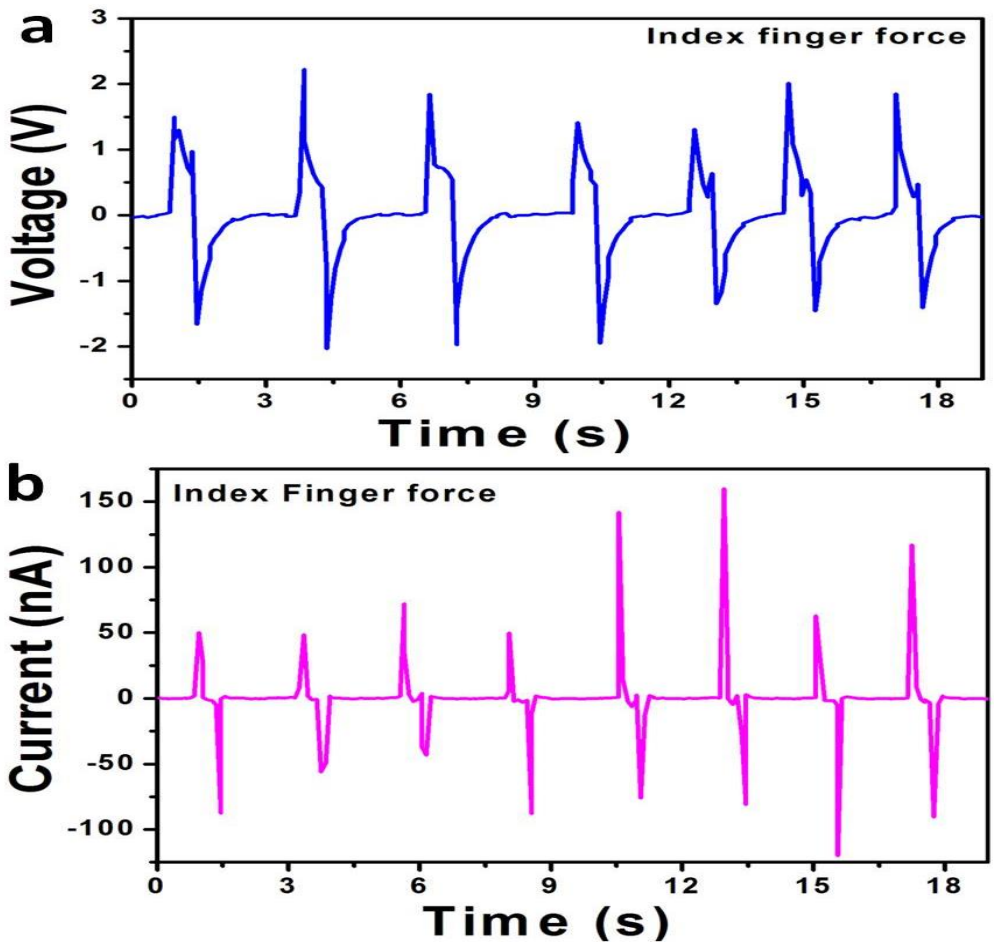

Figure 3.1.14 (a, b) Open circuit voltage and short circuit current of FW-PNG device as a function of periodic biomechanical index finger force

3.4 Conclusions

In summary, self-powered wire (SPW) based-UV sensor was demonstrated successfully by the parallel connection between human hair sized flexible BTO NSs/Ti-wire based piezoelectric nanogenerator (FW-PNG) and TiO_2 NSs/Ti-wire (TW)-UV sensor, respectively. Uniform distribution/continuous radial growth of nanostructures (BTO NSs, TiO_2 NSs) forest obtained on the outer surface of Ti-wire using simple, cost-effective COM method followed by a low-temperature hydrothermal technique. A Raman pattern confirms that the grown TiO_2 nanoneedles, nanoparticles are in anatase phase, and the conversion of TiO_2 to BTO nanorods/

nanoparticles are in tetragonal crystalline phase, respectively. XPS survey analysis confirms that the oxidation state of titanium (Ti) is 4+, barium (Ba) is 2+ and conversion of TiO_2 NSs into BTO NSs creates internal stresses of TiO_6 octahedron in BTO lattice. The internal pressures of TiO_6 octahedron in BTO lattice observed by the slight peak shift of Ti 2p and O 1s peak positions. The FW-PNG device generates peak-to-peak I_{SC}, V_{OC} is ≈600 nA, ≈7 V, and the obtained maximum instantaneous area power density is ≈ 22.5 μW/cm^2 at 10 MΩ upon 2 N load. This type of FW-PNGs occupies less area, more convenient to place on any contour mechanical surfaces, and excellent portability/wearability, respectively. All the results suggest that flexible BTO NSs/Ti-wire, TiO_2 NSs/Ti-wire, and FW-PNGs are potential candidates for developing micro/nanodevices on mechanical contour structures, wire-based self-powered sensors, and flexible energy harvesters.

3.5 References

(1) K. I. Park, S. Xu, Y. Liu, G. T. Hwang, S. J. L. Kang, Z. L. Wang, K. J. Lee, Nano Lett. 10, (2010), 4939-4943.

(2) C. Anuj, B. Muharrem, N. Maarten, E.J. E. Ten, B. Fred, R. Guus, Sci. Rep. 7, 2017, 1-9.

(3) K. Aneesh, A. S. Henry, Nat. Commun. 4, (2013), 1-10.

(4) K. R. Hwan, K. D. Hyeong, X. Jianliang, H. K. Bong, I. P. Sang, P. Bruce, G. Roozbeh, Y. Jimin, L. Ming, L. Zhuangjian, M. Viktor, K. Dae Gon, L. An-Phong, G. N. Ralph, L. K. David, G. O. Fiorenzo, H. Yonggang, K. Zhan, A. R. John, Nat. Mater. 9, 2010, 929-937.

(5) S. Matteo, C. Alessandro, Sensors, 14, 2014, 11957-11992.

(6) X. Yong, Intelligent textile technology based on flexible semiconductor skins, US2006/0255433 A1.

(7) K. Hyunjin, M. K. Seong, B. S. Hyung, K. Hyeok, P. BoongIk, Y. K. Ji, I. S.Jung, I. S.; I. H. Kyu, E. J. Jae, J. P. Jong, K. Ohyun, N. C. Seung, J. P. Young, **Energy Environ. Sci.** 5, 2012, 8932-8936.

(8) S. Ezhilvalavan, T. Tseung-Yuen, Mater. Chem. Phys. 65, 2000, 227-248.

(9) N. Keiichi, N. Shigetoshi, M. Hiroaki, Jpn. J. Appl. Phys. 34, 1995, 5091-5095.

(10) X. Ying, Y. Qi, L. Jing-Feng, J. Mater. Chem. 22, 2012, 23221-23226.

(11) H. Zheng, J. Wang, L. Mohaddes-Ardabili, M. Wuttig, L. Salamanca-Riba, D. G. Schlom, R. Ramesh, Appl. Phys. Lett. 85, 2004, 2035-2037.

(12) M. Chunrui, C. Chonglin, Pulsed Laser Deposition for Complex Oxide Thin Film and Nanostructure, Advanced Nano Deposition Methods, First Edition, Edited by Y. Lin and X. Chen, 2016 Wiley-VCH Verlag GmbH & Co. KGaA.

(13) L. Linglong, L. Lu, W. Zhiguang, L. Yanxi, Y. Yonggang, Z. Dawei, Y. Guang, Y. Jianjun, V. Dwight, Y. Yaodong, Sci. Rep. 5, 2015, 1-7.

(14) J. K. Young, Y. K. Dong, S. W. Sung, W. A. Chang, K. Ill Won, I. K. Angus, K. Seunghyun, K. Jae-Hyeon, H.J. Jong, *ACS Appl. Mater. Interfaces*, 8, 2016, 6504-6511.

(15) Z. H. Ru, W. Aiying, M. V. Paula, Chem. Mater. 21, 2009, 1214-1220.

(16) Y. Dechao, Q. Yu, J. Qingyu, G. Zhaoshuai, S. Wenbin, X. Jin, Z. Yang, F. Qiuxia, S. Xiaoling, Appl. Phys. Lett. 110, 2017, 063901-063905.

(17) P. Yuvasree, N. R. Alluri, C. Arunkumar, K. Sang-Jae, J. Mater. Chem. C. 5, 2017, 415-426.

(18) G. A. T. Sevilla, A. S. Almuslem, A. Gumus, A. M. Hussain, M. E. Cruz, M. M. Hussain, Appl. Phys. Lett. 108, 2016, 094102-094106.

(19) L. Minbaek, C. Chih-Yen, W. Sihong, N. C. Seung, J. P. Yong, M. K. Jong, C. Li-Jen, Z. L. Wang, Adv. Mater. 24, 2012, 1759-1764.

(20) Y. Yeolmae, J. Ji-Won, P. Kyusung, K. Il-Doo, Sci. Rep. 5, 2015, 1-9.

(21) B. Reshma, H. Rajesh, P. Dhanya, O. Satishchandra, Dalton Trans. 40, 2011, 11374-11377.

(22) M. Setvin, J. Hulva, G. S. Parkinson, M. Schmid, U. Diebold, PNAS, 114, 2016, E2556-E2562.

(23) H. Xue, X. Kong, Z. Liu, C. Liu, J. Zhou, W. Chen, S. Ruan, Q. Xu, Appl.Phys.Lett. 90, 2007, 201118-20.

(24) X. Kong, C. Liu, W. Dong, X. Zhang, C. Tao, L. Shen, J. Zhou, Y. Fei, S. Ruan, Appl.Phys.Lett. 94, 2009, 123502-04.

(25) D. Çalışkan, B. Bütün, Ş. Özcan, E. Özbay, J. Vac. Sci. Technol. B, 31, 2013, 020606-8.

(26) W. Dai, X. Pan, S. Chen, C. Chen, W. Chen, H. Zhang, Z. Ye, **RSC Adv.**, 5, 2015, 6311-6314.

(27) H. Y. Lee, Y. T. Hsu, C. T. Lee, Solid-State Electron, 79, 2013, 223–226.

(28) H. Tian, S. Wang, C. Zhang, J. P. Veder, J. Pan, M. Jaroniec, L. Wang, J. Liu, **J. Mater. Chem. A**, 5, 2017, 11615-11622.

(29) E. Chikoidze, T. Tchelidze, E. Popova, P. Maso, N. Ponjavidze, N. Keller, Y. Dumont, Appl. Phys. Lett. 102, 2013, 122112-15.

(30) S. Lei, H. Fan, X. Ren, J. Fang, L. Maa, Z. Liu, J. Mater. Chem. C, 5, 2017, 4040-4047.

(31) C. Ye, Y. Wang, Y. Ye, J. Zhang, G. H. Li, J. Appl.Phys, 106, 2009, 033520-23.

(32) J. R. Fuertes, B. Winkler, T. Bernert, L. Bayarjargal, W. Morgenroth, M. Koch-M¨uller, K. Refson, V. Milman, N. Tamura, Phys. Rev. B, 91, 2015, 214110-18.

(33) N. R. Alluri, C. Arunkumar, V. Venkateswaran, P. Yuvasree, S. Sophia, J. Ji Hyun, K. Sang-Jae, ACS Sustain. Chem. Engg. 5, 2017, 4730-4738.

(34) N. R. Alluri, S. Balasubramaniam, K. Sang-Jae, ACS Appl. Mater. Interfaces, 7, 2015, 9831-9840.

(35) F. Maxim, P. M. Vilarinho, P. Ferreira, I. M. Reaney, I. Levin, Cryst. Growth Des. 11, 2011, 3358–3365.

(36) H. Chen, Y. W. Chen, Ind. Eng. Chem. Res. 42, 2003, 473-483.

(37) X. Wei, J. Cryst.Growth, 286, 2006, 371–375.

(38) V. C. Anitha, A. N. Banerjee, G. R. Dillip, S. W. Joo, B. K. Min, J. Phys. Chem. C, 120, 2016, 9569–9580.

(39) S. Qin, D. Liu, Z. Zuo, Y. Sang, X. Zhang, F. Zheng, H. Liu, X. G. Xu, J. Phys. Chem. Lett. 1, 2010, 238–241.

(40) W.H. Zhang, L. Chen, Y. T. Tao, W. H. Zhang, J. Chen, J. X. Zhang, Physica B 406, 2011, 4630–4633.

(41) I. Popescu, A. Urda, T. Yuzhakova, I. C. Marcu, J. Kovacs, I. Sandulescu, C. R. Chimie 12, 2009, 1072-1078.

(42) W. S. Lee, Y. S. Park, Y. K. Cho, ACS Appl. Mater. Interfaces, 6, 2014, 12189−12195.

(43) X. Li, C. Gao, H. Duan, B. Lu, X. Pan, E. Xie, Nano Energy, 1, 2012, 640–645.

(44) Y. Xie, L. Wei, Q. Li, G. Wei, D. Wang, Y. Chen, J. Jiao, S. Yan, G. Liu, L. Mei, Appl.Phys.Lett., 103, 2013, 261109-12.

(45) S. Sharma, M. Tomar, N. K. Puri, V. Gupta, Procedia Eng. 87, 2014, 1172 – 1175.

CHAPTER-IV

Self-powered luid velocity sensor/light emitting diodes using polymer/Ba(Ti,Zr)O_3 nanocubes hybrid film piezoelectric nanogenerator

4.1 Highlights

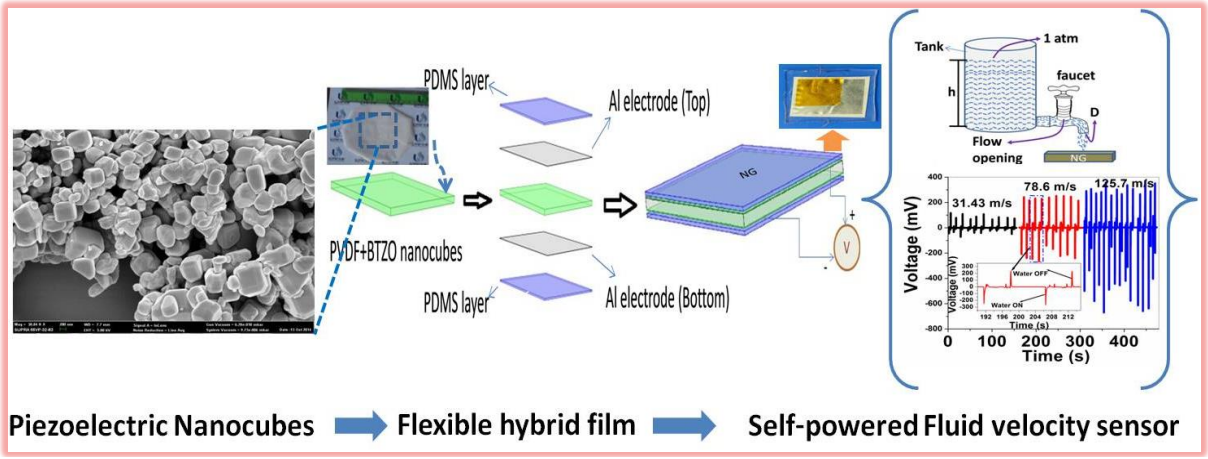

- High crystalline $BaTi_{(1-x)}Zr_xO_3$ (x = 0, 0.05, 0.1, 0.15, and 0.2) nanocubes synthesized using a molten-salt process.
- The BTZO/PVDF flexible nanogenerator exhibits a high output response (11.9 V, 1.35 μA) compared to the BTO/PVDF nanogenerator output of (7.99 V, 1.01 μA) constant load (11 N).
- Demonstrated PNG as a self-powered sensor to measure different water velocities at an outlet pipe.
- Composite PNG has dual functionality (harnessing energy + sensing).

4.2

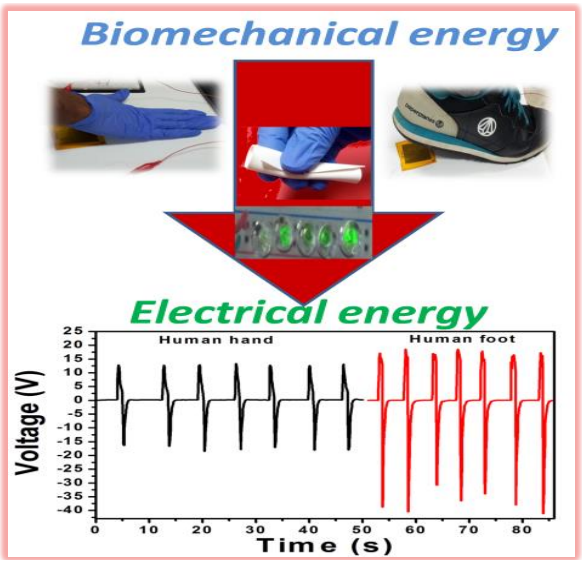

- Cost-effective solution casting technique used to fabricate eco-friendly BTO NCs/PDMS film for harnessing waste biomechanical energy using unconventional harvesting technique.
- Composite PNG generates area power density of 7 mW/cm^2 at 100 MΩ.
- The generated output is sufficient to drive the commercial LEDs.

4.1 Self-powered fluid velocity sensor based on polyvinylidene (PVDF)/B($Ti_{(1-x)}Zr_x$)O_3 nanocubes hybrid film piezoelectric the nanogenerator

4.1.1 Introduction

Self powered portable devices and active transducers play a key role in present and the near future, which can function without any external bias-voltage sources or additional process [1, 2]. Such as self-powered pH sensor[3], temperature[4], vibration[5], ethanol[6], microflow sensors[7] and water motion active transducers[8] have been greatly investigated and successfully implemented. The conventional battery-based sensors have disadvantages such as power consumption, large package size, high system cost[9] and risk of environment pollution[1], which demands the new alternating approach called self-powered technology. The importance of this technology is based on driving a device or sensor by harvesting energy from piezoelectric [10], triboelectric[11], thermal gradient[12] and solar methods[13]. Piezoelectric harvesting method[10], [14] is the most promising as compared to other methods, due to its less affected by external conditions such as humidity, temperature respectively. Nanogenerators using functional materials (piezoelectric ceramics-3D, 2D and 1D structure) have been developed as a disruptive innovation, it generates a voltage in response to mechanical force (and *vice versa*). Piezoelectric nanogenerators (PNGs) using ZnO[10, 15], PVDF[16], $ZnSnO_3$[17], PZT[18, 19], PMN-PT [20], and $BaTiO_3$[14, 21, 22] have been widely examined. Among which PZT based PNGs have more power generation due to its high piezoelectric coefficient (d_{33}) but facing global restriction due to the lead toxicity towards human health problems, bio-incompatibility, and environmental pollution. Therefore, the development of PNGs based on lead-free piezoelectric ceramics has increased great attention due to the environment-friendly and bio-compatibility[23]. Compared with PZT, $BaTiO_3$-based ceramics are

an alternative candidate for the development of PNGs due to the following merits: one is lower piezoelectric coefficient but smaller dielectric constant (possible to improve by doping foreign atoms [24, 25] and second is biocompatibility for implantable biological devices [21, 23].

In this section, demonstrate the flexible PNG based on high performance composite film, composed of BTZO(x =0, 0.05, 0.1, 0.15 and 0.2) nanocubes and poly(vinylidene fluoride) (PVDF) polymer matrix for the first time. High purity bulk $BaTiO_3$ nanocubes (without change of tetragonal structure) has been modified by the substitution of the Zr^{4+} atom (0.72 Å) in place of Ti^{4+} (0.605 Å) site using the molten-salt method. The substitution of Zr^{4+} atom in which Ti^{4+} site, will enhance the piezoelectric coefficient (d_{33}) 100 pC/N ($BaTiO_3$)[26-28] to 174-236 pC/N ($BaTi_{(1-x)}Zr_xO_3$)[29, 30] and electro-mechanical conversion efficiency, which is more acceptable to harvest energy. The electrical characterization (open-circuit voltage and short-circuit current) of as-prepared $BaTi_{(1-x)}Zr_xO_3$/PVDF nanogenerators was studied and demonstrated the lighting five green LEDs simultaneously, without any storage device and successfully harvested biomechanical energy. The maximum open-circuit voltage and short circuit current for $BaTi_{0.9}Zr_{0.1}O_3$ nanocubes/PVDF based PNG reached to 11.9 V and 1.36 μA, which are greater than $BaTiO_3$ nanocubes/PVDF output 7.99 V and 1.01 μA. In addition, we demonstrated $BaTi_{0.9}Zr_{0.1}O_3$/PVDF based PNG as an active sensor. The electrical outputs of this PNG can be examined to estimate their input water velocity (inertial forces) flowing through the outlet pipe. Recently few reports have been published, piezoelectric NGs as active sensors for heart-pulse[31], tire pressure[32], cantilever vibration[33] and wind-velocity detection[2] measurements. This study will expand the choice of materials for PNG and utilization of PNG as the active sensor has more advantages, such as pollution free, low maintenance cost, high operating temperature up to 120 °C and long life time respectively.

4.1.2 Experimental Method

4.1.2.1 Synthesis of $BaTi_{(1-x)}Zr_xO_3$ nanocubes

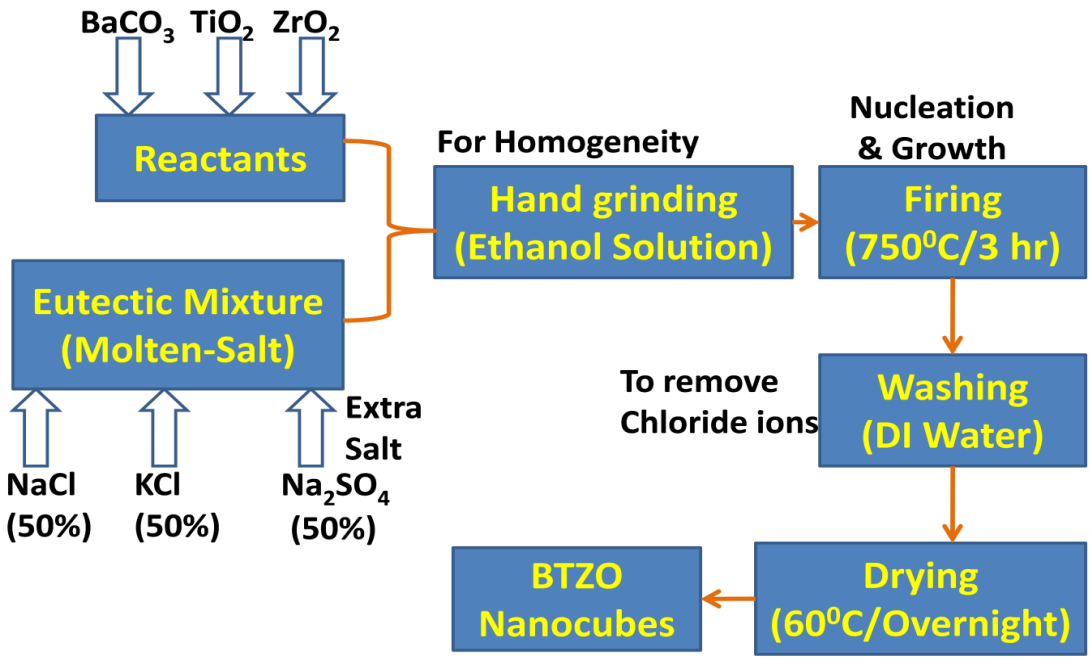

Figure 4.1.1 Process flow chart for $BaTi_{1-x}Zr_xO_3$ nanocubes *via* Molten-Salt method.

The stoichiometric compositions $BaTi_{(1-x)}Zr_xO_3$(x =0, 0.05, 0.1, 0.15 and 0.2) were synthesized by Molten-salt method[34, 35], which is schematically shown in **Figure 4.1.1**. Commercial powders of $BaCO_3$ (99.95%), TiO_2 (98%), and ZrO_2 (99%) were selected as starting materials. The raw materials were weighted according to the stoichiometric ratio and mixed with eutectic mixture of 50% mol NaCl-50% mol KCl flux and an extra salt 25% mol Na_2SO_4 acting as the reaction medium. To obtain a homogeneous powder, the raw materials were mixed by hand-grinding in a mortar and pestle in ethanol solution for 30 minutes. The as-synthesized mixture placed into combustion boat and heated at 750 °C for 3 hr in the furnace. The heating rate is 2.5 °C/min, and the product was taken out of the furnace for cooling naturally after the reaction. Finally, the as-synthesized product was washed with hot deionized water several times until no chloride ions were detected by silver nitrate solution to ensure that the residue of salt was removed exhaustively and then dried at 60 °C overnight. This approach allows the low firing temperature

(750 ˚C /3 hr), enrichment in morphology as compared to BTZO derived with high firing temperature (>1100 °C/2 hr) by solid-state reaction process [29, 36, 37].

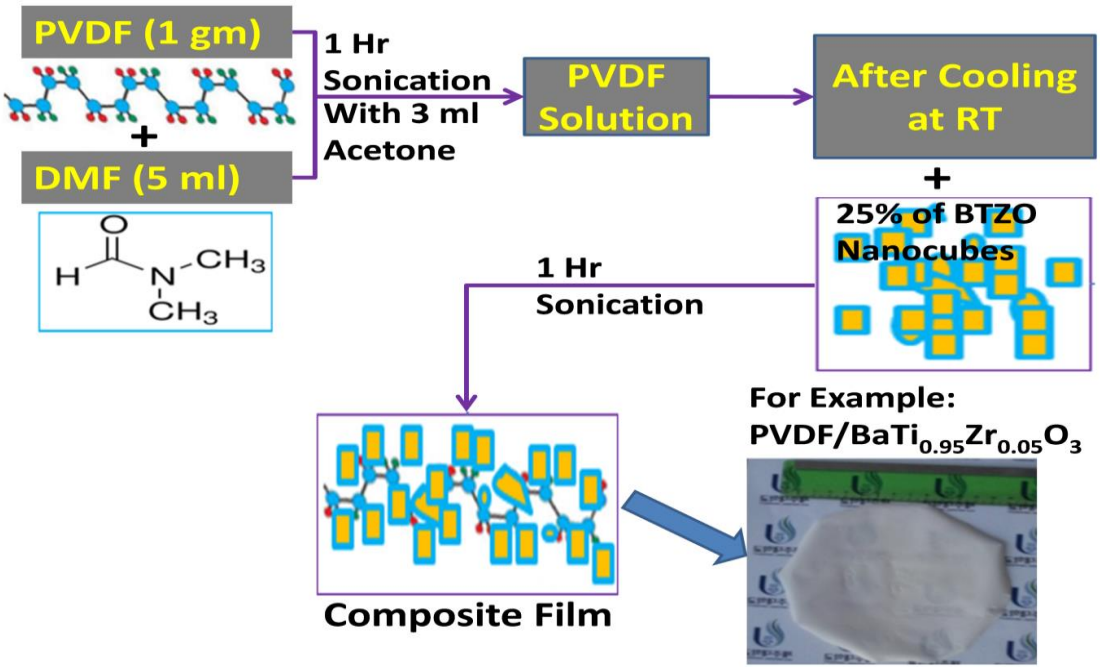

Figure 4.1.2 Fabrication process of PVDF/BTZO hybrid piezoelectric film

4.1.2.2 Hybrid Film & Fabrication of Nanogenerator

The schematic representation of the hybrid (or composite) film using ultrasonication process is shown in **Figure 4.1.2**. A total of (1g) PVDF (Sigma Aldrich) was dissolved in a mixture of (5 mL) N, N-Dimethylformamide (DMF) and (3mL) acetone and homogeneous solution was obtained by sonication process, using a probe sonicator for 60 minutes. Next, 25 wt % of $BaTi_{(1-x)}Zr_xO_3$ (x =0, 0.05, 0.1, 0.15 and 0.2) nanocubes was mixed with the prepared solution and sonication for 1 hr using probe sonicator. The final solution was poured into a Petri dish and dried in a hot-air oven at 60 °C/overnight. The dried film was peeled off from the Petri dish and taken according to the required dimension (2.5 cm X 2.5 cm) of nanogenerator (NG) as shown in **Figure 4.1.3**. The NG was fabricated by coating Al electrodes on top and bottom of the hybrid film through thermal evaporation technique. The electrical connections were established by Cu

wires attached with silver paste on top and bottom of the Al-coated hybrid film. Finally, the polydimethylsiloxane (PDMS) was used as a packaging layer to the NG, to protect the device from external conditions such as mechanical stress, temperature, and humidity respectively. Before electrical characterization, the NG was poled at ambient temperature by applying a high voltage of 8 kV for 24 hr. In order to demonstrate the self-powered sensor, the PNG kept normal to the water flow with a fixed rigid support covered with PE material.

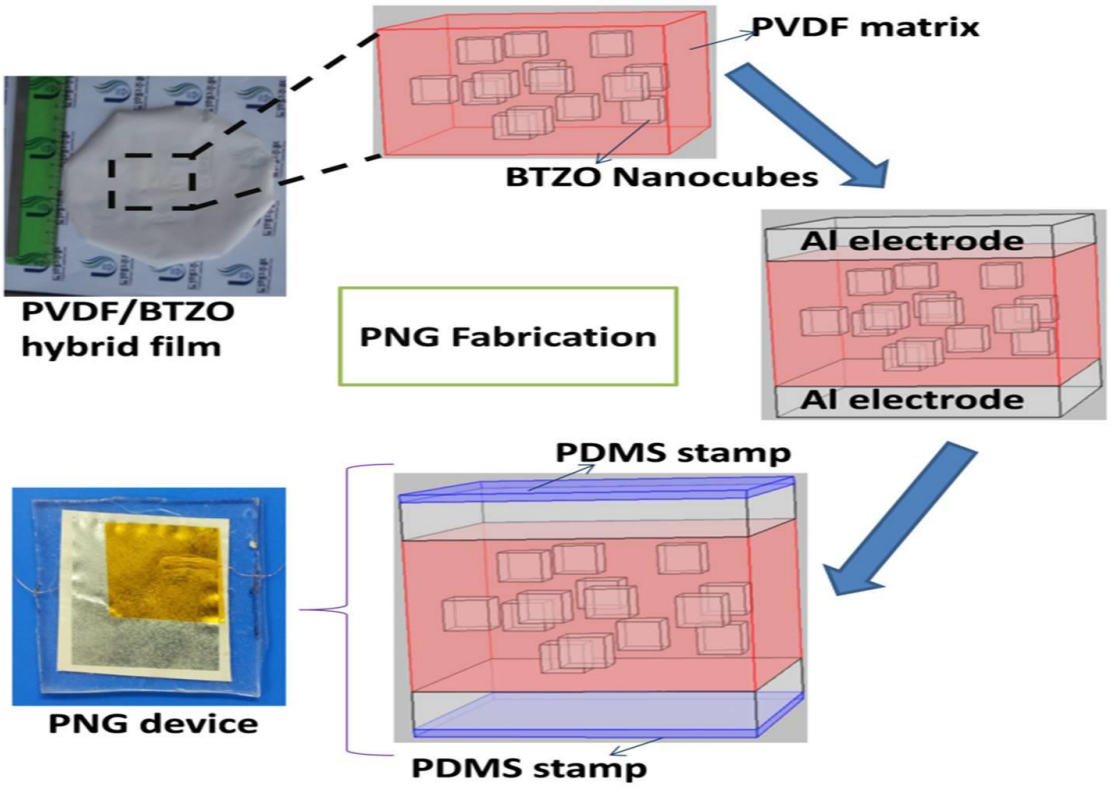

Figure 4.1.3 Fabrication key steps of $BaTi_{0.9}Zr_{0.1}O_3$/PVDF PNG device.

4.1.3 Result and discussion

4.1.3.1 Structural & morphology of BTZO nanocubes/PVDF composite film

A large number of high-quality BTZO nanocubes were synthesized through a molten-salt method. The complete preparation process of BTZO nanocubes is depicted in experimental

section. **Figure 4.1.4a** shows the XRD patterns of as-synthesized BTZO (x = 0, 0.05, and 0.1) piezoelectric nanocubes reveals the single-phase perovskite structure indicating that Zr^{4+} may have entirely diffused into the $BaTiO_3$ lattice to form a solid solution, in which Zr^{4+} (0.72 Å) atom substituted in Ti^{4+} (0.605 Å)-site. The major XRD peaks of BTZO (x = 0, 0.05, 0.1) ascribed to tetragonal crystal structure[34] but with the increase of Zr^{4+} content i.e. x > 0.1 have minor, intermediate phases with the tetragonal crystal structure (**Figure 4.1.5a**), which indicates the doping limit up to x = 0.1 by using the Molten-salt method. The tetragonal structure (ICDD-98-001-3771) is observed by splitting of the diffraction peak at 45° indexed as (002)/(200) respectively[34, 38]. BTZO nanocubes are well-crystallized perovskite structures, but the tetragonal distortion of BTZO, $\delta = (c-a)/a$, is up to 1% in bulk materials, and it is typical identify the line broadening effect[22] by XRD pattern. So that, the detailed dynamic symmetry and structural information was monitored by Raman spectroscopy shown in **Figure 4.1.4b**. Mostly, the $BaTiO_3$ with a cubic structure does not have Raman active modes, but the tetragonal structure has active modes due to the noncentrosymmetric property. The Raman spectra of $BaTiO_3$ nanocubes are identified at 196 cm^{-1} [A_1(TO), E(LO)], 256 cm^{-1} [A_1(TO)], 310 cm^{-1} [B_1(TO+LO), E], 520cm^{-1} [A_1(TO), E] and 720 cm^{-1} [A_1(LO), E], all of which are subjective to a tetragonal phase of $BaTiO_3$[14, 22, 39, 40]. As the increase in Zr^{4+} concentration up to x = 0.15, there is no much considerable peak shift, when x = 0.2, the Raman peak at 256 cm^{-1} appears to be very weak, which indicates the existence of rhombohedral-tetragonal phase[24] (**Figure 4.1.5b**). The Raman shift and XRD pattern indicate the presence of noncentrosymmetric regions formed from the local off-centering of the titanium (zirconium) atoms.

The FT-IR spectra show that Zr^{4+} additives will directly affect the stretching and bending vibration of the crystal lattice ($BaTiO_3$) shown **Figure 4.1.6a**. Generally, the most important

peak for barium titanate corresponds to a wavelength range between 600 – 530 cm^{-1}. This peak is due to the vibration of the bond between titanium and oxygen (Ti–O bond). In proposed work, the $BaTiO_3$ nanocubes were prepared *via* Molten-Salt method having lattice absorption peak at (552 cm^{-1}), which is shifting towards lower wavelength side when increasing the Zr^{4+} substitution into the Ti^{4+} site is shown **Figure 4.1.6b**.

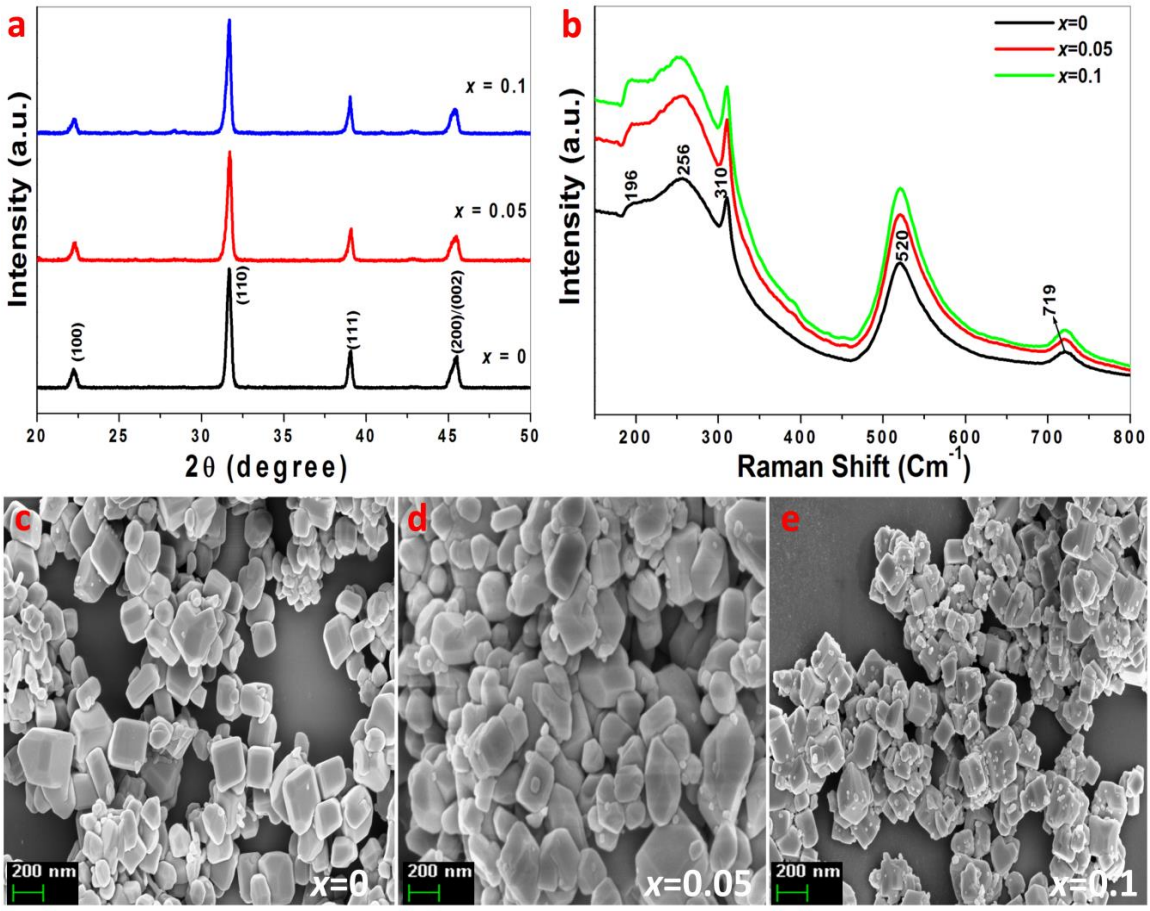

Figure 4.1.4 Structural and surface morphology of $BaTi_{(1-x)}Zr_xO_3$ (x = 0, 0.05 and 0.1) nanocubes processed by Molten-salt method. (a) X-ray diffraction patterns of highly crystalline BTZO nanocubes after calcination (b) Typical Raman spectrum for BTZO nanocubes indicating the formation of the tetragonal crystal structure. (c - e) An FE-SEM image shows the well crystalline surface morphology of BTZO nanocubes at 200 nm scale.

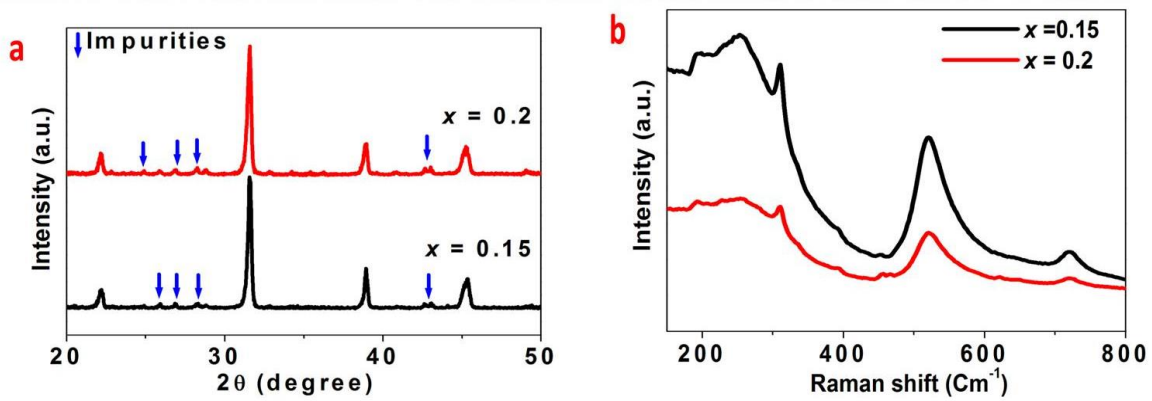

Figure 4.1.5 (a) XRD patterns of $BaTi_{1-x}Zr_xO_3$ nanomaterial for x =0.15 and 0.2. (b) Raman spectra of the resultant materials (x=0.15 and 0.2) confirm the polymorphic nature at room temperature.

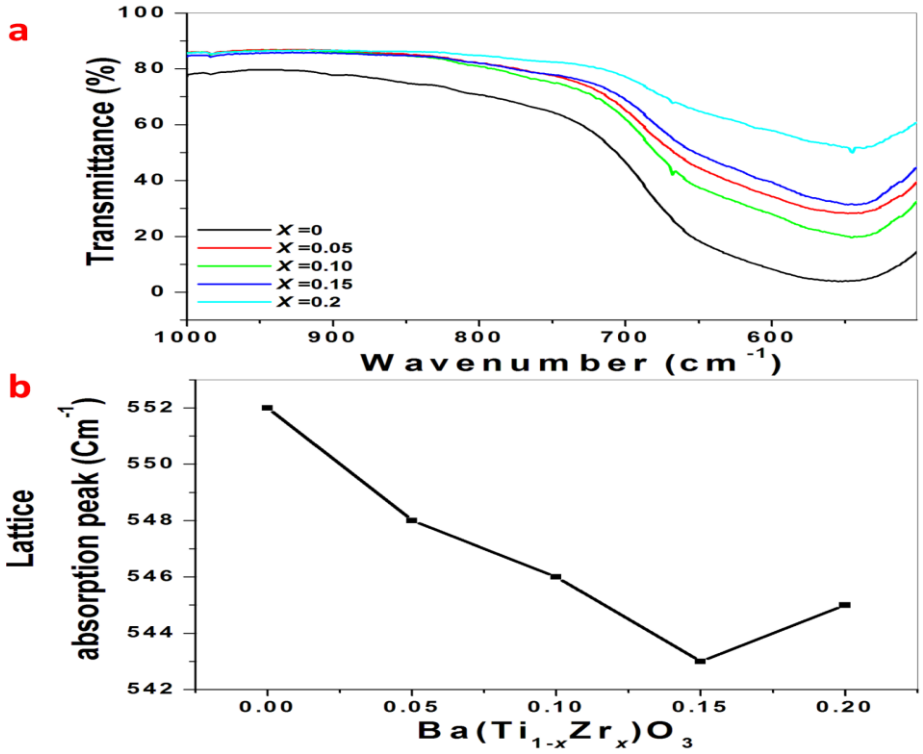

Figure 4.1.6 (a) FTIR spectra of $BaTi_{(1-x)}Zr_xO3$(*x* =0, 0.05, 0.1, 0.15 and 0.2) nanocubes prepared *via* Molten-Salt method. (b) The Lower wavelength shift of $BaTi_{(1-x)}Zr_xO3$ nanocubes, when increase in Zr^{4+} content into Ti^{4+} site.

A field emission scanning electron micrograph (FE-SEM) image depicted in **Figure 4.1.4 (c-e)** reveals the high purity of BTZO nanocubes (200 nm scale). As the increase in Zr^{4+} to $BaTiO_3$, a small size grains are formed other than nanocubes, and at the same time, the shape of the

nanocubes are literally modified. It is a very important issue to identify the doping limit to the $BaTiO_3$ composition without a change in tetragonal structure. The higher concentration of Zr^{4+} atoms into $BaTiO_3$ will result in polymorphic phases with minor impurities. The XRD patterns of as-synthesized BTZO nanocubes (0, 0.05, 0.1, 0.15 and 0.2) are matched and indexed with the reference codes (ICDD) 98-001-3771, 98-011-0292 and 98-044-1874 respectively. FE-SEM image shows **(Figure 4.1.7(a, b))** highly modified BTO nanocubes as well as the formation of minor grains (particle nature) by zirconium atoms (>10%).

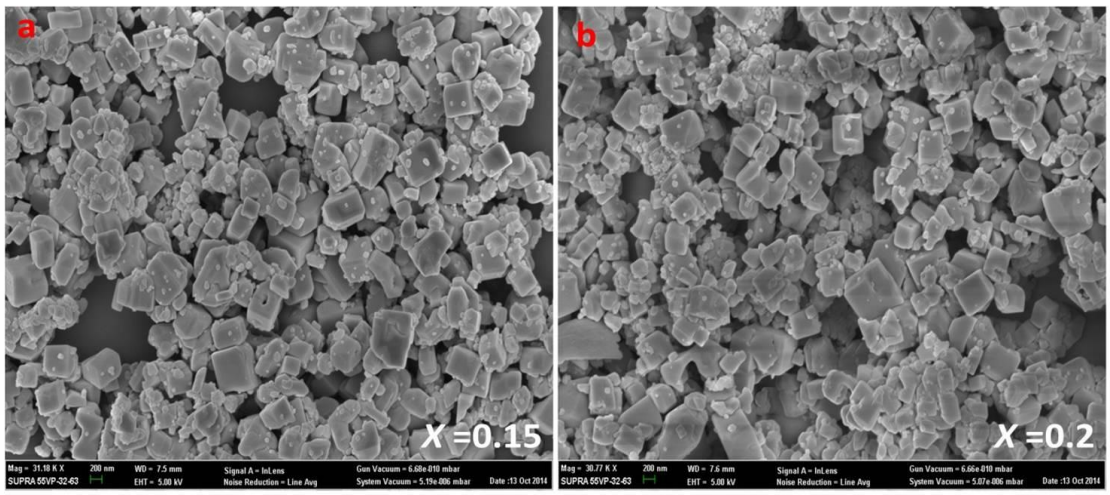

Figure 4.1.7(a, b) Surface morphology of BTZO (x =0.15, 0.2) nanomaterial at 200 nm scale.

Due to the higher concentration of Zr atoms in BTO, the Raman spectroscopy for the phase analysis shows the formation of minor peaks at 250 cm^{-1}, and 310 cm^{-1} confirms the polymorphic phase nature. The high-performance output signals of PNG will depend on the good dispersion of BTZO nanocubes into PVDF matrix and phase formation of piezoelectric materials ($BaTi_{1-x}Zr_xO_3$). Tetragonal BTZO exhibits ferroelectric properties as a result of the lattice distortion of the Ti-ion coordinate with the octahedral oxygen groups and the substitution of Zr-ion in place of Ti-site[29, 38, 39]. **Figure 4.1.8a** shows the Raman shift of $BaTi_{0.9}Zr_{0.1}O_3$/PVDF hybrid film replicates the well processed $BaTi_{0.9}Zr_{0.1}O_3$ nanocubes into PVDF polymer matrix. This indicates

no change in tetragonal structural modes 307 cm^{-1}, 727 cm^{-1} of BTZO nanocubes into PVDF matrix (Sonication process by 1 hr and cured at 60 ˚C / overnight). The inset shows the Raman spectrum of polarized PVDF phase (**Figure 4.1.8a**). The X-ray diffraction is used to identify the characteristic phase of PVDF matrix, indicates the diffraction peak at 20.36° correspond to the polar-β phase[41] (**Figure 4.1.8b**). In sonication process, the sound energy plays a key role to obtain the homogeneous distribution of BTZO nanocubes into PVDF matrix, removal of dissolved gases from liquids by breaking the intermolecular interactions. The surface of the hybrid film, magnified image of a cross-sectional view of the PNG and surface of pure PVDF film was analyzed by FE-SEM, is shown in **Figure 4.1.8(c-e)**.

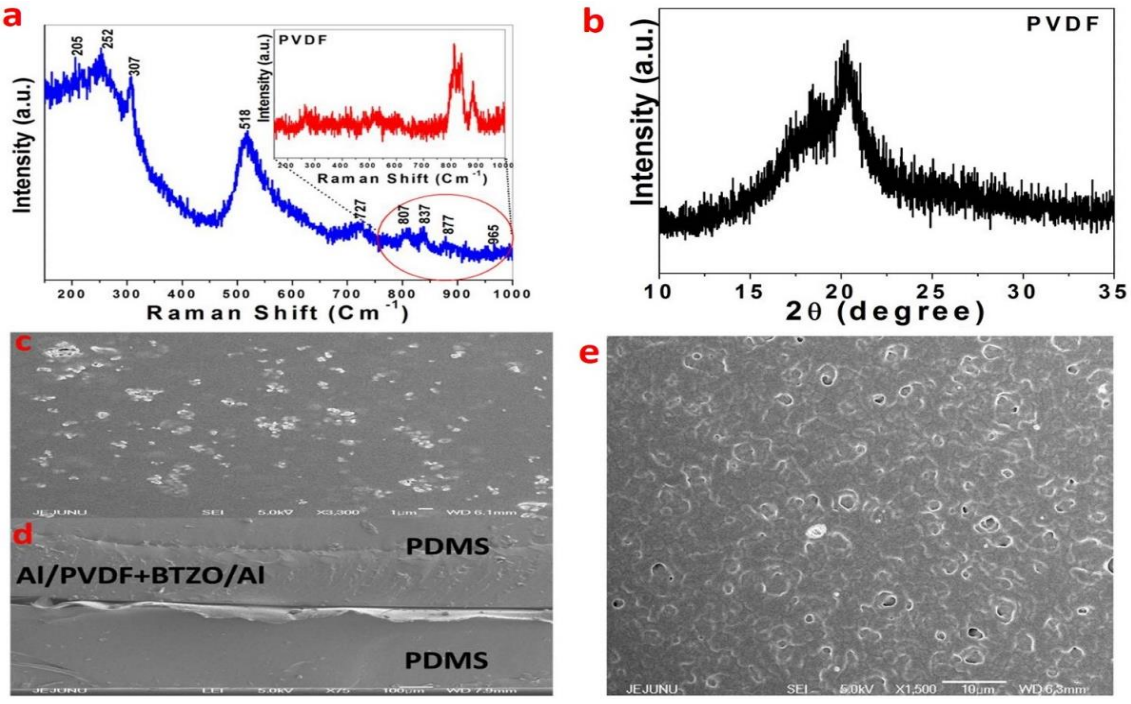

Figure 4.1.8 (a) Typical Raman spectrum of the $BaTi_{0.9}Zr_{0.1}O_3$/PVDF piezoelectric composite film by ultrasonication probe method. The inset shows the Raman spectrum of PVDF polymer matrix (b) XRD pattern of processed PVDF film by Ultra Sonication confirms the existence of the β-phase. (c) FE-SEM image of $BaTi_{0.9}Zr_{0.1}O_3$/PVDF hybrid film showing its well dispersed $BaTi_{0.9}Zr_{0.1}O_3$ nanocubes into polar β-phase of PVDF polymer matrix (d) A magnified cross-sectional FE-SEM image of the PNG device showing its Al coated top and the bottom surface of the hybrid film covered with PDMS stamps. (e) The surface morphology of PVDF film (Scale: 10 μm).

4.1.3.2 Energy harvesting analysis of piezoelectric nanogenerator

The working mechanism of the hybrid film based PNGs was investigated. The working principle of the PNG is based on the piezoelectric properties of BTZO nanocubes, and the creation of an inner piezoelectric field inside the BTZO nanocubes in PVDF matrix, under an applied mechanical load with cyclic frequency. Since Zr^{4+}-ion in place of Ti^{4+}-site will enhance (or reduce) the piezoelectric coefficient, electromechanical coupling factor, which purely depends on the amount of Zr doping[29]. If $Zr \leq 0.1$ has normal ferroelectric properties with an enhanced piezoelectric coefficient (200-300 pC/N[29, 30, 42], 420 pC/N[43] at 100 hr sintering) as compared to $BaTiO_3$ (bulk). When Zr > 0.1 concentration, relaxor ferroelectric behavior with smaller piezoelectricity[29, 30, 42, 43] respectively.

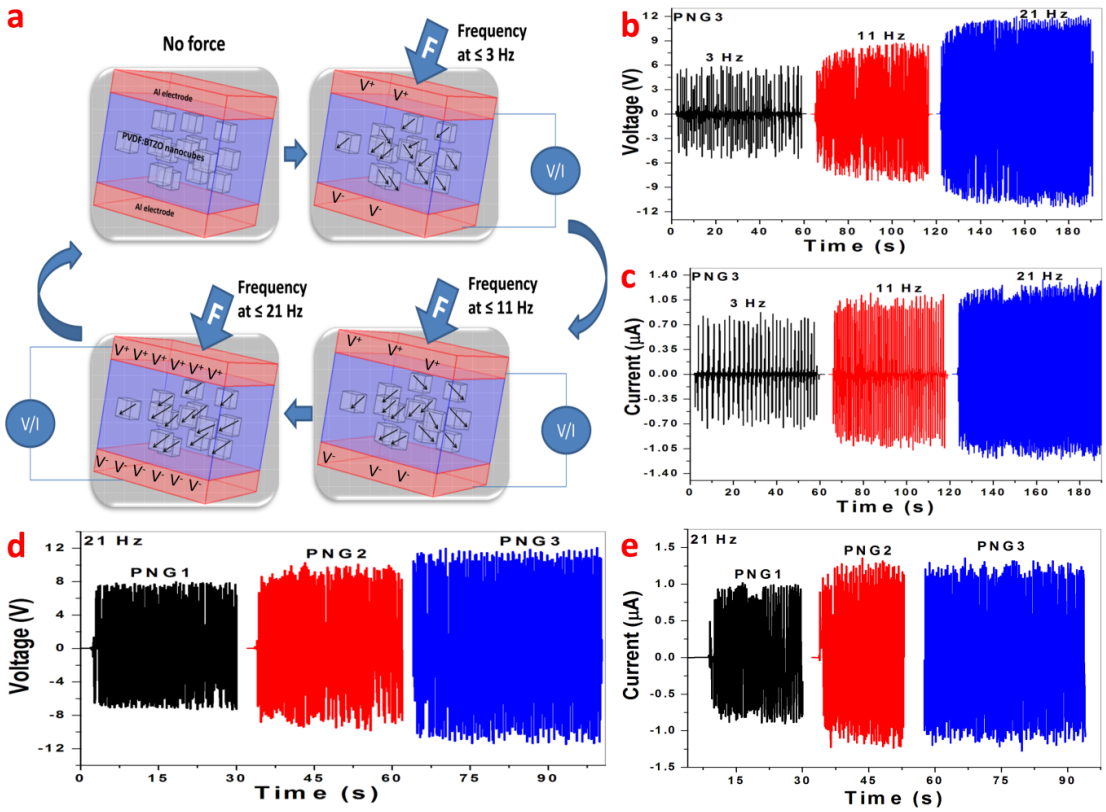

Figure 4.1.9 (a) Proposed mechanism of the BTZO nanocubes: PVDF-based PNG. No output signal is observed in the absence of external mechanical load. The electrical output signal is observed for PNG under external mechanical load (11N) with respect to cyclic frequency (3 Hz, 11 Hz and 21 Hz) of the electro-dynamic shaker. (b, c) The output voltage and current of PNG3

as a function of the cyclic frequency of mechanical load. (d, e) Comparison of the electrical output voltage and current of different PNGs: PNG1, PNG2, and PNG3 upon the application of mechanical load at 21 Hz cyclic frequency.

The piezoelectric potential generation is mainly depending upon the cyclic frequency of the load is shown in **Figure 4.1.9a**. In PNGs, no output signal is observed in the absence of external mechanical load due to the random orientation of the dipoles existing in the hybrid film (BTZO/PVDF), which results in zero net dipole momentum (**Figure 4.1.10)**. An external compressive load (11 N) with low cyclic frequency 3 Hz is applied across PNGs; low piezoelectric-potential is generated across the electrodes. It may be due to either capacitance or the initiation of the piezoelectric behavior. However with the application of same load with high cyclic frequency (3 Hz to 11 Hz and reached to 21 Hz), the piezoelectric potential is reached to the maximum (**Figure 4.1.9(b, c)**), which indicates that the orientation of electric dipoles in hybrid film are in particular direction due to the stress-induced poling effect

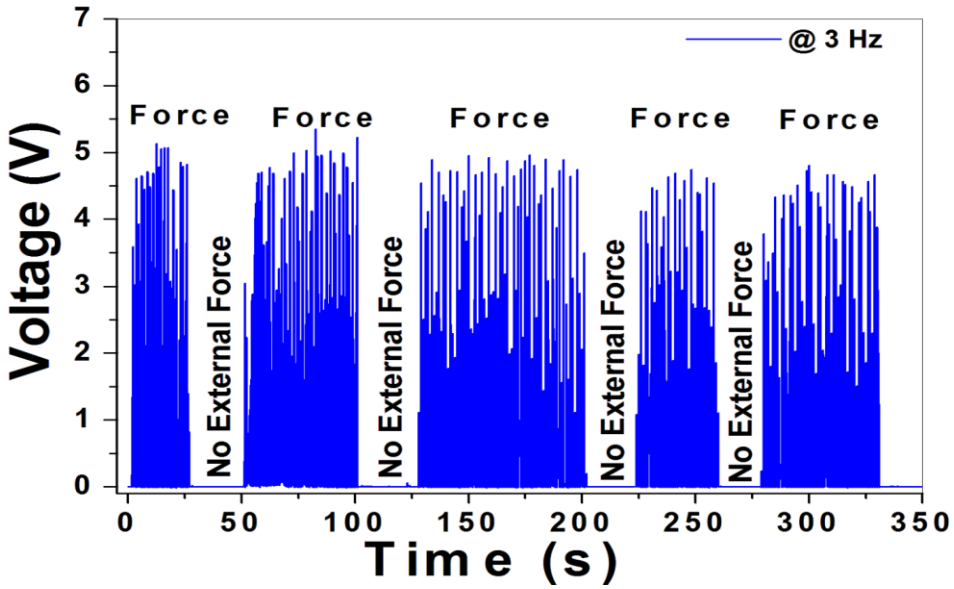

Figure 4.1.10. The electrical output signal is measured for PNG3 under external mechanical load (11N) with respect to cyclic frequency 3 Hz of the electro-dynamic shaker. No output signal is observed in the absence of external mechanical load.

In present work, we correlated the generated piezoelectric potentials of $BaTiO_3$/PVDF (abbreviated as PNG1) and $BaTi_{(1-x)}Zr_xO_3$ (X = 0.05, 0.1)/PVDF based PNGs (abbreviated as PNG2, PNG3) were mechanically triggered by electro-dynamic shaker that provide a dynamic impact with controlled frequency, speed and force. We observed that the voltage, current of a PNGs are affected by the cycling frequencies (3 Hz to 21 Hz) at fixed input amplitude (or load) of the shaker. At the first instant, the electrical output of PNG1 was achieved to be 3.42 V and 0.44 μA by the cyclic pushing-releasing frequency at 3 Hz with a fixed load of the shaker (**Figure 4.1.11(a, b)**). During the pushing process, the dipoles are oriented in perpendicular to the plane of the film. This results in accumulation of opposite charge carriers on top and bottom surface of the $BaTiO_3$/PVDF film, which is collected by external electronic circuitry[22]. Once the external stress is released, the piezoelectric potential vanishes and charge carriers move back to the original state. When the cyclic frequency of the load increases from 3 Hz to 21 Hz, the output varies from 3.42 V, 0.44 μA to 7.99 V and 1.01 μA (**Figure 4.1.11(a, b)**). It indicates the cyclic frequency dependent behavior of hybrid $BaTiO_3$/PVDF film.

The generated piezoelectric potential distribution is mainly due to the stress-induced transient flow of free charge carriers[14, 22, 44], is aroused by active β-phase of PVDF (positive and negative charge carriers displaced in VDF molecule) and due to the non-centrosymmetric $BaTiO_3$, where the atoms displace from the equilibrium positions. It is well known that the β-phase of PVDF have small piezoelectric potential generation[16, 45] as compared to other piezoelectric materials like PZT[18], $BaTiO_3$[14], and KNLN[46] respectively. Here, the PVDF utilizing in two ways, on the one hand it works as substrate support the whole structure. The flexible nature of PVDF will reduce processing time to make the device dimensions for specific applications. On the other hand, PVDF piezoelectric coefficient is negative[16] and while that for $BaTiO_3$ is positive. By

proper poling direction and compressive force, may possible to enhance the electric potential difference across the top and bottom Al electrodes.

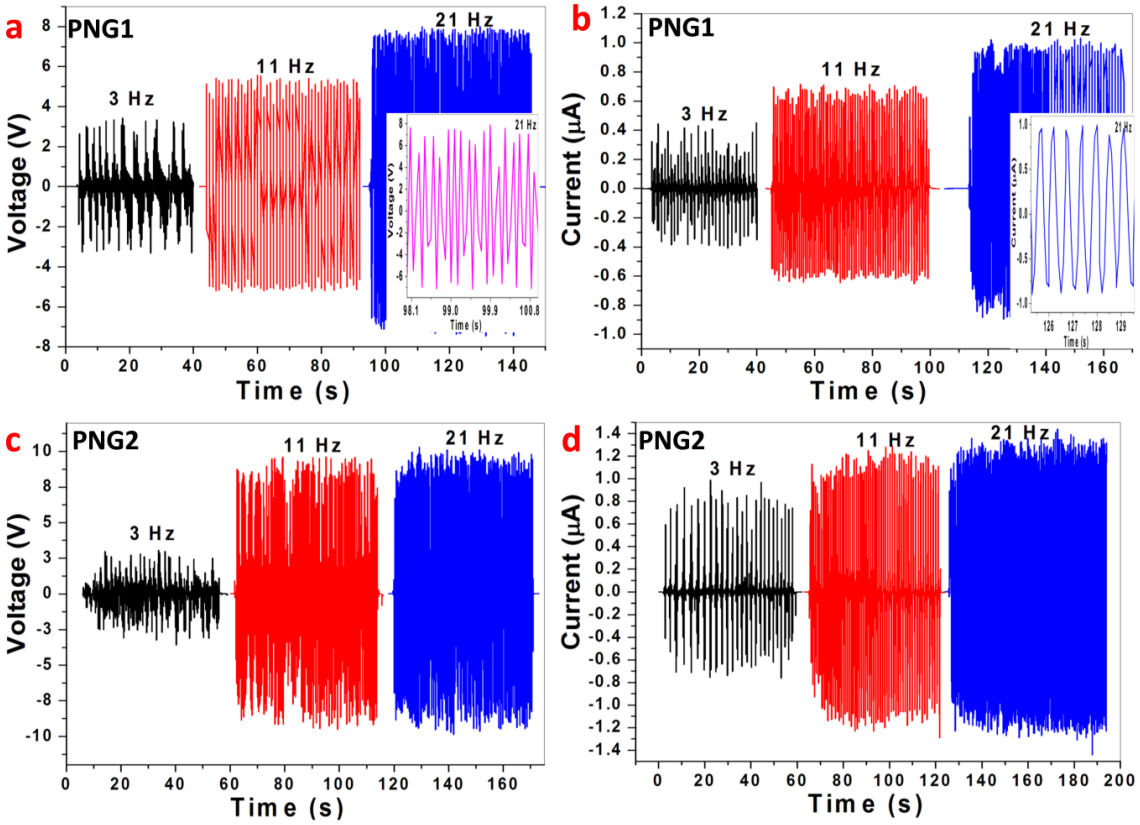

Figure 4.1.11 Typical electrical outputs of PNGs triggered by a shaker with cyclic pushing-releasing frequencies of 3 Hz, 11 Hz and 21 Hz at fixed load 11N. (a, b) Output voltage and current of the PNG1 device ($BaTiO_3$/PVDF hybrid film). The inset shows the enlarged views of voltage and current at frequency 21 Hz with the fixed load. (c, d) Output voltage and current of the PNG2 device ($BaTi_{0.95}Zr_{0.05}O_3$/PVDF hybrid film).

However, we analyzed the contribution of poled PVDF based PNG (Without BTZO nanocubes,) under cyclic frequency 21 Hz with same mechanical load, shows less output (**Figure 4.1.12**) as compared to hybrid film (BTZO/PVDF) based PNG (Figure 4.1.9(d, e)). The un-poled PVDF based PNG has been analyzed shows very low output **(Figure 4.1.13)**, indicates the potential generation is purely based on piezoelectric effect (not triboelectric effect). The

generated piezoelectric potential will depend on the piezoelectric coefficient, can be expressed as:[47, 48]

$$V_{OC} = g_{33}\sigma Yt \qquad \text{(E4.1.1)}$$

Where σ is the strain in the perpendicular direction, g_{33} is the piezoelectric voltage constant $(g_{33} = d_{33}/(\varepsilon_0 K))$, d_{33} is the piezoelectric charge constant, ε_0 is the permittivity of free space, *K* is the dielectric constant or relative permittivity, *Y* is Young's modulus, and *t* is the thickness of the device. According to formula (I), the factors will improve the generated output voltage of the device is as follows: high d_{33}, low relative permittivity (*K*) and high elastic modulus.

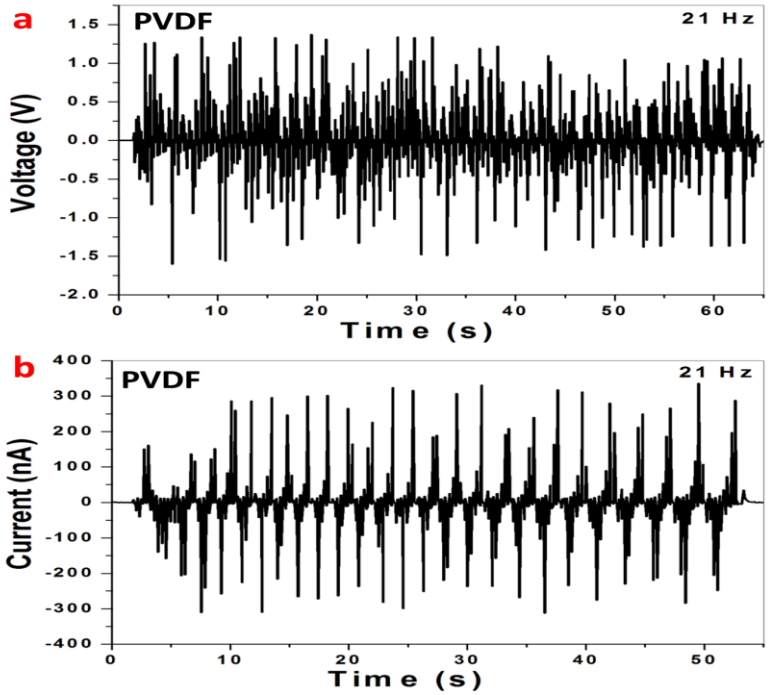

Figure 4.1.12 (a) Open circuit Voltage and (b) Short circuit Current of PVDF based PNG (Poled PVDF sample) triggered by a shaker with the cyclic pushing-releasing frequency of 21 Hz at fixed load 11N.

The $BaTiO_3$ nanocubes embedded with polymer matrix will improve the elastic modulus and reduce the dielectric constant[21]. However, the internal resistance of the piezoelectric film will change according to the driving frequency and mechanical load. At a low driving frequency of mechanical load, the centers of both positive and negative charge carriers may not separate totally; result in smaller piezoelectric potential. While increasing the driving frequency of mechanical load, the centers of both positive and negative charge carriers separation will reach to the maximum value (i.e. the maximum number of dipoles will orient in one direction), corresponds to the generation of higher piezoelectric potential in nanogenerator shown in **Figure 4.1.9(b, c)**.

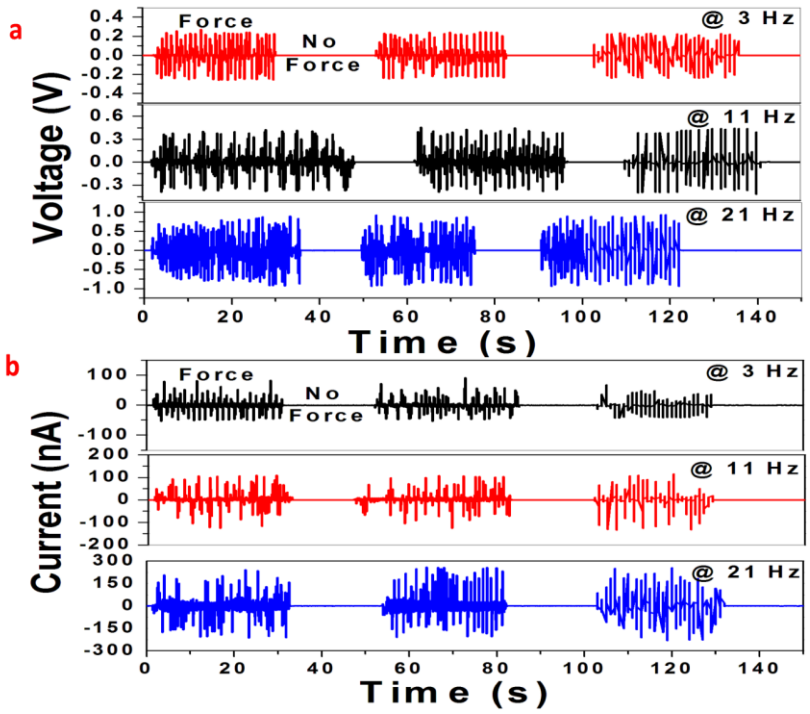

Figure 4.1.13 (a) Open circuit voltage and (b) short circuit current of PVDF based PNG (Without poling) upon cyclic frequencies of 3 Hz, 11 Hz and 21 Hz at constant mechanical load (11N).

Recently, the different cycling-frequency dependent electrical output of PNGs was examined well. According to the fundamental piezoelectric theory[16], the short-circuit current can be written as

$$I = d_{33} EA\varepsilon \qquad \text{(E4.1.2)}$$

Where I is the generated current, d_{33} is the piezoelectric coefficient, E is Young's modulus, A is the cross-sectional area, and ε is the applied strain. The energy conversion efficiency of the PNGs is the ratio of generated electrical energy and applied mechanical energy. After that, we characterized the electrical output of PNG, based on the compositional dependence of nanomaterials (different Zr^{4+} ratios doped to $BaTiO_3$ nanocubes in place of the Ti^{4+} site) embedded with PVDF matrix under the periodic motion of mechanical stress. The result of all PNGs indicates the cyclic frequency dependent behavior at a fixed load. The amplitude of the output voltage and current generated from PNG2 are10.3 V, 1.35 μA at 21 Hz cyclic frequency (load = 11 N), after the doping of 5 % mole content (Zr^{4+}) to $BaTiO_3$ nanocubes. Similarly, the voltage and current for PNG3 are 11.9 V and 1.35 μA after the doping of 10 % mole content (Zr^{4+}) to $BaTiO_3$ shown in **Figure 4.1.9(d, e)**. It clearly shows the enhanced electrical output of Zr doped PNGs as compared to un-doped $BaTiO_3$ based PNG. It may be due to the enhancement in piezoelectric coefficient (d_{33}) of the hybrid film. The increment in d_{33} is due to the coexistence of polymorphic phase boundaries[29], such as orthorhombic (Amm2) + tetragonal (P4mm) to orthorhombic (Amm2) + rhombohedral (R3m) phases. The recent study shows the average piezoelectric response (d_{33} = 290 pC/cm^2 to 285 pC/cm^2) in the composition range $0.02 \leq x \leq 0.08$ ($BaTi_{1-x}Zr_xO_3$) does not vary significantly with the composition, which is greater than $BaTiO_3$ (bulk) piezoelectric coefficient (d_{33} = 150 pC/cm^2) [29]. The phase coexistence may be

possible due to the higher ionic radius of Zr^{4+} ion substitution in Ti^{4+} ion site, which intern creates the lattice distortion by TiO_6 octahedron of $BaTiO_3$. According to formula (I), the V_{OC} is directly proportional to d_{33}, the electrical output voltage increased from 0% to 10% of Zr^{4+} of $BaTiO_3$ along with PVDF matrix, indicates the d_{33} increment behavior. As we increased the doping concentration > 10% of Zr^{4+}-ion into $BaTiO_3$/PVDF based PNG, have lower electrical output as compared to pure $BaTiO_3$ based PNG **(Figure 4.1.14)**, due to the smaller piezoelectric coefficient[29]. The PNGs instantaneous power delivered to the load could be estimated from the following equation:[19, 49]

$$P = \frac{1}{T}\int \frac{V^2(t)}{R} dt \qquad \text{(E4.1.3)}$$

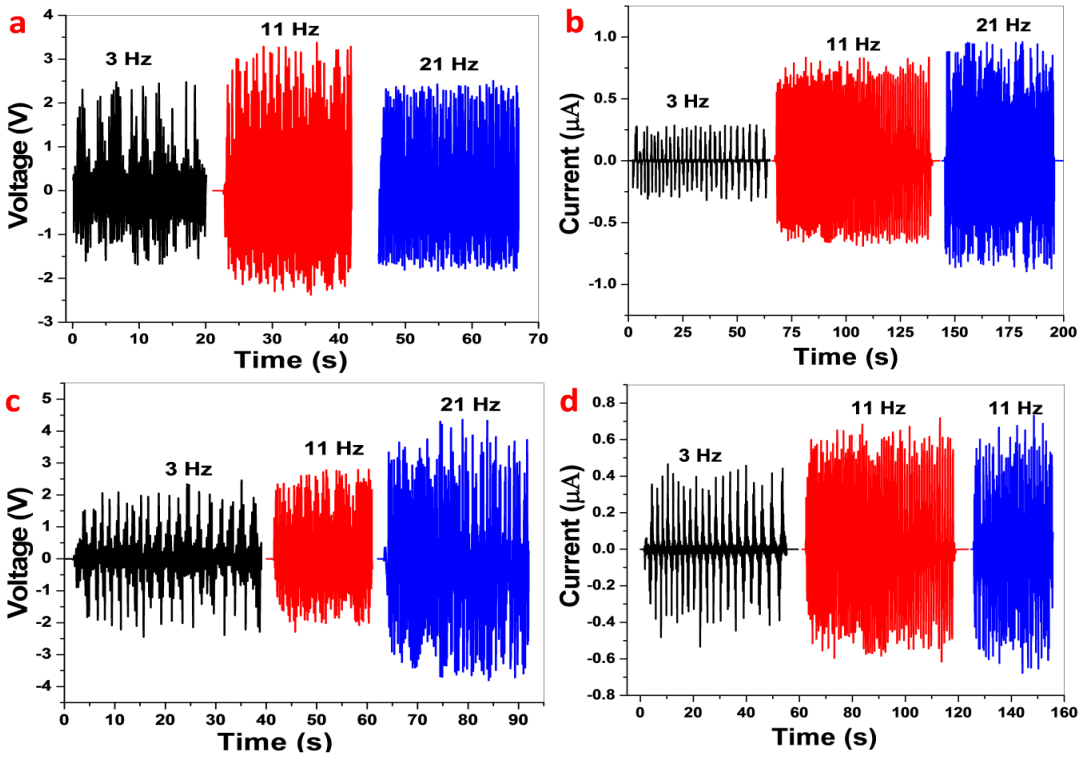

Figure 4.1.14 Typical electrical outputs of PNGs triggered by a shaker with cyclic pushing-releasing frequencies of 3 Hz, 11 Hz and 21 Hz at fixed load 11N. (a, b) Output voltage and

current of PNG4 device ($BaTi_{0.85}Zr_{0.15}O_3$/PVDF hybrid film) (c, d) Output voltage and current of PNG5 device ($BaTi_{0.80}Zr_{0.2}O_3$/PVDF hybrid film).

Where, P is the power and V is the real-time peak voltage across the load resistance R and T is the period of mechanical load. The PNG device is a planar structure; therefore the power scales will depend on the active area (A) of the device. The voltage of PNG3 was measured by connecting output terminals across the variable resistor (R) and correspondingly the instantaneous area power density evaluated by using the above equation (E4.1.3) divided by the area (A) of PNG. The power is maximum (0.14 μW/Cm^2) for PNG3 across the load resistance 10 MΩ at 3 Hz cyclic frequency of the load 11N shown in **Figure 4.1.15a**. It indicates the Maximum optimum load resistance (or equivalent) of the PNG3 device is 10 MΩ. Similarly, the output voltages of all PNGs were evaluated across the resistance 10 MΩ at 3 Hz, 21 Hz cyclic frequency with fixed load 11 N shown in **Figure 4.1.15b**. It clearly shows that the Zr^{4+}doped $BaTiO_3$/PVDF based device have higher power density as compared to pure $BaTiO_3$. The detailed equivalent resistance of a PNG can be evaluated as: [4]

$$R_p = \frac{d}{A\varepsilon_p f} \qquad \text{(E4.1.4)}$$

Where, f is the frequency of the external force and d , A, and ε_p thickness, area, and permittivity of the hybrid film (BTZO/PVDF). Besides the instantaneous area power density, charging ability of the PNG is also measured and analyzed. The experiment was carried at 21 Hz cyclic frequency with external force 11 N is applied to the PNG3. The generated output voltage is rectified to continuously charge a 1 μF capacitor; the output voltage reaches to ≈ 5 V in ≤ 50 s **(Figure 4.1.15c)**. Next, the commercial five green LEDs lit up with generated piezoelectric potential for all devices by using the bridge rectifier circuit without any storage devices **(Figure**

4.1.15d). The durability test is conducted to confirm the mechanical stability of the PNG at 21 Hz cyclic frequency with an applied load 11 N is shown **Figure 4.1.15e**. The current of the PNG3 does not have significant changes during 500 s interval. Next, to estimate the sensitivity of the PNG, the experiment was conducted by successive taping with right-hand finger (gently manner) and the rectified electrical response for all devices was shown in **Figure 4.1.16**. The generated piezoelectric potential is up to 4 V driven by biomechanical force, which is more useful to light the commercial LEDs. It indicates that, proposed energy harvesting device is a potential candidate for remote area applications, where the battery energy is necessary.

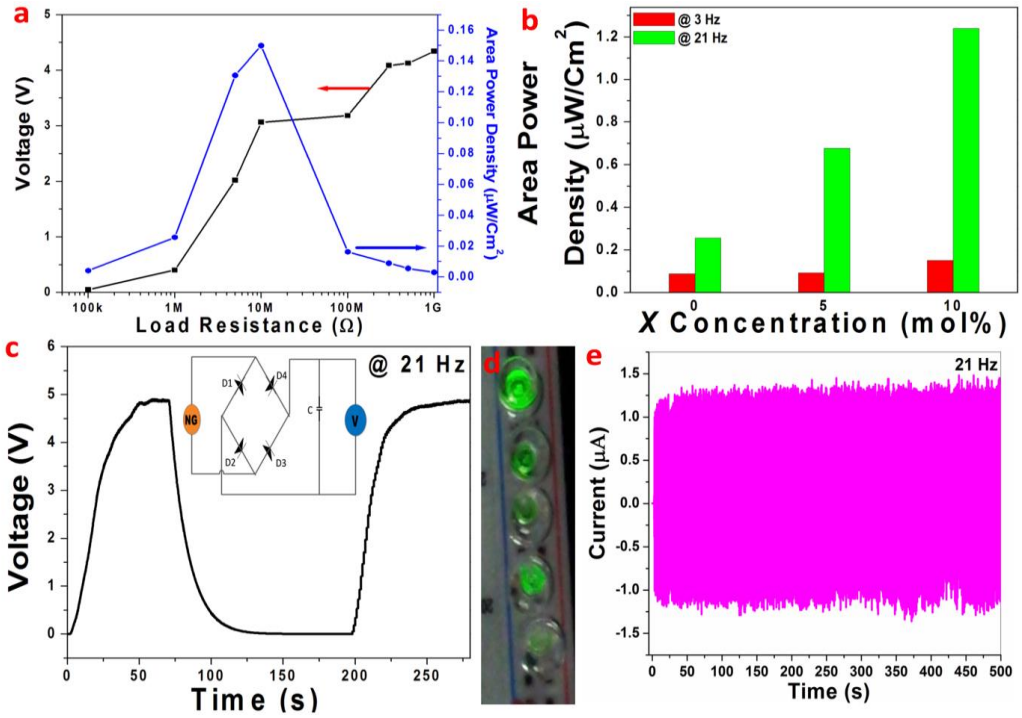

Figure 4.1.15 (a) At the cyclic frequency of 3 Hz with fixed load, output peak voltage and area power density dependence on load resistance of PNG3 device (b) Comparison of area power density of different PNGs (PNG1, PNG2 and PNG3) upon cyclic frequency 3 Hz, 21 Hz of mechanical load at maximum load resistance 10 MΩ, shows the role of Zr^{4+} (x mol%) substitution into $BaTiO_3$ (c) Voltage across a storage capacitor (1μF) when being charge by PNG3 with the full wave bridge rectifier at 21 Hz. (d) Commercial five green LEDs lit up with rectified piezoelectric potential from the PNG3 without any storage device (e) Output current of PNG3 under 21 Hz frequency demonstrating the stability of the nanogenerator.

The polarity test was conducted to confirm the piezoelectric output driven by biomechanical force is shown **Figure 4.1.16d**. The above-mentioned results demonstrate that alternating energy generated from PNG devices is stored in capacitors (or without) and subsequently used for self-powered sensors, implantable devices and low power electronic applications. The PVDF:BTZO nanocubes weight ratio (1 gm: 0.25gm) has been fixed for simplicity. We also observed that, the PNG performance could be varied by changing the weight ratio of PVDF: BTZO, external mechanical stress, electric poling and piezoelectric coefficient of the hybrid film.

Table 4.1 Comparison of the proposed device performance with other reported organic and composite piezoelectric nanogenerators

Material	**Microstructure**	**V_{OC} (V)**	**I_{SC} (nA)**	**References**
PVDF/$BaTiO_3$	Nanocubes	7.99 @ 11 N load	1010 @ 11 N load	Present work
PVDF/$Ba(Ti_{0.95}Zr_{0.05})O_3$	Nanocubes	10.03 @ 11 N load	1350 @ 11 N load	Present work
PVDF/$Ba(Ti_{0.9}Zr_{0.1})O_3$	Nanocubes	11.99 @ 11 N load	1360 @ 11 N load	Present work
$BaTiO_3$/PDMS	Nanotubes	5.5	350	(22)
$BaTiO_3$/MW-CNT/PDMS	Round shape	3.2	350	(40)
$BaTiO_3$ Thin film		1	26	(50)
PAA/13-nm OA-$BaTiO_3$	Cubic-like	1.8	700	(39)
Virus-template BTO/PDMS		6	300	(51)
$BaTiO_3$	Single Nanowire	0.021	1.3	(21)
BZT-xBCT	Nanowires	3.25	55	(52)
PVDF	Single Fibers	0.03	3	(16)
PVDF	Fibers	0.076	39	(45)
PVDF-TrFE		7	58	(53)

However, the proposed PNGs output performance is better and even high output as compared with few published nanogenerator reports based on individual $BaTiO_3$, PVDF and composite

structures is shown in **Table 4.1.** The process used to fabricate the PNGs is relatively simple, cost effective and possible for large scale production. This kind of PNGs has more advantages as compared to the lead based PNGs, due to its sensing capability, biocompatibility[23], nontoxic[25, 46] and eco-friendly behavior [47].

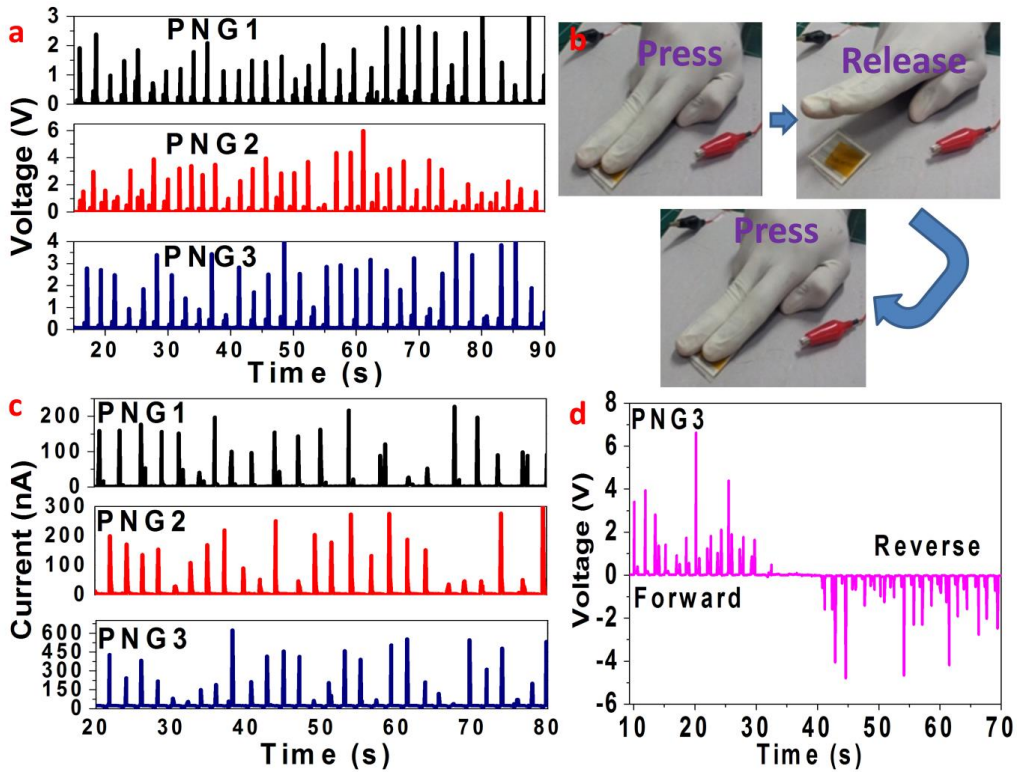

Figure 4.1.16 Rectified electric output of PNGs. (a) open circuit voltage of all PNGs under biomechanical force (b) The optical photograph of the periodic press and release force conditions by right hand finger of human hand (c) Short circuit current of all PNGs under biomechanical force (d) Polarity test was conducted by changing the forward and reverse connections of PNG3 device.

4.1.3.3 Self-powered Fluid Velocity sensor

A flexible PNG can be used as active sensor, capable to measure different water velocity at outlet pipe due to its high sensitivity and high conformability. To demonstrate this, a PNG with a size of 2.5 cm x 2.5 cm was attached to the fixed rigid and placed perpendicular to the water flow shown in **Figure 4.1.17a**. To avoid the direct surface contact between water and PNG,

polyethylene (PE) cover attached on surface of PNG. The electrical response of PNG3 under different water velocities at outlet pipe is shown in **Figure 4.1.18(a, b)**. The PNG was driven by rotating faucet with fixed position having two conditions, water ON and water OFF with periodic time intervals. At water velocity 31.43 m/s, the achieved average output voltage and current of PNG3 is 26 mV and 8 nA during the water ON condition and water OFF condition, the voltage and current are 80 mV and 10 nA respectively. Upon increasing the water velocity from 31.43 m/s to 78.6 m/s and 125.7 m/s, the corresponding output voltage and current reached to 213 mV, 466 mV and 19 nA, 34 nA during the water ON condition.

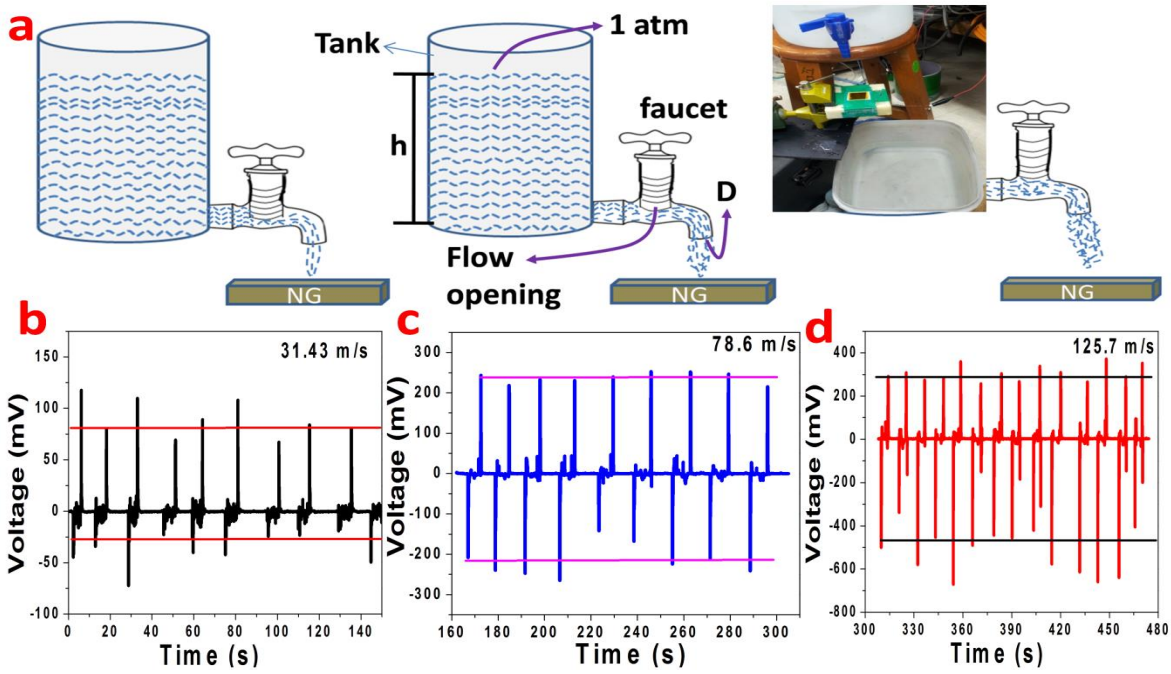

Figure 4.1.17 PNG3 as a self-powered sensor to measure the different water velocities flowing through the outlet pipe. (a) The schematic diagram of the control experiment and inset shows photograph of the controlled experimental setup. (b, c and d) Open circuit voltage of PNG3 under different water velocities 31.43 m/s, 78.6 m/s and 125.7 m/s.

The mechanism involved during water ON and OFF conditions is similar to the force acting on PNG by pushing and releasing load with periodic manner. During the water ON condition, the induced charges moves across the top and bottom surface of the PNG, result in piezoelectric

potentials with different polarities were generated in the same plane of the NG. During water OFF condition, the induced charges will moves back to the original sites. In order to identify the water velocity at outlet pipe, a controlled experiment was performed by rotating a faucet to estimate the amount water falling per second (ml/s). The water flow rate (Q) in pipe as function of faucet rotation (i.e. position) can be approximated as $Q = (V / A)$, where V is the velocity at outlet and A is area of the circular plastic pipe shown in **Figure 4.1.18c**. In order to maintain the constant pressure for different water velocities, a water tank was filled with fixed amount of water having a height (*h*), and pressure (*p* = 1 atm) respectively. By apply the steady–flow energy equation[54] between top surface of the tank and outlet pipe with no heat transfer and no shaft work

$$\frac{P_1}{\rho} + \frac{1}{2}V_1^2 + gh_1 = \frac{P_2}{\rho} + \frac{1}{2}V_2^2 + gh_2 + gh_f \qquad \text{(E4.1.5)}$$

But $P_1 = P_2 = P_{atm}$ (Atmospheric pressure), due to the largely one directional flow acting in the pipe and $V_1 \approx 0,$ and $V_2 \approx V$ is the water velocity at outlet. Therefore the pipe head loss can be written as $h_f = f\frac{L}{D}\frac{V^2}{2g}$ (E4.1.6)

Where L, D and g represents the length, diameter of plastic pipe and specific gravity of water and $f = 0.316/(\mathrm{Re}^{\frac{1}{4}})$ is the friction factor for smooth pipe flow). For a given flow rate Q, the turbulent pressure drop decreases with diameter even more sharply than the laminar flow. In the present case, the diameter of the pipe is kept constant and the flow rate and average water velocity can be controlled by using the faucet. The flow rate of water can be written as $Q = V \times A$, where V is the average velocity of water flowing through the pipe and A is the

area of the pipe respectively. Here the flow rate represents the amount of water collected per 5 seconds by rotating the faucet at particular position and with the help of flow rate equation the average velocity of water has been calculated. The type of flow (laminar or turbulent) can be approximated by using Reynolds number ($\mathrm{Re} = \frac{VD}{\nu}$), where ν is the kinematic viscosity of water ($\frac{\mu}{\rho}$), μ is the dynamic viscosity of fluid in Kg/m. s and ρ is density of water in (Kg/m^3). The calculated Reynolds number is in the range of 10^4 to 10^5 confirms the turbulent flow nature. The basic experiment demonstrates another exciting application of PNG to monitor the water velocity flowing through the pipe. Here the PNG kept exactly perpendicular to the flow channel with the fixed support. By changing the different flow rates through the pipe, the electrical output of PNG3 was shown in **Figure 4.1.17**. The force acing on the PNG will indirectly depend on the water velocity at outlet. The generated piezoelectric potential is due to stress induced transient flow of charge carriers, which are collected by the Al electrodes across the top and bottom of the device.

The average maximum peak power of the PNG under water ON condition as function of different water velocities is shown in Figure 4.1.18. The average maximum peak power (w_e) generated by PNG under impact with water velocities can be evaluated as[16]:

$$w_e = \int VIdt \qquad \text{(E4.1.7)}$$

Where, V and I are the average measured output voltage and current of PNG. The achieved average maximum power is 0.2 nW for 31.43 m/s water velocity and increased up to 15.8 nW for 125.7 m/s. Similarly, the achieved average maximum peak power during water OFF condition was evaluated and shown in **Figure 4.1.18d**, which is quiet less as compared to ON condition. At

water OFF condition a small amount of water droplet's settling on PNG device, which in turn restrict the transient charge carriers motion. The above experiment reveals that, energy harvesting by piezoelectric composite *via* natural water motion, such as home water waste, sea water, rivers and even rains. This can be also useful as active sensor in various fields, like pump monitoring, process controlled field and HVAC (heating, ventilating and air conditioning).

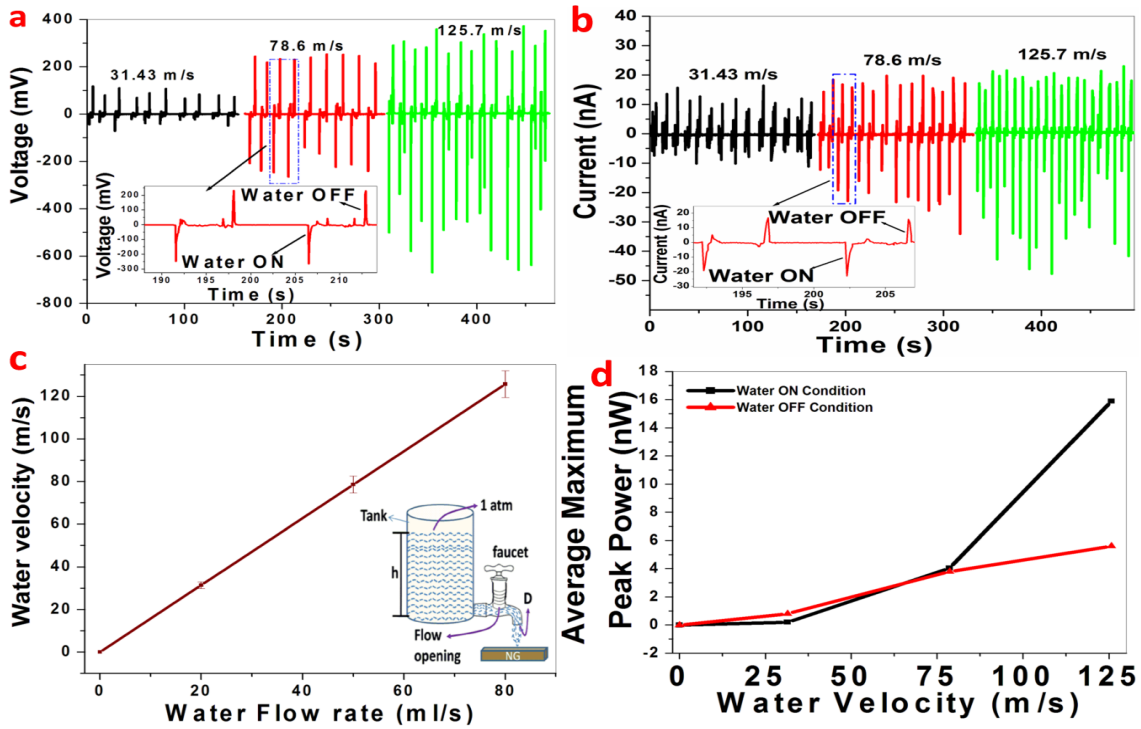

Figure 4.1.18 Demonstration of PNG3 as a self-powered sensor to measure different water velocities flowing through the outlet pipe. (a, b) Open circuit voltage and short circuit current of PNG3 under different water velocities 31.43 m/s, 78.6 m/s and 125.7 m/s. The insets of (a, b) shows output generated under water ON and OFF conditions. (c) Linear relationship between the water velocities (m/s) at outlet pipe and flow rate (ml/s) and the inset shows schematic diagram of the control experiment. (d) The generated average maximum output peak power (W =PI) obtained at different velocities under water ON condition. The inset shows obtained peak power under water OFF condition.

4.1.4 Conclusions

In summary, flexible PNGs were fabricated based on hybrid film composed of BTZO nanocubes and PVDF polymer matrix using an ultrasonication probe process. Next, successfully

demonstrated the PNGs functionality can be useful to interpret as a self-powered sensor, where the battery energy is necessary. The enriched crystalline BTZO nanocubes were successfully synthesized using low processing temperature (750 °C/3 hr) (i.e. molten-salt approach) as compared to the solid state reaction method (>1100 °C/2 hr). The Zr^{4+} doped (<10% mole content) PNG have piezoelectric output power generation (11.9 V, 1.36 μA) as compared to the BTO/PVDF based PNG (7.99 V, 1.01 μA) respectively. We observed the PNG performance will depend on the mechanical load; electric poling and piezoelectric coefficient (i.e. indirectly depend on the BTZO/PVDF weight ratios). This study demonstrates the PNG electrical output will depend on the compositional fluctuation and cyclic frequency of mechanical load. In addition, the generated PNG output power possible to store in capacitors, useful to drive commercial LEDs, low power electronic devices and self-powered sensors. By stability test using a cyclic pushing instrument, superb reproducibility and durability of the PNGs confirmed. Next, we have successfully demonstrated the application of PNG as a self-powered sensor to measure the water velocities at outlet pipe. The PNG based self-powered sensor have possible to operate at high fluid operating temperature (up to 120 °C), high pressure ranges with small device size. The reported PNG results are comparable as well as higher than many other lead free based PNG devices, which are valuable for active sensors, portable devices, pump monitoring and process control fields.

4.1.5 References

(1) Wang, Z. L. Adv. Mater. 2012, 24, 280-285.

(2) Rui, Zhang.; Lin, L.; Jing, Q.; Wu, W.; Zhang, Y.; Jiao, Z.; Yan, L.; Han, R. P. S.; and Wang, Z. L. Energy Environ. Sci. 2012, 5, 8528-8533.

(3) Xu, S.; Qin, Y.; Xu, C.; Wei, Y.; Yang, R.; Wang, Z. L. *Nat. Nanotechnol.* 2010, 5, 366-373.

(4) Yang, Y.; Zhou, Y.; Wu, J. M.; Wang, Z. L. *ACS Nano.* 2012, *6*, 8456–8461.

(5) Yu, A.; Zhao, Y.; Jiang, P.; Wang, Z. L. Nanotechnology. 2013, 24, 055501-055507.

(6) Lin, Z. H.; Cheng, G.; Wu, W.; Pradel, K. C.; Wang, Z. L. *ACS Nano.* 2014, 8, 6440–6448.

(7) Liu, H.; Zhang S.; Kathiresan, R.; Kobayashi T.; Lee, C. Appl. Phys. Lett. 2012, 100, 223905.

(8) Kwon, S. H.; Park, J.; Kim, W. K.; Yang, Y. J.; Lee, E.; Han, C. J.; Park, S. Y.; Lee, J.; and Kim, Y. S. **Energy Environ. Sci.** 2014, **7**, 3279-3283.

(9) Clair, D. St.; Bibo, A.; Sennakesavababu, V. R.; Daqaq, M. F.; Li, G. Appl. Phys. Lett. 2010, 96, 144103.

(10) Wang, Z. L.; and Song, J. Science. 2006, 312, 242-246.

(11) Hu, Y.; Yang, J.; Jing, Q.; Niu, S.; Wu, W.; Wang, Z. L. *ACS Nano.* 2013, *7*, 10424–10432.

(12) Yang, Y.; Guo, W.; Pradel, K. C.; Zhu, G.; Zhou, Y.; Zhang, Y.; Hu, Y.; Lin, L.; Wang, Z. L. *NanoLett.* 2012, 12, 2833-8.

(13) Yang, J.; You, J.; Chen, Chun. Chao.; Hsu, W. C.; Tan, H.R.; Zhang, X. W.; Hong, Z.; and Yang, Y. *ACS Nano.* 2011, 5, 6210-6217.

(14) Shin, S. H.; Kim, Y. H.; Lee, M. H.; Jung, J. Y.; Nah, J. *ACS Nano*. 2014, 8, 2766-2773.

(15) Balasubramaniam, S.; Rajneesh, M.; Thiyagarajan, K.; and Sang-Jae, K. ***RSC Adv.***2013, **3**, 16646-16656.

(16) Chang, C.; Tran, V. H.; Wang, J.; Fuh, Y. K.; Lin, L.; *NanoLett.* 2010, *10*, 726–731.

(17) Wu, J. M.; Chen, K. H.; Zhang, Y.; Wang, Z. L. ***RSC Adv.***2013, **3**, 25184-25189.

(18) Park, K.-I, P.; Son, J. H.; Hwang, G. T.; Jeong C. K.; Ryu, J.; Koo, M.; I, Choi.; Lee, S. H.; Byun, M.; Wang, Z. L.; and Lee, K. J. *Adv. Mater.* 2014, 26, 2514-2520.

(19) Wu, W.; Bai, S.; Yuan, M.; Qin, Y.; Wang, Z. L.; Jing, T. *ACS Nano.* 2012, 6, 6231–6235.

(20) Xu, S.; Yeh, Y. W.; Poirier, G. P.; McAlpine, M. C.; Register, R. A.; and Nan, Y. *NanoLett.* 2013, 13, 2393–2398.

(21) Xia, N.; Fei, W.; Anan, L.; Qi, X.; Zhi, Y.; Yong, Q. *Sci. Adv. Mater.* 2013, 5, 1-7.

(22) Lin, Z. H.; Yang, Y.; Wu, J. M.; Liu, Y.; Zhang, F.; and Wang, Z. L. *J. Phys. Chem. Lett.* 2012, 3, 3599−3604.

(23) Yuan, M. M.; Cheng, L.; Xu, Q.; Wu, W. W.; Bai, S.; Gu, L.; Wang, Z.; Lu, J.; Li, H. P.; Qin, Y.; Jing, T.; and Wang, Z. L. *Adv. Mater.* 2014, DOI: 10.1002/adma.201402868.

(24) Wang, Z.; Zhao, K.; Guo, X.; Sun, W.; Jiang, H. L.; Han, X. Q.; Tao, X. T.; Cheng, Z. X.; Zhao, H. Y.; Kimura, H.; Yuan, G. L.; Y, J.; and Liu, Z. G. *J. Mater. Chem. C.* 2013, 1, 522–530.

(25) Liu, W. F.; and Ren, X. B. *Phys. Rev. Lett.* 2009, 103, 257602-257605.

(26) Fu, H.; Cohen, R. E. *Nature.* 2000, 403, 281−283.

(27) Hernandez, B. A.; Chang, K. S.; Fisher, E. R.; Dorhout, P. K. *Chem. Mater.* 2002, 14, 480−482.

(28) Scott, J. F. Applications of Modern Ferroelectrics. *Science.* 2007, 315, 954−959.

(29) Ajay Kumar, K.; Anatoliy, S.; and Rajeev, R. *J. Appl. Phys.*2013, 114, 014102.

(30) Yu, Z.; Ang, C.; Guo, R.; and Bhalla, A. S. *J. Appl. Phys.*2002, 92, 1489-1493.

(31) Li Z.; and Wang, Z. L. *Adv. Mater.* 2011, 23, 84–89.

(32) Hu, Y.; Xu, C.; Zhang, Y.; Lin, Long.; Snyder, R. L.; and Wang, Z. L. *Adv. Mater.*2011, 23, 4068–4071.

(33) Yu, A.; Jiang, P.; Wang, Z. L. *Nano Energy.*2012 1, 418–423.

(34) Huang, K. C.; Huang, T. C.; Hsieh, W. F. *Inorg. Chem.* 2009, 48, 9180-9184.

(35) Li, B. R.; Shang, W.; Hu, Z. L.; Zhang, N. Q. *Ceram. Int.* 2014, 40, 73-80.

(36) Weber, U.; Greuel, G.; Boettger, U.; Weber, S.; Hennings, D.; and Waser, R. *J. Am. Ceram. Soc.* 2001, 84, 759–66.

(37) Nanakorn, N.; Jalupoom, P.; Vaneesorn, N.; Thanaboonsombut, A. *Ceram. Int.* 2008, 34, 779–782.

(38) Li, W.; Xu, Z.; Chu, R.; Fu, Peng.; and Zang, G. *J. Am. Ceram. Soc.* 2010, 93, 2942–2944.

(39) Kim, Y.; Lee, K. Y.; Hwang, S. K.; Park, C.; Kim, S. O.; and Cho, J. *Adv. Funct. Mater.* 2014, 24, 6262–6269.

(40) Park, K. –I.; Lee, M.; Liu, Y.; Moon, S.; Hwang, G. -T.; Zhu, G.; Kim, J. E.; Kim, S. O.; Kim, D. K.; Wang, Z. L. and Lee, K. J. *Adv. Mater.* 2012, 24, 2999–3004.

(41) Han M.; Zhang, X. S.; Meng, B.; Liu, W.; Tang, W.; Sun, X.; Wang, W.; and Zhang, H. *ACS Nano.* 2013, 7, 8554–8560.

(42) Ricinschi, D.; Ciomaga, C. E.; Mitoseriu, L.; Buscaglia, V.; Okuyama, M. *J. Eur. Ceram. Soc.* 2010, 30, 237–241.

(43) Dong, L.; Donald, S. S.; and Lakes, R. S. *J. Appl. Phys.* 2012,111, 084107-1-10.

(44) Wu, J. M.; Xu, C.; Zhang, Y.; and Wang, Z. L. *ACS Nano* 2012, 6, 4335–4340.

(45) Liu, Z. H.; Pan, C. T.; Lin, L. W.; Huang, J. C.; and Ou, Z. Y. *Smart Mater. Struct.* 2014, 23, 025003-13.

(46) Jeong, C. K.; Park, K. -I.; Ryu, J.; Hwang, G.T.; and Lee, K. J.; *Adv. Funct. Mater.* 2014, 24, 2620–2629.

(47) Balasubramaniam, S.; Thiyagarajan, K.; Nagamalleswara Rao, A.; SoYoon, S.; Taehyun, K.; Zong-Hong, L.; Sang-Jae, K. *Carbon.*2015, 84, 56-65.

(48) Zhang, M.; Gao, T.; Wang, J.; Liao, J.; Qiu, Y.; Xue, H.; Shi, Z.; Xiong, Z.; Chenn, L. *Nano Energy.* 2015, 11, 510-517.

(49) Joe, B.; Nimra, J.; Peter, W.; Mark, S.; Paul, M. W.; Markys, C.; and Steve, D. ***Energy Environ. Sci.*** 2013, **6**, 3035-3045.

(50) Park, K. -I.; Xu, S.; Liu, Y.; Hwang, G, T.; Suk-Joong, L. K.; Wang, Z. L.; and Lee, K. J. *Nano Lett.* 2010, 10, 4939–4943.

(51) Jeong, C. K.; Kim, I.; Park, K. -I.; Oh, M. H.; Paik, H.; Hwang, G.-T.; No, K.; Nam, Y. S.; and Lee, K. J. *ACS Nano.* 2013, *7*, 11016–11025.

(52) Wu, W.; Cheng, L.; Bai, S.; Dou, W.; Xu, Q.; Wei, Z.; Qin, Y. ***J. Mater. Chem. A***, 2013, **1**, 7332-7338.

(53) Pi, Z.; Zhang, J.; Wen, C.; Zhang, Z. B.; Wu, D. *Nano Energy.* 2014, 7, 33–41.

(54) Franke, M. W. Fluid Mechanics, Viscous Flow in Ducts. Frank J. Cerra., Michael Gardner, and James Amar, EDs. McGraw-Hill Kogakusha: Japan, **1979**; pp 305-351.

4.2 Self-powered light emitting diodes using biomechanical-driven output of polydimethylsiloxane (PDMS)/$BaTiO_3$ nanocubes hybrid film nanogenerator

4.2.1 Introduction

Unconventional energy harvesting technologies are playing a key role to reduce the world energy crisis such as power supply and demand. Consuming the natural sources for energy generation creating the pollution and global warming issues, increasing the carbon emissions, this needs to be controlled for better society. Scientists and many researchers believe that, piezoelectric nanogenerator (PNG)[1] is one kind of unconventional approach to harvest the waste mechanical energy in the society such human body movements (walking, running and human finger movements), Ocean waves, wind/water flow and low frequency mechanical vibrations[2]. The traditional nanogenerators output successfully used to power the low power devices such as light emitting diodes (LEDs), liquid crystal displays (LCDs) and sensors[3]. At present time, PNGs using the smart composite materials i.e. organic polymer along with inorganic nanoparticles created intense interest to improve the output power of PNG with low mechanical energy[4, 5]. The use of composite materials for PNG has many advantages such as cost-effectiveness, easy process, eco-friendly, flexible in nature, reducing the internal leakage current, adaptability for large mechanical force, large scale fabrication and possible for high output power as compared to the traditional PNGs using alone inorganic nanostructures[6]. Alternatively many researchers were developed polymer based PNGs using (polyvinylidene fluoride) PVDF and its co-polymers, but these polymers have less piezoelectric coefficient than the inorganic piezoelectric particles[7]. In contrast, composite structures for PNG are more predominant and possible for different device designs to achieve the better output with good reliability and stability. Park et al. demonstrated the feasibility of piezoelectric nanocomposite generator using the $BaTiO_3$ nanoparticles (BTO NPs)/multi-walled carbon nanotubes (MWCNT)/polydimethylsiloxane (PDMS) and extended too many other possible ways using zinc oxide (ZnO), lead zirconate titanate (PZT) and alkaline niobate NPs (KNN) with reasonable output power[8]. Alluri et al. developed the $Ba(ZrTi)O_3$

nanocubes (NCs)/PVDF[2], BTO NPs/Ca-alginate linear and wavy pattern composite worms[5] with reasonable electrical output and the devices itself has capability to measure the various water velocities at an outlet pipe, pH values. S. W. Kim et al.[9] designed the $Na_{0.47}K_{0.47}Li_{0.06}NbO_3$ NCs-PDMS composite film and generated the output voltage 48 V and current density 0.43 μA/cm^2 value with a vertical compressive force 19.7 N at frequency of 3 Hz. Z. H. Lin et al.[10] studied the BTO nanotubes/PDMS composite and the PNG generates an electrical output of 5.5 V and 350 nA respectively. The performance of composite materials based PNG depends on the selection of organic polymer and high piezoelectric coefficient (d_{33}) based inorganic nanoparticles, and its particular weight ratio, thickness of the composite layer and surface morphology of particles (nanocubes, nanotubes, nanofibers etc.). In certain cases, the polymers (PVDF, P(VDF-HFP), P(VDF-TrFE)) used for the development of composite materials can has the dual property such as a supporting layer to hold the nanoparticles and active layer to contribute the additional electrical output[2, 6, 11]. In contrast, PDMS, polycarbonate, (poly(methyl methacrylate)) PMMA and few other polymers will work only for the supporting cross-linker to hold the nanoparticles and does not contribute to improve the piezoelectric output[3, 5, 9, 10]. In order to achieve the high d_{33} of composite material will depend on various factors such as surface morphology of particles, weight ratio of particles in polymer matrix, and electric dipole orientation *via* electrical poling. The reports on BTO nanotubes/PDMS (5.5 V, 350 nA)[10], BTO nanowires/PDMS (7 V, 360 nA)[12], BTO NPs-MWCNTs/PDMS (3.2 V, 350 nA)[8], BTO NCs/PVDF (7.99 V, 1.01 μA)[2], virus template BTO nanostructures/PDMS (6 V, 300 nA)[13], BTO nanofibers/PDMS (2.67 V, 261nA)[14], BTO NPs/bacterial cellulose (14 V, 150 nA/cm^2)[15] based composite materials generates the low electrical output except BTO NPs-P(VDF-HFP) (110 V, 22 μA)[11]. Therefore, an extensive research work is necessary to enhance the piezoelectric output of BTO material along with the

suitable polymer matrix under low input mechanical force condition and for cost-effective fabrication techniques. These kind of reliable PNGs are suitable for remote area locations for harvesting the waste mechanical energy i.e. biomechanical energy, wind/ocean waves and tiny vibrations[1].

In this regard, highly crystalline, lead-free piezoelectric BTO NCs were synthesized using the low temperature molten salt method. Highly flexible, eco-friendly and biocompatible composite film was developed using the simple, low cost solution casting technique, made up of BTO NCs and PDMS matrix (BTP-CF). BTP-CF based PNG fabricated having three major components such as top flexible kapton/aluminum (Al) layer, BTP-CF active layer and bottom flexible kapton/Al. The top and bottom kapton/Al layers was mechanically integrated to the BTP-CF using the fine conductive glue and hot pressing technique used to remove the unwanted air between the layers, placed in oven at 70 ˚C for 30 minutes. A fine PDMS layer was deposited on BTP-CF based PNG (CPNG) to protect from the external damage. All the devices are electrically poled at 8 kV for 24 h at room temperature, for creating the orientation of electrical dipoles in BTO NPs along with PDMS matrix. The piezoelectric performance for all PNG devices was investigated by the application of constant mechanical load 2 N (or 988.2 Pa) and the CPNG device with 15 wt % generates a peak-to-peak voltage and current density of 126.3 V and 77.6 $\mu A/cm^2$. In order to identify the role of PDMS for energy generation, pure PDMS based device (without BTO NPs) has been fabricated and compared with the electrical output of CPNG devices demonstrates that PDMS does not have any piezoelectric property to convert the mechanical energy to electrical energy. The flexibility and rolling capability of the BTP-CF was demonstrated using the digital photographs and the CPNG device cross-sectional image was observed by the FE-SEM technique, demonstrates the thickness of the composite film (≈790 μm)

and no air gap between the device layers (top aluminum/BTP-CF/bottom aluminum). Further, the weight ratio analysis of BTO NPs in PDMS matrix, load resistance analysis, charging capability of commercial capacitors using the CPNG device output, stability test and power up the commercial five green light emitting diodes was investigated successfully. Finally, as fabricated CPNG device (15 wt %) was used to harness the regular biomechanical energy generated from the human hand and foot stress in our daily life. Here, the human foot stress on CPNG device generates higher piezoelectric potential as compared to the potential generated from human hand force. All these results are clearly demonstrates that the CPNG device is a potential candidate to utilize the waste mechanical energy (human body movements, wind/water flow motions, ocean waves and other mechanical vibrations) in the environment.

4.2.2 Experimental Section

4.2.2.1 Synthesis of $BaTiO_3$ nanocubes (BTO NCs)

Highly oriented and well crystalline BTO NCs were synthesized by low cost and low temperature molten salt method [2]. The detailed synthesis procedure was schematically given in **Figure 4.2.1** and well discussed here. Here, the initial precursors are separated into two parts. One is the reactants such as $BaCO_3$ (99.95 %) and TiO_2 (98 %) were taken according to the atomic weight ratios to prepare the target stoichiometric BTO perovskite composition. Second is the eutectic mixture such as 50:50 mol % of NaCl:KCl flux and an extra salt 1 gm of Na_2SO_4 acting as a medium. The reactants and eutectic mixture were grinded thoroughly in mortar and pestle using ethanol solution for 30 minutes. The homogeneous powder was placed in Al_2O_3 boat and kept in open tube furnace for firing at 750 °C for 3 hr. During the heat treatment process, the eutectic mixture was useful for the growth of NCs microstructure and for the homogeneous nucleation. Next, the chloride ions were removed from the obtained product using multiple

washings with hot deionized water and then dried in oven at 60 °C for overnight. Finally, pure single phase perovskite BTO NCs were formed and used for the fabrication of piezoelectric composite film process.

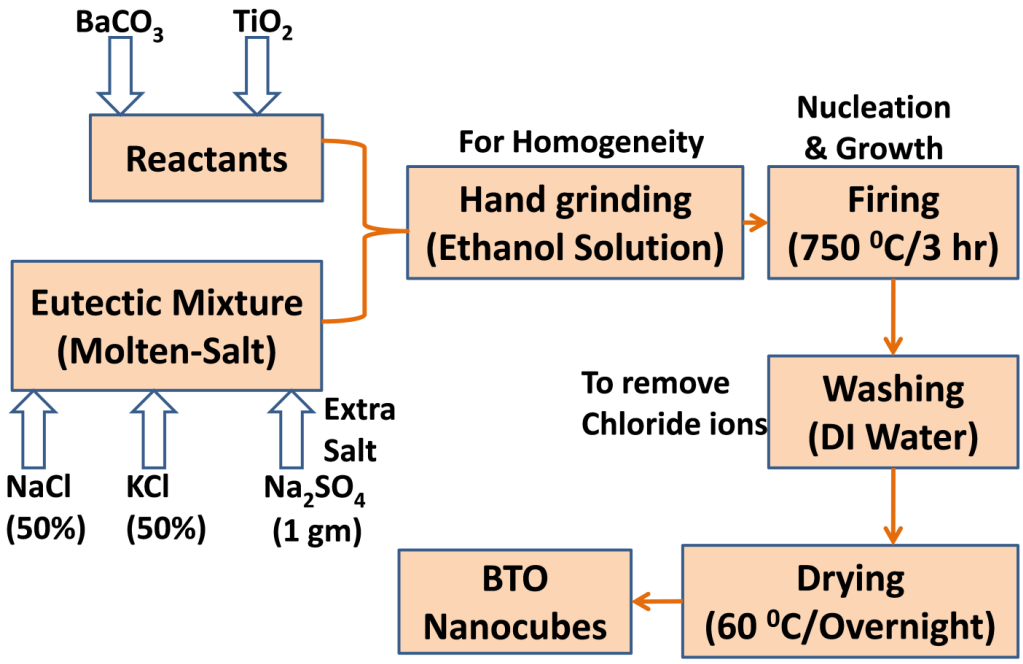

Figure 4.2.1 Schematic for synthesis of BTO NCs by low temperature molten-salt method.

4.2.2.2 Fabrication of piezoelectric BTO NCs/PDMS composite film (BTP-CF)

BTO NCs/PDMS composite film with 5 wt % was fabricated using the solution casting method [2] as depicted in **Figure 4.2.2a** and well discussed here. In which, 10 gm of homogeneous transparent solution was prepared using the PDMS: hardener with 10:1 ratio and 0.5 gm of BTO NCs was dispersed in that solution using the magnetic stirrer with 1000 revolutions per minute. A white homogeneous non-transparent solution was obtained after 30 minutes stirring and poured into the smooth glass petri dish followed by a heat treatment of 70 °C for 30 minutes in hot air oven. After that, as fabricated BTP-CF was peeled off from the glass Petri dish and cut into the required dimensions (4.6 cm x 4.4 cm) for the fabrication of

CPNG. A similar protocol has been followed to prepare the pure PDMS and other BTP-CFs with different weight ratios such as 10, 15, 20 and 25 wt % respectively.

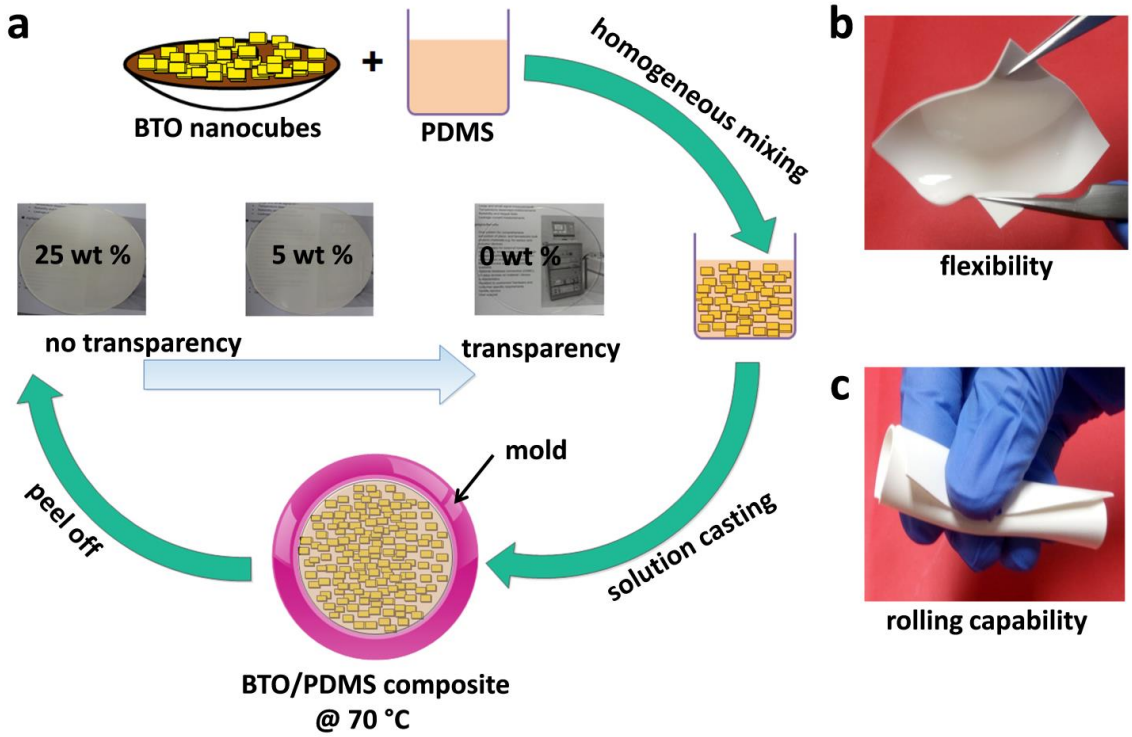

Figure 4.2.2 (a) Fabrication of piezoelectric BTP-CF using the solution casting technique and the inset digital photographs represent the as fabricated BTP-CFs with various weight ratios of BTO NCs to PDMS matrix demonstrates the transparent property. **(b, c)** Digital photographs represent the flexibility and rolling capability of the BTP-CF.

4.2.2.3 Fabrication of BTP-CF based PNG (CPNG) devices

In order to prepare the CPNG device with 5 wt %, as fabricated BTP-CF (5 wt %) was sliced with a dimension of (4.6 cm x 4.4 cm) and sandwiched between the flexible top Al/Kapton film and bottom Al/Kapton film using the hot pressing technique around 30 minutes. Two copper (Cu) wires were attached on top and bottom of the Al electrode using the silver paste for collecting the generated charge carriers through external circuit. To protect the as fabricated CPNG from the external physical damage, a fine pure PDMS layer was used to cover the whole device. After that, the CPNG devices have been electrically poled at 8 kV for 24 h at room temperature to initiate

the permanent electric dipole orientation. Similar fabrication procedure was used to develop the pure PDMS based device and other CPNG devices with different weight ratios (10, 15, 20 and 25 wt %).

4.2.3 Results and discussion

The BTP-CFs made up of different weight ratios of BTO NCs (5, 10, 15, 20 and 25 wt %) to the PDMS matrix, which is fabricated by the simple, low cost solution casting method as shown schematically in Figure 4.2.2a. The detailed fabrication of BTP-CFs was well discussed in experimental section. Pure PDMS film has a low relative permittivity ($\approx\varepsilon_r = 3$), good flexibility, transparent in nature and highly suitable as a supporting polymer matrix to crosslink (or immobilize) the nanoparticle fillers. The substitution of piezoelectric BTO NCs as a filler material into the PDMS matrix will improve the relative permittivity of PDMS matrix, which is due to the high relative permittivity of BTO NCs than PDMS matrix. But the transparent property of PDMS film has been lost, when increasing the weight percentage of BTO NCs to PDMS matrix as shown in **Figure 4.2.2a.** The flexibility and rolling capability of the as fabricated BTP-CF film was depicted in **Figure 4.2.2(b, c).** It indicates that the piezoelectric BTP-CF was suitable for flexible energy harvesting applications and portable, wearable self-powered sensors.

4.2.3.1 Structural and surface morphology of BTP-CFs

Here, the piezoelectric phase of BTO NCs and BTP-CF were characterized, analyzed by the XRD and Raman spectra techniques. **Figure 4.2.3a** shows the XRD spectra of as fabricated BTO NCs, pure PDMS film and BTP-CF (15 wt %), respectively. The XRD spectra of BTO NCs represent the single phase perovskite structure as shown in **Figure 4.2.3a (i).** The calculated average crystallite size and lattice strains are 27.51 nm and 3.86 x 10^{-3}, respectively. The

splitting nature of the diffraction peak position at 45° corresponds to the indexed planes (002)/(200) and the obtained other major peaks are associated to the tetragonal crystal structure of BTO lattice[2]. This structure is more favorable to the high piezoelectric and ferroelectric properties compared to the non-piezoelectric phase (cubic) of BTO lattice. This XRD pattern is well matched with the previously reported ICDD pattern no.98.001-3771. **Figure 4.2.3a(ii)** shows the XRD pattern of pure PDMS and the broad peak at 11.96° represents the amorphous phase of polymer matrix. **Figure 4.2.3a (iii)** represents the XRD pattern of the BTP-CF (15 wt %) indicating the amorphous phase of PDMS and the piezoelectric phase of the BTO NCs. Here, the insulating PDMS matrix unable to change the piezoelectric phase of BTO NCs. So that, the as-fabricated BTP-CFs can works as flexible, piezoelectric active layer for the conversion of mechanical energy to electrical energy. Raman spectroscopy was employed, to understand the dynamic symmetry, lattice vibration of the BTO NCs and phase confirmation of the BTO NCs, BTP-CF as shown in **Figure 4.2.3b**. No active modes available for the cubic phase of BTO lattice. But for the tetragonal phase of BTO[2] have active modes related to the octahedral sites of TiO_6 centers, which correspond to the peaks at 312, 523 and 720 cm^{-1} as shown in **Figure 4.2.3b (i).** PDMS has characteristic peaks at 494 and 713 cm^{-1} related to the symmetrical stretching of the Si-O-Si and Si-C symmetrical stretch and the peak at 1121 cm^{-1} represents the supporting glass substrate peak as shown in **Figure 4.2.3b (ii).** The Raman spectrum of BTO-CF comprises the major active modes of the BTO NCs tetragonal phase and the minor PDMS characteristic peaks completely diffused into the BTO peaks. Lower wavelength phase shift was observed for the BTP-CF compared to the pure BTO NCs pattern represents the stress induced effects. Here, the phase information from the Raman spectra and the XRD pattern is well matched confirming that the existence of the non-centrosymmetric regions from titanium (Ti) atoms.

Surface morphology of BTO NCs, PDMS film and BTP-CF (15 wt %) was characterized and analyzed by the Field Emission Scanning Electron Microscopy (FE-SEM) technique. **Figure 4.2.3c** shows the uniform and high quality crystalline BTO NCs surface morphology at 1 μm scale, synthesized *via* MS method. **Figure 4.2.3d** shows the magnified image of the BTO NCs at 200 nm scale shows the well formation of the BTO NCs with various sizes lies between 100 nm to 400 nm level. Next, the surface morphology of the as-fabricated PDMS and BTP-CF (15 wt %) was analyzed and shown in **Figure 4.2.4(a, b).**

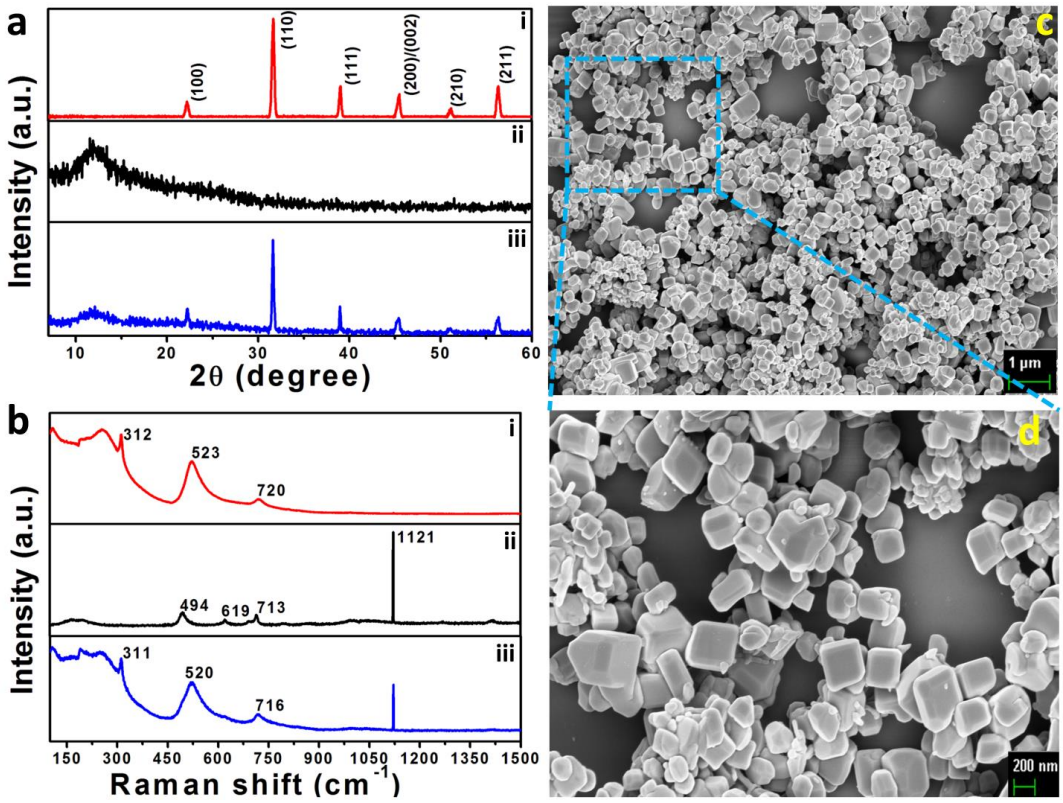

Figure 4.2.3 (a) XRD analysis of the as-synthesized BTO NCs, PDMS film and BTP-CF (15 wt %) **(b)** Raman spectroscopy analysis of the as-synthesized BTO NCs, PDMS film and BTP-CF (15 wt %) **(c, d)** FE-SEM images show the high crystalline BTO NCs at different magnifications at 1 μm and 200 nm scales.

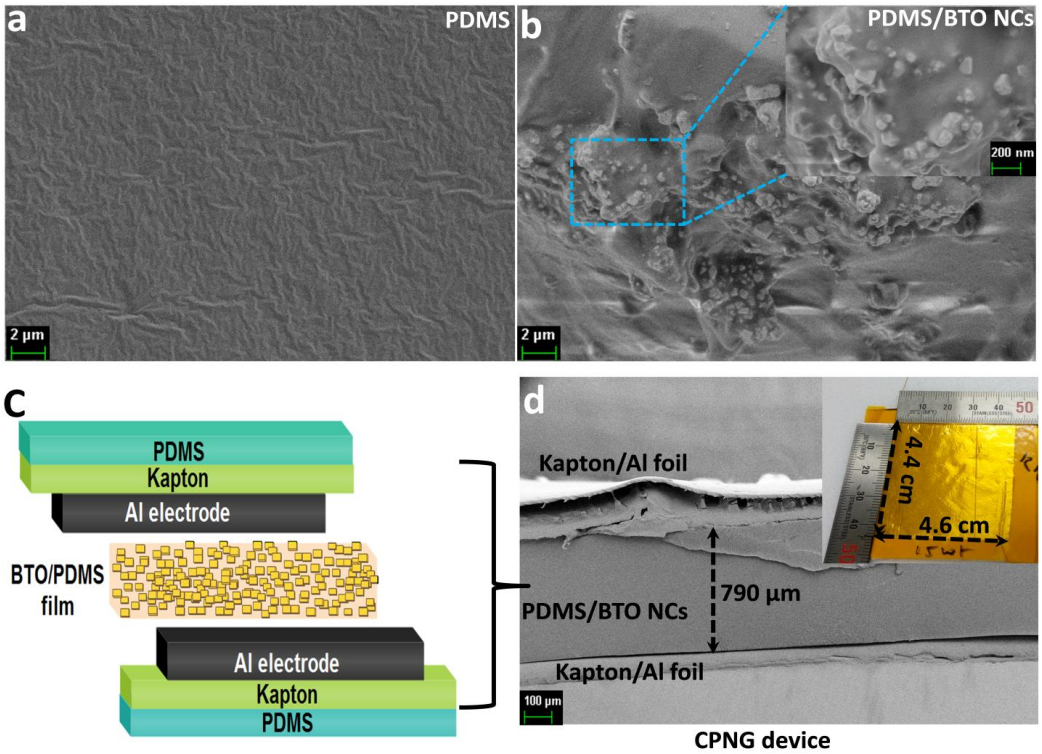

Figure 4.2.4 (a) FE-SEM image shows the smooth surface morphology of pure PDMS film at 2 µm scale. **(b)** FE-SEM image of BTP-CF (15 wt %) shows the well distribution of BTO NCs in PDMS matrix at 2 µm and 200 nm scales. **(c)** Schematic of the CPNG device for harnessing mechanical energy **(d)** Cross-sectional FE-SEM image of the CPNG device at 100 µm scale and the inset shows the digital photograph of CPNG device (4.4 cm x 4.6 cm) without PDMS packaging layer.

Pure PDMS film shows the smooth surface at 2 µm scale and the FE-SEM image of the BTP-CF (15 wt %) at 2 µm and 200 nm scales shows the good distribution of BTO NCs in PDMS matrix as shown in **Figure 4.2.4 (a, b).** The fabricated flexible piezoelectric BTP-CF is useful to harness the waste mechanical energy such as human body movements, wind/water flow and any mechanical vibrations, respectively. This is possible by fabricating the CPNG device using the BTP-CFs. In this work, CPNG device was fabricated having an area of (4.4 cm x 4.6 cm) and verified-analyzed the electrical output behavior using the linear motor force and biomechanical energy (hand & foot). The detailed fabrication procedure of CPNG device was given in the experimental section and the device layers such as PDMS/Kapton/top Al electrode, BTP-CF and

bottom Al electrode/Kapton/PDMS layers were schematically shown in **Figure 4.2.4c.** The cross-sectional FE-SEM image of the CPNG device without PDMS packaging layer at 100 μm scale shown in **Figure 4.2.4d**. The image clearly represents that, there is no air gap formation between the layers during the fabrication of the CPNG device. The inset shows the digital photograph of the as fabricated CPNG device with 15 wt % of the BTP-CF.

4.2.3.2 Piezoelectric potential response of CPNG and self-powered light emitting diodes

The energy harvesting capability of CPNG devices with different weight ratios of BTO NCs in PDMS matrix was performed using the constant mechanical load (988.2 Pa) generated from the linear motor (LinMot-HF01-37) with a fixed acceleration 1 m/s^2. Before that all CPNG devices are electrically poled at 8 kV/24 hr at room temperature, which provides the permanent polarization *via* electrical stress on electric dipoles existing in the BTP-CFs and maximum number of dipoles will align in one particular direction. **Figure 4.2.5 (a,** b) shows the comparison of the open circuit voltage (V_{OC}) and short circuit current density (J_{SC}) of pure PDMS and CPNG device (15 wt %) under constant mechanical load 988.14 Pa.

It clearly demonstrates that the CPNG device (15 wt %) generates high electrical output ($V_{OC\ (peak\text{-}to\text{-}peak)} \approx 126.3$ V, $J_{SC\ (peak\text{-}to\text{-}peak)} \approx 77.69\ \mu A/cm^2$) as compared to the pure PDMS based device output. There is no electric dipole orientation in the pure PDMS matrix and PDMS will act as insulator, could results in zero electrical output. This clearly confirms that PDMS will act as supporting cross-linker to hold the BTO NCs and no contribution for converting mechanical energy to electrical energy. On the other side, CPNG device generates high output performance due to the piezoelectric effect of BTO NCs. As we know that, the piezoelectric coefficient of BTO (≈100-190 pC/N for bulk BTO film) will change according to the shape, particle size, doping, electrical poling and input mechanical force. The working mechanism of CPNG device

for the generation of the electrical energy depends on the generation and collection of free charge carriers top/bottom surface of the BTP-CFs and its Al electrodes. Under no force condition, the CPNG device generates zero electrical output, which is due to the zero net dipole moment. When the constant load (988.2 Pa) acting perpendicular to the CPNG device generates piezoelectric potential which is due to the higher net dipole moment i.e. maximum number of electric dipoles will align in one particular direction by the stress-induced poling effect.

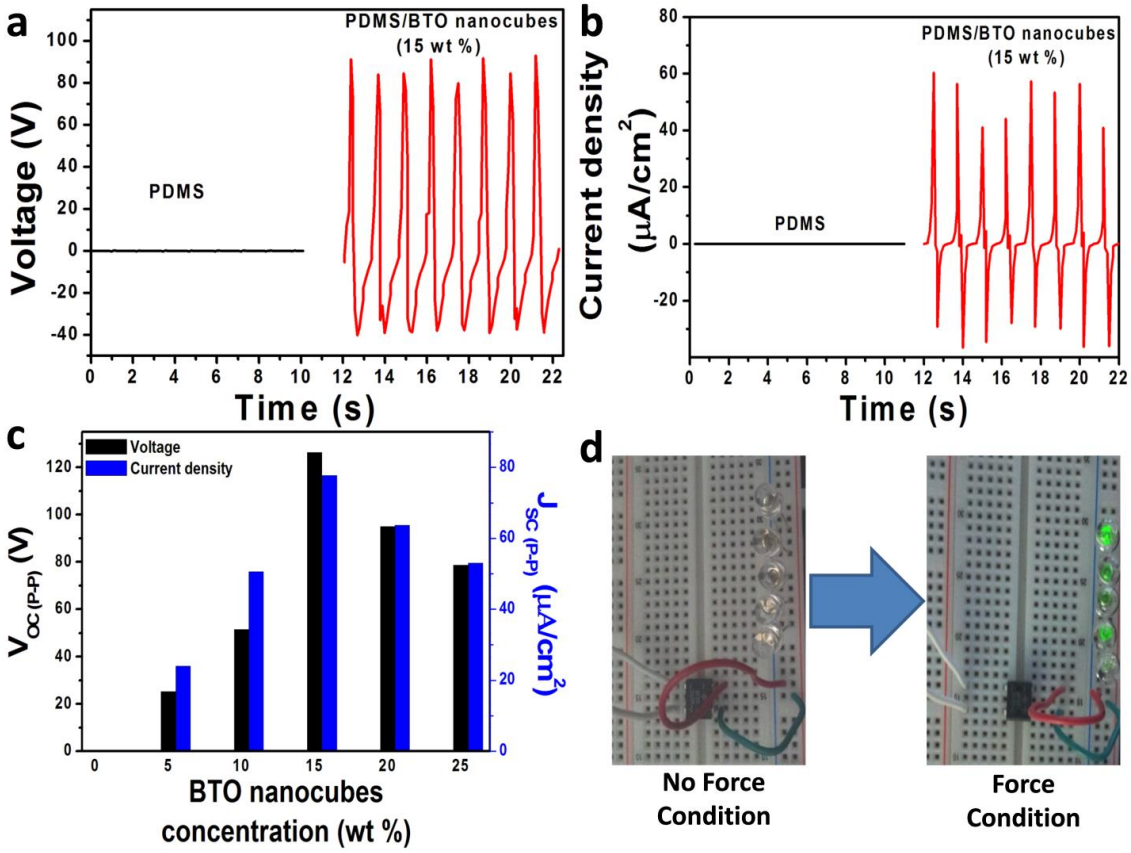

Figure 4.2.5 Electrical response of the various piezoelectric nanogenerators **(a, b)** Comparison of the voltage and current density responses of the pure PDMS and CPNG (15 wt %) devices at 2 N load (988.14 Pa). **(c)** Cumulative comparison of the peak-to-peak voltage and current density responses of the various CPNG devices with BTO NC concentrations at low pressure 988.14 Pa loads. **(d)** Demonstration of the real time application using the generated CPNG device output driving the five green LEDs.

The open circuit voltage from the CPNG device depends on the piezoelectric coefficient and can be evaluated from the equation[2]:

$$V_{OC} = g_{33}\sigma Yt \quad \text{(E4.2.1)}$$

$$g_{33} = {}^{d_{33}}/_{\varepsilon_o K} \quad \text{(E4.2.2)}$$

where t is the thickness of the CPNG device, Y is the young's modulus of the BTP-CF and σ is the strain acting perpendicular to the device. The piezoelectric voltage constant (g_{33}) is directly proportional to the piezoelectric coefficient (d_{33}) and inversely proportional to the relative permittivity (K) of the BTP-CF, respectively.

The maximum output of CPNG device under constant mechanical load depends on the optimum weight ratio of BTO NCs to the PDMS matrix. Weight ratio dependent analysis such as 0, 5, 10, 15, 20 and 25 wt % of BTO NCs to the PDMS matrix was performed to identify the exact weight ratio of BTO NCs and the corresponding electrical response as shown in **Figure 4.2.5c.** Initially, 5 wt % of BTP-CF based CPNG device generates (25 V, 20 μA/cm^2), and increases to (50 V, 50 μA/cm^2) for 10 wt % and reached to the maximum output (126.3 V, 77.6 μA/cm^2) for 15 wt % under constant mechanical load 988.2 Pa. For 20 and 25 wt % of BTP-CF based CPNG devices shows decreasing trend output behavior as compared to the CPNG device (15 wt %) output as shown in **Figure 4.2.5c.** It clearly demonstrate that the higher weight of BTO NCs to the PDMS matrix, will be possible to create the agglomeration and applied force is not possible to act on all the particles and the orientation of electrical dipoles may possible to cancel each other. This creates the low net dipole momentum as compared to the 15 wt % of BTP-CF based CPNG device. So that, in this work 15 wt % of BTO NCs to the PDMS matrix is the optimum weight ratio for achieving the maximum electrical output. The optimized weight percentage (15 wt %) is close enough to the previous results. The generated output from the CPNG device (15 wt %) is sufficient to drive the commercially available low power LEDs. **Figure 4.2.5d** shows the demonstration of driving LEDs using the CPNG device output *via* full

wave bridge rectifier. Under no force condition, LEDs are in OFF state and by the application of constant load on CPNG device lit up the five green LEDs at a time without using any storage capacitor and additional battery energy. This demonstrates that as fabricated BTP-CFs and its nanogenerators are the pave way for unconventional energy harvesting approaches and suitable to harness the waste mechanical energy from the environment such as human body movements, wind/water motions and any kind of mechanical vibrations.

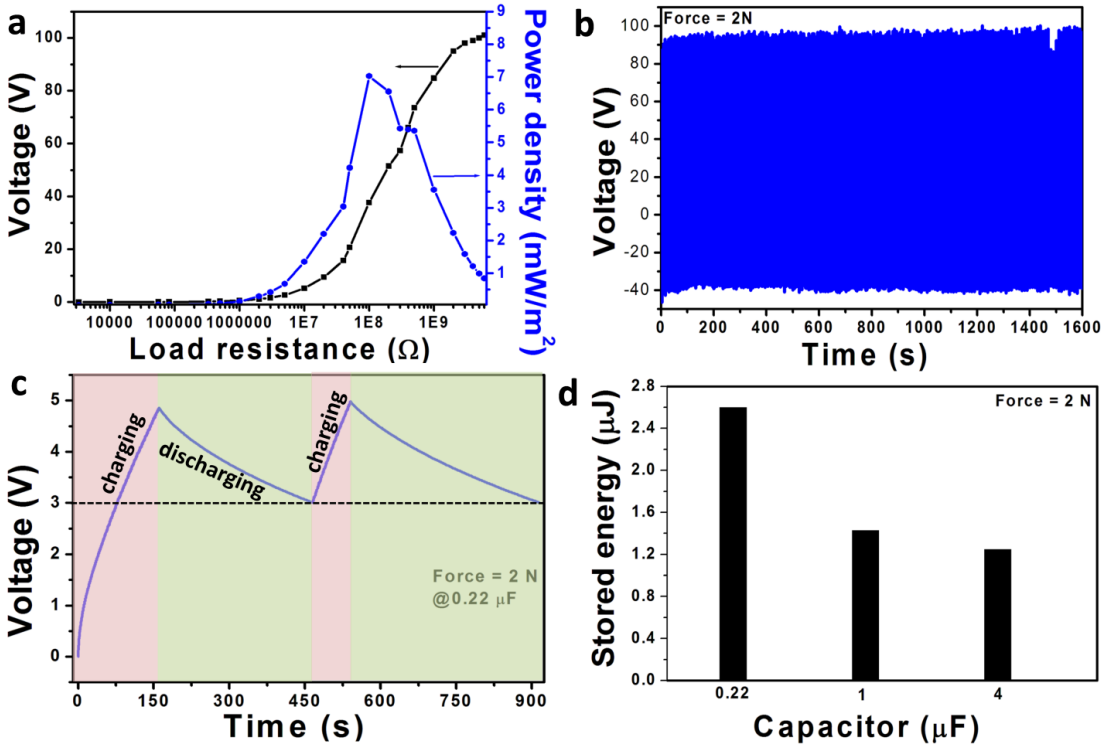

Figure 4.2.6 (a) Load resistance analysis and power density calculations of the CPNG device (15 wt %) at 2 N applied mechanical load (or 988.14 Pa). **(b)** Stability test analysis of the CPNG device at 988.2 Pa (or 2 N) mechanical load. **(c)** Charging and discharging behavior of the commercial capacitor (0.22 μF) using the CPNG device output *via* full wave bridge rectifier. **(d)** Comparison of the stored electrical energy in various commercial capacitors (0.22, 1 and 4) using CPNG device output at constant mechanical load (988.2 pa).

Further studies such as load resistance analysis, power density calculations, stability test, charging capability of commercial capacitor and the stored energy information in various

capacitors has been carried out using the CPNG device (15 wt %) under constant mechanical load 988.2 Pa. The CPNG device output increases, when increasing the load resistance value from 500 Ω to 3 GΩ as shown in **Figure 4.2.6a.** From this, the area power density of CPNG device at 2 N applied load was evaluated by using the equation[2]:

$$P_A = {V^2}/{(R \times A)} \quad \text{(E4.2.3)}$$

Where V is generated output voltage from the CPNG device, R is the load resistance value and A is the active device area of CPNG (4.4 cm x 4.6 cm), respectively.

The area power density (≈ 7 mW/cm^2) for CPNG device is maximum at 100 MΩ load resistance as shown in **Figure 4.2.6a.** This indicates that 100 MΩ is the load matching resistance for achieving maximum output power and suitable for real time applications. Next, the endurance test was carried out to find the stability of the CPNG device during 1600 time interval at 2 N applied load. **Figure 4.2.6b** shows that no change in output voltage of CPNG device over a time interval represents the good stability of CPNG device.

Besides the area power density, the charging analysis of commercial capacitor (0.22 μF) using the CPNG device output through the full wave bridge rectifier was also evaluated and analyzed. **Figure 4.2.6c** shows the charging and discharging curves of 0.22 μF capacitor at 2 N applied load. The capacitor stored maximum voltage of 4.86 V during the time interval 160 seconds at continues input load 2 N and started to decrease the voltage (discharge process) in capacitor whenever the force acting on CPNG device was removed. The charging and discharging cycles of commercial capacitor was repeated to identify that the cyclic stability as shown **in Figure 4.2.6c.** Further the external load capacitor was increased from 0.22 μF to 1 μF and 4 μF, to analyze the storing capability in capacitor from the CPNG device output as shown in **Figure 4.2.6d.** The circuit for experimental demonstration and its charging curve analysis of

various capacitors were given in the **Figure 4.2.7.** Approximately, 1.24 μJ of energy stored in 4 μF commercial capacitor, when 2 N load acting on the CPNG device, which is further increased to 1.42 μJ for load capacitor (1 μF), and 2.59 μJ for 0.22 μF.

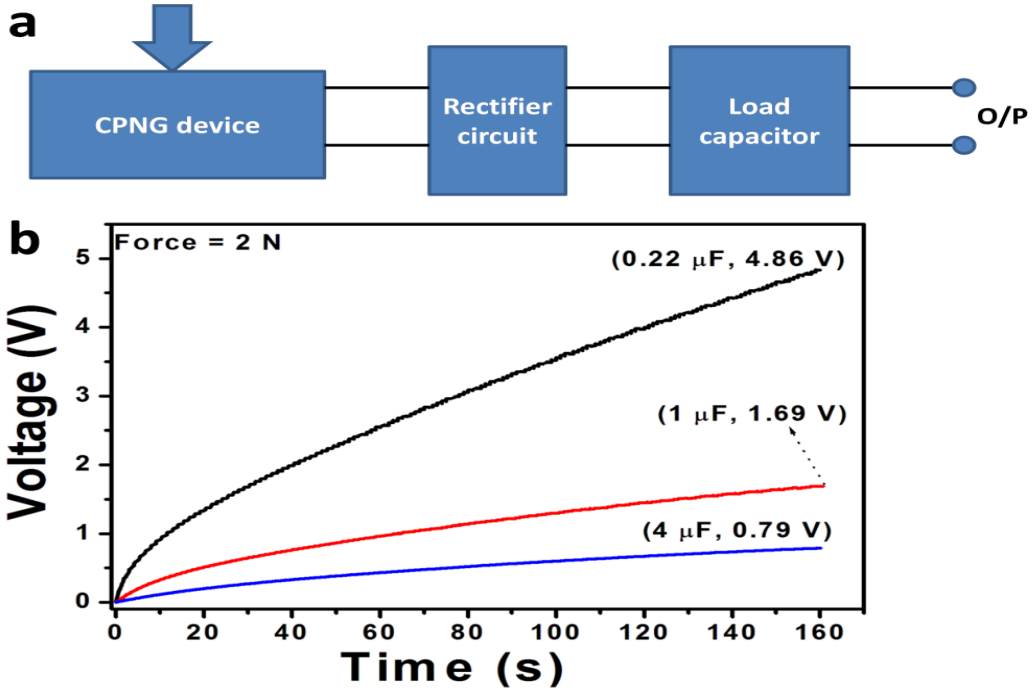

Figure 4.2.7(a, b) Schematic of the capacitance loading effects for the CPNG device **(b)** Charging voltage behavior with respect to various commercial capacitor rating using the output of CPNG device.

The fabricated CPNG device is aimed to harvest the waste biomechanical energy (or natural human body motions). **Figure 4.2.8a** shows the real time experimental demonstration of CPNG device to harness the low frequency waste biomechanical energy. CPNG device generates peak-to-peak voltage ≈ 29 V at the human hand palm force and generates ≈55.9 V at the human foot press and release conditions as shown in **Figure 4.2.8b.** As we know that, the human hand/foot motions lies at low frequency level (≤ 10 Hz) and the generating force is uncertain with respect to the human. The above mentioned results such as CPNG device output with respect to the low mechanical pressure (988.2 Pa) linear motor force, output dependency on weight ratio of BTO

NCs in PDMS matrix, chagrining and stability analysis, driving commercial LEDs and real time biomechanical harvesting suggest that the proposed CPNG device is potential candidate for remote area locations to generate eco-friendly power and also suitable for self-powered sensor applications in various fields[1-16].

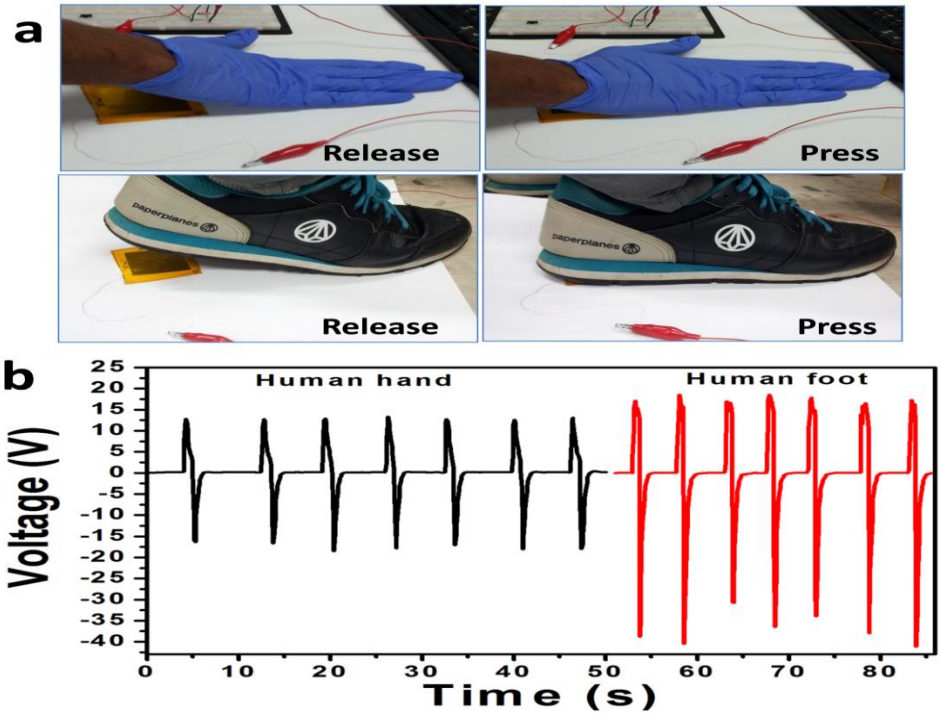

Figure 4.2.8 Real time experimental demonstration of CPNG device to harness the low frequency waste biomechanical energy **(a)** Digital photographs of the human hand and foot release and press conditions act on the CPNG device. **(b)** Comparison of open circuit voltage, when the human hand and foot release/press force act on the CPNG device.

4.2.4 Conclusions

In summary, high quality piezoelectric BTO NCs were synthesized using the low temperature MS method and used to fabricate the efficient, flexible BTP-CF by the simple, cost-effective solution casting technique. The performance of CPNG device was studied by the weight ratio of BTO NCs in PDMS matrix, electrical poling (8 kV/24 h), at constant low mechanical pressure (988.2 Pa), resistance/capacitance loadings and stability test, and at real

time biomechanical hand/foot stress. CPNG device is highly sensitive and generates the high peak-to-peak output voltage (126.3 V), current density (77.6 μA/cm^2) and delivers the maximum area power density 7 mW/cm^2 at 100 MΩ load resistance upon the low mechanical pressure 988.2 Pa. Commercial capacitor (0.22 μF) stored 2.59 μJ of energy during 160 seconds time interval. We also demonstrate that the generated CPNG device output is sufficient to drive the low power commercial five green LEDs without using any storage capacitor and external circuits, which replace the battery energy and reduce the cost factor. At the same time, CPNG device highly sensitive to the biomechanical energy (hand and foot stress) and generates a maximum output voltage 55.9 V during foot stress demonstrates that CPNG is potential candidate to utilize our regular human body physical motions and reliable alternative unconventional energy harvesting approach to solve the partial world energy crisis. The proposed method for fabrication of composite film is cost-effective, eco-friendly, capable for large scale production and the fabricated CPNG device is highly capable to harness the waste mechanical energy in the society.

4.2.5 References

(1) Yang, R.; Qin, Y.; Li, C.; Zhu, G.; Wang, Z.L. *Nano Lett*. **2009**, 9, 1201-1205, 2009.

(2) Alluri, N. R.; Saravanakumar, B.; Sang-Jae, K. *ACS Appl.Mater.Interfaces*, ***2015***, *7*, *9831-9840.*

(3) Alluri, N. R.; Selvarajan, S.; Arunkumr C. A.; Saravanakumar, B.; Jeong, J. H.; Sang-Jae, K. *Sens. Actuator B-Chem*, **2016**, 237, 534–544.

(4) Siddiqui, S.; Kim, D. I.; Duy, L. T.; Nguyen, M. T.; Muhammad, S.; Yoon, W. S.; Lee, N. E. *Nano Energy*, **2015**, 15, 177–185.

(5) Alluri, N. R.; Selvarajan, S.; Arunkumar C.; Saravanakumar, B.; Lee, G. M.; Jeong, J. H.; Sang-Jae, K. *Energy*, **2016,** 1-10.

(6) Shin, S. H.; Kim, Y. H.; Lee, M. H.; Jung, J. Y.; Nah, J. *ACS Nano*, **2014**, 8, 2766-2773.

(7) Whiter, R. A.; Narayan, V.; Narayan, S. K. *Adv. Energy Mater.* **2014**, 4, 1400519-1400525.

(8) Park, K. I.; Lee, M.; Liu, Y.; Moon, S.; Hwang, G. T.; Zhu, G.; Kim, J. E.; Kim, S. O.; Kim, D. K.; Wang, Z. L.; Lee, K. J. *Adv. Mater.* **2012**, *24*, 2999–3004.

(9) Gupta, M. K.; Kim, S. W.; Kumar, B. *ACS Appl. Mater. Interfaces* **2016**, 8, 1766−1773.

(10) Lin, Z. H.; Yang, Y.; Wu, J. M.; Liu, Y.; Zhang, F.; Wang, Z. L. *J. Phys. Chem. Lett*. **2012**, 3, 3599−3604.

(11) Shin, S. H.; Kim, Y. H.; Jung, J. Y.; Lee, M. H.; Nah, J. *Nanotechnology*, **2014**, 25, 485401-485407.

(12) Park, K. I.; Bae, S. B.; Yang, S. H.; Lee, H. I.; Lee, K.; Lee, S. J. *Nanoscale*, **2014**, 6, 8962-8968.

(13) Jeong, C. K.; Kim, I.; Park, K. I.; Oh, M. H.; Paik, H.; Hwang, G. T.; No, K.; Nam, Y. S.; Lee, K. J. *ACS Nano*, **2013**, 7, 11016–11025.

(14) Yan, J.; Jeong, Y. G. *ACS Appl. Mater. Interfaces*, **2016**, 8, 15700-15709.

(15) Zhang, G.; Liao, Q.; Zhang, Z.; Liang, Q.; Zhao, Y.; Zheng, X.; Zhang, Y. *Adv. Sci*. **2016**, *3*, 1500257-1500263.

(16) Selvarajan, S.; Alluri, N. R.; Chandrasekhar, A.; Kim, S. J, *Sens. Actuator. B-Chem*, **2016**, 234, 395–403.

CHAPTER V

Self-powered flexion sensor/electronic display/pH sensor using $BaTiO_3$/bio-polymer hybrid structure nanogenerators

Highlights

- Eco-friendly spherical beads, linear worms and wavy-pattern worms based nanogenerators were developed.
- CBNG device generates (82 V, 227 μA) upon low mechanical pressure 1.70 kPa.
- Piezoelectric-tribolelectric hybrid nanogenerator work as self-powered flexion sensor.
- Length dependant piezoelectric responses of composite worms were analyzed.
- The generated output from these devices can be useful to drive low power consumed electronic device.

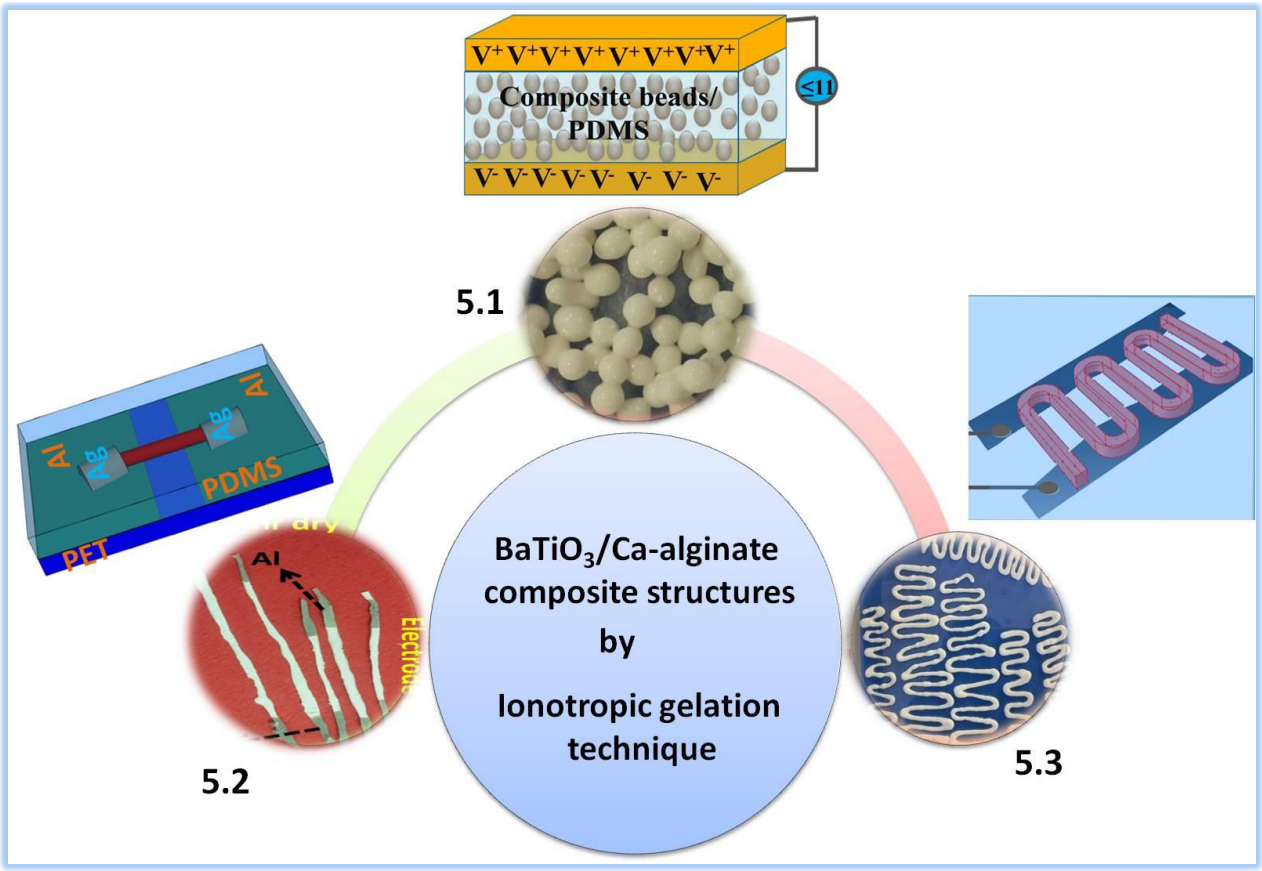

5.1 Self-powered Flexion Sensor by $BaTiO_3$ nanoparticles/Ca-alginate Hybrid Beads/PDMS Film based Piezoelectric-Triboelectric Hybrid Nanogenerator

5.1.1 Introduction

Electrical energy is the primary input source for equipment ranging from entertainment tools to life-saving medical devices, which makes it more favorable to invent alternative energy harvesting technologies such as piezoelectric [1], pyroelectric [2] and triboelectric [3] nanogenerator rather than harvesting energy from natural sources such as water [4], wind [5], solar [6] and thermal [7]. There has been intense interest concerning the use of eco-friendly nanogenerator (NG) technologies to meet the demands of battery-less smart devices (energy harvesting with sensing) and various applications including health monitoring devices, biocompatible devices for in vivo applications [8] and implantable devices [9]. Among these, piezoelectric harvesting [1, 10, 11] is an example that uses single-crystalline, polycrystalline, and composite materials to harness low-frequency mechanical motions such as human body movements and, air/water flow. Over the past decade, research has continuously progressed on NGs using lead $Pb(ZrTi)O_3$ (designated as PZT) [12-15] and lead-free nanostructures (ZnO [16-19], $BaTiO_3$ (designated as BTO) [20, 21], $NaNbO_3$ [22], $(KNa)NbO_3$ (designated as KNN) [23-25] grown on various substrates by different fabrication methods. Prof. Z. L. Wang introduced a conventional ZnO nanowire (NW) array nanogenerator using a vapor–liquid–solid process [1] (and physical vapor deposition) [26], which was later extended upon by other groups with various ZnO nanostructures such as nanorods (fabricated by RF magnetron sputtering followed by a hydrothermal method) [27], nanowalls (fabricated by thermal chemical vapor deposition) [28], and films (fabricated by RF sputtering) [18]. Here, the generated power is normally small (it lies between the uW/cm^3 to mW/cm^3 range), but capable of driving low-power electronic devices, self-powered nanodevices and implantable devices. This small output is due to many factors, such as a lower piezoelectric coefficient (d_{33}), the screening effect induced by the high free carrier density, and the growth of nanostructures on various substrates could not withstand

the critical applied force (or strain) due to the brittleness of ZnO [1, 16-19, 26-28]. Moreover, the output from conventional NGs suffers from environmental factors such as oxygen, humidity, absorption (reducing gases and agents such as ethanol, methanol, formaldehyde, and acetone), radiation, temperature and atmospheric effects [26b]. To resolve these issues, NG studies were extended to include the growth of PZT, BTO and KNN perovskites on substrates such as PZT ribbons [13] (by RF sputtering, deposited on Pt/Ti/SiO2/Si by the sol-gel technique), PZT nanofibers [12] (by electro spinning), PZT thin films [14] (by the sol-gel method followed by a laser lift-off process), PZT nanoparticles on mwCNT [15] (by a heating and stirring method), BTO thin film [21] (by RF sputtering, transferred by soft lithography on plastic substrates), KNN nanofiber [25] (by sol-gel electro-spinning and calcination processes), KNN nanorods [23] (by epitaxial growth on a conducting $SrRuO_3/SrTiO_3$ substrate *via* the hydrothermal method), KN nanowires [24] (by the hydrothermal method). The aforementioned fabrication methods of perovskites materials suitable for large-scale production of high-quality thin films with good crystalline behavior, but the transfer techniques such as soft lithography and laser lift-off process are complicated and result in an increase in the manufacturing cost. Except PZT film fabrication by the sol-gel method followed by a laser lift-off process, the other processes for fabricating pure PZT, KNN and BTO thin films are limited by the low electrical output performance of their devices. Specifically, PZT based NGs (pure or composite devices) have serious drawbacks i.e., lead toxicity will directly affect the intellectual development, neurological development and the genetic transcription of DNA and result in environmental pollution during synthesis (calcination and sintering) [29-31]. This clearly suggest that PZT materials (or devices) require a controlled usage and are not suitable for implantable and health monitoring devices. Therefore, BTO and KNN are alternative biocompatible materials for improving the output performance of NGs, i.e.,

they have higher d_{33} coefficients than ZnO and lower d_{33} coefficients than PZT materials. Since 2010, many researchers have focused on the development of KNN NGs and its performance is related to the high d_{33} (416 pC/N), electromechanical coefficient (k_{33}) (≈ 0.6) and Curie temperature (T_c) of up to 460 °C (comparable to PZT). Untill now, developed KNN NGs generate medium output and have important disadvantages, such as densification, high manufacturing cost, poor piezoelectric properties at room temperature, and high T_c becomes colorless due to the presence of another phase transformation from an ortho-rhombic to a tetragonal symmetry at ~ 200 ºC [23-25, 30, 32-35a]. All these factors restrict the use of the KNN material for practical applications. However, KNN may be suitable for replacing the PZT materials in the near future, but it is not suitable at the moment. On the other hand, pure BTO nanoparticles are biocompatible, easy to synthesize, and low cost and they exhibit good piezoelectric properties at room temperature, except low $T_c \approx 130\ ^0$C. High-output, large scale films with novel microstructures that are fabricated using, low cost and eco-friendly methods are necessary for future generation devices, which is potentially supported by the use of the composite (polymer-nanoparticle) technology [10, 11, 35, 36]. The polymer matrix with nanoparticles (NPs) reduces leakage currents, increases the flexibility, and durability, and withstands large mechanical forces. It is highly desirable to fabricate smart battery-free NGs with a sensing capability and minimum external sensory circuitry for inpatient rehabilitation periods, finger Braille typing and directional bending of the human body.

Here, we adopted BTO NPs and anionic polysaccharide template structures such as calcium alginate polymer (Ca-alg). The functional properties and its electro-mechanical conversion efficiency of BTO NPs directly depend on the applied mechanical pressure, spontaneous polarization, dielectric constant and electric field. Blending BTO NPs with polysaccharides

without altering the BTO tetragonal phase and tuning the functional properties, such as the piezoelectric and semiconductor behaviors, may be an alternative route to achieving high performance innovative micro/nanostructure-based nanogenerators. Here, Ca-alg immobilized the nanoparticles *via* cross linked junctions with divalent cations (Ca^{2+}, Ba^{2+}), which result in a three-dimensional (3D) gel network. Ca-alg can be useful in two ways: first, it can act as a supporting cross-linker to hold the piezoelectric BTO NPs and to form as a spherical composite bead and second, it can contribute additional output through triboelectric polarity because it is an anionic polysaccharide with a relative permittivity (ε_r = 80-85) [37-40]. The physical properties and contribution towards electricity generation of the Ca-alg polymer are analogous to those of many other materials, such as polyvinylidene fluoride (PVDF), polydimethylsiloxane (PDMS), poly(vinylidenefluoride-co-trifluoroethylene) (PVDF-TrFE), polytetrafluoroethylene (PTFE) and paper.

Herein, we report on the development of a novel spherical composite bead based NG (CBNG) device using the eco-friendly ionotropic gelation (IG) technique. The composite film is made up of spherical composite beads (BTO NPs embedded into the Ca-alg beads) and PDMS matrix. We examine the feasibility, the adaptability of the preparation of beads (pure and composite) at micro dimensions by optimizing the weight ratio of alginate (up to 2 wt %) and the functionalities achieved through physisorption between the NPs and polymer matrix. We observe a stable electrical output from the strip-based CBNG (S-CBNG) device, which is highly sensitive and can deliver a maximum amount of positive peak output current (227 μA) and voltage (80 V) with a low applied mechanical pressure (1.70 kPa). This is due to the combined triboelectrification and piezoelectric effects of the S-CBNG device. The generated power density for the S-CBNG device is approximately 16.14 W/m^2 under a low applied mechanical pressure

of 1.77 kPa. This electric power is enough to continuously power-up or drive low power electronic devices, such as monochrome liquid crystal display (LCD) devices and commercial light emitting devices (11 blue and 11 green LEDs), without any storage element. The generation of electrical output and the working mechanism were analyzed by observing the responses of the pure PDMS, PDMS/Ca-alg and composite beads/PDMS devices, and a detailed explanation was presented schematically. We also tested the electrical response of the S-CBNG device under different mechanical pressures (0.170 kPa to 1.77 kPa) and different bending curve angles (0º, 41.1°, 75.5º and 95.2°) which confirm the good reliability of the device. The device was tested with an applied mechanical pressure of 1.77 kPa for 1300 seconds and the corresponding output showed no considerable degradation, which confirms that the S-CBNG device has good stability. Additionally, we demonstrated that the S-CBNG device could function as a non-invasive self-powered wearable flexion (SWF) sensor to measure the tendon-muscle unit force that is created by human finger flexion/extension movements. The optimal location of the SWF sensor and the classification of each finger movement can be established using the electrical outputs of the sensor. These results indicate that the SWF sensor is a smart health monitoring device that is battery free and exhibits a sensing functionality. This is an alternative, reliable approach compared to traditional approaches, such as electromyography sensors [41, 42], fuzzy-based decision-making systems [43] and flexible electrogoniometers [44, 45] for classifying and detecting finger movements. Furthermore, the CBNG devices are cost-effective, durable, flexible, and eco-friendly.

5.1.2 Experimental Method

5.1.2.1 Synthesis of BTO NPs

Highly crystalline BTO NPs were synthesized by adopting the high temperature solid state reaction method. The $BaCO_3$ (99.95 %, High Purity Chemicals) and TiO_2 (98 %, Daejung) precursors were weighed according to the atomic ratio of BTO NPs. To obtain a homogeneous powder, the raw materials were mixed by manual grinding in an acetone medium using a mortar and pestle for 30 min. The grinded mixture was placed in an alumina boat and heated up to 1200 °C for 2 h in an open tube furnace at a heating rate of 2.5 °C/min. The BTO NPs can be formed by the following reaction between the $BaCO_3$ and TiO_2

$$BaCO_3\,(s) + TiO_2\,(s) \rightarrow BaTiO_3\,(s) + CO_2\,(g)$$

The obtained product was removed from the furnace after the reaction completed and cooled down naturally to room temperature. The product was formed in the form of nano-sized particles grouped together as a clusters and reduced these clusters to obtain the fine crystalline and smooth nanoparticles by the manual hand grinding using the mortar and pestle for 1 h. Here there is no sign of agglomeration of BTO NPs. Further, as-synthesized BTO NPs are used for the composite beads formation and investigated the energy harvesting capability.

5.1.2.2 Fabrication of spherical Ca-alginate and composite beads

The fabrication procedure of the Na-alginate (designated as Na-alg) and BTO NPs/Na-alg solutions is schematically shown in **Figure 5.1.1a.** Fabrication of the composite beads using the ionotropic gelation (IG) method involved three key steps: first, a homogeneous aqueous solution of Na-alg was prepared without precipitation of alginic acid. 2 g of alginic acid sodium salt (Sigma–Aldrich) was dissolved in 100 mL of double distilled water under constant stirring at 50 °C for 2 h to obtain a clear transparent solution. Second, the BTO NPs were functionalized using the Na-alg i.e., a fixed 1 wt % of BTO NPs was dissolved in the Na-alg solution by magnetically stirring at 70 °C for 2 h to prevent agglomeration of the BTO NPs. Third, sodium

ions (Na^{1+}) were exchanged with calcium ions (Ca^{2+}) to form the BTO NPs/Ca-alg beads by adding 5 m*l* amount of the homogeneous BTO NPs/Na-alg solution drop wise into 1 M $CaCl_2$ solution. The composite solution was dropped 2 cm away from the $CaCl_2$ solution as shown in **Figure 5.1.2a**. After 30 min of gelation, the beads were removed from the $CaCl_2$ solution, soaked in DI water for 15 min to remove the excess Ca^{2+} ions, and then dried for 24 h at room temperature. A similar approach was followed to fabricate the pure Ca-alg beads. The optical images of the pure and hybrid beads were shown in the **Figure 5.1.2 (b, c)**

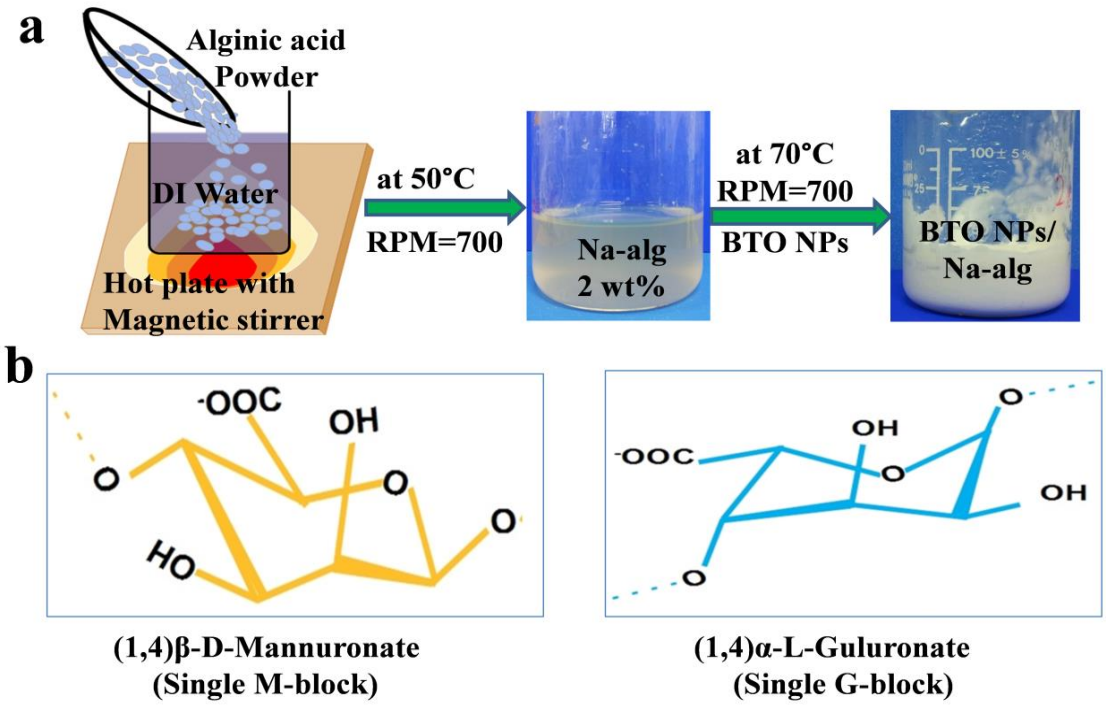

Figure 5.1.1 (a) Fabrication Protocol for the preparation of Na-alg (2 wt %) and BTO NPs/Na-alg (1 wt % / 2 wt %) aqueous solutions represented through schematic manner. **(b)** Schematic illustrations of homo-polymer fractions of Na-alg (M and G block).

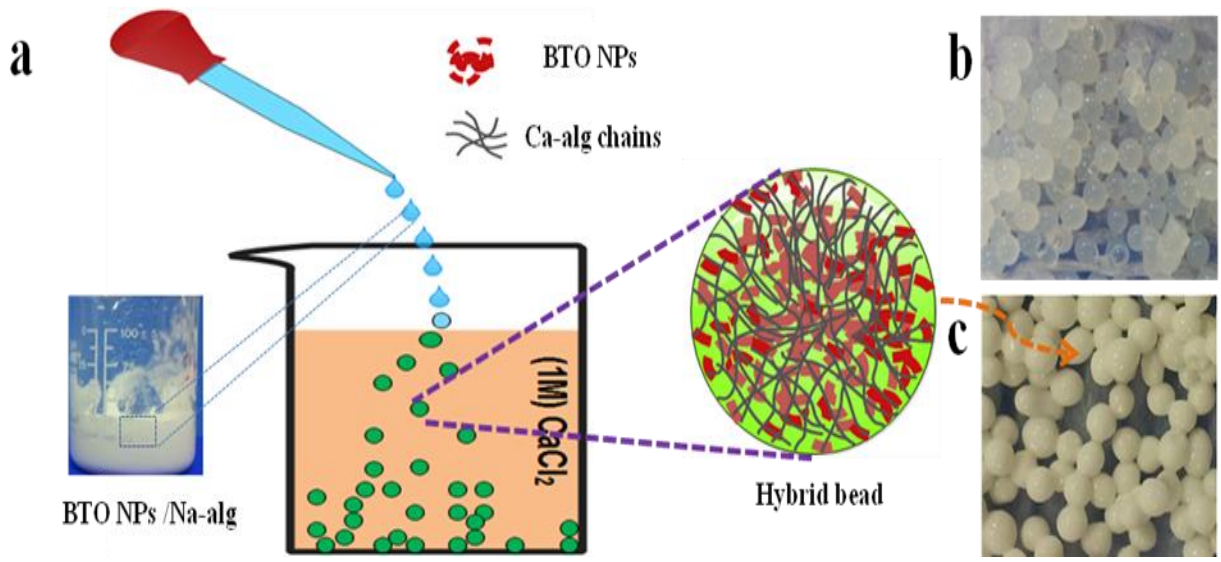

Figure 5.1.2 Fabrication of pure and hybrid beads using the ionotropic gelation (IG) method. **(a)** Schematic representation of hybrid beads fabricated using a 1 M $CaCl_2$ solution. **(b, c)** Optical photographs of the pure and hybrid beads.

5.1.2.3 Fabrication of pure and composite bead based nanogenerators

A BTO NPs-Ca alg/PDMS composite thick film with a concentration of 20 wt % was fabricated. Initially, a polydimethylsiloxane (PDMS) matrix (Slygard 184, Dow Corning Corporation) solution was prepared by rigorously mixing 10 wt % percentage of part A and 1 wt % of part B (the hardener) and then degassed through a vacuum oven for approximately 5 minutes until no air bubbles were observed in the solution. Next, 2.5 g of the as fabricated composite beads were homogeneously dispersed in the final PDMS solution (10 gm) and gently stirred with a spatula. Then, the solution was poured into a glass petri dish and curied at 70 °C for 1 h in a hot oven. The obtained composite layer was cut into the desired dimensions (2 x1.5 cm^2) and two Al foil electrodes were attached on the top and bottom of the composite film to form the CBNG device as shown in **Figure 5.1.3**. External connections were made using Cu wires that were attached to the Al foils with silver paste. Finally, the whole device was sandwiched between thin PDMS layers to protect the film against external mechanical stresses. Before electrical

characterization, the devices were electrically poled at 3 kV for 24 h at ambient temperature. A similar method was followed to fabricate PDMS, Ca-alg/PDMS devices and especially the S-CBNG device (7.5 x 1.5 cm^2) used for the SWF sensor.

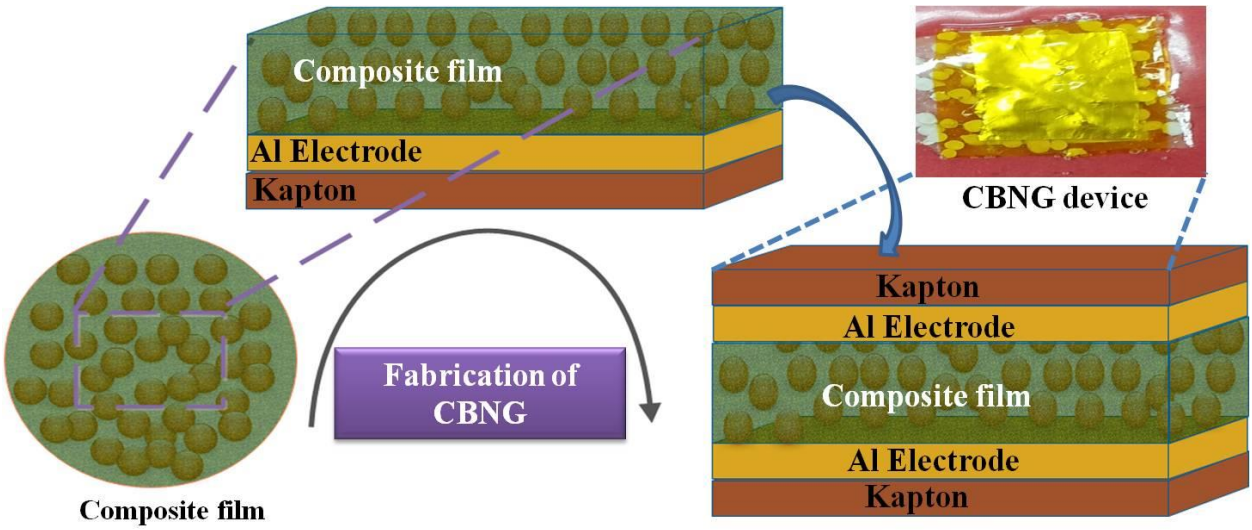

Figure 5.1.3 Schematic diagram for the fabrication of the CBNG device. The top right inset shows an optical photograph of the as-fabricated CBNG device.

5.1.3 Results and Discussion

5.1.3.1 Composites beads, surface morphological and structural analysis

Spherical composite beads were fabricated using the IG method and the fabrication is schematically shown in **Figure 5.1.2**. The whitish-colored composite beads indicated the presence of BTO NPs stacked in the fibrous Ca-alg chains of 1–4-linked β-D-mannuronic acid (M) and its C-5 epimer α-L-guluronic acid (G) [46], as shown in **Figure 5.1.1b.** Pure Ca-alg beads have a diameter (Ø) of 800–900 μm with a crumpled nature, and the magnified image in **Figure 5.1.4a** shows the smooth surface of Ca-alg. In contrast, the composite beads have increased diameters up to 2.2 mm, and magnified image in **Figure 5.1.4b** shows a rough surface and a uniform distribution of BTO NPs in Ca-alg. Here, the diameter of the composite beads

increased due to changes in the viscosity and surface tension of the BTO NPs/Na-alg aqueous solution.

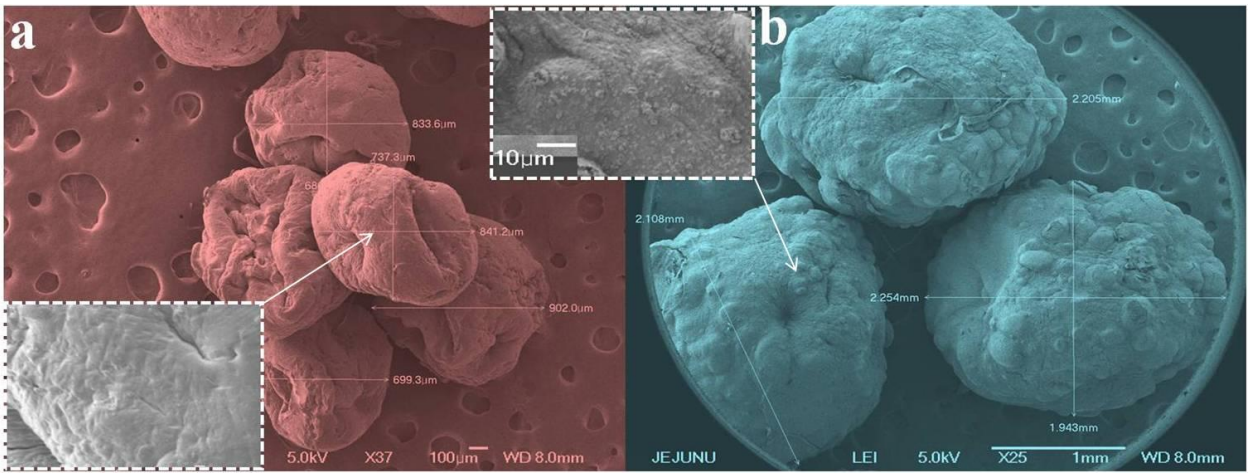

Figure 5.1.4 (a) FE-SEM image of pure beads with a crumpled morphology at a 100-µm scale **(b)** FE-SEM image of spherical hybrid beads at 1 mm scale. The magnified images of pure and hybrid beads that shown the smooth and rough surface at a 10-µm scale.

5.1.3.1.1 Structural analysis (XRD, Raman and FT-IR) of BTO NPs

Before the fabrication of composite beads, the structural properties of high quality BTO NPs were studied using XRD, Raman spectroscopy, FE-SEM and FT-IR techniques. The splitting behavior of the diffraction peak at 45º represents the (002) and, (200) planes, which confirms the tetragonal crystal structure of the BTO NPs, as shown in **Figure 5.1.5a** and is well matched with the reference data (the ICDD-98-001-3771 pattern). The total average crystallite size and lattice strains calculated are 34.04 nm and 0.0031, respectively.

Lattice Strain and Crystallite Size calculations:

The average size of the crystalline domains (ordered) may be smaller than or equal to the grain size. The equation below is applicable for crystallite/grain sizes down to the order of the 2 to 300 nm range. According to the Scherrer equation, the crystalline size and lattice stain can be computed as follows:

$$L = \frac{K\lambda}{\beta \cos(\theta)} \quad and \quad \epsilon = \frac{\beta}{4*\tan(\theta)} \qquad \text{(E5.1.1)}$$

where L = Average crystalline Size (nm)

K = Scherrer constant (0.94 depending upon grain shape)

λ = Wavelength (nm)

β = peak width in radians at full width half maximum

The calculated crystallite size (using equation 1) is approximately 29.876 nm for the major peak intensity positioned at 31.57°, which represents the (110) plane and its corresponding lattice strain is approximately 0.0044. The step wise detailed calculations and the corresponding data are given below:

$$L = \frac{0.94 * (0.154056)}{0.005037 * (0.96228924)}$$

$$L = \frac{0.14481264}{0.00484705}$$

$$\boldsymbol{L = 29.876\, nm}$$

&

$$\epsilon = \frac{0.005037}{4 * 0.28268874}$$

$$\boldsymbol{\epsilon = 0.0044545}$$

To identify the cumulative crystallite size and lattice stain existing in, as fabricated BTO nanoparticles by solid state reaction method, we considered the four major peak intensities posited at 31.57°, 38.94°, 45.36° and 56.24° respectively. By using the above equation, we calculated the crystallite size and lattice strain for each peak and its corresponding data has been given in Table 5.1.1. The obtained total average crystallite size and lattice stain is in the order of 34.04 nm and 0.0031 respectively.

Table 5.1.1 XRD analysis of $BaTiO_3$ nanoparticles

Peak No	Position (Degree)	β(FWHM) (radians)	Cos(θ)	Crystallite Size (nm)	lattice strain
1	31.57	0.005037	0.96228	29.876	0.0044
2	38.94	0.003474	0.94281	44.230	0.0025
3	45.36	0.005036	0.92267	31.169	0.0030
4	56.24	0.005311	0.88196	30919	0.0025
			Average	34.04 nm	0.0031

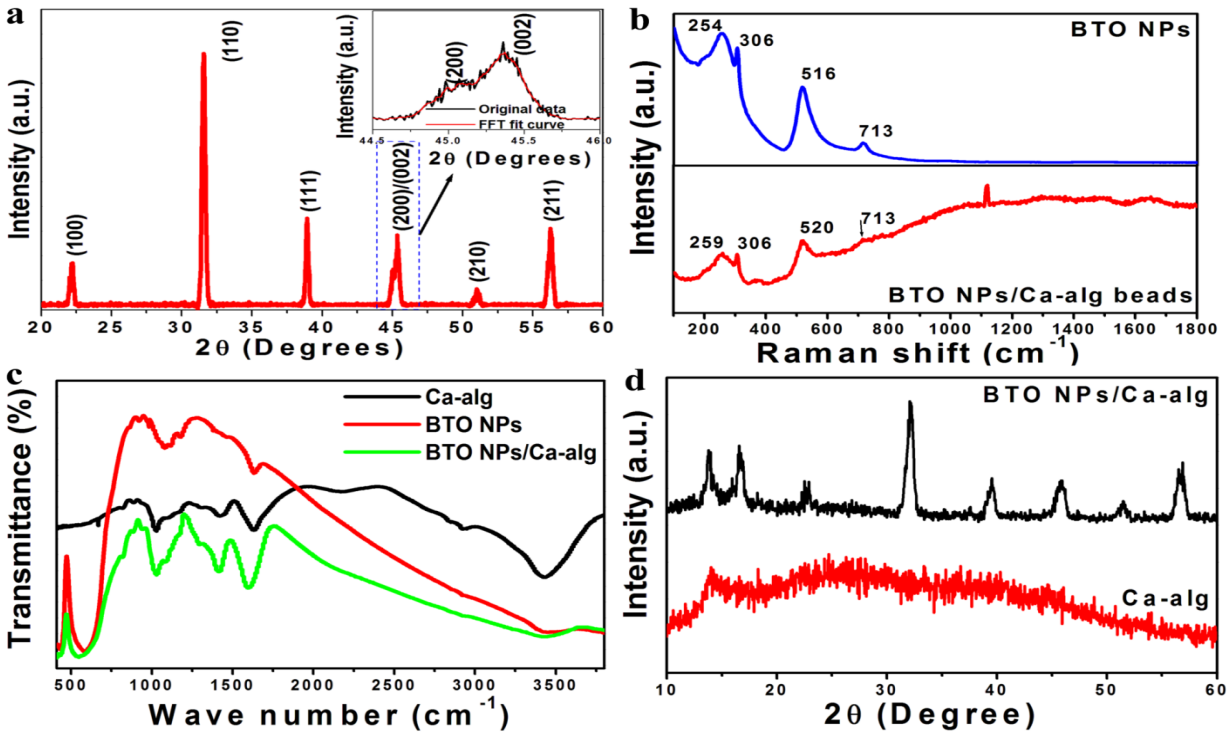

Figure 5.1.5(a) XRD pattern of pure BTO NPs and the inset shows the splitting nature of the peak at 45° **(b)** Raman spectra of BTO NPs and composite beads **(c)** FT-IR spectra of Ca-alg, BTO NPs and BTO NPs/Ca-alg. **(d)** XRD pattern of Ca-alg and BTO NPs/Ca-alg.

Similarly, the Raman active modes of BTO NPs confirm the tetragonal crystal phase, as shown in **Figure 5.1.5b**; which is observed by the characteristic peak positions at 306 cm^{-1} [B_1(TO+LO), E], 516 cm^{-1} [A_1(TO), E] and a few other weak modes such as 258 cm^{-1} [A_1(TO)] and, 713 cm^{-1} [A_1(LO), E]. Both the XRD and Raman patterns of BTO NPs correlate well with

the tetragonal phase [47-50], which confirms the presence of non-centrosymmetric regions that are formed from the local off-centering of titanium atoms. **Figure 5.1.6** shows the FE-SEM image of BTO NPs and confirms the random orientation of the particles at a 100 nm scale. The BTO NPs exhibit a characteristic peak at 600–530 cm^{-1} for the stretching and bending of the Ti–O bond within the TiO_6 octahedra (**Figure 5.1.5c**). A biocompatible, water-insoluble and gelatinous-type of Ca-alg [46, 51] was selected for surface functionalization of the BTO NPs to generate high-performance spherical composite beads for energy harvesting.

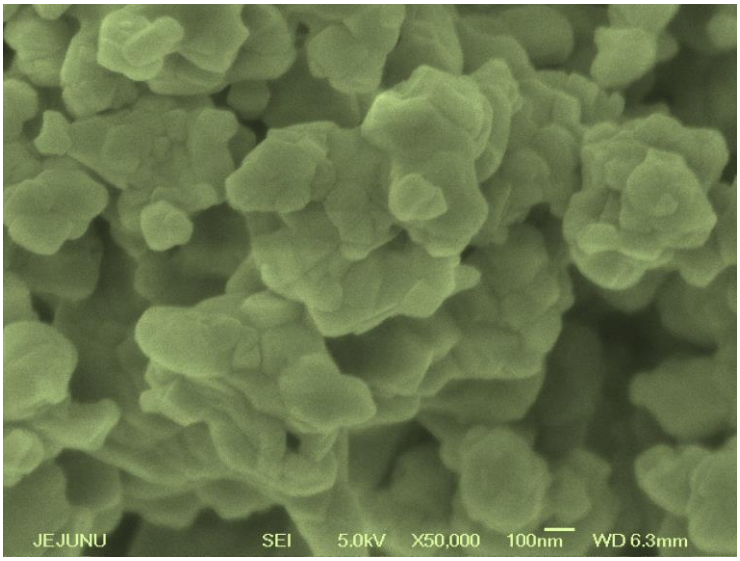

Figure 5.1.6 Surface morphology of as synthesized BTO NPs using solid state reaction method

5.1.3.1.2 Structural analysis (XRD, Raman and FT-IR) of beads

Figure 5.1.5c shows the Fourier transform infrared (FT-IR) spectra of as-synthesized Ca-alg and the BTO NPs/Ca-alg samples. The Ca-alg spectra shows bands at 3428 cm^{-1} for the –OH group, 2930 cm^{-1} for the C–H stretching vibration, and 1628 and, 1422 cm^{-1} for the asymmetric and symmetric vibrations of O=C–O [46]. A shift at lower wavelengths was observed for the composite sample, the peak at 548 cm^{-1} (and 584 cm^{-1} for pure BTO NPs) indicates the internal stresses of TiO_6 in the BTO lattice. In this work, the carboxylate group present on the Na-alg is

able to undergo a sol–gel transition in the presence of multivalent cations (Ca^{2+} ions) to form hydrogel. This gel formation was driven by the interactions between the G-blocks, which associate to form tightly held junctions in the presence of the divalent Ca^{2+} cations. In addition to the G-blocks, MG blocks (weak junctions [46, 52]) can also participate to form good gels. Thus, alginates with high G contents yield stronger gels. The use of Ca-alg as a carrier material for the BTO NPs raises the possibility of selective adsorption of organic and inorganic molecules, depending on their electrical charge, *via* interactions with the negatively charged alginate carboxylate groups. Raman spectroscopy was employed to understand the dynamic symmetry of Ca-alg and the composite sample. The Ca-alg spectra [53, 54] were divided into two categories according to the Raman shifts: shifts < 1300 cm^{-1} represents the vibrations of the polymer backbone and shifts > 1300 cm^{-1} represent the stretching vibrations of the carboxylate functional group. Ca-alg can be differentiated from Na-alg by the COO^{-} stretching band.

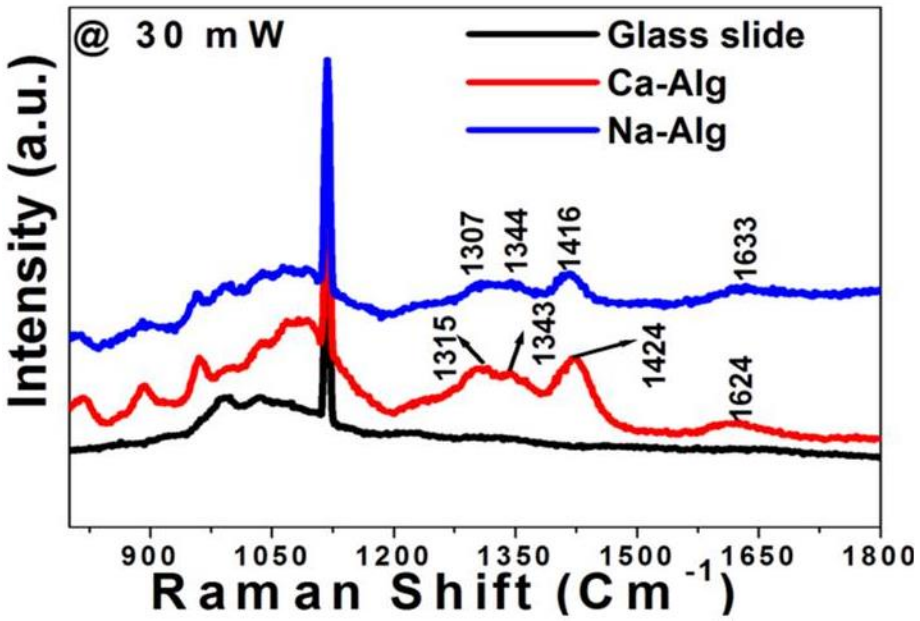

Figure 5.1.7 Raman spectra of the as-prepared Ca-alg and Na-alg samples and a bare glass slide

This band appeared at 1413 cm^{-1} for Na-alg and at 1424 cm^{-1} for Ca-alg [53] as shown in Figure 5.1.7. The Raman spectra of the composite confirm the functionalization of BTO NPs by Ca-alg, as shown in **Figure 5.1.5b**. This indicated that the tetragonal phase of the BTO NPs [11, 50, 55] was not changed when the BTO NPs were mixed with Ca-alg. There was no significant change in the major peak position of the BTO tetragonal phase at 306 cm^{-1} but the observed intensity was much lower than that of pure BTO NPs. The peak at 1119 cm^{-1} corresponds to the glass substrate, and other weak peaks observed from 1350–1700 cm^{-1} are related to the Ca-alg matrix [53, 54]. Overall, the FT-IR and Raman spectra provide direct evidence of physisorption between the BTO NPs and Ca-alg. In this case, the cross linking and gel strength of the polymer depended on the presence of G blocks and their association with Ca^{2+} metal ions. Meanwhile, the G blocks are more likely to interact with BTO NPs and are less dependent on weak hetero blocks (MG) to form the desired microstructures without changing the tetragonal phase of the BTO NPs. This was confirmed by the XRD peak position of the composite at $2\theta = 13°$ for the G block of alginate as shown in **Figure 5.1.5d**.

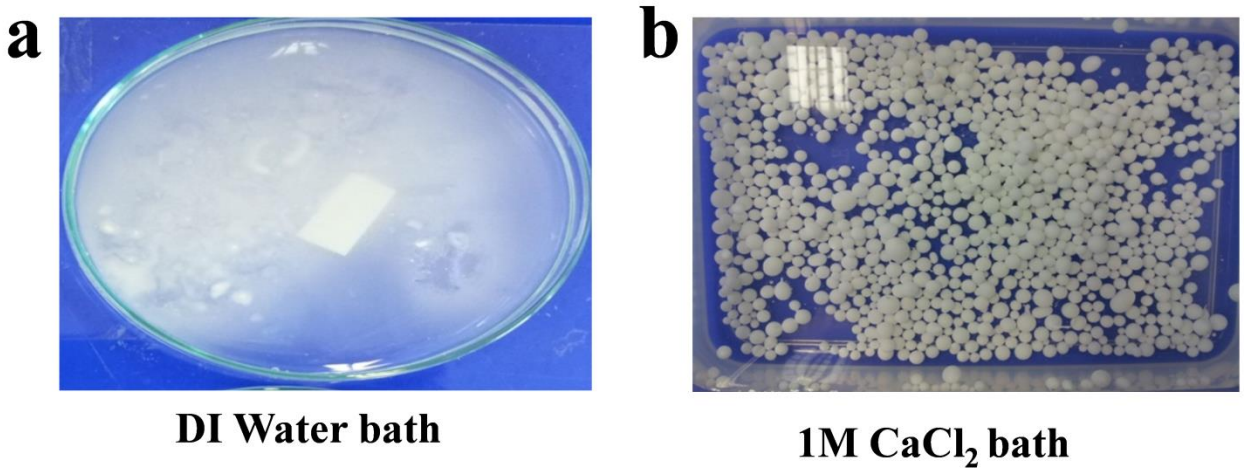

Figure 5.1.8 Formation and ionic gelation strength of Ca-alg **(a)** DI water **(b)** 1 M $Cacl_2$ bath

Next, we confirmed the ionic gelation strength of composite beads under various conditions such as in deionized water (DI) and 1 M $CaCl_2$ solutions. Beads did not form when pure DI water (0 M $CaCl_2$) was used, due to the lack of cross linking Ca^{2+} ions interactions occurred between G-blocks and BTO NPs. Good ionic gelation strength was obtained with a 1 M $CaCl_2$ solution as shown in **Figure 5.1.8**. The G-rich network of Ca-alg and the associated bonds between the metal cations (Ca^{2+} ions) and carboxylate groups are schematically shown in **Figure 5.1.9a**. The physical interaction and good distribution of the BTO NPs along with the G-rich network of Ca-alg are schematically shown in **Figure 5.1.9b**. This schematic was obtained from the FE-SEM images of pure and composite beads as shown in **Figure 5.1.4(f, g)**.

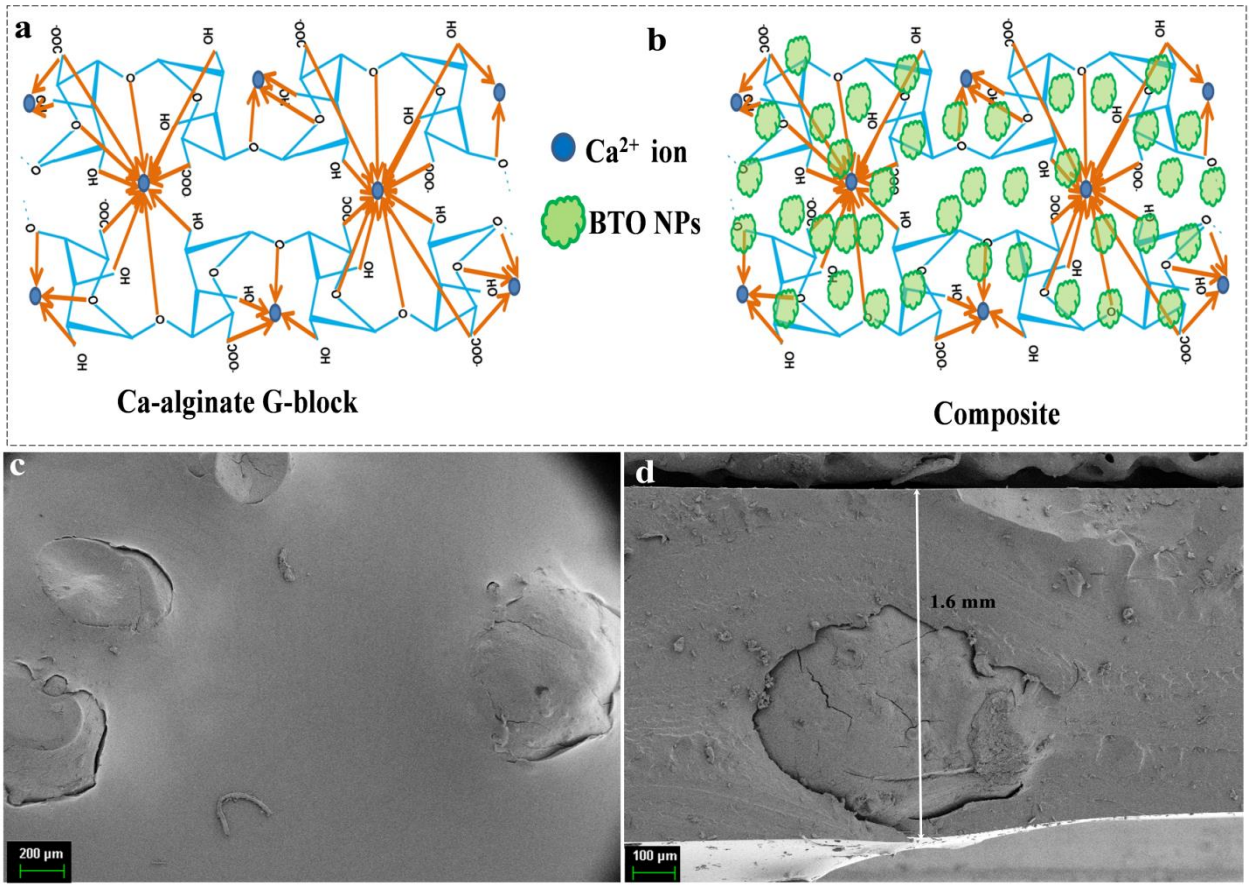

Figure 5.1.9(a) Formation of pure beads *via* ionic interactions between Na-alg and divalent Ca^{2+} cations through G blocks (egg-box model). **(b)** Formation of hybrid beads from the

immobilization and physisorption of BTO NPs with cross-linking of Ca-alg. **(c, d)** Surface morphology and cross-sectional image of composite film at 200 μm and 100 μm scales.

5.1.3.1.3 Energy harvesting performance of CBNG device

The complete fabrication procedure of the thick composite film and CBNG device was given in the experimental section. Initially, we fabricated BTO/Ca-alg beads with a diameter (Ø) ≈2 to 2.4 mm, as shown in **Figure 5.1.4b.** To reduce the thickness of composite film, we need to control and reduce the spherical composite beads. In this work, energy harvesting studies and self-powered flexion sensor studies were carried out by the reducing the spherical composite beads to a diameter (Ø) ≈1.3 to 1.5 mm using pipette droplet with a lower diameter. **Figure 5.1.9c** presents the dispersion of composite beads in PDMS matrix and the surface morphology of the composite. The film thickness is approximately 1.6 mm, which is measured using the cross sectional FE-SEM image of the composite film, as shown in **Figure 5.1.9d**. The device fabrication is schematically illustrated in **Figure 5.1.10a** and the inset image shows as fabricated CBNG device (with an area of 3 cm^2). The energy harvesting performance of the CBNG was investigated using a cyclic frequency-dependent mechanical load of 11 N (in terms of pressure ≈36.67 kPa) was generated from the ET-126 electro-dynamic shaker, which is controlled using the power amplifier (LabWorks Inc., Model No: Pa-138) and sweep function generator (FG-1880B). Initially, a rectified low electric potential (1 V) was generated across the top and bottom Al electrodes when the mechanical load at 3 Hz acted perpendicular to the CBNG device. This was attributed to either the capacitance of the CBNG device or the electric dipole orientation behavior of the BTO NPs [1, 11]. The generated electric potential increased from 1 to 10 V when the cyclic loading frequency was increased from 3 to 20 Hz, as shown in **Figure 5.1.10b**. Above 20 Hz, the electrical output of the CBNG device gradually decreased due to the mismatch

between the optimum working frequency (resonant frequency (f_r)) of the CBNG device and the applied frequency of load**.** No open circuit voltage was observed in the absence of mechanical load, which was attributed to the random orientation of electric dipoles (different directions) or relaxation of electric charges present in the composite film that resulted in a zero net dipole moment as shown in **Figure 5.1.11a**. This behavior indicated that the stress-induced poling effect [1, 11, 55] i.e., the orientation of electric dipoles or generation and transfer of charges in the composite film, was perpendicular to the applied mechanical load.

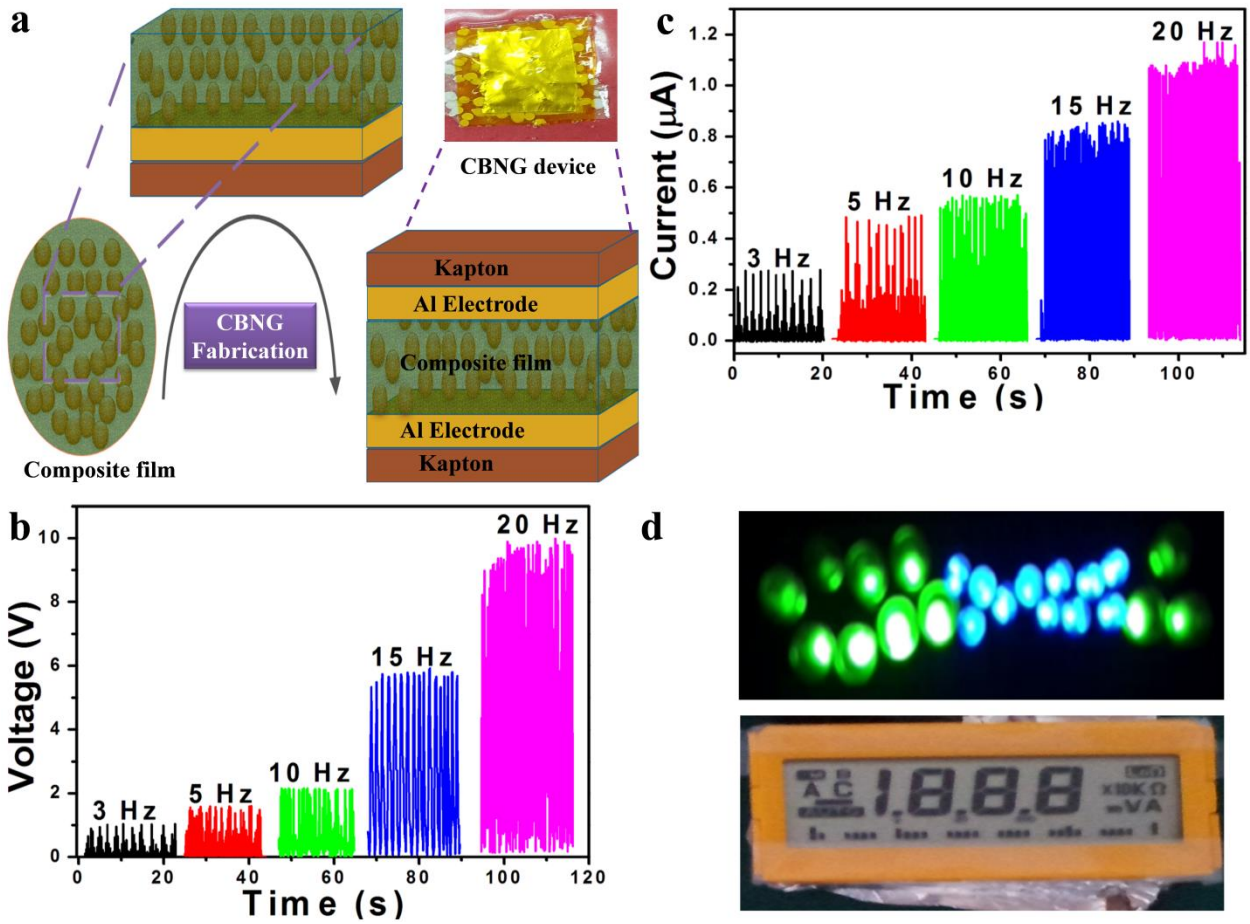

Figure 5.1.10 (a) Schematic diagram for the fabrication of the CBNG device. The top right inset shows an optical photograph of the as-fabricated CBNG device. **(b, c)** Open circuit voltage and short circuit current of the CBNG device as a function of frequency (3, 5, 10, 15 and 20 Hz) with a constant mechanical pressure of 36.67 kPa. **(d)** CBNG device output used to power-up the LEDs and monochrome LCD display.

Similarly, the frequency dependent short circuit current of the CBNG device is shown in **Figure 5.1.10c**. This frequency-dependent electrical response may have resulted from the piezoelectric nature of the BTO NPs with respect to the vibration of the mechanical energy source, which can be analyzed using the equation-E5.1.2:

$$f_r = \frac{\pi}{2}\sqrt{\frac{K_{eff}}{M_{eff}}} \qquad \text{(E5.1.2)}$$

where the effective spring constant [$K_{eff} = K_{piezo}(1/(R_i+R_e))$] is a function of the piezoelectric material, R_i is the internal resistance of the material, R_e is the external resistance and M_{eff} represents the effective mass of the energy harvesting device. The detailed relationships between mechanical stress, electrical output and strain for a piezoelectric harvester were developed using the fundamental piezoelectric theory [11, 56].

Relationship between the electrical quantities and the mechanical force parameters for the piezoelectric energy harvesting devices:

The open circuit voltage (V_{OC}) and short circuit current (I_{SC}) of piezoelectric nanogenerators are directly related to the mechanical parameters such as force and displacement (Z). The relationship can be written as follows (the macroscopic view):

$$F_P = K_{PE}Z + \alpha V_{OC}$$

and

$$I_{SC} = \alpha \dot{Z} - C_P \frac{dV_{OC}}{dt} \qquad \text{(E5.1.3)}$$

where α represents the force factor, F_P is the restoring force of the piezoelectric material, C_P is the clamped capacitance and K_{PE} is the stiffness of the piezoelectric material. The variables C_P, K_{PE} and α defined as follows:

$$K_{PE} = \frac{C_{33}^{E} A}{L}, C_P = \frac{\varepsilon_{33}^{S} A}{L}, \alpha = \frac{e_{33} A}{L} \quad \text{(E5.1.4)}$$

The electromechanical quantities of stress (*T*), strain (*S*), electric field (*E*) and electrical induction (*D*) are obtained by the tensor and electric induction tensor matrices and can be written as follows:

$$E = -\frac{V}{L}, S = \frac{Z}{L}, I = A\frac{dD}{dt}, F_P = AT \quad \text{(E5.1.5)}$$

where *A* and *L* represent the sectional area and thickness of the active working zone of the piezoelectric nanogenerator, respectively. By solving Equation-E5.1.3, the open circuit voltage for the piezoelectric nanogenerator as a function of the piezoelectric coefficient (d_{33}) and relative permittivity can be computed as follows:

$$V_{OC} = g_{33}\sigma Y t \quad \text{(E5.1.6)}$$

where $g_{33}$is the piezoelectric voltage constant ($d_{33} = g_{33}\epsilon_O K$), *Y* and *t* are the Young's modulus of the composite and the thickness of the device, and σ is the strain in the perpendicular direction. The short circuit current can be evaluated by using the equation:

$$I_{SC} = d_{ii} Y A \varepsilon \quad \text{(E.5.1.7)}$$

where d_{ii} is the piezoelectric coefficient, *A* is the cross-sectional area and ε is the applied strain.

5.1.3.1.4 Biomechanical hand force effect on CBNG device output

Figure 5.1.10d shows the ability of the CBNG device to drive 22 LEDs [11 green (Model no: 3BG4UC00) and, 11 blue (Model no: 3BB4SC00)] and a monochrome LCD display (3 ½ LCD display with the maximum reading of 1999 and display size ≈16 mm x 48 mm) by hand tapping, without using any energy storage device. A rapid biomechanical force was applied to establish the sensitivity and maximum energy harvesting capability of the CBNG device. A high

asymmetric electrical response (short circuit current (I_{SC}) = 1.598 mA, open circuit voltage (V_{OC}) = 14.53 V) was observed for the CBNG device under rapid hand-force tapping and releasing conditions as shown in **Figure 5.1.11(b, c)** [57]. This asymmetric output was attributed to the non-symmetric nature of the rapid hand force that acted on the CBNG device, and it also indicated that the application of a large mechanical force to the CBNG device could provide higher electrical response. Such a performance of the CBNG device primarily resulted from two factors: first, the creation of an inner piezoelectric field of BTO NPs within the Ca-alg matrix when the load was applied on the device and second, the generation of triboelectric charges of PDMS/Ca-alg with respect to the Al electrode. Here, a small air gap of 100 to 200 μm may exist between the composite film and the top Al foil[3].

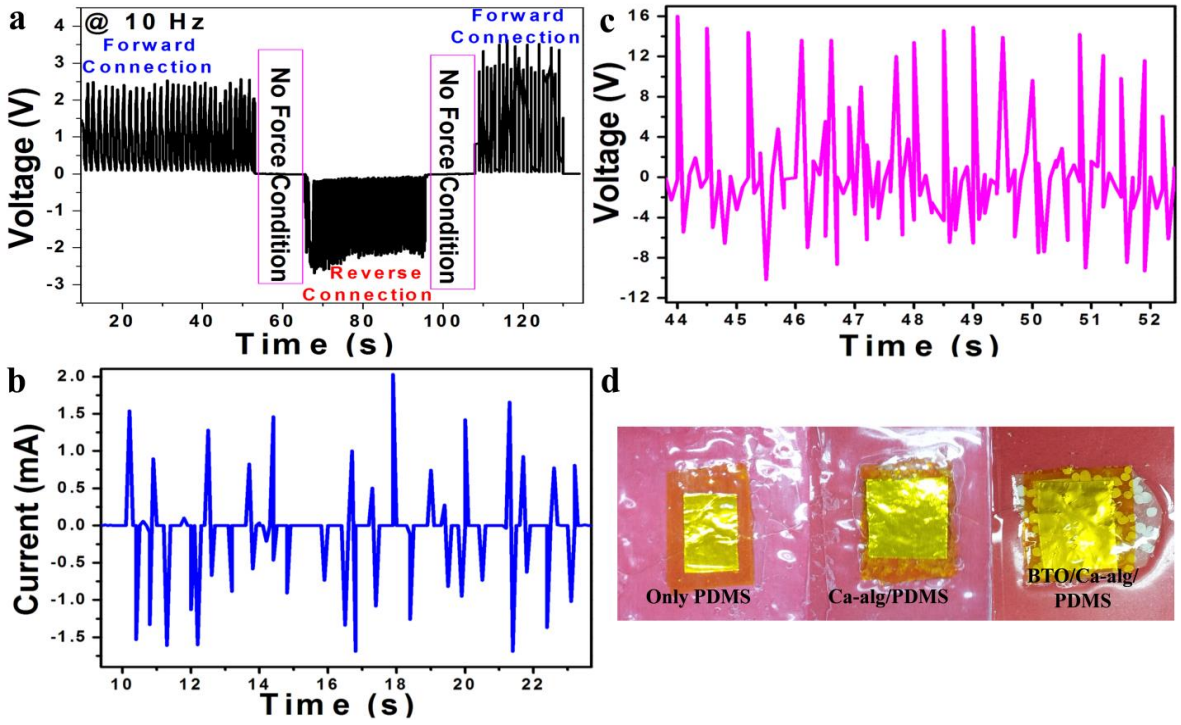

Figure 5.1.11 (a) Rectified open circuit voltage of CBNG device upon the mechanical pressure 36.67 kPa at 10 Hz, confirms the polarity. No electric potential was generated by the device when the pressure was removed. **(b, c)** Current and voltage responses of CBNG device upon the rapid hand force tapping and releasing conditions. **(d)** Digital photographs of as-fabricated PMDS, Ca-alg beads/PDMS and BTO/Ca-alg beads/PDMS (CBNG) devices.

5.1.3.1.5 Constant Load effect and power density calculations of CBNG

However, to confirm this combined piezoelectric-triboelectric working mechanism and the role of Ca-alg for energy harvesting devices including pure PDMS, PDMS/Ca-alg beads and PDMS/Ca-alg-BTO NP beads were fabricated and investigated, as shown in **Figure 5.1.11d**. The generation of electric potential for all devices was experimentally studied by keeping the mechanical pressure of 36.67 kPa constant (at a fixed frequency of 20 Hz) and the corresponding rectified voltage is shown in **Figure 5.1.13a**. Similarly, the obtained rectified short circuit current for all devices was presented in **Figure 5.1.12a.**

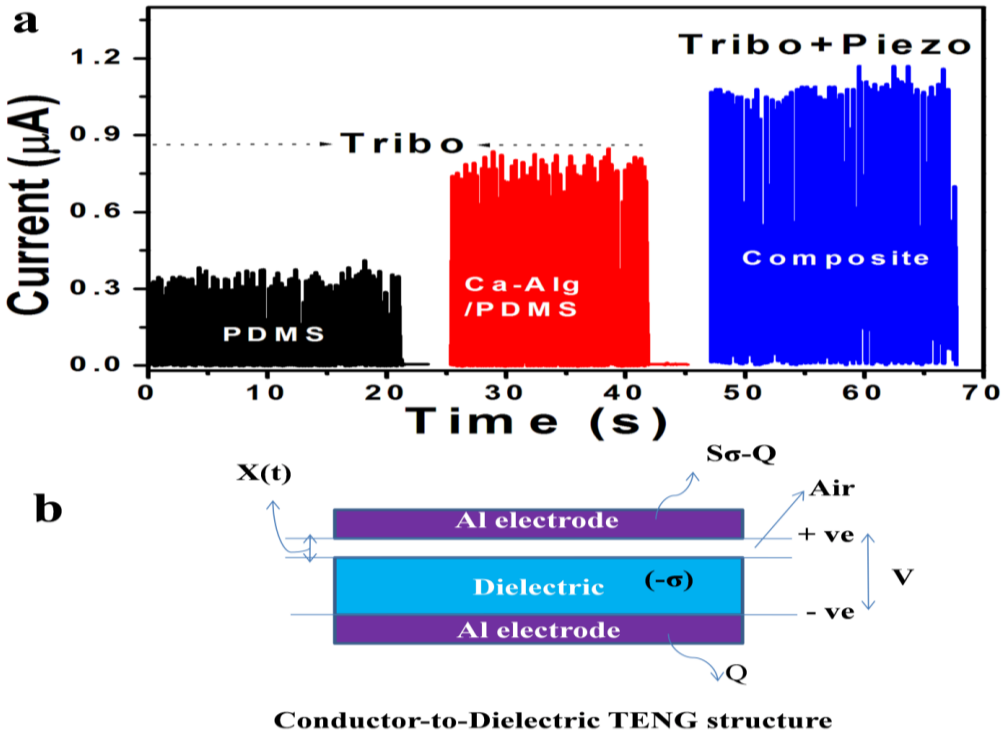

Figure 5.1.12 (a) Rectified short circuit currents for the PDMS, Ca-alg beads/PDMS and CBNG devices under an external mechanical pressure 36.67 kPa at 20 Hz. **(b)** Schematic diagram for the conductor-to-dielectric TENG structure.

Here, the electrical voltage and current outputs measured for pure PDMS [36] are (3 V and, 375 nA) and these can be increased to (6.6 V, 821 nA) by the substitution of Ca-alg beads into the PDMS matrix (without BTO NPs). This electrical response was attributed to a small air

gap between the PDMS/Ca-alg and the top Al foil electrode [3]. This is analogous to the conductor-to-dielectric type of TENG structure shown in **Figure 5.1.12b.**

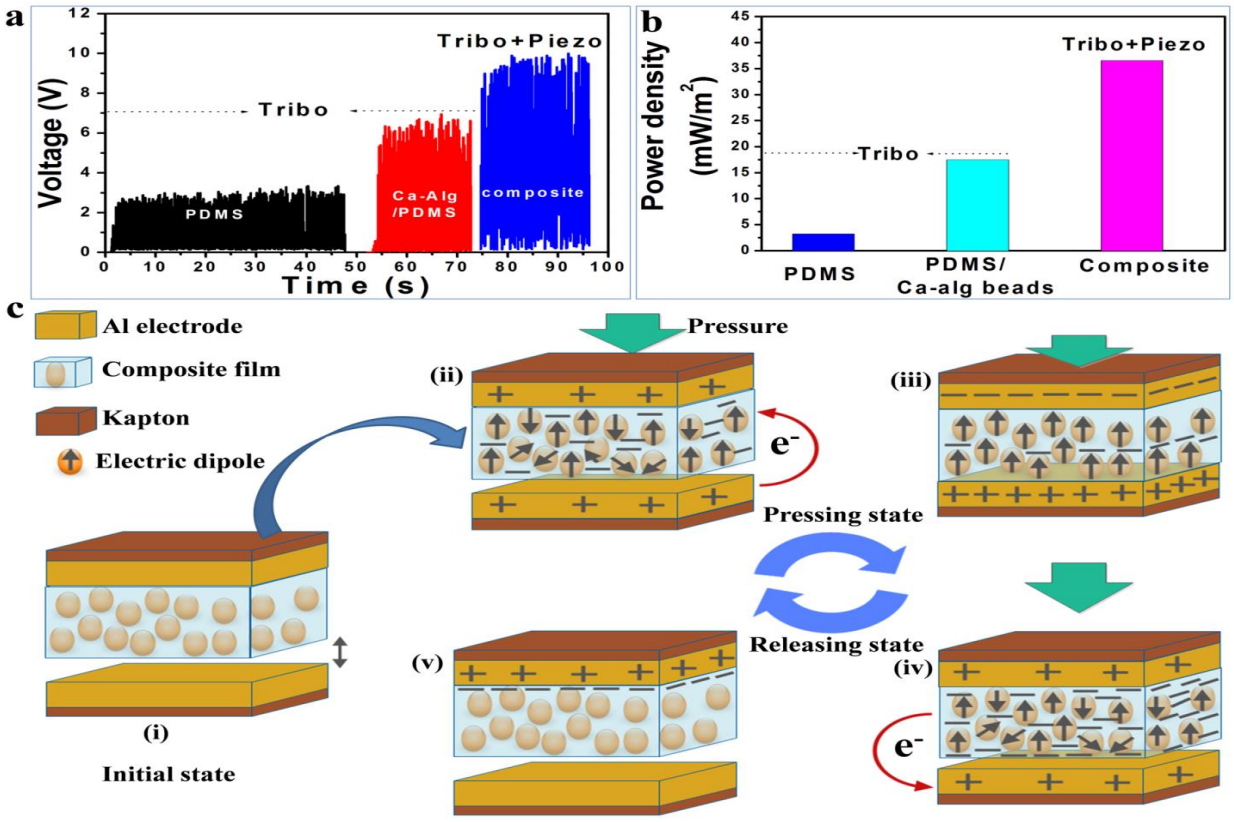

Figure 5.1.13(a, b) Comparison of rectified output voltage and power density of PDMS, Ca-Alg beads/PDMS and CBNG devices under mechanical pressure 36.67 kPa at a cyclic frequency of 20 Hz (triboelectric designated as Tribo and piezoelectric designated as Piezo). **(c)** Piezoelectric-triboelectric working mechanism of CBNG device during pressing and releasing cycles.

Energy harvesting from a triboelectric device: Material Information

Material	Polarity
PDMS (relative permittivity = 3)	Negative
Ca-alg	Negative
Aluminum	Positive
$BaTiO_3$ (relative permittivity = 130)	Negative surface potential

Generally, TENGs have inbuilt capacitance behavior and function primarily because of contact electrification and electrostatic induction. The *V–Q–X* governing relationship that provides the first- order lumped equivalent circuit is a combination of a capacitor connected with an ideal power source. In this study, the PDMS and Ca-alg beads-based NG devices generated considerable electricity. This indicated that there was a small (100 μm to 200 μm) air gap that formed between the top Al foil electrode and the PDMS or Ca-alg beads/PDMS (dielectric layers) during the fabrication process. This configuration is analogous to one of the TENG design modes, i.e., the conductor-to-dielectric type, as shown in **Figure 5.1.12b** (this differs from the dielectric-to-dielectric case). Its corresponding open circuit voltage (from electrodynamics theory) and short circuit charge (charge conservation and Kirchhoff's Law) can be written as follows[8]:

$$V = -\frac{Q}{S\varepsilon_o}\left(d_o + X(t)\right) + \frac{\sigma X(t)}{\varepsilon_o} \qquad \text{(E5.1.8)}$$

$$Q_{SC} = \frac{\sigma S}{\left(1+{}^{C_1(X)}\!/_{C_2(X)}\right)} - \frac{\sigma S}{\left(1+{}^{C_1(X=0)}\!/_{C_2(X=0)}\right)} \qquad \text{(E5.1.9)}$$

$$V_{OC} = \frac{\sigma X(t)}{\varepsilon_o} \;;\; Q_{SC} = \frac{S\sigma X(t)}{(d_o+X(t))} \;;\; C = \frac{\varepsilon_o S}{(d_o+X(t))} \qquad \text{(E5.1.10)}$$

where d_o is sum of the thicknesses of all the dielectrics, V is the induced potential difference between the two plates, $X(t)$ is the distance between the two triboelectric layers with respect to time, S is the areal size of the metal, Q_{SC} is the short circuit charge, C is the capacitance and σ is the static charge density.

In this case, the PDMS/Ca-alg acquired electrons from the Al foil and, left positive charges on the Al electrode. This electrical output clearly confirms that Ca-alg beads (ε_r = 80 to 85) [37-40] trigger the generation of surface charge density on the PDMS/Ca-alg film and, improve the charge transfer ratio between the PDMS/Ca-alg and Al electrode. Next, we observed the

electrical response of the CBNG device (with BTO NPs) under the same mechanical pressure and its output was shown in **Figure 5.1.13a and figure 5.1.12a.**

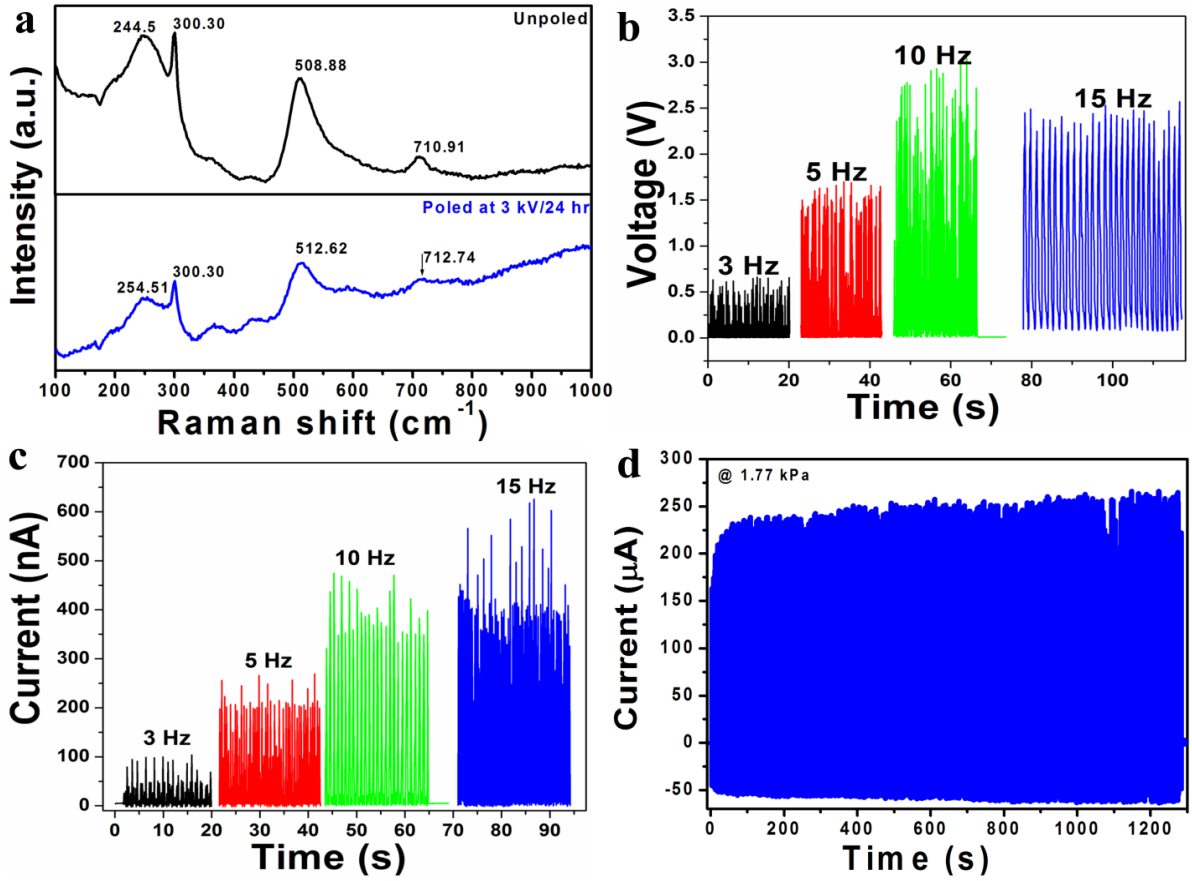

Figure 5.1.14 (a) Raman spectra of poled and unpoled composite film. (b, c) Electrical output of CBNG device (unpoled) under constant pressure 36.67 kPa at various frequencies such as 3, 5, 10 and 15 Hz. (d) Stability test for S-CBNG device during 1300 seconds.

We found that the CBNG device has increased electrical output (10 V, 1.097 μA) compared to the PDMS and, PDMS/Ca-alg devices. The maximum power density achieved for the CBNG device is 36.56 mW/m^2 i.e., which is a twofold increment on the power density of the PDMS/Ca-alg device (17.51 mW/m^2), as shown in **Figure 5.1.13b**. This improvement is due to the additional contribution of piezoelectric fields generated from the BTO NPs. In this case, Ca-alg was unable to change the piezoelectric phase of BTO NPs, but it created internal stresses on the

TiO_6 octahedron of the BTO lattice. The piezoelectricity of the BTO NPs was attributed to the non-centrosymmetric nature of the BTO NPs, i.e., the atoms were displaced from their equilibrium positions. We also evaluated the electrical poling effect (3 kV/24 hr) of the composite film and CBNG devices. The electrically poled composite film shows high intergrain stresses and dislocation ordered vibrations of the Ti-O bond in the BTO lattice, but no change is observed in the crystal structure of BTO, as shown in **Figure 5.1.14a**. This results in high electrical response for the poled CBNG device, as shown in **Figure 5.1.10(b, c**), than the unpoled CBNG output as shown in **Figure 5.1.14(b, c),** under the same mechanical pressure. The comparison of the total average power density (P_T) for all devices reveals that energy harvesting is due to the combination of the piezoelectric effect from BTO NPs and the triboelectric nature of the PDMS/Ca-alg can be written as follows:

$$P_T = P_{\text{Piezoelectric}} + P_{T\text{riboelectric}} \qquad \text{(E5.1.11)}$$

5.1.3.1.6 Working mechanism of CBNG device

The piezoelectric-triboelectric working mechanism of CBNG device was schematically shown in **Figure 5.1.13c**, and it is explained below in detail using the initial state, pressing state and releasing state conditions [35d]. At the initial state, zero charge transfer was observed across the electrodes under no pressure condition, because, there is no direct interaction between the Al electrode/composite layer and the bottom Al electrode, as shown in **Figure 5.1.13c (i)**. At this state, a small amount of induced surface charges potentially exists on the composite film due to electric poling, but these charges are not transferred. When external pressure is applied on top of the CBNG device, the electric dipoles (from BTO/Ca-alg beads) in the composite film start to align in one direction (i.e., generation of a piezoelectric potential), as shown in **Figure 5.1.13c (ii)**. At the same time, during the full contact state the composite film gains electrons from the

bottom Al electrode, which leaves more positive charges on the bottom Al electrode and negative charges on the top Al electrode due to triboelectric process. At this stage, charge transfer is largely triggered by the existing piezoelectric potential in the composite sample, which means more electrons are obtained from the bottom Al electrode, as shown in **Figure 5.1.13c (iii)**. During the releasing state (pressure removal from the CBNG device), the composite film and bottom Al electrode will start to depart from each other, the electrons will flow back from the composite film to the Al electrode, and the aligned electric dipoles will start to deviate from a normal orientation to random orientation, as shown in **Figure 5.1.13c (iv)**. After complete separation of the two active layers, the screened positive charges on the bottom Al electrode completely disappear, and few negative charges potentially exist in the composite film, which leads to the initial state of the CBNG device, as shown in **Figure 5.1.13c (v)**. The full cycle of pressing and releasing states clearly confirms that charge transfer is due to the combined piezoelectric and triboelectric process between the BTO-Ca alg/PDMS composite film and the Al electrode. All these results confirm that the substitution of Ca-alg (ε_r = 80-85), and BTO NPs (ε_r = 150) into the PDMS matrix (ε_r = 3) will improve the dielectric constant of the composite film, leading to increase in the capacitance of the device. This results in high electrical output due to the high surface charge density of the device during the pressing and releasing states

5.1.3.1.7 Various mechanical pressure effect on S-CBNG device output

Next, we fabricated a flexible strip-type CBNG (S-CBNG) device by increasing the CBNG device area up to (7.5 × 1.5 cm^2). This S-CBNG device could act as a self-powered wearable flexion (SWF) sensor for the classification and detection of finger movements *via* tendon-muscle unit forces. Before the device was used as a SWF sensor, the electrical response of the S-CBNG device was monitored under different mechanical pressures (0.17 kPa to 3.55 kPa) and bending

curve angles (0º to 95.5º). This provided information about the energy harvesting capability, reliability and stability of the S-CBNG device under different typical conditions.

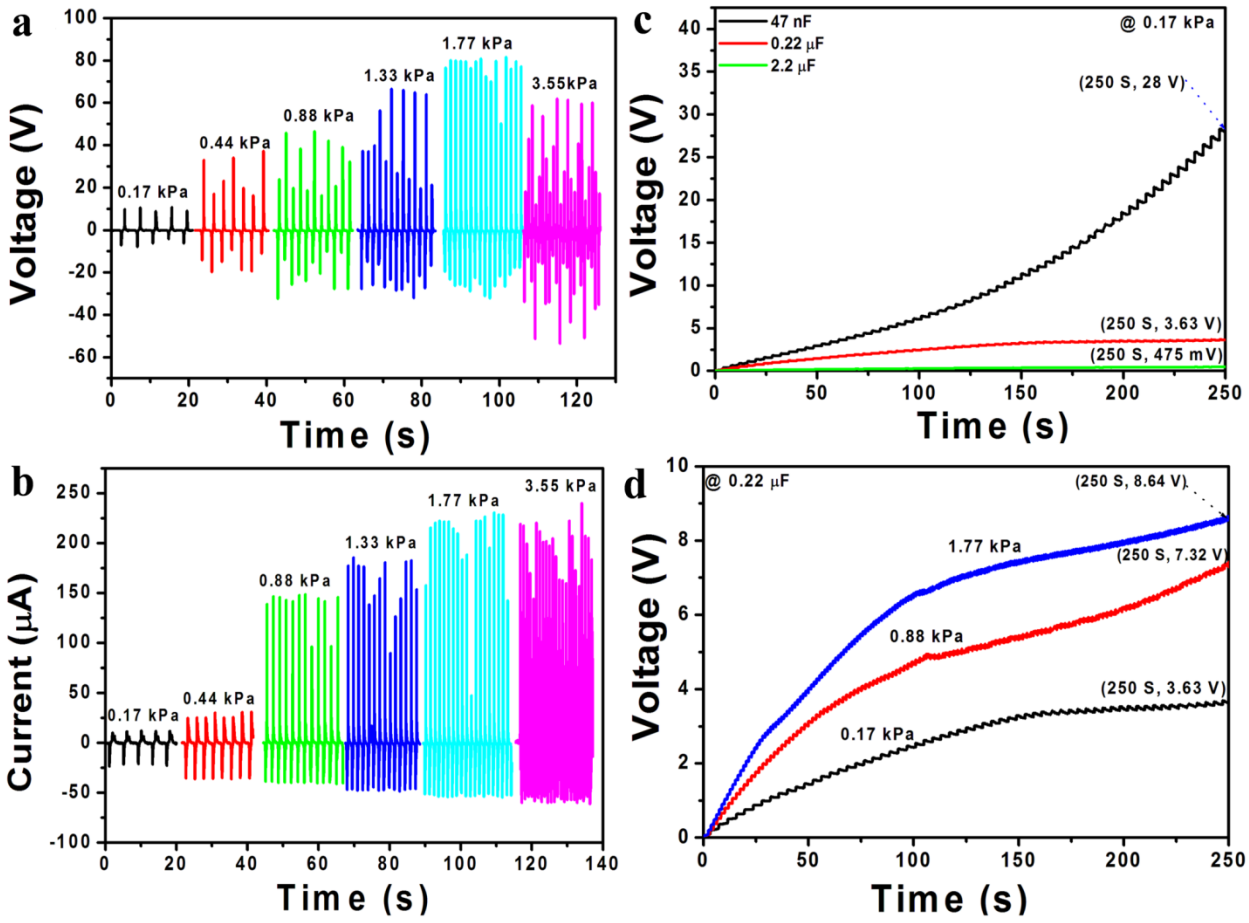

Figure 5.1.15 (a, b) Output voltage and current of the S-CBNG device (11.25 cm^2) under different mechanical pressures. **(c)** Capacitive loading (47 nF, 0.22 μF and 2.2 μF) analysis of the S-CBNG device at 170 Pa during 250 second interval **(d)** Charging of the 0.22 μF load capacitor using the S-CBNG device output at different mechanical pressures.

Controlled mechanical pressures were obtained using a linear motor (LinMot-HF01-37). The generated output voltage and current increased when the mechanical pressure acting on the S-CBNG device increased from 170 Pa to 1.77 kPa as shown in **Figure 5.1.15(a, b)**. The increment of electrical output from (10.5 V, 12 μA) to (80 V, 227 μA) with respect to the increment in mechanical pressure from 0.17 kPa to 1.77 kPa on S-CBNG device shows that the charge

generation on active layers and charge transfer to the electrodes are in linear manner. The higher output response clearly defines that piezoelectric contribution from the BTO NPs and triboelectric contribution from the PDMS/Ca-alginate, Al layers are in perfect phase. Achieving the higher output response of S-CBNG device at low mechanical pressure may be due to the achievement of higher surface charge density of the active layers. Therefore, the acceptable input mechanical force to S-CBNG device (11.25 cm^2) for better electrical performance is 1.77 kPa. When the mechanical pressure acting on the S-CBNG device is greater than 1.77 kPa, the output voltage decreases and shows no noticeable increase. This may be due to the phase mismatch between the piezoelectric/triboelectric charges and the generation of low surface charge density. Moreover, the S-CBNG device is highly sensitive at low mechanical pressures, which is observed by the positive peak response of 10.5 V and, 12 μA obtained at low pressure of 170 Pa, as shown in **Figure 5.1.15(a, b)**. The charging experiments were carried out using different loading capacitors (47 nF, 0.22 μF and 2.2 μF) connected across the rectified output of the S-CBNG device under different mechanical pressures (0.17, 0.88 and 1.77 kPa). **Figure 5.1.15c** shows that the amount of electric potential stored increases from 475 mV to 28 V, when the capacitance value of the load capacitor decreases from 2.2 μF to 47 nF during a 250 second time interval (for an applied mechanical pressure of 0.17 kPa). The 0.22 μF capacitor stored 3.63 V within the 250 second time interval, which is enough to drive any low power electronic device. In contrast, 47 nF load capacitor stored an electric potential of 28 V within the same time, but its discharging time was also very fast compared to μF load capacitors. Among these three capacitors, 0.22 μF is an optimum capacitor that stores an electric potential 3.63 V during 250 seconds and has a reasonable discharge time to drive any low power electronic device. Next, we observed the charging behavior of the S-CBNG device by maintaining a constant load capacitor

(0.22 μF) across the device output and varying the input mechanical pressures from 0.17 kPa, 0.88 kPa and 1.77 kPa, as shown in **Figure 5.1.15d**. It clearly indicates that, the electric potential stored increased from 3.63 V to 8.64 V, when the applied mechanical pressure increased from 0.17 kPa to 1.77 kPa. Compared to the low mechanical pressure that acts on the S-CBNG device, at high pressures, the amount of generated charge is high, which is collected by the external load capacitors. **Figure 5.1.15d** shows the output current of the S-CBNG device under a mechanical pressure of 1.77 kPa during a 1300 second time interval represents the no degradation in output currents confirms the good stability of the S-CBNG device.

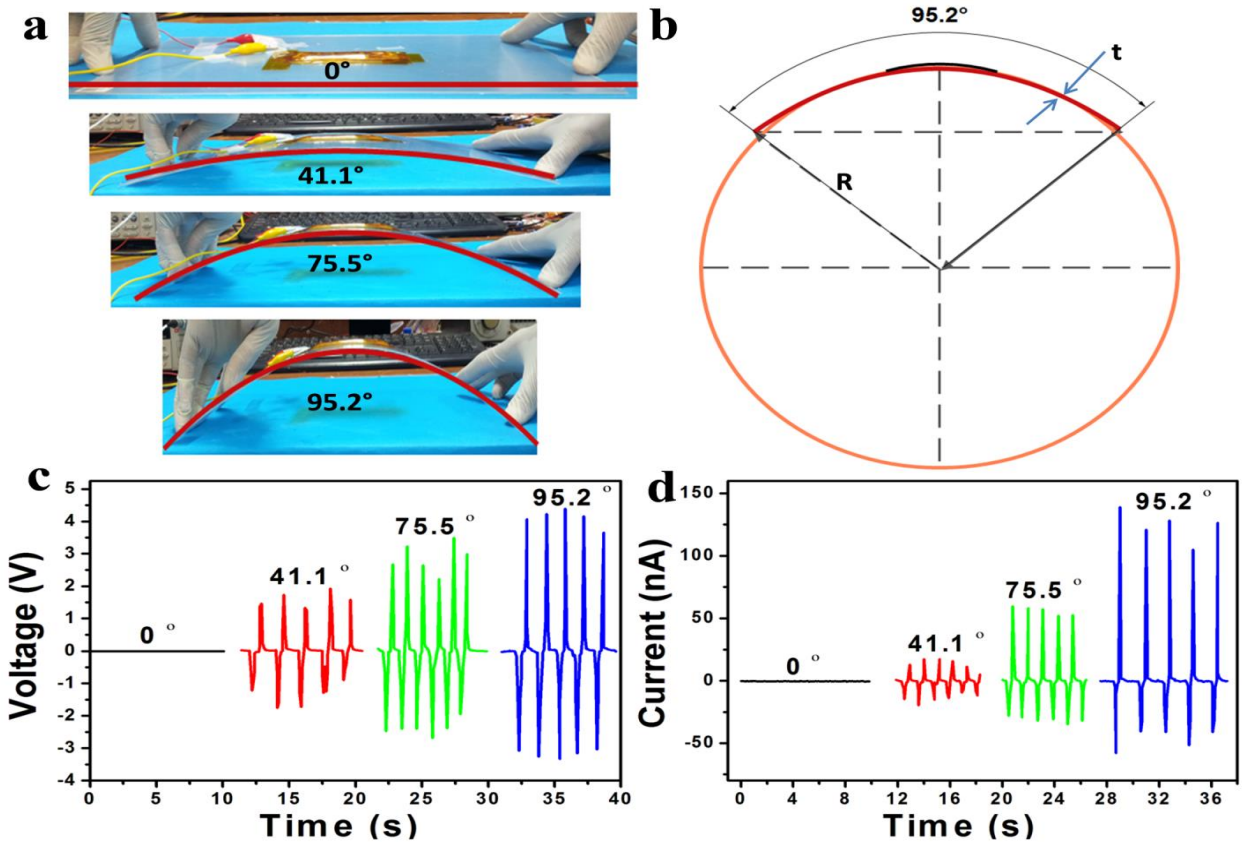

Figure 5.1.16 (a) Optical photographs of the S-CBNG device on a flexible pad and the bending angles (0º, 41.1º, 75.5º and 95.2º) created by human hand. **(b)** Schematic diagram for the strain estimation using the bending radius and angles. **(c, d)** Electrical responses of the S-CBNG device for various bending curve angles.

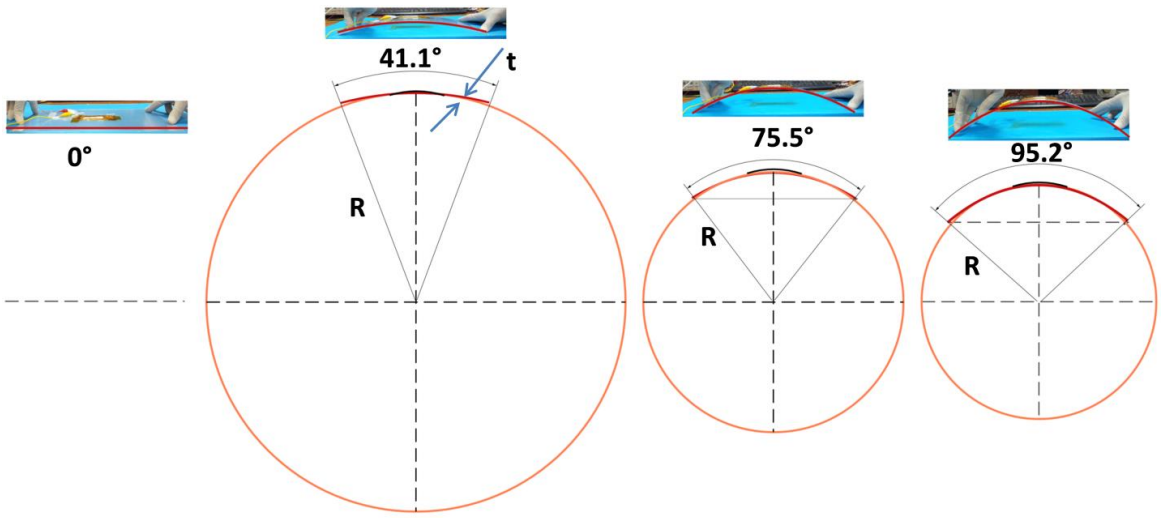

$$Strain \ \ (\varepsilon) = \frac{t}{2R}$$

Figure 5.1.17 Estimation of bending radius profile with respect to the bending angle of flexible pad with S-CBNG device.

5.1.3.1.8 Bending effect on S-CBNG device output

Next, analyzed the electrical response of the S-CBNG device under different mechanical bending curvatures with angles of 0º, 41.1°, 75.5º and 95.2°, as shown in **Figure 5.1.16 (a, b)**. A zero output electrical response was observed when the bending angle is 0º. The generated peak-to-peak voltage (and current) increased from 0 V to 7.5 V (and 0 nA to 160 nA) when the bending angle was increased from 0º to 95.2°, as shown in **Figure 5.1.16 (c, d)**. Increasing the bending angle resulted in an increase in the strain acting on the S-CBNG device. Here, the thickness (t) of the flexible substrate (2.4 mm) is higher than the thickness of the S-CBNG device (1.712 mm). Therefore, the strain on flexible substrate will transfer to the S-CBNG device. Further the applied strain ($\varepsilon = \frac{t}{2R}$) can be calculated using the bending radius (R). The value of R decreases when the bending angle increases, which results in an increase in the applied strain

on the device, as shown in **Figure 5.1.17**. All these results suggest that the S-CBNG device has good energy conversion capability and, impressive reliability at low pressures and it indicates the suitability of the S-CBNG device for active sensors such as flexion and pressure sensors.

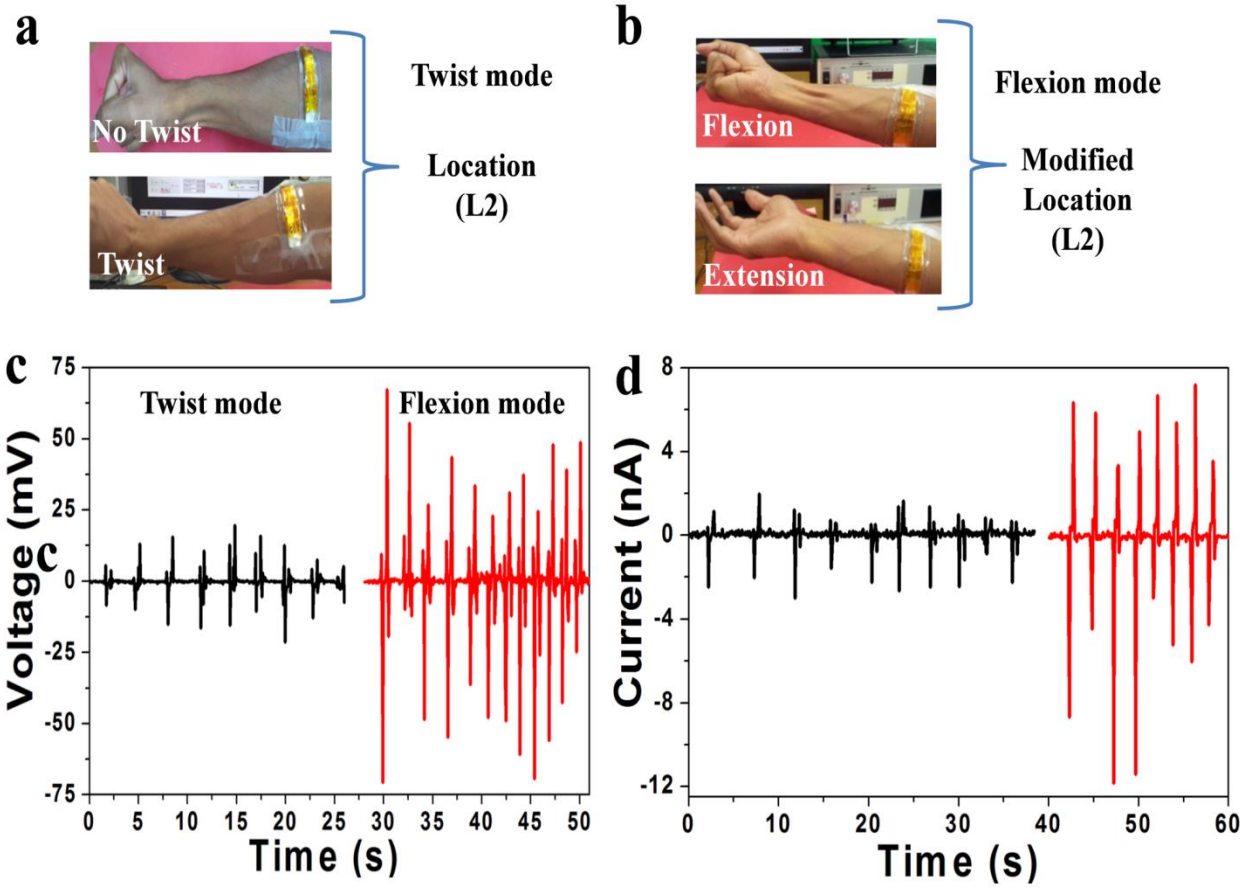

Figure 5.1.18 (a, b) An optical image representing the twist mode conditions at location L2 and the flexion mode conditions at the modified location L2. **(c, d)** Comparative voltage and current of the S-CBNG device on forearm at different locations during the twist/flexion modes.

Table 5.1.2. Comparison of the proposed CBNG device with published reports of composite nanogenerators with different materials.

Material	Fillers Microstructure	Device Area (cm^2)	Mechanical load (Pa) /Strain (%)	Voltage (V)	Current (A)	References
$BaTiO_3$	Nanotubes	1	1 MPa	5.5	350 nA	(50)
$BaTi_{0.9}Zr_{0.1}O_3$/PVDF	Nanocubes	6.25	17.6 kPa	11.9	1.36 μA	(11)
Pb(ZT)O_3-mWCNT	Nanoparticles	-	0.2 MPa	8.6	47 nA	(15)
$BaTiO_3$/MW-CNT/PDMS	Round shape	35	57 kPa	1.5	150 nA	(35c)
$BaTiO_3$	Thin film	0.82	Finger force	1	26 nA	(21)
KNLN-Cu rods/PDMS	Particles	9		12	1.2 μA	(35a)
BTO/PDMS	Nanoparticles	2.25	Linear motor at 1 Hz	60	1 μA	(35d)
PAA/13-nm OA-$BaTiO_3$	Cubic-like	1	0.5 MPa	1.8	700 nA	(59)
ZnO	Hollow hemisphere	≥10	30 kPa	0.2	70 μA	(60)
KNN/PVDF-TrFE	Nanofibers	-	Normal bending	0.98	78 nA	(61)
$ZnSnO_3$	Microbelt	-	≤ 1 %	0.1	80 nA	(62)
BTO NP/Ca-alg/PDMS	Spherical beads	11.25	1.77 kPa	80	227 μA	Present
BTO NP/Ca-alg/PDMS	Spherical beads	11.25	170 Pa	10.5	2 μA	work
Ca-alg/PDMS	crumpled beads	3	36.67 kPa	6.64	821nA	

5.1.3.1.9 Self-powered wearable flexion (SWF) sensor

A control experiment was performed on different parts of the right hand to identify the best location of the S–CBNG device on the forearm to detect finger flexion/extension movements. A thin PDMS layer was used on the bottom and top of the device along with insulated electrical wires to prevent direct contact between the surface of S–CBNG device and the forearm. The electrical response (V_{OC}, I_{SC}) of the S–CBNG device was tested under twisting and non-twisting conditions, as shown in **Figure 5.1.18a**, when the device is located at different areas of the right arm such as the wrist (L1), the forearm (corner part–L2) and near the elbow (L3) as shown in **Figure 5.1.19(a, b).**

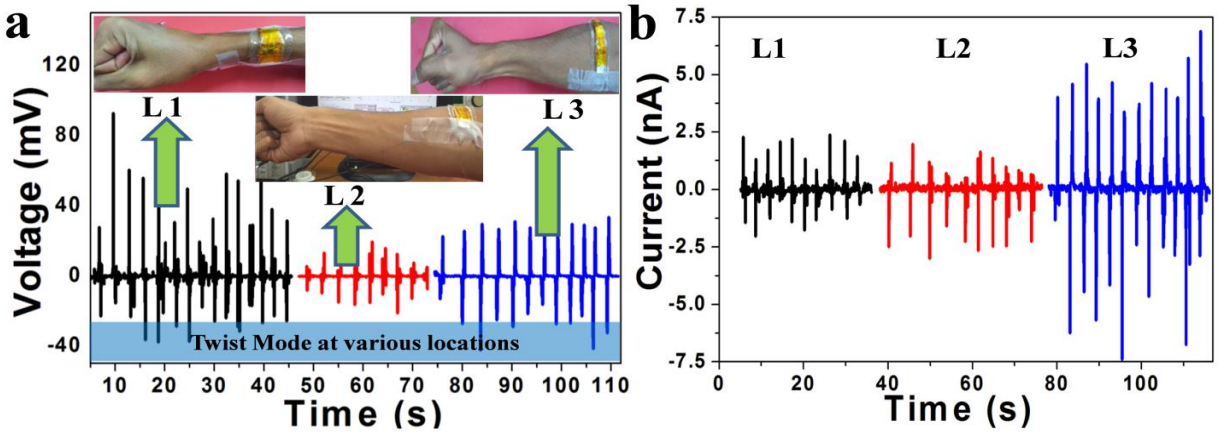

Figure 5.1.19 (a, b) Output voltage and current of S–CBNG placed at different locations (L1, L2 and L3) on the forearm during the twist and no-twist conditions of the forearm.

Finger movements such as flexion and extension were detected by placing the S-CBNG device at locations L1, L2 and L3. However, it was very typical to classify the fingers using the electrical outputs of the S-CBNG device at above locations. The electrical signals were readily detected (they could be classified) but we modified the forearm corner location L2 to be more centered (anterior view) on the forearm and this location is referred to as the "modified L2 location" (**Figure 5.1.20**). The V_{OC} (I_{SC}) values of S–CBNG device at the different L2 positions

during twisting and flexion/extension modes with the clenched fist are shown in **Figure 5.1.18** and **Figure 5.1.19.**

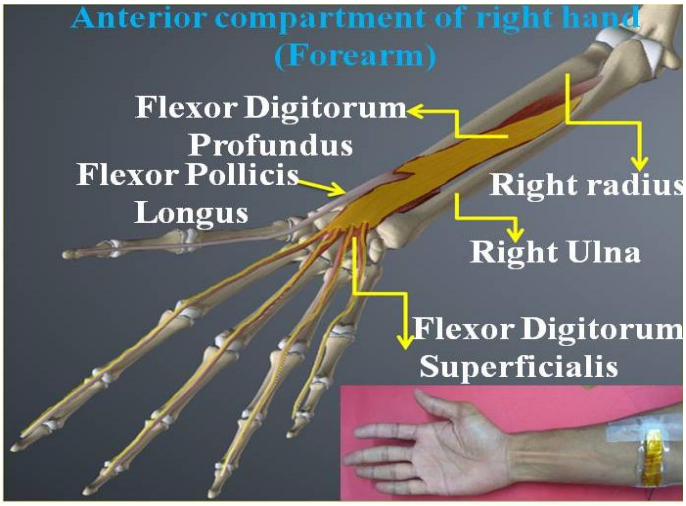

Figure 5.1.20 (a) Anterior compartment of the right hand (forearm) showing the flexor tendons associated with the flexor muscles and finger bones. The bottom right inset shows a digital photograph of the forearm and the device located at the center position of the forearm (anterior view).

The flexion mode generates higher responses (50–60 mV) than the twisting mode (< 10 mV) because of the large mechanical forces provided *via* the tendon-muscle unit forces of the forearm [43]. Later, we tested the electrical response of the S-CBNG device at the modified L2 location during the finger flexion/extension movements of individual fingers (pinky, ring, middle, index and thumb) and the clenched fist and the optical photographs are shown in **Figure 5.1.21a.** Interestingly, the V_{OC} (I_{SC}) output of the S-CBNG device increased from 2.3 mV (0.5 nA) to 10 mV (2.67 nA) from the pinky finger to the index finger and then suddenly decreased to 2.6 mV (0.3 nA) for the flexion/extension of the thumb, as shown in **Figure 5.1.21 (b, c)**. In particular, each and every finger flexion/extension movement generates a particular amount of force (strain) on the S-CBNG device, which in turn generates a corresponding output. The details of the tendon-muscle unit force of a forearm on an S-CBNG device and a schematic diagram of the forearm with the muscles are shown in **Figure 5.1.20** [43, 58]. An optical photograph of an

anterior view of the right hand with an attached S-CBNG device taken during an experiment is shown in the inset of **Figure 5.1.20**. The key to the successful classification and detection of each finger movement resides in understanding how to use and where to place the S-CBNG device, and determining the bending angle and bending rate of the finger. In this study, we selected the maximum bending angle with a slow bending rate (1 to 2 Hz) of the finger. The corresponding output results of the S-CBNG device are given in **Figure 5.1.22(a, b)**. This electrical response is enough to classify and detect the finger flexion/extension movements for the self-powered wearable flexion (SWF) sensor, which is more useful in health monitoring applications. A repeatability test for the SWF sensor was conducted for the clenched fist flexion/extension movements, as shown in **Figure 5.1.23**. The observed electrical output was 60 mV (6 to 8 nA) for different time intervals. This output was high (as shown in **Figure 5.1.23(b, c)**) compared with those of the individual finger flexion/extension movements, as shown in **Figure 5.1.21(b, c)**, which was attributed to the cumulative effect of flexion/extension of all five fingers that created a greater tendon-muscle unit force (a high strain amplitude) on the flexible SWF sensor. The average instantaneous peak power (V_{OC} x I_{SC}) of the SWS sensor during the finger flexion movements is shown in **Figure 5.1.21d**. The achieved maximum peak power varied from 1.15 pW to 0.4 nW during the flexion and extension movements from the pinky finger to the clenched fist. In addition to using the flexible S–CBNG device as an SWF sensor, we used it to monitor regular convex and concave bending movements of the right hand at the wrist position, hand knuckles and elbow; the electrical outputs are shown in **Figure 5.1.24**.

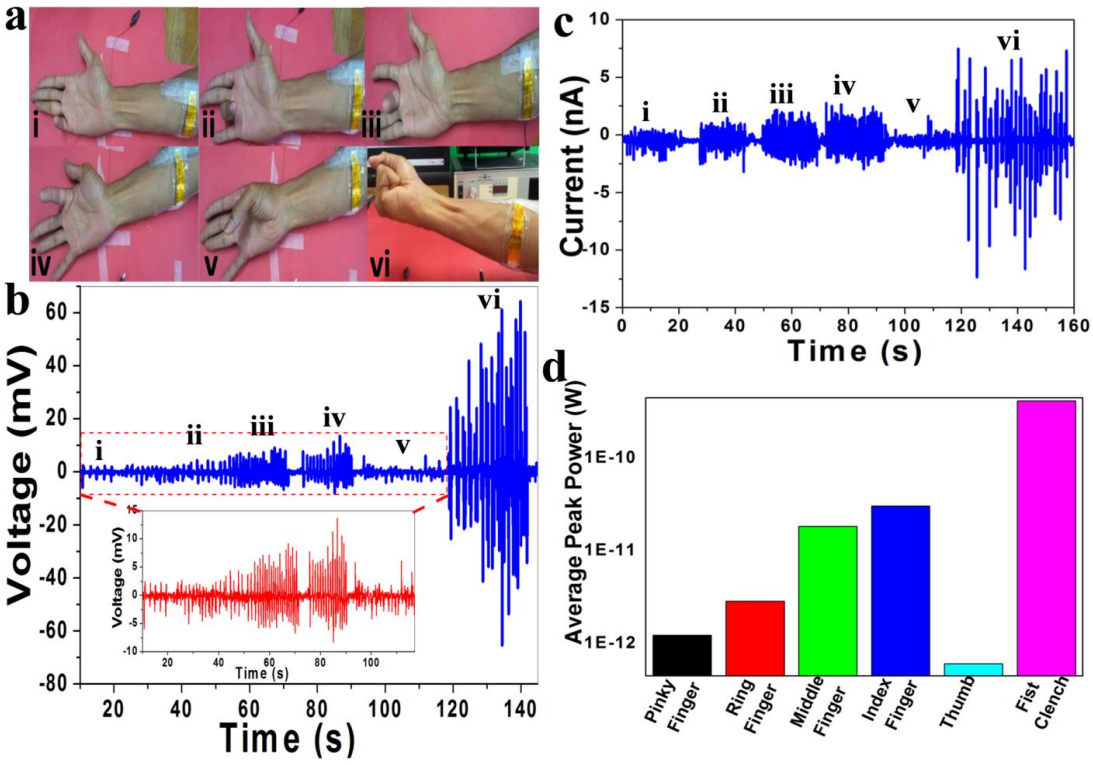

Figure 5.1.21 Demonstration of SWF sensor. **(a)** Digital photographs of flexion movements of individual fingers and clenched fist. **(b, c)** Output voltages and short circuit currents of SWF sensor during flexion/extension movements for the individual finger and clenched fist. **(d)** Average peak powers of the flexible SWF sensor during the flexion movements for the individual finger and clenched fist.

This experiment revealed that S–CBNGs would be useful for monitoring or sensing the motion of human body parts during inpatient rehabilitation, finger Braille typing and directional bending of the human body, while simultaneously acting as an energy harvester. The proposed SWF flexion sensor is non-invasive, sufficiently robust for long-term use and, cost-effective, and it does not require external power, and can easily decode finger movements *via* different voltages (or average peak powers) with good repeatability. This device presents a reliable alternative to existing sensors such as EMG (electromyography) sensors [41, 42] fuzzy-based decision-making systems [43] and flexible electrogoniometers [44, 45] for classifying and detecting finger movements.

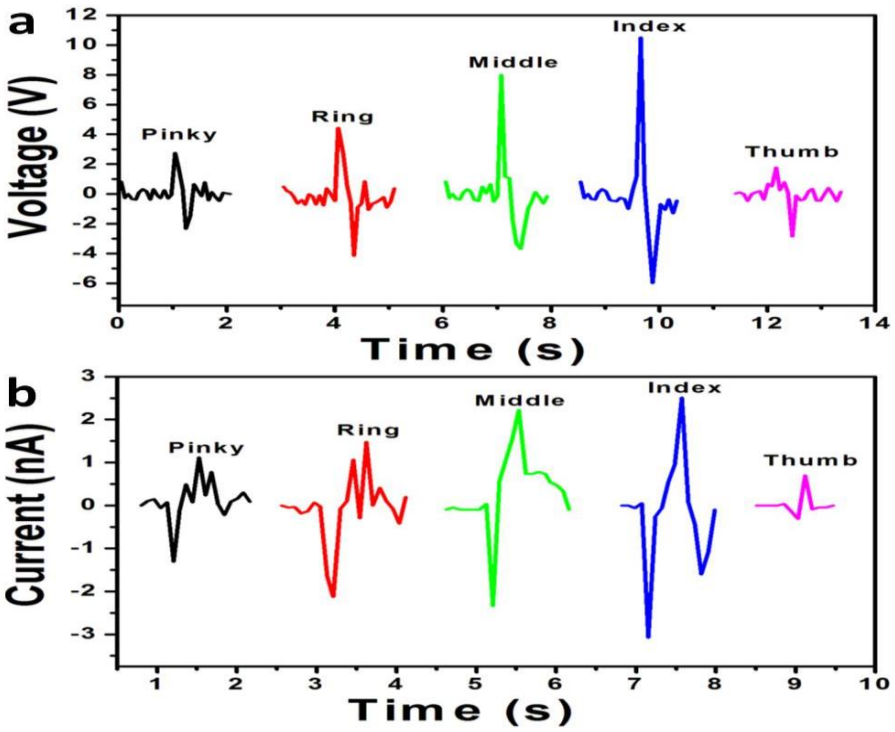

Figure 5.1.22 (a, b) SWF sensor output under maximum bending radius with slow bending rate of different finger flexion/extension movements.

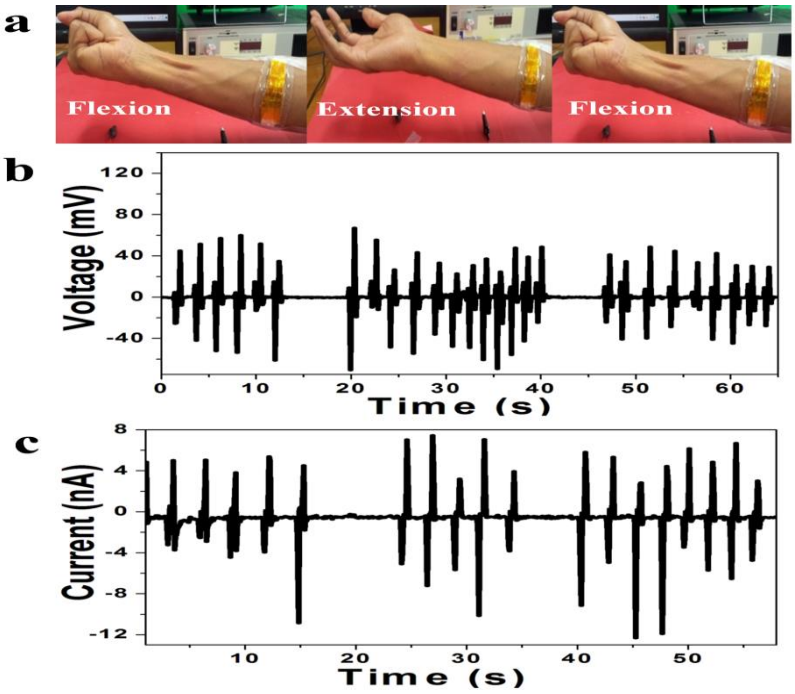

Figure 5.1.23 (a) Optical photograph of the flexion/extension conditions for the clenched fist. **(b, c)** S–CBNG device electrical response for the clenched fist flexion/extension movements represents good repeatability.

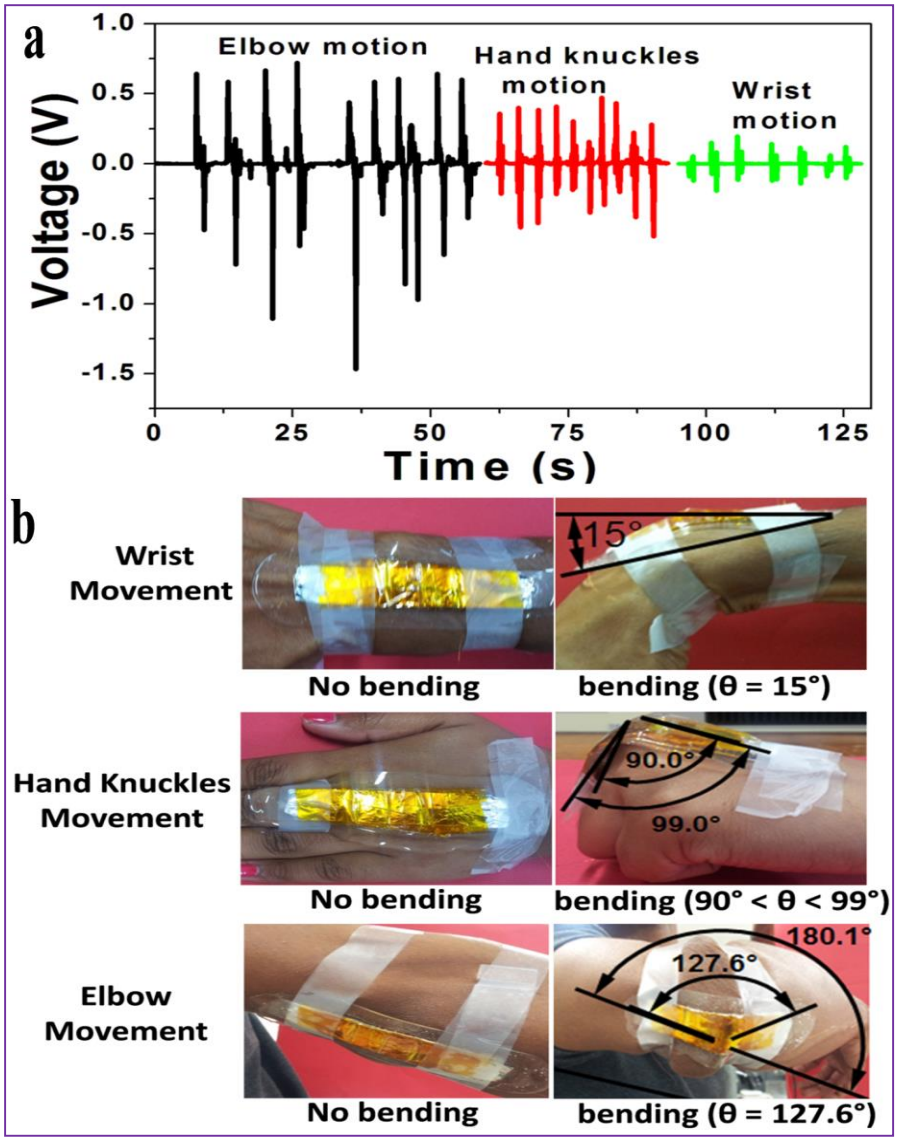

Figure 5.1.24 An S–CBNG device can act as a self-powered sensor to detect tiny bending movements of the human body. **(a)** Open circuit voltage of the S–CBNG device under tiny bending movements of the elbow, hand knuckles and wrist. **(b)** Digital photographs of the various tiny bending movements of the human hand imposing strain on the S–CBNG device.

5.1.4 Conclusions

For the first time, we report on the fabrication of innovative spherical composite (BTO NP/Ca alg) beads using the IG technique; these composite beads are useful for high performance energy conversion and SWF sensor applications. The performance of CBNG was studied by varying the device area, the applied low mechanical pressure (170 Pa to 1.77 kPa) and bending

curve angles, the biomechanical force, the capacitive loading and the electrical poling. The S-CBNG device is highly sensitive and delivers a maximum peak output current (227 μA), a maximum peak output voltage (80 V) and a power density of approximately 16.14 W/m^2 under a low applied mechanical pressure (1.70 kPa). This is due to the combination of triboelectrification and piezoelectric effects of the S-CBNG device. We found that Ca-alginate can be useful as a template structure and an energy harvesting triggering material along with PDMS matrix. We also demonstrated that the, S-CBNG device can act a SWF sensor to measure the tendon-muscle unit force generated by the human finger flexion/extension movements. The location of the sensor, the bending radius (strain amplitude) and a slow bending rate (1 to 2 Hz) enable the successful detection and classification of finger movements using the output signals of the sensor. The results indicate that the S-CBNG device can function as an independent power source and a SWF (smart, battery free) sensor. This is an alternative, reliable approach compared to traditional approaches, such as electromyography sensors, fuzzy-based decision-making systems and flexible electrogoniometers, used for the classification/detection of finger movements. The IG method is a simple, eco-friendly process amenable to large scale production with low cost compared to complex approaches, such as PVD, CVD, vapor-liquid-solid processes, and RF sputtering methods. The fabricated CBNG devices are cost-effective, durable, flexible, and biocompatible. This study will expand the choice of template structured biopolymers (active or supporting) with inorganic nanoparticles for harvesting the mechanical energy and their potential applications in the fields of health monitoring, implantable devices and wireless/communication.

5.1.5 References

[1] Z. L. Wang, J. Song, Science. 312 (2006) 242-246.

[2] Y. Yang, W. Guo, K.C. Pradel, G. Zhu, Y. Zhou, Y. Zhang, Y. Hu, L. Lin, Z.L. Wang, Nano. Lett. 12 (2012) 2833-2838.

[3] J. Chun, J.W. Kim, W.S. Jung, C.Y. Kang, S.W. Kim, Z.L. Wang, J.M. Baik, Energy. Environ. Sci. 8 (2015) 3006-3012.

[4] L.M. Weiland, W.W. Clark, D.G. Cole, Adaptive hydrokinetic energy harvesting. US Patent, **2014**, US 20140001761A1.

[5] D.A. Howey, A. Bansal, A.S. Holmes, Smart Mater. Struct. 20 (2011) 085021-085032.

[6] C. M. Chen, M. H. Chung, T. E. Hsieh, M. O. Liu, J. L. Lin, W. P. Chu, R. M. Tang, Y. S. Tsai, F. S. Juang, Compos. Sci. Technol. 68 (2008) 3041–3046.

[7] R. Hu, B.A. Cola, N. Haram, J. N. Barisci, S. Lee, S. Stoughton, G. Wallace, C. Too, M. Thomas, A. Gestos, M.E. dela Cruz, J.P. Ferraris, A.A. Zakhidov, R.H. Baughman, Nano. Lett. 10 (2010) 838-846.

[8] M. Yuan, L. Cheng, Q. Xu, W. Wu, S. Bai, L. Gu, Z. Wang, J. Lu, H. Li, Y. Qin, T. Jing, Z.L. Wang, Adv. Mater. 26 (2014) 7432-7437.

[9] J. Olivo, S. Carrara, G.D. Micheli, IEEE Sens. J. 11 (2011) 1573-1586.

[10] M. M. Abolhasani, K. Shirvanimoghaddam, M. Naebe, Compos. Sci. Technol. 138 (2017) 49-56.

[11] A. Nagamalleswara Rao, B. Saravanakumar, S.J. Kim, *ACS Appl. Mater. Interfaces*, 7 (2015) 9831-9840.

[12] X. Chen, X. Shiyou, Y. Nan, S. Yong, Nano Lett. 10 (2010) 2133–2137.

[13] J. Kwon, W. Seung, B.K. Sharma, K. Sang-Woo, J.H. Ahn, Energy Environ. Sci. 5 (2012) 8970-8975.

[14] K. Park, J.H. Son, G.T. Hwang, C.K. Jeong, J. Ryu, M. Koo, I. Choi, S.H. Lee, M. Byun, Z.L. Wang, K.J. Lee, Adv. Mater. 26, 2014, 2514–2520.

[15] J.K. Han, D.H. Jeon, S.Y. Cho, S.W. Kang, S.A. Yang, S.D. Bu, S. Myung, J. Lim, M. Choi, M. Lee, M.K. Lee, Sci. Rep. 6 (2016) 1-8.

[16] S.H. Baek, M.R. Hasan, I.K. Park, Nanotechnology 27 (2016) 065401-065408.

[17] M.K. Gupta, J.H. Lee, K.Y. Lee, S.W. Kim, ACS Nano, 7 (2013) 8932–8939.

[18] D. Kim, K.Y. Lee, M.K. Gupta, S. Majumder, S.W. Kim, Adv. Funct. Mater. 24 (2014) 6949–6955.

[19] B. Saravanakumar, S.J. Kim, J. Phys. Chem. C 118 (2014) 8831−8836.

[20] T. Gao, J. Liao, J. Wang, Y. Qiu, Q. Yang, M. Zhang, Y. Zhao, L. Qin, H. Xue, Z. Xiong, L. Chena, Q.M. Wang, J. Mater. Chem. A 3 (2015) 9965–9971.

[21] K.I. Park, S. Xu, Y. Liu, G.T. Hwang, S.J.L. Kang, Z.L. Wang, K.J. Lee, Nano Lett. 10 (2010) 4939–4943.

[22] J.H. Jung, M. Lee, J.I. Hong, Y. Ding, C.Y. Chen, L.J. Chou, Z.L. Wang, ACS Nano 5 (2011) 10041-10046.

[23] P.G. Kang, B.K. Yun, K.D. Sung, T.K. Lee, M. Lee, N. Lee, S.H. Oh, W. Jo, H.J. Seog, C.W. Ahn, I.W. Kim, J.H. Jung, RSC Adv. 4 (2014) 29799-29805.

[24] M.R. Joung, H. Xu, I.T. Seo, D.H. Kim, J. Hur, S. Nahm, C.Y. Kang, S.J. Yoon, H.M. Park, J. Mater. Chem. A 2 (2014) 18547-18553.

[25] Z. Wang, Y. Zhang, S. Yang, Y. Hu, S. Wang, H. Gu, Y. Wang, H.L. Chan, J. Wang, ACS Appl. Mater. Interfaces, 7 (2015) 4921–4927.

[26] (a) G. Zhu, R. Yang, S. Wang, Z.L. Wang, Nano Lett. 10 (2010) 3151–3155. (b) V. Nguyen, R. Zhu, R. Yang, Nano Energy, 14 (2015) 49–61.

[27] Y. Qiu, H. Zhang, L. Hu, D. Yang, L. Wang, B. Wang, J. Ji, G. Liu, X. Liu, J. Lin, F. Li, S. Han, Nanoscale, 4 (2012) 6568-6573.

[28] B. Kumar, K.Y. Lee, H.K. Park, S.J. Chae, Y.H. Lee, S.W. Kim, ACS Nano 5 (2011) 4197–4204.

[29] E. Cross, Nature. 432 (2004) 24-25.

[30] P.K. Panda, J. Mater. Sci. 44 (2009) 5049-5062.

[31] J.M. Shoenung, "Lead compounds" in ceramics and glass materials: structure, properties and processing, Shackelford, J. F.; Doremus, R. H. Eds. **2008**, Page No.151.

[32] C.H. Hong, H.P. Kim, B.Y. Choi, H.S. Han, J.S. Son, C.W. Ahn, W. Jo, J. Materiomics 2 (2016) 1-24.

[33] T.R. Shrout, S.J. Zhang, J. Electroceram. 19 (2007) 113-126.

[34] B.K. Wang, J.F. Li, Adv. Funct. Mater. 20 (2010) 1924–1929.

[35] **(a)** C.K. Jeong, K.I. Park, J. Ryu, G.T. Hwang, K.J. Lee, Adv. Funct. Mater. 24 (2014) 2620-2629 **(b)** K.I. Park, C.K. Jeong, J. Ryu, G.T. Hwang, K.J. Lee, Adv. Energy Mater. 3 (2013) 1539-1544 **(c)** K.I. Park, M. Lee, Y. Liu, S. Moon, G.T. Hwang, G. Zhu, J.E. Kim, S.O. Kim, D.K. Kim, Z.L. Wang, K.J. Lee, Adv. Mater. 24 (2012) 2999-3004 **(d)** B. Shi, Q. Zheng, W. Jiang, L. Yan, X. Wang, H. Liu, Y. Yao, Z. Li, Z.L. Wang, Adv. Mater. 28 (2016) 846-852.

[36] S. Selvarajan, A. Nagamalleswara Rao, C. Arunkumar, S.J. Kim, Sens. Actuator B-Chem, 234 (2016) 395–403.

[37] M. Esch, V.L. Sukhorukov, M. Ku¨ rschner, U. Zimmermann, Biopolymers 50 (1999) 227–237.

[38] S. Ikeda, H. Kumagai, K. Nakamura, Carbohydr. Res. 301 (1997) 51-59.

[39] H. Hajiali, J.A. Heredia-Guerrero, I. Liakos, A. Athanassiou, E. Mele, Biomacromolecules, 16 (2015) 936-943.

[40] H.E.M. Alexandra, D. Lundberg, J.R. Antonio, J.V. Francisco, L. Bjorn, G.M. Maria, O. Ulf, Langmuir, 28 (2012) 4131-4141.

[41] A. Phinyomark, P. Phukpattaranont, C. Limsakul, Expert Syst Appl, 39 (2012) 7420-7431.

[42] S. Đorđević, S. Tomažič, M. Narici, R. Pišot, A. Meglič, Sensors. 14 (2014) 17848-17863.

[43] N.H. Adnan, K. Wan, A.B. Shahriman, S.K. Zaabaa, S. Basah, Z.M. Razlan, D. Hazry, M.N. Ayob, R.M. Nor, A.A. Aziz, Procedia Eng. 41 (2012) 388– 94.

[44] L. Carnaz, C.S. Moriguchi, A.B. Oliveira, P.R.P. Santiago, G.A.P. Caurin, G.Å. Hansson, H.J.C. Gil Coury, Med Eng Phys, 35 (2013) 1629-1637.

[45] P.T. Wang, C.E. King, A.H. Do, Z. Nenadic, Med Eng Phys, 33 (2011) 546-552.

[46] A.B. Al-Sayed, M.M. Yasser, A.M. Eman, M.Y. Mohamed, M.H.K. Mostafa, J. Environ. Chem. Eng. 3 (2015) 1486-1496.

[47] M.T. Buscaglia, M. Bassoli, V. Buscaglia, J. Am. Ceram. Soc. 91 (2008) 2862-2869.

[48] K.C. Huang, T.C. Huang, W.F. Hsieh, Inorg. Chem. 48 (2009) 9180-9184.

[49] W. Li, Z. Xu, R. Chu, P. Fu, G. Zang, J. Am. Ceram. Soc. 93 (2010) 2942-2944.

[50] Z.H. Lin, Y. Yang, J.M. Wu, Y. Liu, F. Zhang, Z.L. Wang, J. Phys. Chem. Lett. 3 (2012) 3599-3604.

[51] S. Sarkar, C. Sudip, C. Bhattacharjee, Ecotoxicol. Environ. Saf. 121 (2015) 263-270.

[52] N.P. Siddhesh, J.E. Kevin, Biomaterials. 33 (2012) 3279-3305.

[53] T. Schmid, A. Messmer, B.S. Yeo, W. Zhang, R. Zenobi, Anal. Bioanal. Chem. 391 (2008) 1907-1916.

[54] M.C.V. Marcelo, P.C. Nancy, C. Ernesto, L. David, M. Betty, O.O.R. Igor, T. Simonet, J. Raman Spectrosc. 41 (2010) 758-763.

[55] S.H. Shin, Y.H. Kim, M.H. Lee, J.Y. Jung, J. Nah, ACS Nano. 8 (2014) 2766-2773.

[56] M. Zhang, T. Gao, J. Wang, J. Liao, Y. Qiu, H. Xue, Z. Shi, Z. Xiong, L. Chenn, Nano Energy. 10 (2015) 510-517.

[57] D. Pan, F. Dai, H. Li, Composites Science and Technology 119 (2015) 34-45.

[58] J. Rafiee, M.A. Rafiee, F. Yavari, M.P. Schoen, Expert Syst Appl, 38 (2011) 4058-4067.

[59] Y. Kim, K.Y. Lee, S.K. Hwang, C. Park, S.O. Kim, J. Cho, Adv. Funct. Mater. 24, (2014) 6262-6269.

[60] J. Chun, K.Y. Lee, C.Y. Kang, M.W. Kim, S.W. Kim, J.M. Baik, Adv. Funct. Mater. 24 (2014) 2038-2043.

[61] H. B. Kang, C. S. Han, J. C. Pyun, W. H. Ryu, C. Y. Kang, Y. S. Cho, Compos. Sci. Technol. 111 (2015) 1–8.

[62] J.M. Wu, C. Xu, Y. Zhang, Z.L. Wang, ACS Nano. 6 (2012) 4335-4340.

5.2 Self-powered Electronic display using the BTO NSs/Ca-Alginate Hybrid Linear Worm Structure & Energy Harvesting Performance

5.2.1 Introduction

Portable and wearable electronics are versatile technologies that may enable future generations to scavenge energy from our daily life environment such as the human body motions, fluidics, and mechanical vibrations. Recently, many energy harvesting (EH) technologies have evolved such as thermoelectric generator (THG), hydroelectric generator (HEG), triboelectric nanogenerator (TNG) and piezoelectric nanogenerator (PNG) devices for portable/wearable applications. Studies show that, a glass fabric based THG developed using the screen-printing technique and it generates high power density [1]. An efficiency of 1.53 % was generated using the THG with eight pairs of segmented legs and the corresponding materials were synthesized by spark plasma sintering [2]. A rational design of multi-unit HEG was fabricated to harvest the water related energy in the environment [3]. Over past decade, rapid and continuous development of PNG and TNG based devices took place, which can convert mechanical energy to electrical energy. Wang et al. [4] developed the basic conventional TNG device structures and it generates high electric power based on four different working modes such as vertical contact-separation mode, lateral sliding mode, single electrode mode and free-standing triboelectric-layer mode. Arunkumar et al. [5] reported the lightweight, cost-effective single-electrode based smart seat TNG device for harvesting energy from the living environment. But these devices suffer from the complicated device design; interference, stability and output performance depend on the growth of various nanostructures (NS) on active triboelectric layers [6]. On the other side, PNG devices were developed using 1D-NS (one-dimensional nanostructures), nanowall, micro belts and thin films, which are useful to harness low frequency mechanical energy. Zhu et al. [7]

studied flexible PNG device using sweeping-printing method and the active layer used for energy generation is horizontally aligned zinc oxide (ZnO) nanowires (NWs). Wang et al. [8] reported the conversion efficiency of the NWs based PNG device is estimated to be 17 % to 30 %. Yang et al. [9] showed the possibility of energy generation from the single lead zirconate titanate ($Pb(ZrTi)O_3$ designated as PZT) wire and its self-powered temperature sensor application. Kumar et al. [10] developed the biocompatible composite PNG for self-powered ultraviolet (UV) photosensor application using the ZnO NWs and the reduced graphene oxide (rGO). It reveals that, the fabricated PNG can generate an output voltage and current of 5.5 V and 0.63 μA, during the foot-stamp operation. They also synthesized the ZnO nanowall for energy generation using the cost-effective hydrothermal method [11]. Wu et al. [12] firstly demonstrated the single-zinc stannate ($ZnSnO_3$) micro belt nanogenerator and it has an energy conversion efficiency of 4.2 to 6.6 % based on the strain 0.8 to 1 % respectively. All these conventional PNGs use various types of ZnO NS and generate the small output power (nW to μW). This can be useful to drive the low power light emitting diodes (LEDs) and monochrome liquid crystal displays (LCDs). Later, the fabrication of PNG devices were extended using the flexible organic polymers, inorganic perovskite NS and organic-inorganic composite films. Pi et al. [13] studied the organic polymer based PNG device and generates a current density ≈ 0.56 μAcm^{-2}. Kim et al. [14] fabricated inorganic nanoparticles based nanocomposite thin films using layer-by layer approach for PNG device. Ni et al [15] reported the single barium titanate ($BaTiO_3$ designated as BTO) nanowire based PNG device and the electrical output is proportional to the strain and strain rate. Kim et al. [16] studied the ferroelectric properties of the organic/inorganic composite films with many number of nanolayers and suggest the suitability for resistive switching memory and energy generation applications. Alluri et al. [17] developed the

zirconium-doped barium titanate (BTZO) nanocubes/poly (vinylidene fluoride) (PVDF) composite films and the generated output voltage ≈11.95 and current ≈1.35 μA respectively. The above mentioned polymer and composite PNGs generates the output power density from uW to mW range. Over the last decade, many researchers demonstrated that the PNG devices can function as a standalone power source and also have a capability to drive various sensors such as UV photo detector output controlled with different wavelengths of light source [10], fluid velocity sensor to measure the different water speeds [17], active gas sensor to detect oxygen, water vapor and hydrogen sulfide (H_2S) gases [18], pH sensor to measure different pH levels of buffer solution [19], composite worm structure output controlled by different pH values of buffer solution [20], and glucose sensor to measure different glucose concentrations of human saliva [21]. These self-powered sensors do not require any external power source (battery) and an additional sensory circuit. Among these EH technologies, PNG device is the most reliable and prominent technology. Other EH technologies may have greater energy conversion efficiencies but suffer from the inherent limitations such as leakage currents, difficulties in maintenance, aging effects (performance degradation), complex working mechanisms, pressure and humidity effects, respectively [6]. In addition, many existing portable devices use batteries as electrical driving source, which consists of complex, sensitive materials with limited life time [22].

The potential use of PNG device is not only limited to the conversion of regular mechanical vibration energy, but also extended to convert the ocean waves, wind, rain drop, vehicle suspension motion and tap water motions to electrical energy. Viet et al. [23] developed floating energy harvester to harness the energy from intermediate and deep water waves. Wu et al. [24] suggested the piezoelectric patches on cantilever and a proof of mass is enough to harvest the wind energy. Alluri et al. [17] explore the feasibility of flexible PNG using the

zirconium-doped barium titanate (BTZO) nanocubes/poly (vinylidene fluoride) (PVDF) film can utilize the tap water motion to harvest the electric power. This device can also have the functionality to sense or generate energy with various speeds of water flow ON/OFF conditions. Ilyas et al. [25] developed an alternating approach for harvesting energy with piezoelectric materials by utilizing rain drop impacts. They thought that the efficiency of the device can be improved by modifying the droplet impact mechanism with the harvester surface by exploring new surface materials to maximize inelastic collision. Xie et al. [26] designed an efficient dual-mass piezoelectric bar harvester, which can convert ambient vibrations of a vehicle suspension system subjected to roughness of road surfaces to electrical energy. They stated the construction and installation of multi-unit piezoelectric bar harvesters in vehicle can generate more energy and have significant impact on automobile industry. Azizi et al. [27] studied the dynamics of a piezoelectric bimorph cantilever energy harvesting device with respect to the harmonic base excitations. They stated that the high output power can be possible to generate at the base excitation frequency coalesced with the first natural frequency of the device. Furthermore studies show that the piezoelectric EH devices are highly efficient to utilize and convert the regular natural contractile and relaxation motions of the heart, lung and diaphragm. In addition, many studies demonstrate the output of PNG devices is also useful to drive pressure sensor and motion sensor, respectively. Chun et al. [28] reported ZnO embossed hollow hemi-spheres thin film for highly responsive pressure sensors and PNGs. They stated for one piece of hemi-sphere layer is stacked over another to form a layer-by-layer matched architecture and the PNG output increases up to 2 times. They also suggested that the stretchable composite films with hemisphere structure based PNG device useful to sense the directional motion of the human body parts [29].

The piezoelectric coefficient (d_{33} or d_{31}), electro-mechanical coefficient (k) and relative permittivity (ε_r) of NS will play a key role for efficient energy conversion. Initially, conventional PNG devices fabricated by lower d_{33} of ZnO NS can generate small output power. Further, the PNG fabrication and output power improved by high d_{33} nanomaterials such as PZT, BTO sodium potassium niobate ($KNaNbO_3$ designated as KNN), and flexible PVDF polymer, respectively. PZT based materials and devices produce high performance [30] but facing global restriction due to lead toxicity and environmental pollution. In this case, KNN and BTO are alternative biocompatible materials with reasonable energy conversion efficiency. To date, the progress on KNN based PNG devices generates medium range outputs [31] and have serious drawbacks such as densification, manufacturing cost [32]. Hong et al. [33] suggest that the KNN material has poor piezoelectric properties at room temperature, which is another demerit for KNN. Shrout et al. [34] demonstrated that the KNN properties are strongly temperature dependent, while degradation occurs through thermal cycling between two ferroelectric states. Certainly, BTO and doped BTO based devices are eco-friendly, cost-effective and generate higher or equal to the PZT device output performance. These PNG devices are suitable for self-powered biosensors and implantable devices in health monitoring applications. The main disadvantage of pure BTO nanomaterials is brittle nature and the devices cannot withstand at high mechanical forces, which can be solved by the composite technology [35]. Recent studies show the composite PNG devices have greater energy conversion efficiency, reducing internal leakage currents and can sustain at high input mechanical forces. These PNG devices are made up of inorganic piezoelectric NS as a filler material along with the organic polymer matrix. Another serious factor for approaching the composite technique is manufacturing cost, which depends on the fabrication of active piezoelectric material. To date, physical vapor deposition

(PVD) [36], chemical vapor deposition (CVD) [37], hydrothermal [11], and vapor transport techniques [10], are established for developing the micro/nanostructures such as nanowires, micro belts, nanowall, and composite films. Kim et.al [14] developed layer-by-layer (LbL) assembly of oleic acid ligands (OA)-BTO nanoparticles (NPs) ultrathin film and explained the effect of amine, carboxylic acid functionalized polymers to enhance the piezoelectric power output and ferroelectric properties. But these techniques suffer from high costs, small-scale production and long processing times. Here, the hydrothermal synthesis is cost-effective but the drawback of prolonged reaction times and less reproducibility of NS due to the addition of fresh solution to the previous solution [38]. Hence piezoelectric composite technology is the best approach for low manufacturing cost, but needed to develop the novel micro-structures other than regular composite films, which can reduce the device area, increase the flexibility/portability, biodegradable property, and efficient energy conversion at low frequency, stability and non-interference of the electrical output.

In this work, a new type of linear worm structure i.e. BTO NPs/calcium alginate (Ca-alg) composite was prepared using the ionotropic gelation (IG) technique. Here, Ca-alg extracted from the brown seaweeds used to form a three dimensional (3D) gel network. The Ca-alg biopolymer blocks (M or G) are formed by the cross linked junctions with mono or divalent cations (Ca^{2+}), leading to a 3D gel network that immobilized the BTO NPs to form as a 1D-composite linear worm structure. In comparison with the small-scale fabrication of poly-crystalline single nanowires and thin films, the IG method is eco-friendly, and it has high potentiality, adaptability for the preparation of flexible worms of tailored lengths, compositions, and functionalities achieved through physisorption between the NPs and the polymer matrix. Further portable, laterally aligned 1D-composite linear worm based piezoelectric nanogenerator

(WPNG) with high energy conversion efficiency at low frequency and WPNG devices of multiple lengths were fabricated and studied. The maximum open circuit voltage (V_{OC}) ≈10.90 V and short circuit current (I_{SC}) ≈1.88 μA for single flexible WPNG device was generated by rapidly tapping with biomechanical hand force. The device has composite worm length (L) ≈3.5 cm, diameter (D) ≈550 μm and the generated output is sufficient to drive monochrome LCD and commercial LEDs (11 blue and 11 green). The performance of WPNGs was higher than many published reports of polycrystalline single nanowire or micro belts based nanogenerators (Table 5.2.1). This may be due to the contribution of space charge polarization according to the maximum number of BTO NPs along the length of the worm. Next, the portability of a single worm (having L= 2.5 cm, D=550 μm) based WPNG device by placing it on the insole of a shoe to harness the low mechanical energy of human foot motion has been demonstrated. Then, we evaluated by the effects of integrating two WPNGs connected in series/parallel, depending on the requirements of an electrical performance and the results indicated that, this was a promising candidate method for portable, wearable applications and possibly suitable for self-powered sensor applications.

5.2.2 Experimental Method

High quality piezoelectric BTO NPs were synthesized using a conventional solid state-reaction (SSR) method [39] and given the detailed explanation in the section 5.1.2.1.

5.2.2.1 Fabrication of BTO NPs/Ca-alg linear worms

Fabrication of pure (Ca-alg) and composite (BTO NPs/Ca-alg) linear worm structures prepared by an IG method involves three key steps (**Figure 5.2.1a**). First, to prepare the sodium alginate (Na-alg) homogeneous aqueous solution with no alginic acid precipitation, which is obtained by the commercially available alginic acid sodium salt (Sigma-Aldrich) ~ 2 g, was

dissolved in 100 mL double-distilled water (DI water) under constant stirring at 50 °C for 2 h to form a clear transparent solution. The second step was the functionalization of BTO NPs using Na-alg biopolymer, i.e. a fixed weight percentage of BTO NPs (1 wt %) was dissolved in Na-alg solution by stirring magnetically at 70 °C for 2 h with no agglomeration of BTO NPs. The third step involved the exchange of sodium ions (Na^{+}) by calcium ions (Ca^{2+}) and ionic gelation of BTO NPs/Ca-alg linear worms by squeezing the homogeneous solution of BTO NPs/Na-alg through a plastic syringe (without needle) of 5 mL volume into a calcium chloride ($CaCl_2$) bath (1 %w/w). After 30 minutes of gelation, the worms were removed from the $CaCl_2$ solution and soaked in deionized water for 15 minutes to remove excess Ca^{2+} ions and then dried for 24 h at room temperature. A similar approach was followed to prepare pure (Ca-alg) worms.

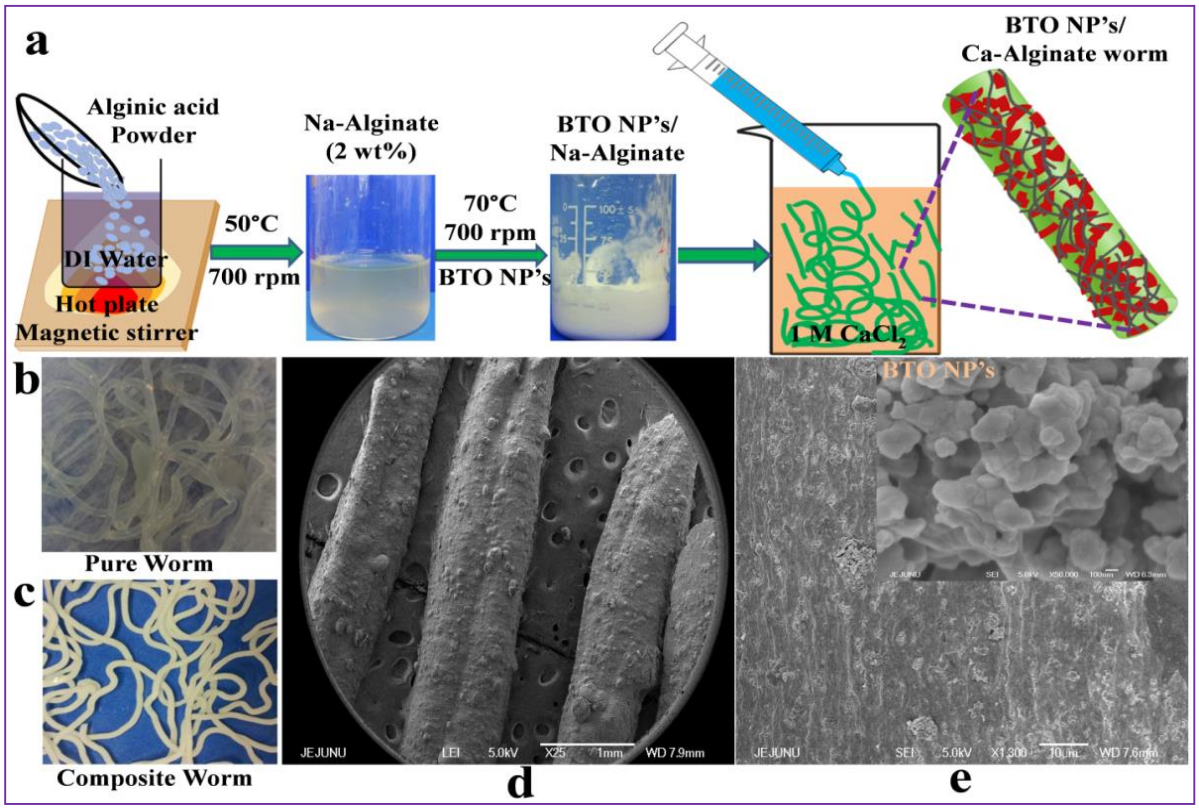

Figure 5.2.1.(a) IG method for composite linear worm. **(b, c)** Digital image of transparent (Ca-alg) and non-transparent (BTO NPs /Ca-alg) worm structures. **(d, e)** Surface morphology of the composite linear worm shows a rough surface at 1 mm scale and magnified image shows good

distribution of BTO NPs in Ca-alg chains at 10 μm scale. The inset shows highly crystalline random BTO NPs synthesized by SSR method at 100 nm scale.

5.2.2.2 Fabrication of flexible, laterally aligned composite linear worm based piezoelectric nanogenerators (WPNGs)

Fabricated composite linear worms were seized according to the required dimensions (L = 1.5, 2.5 and 3.5 cm, D ≈ 550 μm) for WPNG devices. The WPNG was fabricated by attaching the adhesive side of aluminum (Al) foil on polyethylene terephthalate (PET) as a substrate (4 x 1.5 cm). For WPNGs, electrodes were fabricated by attaching Al foil having a thickness of 18 μm and finite length of ≈1 cm on flexible PET. The two Al foils were separated by a fixed distance. Next, a linear worm of required dimension was aligned laterally and placed exactly on top of two Al foils and tightly attached using silver paste. The electrical connections were established with copper (Cu) wires attached to the silver paste on both sides of the linear worm. Finally, polydimethylsiloxane (PDMS) was used as a packing layer for the WPNG to protect the device from external conditions such as mechanical stress, temperature and humidity. Before electrical characterization, the WPNG devices were electrically poled at 3 kV for 24 h at ambient temperature.

5.2.3 Results and discussion

5.2.3.1 Structural and solubility conditions of composite structures

Complete protocols for Na-alg, BTO NPs/Na-alg, and BTO NPs/Ca-alg composites are shown in **Figure 5.2.1a.** The right inset shows a schematic representation of a finite linear composite worm having a good distribution of BTO NPs (≥ 100 nm) along with Ca-alg chains. Generally, Ca-alg can form several possible shapes such as fiber mats for regenerative medicine [40], hydrogel beads for removal of metal ions in aqueous solution [41], 3D porous scaffolds for

cell therapy [42], and scaffolds with predesigned core/shell structures for bone tissue engineering applications [43].

The strategy was to incorporate piezoelectric BTO NPs into template worm structure of alginate for portable energy harvesting and self-powered sensor applications. **Figure 5.2.1(b, c)** shows optical images of a pure Ca-alg (transparent) and a composite worm (whitish color, non-transparent) with finite lengths having the same diameter. As fabricated linear composite worms were suitable for large-scale production, which is more useful in potentially diverse applications. Here, the formation mechanism of pure worm was related to the sol-gel transition between the multivalent cations (specifically with Ca^{2+} ions) due to the existing carboxylate groups of the biopolymer. The Na-alg chelate with Ca^{2+} ions forms 3D hydrogels and gel formation was driven by interactions between G-blocks which associate to form tightly held junctions in the presence of divalent (Ca^{2+}) cations.

The surface morphology of composite worm was analyzed under a field emission scanning electron microscope (FE-SEM) at 1 mm and 10 μm scales, as shown in **Figure 5.2.1(d, e)**; the immobilization of BTO NPs in Ca-alg chains was observed. The inset shows high-quality BTO NPs at 100 nm scale, synthesized using a high-temperature solid state reaction (1200 ^{0}C for 2 h). The tetragonal crystal structure with a single phase of BTO NPs was identified by the major characteristic peaks and the splitting behavior of the diffraction peak position at 45º, indexed with (002)/(200) as shown in left inset **Figure 5.2.2a** [44]. It was consistent with the ICDD-98-001-3771 pattern. Raman spectroscopy was employed to understand the dynamic symmetry of as synthesized samples. The right inset presents the two strong peak positions at 305.87 cm^{-1} and 517 cm^{-1}, indicating the presence of an asymmetric Ti^{4+} ion in the BTO lattice confirming a tetragonal structure of BTO NPs [17]. Both X-ray diffraction (XRD) and Raman patterns showed

good correlations with the tetragonal phase of BTO NPs indicating the formation of non-centrosymmetric regions through local off-centering of titanium atoms.

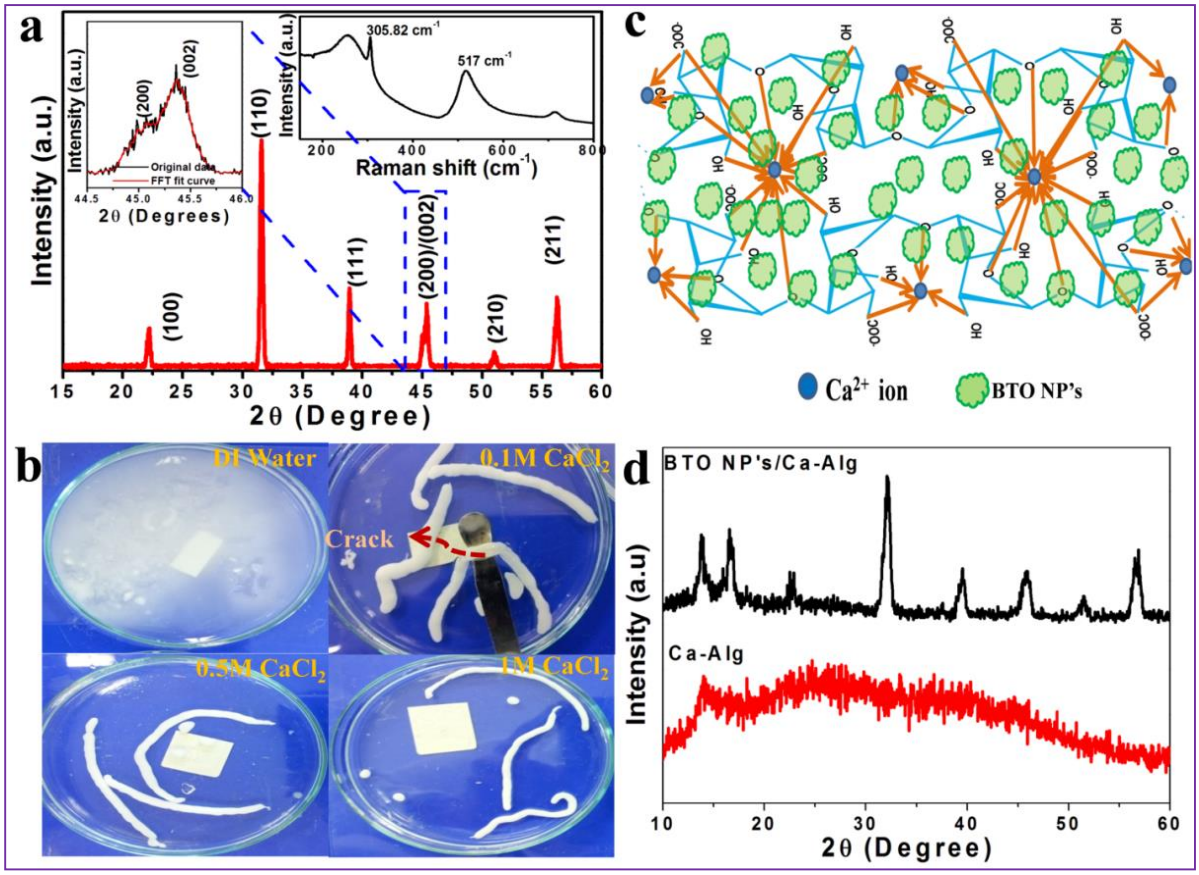

Figure 5.2.2(a) Typical XRD pattern of BTO NPs. The left inset shows the splitting nature of the diffraction peak position at 45° confirming the tetragonal structure. Right inset shows Raman spectrum of BTO NPs active vibration modes. **(b)** Stability and solubility of the composite worms under different concentrations of $CaCl_2$ bath solutions [1 M, 0.5 M, 0.1 M and 0 M (DI Water)]. **(c)** Schematic illustration for the formation of composite worms using a 3D gel network (egg box model). **(d)** XRD patterns of amorphous Ca-alg and crystalline composites.

Next, the ionic gelation strength of composite worms was confirmed under various $CaCl_2$ weight percentages (0, 0.1, 0.5 and 1 M), as shown in **Figure 5.2.2b**. No formation of worms was observed when processed with pure DI water (0 M $CaCl_2$) due to the lack of Ca^{2+} ions (and thus also of G-blocks). But with 0.1 M and 0.5 M $CaCl_2$ solutions, composite worms were formed but with less ionic gelation strength and multiple cracks. However, good ionic gelation

strength, and longevity of worms was achieved with 1 M $CaCl_2$ as shown in **Figure 5.2.22b**. The purity of copolymer such as composition, sequence, and molecular weight will vary with the source and species. Thus, alginates with high G contents yielded stronger gels. Use of Ca-alg as a carrier material for BTO NPs opens the possibility of a selective adsorption of organic and inorganic molecules [16] depending on their electrical charge, due to interactions with the negative carboxylate groups on the alginate. Pure and BTO NPs/Ca-alg composite worms were used for energy harvesting applications and are also suitable to drive low-power electronic devices (LCD display, LEDs) and self-powered devices. The immobilization of BTO NPs, along with G-blocks of Ca-alg caused by physisorption, is shown schematically in **Figure 5.2.2c**. In addition to G-blocks, MG blocks will also participate, forming weak junctions. The amorphous nature of Ca-alg [45] and the crystalline behavior of the composite were confirmed by the XRD pattern as shown in **Figure 5.2.2d**. The XRD peaks between 10° to 20° for the composite confirmed that the crystalline nature of the Ca-alg [46] did not influence the tetragonal crystalline structure of BTO NPs and provides flexibility, and longevity to the composite through homopolymeric and hetero-polymeric blocks. Furthermore, Fourier transform infrared spectroscopy (FTIR) was used to confirm physisorption between the BTO NPs and Ca-alg. **Fig. 5.2.3** presents FTIR spectra for as-synthesized samples: BTO NPs, Ca-alg, and BTO NPs/Ca-alg. In the Ca-alg spectrum, the bands at 3428 cm^{-1} and 2930 cm^{-1} indicated OH groups and stretching vibrations of C-H groups respectively, and the bands at 1628 cm^{-1}, 1422 cm^{-1} were attributed to the asymmetric, and symmetric vibrations of O=C-O bonds [45]. Similarly, stretching and bending of the BTO lattice can be analyzed with the characteristic peak at 600-530 cm^{-1} due to the bond between Ti-O in TiO_6 octahedron of the $BaTiO_3$ lattice [17]. In this case, the characteristic peak for the composite had a lower wavelength shift i.e. 548 cm^{-1} as

compared to the characteristic peak of 584 cm^{-1} for BTO NPs indicating the internal stresses of TiO_6 in the BTO lattice. Other groups, such as OH, C-H, and O=C-O, also showed small changes in peak positions. Overall, solubility tests, the XRD pattern, and the FTIR spectra provided direct evidence for physisorption between the BTO NPs and Ca-alg polymer.

5.2.3.2 Energy harvesting performance of worm structure piezoelectric nanogenerator

Laterally aligned linear composite WPNGs were fabricated and analyzed the energy harvesting performance using an electrodynamic shaker operated at various frequencies (3, 10, 15 and 20 Hz). **Figure 5.2.5a** shows the different lengths of flexible composite worms under dry conditions for 12 hr, and 24 hr at room temperature and Al electrode coating on two ends of the worms using a thermal evaporator. However, the Al coating on two ends of each worm was not suitable (partially conductive), alternatively a low cost Al foil/ flexible polyethylene terephthalate (PET) substrate was selected to acquire the generated charge carriers.

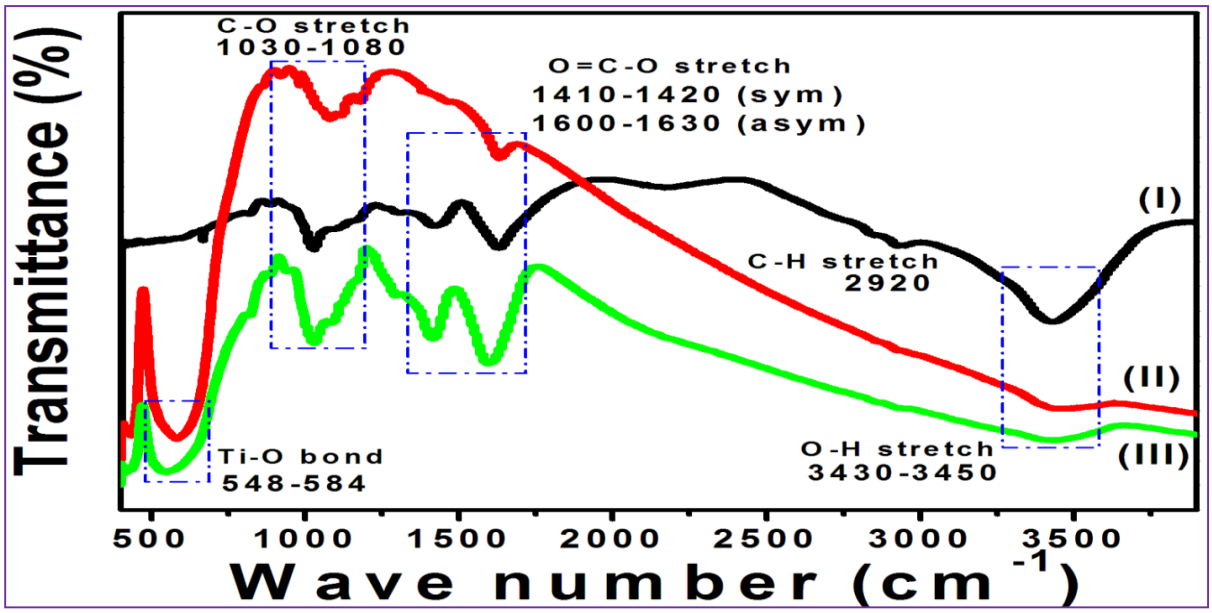

Figure 5.2.3 FT-IR spectra of as-synthesized all samples: (I) pure Ca-alg (II) BTO NPs (III) composite (BTO NPs/Ca-alg).

The electrical output voltage (V_{OC}) was obtained by connecting the WPNG (L = 2.5 cm, D = 550 μm) output terminals as the input to full-wave bridge rectifier as shown in **Figure 5.2.4a**. Initially, the WPNG has low piezoelectric potential developed across the two ends of opposite electrodes with a low driving frequency (3 Hz) of mechanical load. This may be due to the capacitance nature or initialization of the piezoelectric response of the device [17]. The V_{OC} (and current (I_{SC})) of WPNG device increased from 1 V to 5.5 V (and 140 nA to 590 nA), when the driving frequency of the constant load varied from 3 to 20 Hz as shown in **Figure 5.2.4b (and Figure 5.2.7a)**.

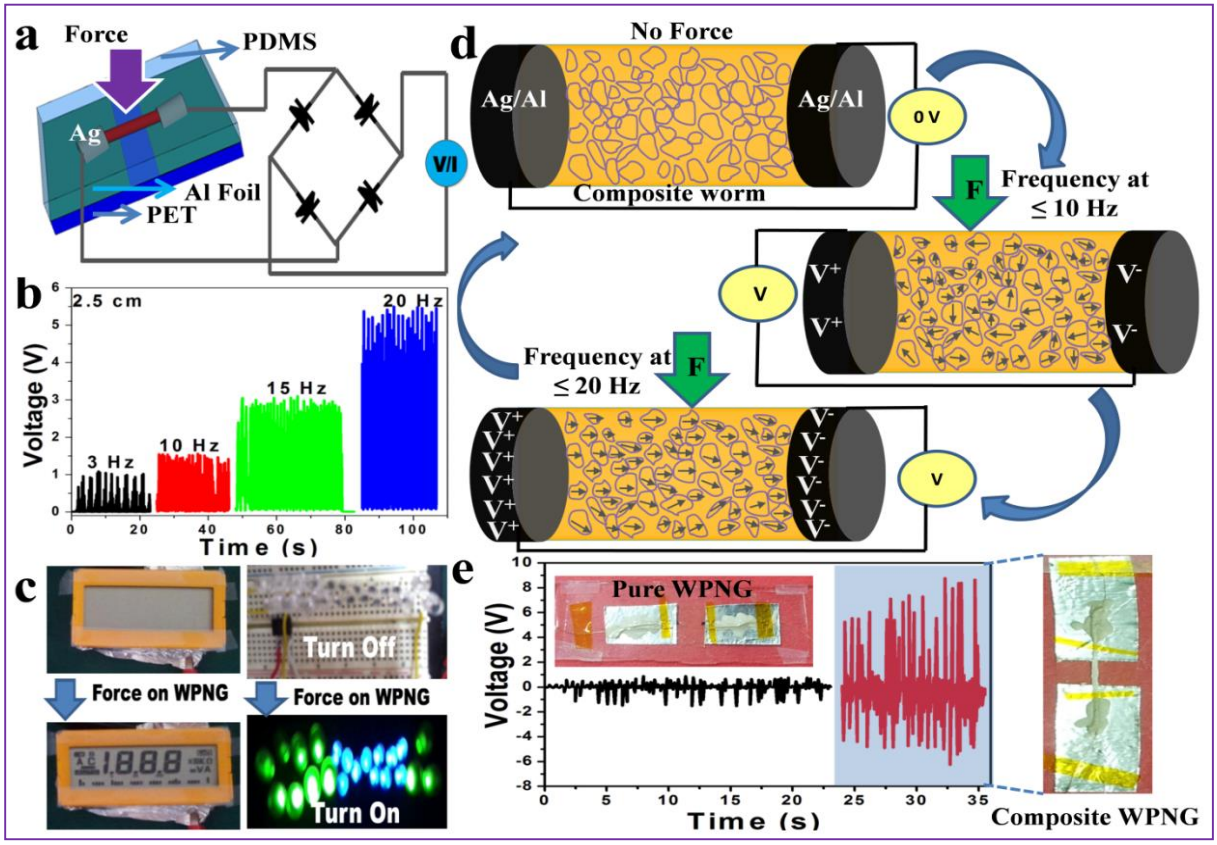

Figure 5.2.4 (a) Schematic diagram of WPNG device output connected to a full wave bridge rectifier. **(b)** Rectified V_{OC} of the WPNG device (L= 2.5 cm, D = 550 μm) under frequency (3, 10, 15 and 20 Hz) dependent mechanical load (11 N). **(c)** A monochromic LCD display and 22 LEDs (11 green, 11 blue) could be lit up by the rectified V_{OC} of the WPNG with no storage device. **(d)** Working mechanism of the WPNG device through schematic illustration. No

potential developed across the two ends of the Al/Ag electrode under the no force condition. An electric potential was developed across the electrodes with the frequency-dependent load (11 N). **(e)** Comparative voltages of pure and composite worms of length 2.5 cm having constant diameters; inset shows optical photographs of the as fabricated WPNG devices.

These results indicated cyclic frequency-dependent behavior of WPNG device at constant load. The single worm (L = 2.5 cm, D = 550 μm) based nanogenerator results are quite high when compared with many published reports of on BTO single nanowire, ZnO nanowire, $KNbO_3$ nanowires, and $ZnSnO_3$ micro belt devices (given in **Table 5.2.1).** Next, the generated output of WPNG device can be useful to drive commercial LEDs and monochrome LCD displays with no storage unit. **Figure 5.2.4c** shows the series connection of LEDs (11 blue and 11 green) and the LCD display was turned OFF during the no force condition and turned ON upon the force acting on WPNG device. The working mechanism of the linear WPNG device is schematically shown in **Figure 5.2.4d.** Zero potential was developed across the Al/Ag electrodes of the WPNG during no force conditions. The device generated a maximum piezoelectric potential across the electrodes when the cyclic frequency (3 to 20 Hz) dependent mechanical load acted on it. This is due to the orientation of electric dipoles along the length of composite worm as shown in **Figure 5.2.4d**. The frequency dependence as a function of piezoelectric material with respect to the vibration mechanical load can be expressed as:

$$f_r = \left(\frac{\pi}{2}\right)\sqrt{\frac{K_{eff}}{M_{eff}}} \qquad \text{(E5.2.1)}$$

Where $K_{eff} = K_{piezo}({}^{1}/_{(R_i + R_e)})$ is the effective spring constant as a function of the piezoelectric material, M_{eff} is the effective mass of the energy harvesting device, R_i represents the internal resistance of the material and R_e is the external resistance.

Table 5.2.1: Comparison of the laterally aligned single linear WPNG devices with published reports on single micro belt, fiber, nanowire and thin film based nanogenerators.

Material	Structure	V_{OC} (V)	I_{SC} (A)	References
$BaTiO_3$	Single Nanowire	0.021	1.3 n	[**15**]
BZT-xBCT	Nanowires	3.25	55 n	[**51**]
ZnO	Hollow hemisphere	0.2	-	[**28**]
ZnO/PVDF	Nanowires	40-55 m	-	[**52**]
CdTe (Zinc blende)	Single nanowire	0.3	40 n	[**53**]
$ZnSnO_3$	Microbelt	110 m	80 n	[**12**]
PVDF	Fibers	0.076	39 n	[**54**]
$BaTiO_3$/MW-CNT/PDMS	Round shape	3.2	350 n	[**55**]
$BaTiO_3$	Thin film	1	26 n	[**56**]
PAA/13-nm OA-$BaTiO_3$	Cubic-like	1.8	700 n	[**14**]
BTO NPs/Ca-alg	Worm (L = 1.5 cm)	5.59	1.14 µ	Present work @ Hand force
BTO NPs/Ca-alg	Worm (L = 2.5 cm)	7.39	1.57 µ	
BTO NPs/Ca-alg	Worm (L = 3.5 cm)	10.90	1.88 µ	

Further, the effect of the template polymer for energy harvesting was estimated. A transparent WPNG device (L = 2.5 cm, D = 550 μm) without BTO NPs showed less output than the composite WPNGs (with BTO NPs) up on hand force as shown in **Figure 5.2.4e**. It shows that, the polymer effect for energy harvesting is negligible and supports only as a template structure (worm microstructure) to hold BTO NPs. This confirms that the energy harvesting is only due to the piezoelectric properties of BTO NPs and its electric dipole orientation with respect to the load. The inset in **Figure 5.2.4e** shows optical images of as fabricated WPNGs with and without BTO NPs. Here, the charge accumulation is dependent mainly on the type of piezoelectric mode such as d_{31} ($t_{piezo}>L_{piezo}$) or d_{33} ($L_{piezo}>t_{piezo}$), which will depend on the thickness, the length of the active piezoelectric material, and the location of the electrodes. In this case, the length of the piezoelectric worm (1.5 to 3.5 cm) was much greater than the thickness ≈550 μm of worm i.e. d_{33} mode and the electrodes were placed adjacent to the two ends of worm. The piezoelectric voltage constant (g_{ii}) was directly proportional to the piezoelectric charge coefficient (d_{ii}) and the transient flow of electrons with respect to the external mechanical load, in case of which tuning of the piezoelectric potential inside the composite worm [8] will play a major role in macroscopic piezoelectric potential.

5.2.3.3 Length dependent output of WPNGs & self-powered electronic display

A quantitative analysis of the length dependence of piezoelectric worms for energy harvesting was undertaken by fabricating WPNGs of different lengths 1.5, 2.5 and 3.5 cm and an approximately constant diameter 550 μm, as shown in **Figure 5.2.5c**. The electrical response (V_{OC}, I_{SC}) for all WPNGs was obtained and analyzed by hand force. For worm length ≈1.5 cm, the harvested energy was approximately ≈6 V, and ≈1 μA by hand force. The generated output of WPNG device was increased to ≈10.90 V and ≈1.88 μA, by increasing the worm length up to 3.5

cm as shown in **Figure 5.2.6 and Figure 5.2.7b.** An asymmetric electrical response was observed for all WPNGs, which was due to the non-symmetric nature of the biomechanical hand force. Periodic loads on WPNG devices results in a back-and-forth of charge carriers across the electrodes in a laterally aligned linear worm. The generated piezoelectric potential can be evaluated using fundamental piezoelectric theory as [47]:

$$V_{OC} = \int g_{ii}\, \varepsilon(l) \lambda dl \qquad \text{(E5.2.2)}$$

where the piezoelectric voltage constant $g_{ii} = d_{ii}/(\varepsilon_r \varepsilon_0)$, $\varepsilon(l)$ is the strain along the worm, d_{ii} is the piezoelectric coupling coefficient, λ is the elastic modulus, $(\varepsilon_0, \varepsilon_r)$ are the permittivity of free space and the relative permittivity of the composite linear worm respectively.

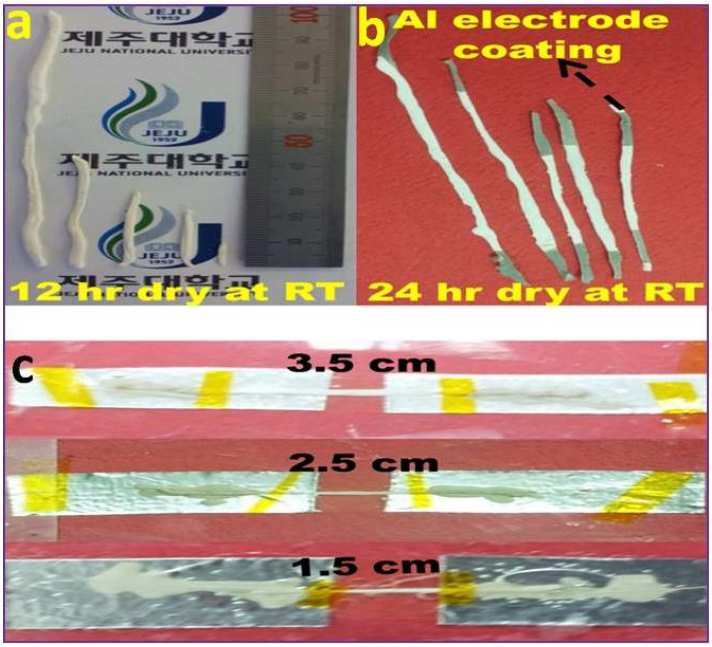

Figure 5.2.5 (a) Multiple lengths of linear worms at dry conditions like after 12 hr and 24 hr dry at room temperature with Al electrode coating by thermal evaporator. **(c)** Digital images of as fabricated laterally aligned WPNGs with various lengths of worms (1.5, 2.5 and 3.5 cm).

The relationship between the electrical quantities, and mechanical parameters (stress, strain) of the piezoelectric harvester was approximated using piezoelectric theory. For real-time

applications, understanding the instantaneous WPNG power across the load resistance is necessary, and can be estimated with the following equation-E5.2.3 [48]:

$$P = {}^{1}/_{T} \int ({}^{V^2(t)}/_{R})\, dt \qquad \text{(E5.2.3)}$$

where P is the developed power, V is the real-time peak voltage across load resistance R, and T is the time period of the mechanical load.

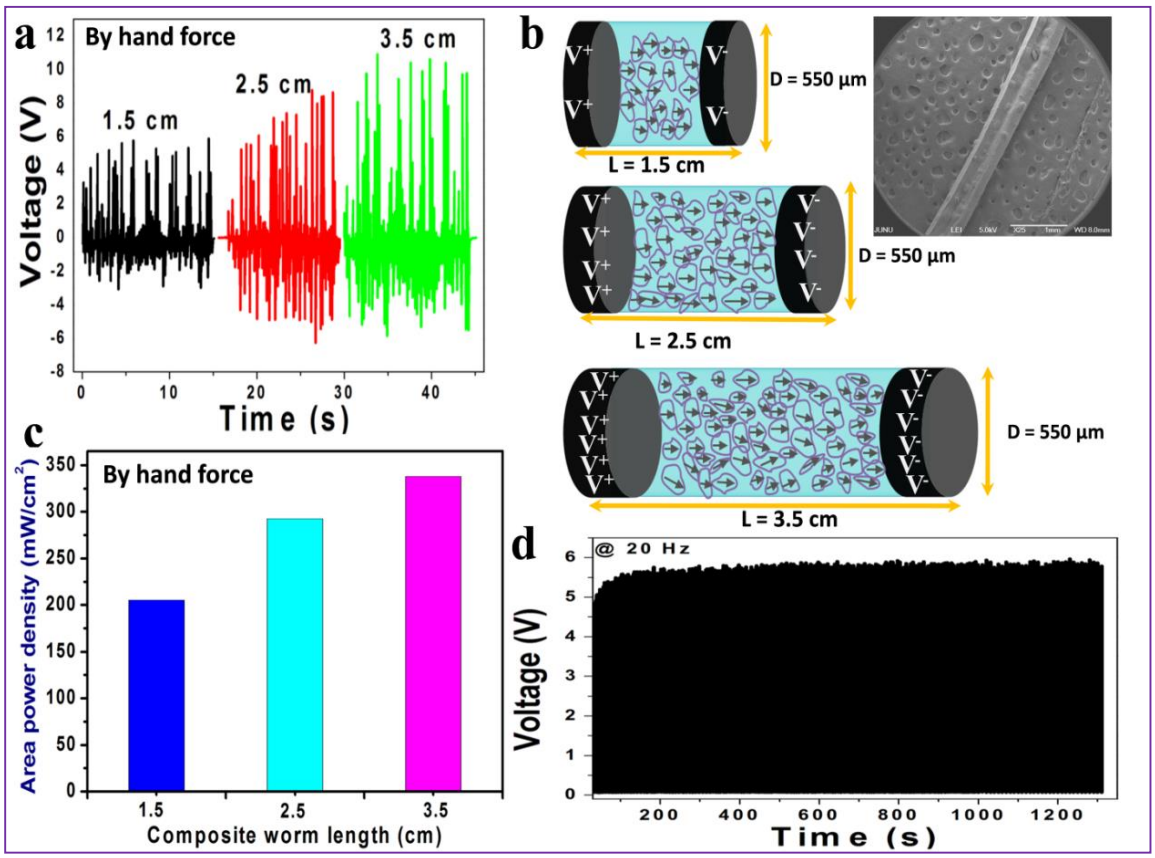

Figure 5.2.6 (a) The V_{OC} of WPNG devices with various lengths of composite worm (1.5, 2.5, and 3.5 cm) under rapid periodic hand force (tapping and release conditions). **(b)** Schematic illustration of the piezoelectric potential generation with respect to the composite worm length under constant force. The inset shows the FE-SEM image of composite worm. **(c)** Comparative area power density *vs* composite worm length with respect to the hand force**. (d)** Stability test of the WPNG device (2.5 cm) at 20 Hz frequency of 11 N.

Figure 5.2.6b shows the estimated schematic illustration of length dependent working mechanism of WPNG device, which purely depends on the number of piezoelectric NPs and its

electric dipole orientations along the worm lengths (1.5 cm, 2.5 cm, and 3.5 cm) with constant diameter. Here, the increment in composite worm length results in increasing the BTO NPs contribution along the worm length and the corresponding cumulative effect of the electric dipole orientations in composite worm will enhance as shown in **Figure 5.2.6b**.

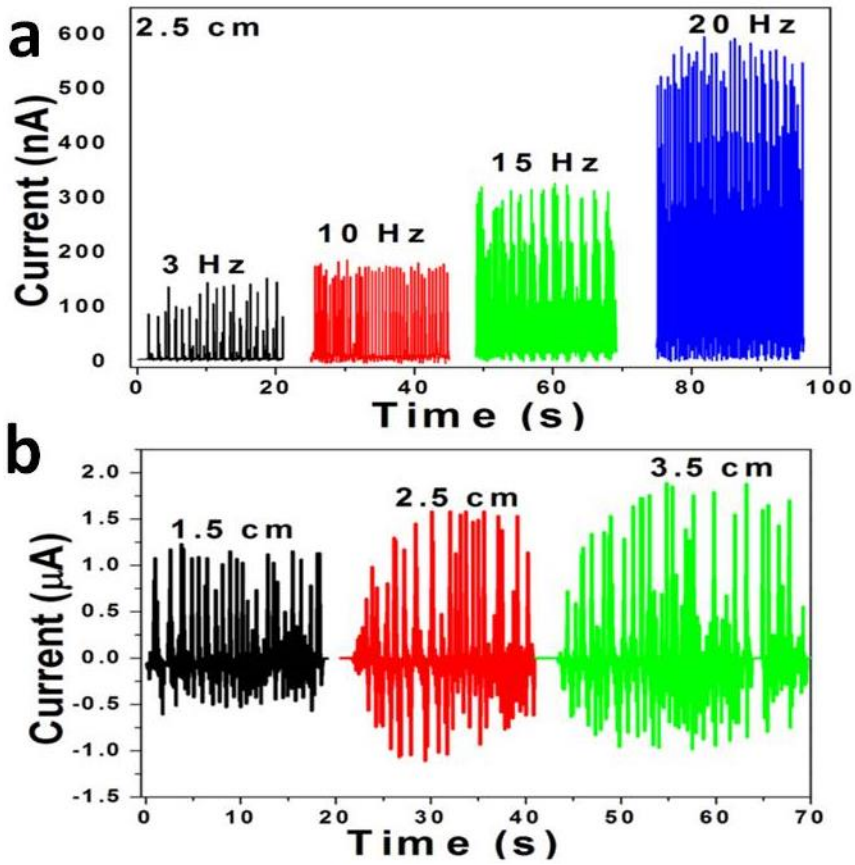

Figure 5.2.7 (a) The I_{SC} of WPNG (2.5 cm) under the mechanical load (11 N) as a function of cyclic frequency **(b)** The I_{SC} of WPNG devices with various lengths of composite worm (1.5, 2.5 and 3.5 cm) upon rapid periodic hand force (tapping and release conditions).

The inset of **Figure 5.2.6b**, indicate an FE-SEM image of the composite worm and the magnified image shows the BTO NPs in polymer matrix. **Figure 5.2.6 (a, c)** is the direct evidence for enhancement of piezoelectric performance with respect to the composite worm length upon the bio-mechanical hand force. A long-term test was conducted to confirm the

mechanical endurance of the WPNG device (L = 2.5 cm, D = 550 μm). Measurements were carried out for more than 1300 seconds at a 20 Hz frequency of periodic load (**Figure 5.2.6d**) and the output voltage for the WPNG was 5.92 V. There was no significant change in output voltage even after more than 1300 seconds, indicating that the device had long-term stability. **Figure 5.2.8a** shows the load resistance analysis of WPNG device and the obtained load matching resistance is approximately ≈1 MΩ. As expected, the output voltage increased from 0.0011 V to 5.92 V when increasing the resistive loads from 47 Ω to 5 GΩ due to ohmic losses of the device at constant mechanical load. The power density was maximum (≈ 74.189 mW/m^2) for WPNG (L = 2.5 cm, D = 550 μm) across a load resistance of 1 MΩ at 20 Hz cyclic frequency of the mechanical load as shown in **Figure 5.2.8a**. Besides the power density, the charging ability of the WPNG device was also measured as shown in **Figure 5.2.8b**. The generated output voltage from the WPNG device was rectified continuously and connected across a capacitor (0.1 μF), which charged up to 2.3 V during 5 s under a 20 Hz cyclic frequency of mechanical load.

The laterally aligned WPNG device was intended for portable, wearable consumer electronics using low-frequency based energy from human foot stress. An experimental demonstration of a portable low frequency-based multi-unit energy harvester (integrating the WPNG devices) and its output, connected to a full wave bridge rectifier is shown in **Figure 5.2.9a**. The optical image indicates the WPNG location on the insole to evaluate its energy conversion depending on foot stress **(Figure 5.2.9b)**. Polydimethylsiloxane (PDMS) was used as a packing layer for the WPNG device to avoid undesirable noise, and direct contact between the human foot and the energy harvesting device. Initially, the individual electrical responses of two single WPNG devices (L = 2.5 cm, D ≈ 550 μm) was evaluated with the periodic stress and release of a human foot stamp as shown in **Figure 5.2.9(c, d)**. The maximum generated open

circuit voltage and short circuit current of the two individual WPNGs reached 0.3 V and 40 nA, respectively. Here, the energy harvesting mechanism is quite similar to the energy harvesting by hand force. Generally, the existing mechanical energy in the environment is always fluctuating and depends on its frequency, the source of mechanical energy.

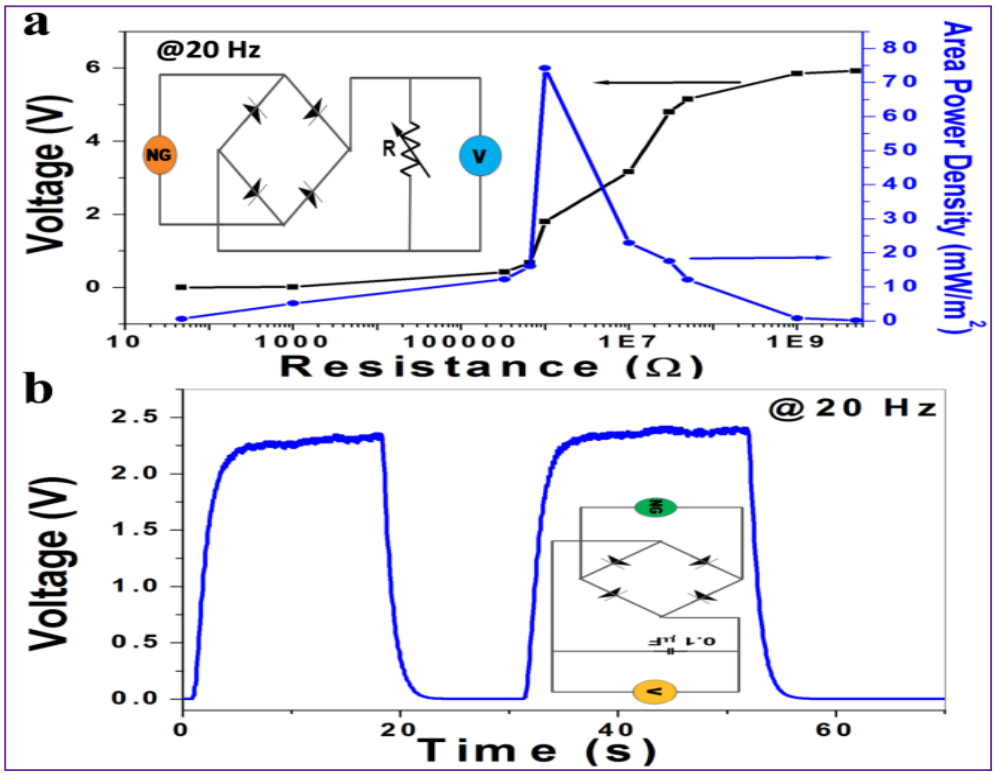

Figure 5.2.8 (a) WPNG (2.5 cm) device load matching analysis and its area power density at 20 Hz of mechanical load (11 N). **(b)** Charging analysis of the commercial capacitor (0.1 µF) storing voltage when it was connected parallel to the WPNG device (2.5 cm) through a full wave bridge rectifier (at 20 Hz frequency of 11 N).

Further, the electrical response of multi-unit energy harvester was analyzed i.e. integration of two WPNGs in series or parallel mode depending on the requirement [49]. The generated V_{OC} of the integrated devices in series mode could reach to 0.8 V and the I_{SC} of integrated devices in parallel mode can reach to ≈90 nA, as shown in **Figure 5.2.9(c, d)**. It clearly indicates that the generated V_{OC} and I_{SC} can be improved by integrating different WPNGs in various connection modes depending on the application [50]. These results indicate that the generation of electrical

energy depends on device dimensions, frequency dependent load, electrical poling, and the internal resistance of the worm suggesting the general suitability of wearable, portable energy harvesting devices for remote area applications.

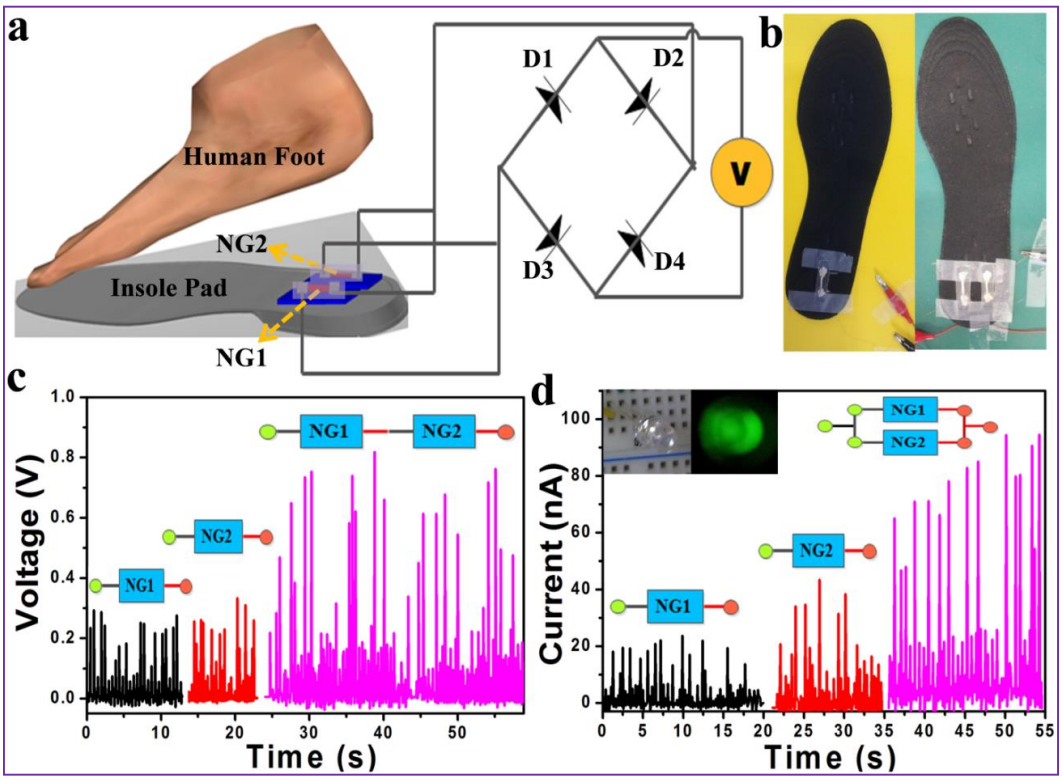

Figure 5.2.9 (a) Schematic diagram of a power-generating shoe insole based on flexible integrated WPNG devices and electrical output generated by human foot stress when connected to a full wave bridge rectifier **(b)** Digital photographs indicate a single WPNG and two WPNGs placed on the insole of a shoe **(c)** The V_{OC} of individual WPNGs (NG1, NG2) and integrated output based on low frequency human foot motion. **(d)** The I_{SC} of individual WPNGs and integrated output based on low frequency human foot motion. The inset shows a green LED turning OFF/ON during periodic human stress on the WPNGs.

Conclusions

In summary, a portable, efficient, and laterally aligned piezoelectric worm-based nanogenerator was reported to harvest the low frequency mechanical energy (human foot motions). The IG fabrication protocol for the 3D gel network of the BTO NPs/Ca-alg composite

worm was relatively simple, non-toxic, eco-friendly, and amenable to do large-scale fabrication. The feasible approach provides a cost-effective method to use the biopolymer template microstructures in the field of piezoelectric energy harvesting, as compared with high-cost, and time-consuming conventional films prepared by CVD, or PVD techniques and single wires (or rods) prepared by vapor transport, or hydrothermal methods. Commercial LEDs and a monochrome LCD could be powered by aligned WPNGs. The WPNG output voltage increased by up to 1.5 times, when the length of the worm increased from 1.5 to 3.5 cm, respectively. Similarly, the output voltages increased about five-fold for a worm length of 2.5 cm (diameter = 550 μm) when the cyclic frequency of the mechanical load changed from 3 to 20 Hz. The proposed flexible WPNG energy conversion efficiency was high, and comparable to that of previously published reports, suggesting the suitability of IG method and its biopolymer template structures for energy harvesting applications. This WPNG is powerful enough to act as an energy harvesting unit for power sources, portable and wearable self-powered systems.

References

[1] Kim SJ, We JH, Cho BJ. **Energy Environ. Sci** 2014;**7:**1959-1965.

[2] Li S, Pei J, Liu D, Bao L, Li JF, Wu H, Li L. Energy 2016;113:35-43.

[3] Liang Q, Yan X, Liao X, Cao S, Zheng X, Si H, Lu S, Zhang Y. NanoEnergy 2015; 16:329-338.

[4] Wang ZL, Chen J, Lin L. Energy Environ. Sci 2015;8:2250-2282.

[5] Arunkumar C, Nagamalleswara Rao A, Saravanakumar B, Sophia S, Kim SJ. *ACS Appl. Mater. Interfaces* 2016;8(15):9692–9699.

[6] Nguyen V, Yang R. NanoEnergy 2013;2:604–608.

[7] Zhu G, Yang R, Wang S, Wang ZL Nano Lett 2010;10:3151–3155.

[8] Wang ZL, Song J. Science 2006;312:242-246.

[9] Yang Y, Zhou Y, Wu JM, Wang ZL. ACS Nano 2012;6:8456-8461.

[10] Saravanakumar B, Thiyagarajan K, Nagamalleswara Rao A, SoYoon S, Kim T, Lin ZH, Kim SJ. Carbon 2015;84:56-65.

[11] Saravanakumar B, Kim SJ. J. Phys. Chem. C 2014;118:8831-8836.

[12] Wu JM, Xu C, Zhang Y, Wang ZL. ACS Nano 2012;6:4335-4340.

[13] Pi Z, Zhang J, Wen C, Zhang Z, Wu D. Nano Energy 2014;7:33–41.

[14] Kim T, Lee KY, Hwang SK, Park C, Kim SW, Cho J. Adv. Funct. Mater 2014;24:6262–6269.

[15] Ni X, Fei W, Anan L, Qi X, Zhi Y, Yong Q. Sci Adv Mater 2013;5:1-7.

[16] Kim Y, Kook K, Hwang SK, Park C, Cho J. ACS Nano 2014;8:2419–2430.

[17] Nagamalleswara Rao A, Saravanakumar B, Kim SJ. ACS Appl. Mater. Interfaces 2015;7:9831-9840.

[18] Xue X, Nie Y, He B, Xing L, Zhang Y, Wang ZL. Nanotechnology 2013;24:225501-225506.

[19] Saravanakumar B, Soyoon S, Kim SJ. *ACS Appl. Mater. Interfaces*. 2014;6:13716–13723.

[20] Nagamalleswara Rao A, Sophia S, Arunkumar C, Saravanakumar B, Jeong JH, Kim SJ. Sens. Actuator B-Chem 2016;237:534–544.

[21] Sophia S, Nagamalleswara Rao A, Arunkumar C, Kim SJ. Sens. Actuator B-Chem 2016;234:395–403.

[22] Pistoia G. Batteries for portable devices,2005,Elsevier,ISBN: 978-0-444-51672-5.

[23] Viet NV, Xie XD, Liew KM, Banthia N, Wang Q. Energy 2016;112:1219-1226.

[24] Wu N, Wang Q, Xie X. Smart Mater. Struct 2013;22:095023-095031.

[25] Ilyas MA, Swingler J. Energy 2015;90:796-806.

[26] Xie XD, Wang Q. Energy 2015;86:385-392.

[27] Azizi S, Ghodsi A, Jafari H, Ghazavi MR. Energy 2016;96:495-506.

[28] Chun J, Lee KY, Kang CY, Kim MW, Kim SW, Baik JM. Adv. Funct. Mater 2014;24:2038–2043.

[29] Chun J, Kang NR, Kim JY, Noh MS, Kang CY, Choid D, Kim SW, Wang ZL, Baik JM. NanoEnergy 2015;11:1–10.

[30] Park KI, Son JH, Hwang GT, Jeong CK, Ryu J, Koo M, Choi I, Lee SH, Byun M, Wang ZL, Lee KJ. Adv. Mater 2014;26:2514–2520.

[31] Xue QT, Wang Z, Tian H, Huan Y, Xie QY, Yang Y, Xie D, Li C, Shu Y, Wang XH, Ren TL. AIP Adv 2015;5:017102-017108.

[32] Panda P K. J. Mater. Sci 2009;44:5049-5062.

[33] Hong CH, Kim HP, Choi BY, Han HS, Son JS, Ahn CW, Jo W. J. Materiomics 2016;2:1-24.

[34] Shrout TR, Zhang SJ. J. Electroceram 2007;19:113-126.

[35] Park KI, Lee M, Liu Y, Moon S, Hwang GT, Zhu G, Kim JE, Kim SO, Kim DK, Wang ZL, Lee KJ. Adv. Mater 2012;24:2999-3004.

[36] Fan Z, Lu JG. Nanosci. Nanotechnol 2005;5:1561-1573.

[37] Menzel A, Subannajui K, Bakhda R, Wang Y, Thomann R, Zacharias M. J. Phys. Chem. Lett 2012;3:2815-2821.

[38] Shin DM, Tsege EL, Kang SH, Seung W, Kim SW, Kim HK, Hong SW, Hwang YH. NanoEnergy 2015;12:268–277.

[39] Buscaglia MT, Bassoli M, Buscaglia V, Vormberg R. J. Am. Ceram. Soc 2008;91:2862-2869.

[40] Hajiali H, Heredia-Guerrero JA, Liakos I, Athanassiou A, Mele E. Biomacromolecules 2015;16:936-943.

[41] Algothmi WM, Bandaru NM, Yu Y, Shapter JG, Ellis AV. J. Colloid Interface Sci 2013;397:32-38.

[42] Chen CY, Ke CJ, Yen KC, Hsieh HC, Sun JS, Lin FH. Theranostics 2015;5:643-655.

[43] Luo Y, Lode A, Wu C, Chang J, Gelinsky M. ACS Appl. Mater. Interfaces 2015;7:6541-6549.

[44] Gao T, Liao J, Wang J, Qiu Y, Yang Q, Zhang M, Zhao Y, Qin L, Xue H, Xiong Z, Chen L, Wang QM. J. Mater.Chem. A 2015;3:9965-9971.

[45] Al-Sayed AB, Moustafa YM, Motawea EA, Yehia MM, Khalil Mostafa MH. J. Environ. Chem. Eng 2015;3:1486-1496.

[46] Hosseini SM, Hosseini H, Mohammadifar MA, German JB, Mortazavian AM, Mohammadi A, Darani KK, Aliabadi SS, Khaksar R. Carbohydr. Polym 2014;103:573-580.

[47] Chen X, Xu S, Yao N, Shi Y. Nano Lett 2010;10:2133–2137.

[48] Wu W, Bai S, Yuan M, Qin Y, Wang ZL, Jing T. ACS Nano 2012;6:6231-6235.

[49] Shin SH, Kim YH, Lee MH, Jung JY, Nah J. ACS Nano 2014;8:2766-2773.

[50] Lin ZH, Yang Y, Wu JM, Liu Ying, Zhang F, Wang ZL, J. Phys. Chem. Lett 2012;3:3599-3604.

[51] Wu W, Cheng L, Bai S, Dou W, Xu Qi, Wei Z, Qin Y. J. Mater. Chem. A 2013;1:7332-7338.

[52] Lee M, Chen CY, Wang S, Cha SN, Park YJ, Kim JM, Chou LJ, Wang ZL. Adv. Mater 2012;24:1759-1764.

[53] Hou TC, Yang Y, Lin ZH, Ding Y, Park C, Pradel KC, Chen LJ, Wang ZL. NanoEnergy 2013;2:387-393.

[54] Liu ZH, Pan CT, Lin LW, Huang JC, Ou ZY. Smart Mater. Struct 2014;23:025003-025013.

[55] Park KI, Lee M, Liu Y, Moon S, Hwang GT, Zhu G, Kim JE, Kim SO, Kim DK, Wang ZL, Lee KJ. Adv. Mater 2012;24:2999-3004.

[56] Park KI, Xu S, Liu Y, Hwang GT, Kang SJL, Wang ZL, Lee KJ. Nano Lett 2010;10:4939-4943.

5.3 Self-powered pH Sensor using the Wave-Pattern Hybrid Worm Structure based PNG and Linear Worm Structure pH Sensor

5.3.1 Introduction

Alternative energy harvesting technologies like piezoelectric [1, 2], triboelectric [3], photovoltaic [4] and thermoelectric [5] devices can act as an independent power source using the environmental energies such as water motion [3, 6], human body movements [3], sun-light [2, 4], and air/wind flow [3, 7]. The output energy from these technologies is electrical energy, even though these are operated by various types of input energies such as sound, mechanical, wind, thermal and chemical energies. This electrical energy can be useful for broad range of applications from life-saving medical devices [7-12] to portable devices [13-19]. On the contrary, other energies such as sound, thermal, chemical, mechanical and wind energies are useful energies, but these have inherent limitations for broad range applications. Meanwhile, the alternative piezoelectric harvesting technology generates electric power from $\mu W/m^2$ to W/m^2 by utilizing the sound, mechanical, wind and nuclear energies as an input energy source [20]. Moreover, the piezoelectric harvester with different micro/nanostructure materials has several merits such as low leakage current, biocompatible, highly stable from the interferences like temperature, pressure and humidity. But it has two ample drawbacks: one it suffers the development of highly efficient nano/micro structures by alone brittle piezoelectric ceramics with small scale production, high cost and time-consuming techniques like sol-gel, hydrothermal, physical vapor deposition (PVD) and chemical vapor deposition (CVD) techniques. Second, the fabrication of energy harvester and its performance was restricted by smaller dimension of single nanowire/belt [6-9]. It directs to find alternative method [10, 11] for innovative structures with

high energy conversion, sustainable at large input mechanical force and mass production with low cost.

However, the tuning of piezoelectric coefficient in nanomaterial is the key factor for achieving high energy conversion efficiency. This is possible in many ways such as the crystallographic orientation of lattice helps to increase an anisotropic properties of polycrystalline materials, creating internal stresses, doping foreign atoms into parent lattice and lowering dielectric constant of material respectively [2, 8-10, 20, 22]. Recent reports explore the reliable, large-scale nano/micro structures provides a low cost, high energy efficient conversion with compact working area and wearable property by the combination of piezoelectric nanoparticles (ZnO, $BaTiO_3$, PZT) along with the template polymers. This is due to the transfer of large mechanical force on active piezoelectric material *via* polymer matrix to tune the maximum piezoelectricity and provides the greater flexibility. Here, the selection of polymer matrix is a crucial factor to achieve the dual-functionality like energy harvesting and pH dependence with the same micro/nanostructure. Monitoring the pH value is a critical issue in many applications such as in-vivo biomedical, food monitoring, clinical and lubricant fields depend on pH variation processes [27]. Up to now TiO_2 [28], RuO_2 [29], SnO_2 [30], V_2O_5 [31] and ZnO [32, 33] metal oxides and surface plasmon resonance (SPR) based fiber optic sensors [34] were used for pH sensing/monitoring.

In order to overcome the above limitations, we developed the dual functional behavior of piezoelectric composite worm structures such as energy harvesting and sensing using ionotropic gelation (IG) approach [21]. The energy harvesting realized by innovative laterally aligned composite linear worm (CLW) and wavy pattern worms (CWPW) with multiple lengths consists of highly crystalline $BaTiO_3$ nanopartilces (BTO NPs) along with the 3D gel network of Ca-

alginate (Ca-alg). The proposed single CWPW device has greater peak-peak $V_{OC} \approx 21.12$ V and $I_{SC} \approx 2.53$ μA (L = 1.95 cm, D = 0.055 cm) as compared to the single nanowire/micro belts. This is due to the crystallographic orientation of BTO lattice, lowering dielectric constant, internal stress of TiO_6 octahedron in BTO lattice and may be due to the acceptance of large mechanical force. This technique will solve the brittle nature and cracking of piezoelectric materials under the large mechanical force, mass production of worms with low cost and easy to fabricate multiple lengths based devices for greater energy conversion, flexibility. Next, we demonstrated the CLW as pH sensor under solutions with different pH values (alkaline value: 12-8) and self powered concept was realized by considering the CWPW device as power source unit. The pH solution dependent conductivity of CLW by metal (M)-semiconductor (S)-metal (M) interface is well matched with the electrical response of self-powered pH sensor. The proposed technique can pave way for developing the dual functional composites, which are more suitable in the fields of theranostics, vibration and portable devices with low cost, eco-friendly with high performances.

5.3.2 Experimental method

5.3.2.1 Synthesis of $BaTiO_3$ nanoparticles

Highly crystalline BTO NPs were synthesized by high temperature solid state reaction method. The precursors $BaCO_3$ (99.95%, High purity chemicals-CAS No: 052880) and TiO_2 (98%, Daejung-CAS No: 1317-70-0) were subjected to taken as starting raw materials with proper atomic ratio of $BaTiO_3$. The weighted raw materials were mixed homogeneously by hand grinding through mortar and pestle using acetone medium. Next, the mixed powder was placed in commercially available Al_2O_3 boat. Then the heat treatment was followed with a heating rate 2.5 °C/min until it reaches to 1200 °C, and maintained, soaked around two hours in open tube

furnace. After that, the furnace has been cooled down to room temperature naturally and the desired high crystalline BTO NPs has been collected.

5.3.2.2 Fabrication of nonlinear, handy CWPW and CLW structures

The fabrication of transparent Ca-alg and non transparent BTO NPs/Ca-alg worm structures using IG approach involved three processing steps (**Figure 5.3.1**). First step, to prepare the homogeneous aqueous Na-alg (2 Wt %, Sigma-Aldrich, CAS No: 9005-38-3) solution under constant stirring at temperature 50 °C for two hours. Similarly, the homogeneous Na-alg/BTO NPs composite solution (2 wt %/ 1 wt %) were prepared without any agglomeration of BTO NPs under constant stirring at 70 °C for two hours. Second step, involved exchange of sodium ions (Na^+) by calcium ions (Ca^{2+}) i.e. ionic gelation of BTO NPs/Ca-alg nonlinear worms can be obtained by squeezing the homogeneous solution of BTO NPs/Na-alg through a pipette dropper having 5 ml amounts of solution into 1 M calcium chloride (Daejung-CAS No: 10043-52-4). After 30 minutes of gelation the non-linear composite worms were removed from $CaCl_2$ solution and soaked in deionized water for 15 minutes to remove the excess Ca-ions and then dried for 24 hr at room temperature. Third step, involved free handy drawing of BTO NPs/Ca-alg composite wavy pattern worm (CWPW) structures with tailored lengths having multiple crests were as shown in **Figure 5.3.1(a, c)**. Similar approach, has been followed to fabricate the handy pure wavy pattern worm (only alginate) by pipette dropper, but it was not achieved may be due to the difference in viscosity and surface tension of Na-alg solution as compared to the composite solution (BTO NPs/Na-alg). The composite solutions are more suitable to fabricate flexible, reliable CWPW structures for energy harvesting. Similar approach has been followed to fabricate the linear and non-linear worm structures using pure and composite solutions.

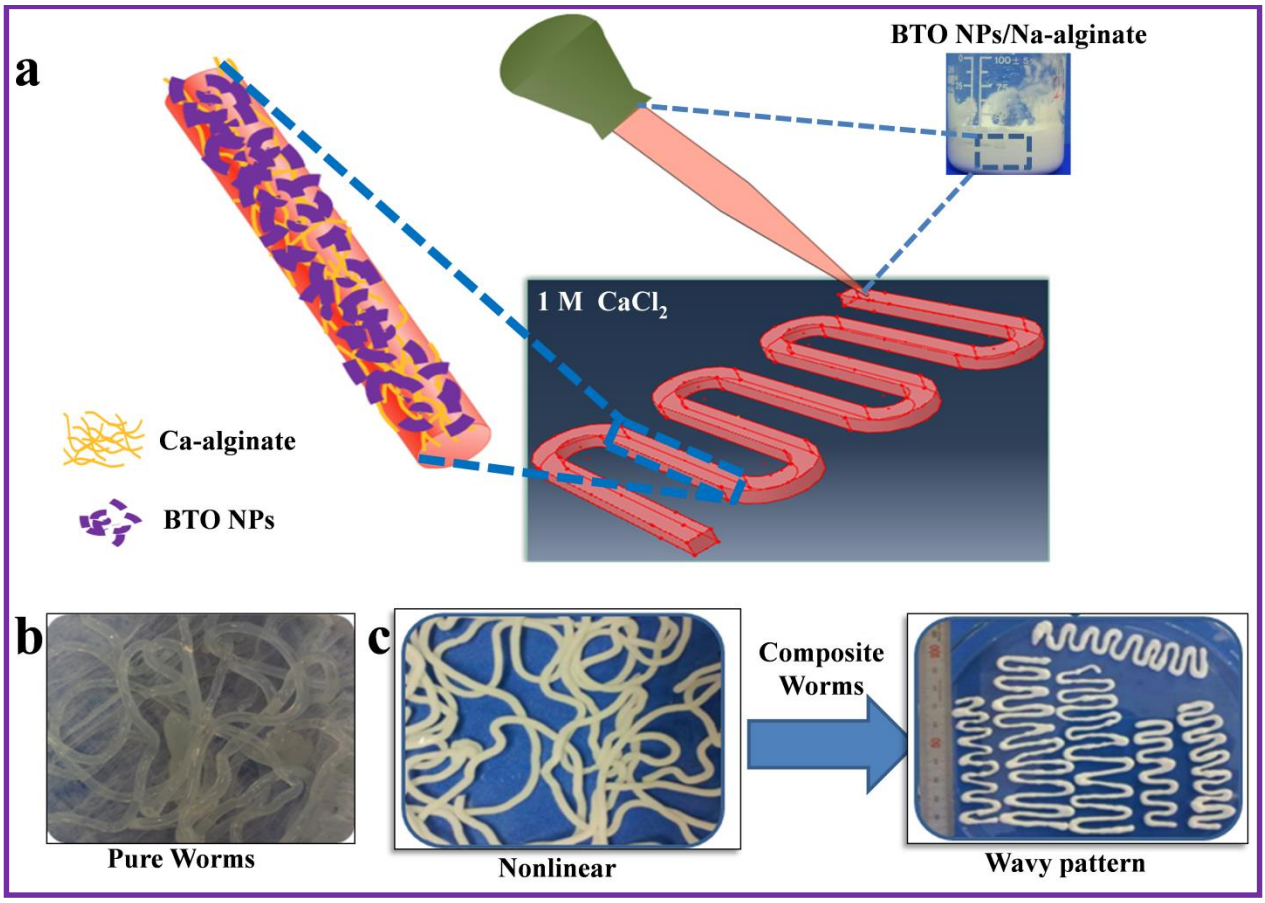

Figure 5.3.1(a) Fabrication protocol for pure and composite worms using IG method. Magnified right and left parts showed the BTO NPs/Na-alginate solution and linear worm portion. **(b)** Optical image of pure Ca-alginate worms (**c**) Optical image of composite worms (BTO NPs/Ca-alginate) i.e. nonlinear to wavy pattern by free hand drawn with multiple dimensions.

5.3.2.3 Fabrication of flexible, laterally aligned CWPW piezoelectric nanogenerators

CWPW structures were taken according to the required dimensions such as L≈0.85 cm, W≈1.5 cm for fabricating the flexible CWPW devices as shown in **Figure 5.3.2a**. The CWPW structure was placed on two Al foil based electrodes were attached on the flexible polyethylene terephthalate (PET) and separated with finite distance and schematically shown in **Figure 5.3.2b**. The silver paste was used to attach the CWPW pattern on aluminum (Al) foils and copper (Cu) wires used for external connections to measure the electrical output. The silver paste can be useful in two ways, one is to attach the wavy pattern on Al foil and other is to acquire the charge

accumulation on each crest of composite wavy pattern. Finally, the polydimethylsiloxane (PDMS) matrix was used as a packaging layer for CWPW device to protect from the physical damage and the interaction with surrounding environments like temperature, humidity. Lastly, the fabricated devices have been electrically poled at 3 kV for 24 hr at room temperature for the activation and alignment of electric dipoles in worms.

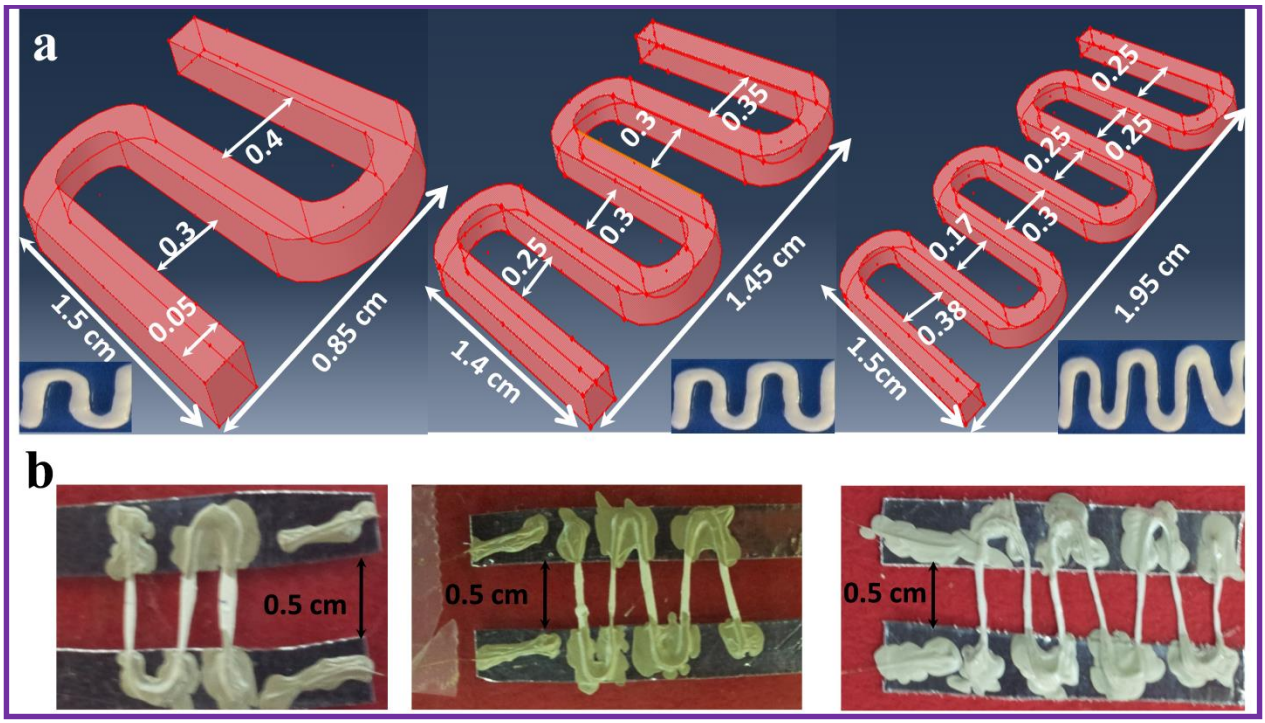

Figure 5.3.2 (a) Schematic illustrations of handy drawn CWPW structures with tailored lengths by increasing number of crests of wave. The inset shows optical images of CWPWs without dry condition. **(b)** Optical images of as-fabricated CWPW devices for harvesting low frequency biomechanical energy.

5.3.2.4 Fabrication of CLW pH sensor

Composite linear worm (CLW) pH sensor was fabricated with the help of as-prepared composite linear worm having dimensions (L= 2 cm, D = 0.055 cm) by IG method. The single linear worm positioned on flexible PET substrate and both ends of the worm were attached using silver paste. The external connections for linear worm pH sensor were taken by Cu-wires for

electrical characterization. A fine epoxy resin layer was covered on both electrodes to avoid the unwanted interactions between pH buffer solutions and electrodes, which provide electrical isolation. The realization of self-powered pH sensor accomplished by the parallel connection between the CWPW energy harvester and CLW pH sensor, and the measurements were carried out under different pH solutions from 12 to 8.

5.3.3 Results and discussion

5.3.3.1 Structural and surface morphology

The CLW and CWPW were fabricated using IG method [35] consists of piezoelectric BTO NPs and 3D gel network of Ca-alg polymer. The complete fabrication protocol was given in experimental section and as-prepared composite solutions were shown in **Figure 5.3.1a**. Before the fabrication of composite worm structure, a highly crystalline BTO NPs having tetragonal crystal structure was synthesized by high-temperature solid-state reaction [36]. **Figure 5.3.1a** represents schematic diagram of CWPW structure and magnified left portion indicates the linear worm part represents the physisorption between BTO NPs (≥ 100 nm) and Ca-alg matrix. The composite formation using egg-box model was systematically discussed in chapters 5.1 and 5.2. Initially, we fabricated the transparent Ca-alg and non-transparent composite (BTO NPs/Ca-alg) worm structures (non-linear) and its digital photographs were given in **Figure 5.3.1(b, c).** Later, we designed CWPW by free hand drawn in controlled dimensions (length and width wise) using BTO NPs/Na-alg composite solution. The solution has been seized into the pipette dropper (5 ml) and the patterns were drawn in to glass petridish. Next, the drawn pattern was completely covered with 1 M $CaCl_2$ aqueous solution to undergo an ionic gelation in the form of required wavy patterned 3D gel network (**Figure 5.3.1c**). Finally, the obtained pattern was washed in DI

water and dried at room temperature for 24 hrs to form a desired flexible, solid CWPW structure. The structural bonding vibrations (symmetric, asymmetric) and piezoelectric phase of BTO NPs for composite structures [9] using an FT-IR and XRD techniques was discussed in Chapter 5.1 and 5.2.

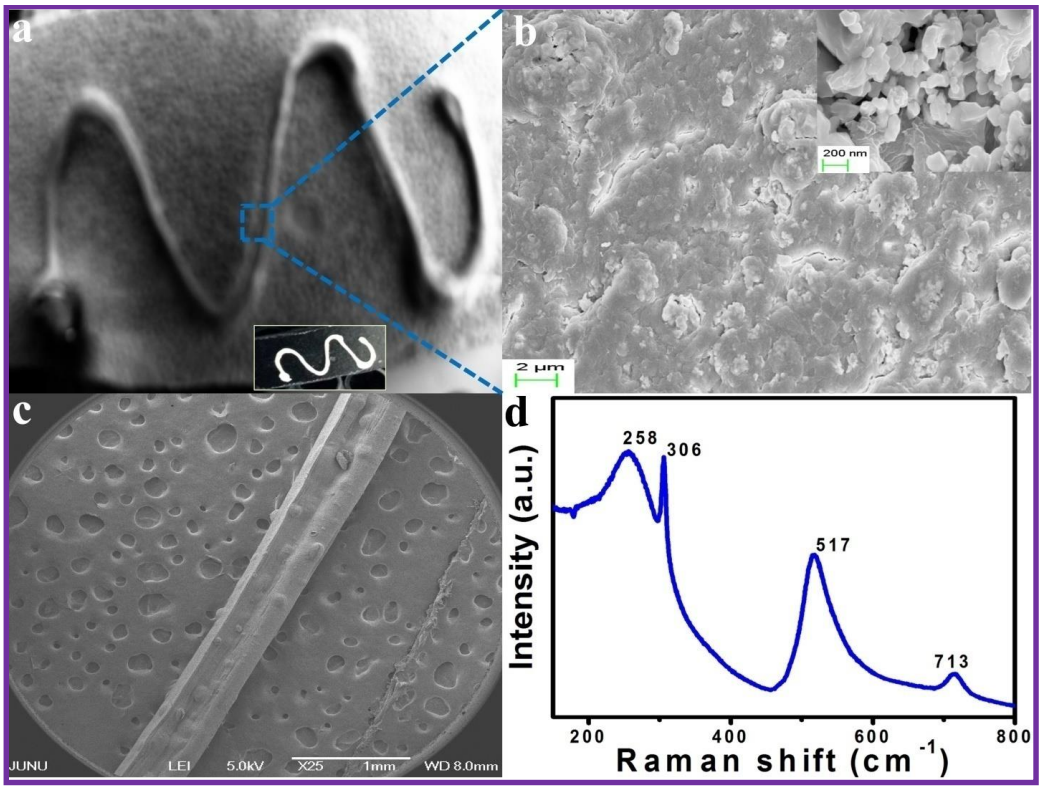

Figure 5.3.3 (a) A FE-SEM image of CWPW (1 mm scale). **(b)** Magnified portion represents the rough surface at 2 µm and 200 nm scales. **(c)** A FE-SEM image of CLW (1 mm scale). **(d)** Raman active modes of pure BTO NPs confirms tetragonal phase.

The FE-SEM image of as-fabricated CWPW structure with multiple numbers of crests (troughs) at 1 mm scale, and the digital photograph (inset) is shown in **Figure 5.3.3a.** The magnified image shows rough surface morphology on CWPW structure confirms the good distribution of BTO NPs along with Ca-alg chains at 2 µm, 200 nm scales as shown in **Figure 5.3.3b**. The crest to crest separation of the CWPW structure is about ≈ 1 cm and the length of worm is ≈ 1.6 cm. The thickness of composite worm is around 0.055 cm throughout the length

and amplitude of CWPW is on the order of 0.35 cm to few centimeters. Similarly, **Figure 5.3.3c** shows an FE-SEM image of CLW structure at mm scale. Before that, the randomly oriented crystalline nature of BTO NPs at 100 nm scale as shown in **Figure 5.1.6** and its Raman active modes were given in **Figure 5.3.3d**. The two major characteristic peaks appear at 306 cm^{-1}, 512 cm^{-1} confirms the tetragonal phase of BTO NPs and well matched with the XRD pattern data [9].

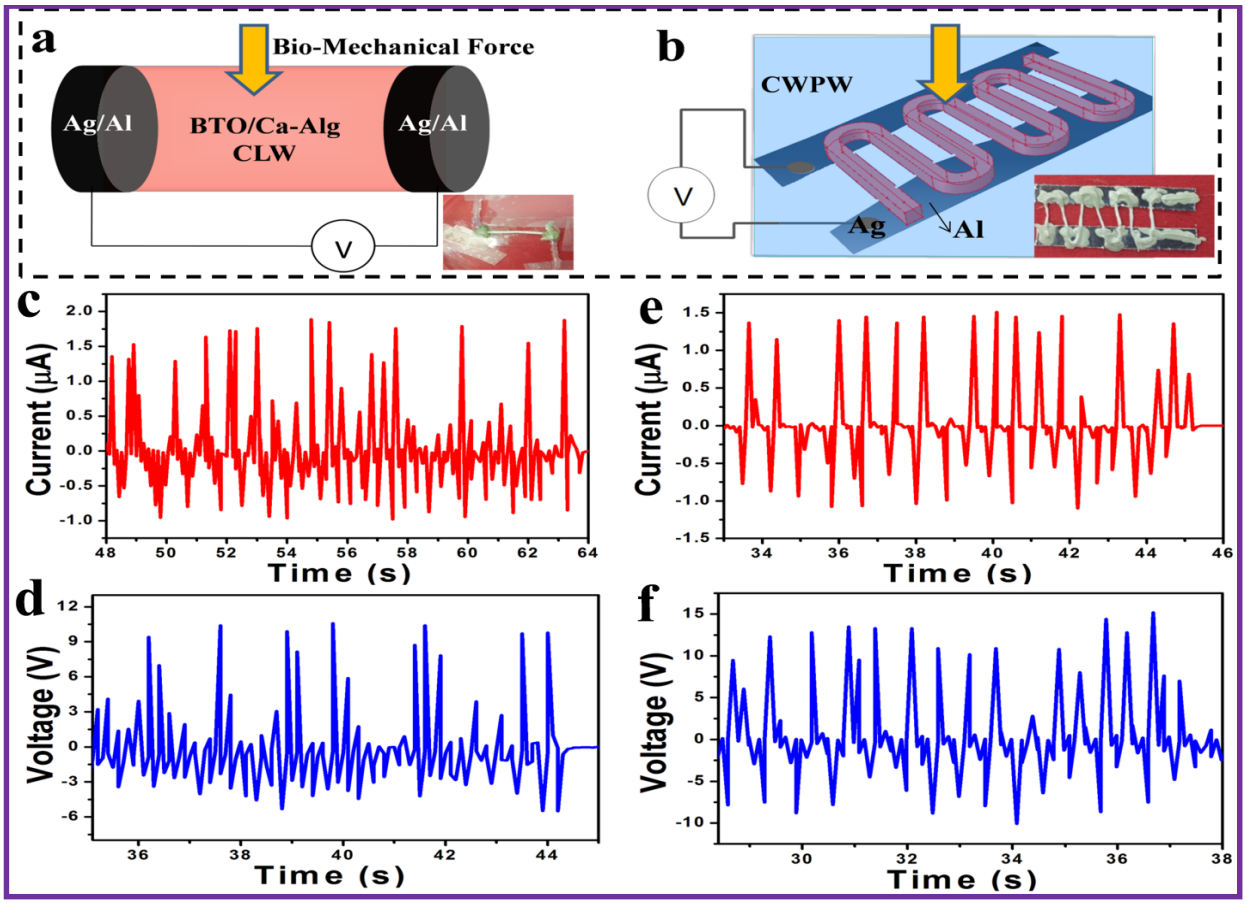

Figure 5.3.4(a, b) Schematic diagrams of laterally aligned CLW and CWPW devices and inset shows the optical images of as-fabricated devices. (c, d) CLW device outputs when a non-uniform hand force acting on devices. (e, f) CWPW device outputs when a non-uniform hand force acting on devices.

5.3.3.2 Energy harvesting and working mechanism

The recent developments in sensor technology have brought up with the novelties in independently powering systems [1-3, 5, 9, 32, 37]. For that, we developed a novel free hand

drawn CWPW and CLW based energy harvesters for converting tiny bio-mechanical energy into electrical power was schematically shown in **Figure 5.3. 4(a, b)**. Inset figures represent the digital photographs of as fabricated energy harvesting devices. Initially, the electrical response of CLW device (L = 3.5 cm, D = 0.055 cm) was obtained by hand force such as peak to peak V_{OC} = 15.21 V and I_{SC} = 2.56 μA as shown **Figure5.3. 4(c, d)**.

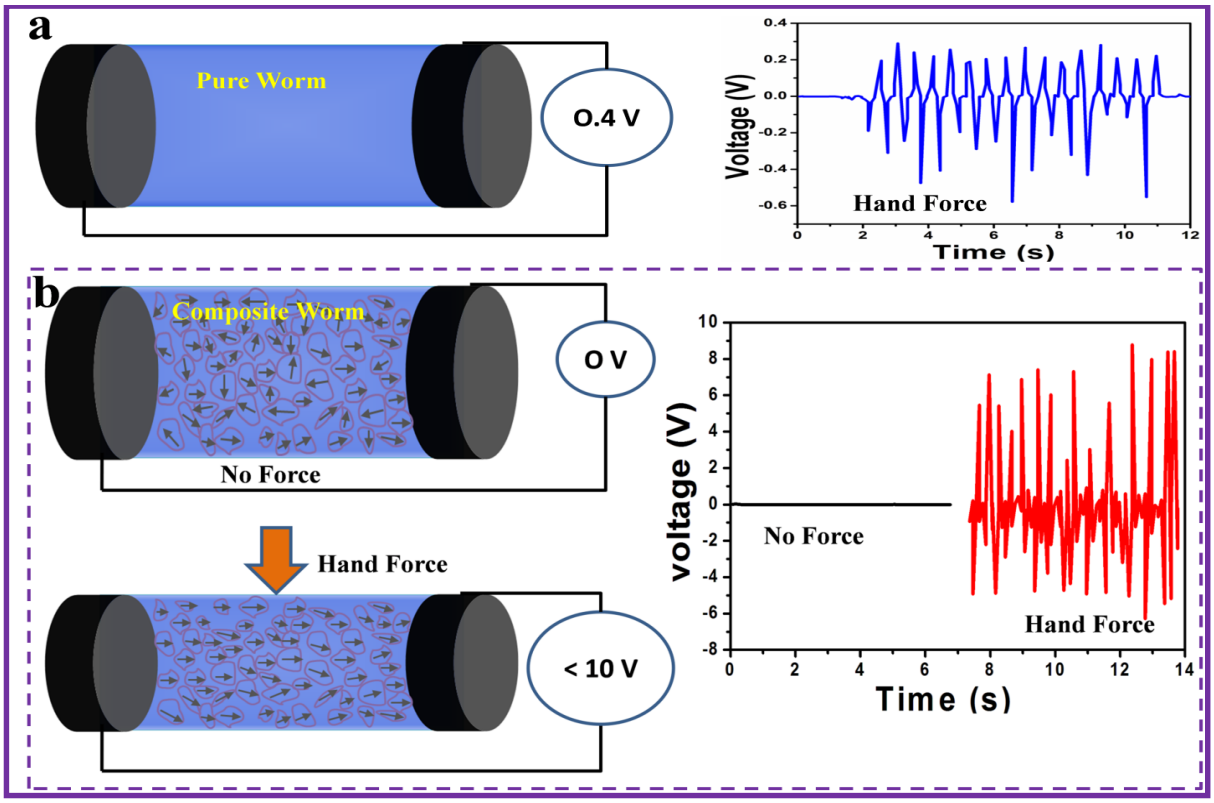

Figure 5.3.5 (a) Schematic diagram of pure worm based device (L= 2.5 cm, D = 0.055 cm) and its output voltage as a function of hand force. **(b)** Schematic illustrations of composite worm based device (L= 2.5 cm, D = 0.055 cm) without and with hand and its corresponding output voltages.

In order to understand the role of Ca-alg for energy harvesting, we fabricated and analyzed the worm based devices with and without BTO NPs having similar dimensions. We found that the pure worms have negligible output as compared to composite worm (**Figure 5.3. 5**) shows Ca-alg dependency for harvesting is very less. Next, we observed the electrical response of

CWPW device (achieved peak to peak V_{OC} = 21.12 V and I_{SC} = 2.53 μA) with 1.95 cm length and 0.055 cm diameter having three crests and troughs respectively. The CWPW device (L = 1.95 cm) exhibits good electrical output variation and better response as compared to the CLW device (L = 3.5 cm) as shown in **Figure 5.3. 4(e, f)**. Here, the working mechanism attributes longitudinal mode with alternating hand force transferred to the device *via* PDMS packaging layer and resulted in charge generation along the composite worm could collect through adjacent Al/Ag electrodes. Here, the charge generation is mainly due to the d_{33} mode (i.e L_{piezo}>t_{piezo}) and its corresponding open circuit voltage (V_{OC}) can be computed as: [38, 39]

$$V_{OC} = \int g_{33}\, \varepsilon(l) E_{CW} dl \tag{1}$$

Where the piezoelectric voltage constant is $g_{33} = \frac{d_{33}}{\varepsilon_r \varepsilon_0}$ (in terms of Vm/N), d_{33}, E_{CW}, ε_r are piezoelectric coupling coefficient, elastic (young's) modulus, relative permittivity of the active piezoelectric material (for bulk BTO film d_{33} = 100 pC/N to 190 pC/N, $E_{CW} \leq$ 100 GPa, ε_r = 1700 at room temperature) [40-42], ε_0 is permittivity of free space (8.8541×10^{-12} F/m), and $\varepsilon(l)$ is strain along the worm. Meanwhile, the stress function $\sigma(l)$ of composite worm along the longitudinal direction in terms of young's modulus and poisons ratio ($\vartheta = 0.35$) can be approximated as [38, 39]:

$$\sigma(l) = \frac{F}{A} = E_{CW}\left(\frac{\sigma_{xx}}{E_{11}} - \frac{\sigma_{yy}}{E_{11}}.\vartheta - \frac{\sigma_{zz}}{E_{11}}.\vartheta\right) = E_{CW}\, \varepsilon\,(l) \tag{2}$$

Where F is applied mechanical force on energy harvester (N), l and A are length and area of the active piezoelectric material, E_{11} is longitudinal modulus of composite, σ_{xx}, σ_{yy}, and σ_{zz} are stresses along three directions such as *x*, *y* and *z*. By solving equations 1 and 2, we can obtain a precise equation to calculate the maximum open circuit voltage (V_{max}): [39, 43]

$$V_{max} = F g_{33} \left(\frac{l}{A}\right) \quad (3)$$

Here, the piezoelectric voltage constant (g_{33}) is an unknown factor which depends on the intrinsic properties of material and its type of nanostructures (like thin film, nanorods and composites). For example, the evaluated piezoelectric voltage constant ($g_{33} = 0.002649$ mV/N) [44] for single composite linear worm (CLW) device using the open circuit voltage (15.21 V) obtained by experimentally with an applied mechanical force 10 N (Generally, the human hand force will fluctuate 10 N to 30 N depending on the hand movement) on device has dimensions $l = 0.035\, m$ and $A = 6.095 \times 10^{-5}\ m^2$ respectively. By considering the BTO thin film (d_{33} = 100 pC/N and ε_r = 1700) value for $g_{33} = 0.006643$ mV/N [40, 44, 45], the calculated piezoelectric potential reached around 40 % with a simple approach (cost-effective) based single composite linear worm structure nanogenerator ($l = 3.5\ cm$ and $D = 0.055\ cm$). We also tested the electrical response of CWPW device using the mechanical linear motor with different accelerations (0.1, 1 and 2.5 m/s^2) as shown in **Figure 5.3. 6(a, b)**. Stable electrical output has been observed using 0.1 m/s^2 acceleration of linear motor. When we apply high acceleration (1 and 2.5 m/s^2) of constant load (motor) on CWPW device, there is no significance increment in output voltage and similarly, the current peak pattern was totally unstable. It indicates that the optimum acceleration of load is around 0.1 m/s^2 to achieve maximum electrical response for CWPW device. In order to estimate the stability of CWPW device, we performed the stability test analysis at 0.1 m/s^2 of linear motor as an input force. The output voltage is stable up to 1200 seconds shows the good stability (**Figure 5.3. 6c**), suggest the suitability for real-time applications. Next, the load resistance analysis, power density calculations for CWPW device were carried out at 0.1 m/s^2 of linear motor. The output voltage increases gradually when increasing the external load resistance across

CWPW device as shown in **Figure 5.3.6d**. The obtained maximum power density across the load resistance 400 MΩ is ≈7.5 mW/m^2. Here, the strategy is mainly focused on length dependent nature (by increasing No. of crests of wave pattern) of CWPW structure-based energy harvester having constant thickness of worm (≈ 0.055 cm) with approximately fixed width of CWPW structure. The schematic diagrams of different CWPW structures with desired dimensions and its corresponding digital photographs of as-fabricated devices were shown in **Figure 5.3.2 (a, b)**. The BTO NPs weight ratio dependent electrical response of CWPW-1 devices has been observed by fabricating CWPW-1 structures with one crest and trough (L =0.85, W= 1.5 and t = 0.055 cm) and using the biomechanical hand force. Here, the Ca-alginate weight ratio (2 wt %) has been fixed and varies BTO NPs weight ratio such as 0.3, 0.6, 0.8, and 1 wt % respectively. The generated electrical response for CWPW-1 devices increases by increasing the weight ratio of BTO NPs as shown in **Figure 5.3.7(a, b)**. In present work, the optimized piezoelectric nanoparticles weight ratio up to 1 percentage, beyond this the fabrication of CWPW structures is quite typical due to the variation in viscosity and surface tension of composite solution for free hand drawing of CWPW structures. Changing the alginate weight ratio or adding extra surfactants to the composite solution (modification of surface tension) are the variable parameters to improve the piezoelectric nanoparticles weight ratio greater than 1 wt %. Initially, we fabricated and analyzed the electrical response of CWPW-1 device with one crest and trough of wave (L≈0.85 cm, W≈1.5 cm) as shown in **Figure 5.3.8(a, b)**. The inset shows digital photographs of as fabricated CWPWs in the form of 3D gel networks (without dry condition) with multiple dimensions. The CWPW-1 device generates peak-peak V_{OC} ≈ 2.59 V, I_{SC} ≈ 0.725 μA using periodic hand force. This is due to the generation of piezoelectric potential in wavy

worm structure drives the flow of external electrons produces an electrical output. We also observed the electrical response of CWPW-2 (1 wt % BTO NPs with two crest and troughs) and CWPW-3 (1 wt % BTO NPs with three crest and troughs) and compared with CWPW-1 electrical output

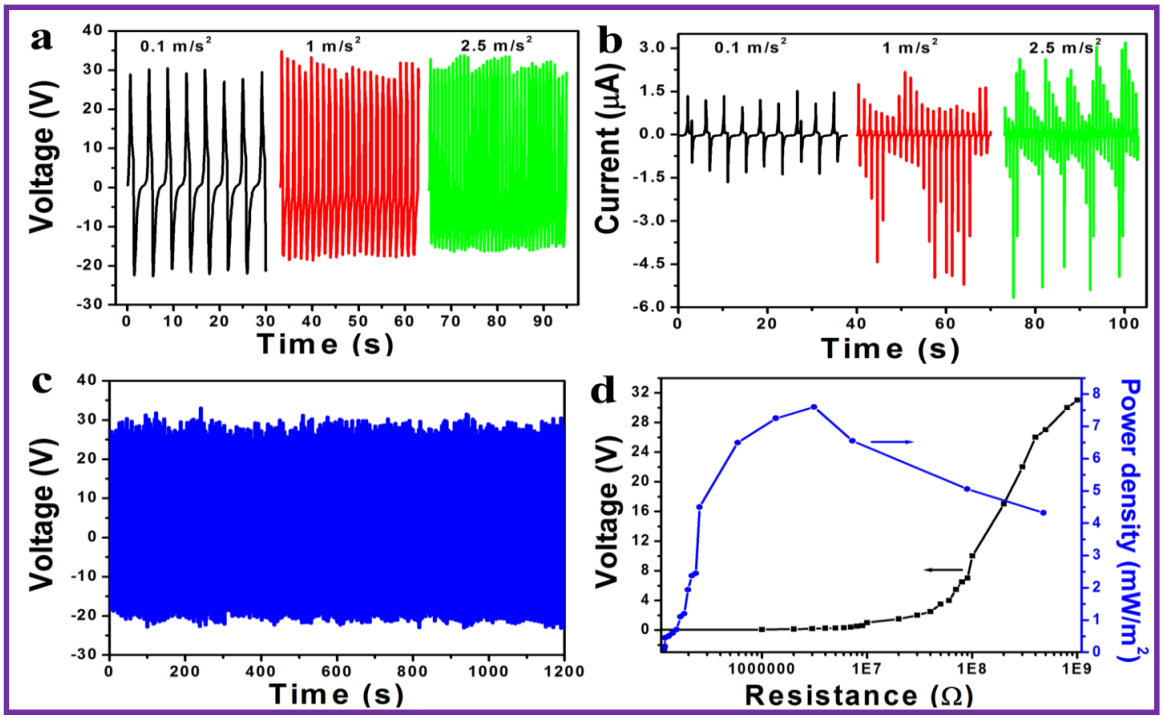

Figure 5.3.6 (a, b) Output voltage and current of CWPW device during various input accelerations (0.1, 1 and 2.5 m/s^2) of linear motor (load). **(c)** Stability test for CWPW device up to 1200 seconds when a constant input acceleration (0.1 m/s^2) of linear motor acting on device. (d) Load resistance analysis and power density evaluation for CWPW device using constant input acceleration (0.1 m/s^2) of linear motor.

Interestingly, we found the enhanced peak to peak $V_{OC} \approx 2.59$ V, $I_{SC} \approx 0.725$ μA for 0.85 cm lengthy wavy worm to $V_{OC} \approx 9.87$ V, $I_{SC} \approx 1.344$ μA for 1.4 cm length and maximized up to $V_{OC} \approx 21.12$ V, $I_{SC} \approx 2.53$ μA for 1.95 cm lengthy worm structure as shown in **Figure 5.3.8(a, b)**. This study proves that, the generated piezoelectric potential is length dependent nature of CWPW structures. The length dependent peak-peak voltage, current and power density was

graphically shown in **Figure 5.3.9 (a, b)**. The increased electrical output is not only on length but also may be due to lowering relative permittivity, tuning of piezoelectric coefficient (d_{33}) in positive direction and high elastic modulus. It may be aroused with supporting bio-polymer immobilized the BTO NPs and electrically aligned all the dipoles along the length of composite worm structure. Generally, pure bulk BTO NPs has higher relative permittivity will be decreased naturally whenever it processed with any polymer matrix consequently d_{33} may possible to increase.

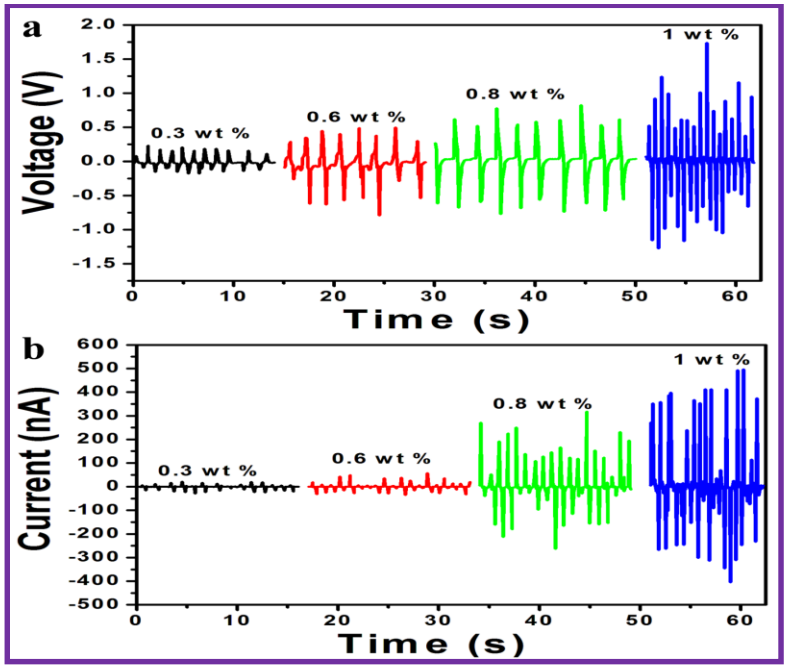

Figure 5.3.7(a, b) Open circuit voltage and short circuit current of CWPW devices when the biomechanical hand force acting on devices (CWPWs made by different weight ratios of BTO NPs).

In order to prove the piezoelectric potential generation of CWPW device experimentally we opted to drive the LED sign-lighting ("N" and "M" letters) connected with multiple green and blue LEDs in series manner upon taping the device with hand force as shown in **Figure 5.3.8c**. Additionally, the CWPW device output is used to charge the commercial capacitors (47 nF, 0.22 μF and 2.2 μF) at various input accelerations (0.1, 1 and 2.5 m/s^2) of linear motor as shown in

Figure 5.3.9(c, d). An optical photograph of the as-fabricated CLW and CWPW devices with equal length is shown in **Figure 5.3.10(a, b)**. The CWPW device shows higher output as compared to the CLW device output confirms that the non-linear part of the CWPW device has a considerable effect on device electrical response as shown in **Figure 5.3.10(c, d)**. It indicates that the crest part and distance between two crests will also effect on the device performance. All the above results confirm that efficient energy conversion (mechanical to electrical) depend on the selection of supporting polymer along with brittle piezoelectric nanoparticles, developed microstructures with electrode interfaces and device dimensions.

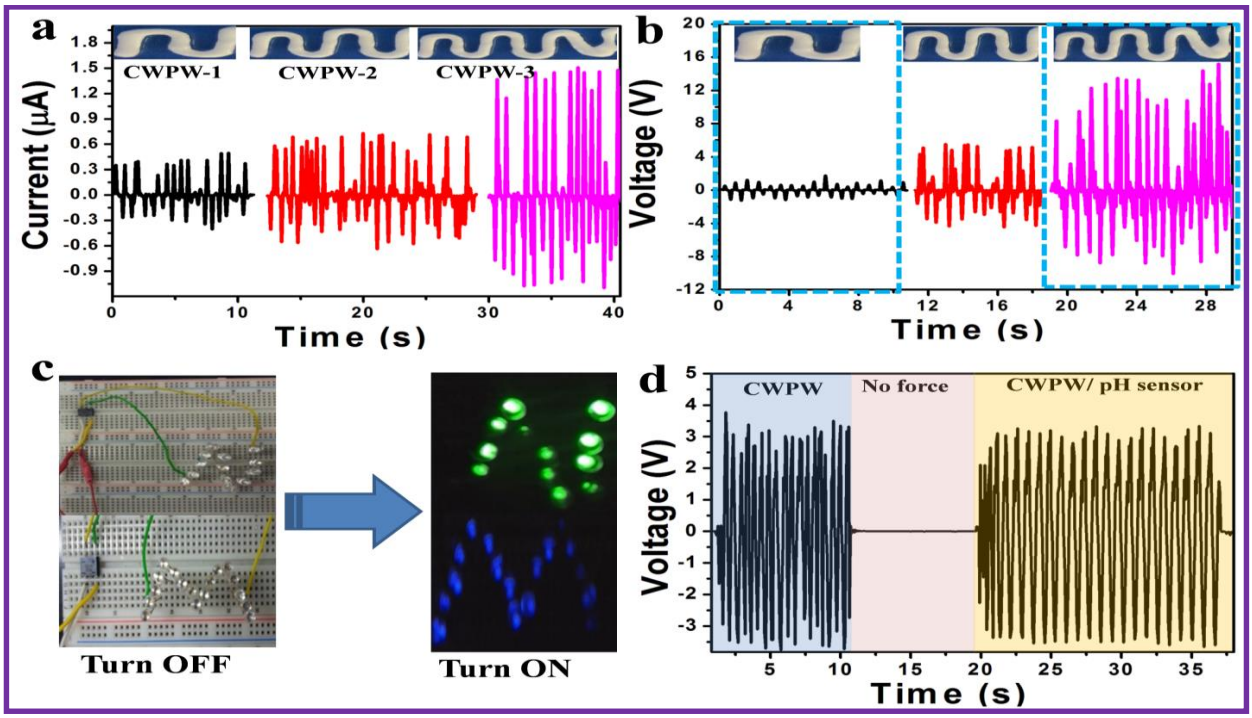

Figure 5.3.8(a, b) Length dependent electrical output of devices such as CWPW-1 (L = 0.85 cm) CWPW-2 (L = 1.4 cm) and CWPW-3 (L = 1.95 cm). The inset shows as synthesized CWPW patterns with multiple dimensions (without dry). **(c)** CWPW device output driving the LED sign letters "N" and "M" letters. **(d)** Three regions of V_{OC}: One is CWPW device output when an input mechanical forces 11 N at 14 Hz cyclic frequency. Second part represents the zero V_{OC} when no force condition and third part is CWPW device output driving CLW pH sensor (L = 2 cm, D = 0.055 cm) under no pH solution.

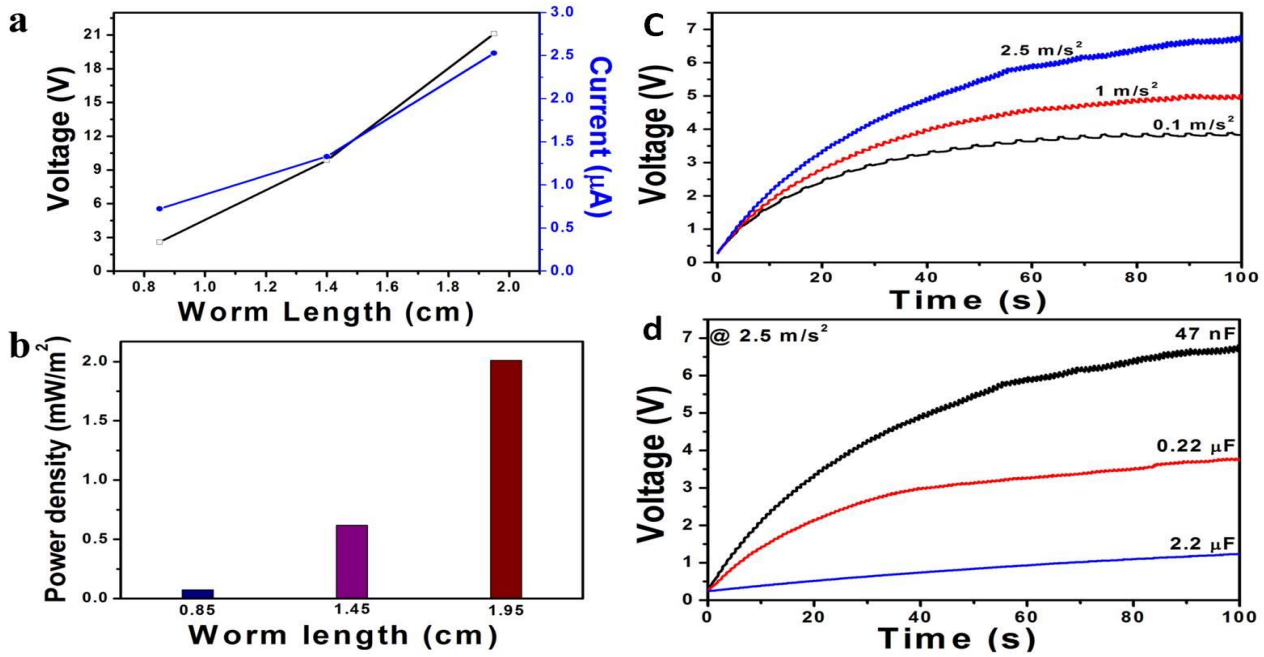

Figure 5.3.9 (a) Open circuit voltage and short circuit current of all CWPW devices *vs* CWPW length. **(b)** Output power of all CWPW devices when increasing the CWPW lengths such as 0.85, 1.4 and 1.95 cm. **(c)** The generated output voltage charging the commercial capacitor (47 nF) using full wave bridge rectifier at different accelerations of mechanical load (by linear motor). **(d)** The generated output voltage charging the various commercial capacitors using full wave bridge rectifier at constant acceleration of mechanical load.

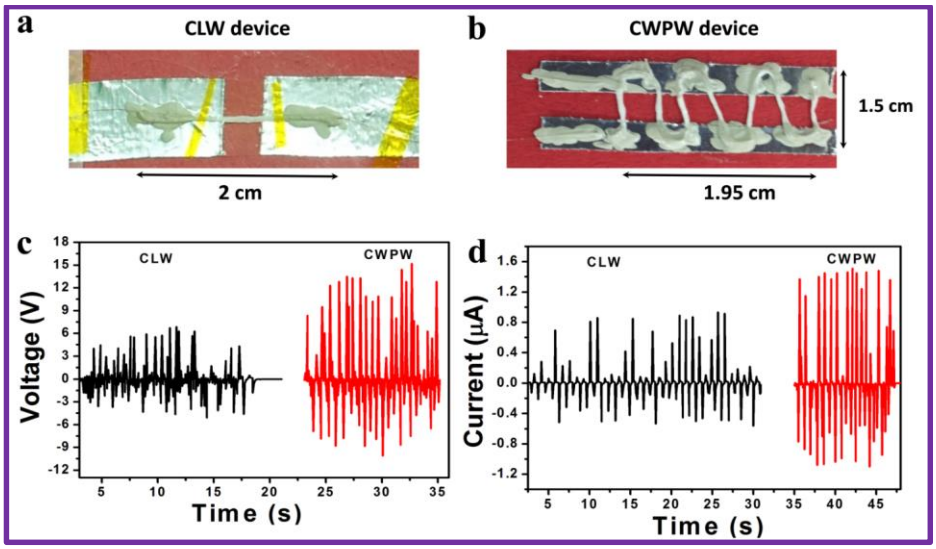

Figure 5.3.10(a, b) Optical photographs of as-fabricated CLW and CWPW devices having approximately equal length (L = 2cm) **(c, d)** Comparison of open circuit voltage and short circuit current for both devices, when the bio-mechanical force acting perpendicularly to the devices.

5.3.3.3 Self-powered CLW pH Sensor

To explore the potentiality and dual functionality of composite worm structures we demonstrated the CWPW device (L = 1.95 cm, D = 0.055 cm) as energy harvester and CLW (metal-semiconductor-metal interface) as a pH dependent sensing element. It is highly desirable to monitor the pH variations because many application fields such as in-vivo biomedical, clinical, lubricant, food monitoring related to biological and chemical processes depend on pH variations. Therefore, we implemented a self-powered pH sensor using the parallel connection between innovative microstructures of CWPW and CLW devices to monitor pH variations. First, we evaluated the energy conversion efficiency of the CWPW device by periodic hand force, but to drive the pH sensor the nonuniform hand force on energy harvesting device is not an optimum. For that, we used mechanical shaker force (ET-126) for harvesting mechanical to electrical energy. **Figure 5.3.8d** shows the three regions of electrical outputs for self-powered pH sensor. One is CWPW device output (peak-peak $V_{OC} \approx 6.646$ V), when an input mechanical force 11 N at 14 Hz cyclic frequency.

Second part represents the zero V_{OC} when no force condition and third part is CWPW device output driving CLW pH sensor (L = 2 cm, D = 0.055 cm) under no pH solution (as shown in **Figure 5.3.11a**). Under no pH buffer solution, there is no considerable potential drop across CLW pH sensor peak-peak $V_{OC} \approx 6.524$ V, which is due to the matching of high internal resistance for both devices made up of same polycrystalline material and polymer. To avoid the short circuit of CLW pH sensor under the medium of various basic regions of pH values [18], the electrode interface region was covered with nonconductive epoxy resin i.e. electrical isolation. Similarly to protect from the physical damage of CWPW harvester under mechanical loading, a soft and flexible PDMS matrix was poured onto the device.

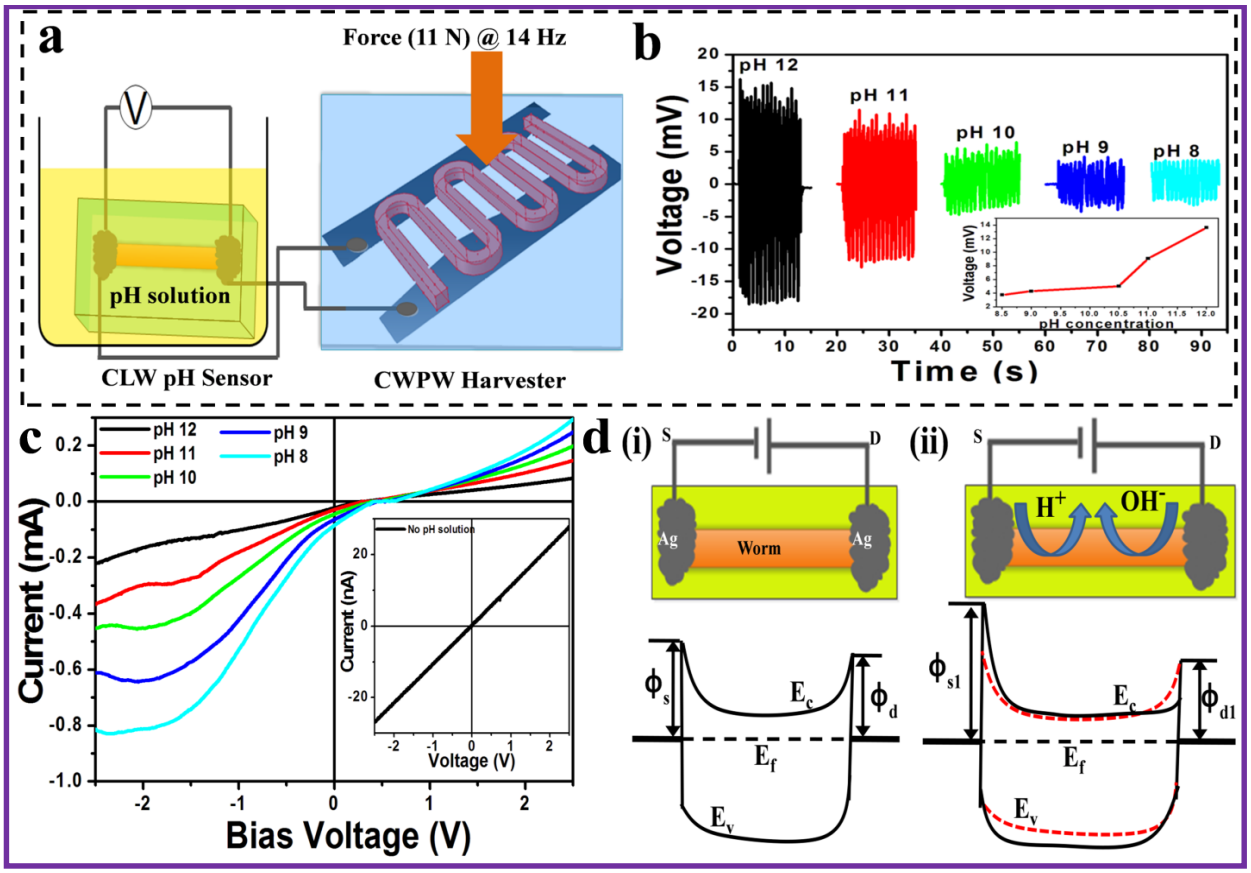

Figure 5.3.11 Demonstration of self-powered pH sensor: **(a)** Schematic diagram of CWPW device and CLW pH sensor under pH buffer solution established through parallel connection. **(b)** CLW pH sensor output voltages as a function of different basic pH solutions and inset shows positive peak output voltage under various pH solutions. **(c)** I-V curves of CLW pH sensor as a function of different basic region pH solutions with bias voltage ± 2.5 V. **(d)** Illustration of energy band diagram for the enhancement of electrical conductivity of worm (i) without pH solution (ii) with pH solution.

Finally, the obtained peak-peak voltage of CLW pH sensor under pH buffer solution with pH 12 is around 33 mV. This is quite less as compared to the electrical response of peak-peak $V_{OC} \approx$ 6.524 V under no pH buffer solution. The reason may be due to the changes in chemical environment species (H^+, OH^-) across pH sensor which modifies the depletion between M-S-M interfaces and swelling behavior. The electrical response of pH sensor changed from peak-peak $V_{OC} \approx$ 33 mV to peak-peak $V_{OC} \approx$ 7.03 mV when the pH buffer solution changed from 12 to 8

indicates lowering the resistance across pH sensor as shown in **Figure 5.3.11b**. A nonlinear behavior was observed by plotting the observed positive peak voltage as a function of pH concentration shown in inset **Figure 5.3.11b**.

To justify the above results and identifying the physical behavior of M-S-M interface, we employed the simple I-V technique for CLW pH sensor with a bias voltage ± 2.5 V and its corresponding results were shown in **Figure 5.3.11c**. Three fold increments were observed for CLW pH sensor (nA to mA) under no solution to pH solution 8 respectively. The ohmic behavior of M-S-M interface was changed to Schottky behavior under the pH solution was confirmed by I-V curves. In order to illustrate the pH-dependent piezoelectric potential could affect the Schottky barrier height (SBH) at source and drain contacts and its corresponding schematic band diagrams were shown in **Figure 5.3.11d**. Without pH solution, the CLW pH sensor shows symmetric effect at both contacts (I-V curve) with respect to bias voltage i.e SBH at source side and drain side has approximately equal heights confirms there is no screening effect as shown in **Figure 5.3.11d(i)**. The introduction of pH solution modifies the local contacts at source and drain owing to the polarity of piezoelectric potential. At the same time, linear worm structure undergoes into swelling state and bending outward direction (compressive force) initiates the piezoelectric charge carriers at both ends of local contacts. Which is the reason for I-V curves shown an asymmetric effect and its estimated energy band diagram was given in **Figure 5.3.11d(ii)**. In general, negative piezoelectric potential side SBH could raise (i.e source side-solid black line) possible to change the symmetric to asymmetric nature, while positive piezoelectric potential side lowers the barrier height changing asymmetric to symmetric nature [46-49]. In present case, the resistance of linear worm not only depends on pH chemical environment, swelling and compressive bending but also depends on carrier density,

crystallographic orientation of BTO NPs at local contacts (both ends of linear worm). Both self-powered pH sensor and I-V characterization results of linear worm pH sensor are the direct evidence for the change in resistance of worm under different basic pH solutions. This study proves that, the dual functionality of composite worm structures such as a driving power source unit for nanoelectromechanical systems (NEMS)/ microelectromechanical systems (MEMS) and a bio-sensing element to monitor or sense bio, chemical, and physical stimuli.

5.3.4 Conclusions

We successfully demonstrated the tailored length based laterally aligned composite worm structures (CWPW, CLW) through IG technique. Dual functionality of worms has been explored by energy harvesting performance using bio-mechanical force (low frequency), linear motor, and its pH dependent conductivity. We found that, the CWPW structures enable high piezoelectric potential generation and tuneable piezoelectricity by increasing the number of crests for wavy patterns, weight ratio of piezoelectric nanoparticles, electric polling and mechanical force. In addition to self-powered pH sensor, we demonstrated the CWPW device as an independent power source unit to drive the LEDs arranged as “N” and “M” letters. Furthermore, our approach shows pave way for template bio-polymer along with piezoelectric nanoparticles generates high efficient energy harvesting with various multifunctional utilities. Firstly, tailored dimensions of composite worm structures for the aptness of portability, wearability point view and second is mass production of composites with different nano/microstructures like worms, beads, nano-hydrogels and thin films.

5.3.5 References

[1] S. Xu, Y. Qin, C. Xu, Y. Wei, R. Yang, Z. L. Wang, Nat. Nanotechnol. 5, 2010, 366-373.

[2] B. Saravanakumar, K. Thiyagarajan, A. Nagamalleswara Rao, S. SoYoon, K. Taehyun, Z. H. Lin, S. J. Kim, Carbon. 84 (2015) 56-65.

[3] Z. L. Wang, **Faraday Discuss. 176** (2014) 447-458.

[4] Z. Huang, S. Yang, H. Zhang, M. Zhang, W. Cao, Sci. Rep. 5 (2015) 1-10.

[5] F. Zhang, Y. Zang, D. Huang, C. Di, D. Zhu, Nat. Commun. 6 (2015) 1-10.

[6] T. Jiang, L. M. Zhang, X. Chen, C. B. Han, W. Tang, C. Zhang, L. Xu, Z. L. Wang, *ACS Nano*. 9 (2015) 12562–12572.

[7] Z. Wen, J. Chen, M. H. Yeh, H. Guo, Z. Li, X. Fan, T. Zhang, L. Zhu, Z. L. Wang, Nano Energy, 16 (2015) 38–46.

[8] M. Yuan, L. Cheng, Q. Xu, W. Wu, S. Bai, L. Gu, Z. Wang, J. Lu, H. Li, Y. Qin,T. Jing, Z. L. Wang, Adv. Mater. 26 (2014) 7432–7437.

[9] A. Nagamalleswara Rao, B. Saravanakumar, and S. J. Kim, ACS Appl. Mater. Interfaces. 7 (2015) 9831-9840.

[10] J. S. Lee, K. Y. Shin, O. J. Cheong, J. H. Kim, J. Jang, Sci. Rep. 5 (2015) 1-8.

[11] W. Tang, J. Tian, Q. Zheng, L. Yan, J. Wang, Z. Li, Z. L. Wang, *ACS Nano*, 9 (2015) 7867–7873.

[12] K. Song, J. H. Han, T. Lim, N. Kim, S. Shin, J. Kim, H. Choo, S. Jeong, Y. C. Kim, Z. L. Wang, J. Lee, Adv. Healthcare Mater. 2016, 5, 1572-1580.

[13] J. Zhao, Z. You, Sensors, Sensors, 14 *(*2014) 12497-12510.

[14] C. Hu, L. Cheng, Z. Wang, Y. Zheng, S. Bai, Y. Qin, Small, 12 (2016) 1315-1321.

[15] L. Lin, Y. Hu, C. Xu, Y. Zhang, R. Zhang, X. Wen, Z. L. Wang, NanoEnergy, 2 (2013) 75–81.

[16] K. Y. Lee, M. K. Gupta, S. W. Kim, NanoEnergy, 14 (2015) 139–160.

[17] G. Zhu, W. Q. Yang, T. Zhang, Q. Jing, J. Chen, Y. S. Zhou, P. Bai, Z. L. Wang, *Nano Lett*, 14 (2014) 3208–3213.

[18] C. Arunkumar, A. Nagamalleswara Rao, B. Saravanakumar, S. Sophia, S. J. Kim, *ACS Appl. Mater. Interfaces*, 8 (2016) 9692–9699.

[19] Z. L. Wang, G. Zhu, Y. Yang, S. Wang, C. Pan, Mater. Today, 15 (2012) 532-543.

[20] Y. Hu, Z. L. Wang, NanoEnergy, 14 (2015) 3-14.

[21] J. M. Wu, C. Xu, Y. Zhang, and Z. L. Wang, *ACS Nano. 6* (2012) 4335-4340.

[22] M. Zhang, T. Gao, J. Wang, J. Liao, Y. Qiu, H. Xue, Z. Shi, Z. Xiong, L. Chen, NanoEnergy. 11 (2015) 510-517.

[23] T. C. Houa, Y. Yang, Z. H. Lin, Y. Ding, C. Park, K. C. Pradel, L. J. Chen, Z. L. Wang, NanoEnergy. 2 (2013) 387-393.

[24] X. Ni, F. Wang, A. Lin, Q. Xu, Z. Yang, and Y. Qin, Sci. Adv. Mater. 5 (2013) 1-7.

[25] S. Stassia, V. Caudab, C. Ottonea, A. Chiodoni, C. F. Pirria, G. Canavese, NanoEnergy. 13 (2015) 474-481.

[26] J. Chun, N. R. Kang, J. Y. Kim, M. S. Noh, C. Y. Kang, D. Choi, S. W. Kim, Z. L. Wang, J. M. Baik, NanoEnergy. 11 (2015) 1-10.

[27] L. Maiolo, S. Mirabella, F. Maita, A. Alberti, A. Minotti, V. Strano, A. Pecora, Y. Shacham-Diamand and G. Fortunato, App. Phys. Lett. 105 (2014) 093501-4.

[28] W. S. Lee, Y. S. Park, Y. K. Cho, ACS Appl. Mater. Interfaces. 6 (2014) 12189-12195.

[29] A. Sardarinejad, D.K. Mauryaa, M. Khaled, K. Alameha, Sens Actuators A Phys. 233 (2015) 414-421.

[30] Y. Cheng, P. Xiong, C. Steven Yun, G. F. Strouse, J.P. Zheng, R. S. Yang, Z. L. Wang, Nano let. 8 (2008) 4179-4184.

[31] A. V. Grigorieva, S. M. Badalyan, E. A. Goodilin, M. N. Rumyantseva, A. M. Gaskov, A. Birkner, and Y. D. Tretyakov, Eur. J. Inorg. Chem. 33 (2010) 5247-5253.

[32] B. Saravanakumar, S. Soyoon and S. J. Kim, ACS Appl. Mater. Interfaces. 6 (2014) 13716-13723.

[33] A. Menzel, K. Subannajui, F. Güder, D. Moser, O. Paul, and M. Zacharias, Adv. Funct. Mater. 21 (2011) 4342-4348.

[34] S. Singh, B. D. Gupta, Sen. Actuator B-Chem. 173 (2013) 268-273.

[35] A. A. Bark, Y. M. Moustafa, E. A. Motawea, M. M. Yehia, M. M. H. Khalil, Journal of Environmental Chemical Engineering. 3 (2015) 1486-1496.

[36] M. T. Buscaglia, M. Bassoli, V. Buscaglia, and R. Vormberg, J. Am. Ceram. Soc. 91 (2008) 2862-2869.

[37] Z. L. Wang, Adv. Mater. 24 (2012) 280-285.

[38] X. Chen, S. Xu, N. Yao, and Y. Shi, Nano let. 10 (2010) 2133-2137.

[39] B. Kumar and S. W. Kim, J. Mater. Chem. 21 (2011) 18946-18958.

[40] Y. Qi, M. C. McAlpine, Energy Environ. Sci. 3 (2010) 1275–1285.

[41] G. Mader, H. Meixner, P. Kleinschmidt, J. Appl. Phys, 58 (1985) 702-704.

[42] B. L. Cheng, M. Gabbay, W. Duffy, G. Fantozzi, Journal of materials science, 31 (1996) 4951-4955.

[43] B. M. Y. Choi, D. Choi, M. J. Jin, I. Kim, S. H. Kim, J. Y. Choi, S. Y. Lee, J. M. Kim, S. W. Kim, Adv. Mater. 21 (2009) 2185–2189.

[44] L. M. Swallow, J. K. Luo, E. Siores, I. Patel, D. Dodds, Smart Mater. Struct. 17 (2008) 025017-025023.

[45] J. Kwon, W. Seung, B. K. Sharma, S. W. Kim, J. H. Ahn, Energy Environ. Sci. 5 2012 8970-8975.

[46] Z. L. Wang, MRS Bulletin. 37 (2012) 814-827.

[47] S. Niu, Y. Hu, X. Wen, Y. Zhou, F. Zhang, L. Lin, S. Wang, and Z. L. Wang, Adv. Mater. 25 (2013) 3701-3706.

[48] F. Xue, L. Zhang, W. Tang, C. Zhang, W. Du and Z. L. Wang, ACS Appl. Mater. Interfaces. 6 (2014) 5955-5961.

[49] S. Sophia Selvarajana, A. Nagamalleswara Rao, C. Arunkumar, S. J. Kim, Sens. Actuator B 234 (2016) 395–403.

Chapter VI

Self-powered acceleration sensor using enhanced electroactive β-phase of PVDF/activated carbon hybrid film nanogenerator

Highlights

- The use of sonication process originates the high electroactive β-phase of PVDF without requirement of additional electrical poling process.
- This β-phase content of PVDF improved and stabilizes up to ≈91.75 % by the substitution of sheet type AC fillers in PVDF matrix solution with 30 V/V %.
- C-NG generates the instantaneous power density of ≈63.07 mW/m^2.
- C-NG device itself can act as a self-powered acceleration sensor and the output voltage shows linear behavior between the input accelerations 0.5 to 5 m/s^2 of shaft load.

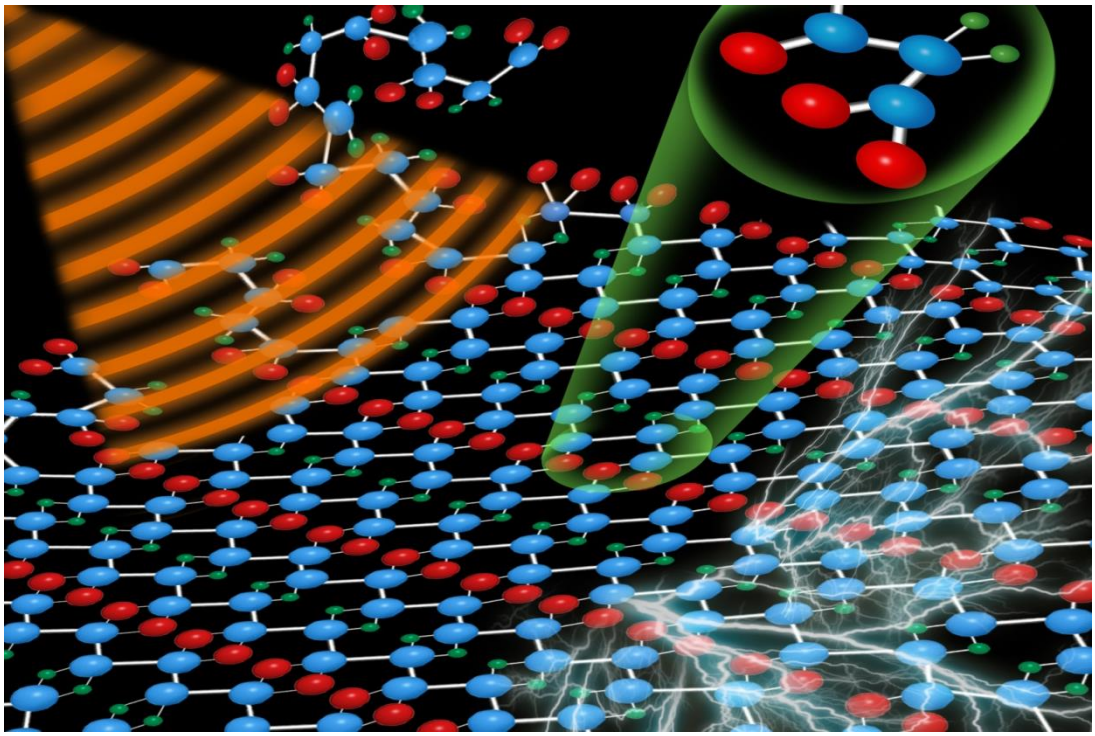

6.1 Introduction

Battery-free piezoelectric active sensors are the key source for the future and emerging smart technologies, which can measure various types of mechanical motions such as force, acceleration, fluid (or air) flow, human finger movements, photosensor, glucose and pH concentrations into useful and readable electrical signals[1-6]. These types of active sensors have many advantages such as good reliability, cost-effectiveness, eco-friendly, light weight, flexibility, portability, no requirement of additional sensory circuit and no external battery energy. Recently, many energy harvesting technologies were developed to demonstrate the feasibility of self-powered or battery-free active sensors. Piezoelectric[1-7], pyroelectric[8], triboelectric[9, 10], thermoelectric[11] and photovoltaic effects[12] are the origin for this type of technologies or nanogenerators. Further, the performance of these effects will always depend on the type of materials, growth of nanostructures and device designs. Among them, piezoelectric nanogenerator technology is the most promising, reliable, low cost, high sensitive for low frequency mechanical energies and possible for industrialization in various fields such automotive, medical and wearable electronics. Until now, a lot of research work and continuous progress was happening on the piezoelectric nanogenerator performance, device designs and growth of various nanostructures on plastic substrates. High piezoelectric coefficient based inorganic materials such as $Pb(ZrTi)O_3$, ZnO, $BaTiO_3$, $(KNa)NbO_3$, $ZnSnO_3$, CdS were widely used and extensively studied for generating enough electrical energy to drive the low power electronic devices[1-7, 13-18]. But the inorganic materials have disadvantages like brittleness, cost intensive, long term durability and few materials are toxic in nature. In contrast, organic polymer based devices such as poly(vinylidene fluoride) (designated as PVDF) and its co-polymers poly(vinylidenefluoride-co-trifluoroethylene) (designated as P(VDF-TrFE)), poly(vinylidene fluoride-co-hexafluropropylene) (designated as P(VDF-HFP)) with different surface morphologies were widely studied even though it has a low

piezoelectric coefficient than inorganic materials based devices[19-23]. Because the organic polymers have advantages such as flexibility, adaptability with device structure (flat, bending and fiber), high durability, easy to process, biodegradable and also generate reasonable energy conversion efficiency to drive low power electronic devices. PVDF have better piezoelectric properties compared to the other existing organic polymers, large deformation is possible without cracks, chemically stable and have multi functional properties other than piezoelectric such as ferro and pyro electric properties. Mendez et al.[24] demonstrated the quantification of various phases (α, β, γ, δ and ε) under different processing conditions and how the filler substitution will improve the phase content and mechanical properties. They also stated that the nucleation of β-PVDF with carbon nanotubes (CNTs) has been achieved with the solution sonication and mechanical mixture approaches. It was found that, α-phase coexists with the β-phase in the composite (PVDF/CNTs) prepared by solution sonication, while no β-phase can be observed in the composite prepared from the mechanical mixture route. The non-polar α-phase[25] of PVDF has zero electric dipole moment due to the anti-parallel alignment of -CH_2-/-CF_2- electric dipoles to the polar axis, not useful for the energy conversion applications. Whereas polar β-phase generates high electric dipole moment due to the parallel alignment of -CH_2-/-CF_2- electric dipoles to the polar axis (i.e. piezoelectric property) useful for the conversion of mechanical energy into electrical energy. The γ-phase of PVDF is semi-polar phase has less piezoelectric property compared to β-phase but higher than non-polar α-phase of PVDF. So that β and γ-phases of PVDF are favorable for good piezoelectric properties[25]. Recently, the role of fillers surface charge on the nucleation of electro-active polar phase of PVDF was reported[26] and claimed that the electrical interactions due to the presence of negative nanoparticle surfaces will interact with the positive charge density of the polymeric CH_2 groups. The use of appropriate

surfactants causes variations in the surface charge of nanoparticles opening the possibility of β-phase nucleation in different nanofillers, leading to hybrid composites that can take advantage of the properties of the fillers and the electro-active phase of the polymer[26]. PVDF polymer with different surface morphology were developed using various methods such as flat film by solution casting, hot press method, processed with hydrated chemicals[2, 25, 27], and mesoporous structure by template assisted[19, 20] respectively. All these techniques require external electrical poling treatment or mechanical stretching to achieve the polar phase of PVDF from the non-polar phase due to the re-orientation of -CH_2-/-CF_2- electric dipoles. This will create the permanent electroactive β-phase of PVDF matrix, which is useful for various applications such as conversion of tiny mechanical energy into electrical energy, piezo-separator in supercapacitors and battery, photocatalytic membrane reactor in water and flexible sensors. On the other side superhydriphobic fibrous films[28], composite nanofibers[29-31] was developed by electro spinning process. These films doesn't require any additional electrical poling process, but the fabrication process requires high applied electric fields such as 20 kV, 25 kV and 35 kV and lot of care has to be taken on various parameters like flow rate of liquid (mL/h), needle inner diameter (mm) and travelling distance (cm) respectively.

Recently, many techniques have been established to synthesize the electroactive β-phase (or self-polarization) of PVDF such as in-situ process[32], Langmuir-Blodgett deposition method[33], phase inversion[34] and substitution of fillers[35-41], where the external electrical poling is permanently removed. Among them, the substitution of fillers in PVDF matrix is easiest, low cost and easily scalable for large scale fabrication of films for harvesting and sensor applications. Here the fillers may be carbon related compounds such as graphene oxide (GO)[35], reduced GO (rGO)[36], and graphene[28, 32, 37] or inorganic nanoparticles such as TiO_2[38], ZnO[39], Fe_2O_3[40], and Ce^{3+}

[32]. The immobilization of fillers with particular weight ratio in PVDF matrix improves not only electroactive β-phase, but also improves the mechanical stiffness and thermal stability of PVDF film. Garain et al.[32] demonstrates the possibility of self-polarization behavior of PVDF/graphene fiber by the substitution of Ce^{3+} and another study shows the fabrication of self-poled transparent Ce^{3+}-PVDF composite film with intense photoluminescence in the UV region and suitability for the energy harvesting application. Sumanta et al.[41] developed the self-poled PVDF/AlO-rGO composite film and the corresponding nanogenerator shows high power density and energy conversion efficiency. Here, AlO-rGO acts as nucleating agent for the formation of electroactive β-phase of PVDF matrix. All these approaches pave way the elimination of external electrical poling of PVDF structures and improve the performance of energy generation, mechanical stiffness and thermal stability. Thus an alternative approach is required to develop the self-poled pure PVDF films and composite films for efficient conversion of mechanical energy to electrical energy along with the self-powered sensing property to measure the physical input parameters such as pressure, air and acceleration. Considering these, we have developed the flexible piezoelectric nanogenerator using the self-poled pure PVDF film and composite PVDF-activated carbon (C-PVDF-AC) films that can overcome the limitations of additional electrical poling, high electrical output and sensing property without any additional battery source.

In this section, a self-poled pure PVDF film was developed using the sonication process having sound energy as an input source originates the high electroactive β-phase of PVDF (≈73.04 %) without requirement of additional electrical poling process. This β-phase content of PVDF further improved and stabilizes up to ≈91.75 % by the substitution of sheet type AC fillers in PVDF matrix solution with a volume percentage of 30 V/V %. Here, AC fillers act as electrical conduction path between the $-CH_2-/-CF_2-$ electric dipoles of PVDF. Un-poled PVDF

nanogenerator (P-NG) and composite nanogenerator (C-NG) with 30 V/V % generate high peak-to-peak output voltage and currents are (37.77 V, 299 nA) and (37.87 V, 0.831 μA) upon the applied pressure of ≈6.6 kPa. The electrical performance of as-fabricated NG devices were tested with poling (8 kV/24 h at room temperature) and without poling conditions under constant mechanical force. It explains that the electrical poling process of these devices, no significant change in P-NG device output, but C-NG (30 V/V %) device output has considerable variation such as voltage increment change ≈30 % and current increment change around ≈96 % respectively. C-NG device generated the power density of ≈63.07 mW/m^2, which is sufficient to drive the LEDs and display systems. Finally, SAS was demonstrated experimentally to measure the various accelerations (0.1, 0.5, 1, 2, 3 and 5 m/s^2) of linear motor shaft load (2 Kg) without using any external battery energy and additional sensory circuit. Further, the charge accumulation behavior in commercial capacitor, driving 22 commercial LEDs using the C-NG device output and its stability test analysis were performed.

6.2 Experimental Method

6.2.1 Synthesis of PVDF/Activated carbon hybrid film by ultrasonication followed by solution casting technique

The fabrication procedure of pure PVDF and C-PVDF-AC films using the sonication technique is schematically shown in **Figure 6.1.1.** Fabrication of the C-PVDF-AC film involved four key steps: first, a homogeneous PVDF solution was prepared without precipitation of PVDF powder (Sigma-Aldrich). A total of 2 g of PVDF power with α-phase was dissolved in a mixture of 10 mL N,N-dimethylformamide (DMF), (DaeJung chemicals Ltd.), and 6 mL of acetone under the sonication process (amplitude 35 %) using a probe sonicator (Sonics, Vibra cell-VC 750 Watt) for 90 min to obtain a clear transparent solution. Second, a homogeneous suspension of AC with sheet like microstructure was obtained from the sonication process (1 h) of 1 g of AC

powder (DaeJung chemicals Ltd.) with 10 mL DMF solution. Third, the C-PVDF-AC solutions were prepared with various concentrations of PVDF solution and AC/DMF solution such as 10, 20 and 30 V/V % solutions using the sonication process (amplitude 35 %) for 1 h. Four, as prepared final C-PVDF-AC solutions were poured into a petri dish and dried in hot-air oven at 70 °C overnight for removing the residual solvents (DMF/acetone) and to form the C-PVDF-AC films with 10, 20 and 30 V/V % concentrations with good crystalline nature. A similar approach was followed to fabricate the pure PVDF film.

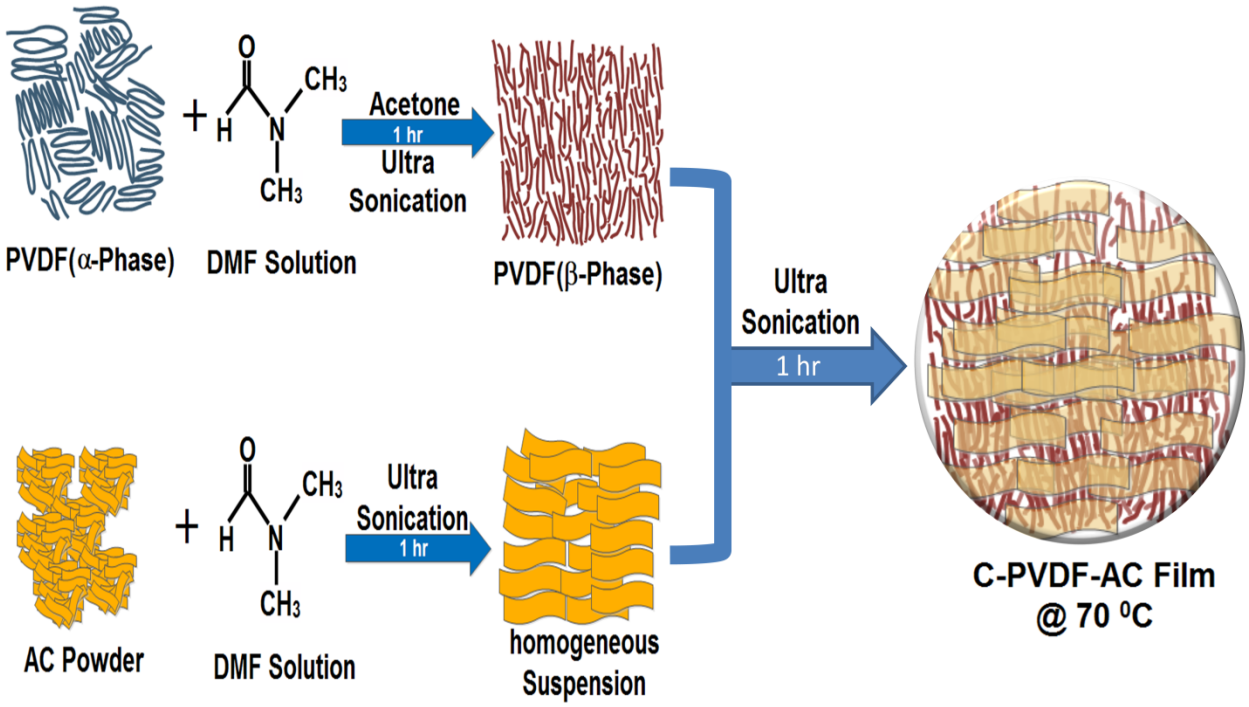

Figure 6.1.1 Schematic for the preparation of electroactive β-phase of pure PVDF and C-PVDF-AC films using sonication process followed by heat treatment.

6.2.2 Synthesis of PVDF film using magnetic stirring process

The PVDF transparent solution was prepared by dissolving 2 gm of commercially purchased PVDF powder in the mixture of 10 mL N,N-dimethylformamide (DMF), 6 mL of acetone and magnetically stirred at a temperature of 60 ^{0}C for 2 h. The obtained PVDF transparent solution

was poured into a glass Petri dish and soaked at 70 ^{0}C overnight for the removal of residual solvents (DMF/acetone) and to form as a flexible PVDF film.

6.2.3 Fabrication of flexible composite nanogenerator (C-NG)

As fabricated C-PVDF-AC film (10 V/V %) was cut into the desired dimensions (2 x1.5 cm^2) and two Al foil electrodes were attached on the top and bottom of the composite film to form the C-NG device. External connections were made using copper (Cu) wires that were attached to the Al foils with silver paste. Finally, the whole device was sandwiched between thin polydimethylsiloxane (PDMS) layers to protect the film against external mechanical stresses. A similar method was followed to fabricate P-NG and C-NGs (20 and 30 V/V %). Here, the electrical response characterizations for as-fabricated NG devices were performed under two conditions such as without poling and with poling (8 kV for 24 h at room temperature (RT)). Which gives the better insight about the electro-active β-phase content of sonication derived PVDF and its composite films.

6.3 Results and Discussion

6.3.1 Structural and dielectric constant analysis of flexible composite films

Formation of the polar β-phase of PVDF and C-PVDF-AC films were synthesized using the ultrasonication process. The complete fabrication protocol of piezoelectric films is depicted in experimental section. **Figure 6.1.2(a, b)** shows the X-ray diffraction (XRD) pattern of commercial PVDF powder (Sigma-Aldrich) and as-synthesized films such as pure PVDF and C-PVDF-AC films. The XRD peaks of PVDF powder at 18.28°, 19.92° and 26.6° clearly confirms the non-polar α-phase ($TG^{+}TG^{-}$) of PVDF and the corresponding reflections can be indexed as (020), (110) and (021) respectively[42]. The non-piezoelectric phase (α-phase) of PVDF has been

transformed into highly crystalline induced electroactive β-phase *via* ultrasonication process along with suitable solvents such as DMF and acetone. This β-phase can be observed by the XRD peak at 20.2° and at the same time all other peaks related to α-phase such as 18.28° and 26.6° were considerably reduced as shown in **Figure 6.1.2b (black)**[41, 42].

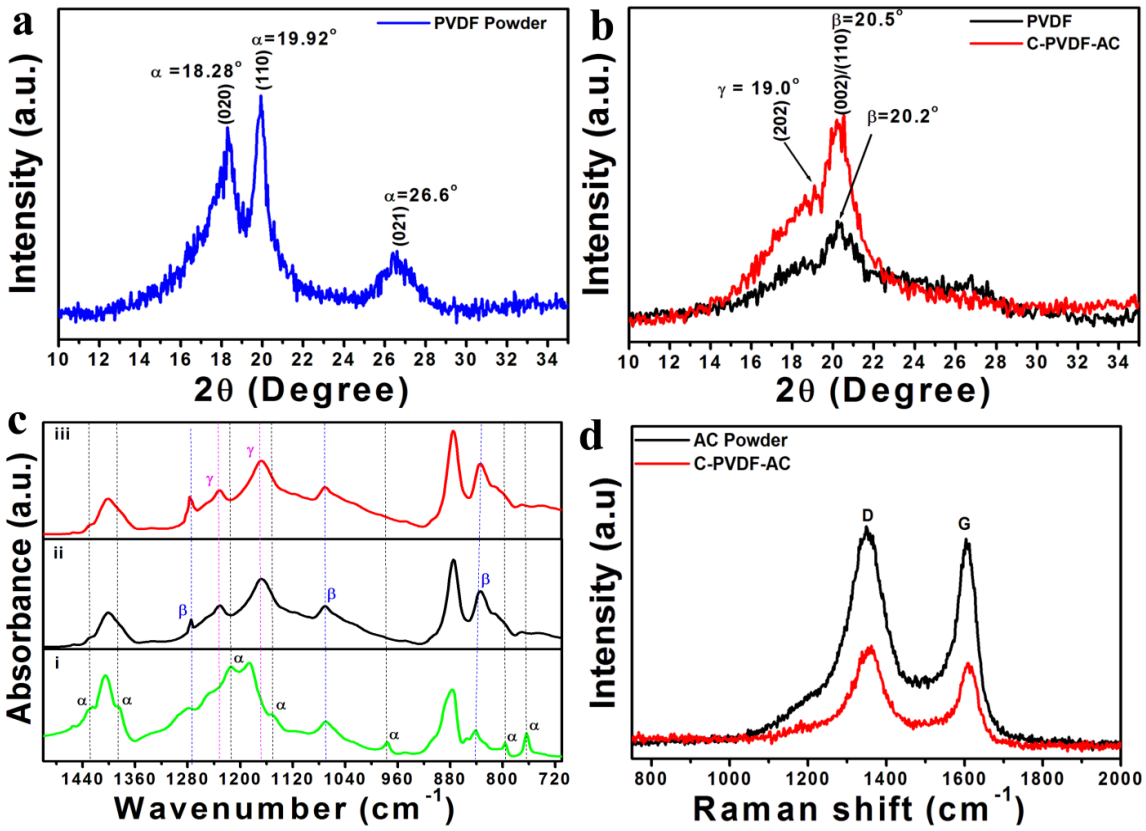

Figure 6.1.2 Structural characterizations of as-synthesized films **(a)** XRD pattern of commercial PVDF powder **(b)** XRD pattern of PVDF film and C-PVDF-AC film (30 V/V %) **(c)** FT-IR spectra of **(i)** PVDF powder **(ii)** pure PVDF film **(iii)** C-PVDF-AC film (30 V/V %) **(d)** Raman spectra of AC powder and C-PVDF-AC film (30 V/V %).

The β-phase contains all trans-conformation (TTTT) and exhibits good piezoelectric behavior by achieving the non-zero dipole moment via the opposite sides of hydrogen (H) and fluorine (F) along with the backbone chain as shown in **Figure 6.1.3**. This specific chain formation in PVDF will create the considerable amount of remnant polarization, which is useful

for energy harvesting and sensor applications. In ultrasonication process, the sound energy plays a key role to alter the -CH_2-/-CF_2- dipoles by breaking the intermolecular interactions and obtained the homogeneous transparent solution, poured into the glass Petri dish followed by heat treatment at 70 °C overnight for achieving the piezoelectric PVDF films. Here, the mechanical stretching and stress induced effects during the sonication process will be the responsible for the formation of polar β-phase. This method clearly suggests that the removal of traditional electrical poling of PVDF film for achieving the piezoelectric properties.

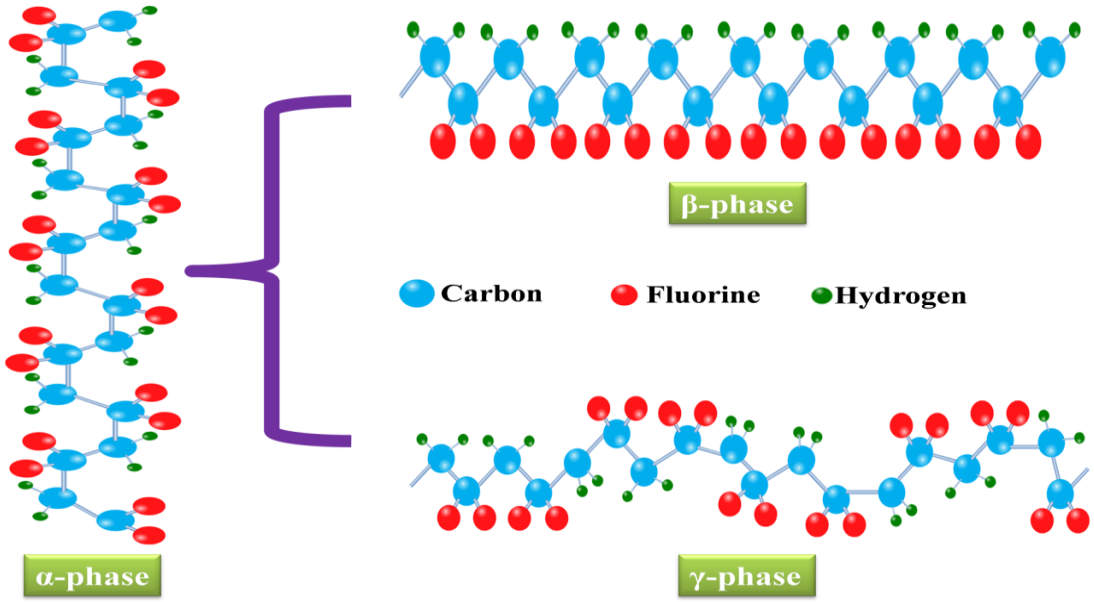

Figure 6.1.3 Schematic for the phase conversion of PVDF phases (α-phase to β and γ phases).

Further, the sheet type morphology of AC along with the DMF solvent and the previous PVDF solution by sonication process (≈1 h) were mixed with particular volumes such as 10, 20 and 30 V/V %. **Figure 6.1.4a** depicts the XRD pattern of the commercial AC powder shows the broad peaks from 20° to 29° and from 40° to 45° represents the graphitic microcrystallites corresponds to the (002) and (100)/(101) planes of the graphitic structure. These composite solutions (AC/PVDF/DMF) were rigorously mixed using the sonication process for 1 h, for achieving proper nucleation, growth and enhancement in dipole orientation.

Figure 6.1.2b (red color) represents XRD pattern of as-synthesized C-PVDF-AC film shows slightly reduced broadness of β-phase peak ≈ 20.5°and sharpness has been increased than the β-phase peak (≈20.2°) of pure PVDF film. Regarding the broadness and increasing intensity of XRD peak clearly confirms the improvement in crystalline nature due to the generation of considerable amount of temperature by double time sonication process and the molecular movement restriction between the PVDF chains and sheet type AC. This is nothing but a specific attraction of -CH_2- dipoles towards the delocalized π electrons present in AC, resulting in the formation of high electroactive phases of PVDF. Moreover, a small shoulder peak was generated between 18.5° to 20.2° and indexed as (202) represents the lower content of semi-polar γ-phase of PVDF[41].

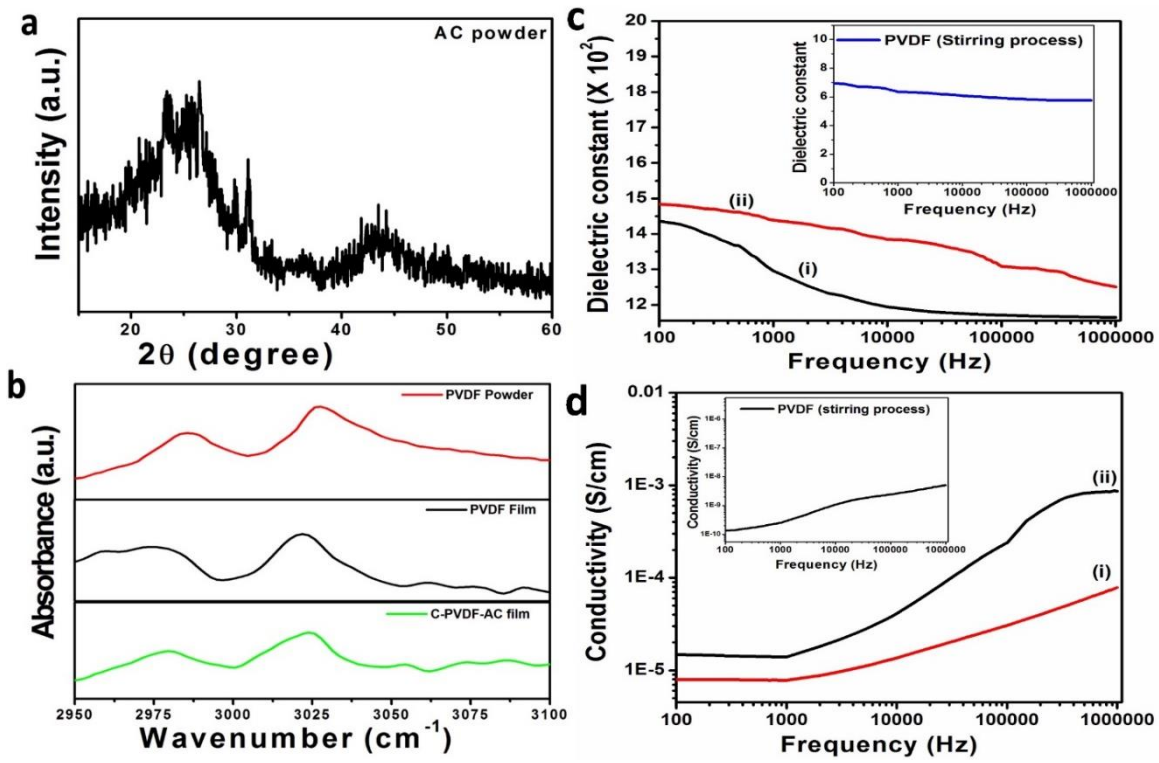

Figure 6.1.4 (a) XRD pattern of the commercial AC powder **(b)** FT-IR spectra of commercial PVDF powder and as-synthesized films such as pure PVDF film and C-PVDF-AC film (30 V/V %). **(c, d)** Frequency dependent dielectric constant and conductivity analysis at room temperature for sonication derived PVDF and C-PVDF-AC films (30 V/V %). The inset shows

the frequency dependent dielectric constant and conductivity of the PVDF film (*via* stirring process).

Generally, to improve the β-phase in PVDF, electrical poling and mechanical stretching processes are required to align the electric dipoles in PVDF. But in this case, both these processes were happening automatically during the sonication process followed by heat treatment in hot air oven at 70 °C overnight. The higher fraction of β-phase content in pure PVDF film and C-PVDF-AC film clearly confirms the removal of additional electrical poling process at room temperature. Therefore, it is expected that the PVDF and C-PVDF-AC films should have better piezoelectric/ferroelectric response and is directly proportional to the degree of electric dipole orientations and β-phase crystallinity.

Further, infrared vibrational spectroscopy (IR) studies were carried out to analyze the absorption bands related to the exact phases (α, β and γ) of commercial PVDF powder, as synthesized PVDF and C-PVDF-AC films as shown in **Figure 6.1.2c. Figure 6.1.2c(i)** shows the commercial PVDF powder spectra and the corresponding absorption bands at 763, 796, 975, 1149, 1214, 1384, and 1425 cm^{-1} are related to the major non-polar α-phase content and the bands at 840 cm^{-1} related to the minor polar β-phase content and the band at 1070 cm^{-1} describes the linear behavior with thickness of the composite film[36, 41]. The sonication process followed by heat treatment of PVDF/DMF and PVDF-AC/DMF precursors gives the PVDF and C-PVDF-AC films and the corresponding absorption bands spectra were shown in **Figure 2c(ii, iii).** The IR spectra of both films clearly shows that the absorption bands related to α-phase content were considerable diminished and at the same time the polar β-phase bands (833, 1070 and 1273 cm^{-1}) were raised and the semi-polar γ-phase absorption bands (1168, 1232 cm^{-1}) were newly generated[37, 42]. So the transformation of α-phase to β-phase (or γ-phase) is due to the vibrational stretching of molecular dipoles (-CH_2-/-CF_2-) in PVDF. This is because of the mechanical

stretching and stress induced effects in PVDF polymer, which are aroused by the sonication process followed by heat treatment. The sheet like AC in PVDF stabilizes the β-phase fractions and well improved the γ-phase content by aggregating all locally ordered trans-conformations. This is due to the electrostatic interaction between the AC (delocalized π electrons) and -CH_2-/-CF_2- dipoles of PVDF polymer. The vibrational bands at 3027 cm^{-1} represent the asymmetrical stretching of (-CH_2-) dipole and the peak at 2985 cm^{-1} represent the symmetric stretching of (-CH_2-) for PVDF and composite films as shown in **Figure 6.1.42b**[36]. The wavelength shifts and peak broadening of these bands confirms the interfacial interaction between the PVDF and AC sheets. The relative β-phase fractions in the PVDF film and C-PVDF-AC film can be evaluated using the equation[37, 42]:

$$F_\beta = \frac{X_\beta}{X_\alpha + X_\beta} = \frac{A_\beta}{1.26\, A_\alpha + A_\beta} \qquad 1$$

Where X_β and X_α are the % crystallinity of corresponding phases, A_β (β-phase) and A_α (α-phase) are the absorption band intensities at 840 cm^{-1} and 763 cm^{-1}, The value 1.26 is the ratio (K_β/ K_α) of absorption coefficients of respective wave numbers such as $K_{\beta,840}$ = 7.7 × 104 cm^2 mol^{-1} and $K_{\alpha,763}$ = 6.1 × 104 cm^2 mol^{-1} respectively. The relative fraction of β-phase content in PVDF powder sample was evaluated using the above equation is ≈46.8 %. The electroactive β-phase reaches to a maximum of ≈73.04 % (relative content with respect to other phases present) for pure PVDF film obtained by the sonication process followed by heat treatment (70 °C/overnight). Further, the β-phase stabilizes and increased up to ≈91.75 % when the AC fillers and PVDF volume percentage values reaches to 30 V/V % for the composite film. Beyond this volume percentage, composite film formation is not in flat manner and crumpled in nature with multiple cracks. This is due to agglomeration of high AC filler content in polymer matrix, which is not allowed to nucleate completely and diffuse into polymer matrix. So that we restricted the volume

percentage of sheet like AC filler content into PVDF polymer matrix ≈ 30 V/V % and further piezoelectric energy harvesting and self-powdered sensor studies were carried out with in this volume percentage. The frequency dependent dielectric constant and electrical conductivity of PVDF film (*via* magnetic stirring and sonication processes) and C-PVDF-AC film (*via* sonication process) was measured between the operating frequency 100 Hz to 1 MHz at room temperature. The enhancement in dielectric constant of PVDF film *via* sonication process represents the enhancement of electric dipole-dipole interactions and well alignment in particular direction (**Figure 6.1.4c**). Here, the sound energy creates higher mechanical stretching and stress induced effects on PVDF molecular chains, which intern results in-situ orientation of CH_2/CF_2 electric dipoles of PVDF. Further, C-PVDF-AC film shows higher dielectric constant ≈1483 at 100 Hz (**Figure 6.1.4c**), which is due to the interfacial interaction between AC fillers and PVDF molecular chains. This attributes to the accumulation of mobile charge carriers at the interfaces between AC fillers and PVDF.[37, 43-45] Moreover, electrical conductivity of C-PVDF-AC at room temperature is higher than pure PVDF film as shown in **Figure 6.1.4d.** The enhancement is mainly due to the charge separation, charge distribution and synergy effect in composites. Optimized AC filler content in composites reduces the inter-particle distance between particles and PVDF molecular chains and subsequently improves the conductivity of composite. The increment in dielectric constant and electrical conductivity of composite film may possible to improve the piezoelectric property of film. **Figure 6.1.2d** shows the Raman spectra of the AC powder and C-PVDF-AC film contains two intense vibrational bands related to the sp^2 carbon atoms belonging to disordered microcrystalline domains. The band at 1348 cm^{-1} is assigned to lattice breathing mode with A_{1g} symmetry (structural disorder) and the band at 1603 cm^{-1} assigned to bond stretching of pairs of sp^2 carbon atoms either in chain or aromatic rings [37, 46].

For composite film, the D band peak intensity is higher than the G band intensity, indicates the defect induced transitions are higher compared to the pristine AC.

6.3.2 Surface morphology of the composite films

The surface morphology of the PVDF film, AC powder and C-PVDF-AC film were analyzed using the FE-SEM images. Fabrication of pure PVDF film using sonication process shows rough surface without any micro pores at 20 μm scale as shown in **Figure 6.1.5a**. The homogenous dispersion of AC in DMF solvent shows the sheet like morphology of the AC as shown in **Figure 6.1.6b.** The dispersion of sheet like AC in PVDF creates the randomly oriented irregular rough surface having micro pores ≤ 2 μm as shown in **Figure 6.1.6(c, d).** The sheet like AC fillers are not observed on the surface of C-PVDF-AC film may be due to the well dispersion of AC fillers in homogenous PVDF solution.

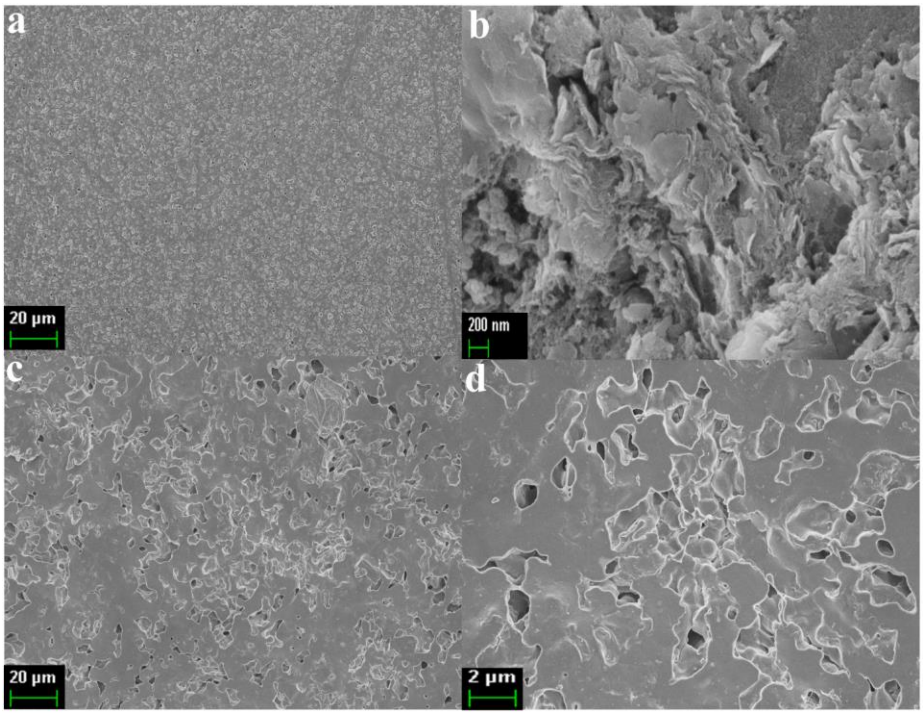

Figure 6.1.5 Surface morphological analyses of as-synthesized samples **(a)** PVDF film at 20 μm scale **(b)** DMF treated AC powder at 200 nm scale **(c, d)** C-PVDF-AC film (30 V/V %) at 20 μm and 2 μm scales.

6.3.3 Piezoelectric potential response of P-NG

The piezoelectric response of an electroactive β-phase of pure PVDF and C-PVDF-AC films (10, 20 and 30 V/V %) were analyzed by fabricating the corresponding flexible piezoelectric nanogenerators and the device electrical responses upon the constant mechanical force was observed in terms of open circuit voltage (V_{OC}) and short circuit current (I_{SC}). **Figure 6.1.6a** shows the schematic representation of pure PVDF based piezoelectric nanogenerator (P-NG) layers (PVDF film, Al electrodes and protecting PDMS package stamps) and a perpendicular mechanical force act on it. The magnified part shows the cross-sectional FE-SEM image of pure PVDF film reveals the thickness ≈94 μm as shown in **Figure 6.1.6b.** The self-polarization effect (electroactive β-phase) of as-synthesized pure PVDF film has been verified and experimentally demonstrated by the piezoelectric effect based voltage response. Generally, low electrical response will generate for the non-electrically poled P-NG device (without self-polarization) upon the constant mechanical force. This is due to the higher content of non-polar regions (α-phase, TG+TG-) exist in the polymerized PVDF film i.e. the electric dipoles ($-CH_2-/-CF_2-$) are arranged to the polar axis in anti-parallel manner. This results in low piezoelectric potential across the electrodes, when applied a mechanical force on P-NG device. But in this case, the un-poled P-NG device generates high piezoelectric voltage (V_{OC}) ≈ 37 V and I_{SC} ≈299 nA with a simple mechanical force (2 N or ≈6.6 kPa) act on it as shown in **Figure 6.1.6(c, d)**.This behavior clearly indicates that the as-fabricated PVDF film (un-poled) has high polar content regions (TTTT) i.e. orientations of electric dipoles ($-CH_2-/-CF_2-$) in the thickness direction are arranged to the polar axis in parallel manner (self-polarization), which is favorable to the generation of high piezoelectric response with respect to the mechanical force.

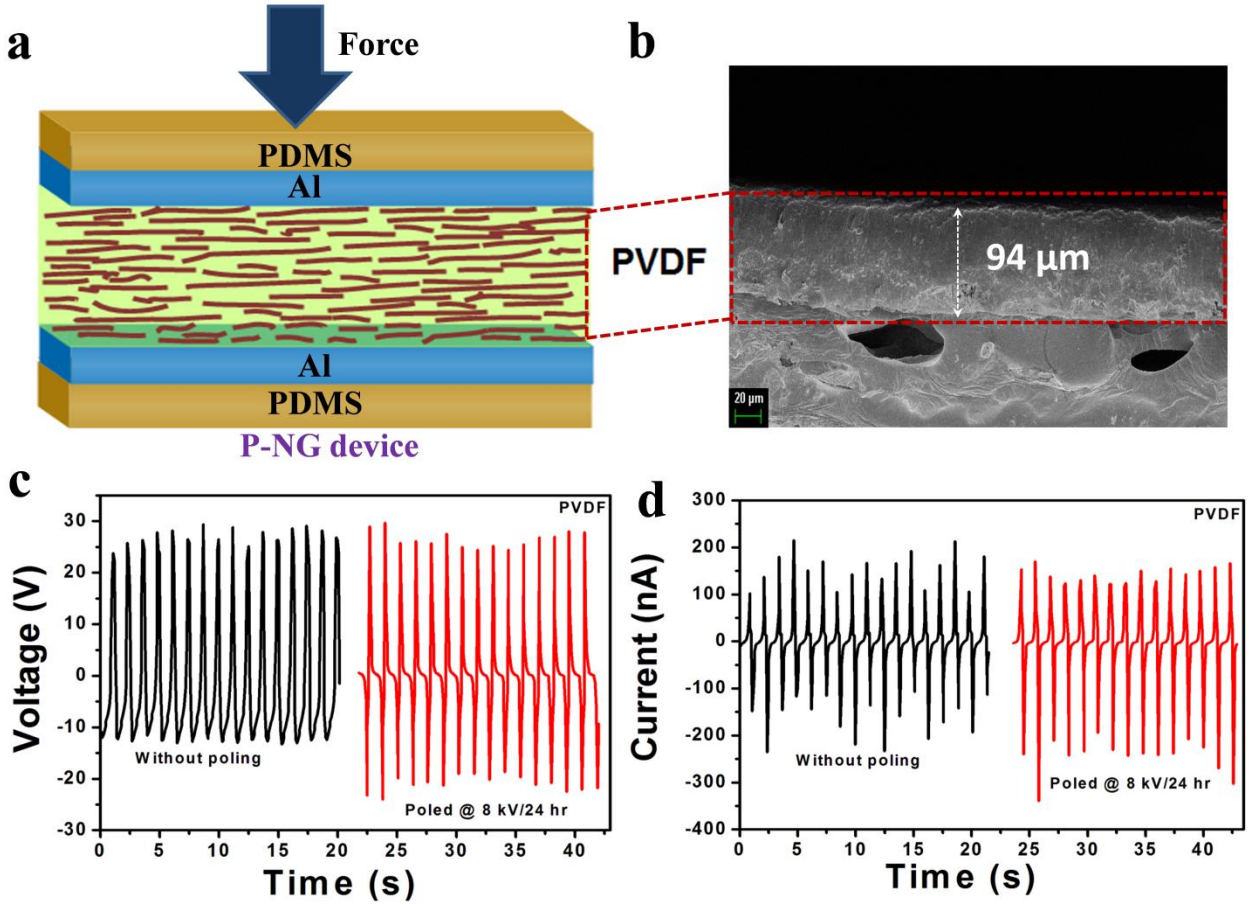

Figure 6.1.6 (a) Schematic diagram shows the P-NG device layers **(b)** Cross-sectional FE-SEM image of the pure PVDF film at 20 µm scale. **(c, d)** Open circuit voltage and short circuit current of the poled and un-poled P-NG devices upon the mechanical force 2 N (or ≈6.6 kPa).

As the perpendicular periodic mechanical force press/release conditions, generates the electrons will flow back and forth between the top/bottom electrodes through the external electronic circuit. The self-polarization of PVDF film was confirmed by the comparison of electrical responses of PVDF based P-NGs with electrical poled (8 kV for 24 h at RT) and un-poled conditions. Here, the input applied mechanical force and device area kept as constant parameters. **Figure 6.1.6(c, d)** shows the comparative electrical responses of both P-NG devices (poled and un-poled) upon mechanical force (≈6.6 kPa), shows negligible difference between them. It indicates that, no additional electrical poling is required for the as-fabricated PVDF film

(sonication process followed by heat treatment) and a direct experimental evidence for self-polarization (electroactive β-phase) of pure PVDF film. The excellence of sonication process was demonstrated by the comparison of electrical responses of sonication process derived PVDF results to the magnetic stirring process derived PVDF (8 kV/24 h poling at RT) results as shown in **Figure 6.1.7(a,b)**.

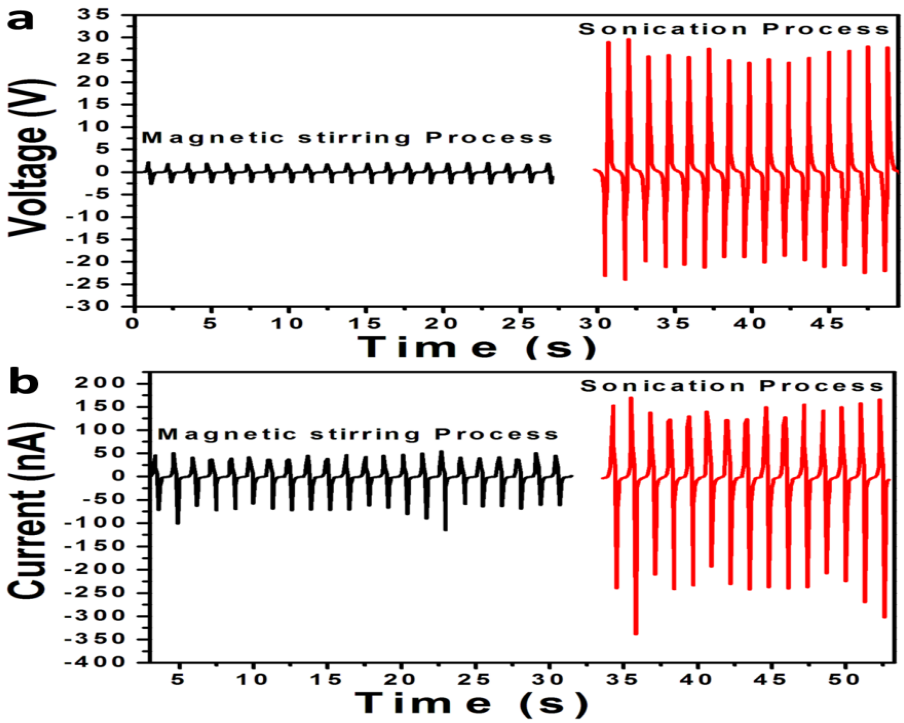

Figure 6.1.7(a, b) Comparative electrical responses of PVDF film based devices upon constant mechanical force (≈2 N). Here the PVDF films were prepared under two different methods such as magnetic stirring process and sonication process.

It clearly represents that, sonication process derived PVDF film (without poling) has superior piezoelectric properties than stirring process derived poled PVDF film. During sonication process, the PVDF molecular chains will experienced a higher mechanical stretching and stress induced effects by the ultrasound energy resulting in-situ orientation of the -CH_2-/-CF_2- electric dipoles of PVDF film. The existence of electroactive β-phase of PVDF film (un-

poled) were confirmed through structural, IR studies and well matched with the high piezoelectric electrical response of the un-poled P-NG device[36, 37, 41, 42].

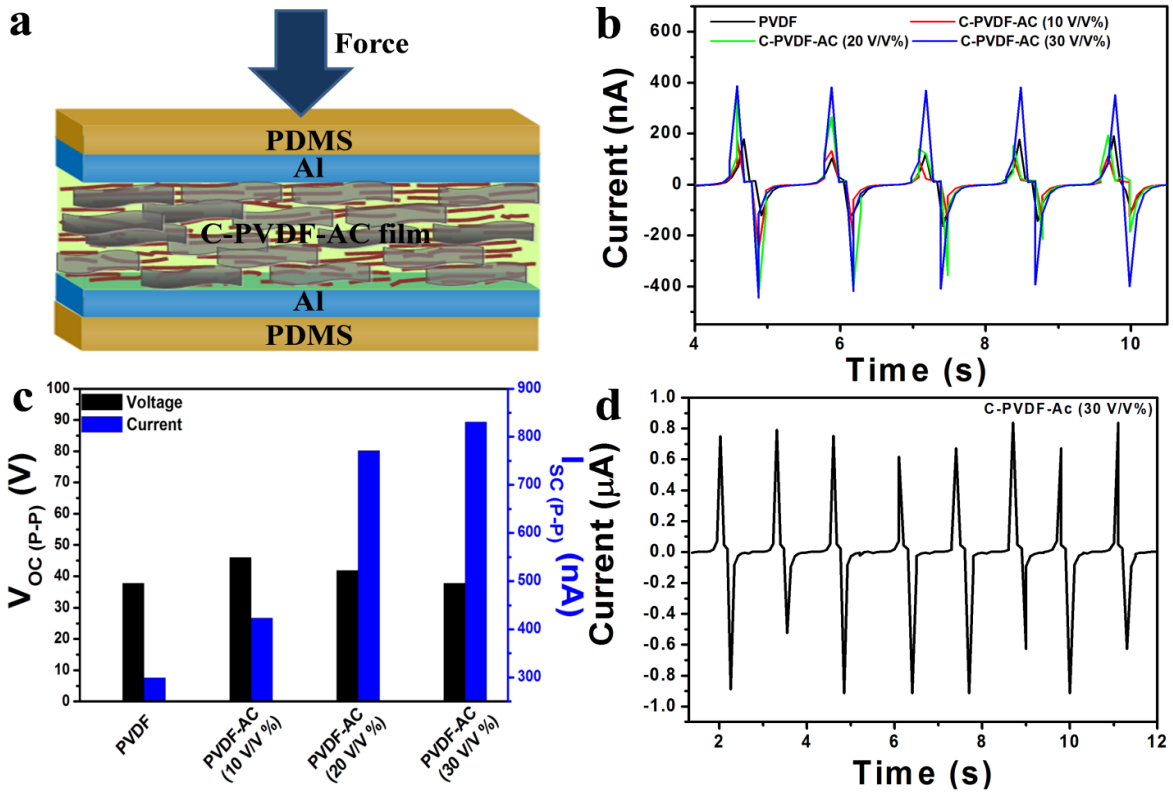

Figure 6.1.8 (a) Schematic diagram shows the C-NG device layers **(b)** Comparative current response of various un-poled C-NG devices upon the mechanical pressure (6.6 kPa) **(c)** Cumulative peak-to-peak voltage and current comparison with different volume percentage of PVDF and AC such as 0, 10, 20 and 30 V/V % (other side, greater than 30 V/V %, the film formation is not good and AC fillers are fully agglomerated). **(d)** Short circuit current of poled C-NG device (30 V/V %) upon constant mechanical force (6.6 kPa).

The substitution of sheet like AC fillers in PVDF film improved and stabilizes the β-phase crystalline nature was confirmed by XRD and FT-IR studies[35-37, 41]. **Figure 6.1.8a** shows the schematic diagram of the C-NG device structure using C-PVDF-AC films with various volume percentages such as 10, 20 and 30 V/V % and the corresponding thickness of the films were slightly increases (104 μm, 109 μm and 111 μm) with increasing the AC/PVDF volume percentages (10, 20 and 30 V/V %) as shown in **Figure 6.1.9.** Here, the mold used for film

formation was kept as constant parameter and variable content is the amount of pouring PVDF/AC solutions resulting in higher thicknesses of the films. The C-PVDF-AC films have slightly higher thickness compared to the pure PVDF film thickness ≈94 μm.

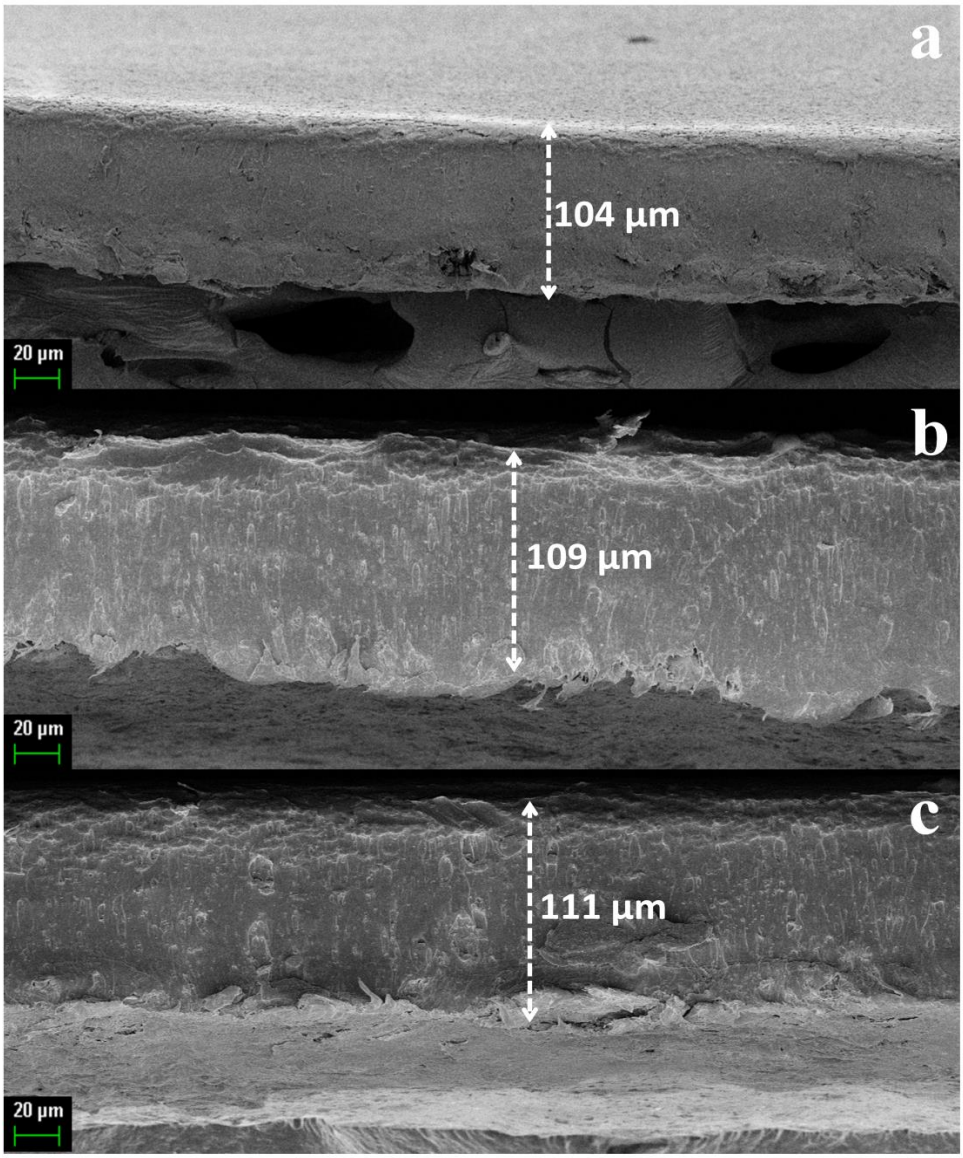

Figure 6.1.9 Cross-sectional FE-SEM image of the C-PVDF-AC films with different volume concentrations at 20 μm scale **(a)** 10 V/V % **(b)** 20 V/V % and **(c)** 30 V/V %.

Figure 6.1.8b shows the comparison of I_{SC} for all fabricated C-NG devices without poling condition under constant force (≈6.6 kPa). This reveals that the output current increases with increasing the AC filler content in PVDF film, because of the electrostatic interaction

between the delocalized π electrons present in AC and -CH_2-/-CF_2- electric dipoles of PVDF film. **Figure 6.1.8c** shows the comparison of cumulative peak-to-peak open circuit voltage (V_{OC}) and short circuit current (I_{SC}) of un-poled PVDF and C-NG devices under constant mechanical force.

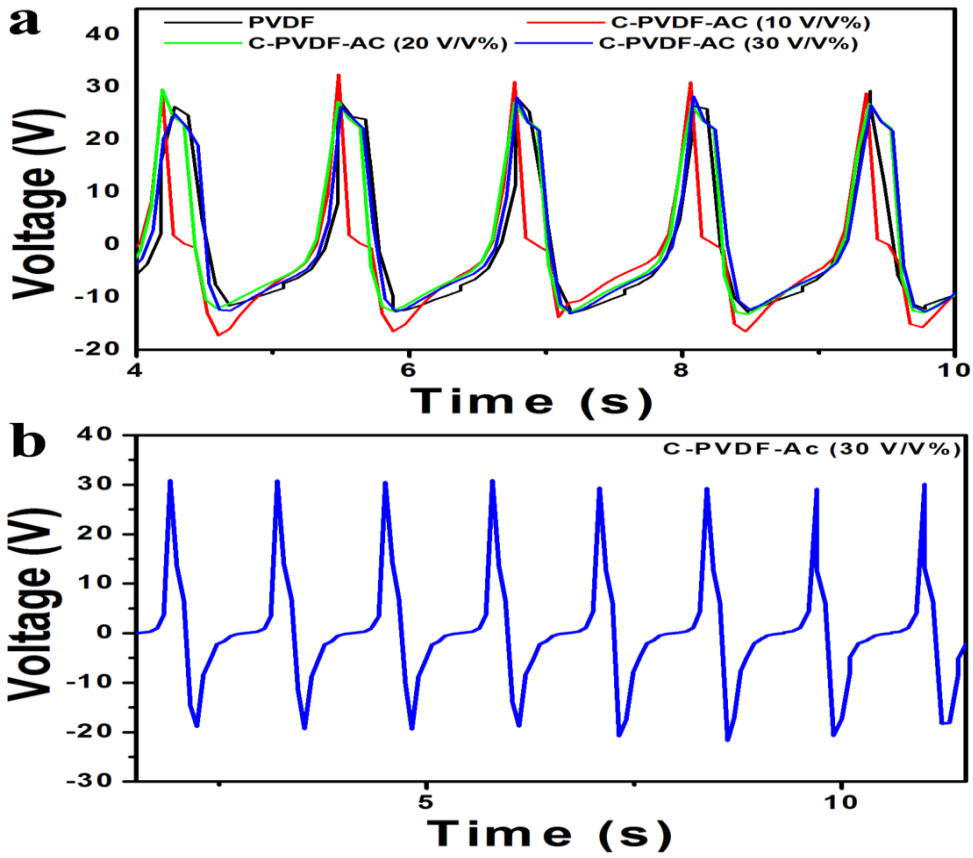

Figure 6.1.10 (a) Comparative voltage response of various un-poled C-NG devices upon the mechanical force (2 N). (b) Open circuit voltage of poled C-NG device (30 V/V %) upon constant mechanical force (2 N).

The real time experimental data was given in **Figure 6.1.10a (and Figure 6.1.8b).** The results demonstrate that, substitution of AC fillers into PVDF could not reduce the electroactive β-phase content (self-polarization) of PVDF film. Additionally, it improved the crystalline nature of PVDF and stabilizes the electroactive β-phase content. It resulting that, C-NG devices shows superior piezoelectric response compared to P-NG device as shown in **Figure 6.1.8c**. Here, the I_{SC} have proportional relationship with AC filler content in the PVDF matrix i.e. the percentage

increment of I_{SC} is ≈41.7 % for C-NG device (10 V/V %), 158.15 % for C-NG device (20 V/V %) and 178.08 % for C-NG device (30 V/V %) compared to I_{SC} of P-NG device (pure PVDF).

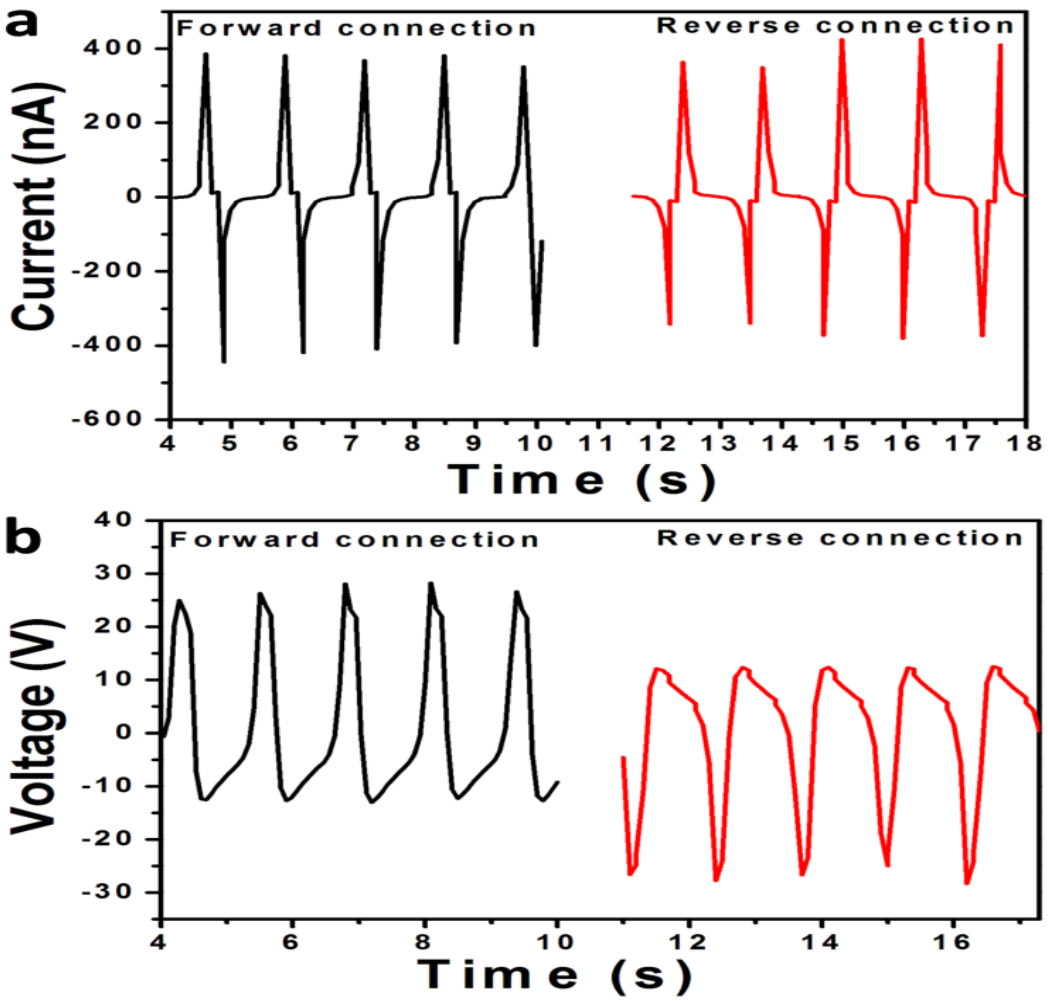

Figure 6.1.11 Switching-polarity test of un-poled C-NG device up on mechanical force 2 N. (a) Current response and (b) Voltage response.

But the change of V_{OC} is small i.e. the percentage increment of V_{OC} is ≈21 % for C-NG device (10 V/V %), 20 % for C-NG device (20 V/V %) and 0.31 % for C-NG device (30 V/V %) compared to the V_{OC} of pure PVDF device. The increment of current in C-NG devices explains the improvement of electrostatic interaction between delocalized π electrons in AC and molecular movements of PVDF resulting in the generation of more free charge carriers through

direction of film thickness[41]. Switching polarity test was performed for C-NG device (30 V/V %) to confirm that the output was coming from C-NG device or not. The phase shift was observed between the output signals with respect to the forward and reverse connections of C-NG device as shown in **Figure 6.1.11 (a, b)** and **Figure 6.1.12 (a, b).** It describes that the output signals are coming from C-NG device and not by other sources. Moreover, the cross-sectional FE-SEM analysis of C-NG device (30 V/V %) was performed and the corresponding image is shown in **Figure 6.1.12c.** It confirms that there is no air gap between the active layers (Al/PVDF-AC/Al) suggests that no influence of triboelectric effect in output response.

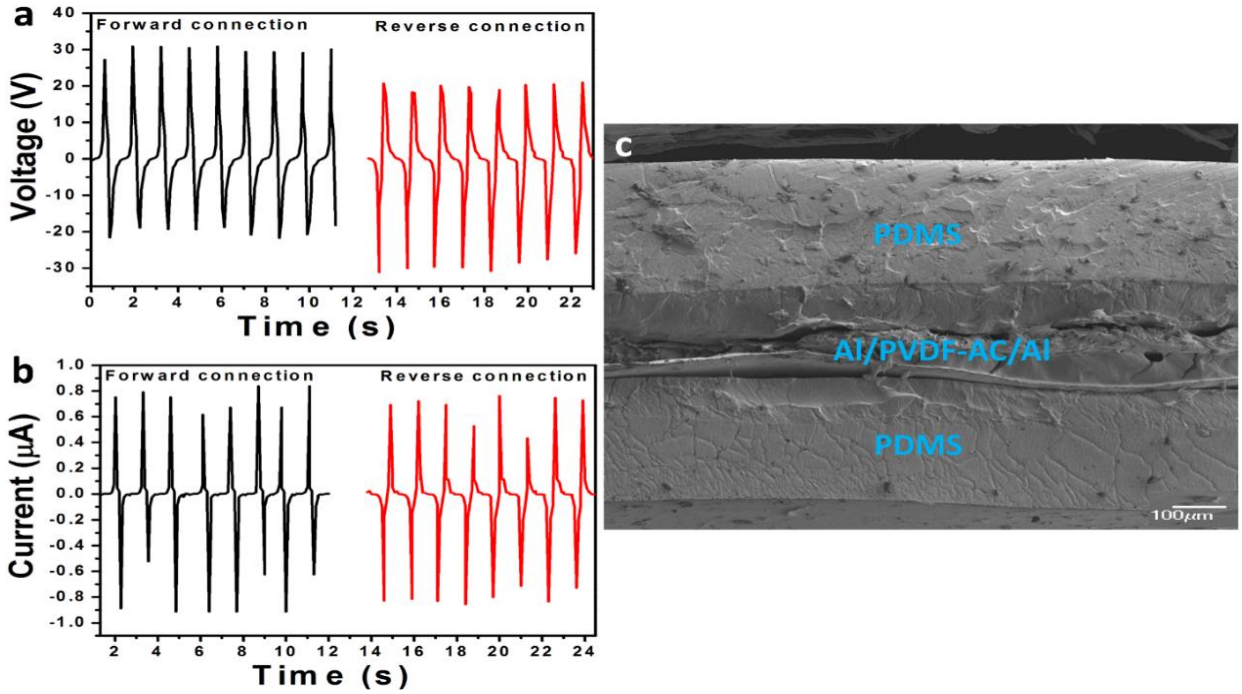

Figure 6.1.12 Switching-polarity test of poled C-NG device (8 kV/24 h at RT) up on mechanical force 2 N. (a) Voltage response, (b) Current response and (c) Cross-sectional FE-SEM image of C-NG device (30 V/V %) at 100 μm scale.

6.3.4 Self-powered acceleration sensor using flexible C-NG device

Further studies, such as flexible self-powered acceleration sensor (SAS) application, capacitance loading effects, load resistance analysis, power density calculations and stability test

were carried out using the C-NG device (30 V/V %). The C-NG device (> 30 V/V %) does not possible to fabricate due to the cracks appeared in composite film formation, crumpled nature and agglomeration of AC filler content in PVDF matrix. Before that, electrically poled (8 kV/24 h at room temperature) C-NG device (30 V/V %) electrical performance was obtained under constant periodical mechanical pressure ≈6.6 kPa. **Figure 6.1.8d (**and **Figure 6.1.12b)** shows the superior electrical response ≈49.6 V and ≈1.63 μA compared to the un-poled C-NG device response ≈ 37.87 V and ≈ 831.46 nA, respectively. There is a pleasant electrical poling effect on C-NG device electrical response; due to the enhancement in permanent polarization of the composite film which improves the piezoelectric behavior. Here, AC fillers act as electrical conduction path between PVDF chains, that creates the electrically stress induced effect on molecular dipoles resulting in the re-orientation of dipoles to the polar in parallel manner. But this kind of poling effect was not observed in the P-NG device based on electroactive β-phase crystallinity (73.04 %) of pure PVDF film. This clearly demonstrates that, AC fillers and electrical poling of C-NG device (30 V/V %) further improves the electroactive β-phase crystallinity from 73.04 % to (91.75 %) respectively. The piezoelectric films (PVDF and C-PVDF-AC) derived from the sonication process and its P-NG, C-NG device outputs are comparable and much high response compared to the published reports of PVDF film based devices as shown in **Table-6.1.**

Next, the C-NG device can be used a self-powered acceleration sensor (designated as S-AS) to measure the various accelerations (0.1, 0.5, 1, 2, 3, 5, 7 and 9 m/s^2) of the fixed linear motor shaft mass (2 Kg) and the corresponding electrical responses were shown in **Figure 6.1.13(a, b)**. It is highly desirable to develop the self-powered accelerometers without use of commercial battery energy and extra sensory circuits, due to its wide range of applications in

various fields such as industrial and engineering fields (to measure vehicle or machine acceleration and vibrations), structural monitoring fields (to measure the quality of building structures driving from various shock and vibrations, heavy wind flow speeds and heavy load detection limits on bridges) and portable electronics (to measure automatic collision detection, pedometers).

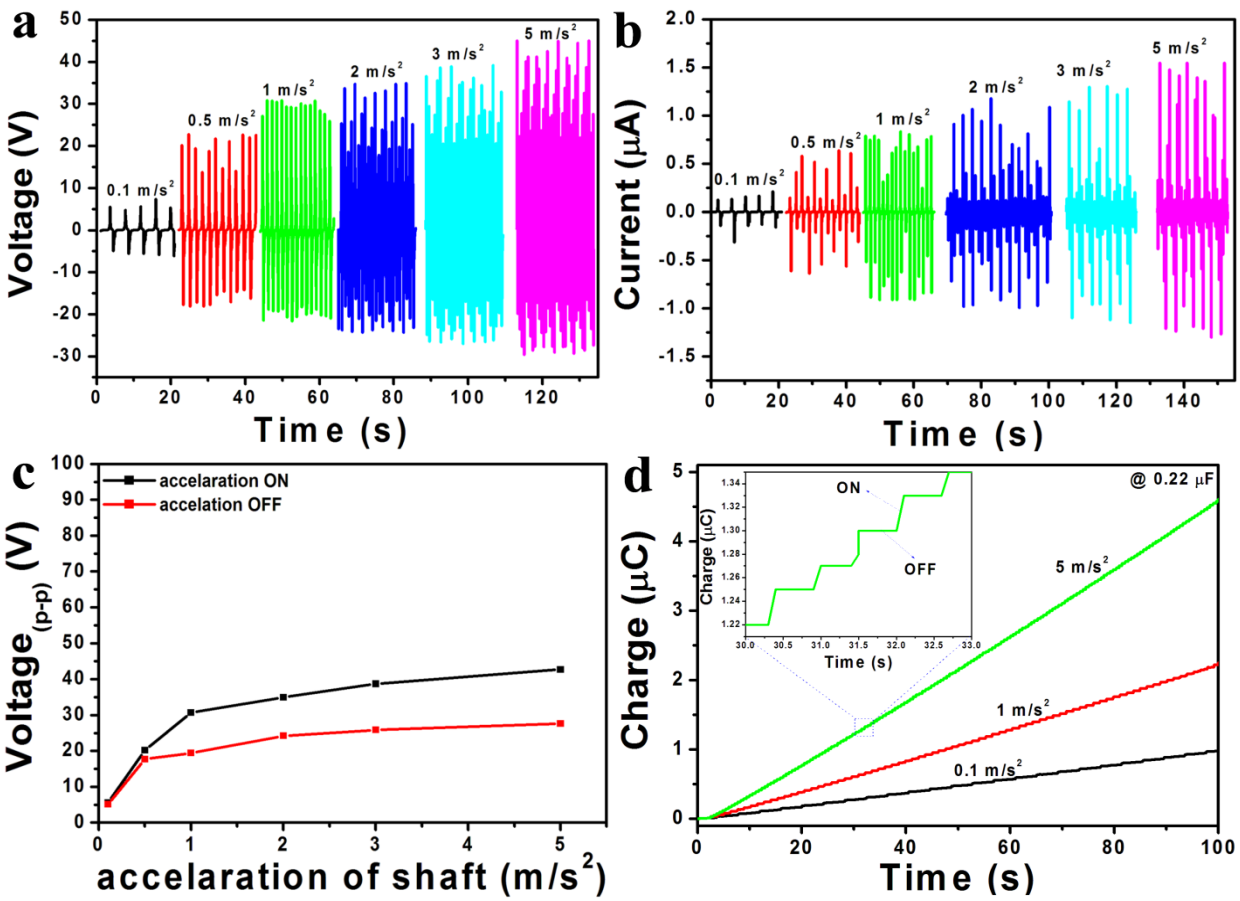

Figure 6.1.13 C-NG acts as a self-powered acceleration sensor. **(a, b)** Open circuit voltage and short circuit current of S-AS upon various accelerations (0.1, 0.5, 1, 2, 3 and 5 m/s^2) of shaft load (2 Kg) act on it. **(c)** Cumulative output voltage of S-AS upon various accelerations ON and OFF conditions. **(d)** Charge accumulation behavior in 0.22 μF capacitor using the output of S-AS upon 0.1, 1 and 5 m/s^2 accelerations of shaft load.

Table 6.1 Comparison of the proposed composite nanogenerator output with respect to the previously published reports.

Active film	Poling condition	Device Area (cm^2)	Pressure/Force	Voltage (V)	Current (μA)	Ref.
Ce^{3+}-PVDF/Graphene	Not poled	12	6.6 kPa	11	0.07	32
PVDF	Not poled	-	100 N	3	-	34
Fe-rGO/PVDF	Not poled	6	12 kPa	5.1	0.25	36
GAg-PVDF	Not poled	1.22	5.2 kPa	0.1	0.0001	37
ZnO-PVDF	Not poled	7.2	8.43 kPa	28	0.45	39
AlO-rGO-PVDF	Not poled	7.82	46.8 kPa	36	0.8	41
PVDF	Not poled	3	6.6 kPa	37	0.29	Present work
C-PVDF-AC (30 V/V %)	Not poled	3	6.6 kPa	37.87	0.83	Present work
C-PVDF-AC 30 V/V %	Poled (8 kV/24 hr)	3	6.6 kPa	49.6	1.63	Present work

As an experimental demonstration, S-AS device having an active area 2 cm x 1.5 cm was placed on fixed rigid stand and directed perpendicular to the linear motor shaft mass (2 Kg). To protect the device from mechanical failure, a thin insulating PDMS packaging layer was attached on top of the S-AS device. The S-AS device driven by various controlled accelerations of linear motor shaft having a fixed mass ≈2 Kg with two conditions such as acceleration ON and OFF over periodic time intervals.

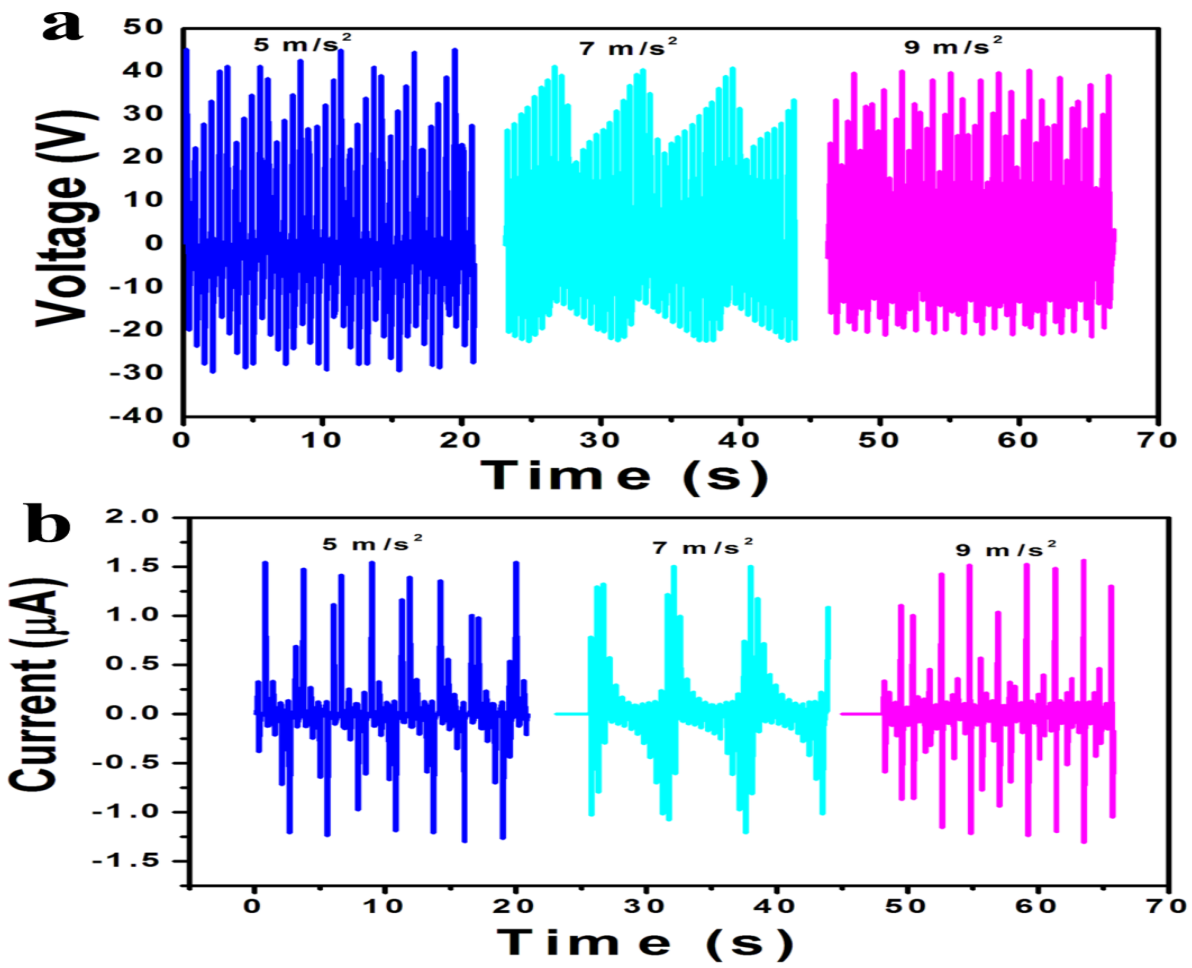

Figure 6.1.14(a, b) Open circuit voltage and short circuit current of S-AS upon various accelerations (5, 7 and 9 m/s^2) of shaft load (2 Kg) act on it.

In **Figure 61.13(a, b)**, the positive peaks correspond to the electrical response of S-AS, when an acceleration of fixed mass acting on device (ON condition) and negative peaks corresponds to the electrical response of S-AS device, when an acceleration of fixed mass releasing from the device (OFF condition). At an acceleration of 0.1 m/s^2, the average output voltage and current of S-AS are 5.49 V and 164.5 nA during acceleration ON condition and acceleration OFF condition, the average voltage and current are 5.1 V and 140.9 nA, respectively. Upon increasing the acceleration (ON condition) of fixed linear shaft mass from 0.1 to 0.5, 1, 2 3 and 5 m/s^2, the corresponding output voltages and currents are reached to 20.19, 30.66, 34.96,

38.7, 42.75 V and 441.1, 807.6, 1070, 1150, 1420 nA, respectively. Similar kind of behavior is observed for the acceleration OFF condition as shown in **Figure 6.1.13(a, b)**. Here, the working mechanism involved during acceleration of shaft ON and OFF condition is similar to the force acting on the C-NG device by pushing and releasing load with periodic manner. During the acceleration ON condition, the electric dipoles in the composite film will orient to the polar axis in a parallel manner and induce charges across the top and bottom of the device, resulting in a piezoelectric potential difference in perpendicular to the force direction. During acceleration OFF condition, the generated charge carriers will move back to their original direction. Figure .6c shows the cumulative peak-to-peak voltage response of S-AS during various accelerations of shaft ON and OFF conditions shows the linear output behavior between 0.5 to 5 m/s^2 accelerations. Beyond 5 m/s^2 acceleration, the S-AS output response such as voltage and current shows the decreasing trend behavior and discontinuous peak pattern as shown in **Figure 6.1.14(a, b).** It suggests that the proposed S-AS device is more applicable for low and medium range of accelerometer applications without using any additional sensory circuitry and battery energy. Further, the charge accumulation behavior in commercial 0.22 μF capacitor using the output of S-AS device upon various accelerations (0.1, 1 and 5 m/s^2) of shaft load was observed over a periodic time interval of 100 seconds as shown in **Figure 6.1.15d**. Upon increasing the accelerations from 0.1 to 1 and 5 m/s^2, the charge accumulation (Q) in 0.22 μF capacitor is 0.9829 μC to 2.217 μC and 4.579 μC during 100 seconds time interval. The evaluated stored energies ($U = \frac{1}{2}\frac{Q^2}{c}$) on a capacitor ($c = 0.22\ \mu F$) are 2.194 μJ, 0.011 mJ and 0.04763 mJ upon various input accelerations (0.1, 1 and 5 m/s^2) on S-AS device. The stability test of S-AS device was performed using the maximum acceleration (5 m/s^2) of shaft load (2 Kg) during the time interval ≈1200 seconds. The electrical response of S-AS device was measured after four months,

shows no degradation in output response. It suggests that, as-fabricated composite film based device has good stability and electrical response not disappeared over a period of time. **Figure 6.1.16a** shows the voltage stability of S-AS device presents no degradation and uncertainties in the output confirms good endurance of sensor.

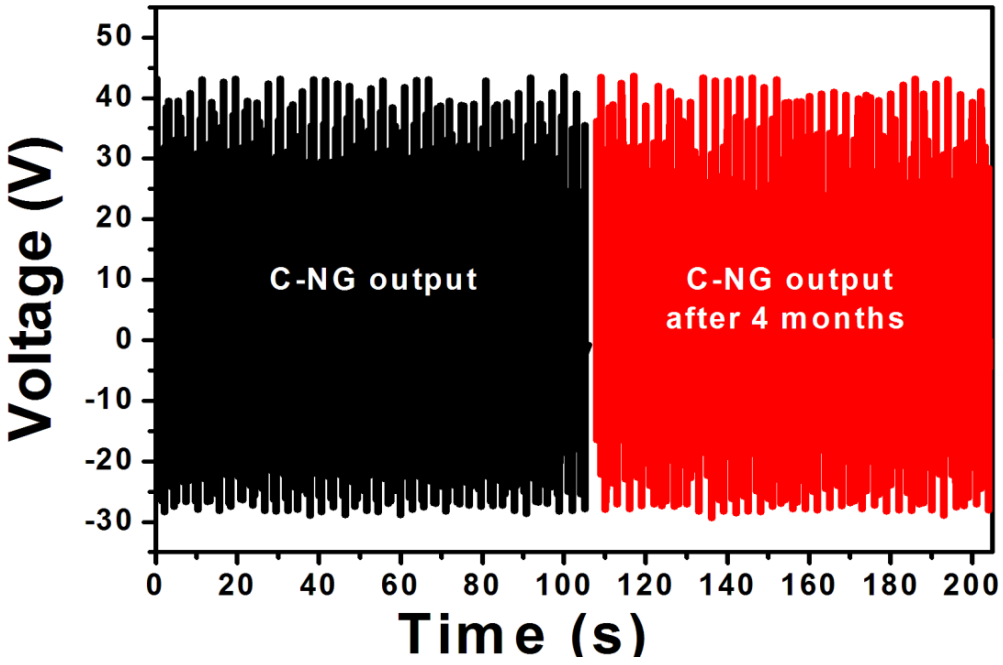

Figure 6.1.15 Open circuit voltage of C-NG device (or S-AS) up on the periodic acceleration of 5 m/s^2 of shaft mass 2 kg (i.e. 10 N).

Figure 6.1.16b represents the load resistance analysis and area power density calculations of C-NG device (30 V/V %) or S-AS sensor upon the acceleration of 5 m/s^2 of shaft load. The load resistance analysis was performed using the variable resistor unit ranging from 50 kΩ to 5 GΩ connected across the output terminals of C-NG device *via* full wave bridge rectifier circuit and corresponding output voltage (V) as shown in **Figure 6.1.16b** (black color). C-NG is a planar device structure and the corresponding delivered power depends on active area (A ≈ 2 cm x 1.5 cm) of device, external load matching resistance (R). The instantaneous area power density (P_a) of C-NG device can be evaluated using the equation[3]:

$$P_a = \frac{V^2}{A \times R} \qquad 2$$

The generated power density has increment behavior, when increasing the external load resistance across the C-NG device (upon 5 m/s^2 acceleration of shaft load) and is maximum (63.07 mW/m^2) at 100 MΩ load resistance as shown in **Figure 6.1.16b**. Beyond 100 MΩ load resistance, the generated C-NG device power density has decrement behavior. It confirms that 100 MΩ load resistance is the perfect load matching resistance to C-NG device for achieving the maximum powder density to drive low power electronic devices.

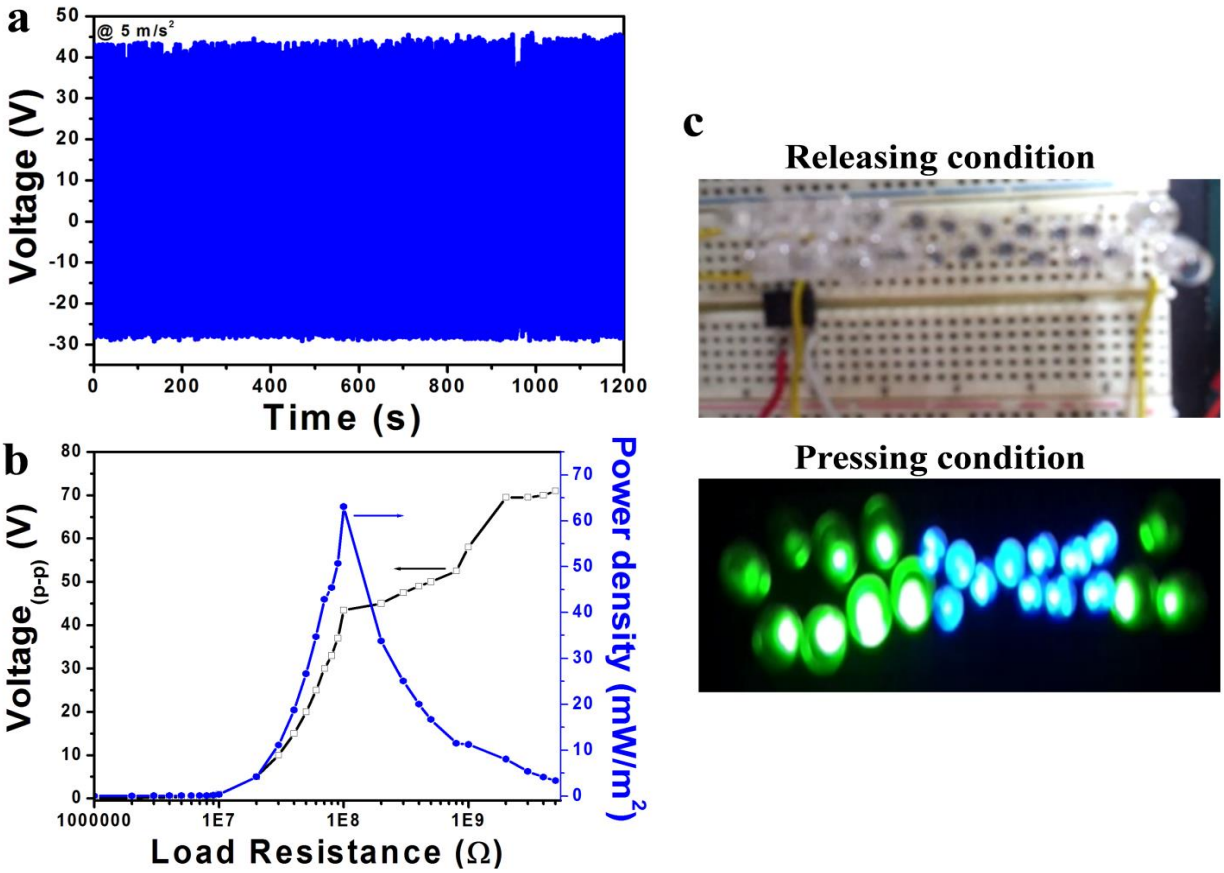

Figure 6.1.16 (a) Stability test of C-NG device (or S-AS) upon load at 5 m/s^2. **(b)** Load resistance analysis and powder density calculations of C-NG device upon the acceleration of 5 m/s^2 of load. **(c)** Turn OFF/ON of twenty-two commercial LEDs using the C-NG device output up on constant periodical mechanical force (10 N) OFF/ON conditions.

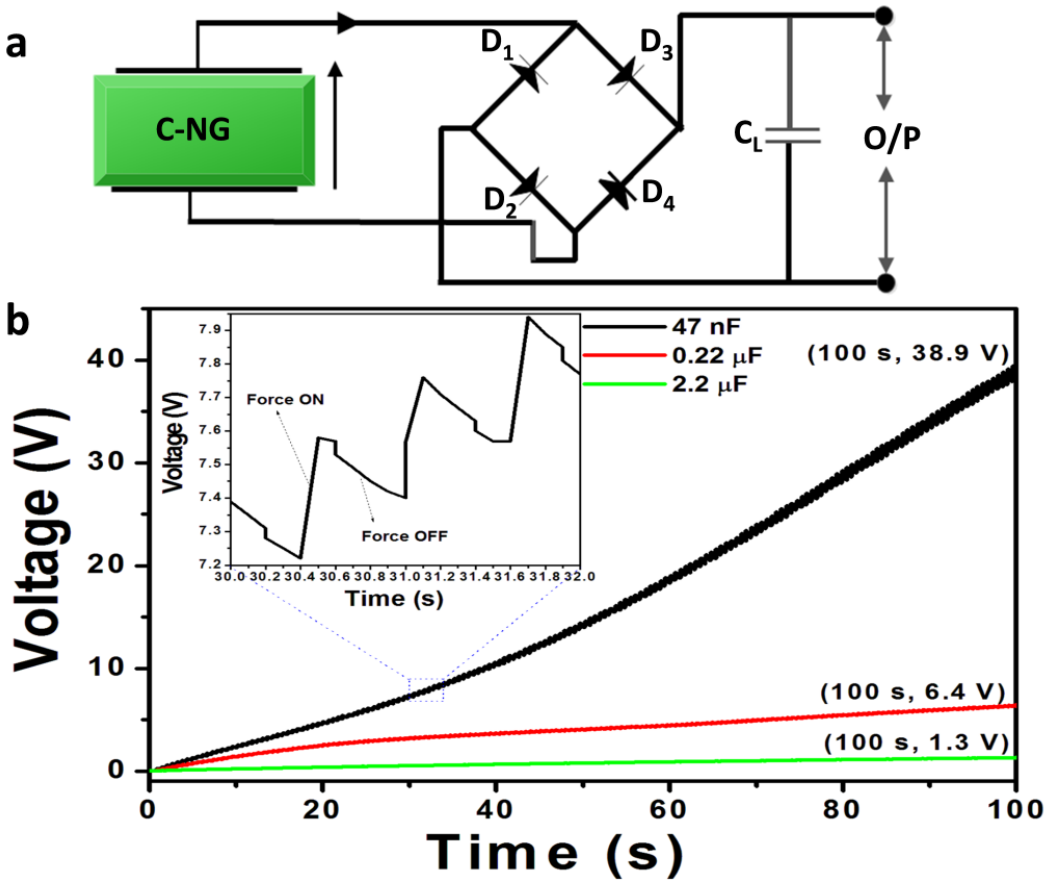

Figure 6.1.17 (a) Schematic diagram for the charging experiment using C-NG device (b) Charging behavior of various load capacitors (47 nF, 0.22 μF and 2.2 μF) across the C-NG device output up on the acceleration ≈5 m/s^2 of shaft mass 2 Kg.

The C-NG device output terminals were connected to various commercial capacitors (47 nF, 0.22 μF and 2.2 μF) *via* full wave bridge rectifier and analyzed the charging behavior as shown in **Figure 6.1.17a**. Initially, 38.9 V stored in 47 nF capacitance of the load capacitor during the time interval of 100 seconds under constant force on C-NG device. Next, the voltage stored in capacitor has been decreased from 38.9 V to 6.4 V and 1.3 V, when increasing the load capacitor value across C-NG device from 47 nF to 0.22 μF and 2.2 μF as shown in **Figure 6.1.17b**. The inset figure shows the magnified image of charging peak behavior during the force ON and OFF conditions on C-NG device. This behavior is well matched with the previous

reports and suggests that the C-NG device output is useful to charge the various commercial capacitors for driving the low power electronic device. In order to demonstrate the real time utility, twenty-two commercial LEDs (11 green and 11 blue) were connected in series and lit up using the generated electric power from C-NG device up on mechanical force ≈10 N as shown in **Figure 6.1.16c**. Therefore, sonication process with high micro tip amplitude derived pure PVDF, composite film have self-polarization behavior (high fraction of electroactive β-phase content) than the films derived by other methods such as stirring, phase inversion and electro-spinning processes, which eliminates the external electrical poling process and generates higher electrical output response upon the low mechanical pressure. This kind of devices itself can work as a standalone power sources and can also be useful as battery-free active sensor in various fields such as automobile industry, health and structural monitoring sectors.

6.4 Conclusions

In summary, a novel flexible and highly reliable SAS was demonstrated using the sonication process derived C-PVDF-AC film. The proposed sonication process of PVDF and composite films removes the additional step i.e. conventional electrical poling process. Here, AC fillers in PVDF stabilizes and improves the electroactive β-phase of PVDF and also act as electrical conduction path between the -CH_2-/-CF_2- electric dipoles of PVDF. Enhancement in dielectric constant and electrical conductivity of sonication derived PVDF and composite films demonstrate the improvement of electric dipole-dipole interactions and interfacial interaction between AC fillers and PVDF molecular chains. This attributes to the accumulation of mobile charge carriers at the interfaces between AC fillers and PVDF. Un-poled P-NG and C-NG (30 V/V %) devices generate high peak-to-peak output voltage and currents are (37.77 V, 299 nA) and (37.87 V, 0.831 μA) upon the applied pressure of ≈6 .6 kPa. No significant change in P-NG

device output was observed at poled and un-poled conditions. But the composite devices i.e. C-NG (30 V/V %) output has significant variation at electrical poling condition (V increases 30 % and I increases 96 %). The obtained instantaneous power density of C-NG device ≈63.07 mW/m^2 is sufficient to drive the low power electronic devices such as LEDs and display systems. Experimentally demonstrated that the C-NG device itself act as a SAS to measure the various accelerations of linear motor shaft load without using any external battery energy and additional sensory circuit. The charge accumulation behavior in commercial capacitor, driving 22 commercial LEDs using the C-NG device output and its stability test analysis were confirmed that C-NG is an unconventional energy harvesting approach to harvest the waste mechanical energy. All the above results, suggest that the proposed C-NG device can act as a standalone power source and can also work as an active sensor in various fields such portable electronics, implantable devices and automobile industries.

6.5 References

(1) J. Chun, K. Y. Lee, C. Y. Kang, M. W. Kim, S. W. Kim, J. M. Baik, *Adv. Funct. Mater*., 2014, **24**, 2038–2043.

(2) N. R. Alluri, B. Saravanakumar, S. J. Kim, *ACS Appl. Mater. Interfaces*, 2015, **7**, 9831–9840.

(3) X. Chen, J. Shao, N. An, X. Li, H. Tian, C. Xua, Y. Ding, ***J. Mater. Chem. C* 2015, 3,** 11806-11814.

(4) B. Saravanakumar, K. Thiyagarajan, N. R. Alluri, S. SoYoon, K. Taehyun, Z.H. Lin, S.J. Kim, *Carbon* 2015, **84**, 56–65.

(5) N. R. Alluri, S. Selvarajan, A. Chandrasekhar, S. Balasubramaniam, J. H. Jeong, S. J. Kim, *Sens. Actuator B-Chem* 2016, **237**, 534–544.

(6) S. Selvarajan, N. R. Alluri, A. Chandrasekhar, S. J. Kim, *Sens. Actuator B-Chem*, 2016, **234**, 395–403.

(7) S. Xu, Y. Qin, C. Xu, Y. Wei, R. Yang, Z. L. Wang, *Nat. Nanotechnol*. 2010, **5**, 366–373.

(8) Y. Yang, W. Guo, K. C. Pradel, G. Zhu, Y. Zhou, Y. Zhang, Y. Hu, L. Lin, Z. L. Wang, *Nano Lett.* 2012, **12**, 2833–2838.

(9) Z. L. Wang, ***Farad. Discuss*. 2014, 176**, 447-458.

(10) A. Chandrasekhar, N. R Alluri, B. Saravanakumar, S. Selvarajan, S. J. Kim, *ACS Appl. Mater. Interfaces 2016, **8**,* 9692–9699.

(11) Y. Zhao, D. Maurya, A. Miner, G. A. Khodaparast, S. Priya, *Energy Harvesting and Systems*, 2015, **2**, 55–62.

(12) M. Law, L. E. Greene, J. C. Johnson, R. Saykally, P. Yang, *Nat. Mater*. 2005, **4**, 455-459.

(13) J. K. Han, D. H. Jeon, S. Y. Cho, S. W. Kang, S. A. Yang, S. D. Bu, S. Myung, J. Lim, M. Choi, M. Lee, M. K. Lee, *Sci. Rep*. 2016, **6**, 1-8.

(14) M. K. Gupta, J. H. Lee, K. Y. Lee, S. W. Kim, *ACS Nano*, 2013, **7**, 8932–8939.

(15) K. I. Park, S. Xu, Y. Liu, G. T. Hwang, S. J. L. Kang, Z. L. Wang, K. J. Lee, *Nano Lett*. 2010, **10**, 4939–4943.

(16) Z. Wang, Y. Zhang, S. Yang, Y. Hu, S. Wang, H. Gu, Y. Wang, H. L. W. Chan, J. Wang, *ACS Appl. Mater. Interfaces* 2015, **7**, 4921−4927.

(17) S. Paria, S. K. Karan, R. Bera, A. K. Das, A. Maitra, B. B. Khatua, *Ind. Eng. Chem. Res. 2016*, ***55***, 10671–10680.

(18) Y. F. Lin, J. Song, Y. Ding, S. Y. Lu, Z. L. Wang, *Appl. Phys. Lett*. 2008, **92**, 022105-022107.

(19) Y. Yu, H. Sun, H. Orbay, F. Chen, C. G. England, W. Cai, X. Wang, *Nano Energy* 2016, **27**, 275–281.

(20) L. Xing, Y. Nie, X. Xue, Y. Zhang, *Nano Energy* 2014, **10**, 44–52.

(21) C. Chang, V. H. Tran, J. Wang, Y. K. Fuh, L. Lin, *Nano Lett.* 2010, **10**, 726–731.

(22) X. Chen, H. Tian, X. Li, Y. Zhou, J. Shao, Y. Ding, N. An, ***Nanoscale* 2015, 7,** 11536-11544.

(23) D. Mandala, K. Henkelb, D. Schmeißerb, ***Phys. Chem. Chem. Phys*. 2014, 16,** 10403-10407.

(24) P. Martins, A.C. Lopes, S. L. Mendez, *Prog. Polym. Sci*. 2014, **39**, 683–706.

(25) M. Sharma, G. Madras, S. Bose, *Phys.Chem.Chem.Phys*. 2014, **16**, 14792-14799.

(26) P. Martins, C. Caparros, R. Gonçalves, P. M. Martins, M. Benelmekki, G. Botelho, S. L. Mendez, *J. Phys. Chem. C* 2012, **116**, 15790−15794.

(27) X. Li, S. Chen, K. Yao, F. E. H. Tay, *J. Polym. Sci. Part B Polym. Phys*, 2009, **47**, 2410-2418.

(28) R. Moradi, J. K. Sabet, M. S. Niassar, M. A. Koochaki, *Polymers*, 2015, 7, 1444-1463.

(29) J. N. Pereira, V. Sencadas, V. Correia, J. G. Rocha, S. L. Méndez, Sens. Actuator A-Phys, 2013, **196**, 55-62.

(30) J. Chang, L. Lin, *RSC Nanoscience and Nanotechnology* 2015, January (**35**), 142-173.

(31) B. S. Lee, B. Park, H. S. Yang, J. W. Han, C. Choong, J. Bae, K. Lee, W. R. Yu, U. Jeong, U-In Chung, J. J. Park, O. Kim, *ACS Appl. Mater. Interfaces*, 2014, **6**, 3520–3527.

(32) S. Garain, S. Jana, T. K. Sinha, D. Mandal, *ACS Appl. Mater. Interfaces* 2016, **8**, 4532–4540.

(33) S. Chen, X. Li, K. Yao, F. E. H. Tay, A. Kumar, K. Zeng, *Polym. J*. 2012, **53**, 1404-1408.

(34) N. Soin, D. Boyer, K. Prashanthi, S. Sharma, A. A. Narasimulu, J. Luo, T. H. Shah, E. Siores, T. Thundat, *Chem. Commun.* 2015, **51**, 8257-8260.

(35) A. A. Issa, M. A. A. S. Al-Maadeed, M. Mrlík, A. S. Luyt, *J. Polym. Res*. 2016, **23**, 232.

(36) S. K. Karan, D. Mandal, B. B. Khatua, ***Nanoscale* 2015, 7,** 10655-10666.

(37) T. K. Sinha, S. K. Ghosh, R. Maiti, S. Jana, B. Adhikari, D. Mandal, S. K. Ray, *ACS Appl. Mater. Interfaces, 2016, **8**,* 14986–14993.

(38) W. L. Ong, M. Gao, G. W. Ho, *Nanoscale*, 2013, **5**, 11283–11290.

(39) S. Jana, S. Garain, S. K. Ghosh, S. Sen, D. Mandal, *Nanotechnology*, 2016, **27,** 445403-445114.

(40) O. D. Jayakumar, B. P. Mandal, J. Majeed, G. Lawes, R. Naik, A. K. Tyagi, *J. Mater. Chem. C* 2013, 1, 3710–3715.

(41) S. K. Karan, R. Bera, S. Paria, A. K. Das, S. Maiti, A. Maitra, B. B. Khatua, *Adv. Energy. Mater*. 2016, **6**, 1601016-1601027.

(42) L. Li, M. Zhang, M. Rong, W. Ruan, *RSC Adv*. 2014, **4**, 3938–3943.

(43) S. K. Ghosh, A. Biswas, S. Sen, C. Das, K. Henkel, D. Schmeisser, D. Mandal, *Nano Energy*, 2016, **30**, 621–629.

(44) S. K. Ghosh, T. K. Sinha, B. Mahanty, D. Mandal, *Energy Technol*. 2015, **3**, 1190-1197.

(45) Y. Sui, W. T. Chen, J. J. Ma, R. H. Hu, D. S. Liu, *RSC Adv*. 2016, **6**, 7364–7369.

(46) Y. Li, Q. Zhang, J. Zhang, L. Jin, X. Zhao, T. Xu, Sci. Rep. 2015, **5**, 1-10.

Chapter VII

Self-powered muscle monitoring system/air-pressure sensor based on PDMS/(BaCa)(SnTi)O_3 hybrid film nanogenerators

7.1 Highlights

- A feasible groove technique developed to fabricate adaptable HS-CSPNG devices to monitor all non-linear motions of human body movements.
- Single HS-CSPNG generates high electrical response 130 V and 0.8 μA.
- Demonstrated self-powered muscle monitoring system using HS-CSPNGs.

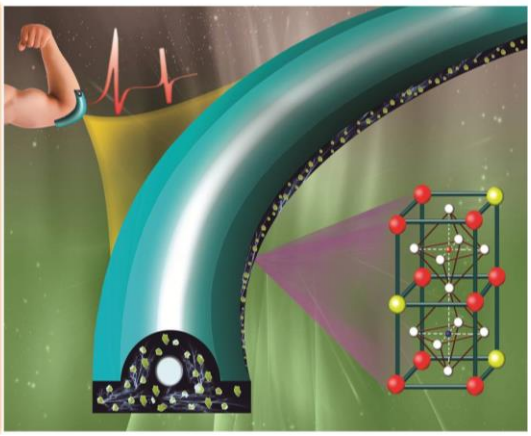

7.2

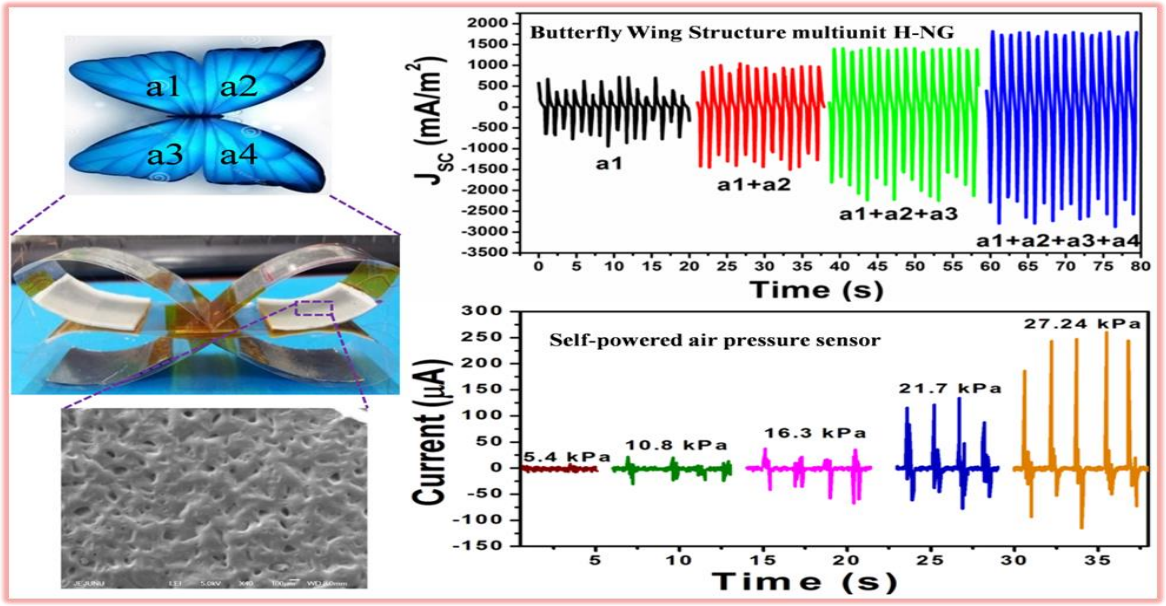

7.1 Groove technique derived adaptable piezoelectric hemispherical composite strips for self-powered muscle monitoring system

7.1.1 Introduction

Smart adaptable/wearable technologies attract immense attention due to its broad range of applications in various fields such health monitoring electronic devices, security surveillance systems, pollution/carbon-free unconventional energy harvesting technologies and smart textile electronics[1-5]. Currently, existing wearable technology uses an external power source unit (rechargeable battery sources) to drive the device, sensing unit and other communication components. The use of battery source increased the complexity (typical electrical wiring) in circuit design, overheating issues in components, limited lifetime and restricted for a broad range of applications. To overcome these issues, many research groups showed the possibility to replace an external battery using various types of instantaneous/continuous power generating units. Piezoelectric nanogenerator (P-NG)[6], triboelectric nanogenerator (T-NG)[5], thermoelectric generator (TG), solar cells[4] and biofuel cells[3] generates electricity by the use of various mechanical motions from the human body movements, fluid/wind motions, vibrations from the machine parts and temperature gradient. The generated energy from these power sources is cost-effective, eco-friendly and pollution-free energy. Sometimes, NG device itself can work as sustainable power source and sensing unit to measure various physical, chemical, biological, optical stimuli named as self-powered sensor or system (SPS)[1-9]. Over the last decade, various prototypes of SPS using planar P-NG technology were reported to monitor the human body part movements such as a finger, foot, elbow, knee joint, neck rotation and inhale/exhale breathe conditions[9-13]. Existing planar P-NG devices are suitable to measure one or two body part movements, but not suitable to measure all or maximum human body part movements due to the

lack of adaptability/flexibility in shape concerning the shape of the human body part. Moreover, the sensing, monitoring capability of P-NG was too poor due to the low piezoelectric performance of materials used for the device. All these things demonstrate that the traditional planar P-NG technology restricted to transfer on typical non-linear surfaces and not possible to harness/measure the non-linear motions[9-15]. A cost-effective, eco-friendly fabrication technology is required to prepare adaptable/flexible composites for adaptable P-NG devices with a high degree of flexibility in shape, biocompatibility, large-scale designing, enough power generation, and can also have a capability to monitor or sense all human body parts without using external storage components.

In this work reports the first use of groove technique for fabricating the hemispherical shaped flexible piezoelectric composite strips (HS-FPCSs) with multiple in lengths. Adaptable hemispherical shaped-composite strip based piezoelectric nanogenerator (HS-CSPNG) was fabricated using the flexible adhesive bandage (one side) as a base substrate, HS-FPCS acts as a piezoelectric layer, Ti-metal wire as inner electrode and silver (Ag) layer acts as a top electrode, respectively. HS-FPCS consists of one side hemispherical shape, the rectangular flat base is on another side, and the center part is Ti-metal wire acts as an inner electrode as well as supporting material to hold the composite material. This method offers the working mechanism related to the electric dipole orientation perpendicular to the plane of HS-FPCS, and scalable lengths of HS-FPCS was designed using cost-effective groove technique. Contrary to literature reports, this HS-CSPNG utilized as adaptable, bendable and on-demand parallel/series integration of HS-CSPNGs.

7.1.2 Experimental Methods

7.1.2.1 Synthesis of $(BaCa)(SnTi)O_3$ nanoparticles

Piezoelectric NPs such as $Ba_{0.7}Ca_{0.3}TiO_3$ (BCT), $BaSn_{0.12}Ti_{0.88}O_3$ (BST) and $0.3Ba_{0.7}Ca_{0.3}TiO_3$-$0.7BaSn_{0.12}Ti_{0.88}O_3$ (0.3BCT-0.7BST) were fabricated using a high temperature SSR method. The raw materials $BaCO_3$ (99.95% purity, High purity chemicals Ltd.), TiO_2 (98% purity, Daejung), SnO_2 (99.99% purity, Sigma–Aldrich) and $CaCO_3$ (99.99% purity, High purity chemicals Ltd.) were weighed to obtain the desired atomic ratio of the piezoelectric system. Initially, the raw materials were mixed homogeneously by manually grinding for 1 h in a mortar and pestle with ethanol as the medium. Heating the mixed powder in an alumina crucible at 1,300 °C for 3 h at a heating rate of 3.33 °C/min provided the desired crystalline quality. After cooling, the sample was again manually ground for 30 min.

7.1.2.2 Fabrication of hemispherical composite strips

Figure 7.1.1 shows the schematic diagram of cost-effective groove technique for the fabrication of HS-FPCSs made up of high-performance $0.3Ba_{0.7}Ca_{0.3}TiO_3$-$0.7BaSn_{0.12}Ti_{0.88}O_3$ nanoparticles (designated as BCST NPs) into polydimethylsiloxane (PDMS) matrix. The BCST NPs have high piezoelectric coefficient (d_{33}) is 530 pC N^{-1}, and planar electromechanical coupling coefficient (k_p) is 55 %, respectively[16]. The fabrication procedure consists of five major steps: (i) Generation of pre-defined hemispherical groove shape on flat thick PET sheet by the removal of required part from the PET surface (ii) Placing the Ti-metal wire (Ø ≈0.1 mm) exactly at the center of groove by the support of rigid stands. This Ti-metal wire has a dual purpose, one it will act as an inner electrode to obtain the accumulated charge carriers during the mechanical force act on it and second is supporting wire to retain the formed hemispherical shape without any bending curvatures. (iii) Pouring the limited amount of as-prepared

PDMS/BCST NPs (10 wt %) composite solution into that groove. (iv) Heat treatment of as-poured composite solution along with the groove at 70 °C for 30 minutes for achieving good solidification (v) As-obtained product peel off from the PET surface called as HS-FPCS and its optical photograph shown as inset image.

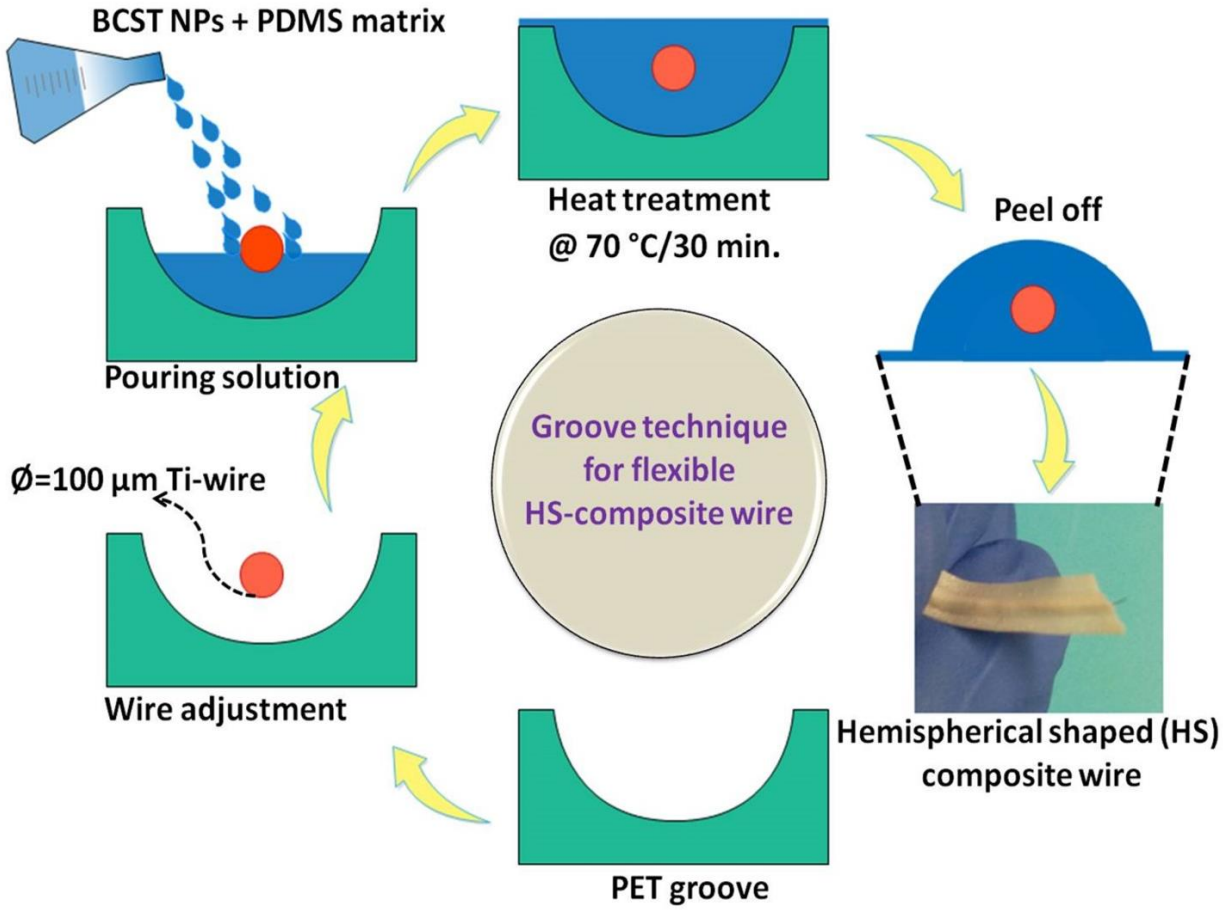

Figure 7.1.1 Schematic representation of groove technique for the fabrication of HS-FPCSs and the inset shows a digital photograph of as-fabricated single HS-FPCS.

7.1.2.3 Fabrication of adaptable hemispherical composite strips PNG

The fabrication procedure of adaptable HS-CSPNG device shown in **Figure 7.1.2**. Here, the HS-FPCS transferred on to a one-sided adhesive bandage and attached with the conductive glue. The left inset images of **Figure 7.1.2** demonstrate the feasible fabrication of multiple lengths of HS-FPCS and its flexibility demonstration using the light twist and full twist conditions. The top

surface of the strip coated with the Ag electrode using the brush coating technique serves as a top electrode and inner Ti-metal wire used as a second electrode to collect the accumulated charge carriers across the outer/inner surfaces. Finally, the whole device packed with the flexible PDMS stamp without the existence of air gap between the layers, which will minimize the triboelectric contribution. The inset image of **Figure 7.1.2** (right) shows the as-fabricated HS-CSPNG device and can be easily attached to any contour (or non-linear) surfaces to harness or monitor the mechanical motions.

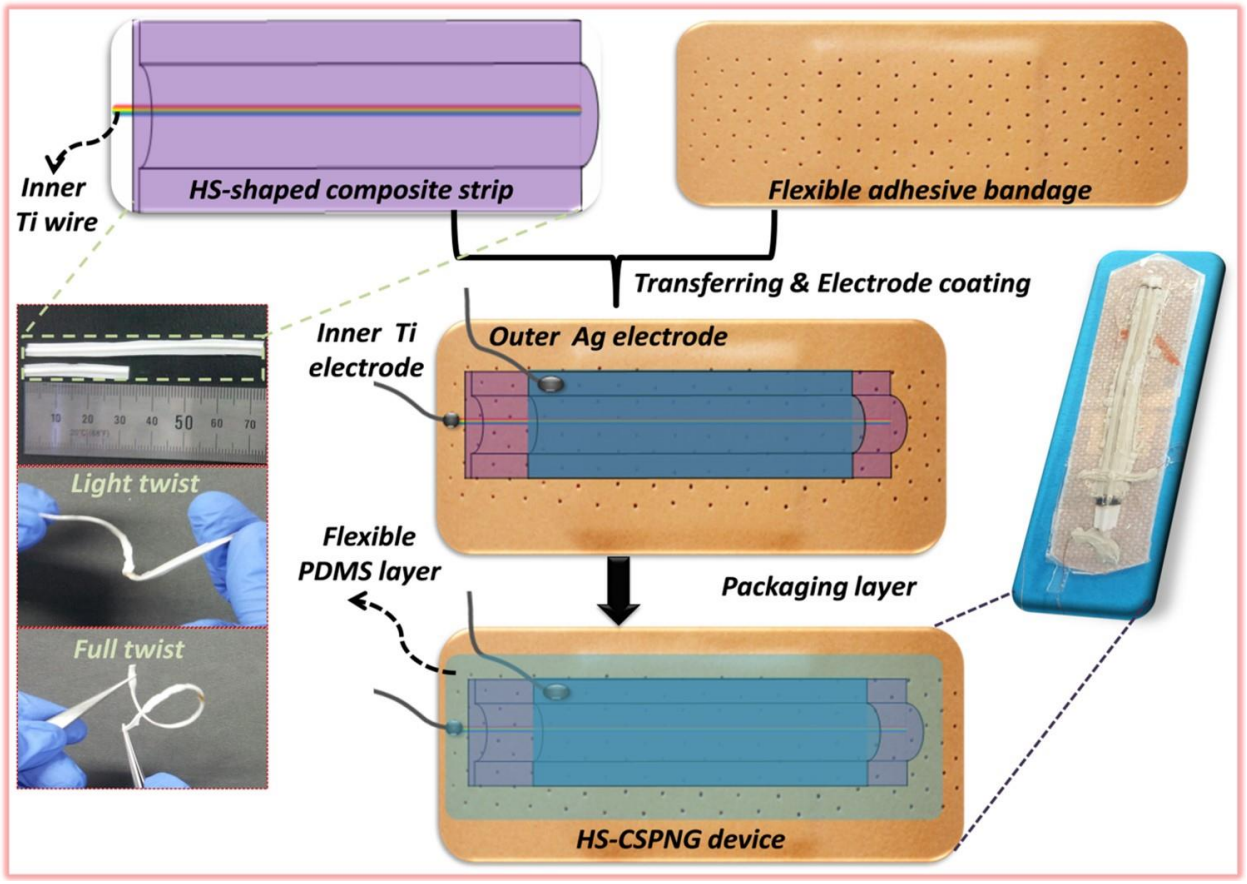

Figure 7.1.2 Schematic representation of the adaptable HS-CSPNG device and the right inset shows the digital photograph of as-fabricated adaptable HS-CSPNG. The left inset shows the demonstration of feasible fabrication of multiple lengths of HS-FPCS and its flexibility showed using the light twist and full twist conditions.

7.1.3 Results and Discussion

7.1.3.1 Structural and ferroelectric hysteresis loop analysis

High quality nanocrystalline particles such as BST, BCT and 0.3BCT-0.7BST nanoparticles (designated as BCST NPs) were synthesized using the high temperature (1300 °C/2 h) solid state reaction method. **Figure 7.1.3(a, b)** shows the XRD patterns of as-prepared NPs and the corresponding presence of multiple phases, tetragonal (T), orthorhombic (O), and rhombohedral (R), was confirmed by the splitting of peaks at 45–46° and 56°. Here, BCT NPs pattern confirms that the intensity of the $(200)_T$ peak was greater than that of the $(002)_T$ peak, which confirms the T-phase (matched with PDF#05-0626). BST NPs pattern confirms that the $(200)_T$ and $(002)_T$ peaks merged into a broad peak $(202)_R$, which determines the existence of the R-phase (matched with PDF#85-0368). These phase variations were attributed to the substitution of foreign atoms having different ionic radii, i.e., Sn^{4+} (0.69 Å) and Ca^{2+} (1.34 Å), into Ti^{4+} (0.605 Å) and Ba^{2+} (1.61 Å) atomic sites of the $BaTiO_3$ (BTO) lattice, which created internal lattice strains in various directions. The dual system BCST NPs pattern confirms the existence of multiple phases i.e. the splitting of peaks at 45–46° and 56°, which is well matched with the reference pattern ID (PDF#81-2200).

Here, BCST NPs synthesized by high-temperature solid-state reaction (1300 °C/2 h) having the multiphase coexistence of BCST NPs such as major tetragonal (T) and minor orthorhombic (O) confirmed by the Raman spectroscopic data as shown in the inset of **Figure 7.1.4**. The presence of longitudinal as well as transverse vibrational active mode at peak position 312 cm^{-1} referring to the major T-phase and broadband discontinuously drops between the peak positions 240–270 cm^{-1} referring to the T/O phase transition[17]. Next, as-prepared BCST NPs mixed into PDMS matrix with particular weight ratio, i.e., 10 wt % and its phase confirmation was

evaluated by the Raman spectroscopy as shown in **Figure 7.1.4.** Pure PDMS spectra have major characteristic peaks at 2972, 2911, 713, 688, 620 494 cm^{-1} corresponds to various vibration modes such as CH_3 asymmetric stretching, CH_3 symmetric stretching, Si-C symmetric stretching, Si-CH_3 symmetric stretching, Si-C symmetric stretching and Si-O-Si symmetric stretching, respectively. Remaining peaks at 1100, 2100 to 2200 cm^{-1} represents the base glass substrate peaks. The composite Raman spectra show the combined BCST NPs, and PDMS matrix major active modes demonstrate the successful formation of composite strip. Here, the piezoelectric phase of BCST NPs was not changed even after processing with the PDMS polymer.

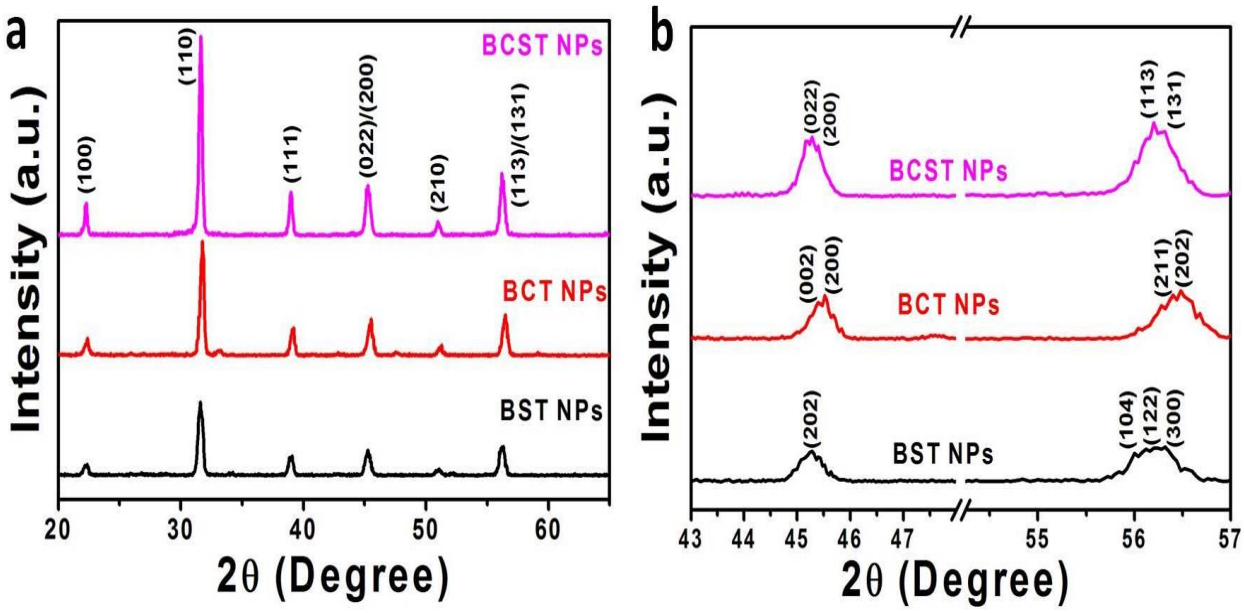

Figure 7.1.3 (a, b) X-ray diffraction patterns of the as-prepared BST, BCT and BCST NPs.

Figure 7.1.5a shows the FE-SEM image of the top surface morphology of HS-FPCS shows the existence of slight roughness which is due to the good distribution of the BCST NPs in PDMS matrix (inset figure). **Figure 7.1.5b** represents the cross-sectional view of HS-FPCS demonstrates the existence of inner Ti-metal wire electrode at the center of the hemispherical PDMS/BCST NPs composite zone.

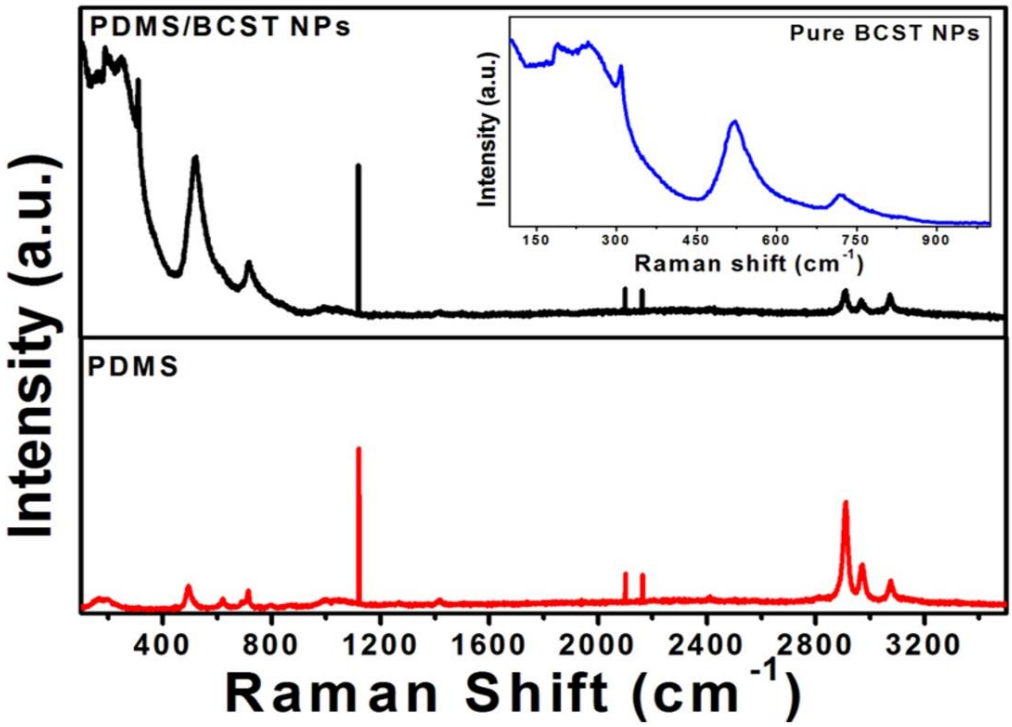

Figure 7.1.4 Raman patterns of pure PDMS and BCST NPs/PDMS composite strip. The inset shows the Raman pattern of pure BCST NPs.

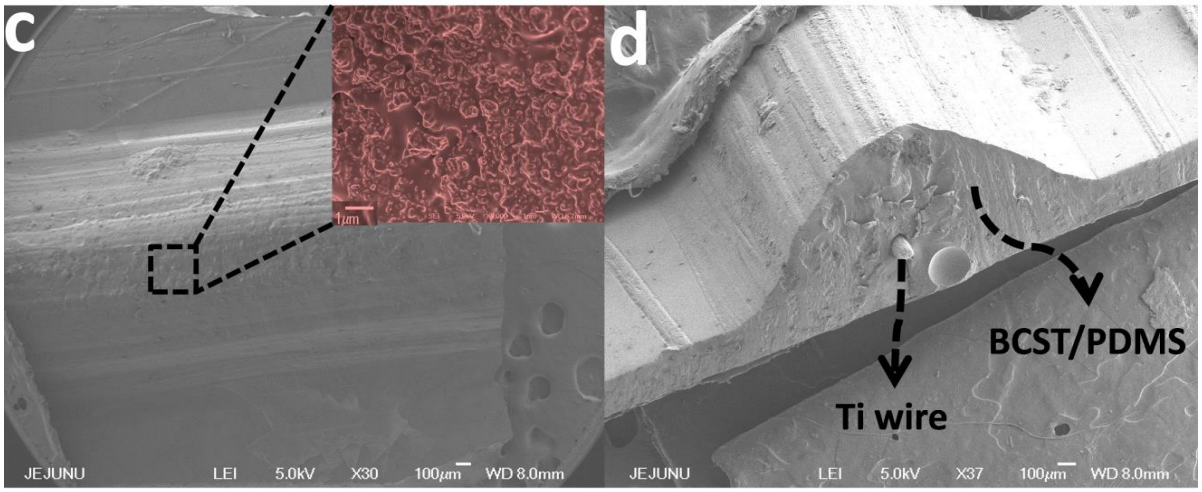

Figure 7.1.5 (a, b) Surface morphology and cross-sectional FE-SEM image of as-fabricated HS-FPCS. The inset shows the good surface roughness of composite strip.

7.1.3.2 Ferroelectric hysteresis loop and elemental composition analysis

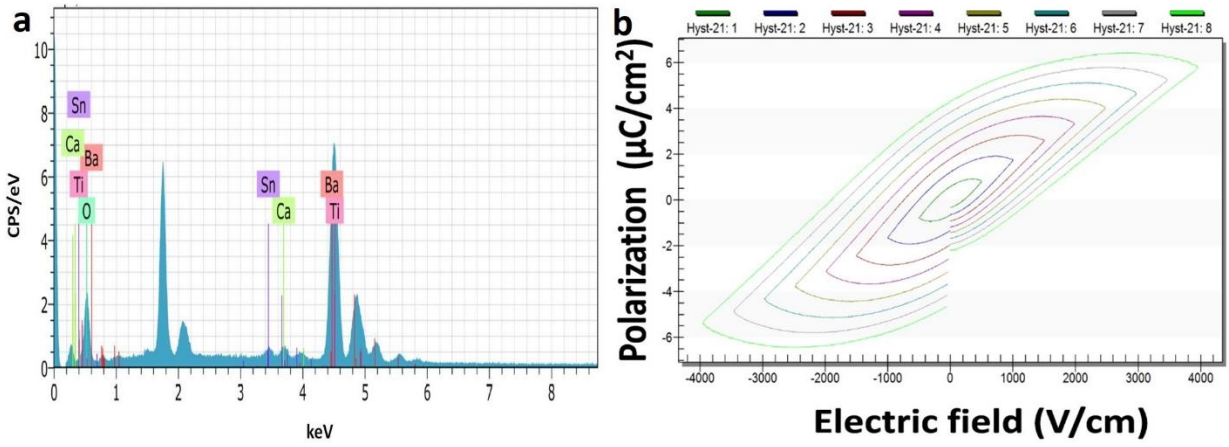

Figure 7.1.6 (a) Energy dispersive X-ray spectroscopy analysis of BCST NPs. **(b)** Polarization vs electric field response of BCST NPs pellet.

The existence of all chemical elements (Ba, Ca, Sn, Ti, and O) in BCST NPs confirmed by performing the energy dispersive X-ray spectroscopy analysis as shown in **Figure 7.1.6a**. The saturated polarization is ≈6.3 μC/cm^2 (at 4 kV/cm) obtained from the polarization *vs* electric field measurement of BCST pellet as shown in **Figure 7.1.6b.**

7.1.3.3 Electrical response analysis of hemispherical composite strips based PNG device

A periodic biomechanical hand force on HS-CSPNG device generates the piezoelectric potential generation. Fabricated three similar HS-CSPNG devices at a time named as HS-CSPNG 1, HS-CSPNG 2 and HS-CSPNG 3 and the corresponding obtained piezoelectric potentials shown in **Figure 7.1.7a**. The generated average peak-to-peak open circuit voltage ($V_{OC\ (P\text{-}P)}$) for all HS-CSPNG devices lies between the ranges of 100 to 130 V, respectively. Similarly, the generated average peak-to-peak short-circuit current ($I_{SC(P\text{-}P)}$) for three devices upon biomechanical periodic hand force is 800 nA as shown in **Figure 7.1.7b.** It demonstrates that as-fabricated HS-CSPNG devices based hemispherical composite strips are potential candidates to convert the waste bio-mechanical energy into useful electrical energy.

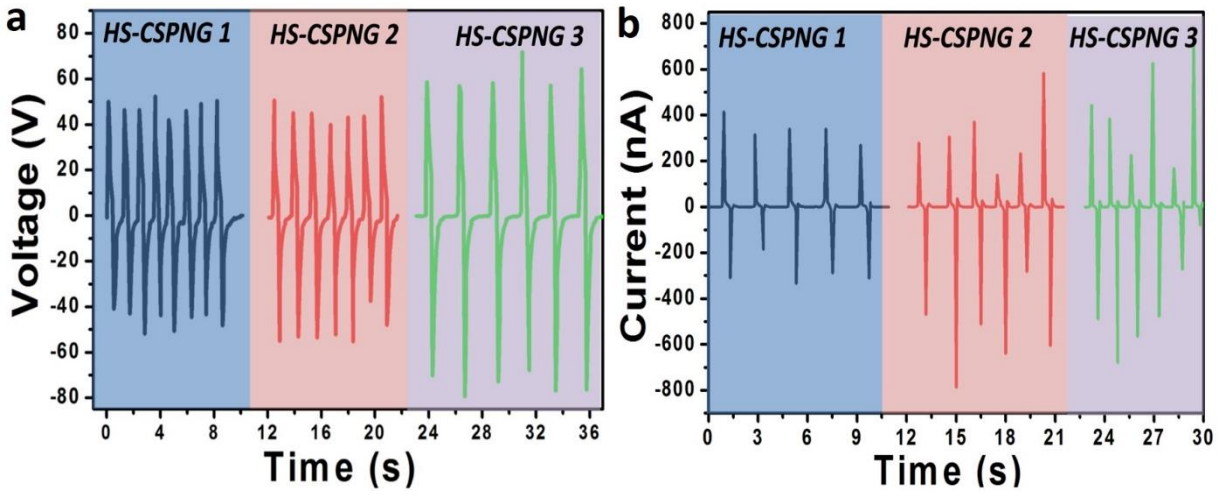

Figure 7.1.7 (a, b) Comparison of output voltage/current signals of different adaptable HS-CSPNGs during periodic bio-mechanical hand force.

Switching-polarity test of HS-CSPNG was performed using biomechanical hand force to confirm that the generated electrical output is coming from the device, not from any external sources. **Figure 7.1.8 (a, b)** shows the generated I_{SC} of HS-CSPNG device during forward/reverse connections upon hand force. Good phase shift was observed between the output signals of HS-CSPNG device during forward/reverse connections demonstrates that the generated electrical output is coming from the device, not from any external sources. The working mechanism of HS-CSPNG depends on three major steps: one is no force condition but poled HS-CSPNG device (8 kV for 24 h), second is a perpendicular force acting on the device, and third is force removal condition, respectively. In no force condition, the poled HS-CSPNG device has permanent polarization, which is due to the alignment of a maximum number of electric dipoles in BCST NPs/PDMS composite strip during external electrical poling process. But no charge carriers are transferred to the outer/inner electrodes of the device and the generated electrical output is zero, as schematically shown in **Figure 7.1.9a(i).** Whenever a perpendicular force acts on the devices, all existed electric dipoles in BCST NPs/PDMS composite strip was aligned into one direction and a potential difference created between the

accumulated positive/negative charge carriers on composite strip surface. Which is collected inductively through the electrodes, and the generated electrons are moving in the clockwise direction as schematically shown in **Figure 7.1.9a(ii)**. During the force released condition, the excited electric dipoles in HS-CSPNG device gets relaxed. The accumulated charge carriers will move back to the original position, and generated electrons will move in the anti-clockwise direction as schematically shown in **Figure 7.1.9a (iii)**.

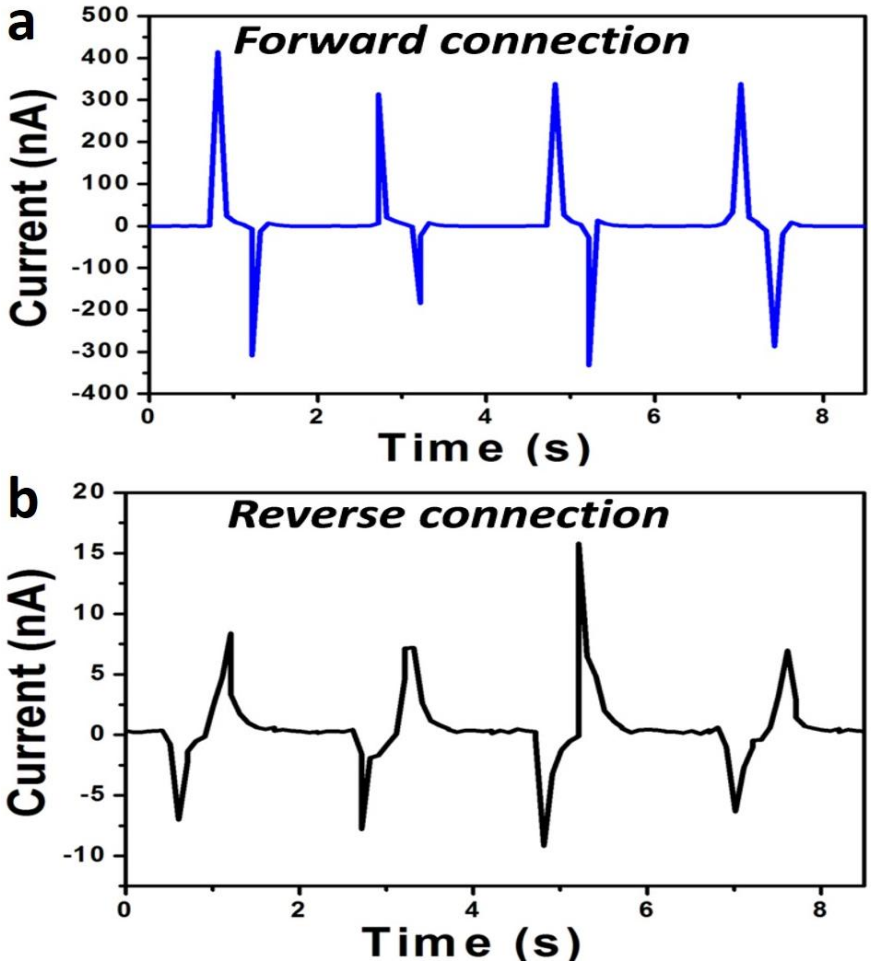

Figure 7.1.8 (a, b) Switching polarity test represents the perfect phase reversal between the output current signals of HS-CSPNG upon hand force (forward/reverse connections).

Next, HS-CSPNG device tested under the periodic mechanical force (2 N) generated by the linear motor (company name) and the corresponding $V_{OC} \approx 52$ V and $I_{SC} \approx 600$ nA shown in

Figure 7.1.9(b, c). The load resistance analysis and evaluation of instantaneous area power density of HS-CSPNG device upon mechanical force 2 N shown in **Figure 7.1.9d**. Here, the V_{OC} value decreases whenever the load resistance value decreased from 1 GΩ to 1 kΩ across the HS-CSPNG output terminals. The instantaneous area power density (P_A) was calculated using the equation $P_A=((V_{OC})^2/R_L x A)$[11] and the achieved maximum power density $P_{A,max}\approx 0.8\ mW/m^2$ at the load resistance value is 10 MΩ. Remaining all other resistances, the achieved P_A is less than the $P_{A,max}$ and the obtained load matching resistance for practical applications is 10 MΩ. **Figure 7.1.9e** shows the durability test of HS-CSPNG device upon 2 N mechanical force and demonstrates that no change in the output voltage over the interval of 1500 seconds.

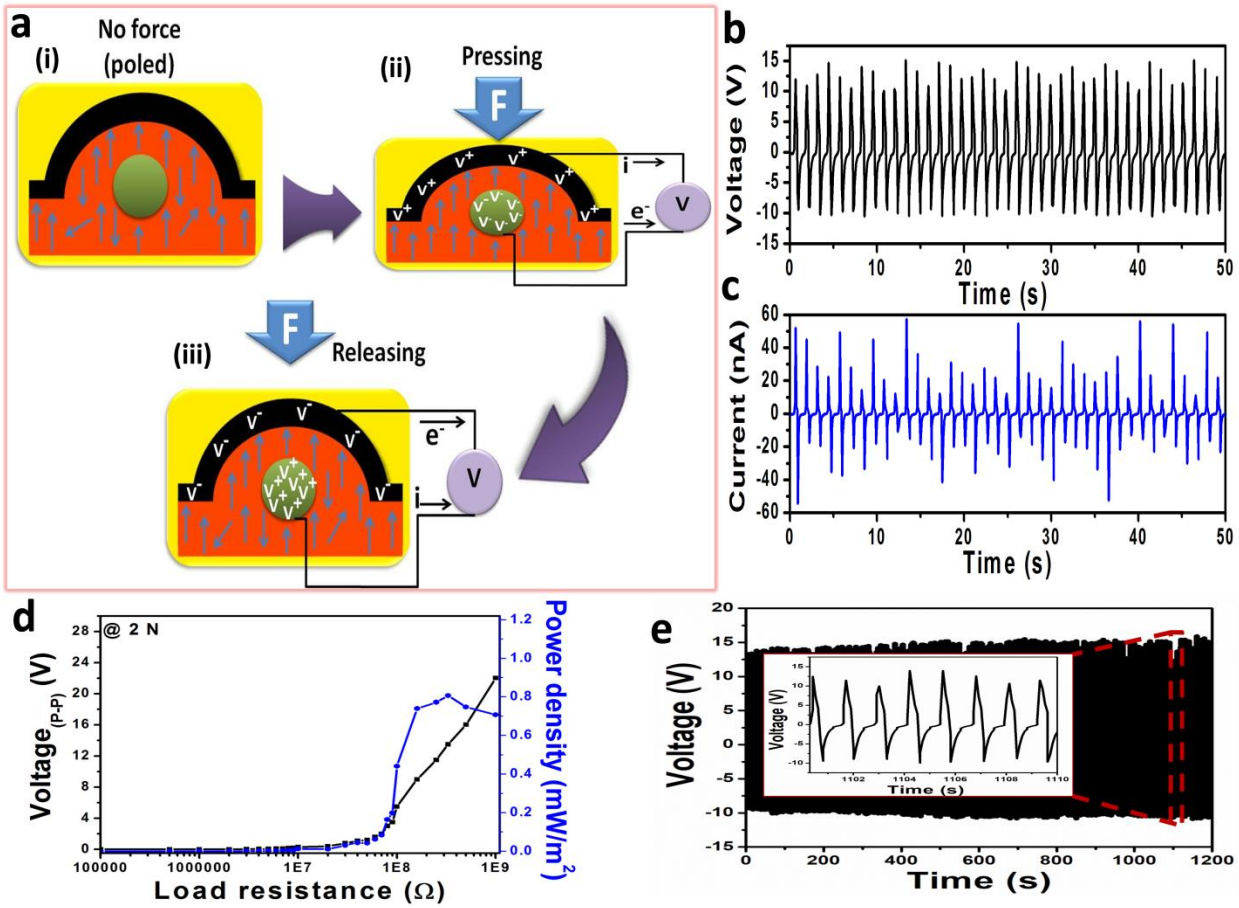

Figure 7.1.9 (a) Schematic representation of working mechanism of the adaptable HS-CSPNG device under various conditions such as no force (poled), pressing and releasing conditions. **(b-d)** The output voltage, current, load resistance analysis, and instantaneous area power density of

adaptable HS-CSPNG upon periodic acceleration (1 ms^2) of shaft load 2 N. **(e)** Stability test of adaptable HS-CSPNG upon 2 N over a periodic time interval of 1200 seconds. The inset shows the enlarged image of the output voltage at 1100 seconds.

It suggests that the as-fabricated HS-CSPNG device is highly stable and practically suitable for real-time monitoring applications. For that flexible energy harvesting glove (FEHG) was implemented using the as-fabricated three HS-CSPNG devices and tested to harness the waste biomechanical energy under two different conditions such as perpendicular/bending force to the HS-CSPNG. **Figure 7.1.10a** shows the photographs of FEHG at various conditions such as no force, single finger force on HS-CSPNG 1, two fingers force on two devices (HS-CSPNG 1 and HS-CSPNG 2) at a time, three fingers force on three devices (HS-CSPNG 1, HS-CSPNG2 and HS-CSPNG 3) at a time. The combined electrical output of three HS-CSPNG devices was obtained by the series connection between them as shown in **Figure 7.1.10b**. **Figure 7.1.10(c, d)** represents the generated $V_{OC\ (P\text{-}P)}$ and $I_{SC\ (P\text{-}P)}$ of FEHG upon finger force acting perpendicular to the HS-CSPNG devices. It generates average $V_{OC\ (P\text{-}P)}$ ≈10 V for a single device, 30 V for two devices and 50 V for three devices, but in the average $I_{SC(P\text{-}P)}$ case generates 30 nA for all devices configurations. It satisfies the series connection between the three HS-CSPNG devices and well matches with the previous reports. Similarly, the bending force conditions (ON/OFF) generated on FEHG by placing the hand gripper one handle against to the palm and performed the squeeze/release exercise. **Figure 7.1.10e** shows the photographs of the hand gripper, squeeze/release conditions and the flexion/extension of the human hand. Here, the squeezing condition of hand gripper using the FEHG is nothing but a “Flexion (bending force ON)” and releasing condition is “Extension (bending force OFF).” **Figure 7.1.10(f, g)** represents the generated electrical output (2 V, 4 nA) of the single HS-CSPNG device during the flexion/extension of FEHG and the series connection between all HS-CSPNG devices in FEHG

can be possible to enhance the electric output. The perpendicular/bending force results of FEHG demonstrate the potential usefulness of the next generation energy harvesting technology to harness the waste bio-mechanical energy.

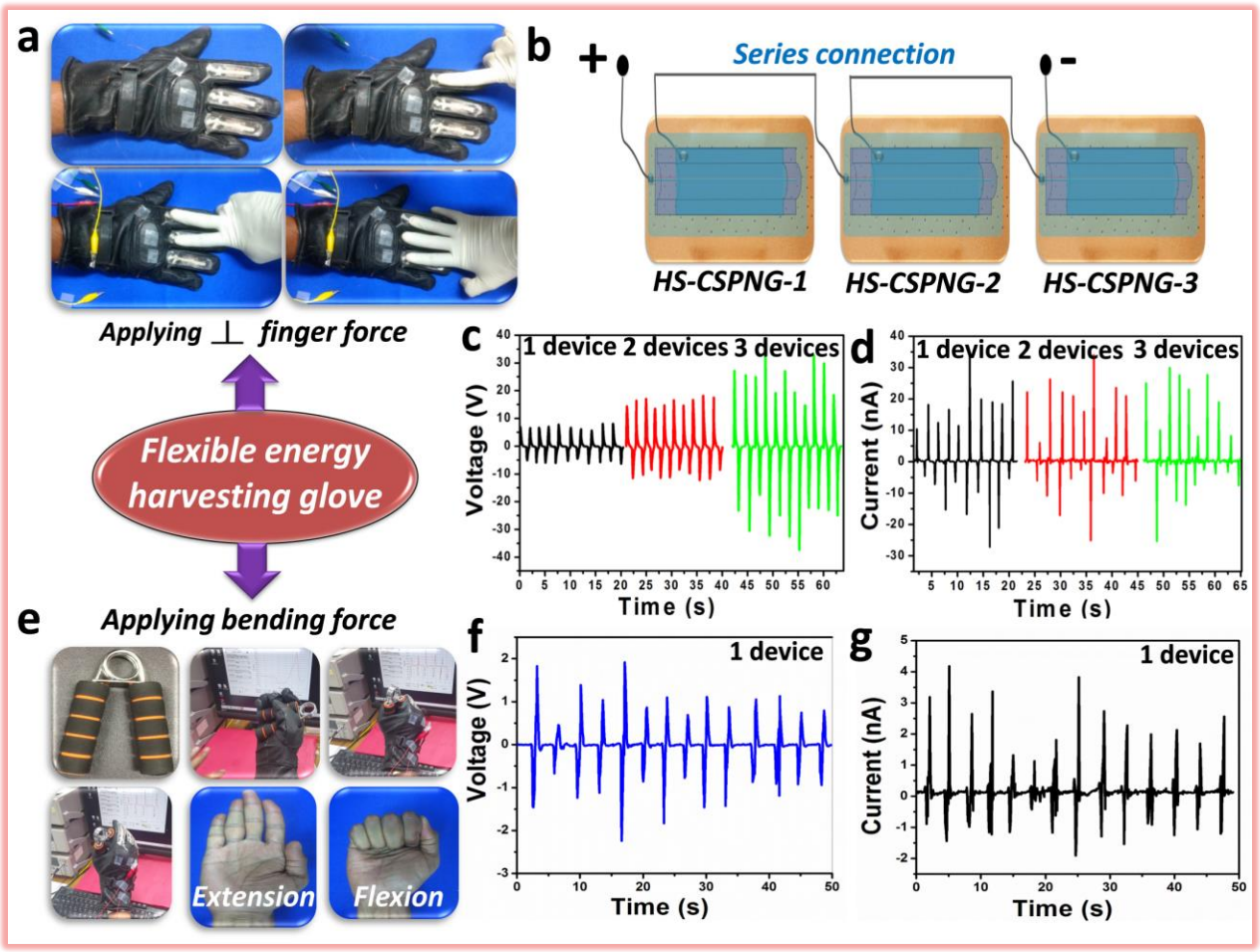

Figure 7.1.10 Demonstration of flexible energy harvesting glove (FEHG) using multiple adaptable HS-CSPNG devices under perpendicular/bending forces: **(a)** Digital photographs shows the FEHG under various conditions such as no force and perpendicular force *via* single, two and three fingers. **(b)** The schematic diagram shows the series connection of three HS-CSPNG device outputs. **(c, d)** Output voltage/current signals of FEHG upon single, two and three fingers force conditions. **(e)** Applying bending force to FEHG *via* commercially purchased hand gripper and its digital photographs represents flexion/extension conditions. **(f, g)** Output voltage/current signals of single HS-CSPNG in FEHG during flexion/extension of hand using hand gripper.

7.1.3.4 Self-powered muscle monitoring system by multiple HS-CSPNGs

The HS-CSPNG prototype not only suitable to harness the waste mechanical energy but also useful to monitor/sense the various human body part movements and its muscle conditions. The existing conventional planar P-NG design is suitable to sense only one or two human body part movements either finger or elbow joints without any batter source, but not suitable for monitoring maximum human body part movements at a time. This is due to the lack of adaptability in P-NG device design, high planar device area, low electrical output performance of flexible devices and poor repeatability. For that, highly flexible, adaptable, eco-friendly, battery-less and high output performance based HS-CSPNG devices (*via* cost-effective groove technique) developed, and it can also work as a self-powered muscle monitoring system (SP-MMS) for sensing the muscle or joint movements. The advantage of single SP-MMS prototype is capable of measuring/monitoring the maximum human body part movements/rotations such as spinal cord, jaw, throat, elbow, knee, foot stress, finger force and breathes condition as shown in **Figure 7.1.11**. This type of strip device design and its large scale, cost-effective manufacturing methods are highly reliable and much needed for the development of advanced rehabilitation electronic devices. **Figure 7.1.11a** shows the human body schematic diagram and the adaptability of SP-MMS device at various locations without changing the device area. The obtained positive/negative output voltage responses of SP-MMS are +45 mV/-60 mV for jaw open/closed condition, +100 mV/-200 mV for spinal cord right/left rotations and +2.5V/-2.5 V for foot stress/release condition as shown in **Figure 7.1.11 (b-d)**.

During the jaw open condition, the mandible gets stretched will resulting stretching force on SP-MMS device generates the positive voltage spike. During the jaw closed condition, the mandible comes to normal position and the applied stretching force on SP-MMS is removed,

generates the negative voltage spike as shown in **Figure 7.1.11b**. The right side of **Figure 7.1.11b** shows the photographs were taken during the experimental demonstration of jaw open/closed conditions. A similar response observed during the foot stress/release conditions with increased positive/negative spike amplitudes. The left/right rotations and neutral condition of the spinal cord of human were monitored keenly with the good repeatability in output using SP-MMS, and the corresponding digital photographs show the implanted device location as shown in **Figure 7.1.11c**. The perfect phase shift was observed between output voltage signals during the right rotation to the neutral point and left rotation to neutral point demonstrate the true response, working/adaptable ability of SP-MMS. **Figure 7.1.11(e)** shows the obtained positive/negative output voltage responses of SP-MMS are +50 mV/-100 mV for normal breathing with the closed/open throat. The (+2 V/-3 V) for bending/releasing of the elbow, liquid crystal display (LCD) ON/OFF using finger force ON/OFF and +40 V/-30 V for knee joint bending/releasing shown in **Figure 7.1.11(f-h)**. During closed throat breathe condition, the surrounding muscles of the throat gets partially flexed, and the resulting force will act on the SP-MMS generates positive voltage spike. During open throat breathe condition, the muscles of the throat relaxed, and SP-MMS generates negative voltage spike. Enhanced positive/negative spike amplitude was observed for the elbow and knee joint bending/releasing conditions. All the above results demonstrate that the SP-MMS is a potential candidate for rehabilitation medical electronic devices to monitor or diagnose muscle movements in various parts of human body. Moreover, the SP-MMS has good adaptability in various locations, highly sensitive concerning movements, eco-friendly nature, battery-less operation, and additional components are not required.

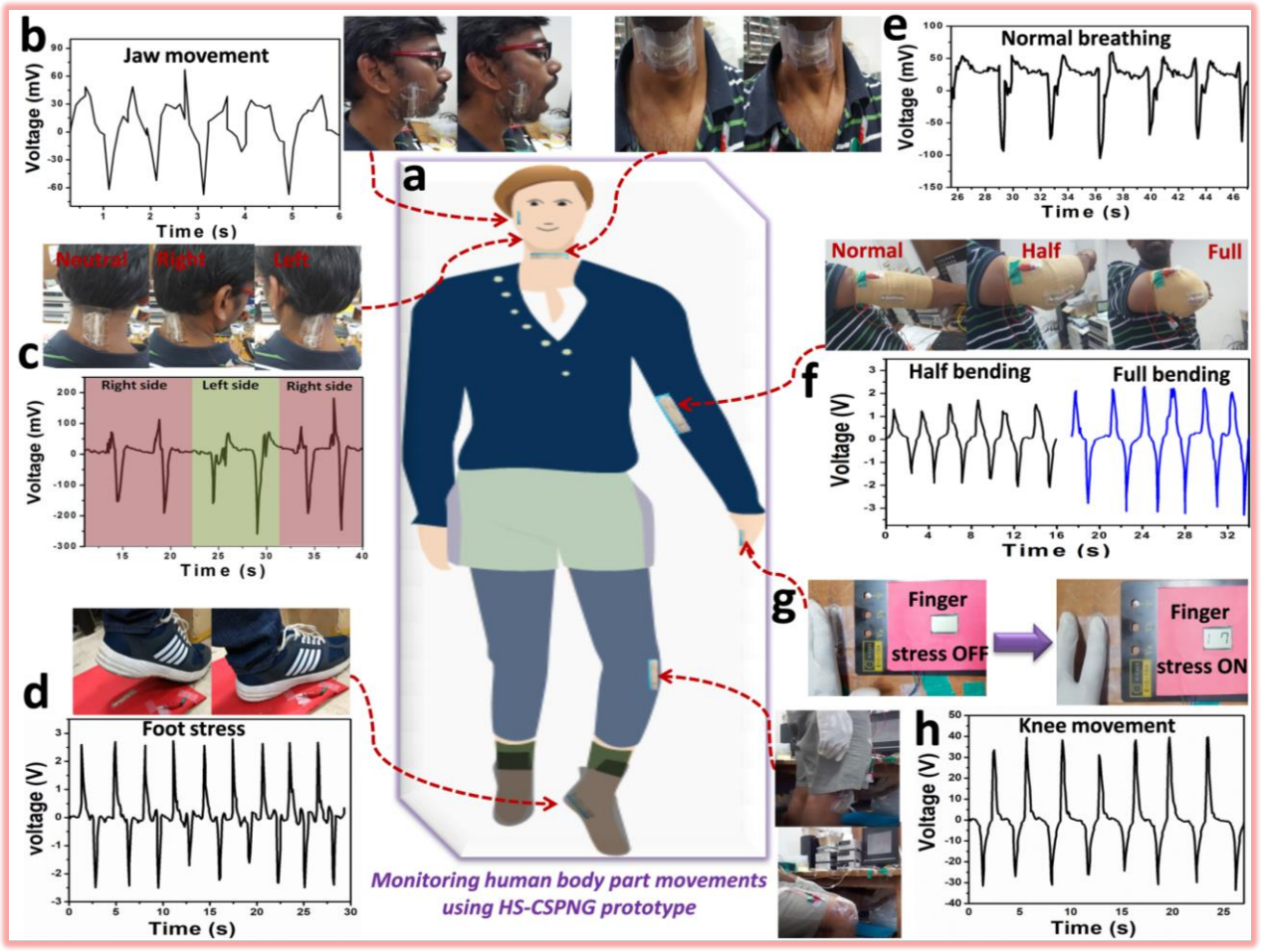

Figure 7.1.11 Demonstration of self-powered muscle monitoring system (SP-MMS) using adaptable HS-CSPNG. **(a)** Schematic diagram of the human body and the location of various SP-MMSs to monitor or diagnosis the maximum human body movements (spinal cord, jaw, throat, elbow, knee, foot stress, finger force, and breath condition) at a time or different time intervals. **(b-d)** Output voltage responses of SP-MMSs upon the jaw movements, spinal cord right/left rotations and neutral position, and foot stress/release conditions. **(e, f)** Output voltage responses of SP-MMSs during the throat inhale/exhale conditions, elbow bending (half/full)/release movements. **(g)** Low power consumed display lit up/off upon finger stress on/off on SP-MMS. **(h)** High electrical output voltage response of SP-MMS during the knee joint bending/releasing conditions.

7.1.4 Conclusions

In summary, for the first time highly adaptable HS-FPCS were fabricated using the simple, cost-effective and eco-friendly groove technique. The energy harvesting performance of the adaptable

HS-CSPNG device was investigated using the biomechanical hand force as well as periodic linear motor shaft load (2 N) at 1 ms^2 forward/backward acceleration. HS-CSPNG can generate the maximum amount of output voltage/current are 130 V, 800 nA and switching polarity test of current confirming that the generated electrical response is from the device, not from any other sources. Moreover, the detailed working mechanism, repeatability test, reproducibility test, electrical response at constant mechanical load (2 N), load resistance analysis, instantaneous power density calculations, and stability test performance evaluated successfully. The adaptability/flexibility of HS-CSPNG device was tested by placing the multiple devices at different non-linear surface locations of the human body part and observed the electrical responses by moving or rotating the respective joints. It demonstrates that the proposed groove technique has many advantages such as the on-demand design of various types of groove-based piezoelectric strips, easy to transfer on any non-linear supporting substrates, a high degree of flexibility in shape, large-scale production of all the groove design types, high output performance in typical environments and cost-effective/eco-friendly approach. The developed HS-CSPNG devices are potential candidates for developing the self-powered muscle monitoring systems without using any additional storage components. This type of adaptable, flexible strip based PNGs is highly suitable to measure any non-linear surfaces motions/rotations compared to traditional planar PNG devices.

7.1.5 References

1. M. Lee, C. Y. Chen, S. Wang, S. N. Cha, Y. J. Park, J. M. Kim, L. J. Chou, Z. L. Wang, *Adv. Mater*. 2012, **24**, 1759–1764.
2. M. Zhang, T. Gao, J. Wang, J. Liao, Y. Qiu, Q. Yang, H. Xue, Z. Shi, Y. Zhao, Z. Xiong, L. Chen, *Nanoenergy*, 2015, **13**, 298-305.
3. W. Jia, X. Wang, S. Imani, A. J. Bandodkar, J. Ram´ırez, P. P. Mercier, J. Wang, *J. Mater. Chem. A*, 2014, **2**, 18184–18189.
4. A. E. Ostfeld, A. M. Gaikwad, Y. Khan, A. C. Arias, *Sci. Rep*. 2016, **6**, 1-10.
5. A. Chandrasekhar, N. R. Alluri, M. S. P Sudhakaran, Y. S. Mok, S. J. Kim, ***Nanoscale***, 2017,**9**, 9818-9824.
6. N. R. Alluri, S. Selvarajan, A. Chandrasekhar, B. Saravanakumar, J. H. Jeong, S. J. Kim, *Compos. Sci. Technol*, 2017, **142**, 65-78.
7. S. Siddiqui, D. I. Kim, E. Roh, L. T. Duy, T. Q. Trung, M. T. Nguyen, N. E. Lee, *NanoEnergy* 2016, **30**, 434–442.
8. Z. L. Wang, Piezoelectric nanogenerators for self-powered nanosensors and nanosystems, J. Webster (ed.), Wiley Encyclopedia of Electrical and Electronics Engineering. Copyright © 2012 John Wiley & Sons, Inc, 1-20.
9. N. R. Alluri, B. Saravanakumar, S. J. Kim, *ACS Appl. Mater. Interfaces*, 2015, 7, 9831–9840.
10. X. Ren, H. Fan, Y. Zhao, Z. Liu, *ACS Appl. Mater. Interfaces*, 2016, **8**, 26190–26197.
11. N. R. Alluri, A. Chandrasekhar, V. Vivekananthan, Y. Purusothaman, S. Selvarajan, J. H. Jeong, S. J. Kim, *ACS Sustainable Chem. Eng*, 2017, **5**, 4730–4738.
12. Z. Liu, S. Zhang, Y. M. Jin, H. Ouyang, Y. Zou, X. X. Wang, L. X. Xie, Z. Li, *Semicond. Sci. Technol.* 2017, **32** 064004.
13. S. Siddiqui, D. I. Kim, L. T. Duy, M. T. Nguyen, S. Muhammad, W. S. Yoon, N. E. Lee, *NanoEnergy*, 2015, **15**, 177–185.
14. Q. Zheng, H. Zhang, H. Mi, Z. Cai, Z. Ma, S. Gong, *NanoEnergy* 2016, **26**, 504–512.
15. K. I. Park, M. Lee, Y. Liu, S. Moon, G. T. Hwang, G. Zhu, J. E. Kim, S. O. Kim, D. K. Kim, Z. L. Wang, K. J. Lee, *Adv. Mater*. 2012, **24**, 2999–3004.
16. D. Xue, Y. Zhou, H. Bao, J. Gao, C. Zhou, X. Ren, Appl. Phys. Lett. 2011, 99, 122901-3.
17. L. F. Zhu, B. P. Zhang, L. Zhao, J. F. Li, *J. Mater. Chem. C*, 2014, **2**, 4764-4771.

7.2 Self-powered air pressure sensor using high output butterfly wing-structure type multiunit-hybrid nanogenerator

7.2.1 Introduction

The development of alternative energy harvesting systems such as a piezoelectric (P)[1] triboelectric (T) [2], and pyroelectric (Py) [3] nanogenerators (NGs) are of great interest in recent days. Strongly needed to control the energy harvesting from the traditional energy sources (e.g., fossil fuels, nuclear, and hydroelectric). Moreover, electricity use has increased tremendously due to lifestyle choices of humans, climate change, and regulatory policies of power management sectors. The enhancements of high electrical output, instantaneous power density, and cost-effective device designs for alternative energy harvesting systems will be key factors in solving the above- mentioned issues. This type of energy generation is eco-friendly, costeffective, and biocompatible. Over the last decade, the performance of individual systems (PNGs and T-NGs) has improved greatly due to the growth of various nanostructured materials, device designs, and composite films. The P-NG power density has improved several orders (from μW/cm2 to mW/cm2) by incorporating various materials such as polyvinylidene fluoride (PVDF) [4–6], ZnO [7], PbZrTiO3 (PZT) [8], BaTiO3 (BTO) [9], and composite materials (ZnOnanotubes-polycarbonate [10], BTO/PVDF [11], BTO/calcium alginate linear worm/beads structure [12, 13], BTO nanocubes/PDMS [14]). The T-NG performance has improved substantially (up to W/m2) via enhancement of the surface charge density (SCD) of a dielectric film [15], and the relative permittivity and porosity [16], compressibility [17], and surface potential of the triboelectric material. The aligning graphene sheets or conducting nanofillers in the PDMS matrix improves the electrical output performance of the T-NG device [19, 20]. These individual systems (P-NGs and T-NGs) generate considerable amounts of power density, which is useful to

start up or drive low-power consuming electronic applications. However, they still suffer from complex device designs, environmental issues, unstable outputs over long periods, dependency on nanostructured materials, and operation difficulties under robust conditions. A new approach is required to resolve the above issues, i.e., the hybridization of material properties, device designs, and working principles [21–29].

Recently, a few researchers have explored hybrid nanogenerators (H-NGs) to improve the power density and reduce the complexity of the device design. These H-NGs have included the piezoelectric-triboelectric (P-T) [22-26], piezoelectric-pyroelectric (P-Py) [27, 28], and piezoelectric-triboelectric-pyroelectric (P-T-Py) [21, 29] types; however, their performance remains inadequate. The literature suggests that the concept/development of an H-NG can be achieved using two approaches. One is the external integration [22–24] of two or more individual systems, i.e., the separate output terminals of two systems connected *via* a full-wave bridge rectifier. Second, internal integration [25, 26], i.e., one of the active triboelectric layers in the T-NG device structure replaced by a multifunctional composite material, i.e., a P-T composite layer or P-T-Py composite layer. Through the external integration mode, the possibility of mismatch between the positive and negative output signals is very high and may reduce the generated hybrid output. Moreover, this type of H-NG or integration is not suitable for real-time applications because of the increased complexity in device design and additional circuit components are required to obtain the hybrid output. To date, few papers published on this concept (r-shaped [22], arc-shaped [23], three-dimensional (3D)-fiber shaped [24] and Dshaped [30]) and the obtained power density is not high as that achievable with individual P-NGs and T-NGs. In contrast, the internal integration mode (rectangular [25] cantilever-resonator [26] and circular [31] designs) has more advantages. This mode uses fewer fabrication layers (or)

films for the H-NG (≤ five layers), a full-wave bridge rectifier is not needed to obtain the hybrid output, and the mismatch between the output terminals is much less because it has only two electrodes. Additionally, it is more suitable for practical applications because the device designs can be less complicated. But the recent report demonstrates that the significant output power response (1100 V, 1.5 mA) [32] achieved in an air atmosphere and 570 mA/m2 in vacuum condition [33] with the artificial control of ferroelectric properties based composite as one active layer in T-NG device design (contact-separation). However, there is a possibility to improve the hybrid output by concentrating on few critical factors such as the selection of efficient multifunctional nanomaterials for composite structures, surface modification aspects, cost-effective designs (single or multi-unit), and optimal contact separation between the active layers.

In this study, a new type of butterfly wing structure (BWS)-based multi-unit H-NG device reported for the first time. It consists of four simple arc-shaped H-NGs and can generate a very high current density of 2500 mA/m^2. The enhanced current density mainly attributed to the high SCD resulting from the combined triboelectric effect (polydimethylsiloxane (PDMS), Al layer) and piezoelectric effect from lead-free 0.3Ba0.7Ca0.3TiO3-0.7BaSn0.12Ti0.88O3 nanoparticles (0.3BCT-0.7BST NPs). These lead-free piezoelectric NPs display a high εr ≈3800 and d_{33} ≈530 pC/N [34] near room temperature (RT), similar to PZT, and are well-suited for energy harvesting, actuation, and sensor applications. The SCD of H-NG concerning the surface modifications (flat, micropillars, irregular network) of the composite layer (10 wt %), contact–separation distance between the layers, and the weight ratio of NPs investigated thoroughly. Initially, the P-NG, T-NG, and H-NG device modes analyzed with a simple flat composite film, and the efficient energy harvesting mode was left for further study. Next, various cost-effective surface modifications (micropillars and an irregular network) of composite layer led to an

increment in the electrical response (≈10 folds in voltage-wise). Open-circuit voltage (VOC(P-P)) = 572 V and short-circuit current (ISC(P-P)) = 1.752 mA for the irregular surface-based H-NG is higher when compared with VOC(P-P) = 53 V and ISC(P-P) = 2.366 μA for P-NG. The power density of a single H-NG with an irregular surface was four-times higher, and that of the micro-pillared surface was double that of the H-NG with a flat surface (333 W/m2). Investigated the various studies such as various input accelerations, switching polarity test, load resistance analysis, and charge accumulation behaviors of H-NGs. Demonstrated the real-time capacitor/Li-ion coin cell charging analysis, powering-up 100 green light-emitting diodes forming the word "NU" and surface charge density dependency with the composite morphology. Finally, a self-powered air pressure sensor demonstrated using the BWS-based multi-unit H-NGs under various air pressures ranging from 5.4 to 27.24 kPa, respectively. Here, the H-NGs contact and separation in the BWS closely resembled the up-down flapping movements of natural butterfly wings. The improved output power of the H-NG has a simple device design, high piezoelectricity at room temperature, cost-effective surface modifications, and optimal contact separation distances will accelerate the development of next-generation energy harvesting devices.

7.2.2 Experimental Methods

Piezoelectric nanoparticles were synthesized using a high-temperature solid-state reaction (SSR) method. Various surface morphologies of the composite films were developed using the solution casting technique (SCT). The corresponding P-NG (without an air gap), T-NG (with air gap), and H-NG devices (with air gap) were fabricated using the conventional approach.

7.2.2.1 Synthesis of BCT, BST, and 0.3BCT-0.7BST piezoelectric NPs

Piezoelectric NPs such as $Ba_{0.7}Ca_{0.3}TiO_3$ (BCT), $BaSn_{0.12}Ti_{0.88}O_3$ (BST) and $0.3Ba_{0.7}Ca_{0.3}TiO_3$-$0.7BaSn_{0.12}Ti_{0.88}O_3$ (0.3BCT-0.7BST) [30] were fabricated using a high-

temperature SSR method. The raw materials $BaCO_3$ (99.95% purity, High purity chemicals Ltd.), TiO_2 (98% purity, Daejung), SnO_2 (99.99% purity, Sigma–Aldrich) and $CaCO_3$ (99.99% purity, High purity chemicals Ltd.) were weighed to obtain the desired atomic ratio of the piezoelectric system. Initially, the raw materials were mixed homogeneously by manually grinding for one h in a mortar and pestle with ethanol as the medium. Heating the mixed powder in an alumina crucible at 1,300°C for 3 h at a heating rate of 3.33°C/min provided the desired crystalline quality. After cooling, the sample was again manually ground for 30 min.

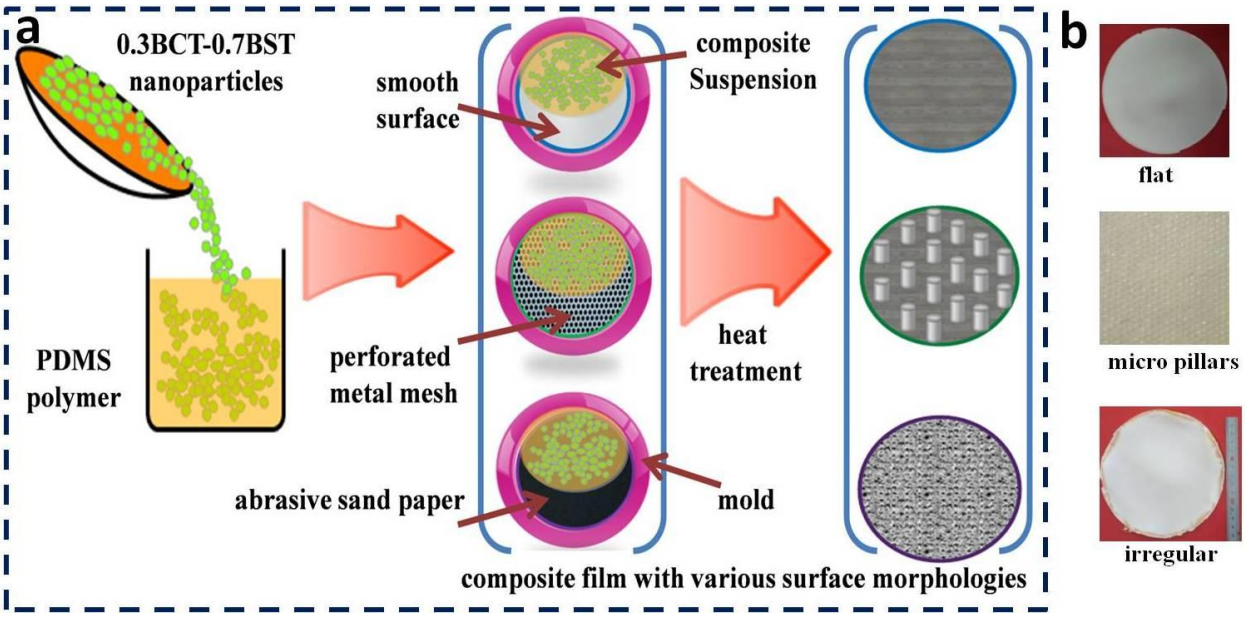

Figure 7.2.1(a) Schematic diagram of the fabrication protocol for $0.3Ba_{0.7}Ca_{0.3}TiO_3$-$0.7BaSn_{0.12}Ti_{0.88}O_3$/polydimethylsiloxane (0.3BCT-0.7BST/PDMS) composite layers with different surface morphologies (flat, micropillars, and irregular network). **(b)** As-fabricated composite surface morphologies depicted through optical photographs.

7.2.2.2 Fabrication of various hybrid film surface morphologies

The 0.3BCT-0.7BST/PDMS composite (or hybrid) films with various surface morphologies (flat, micropillars, and an irregular network) prepared using the simple SCT method as shown in **Figure 7.2.1**. The flat composite surfaces prepared by mixing a

homogeneous PDMS: hardener (10:1) solution with 0, 1, 5, 10 and 15 wt% 0.3BCT-0.7BST NPs. This solution was poured into a glass Petri dish (Duran group) and heated at 70°C for 1 h in an oven. Next, the composites were peeled from the dish and cut into the required dimensions (3 × 2.5 cm^2) for the P-NG. The flat composite surface based P-NG (10 wt% of 0.3BCT-0.7BST NPs) displayed good performance and utilized in the T-NG configuration (contact–separation mode), which exhibited a high conversion of mechanical energy to electrical energy. Micropillar and irregularly surfaced composite films were prepared using a perforated metal mesh purchased from the local Jeju city market (thickness of the hole ≈400 μm & diameter of circular hole ≈705 μm). The aspect ratio of metal mesh [thickness: diameter] is ≈ 1.76 to 1.82 and abrasive sandpaper (Silicon carbide sandpaper, Grade number: P60, C-Cw, Croco abrasive) as substrates in the molds shown in Figure 7.2.2. The optical images of the as-prepared composite films having flat, micro-pillars and irregular surface morphologies shown in **Figure 7.2.1b.**

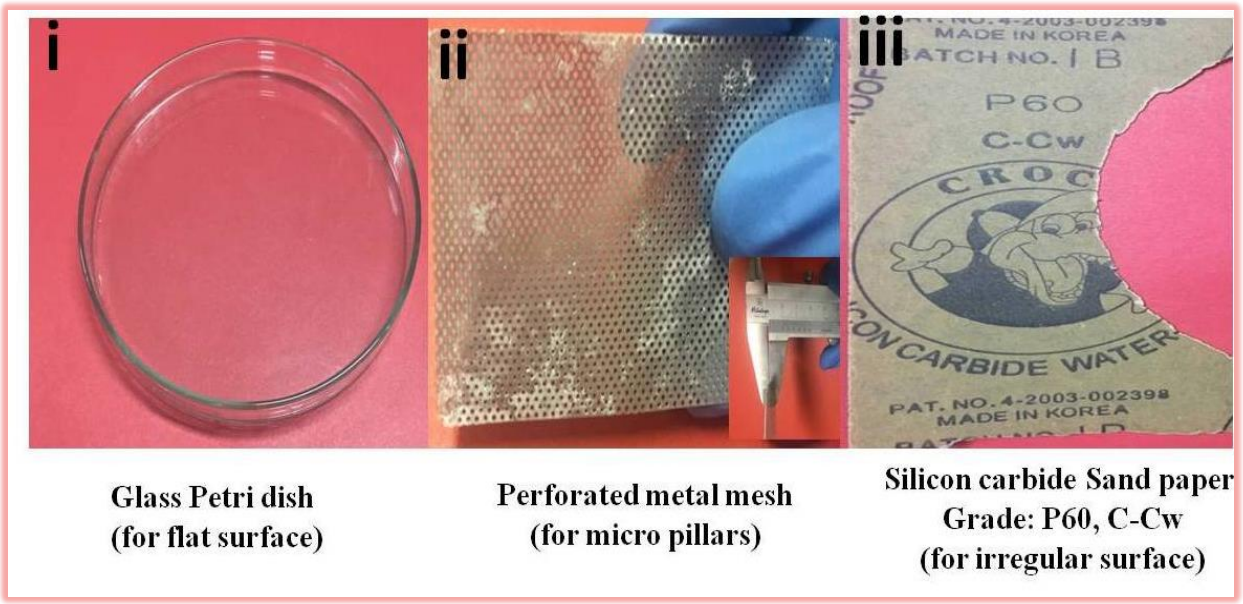

Figure 7.2.2 Optical images of the commercially purchased molds for surface roughness such as **(i)** Glass Petri dish (Duran Group) **(ii)** metal mesh purchased from local Jeju city market **(iii)** Silicon carbide sand paper (Croco abrasive)

7.2.2.3 Fabrication of P-NG, T-NG and H-NG modes

Three modes of NGs such as P-NG, T-NG, and H-NGs (piezoelectric-triboelectric) were made using the 0.3BCT-0.7BST/PDMS composite (containing 10 wt% of piezoelectric NPs) and aluminum (Al) layer. P-NGs were fabricated using composite films with different weight ratios (0, 1, 5, 10 and 15 wt% NPs in PDMS). Film samples were cut to the required device dimensions (3×2.5 cm^2) and sandwiched between a Kapton/Al top electrode and polyethylene terephthalate (PET)/Al bottom electrode without any air gap by hot pressing for 30 min **[Fig. 2b(i)]**. As-fabricated P-NGs electrically poled at 3 kV for 24 h at room temperature. An arc-shaped T-NG device was fabricated using a pure PDMS film having the same thickness as that of the P-NG device active layer. The fabrication protocol consisted of two steps. First, the PDMS film (3×2.5 cm^2) was attached to an Al electrode/PET layer that was the bottom layer of the T-NG; Al electrode/Kapton used as the top layer. Second, both parts were attached to an arc-shaped PET substrate having a fixed (25 mm) contact–separation distance. Finally, the H-NG device was fabricated by electrically poling (3 kV for 24 h) the flat composite film (0.3BCT-0.7BST NPs/PDMS containing 10 wt% NPs) as an active layer. The remaining fabrication steps were similar to those of the T-NG device with a contact–separation distance of 25 mm **[Fig. 2b(ii)]**. Similarly, arc-shaped H-NGs with 10 and 15 mm contact–separation distances and various surface morphologies (micropillars, irregular network) of the composite film were studied. The electrical response of the NGs was obtained using copper wires attached with silver paste to the back of each electrode, followed by heating at 70°C for 15 min in an oven. Last, a highly efficient BWS- type multi-unit H-NG device constructed from four arc-shaped H-NG wings (with an irregular surface). Two wings oriented in the forward direction and two in the backward direction such that their movements overlapped at the center point, which was a fixed neutral

location. The forward (or backward) two wings were formed by folding both ends of a single large PET strip and attaching it to the center point using double-sided adhesive Kapton tape. The contact–separation distance between the two opposite active layers of the four H-NGs was fixed at 10 mm.

7.2.3 Results and Discussion

7.2.3.1 Structural and surface morphological analyses

A thick composite film as an active layer for mechanical energy scavenging was fabricated using the SCT approach. Composite films having various surface morphologies (flat, micropillars, and an irregular network) were developed using cost-effective masks in fixed molds, i.e., a flat surface, a perforated metal mesh, and abrasive sandpaper. The crystalline structure and surface morphology of BCT, BST, and 0.3BCT-0.7BST NPs was studied using XRD, Raman spectroscopy, and FE-SEM. Dezhen et al. [34] reported a large d_{33} of 530 pC/N, a high ε_r of 3800, and an electromechanical coupling coefficient (k_3) of 0.55 for 0.3BCT-0.7BST NPs at room temperature. These properties attributed to the coexistence of multiple phases (i.e., rhombohedral-R, tetragonal-T, and orthorhombic-O), which is similar to the morphotropic phase boundary (MPB) of BZT-50BCT NPs [34]. SSR method followed to prepare all of the NPs, which described in the experimental section. The crystalline phase information of 0.3BCT-0.7BST NPs by XRD technique was explained in detailed manner through section 7.1. Raman spectroscopy was used to better understand the dynamic symmetry of the dual system (majority T-phase) (**Figure 7.2.3a**). The peak at 312 cm^{-1} represents the presence of longitudinal as well as transverse vibrational active modes, which correspond to the major T-phase; the broad peak at 240–270 cm^{-1} corresponds to the T/O phase transition. **Figure 7.2.3(b-d)** shows FE-SEM

images of BST, BCT, and 0.3BCT-0.7BST NPs having a random orientation with highly crystalline surface morphologies.

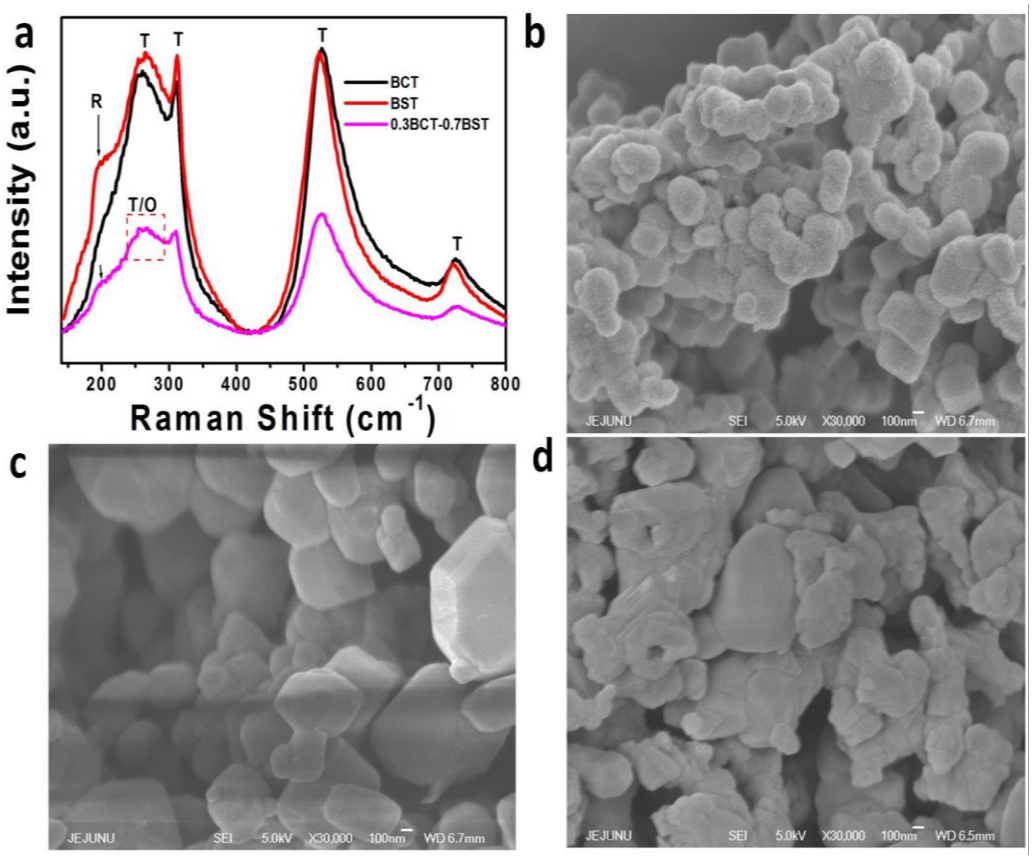

Figure 7.2.3. S1. (a) Raman spectra of $BaSn_{0.12}Ti_{0.88}O_3$ (BST), $Ba_{0.7}Ca_{0.3}TiO_3$ (BCT), $0.3Ba_{0.7}Ca_{0.3}TiO_3$-$0.7BaSn_{0.12}Ti_{0.88}O_3$ nanoparticles (0.3BCT-0.7BST NPs) as synthesized by the solid-state reaction (SSR) method. **(b-d)** Field-emission scanning electron microscopy (FE-SEM) images of randomly oriented crystalline BST, BCT, and 0.3BCT-0.7BST NPs. The scale bar represents 100 nm.

Flat composite thick films were fabricated using different weight ratios of 0.3BCT-0.7BST NPs (0, 1, 5, 10 and 15 wt %) as fillers and PDMS as the matrix. The transparency of PDMS decreased with increasing weight fraction of 0.3BCT-0.7BST NPs (**Figure 7.2.4**). **Figure 7.2.5a** shows a schematic diagram of the NG device layers consisting of PET/Al (bottom electrode), a composite film (active layer), and Al/Kapton (top electrode). Magnified SEM images of the active layer show the various surface morphologies **(Figure 7.2.5(c–e)).** The flat surface shows

no surface roughness, but the irregular composite surface morphology is not smooth and contains micropores of size ranging from 100 to 300 μm. Both the flat composite film and the irregular composite film had a thickness of 800 μm (**Figure 7.2.6**). However, the thickness of the micropillar composite film depended on the thickness of the base layer (250 to 300 μm) and the height of the micropillars (400 μm). Thus, the estimated thickness of the micropillar composite film ranged from 650 to 700 μm and the distance between two micropillars was 500 μm (inset of **Figure 7.2.5e**).

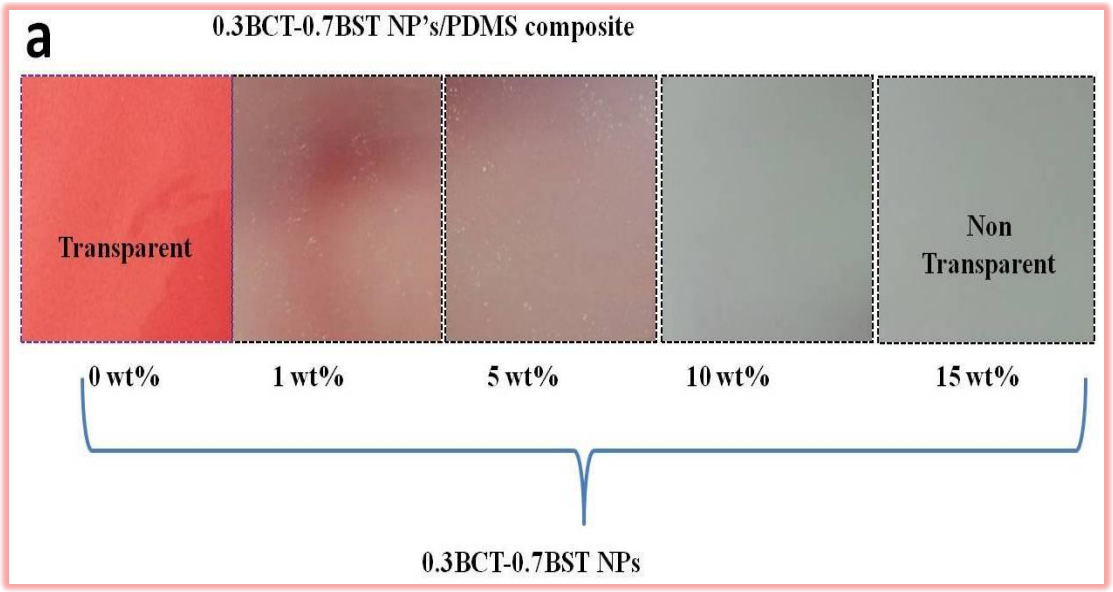

Figure 7.2.4 (a) Optical photographs of flat composite films in polydimethylsiloxane (PDMS) showing the loss of transparency with increasing weight fraction of NPs in the PDMS matrix.

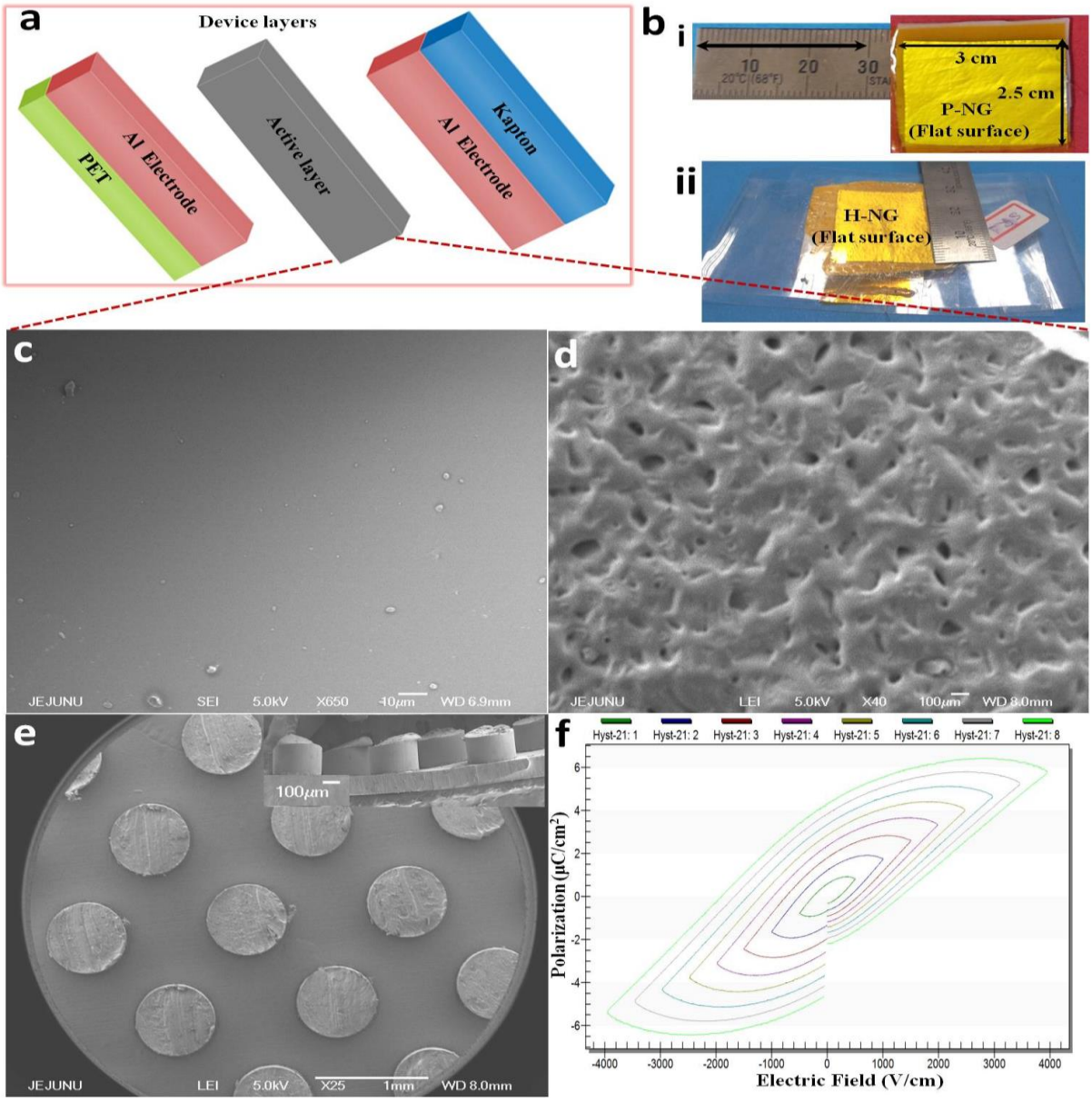

Figure 7.2.5 (a) Schematic representation of device layers for the piezoelectric-, triboelectric-, and hybrid-nanogenerator (P-NG, T-NG, and H-NG, respectively) modes. **(b)** Photograph of (i) P-NG and (ii) H-NG devices are having a flat composite surface (10 wt% of NPs). **(c)** Field-emission scanning electron microscopy (FE-SEM) images of the flat surface, **(d)** irregular network and **(e)** micropillars (inset shows the height of the pillars). **(f)** Polarization *vs.* electric field (*P–E*) hysteresis loop of a 0.3BCT-0.7BST pellet (sintered at 1100°C for 2 h) at room temperature.

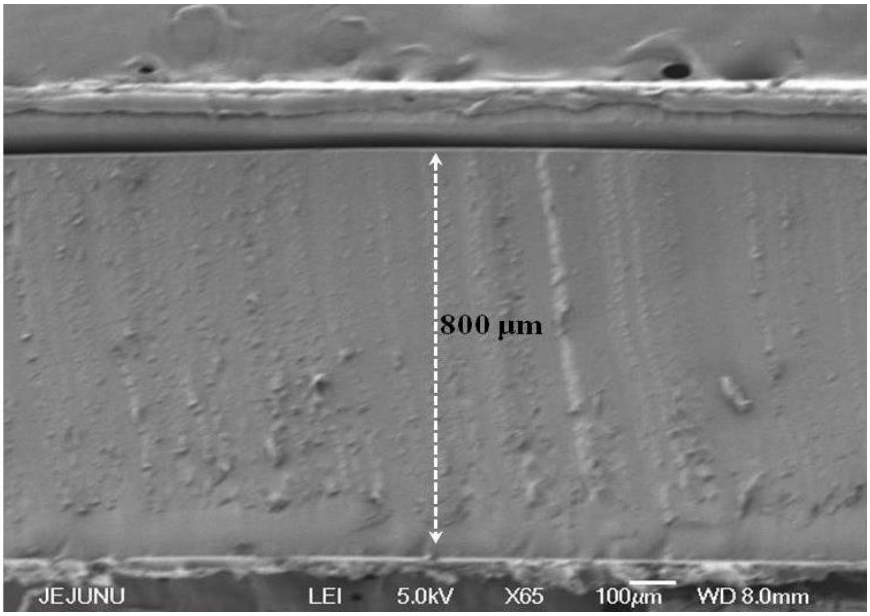

Figure 7.2.6 Cross-sectional field-emission scanning electron microscopy (FE-SEM) image of the piezoelectric nanogenerator (P-NG) device at the 100-µm scale.

7.2.3.2 Harvesting energy using P-NG, T-NG, and H-NG modes

Initially, P-NGs (3 × 2.5 cm^2) were made using flat composite films with different weight fractions of NPs and the fabrication procedure given in the experimental section. **Figure 7.2.5c and Figure 7.2.6** shows the SEM image of the P-NG (10 wt% of NPs) surface and the cross-sectional SEM of the device. **Figure 7.2.7a** is a schematic diagram of the P-NG device. **Figure 7.2.7b** shows the peak-to-peak V_{OC} and I_{SC} for all weight fractions of P-NGs upon a constant loading of 30 N. The electrical output increased with increasing weight fraction of NPs (up to 10 wt %), but the electrical output steadily decreased beyond 10 wt%. Here, d_{33} values changed by 382 and 147% for P-NGs containing 1–5 wt% and 5–10 wt%, respectively. However, at 10–15 wt%, the percentage change in d_{33} was minimal, i.e., 6.35%; the effective permittivity (ε_{eff}) varied linearly with respect to the weight fraction of NPs in the PDMS matrix. The percentage change of ε_{eff} dominated the change in the d_{33} coefficient and controlled the generation of a

cumulative electric dipole momentum of the composite film when the NPs content exceeded 10 wt% in the PDMS matrix (**Figure 7.2.8**).

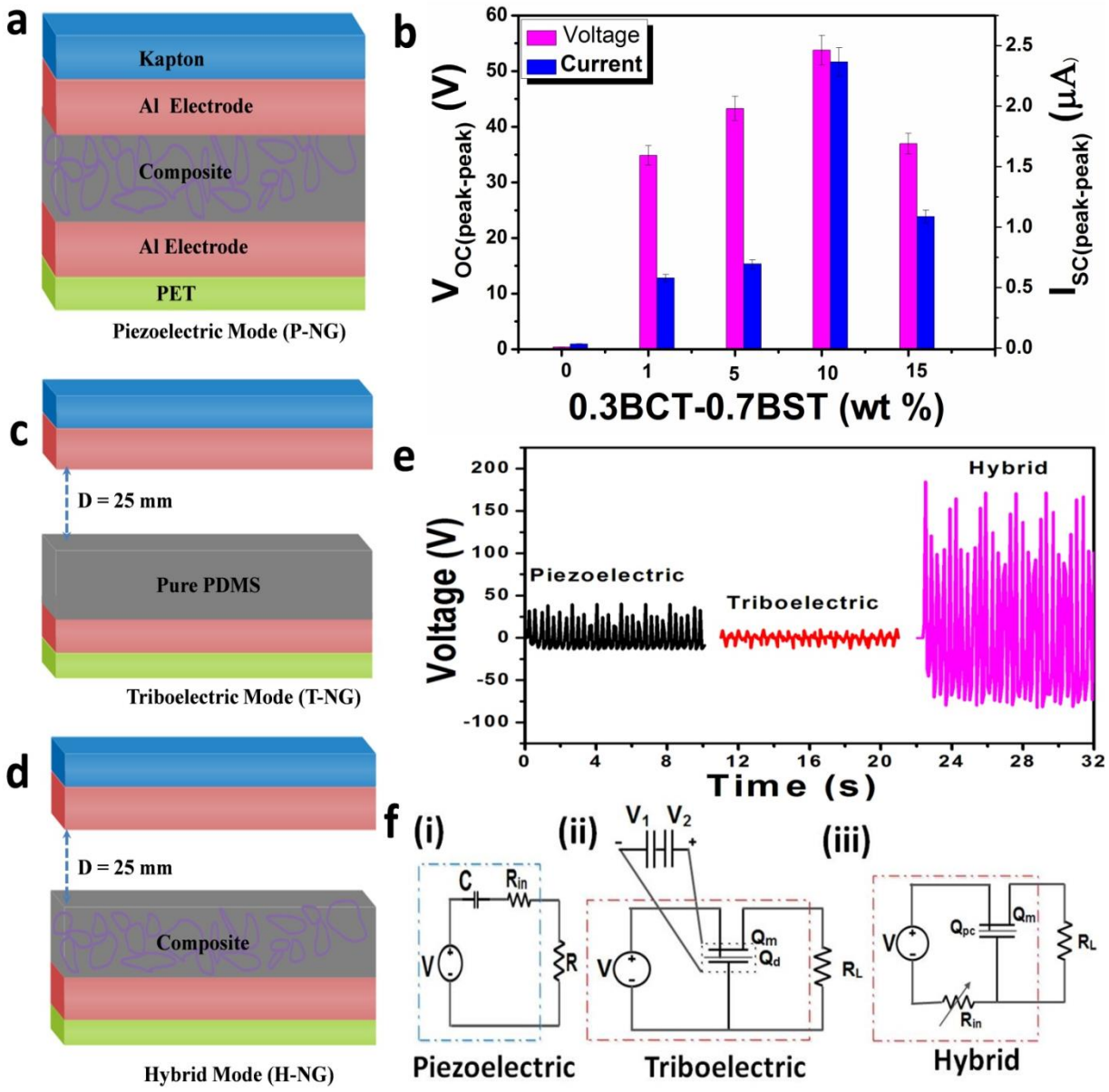

Figure 7.2.7 (a) Schematic diagram of a P-NG device having dimensions of 3 × 2.5 cm^2. **(b)** Peak-to-peak data open-circuit voltage (V_{OC}) and short-circuit current (I_{SC}) of the P-NG device as a function of weight percentage of nanoparticles (NPs) in the PDMS matrix upon 30-N loading (2 kg shaft mass × 15 m/s^2). **(c, d)** The simple PDMS-based T-NG and composite layer-based H-NG schematic designs. **(e)** The generated P-NG, T-NG, and H-NG output voltages (upon 30-N loading) are compared. **(f)** Estimated equivalent circuit diagrams for (i) P-NG, (ii) T-NG, and (iii) H-NG modes using the internal resistance and variable capacitors.

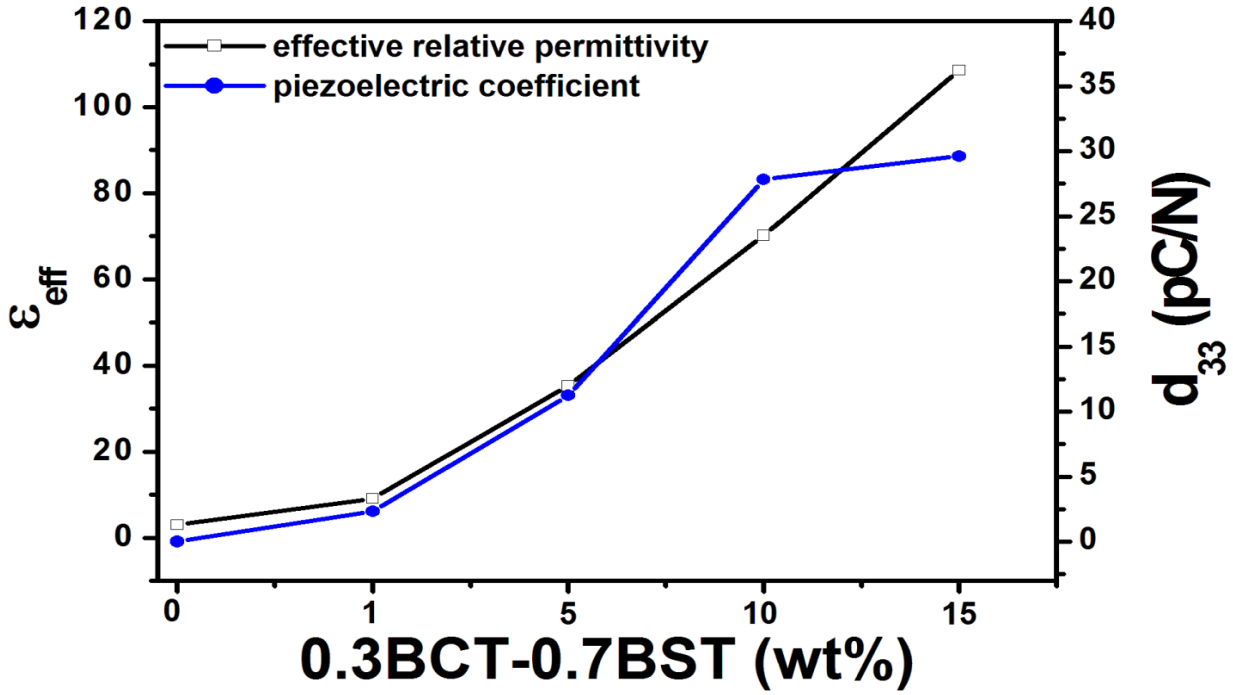

Figure 7.2.8 Theoretical calculations of the effective permittivity (ε_{eff}) and piezoelectric coefficient (d_{33}) of composite layers made with different weight fractions of 0.3BCT-0.7BST NPs in the PDMS matrix.

7.2.3.3 Theoretical calculation of the ε_{eff} and d_{33} parameters

The relative permittivity of the PDMS matrix (ε_{pdms} = 3) can be improved by incorporating piezoelectric NPs (0.3BCT-0.7BST) having high relative permittivity (ε_{piezo} = 3800) at room temperature. Herein, the composite films were prepared with 0, 1, 5, 10, and 15 wt% piezoelectric NPs in the PDMS matrix. The corresponding effective permittivity (ε_{eff}) of the composite thick films can be calculated as follows:

$$\varepsilon_{eff} = \varepsilon_{pdms} f_{pdms} + \varepsilon_{piezo} f_{piezo} , \qquad \text{(E7.2.1)}$$

where f_{pdms} and f_{piezo} are the volume fractions of the PDMS matrix and piezoelectric nanoparticles, respectively. **Figure 7.2.8** shows the calculated effective relative permittivity values of the composite films; there is a nearly linear relationship with the piezoelectric nanoparticle content. According to fundamental piezoelectric theory, the piezoelectric coefficient

(d_{33}) of composite films can be estimated using the piezoelectric voltage constant (g_{33}) and the effective relative permittivity (ε_{eff}) of the composite film as follows:

$$d_{33} = g_{33} \times (\varepsilon_{eff}\varepsilon_o) , \qquad \text{(E7.2.2)}$$

where g_{33} is an unknown factor that depends on the intrinsic properties of the material and its type of nanostructure, e.g., thin films, nanorods, and composites. This g_{33} can be obtained by using the experimentally generated maximum open-circuit voltage (V_{max}) of the corresponding composite film-based devices upon a constant load (F) as follows:

$$V_{max} = F \times g_{33} \times (\frac{l}{A}) , \qquad \text{(E7.2.3)}$$

where l and A are the length and area of the piezoelectric composite device. In the present case, the obtained V_{max} (for poled devices) were 34.87, 43.29, 53.75, and 36.97 V for the weight ratios of 1, 5, 10, and 15 wt% piezoelectric NPs, respectively, in the PDMS matrix under a constant perpendicular load of 30 N (2 kg × 15 m/s^2). All of these composite devices had the same length ($l = 0.03$ m) and area ($A = 0.00075$ m^2). Using the above results, we calculated the piezoelectric voltage constant values of 0.029058, 0.036075, 0.044791, and 0.030808 V·m/N for the composite films containing 1, 5, 10, and 15 wt%, respectively, of NPs. We can obtain *t* from the change in the piezoelectric coefficient (d_{33}) values for the poled piezoelectric composite film-based devices using the piezoelectric constant and effective relative permittivity values of the various composite films and Equation (E7.2.2). **Figure 7.2.8** shows the change of d_{33} values as a function of weight fraction of the composite films poled at 3 kV for 24 h. The percentage change of d_{33} varied rapidly for the 1–5 wt% (382%) and 5–10 wt% (147%) cases. But for the 10–15 wt% case, the percentage change of d_{33} was very small value, i.e., 6.35%, and the observed lower electric output voltage (36.97 V) clearly demonstrated that the substitution of piezoelectric NPs in the PDMS matrix had reached its maximum effective value. Thus, 10 wt% NPs was the

optimal content for the poled composite film. The calculated g_{33} and d_{33} values for the unpoled composite film containing 10 wt% of NPs were 0.01375 ($^{V.m}/_{N}$) and 8.5472 pC/N. The d_{33} value (26.8429 pC/N) of the poled composite film (10 wt%) was more than three-fold higher than that (8.5472 pC/N) of the unpoled composite film. A higher weight fraction of the piezoelectric NPs in the PDMS matrix could lead to agglomeration as shown in Figure 7.2.9. In this case, the applied force on the P-NG device may not be distributed uniformly over all of the NPs. It would lead to a non-uniform orientation of the electric dipoles, and some of the electric dipole moments in the film could cancel each other. This mechanism would account for the low electrical output for the composite P-NG device prepared with greater than 10 wt% of NPs. Moreover, the switching polarity test of the P-NG device (10 wt %) upon 30 N of applied force demonstrated a phase shift between the output electrical signals during forward/reverse connections. This behavior confirmed that the generated output was a true output and not from other sources (**Figure 7.2.10).**

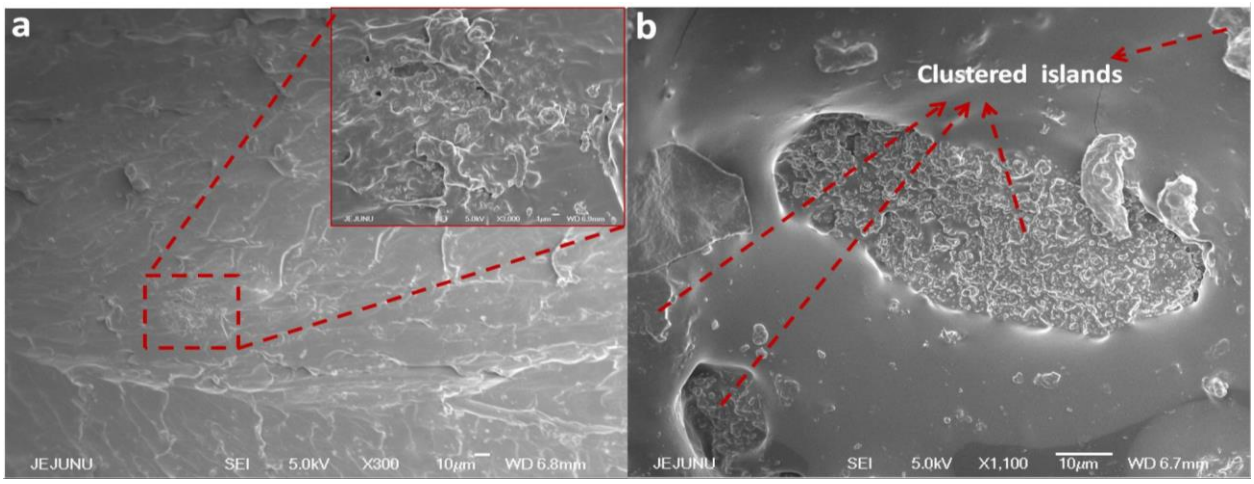

Figure 7.2.9 Cross-sectional morphology of the composite films with weight percentage of the nanoparticles at 10 μm and 1 μm scales: **(a)** 10 wt % and **(b)** 15 wt %.

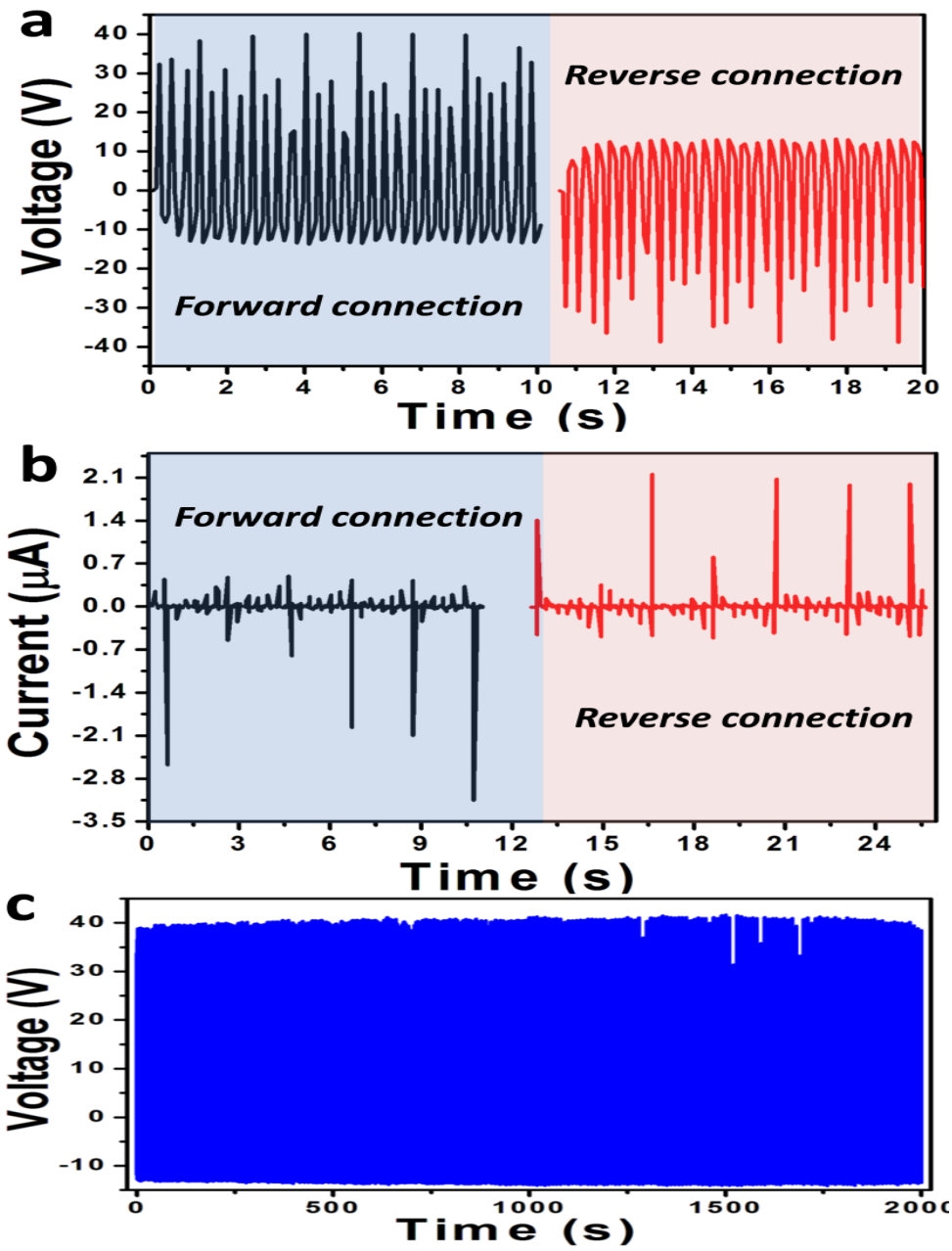

Figure 7.2.10 Switching polarity test results for the P-NG device (10 wt% with electrical poling of 3 kV for 24 h**). (a, b)** V_{OC} and I_{SC} results for the P-NG device (forward/reverse connections) upon 15 m/s^2 of linear motor shaft acceleration (30 N) operated between fixed distances of 10–100 mm. **(c)** Stability test results for the poled P-NG device upon 30 N of loading over 2,000 s.

The pure PDMS flat film (without piezoelectric NPs) generated negligible output ($V_{OC(p\text{-}p)}$ 0.4 V, $I_{SC(p\text{-}p)}$ 35 nA) compared with the composite flat film device (**Figure 7.2.7b**). This small

output arises from the pure PDMS device (**Figure 7.2.11 (c, d))** is attributed to a small air gap (≤ 100 μm) between the PDMS and Al layer. The maximum electrical output ($V_{OC(p-p)}$ = 53.75 V, $I_{SC(p-p)}$ = 2.366 μA) observed for the poled (3 kV for 24 h) P-NG device (10 wt% of NPs) upon 30 N load (**Figure 7.2.11(a, b)**). The optimized force 30 N obtained by performing the force-dependent analysis of P-NG device and the corresponding results shown in Figure 7.2.11. It confirmed that the piezoelectric contribution of the NPs. The room-temperature measurement of the polarization–electric field (*P–E*) hysteresis loop was used to analyze the ferroelectric/piezoelectric behavior of 0.3BCT-0.7BST NPs pellets (diameter: 13 mm; thickness: 1.3 mm) prepared at 1100°C for 2 h (**Figure 7.2.5f**). The as-prepared NPs displayed nonlinear ferroelectric behavior and had a remnant polariztion of 6–6.5 μC/cm^2. This poled P-NG device had higher output than the unpoled P-NG output ($V_{OC(p-p)}$ = 16.5 V, $I_{SC(p-p)}$ = 330 nA) (**Figure 7.2.12 (e, f)**), which confirmed the orientation of the electric dipoles in piezoelectric NPs during electrical poling.

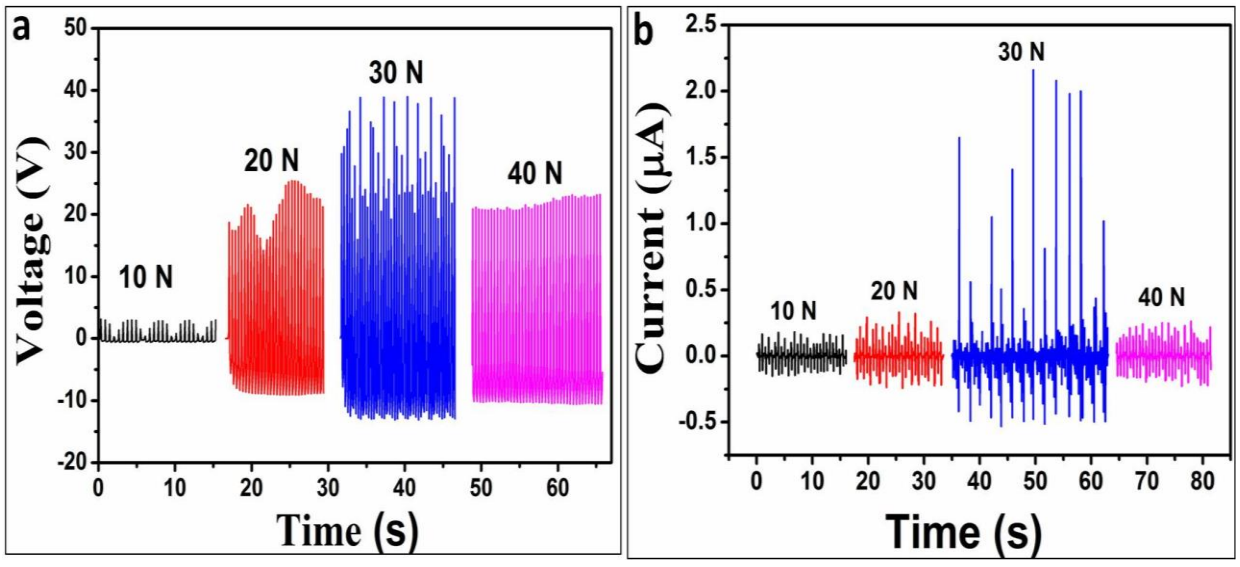

Figure 7.2.11(a, b) The electrical response of P-NG device (10 wt % of NPs) as a function of applied mechanical force.

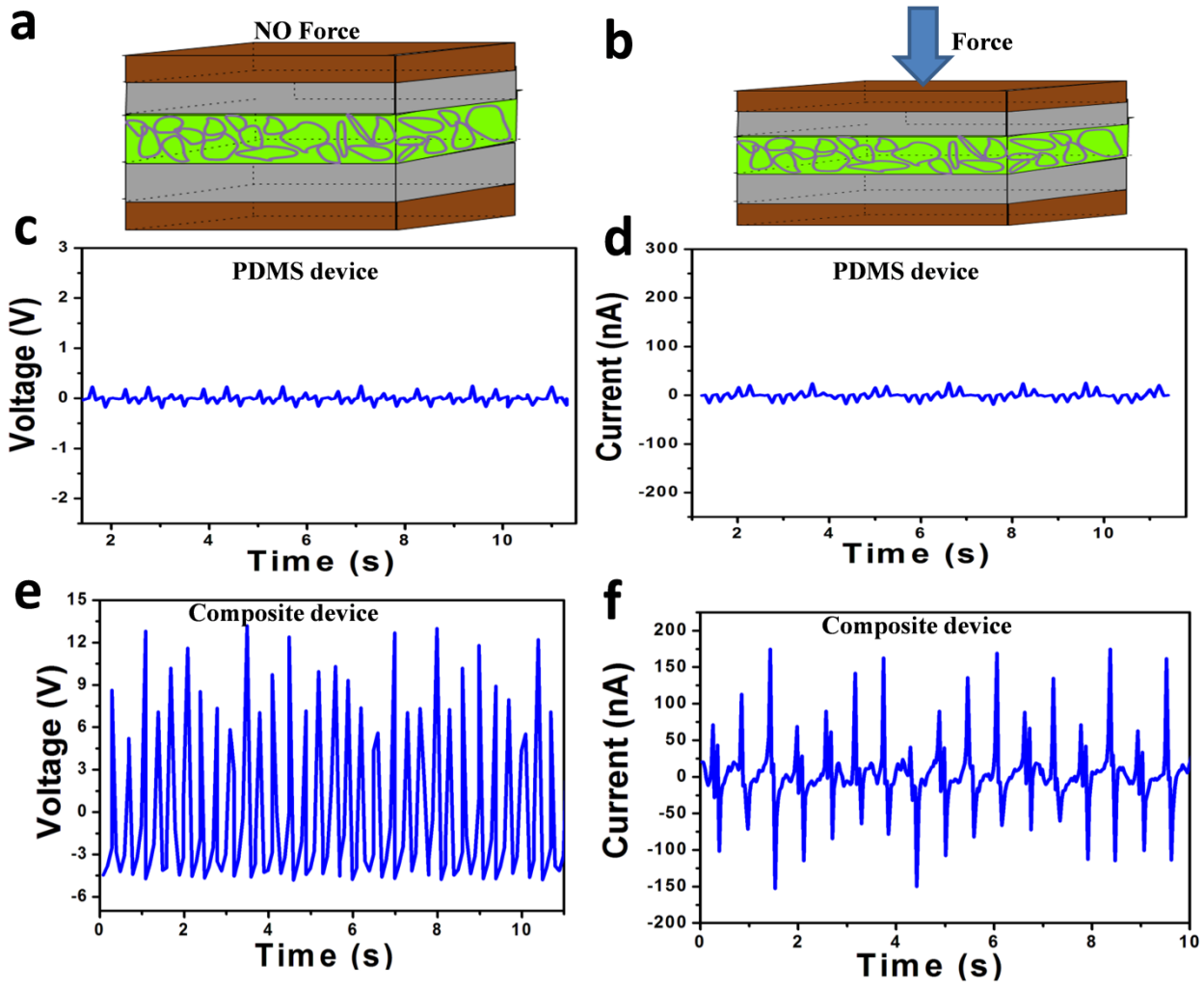

Figure 7.2.12 (a, b) Schematic diagram of the P-NG device under various force conditions. **(c, d)** Open-circuit voltage (V_{OC}) and short-circuit current (I_{SC}) results for the pure PDMS device upon 15 m/s^2 of linear motor shaft acceleration (30 N) operated between fixed distances of 10–100 mm. **(e, f)** V_{OC} and I_{SC} results for the P-NG device (10 wt% without poling) upon 15 m/s^2 of linear motor shaft acceleration (30 N) operated between fixed distances of 10–100 mm.

The durability test performed for the P-NG (10 wt% of NPs) device upon 30 N loading during 2,000 s showed no change in output, indicating good stability (**Figure 7.2.10c**). The enhanced electrical output was due to the substitution of Sn^{4+} and Ca^{2+} ions into Ti^{4+} and Ba^{2+} sites of the BTO lattice, which decreased the Curie temperature (130°C for the pristine BTO system) to room temperature. Due to the presence of the MPB, a low-energy barrier for

polarization rotation, extension and domain wall motion created the high piezoelectric performance [34, 35].

Figure 7.2.7c shows the as-fabricated simple T-NG device with a contact–separation distance of 25 mm between the flat PDMS active layer and the Al layer. The generation of a $V_{OC(p\text{-}p)}$ of 9 V when a constant mechanical force of 30 N was applied may have been due to a triboelectric effect and electrostatic induction. The low output of the simple PDMS-based T-NG device is due to the low induced surface-charge transfer between PDMS and Al layers. It resulted from the high contact–separation distance between two triboelectric active layers, the absence of surface modification and growth of nanostructures on both active layers (Al and PDMS layer), and the greater thickness of the PDMS layer (600 μm). Load resistance analysis evaluated the instantaneous power density [$P_a = (V^2)/R \times A$] of P-NG and T-NG devices under 30 N loading (**Figure 7.2.13(a, b)**). The peak-to-peak output voltage decreased for both devices as the load resistance decreased from 1 GΩ to 5 kΩ. The P-NG device delivered an instantaneous power density of 26.07 mW/m^2 at a load resistance of 70 MΩ, while the T-NG device delivered a maximum power density of 3.072 mW/m^2 at a load resistance 10 MΩ. It confirmed that the optimized load-matching resistances for the P-NG and T-NG devices were 70 and 10 MΩ, respectively. It also confirmed that the present T-NG (2.5 cm contact-separation distance) had a smaller internal resistance than the P-NG, which was central to achieving the low electrical output voltage response from the T-NG device. The NG output could be enhanced by small changes in the modulating device design/shape, an active layer, or integrating principle effect with a hybrid active layer. All of these factors may help to increase the generated electrical output from an NG significantly. In this work, the pure PDMS film in the T-NG device replaced

with the electrically poled (3 kV for 24 h at room temperature) piezoelectric hybrid flat film (10 wt% of NPs). This device referred to as the hybrid device (H-NG) is shown in Figure 7.2.7d. The H-NG generated a high $V_{OC(p\text{-}p)}$ of 250 V under the same load (30 N), i.e., a 5-fold improvement over the P-NG mode and 28-times better than the T-NG mode.

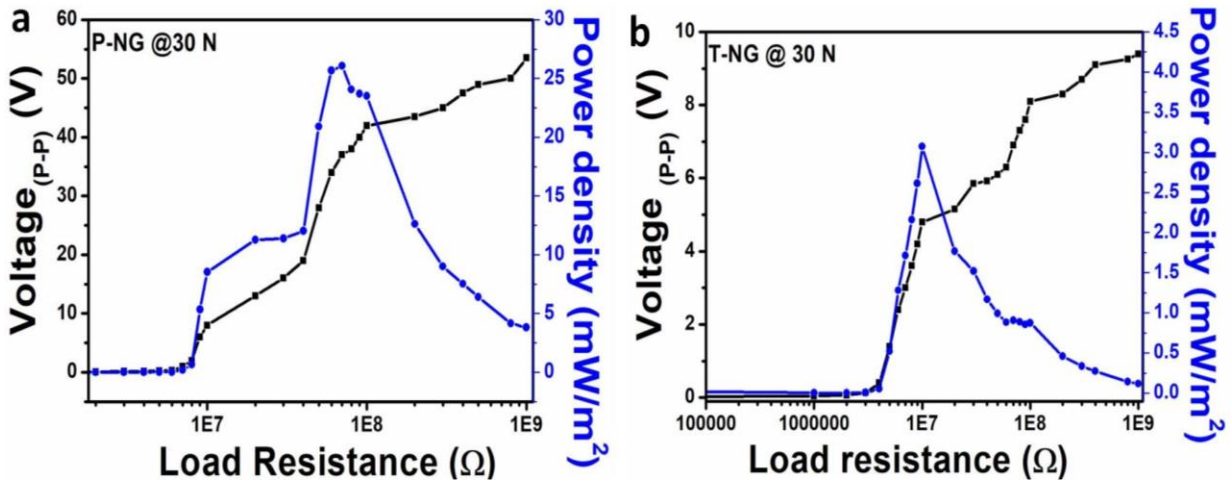

Figure 7.2.13. Load resistance analysis of the P-NG and triboelectric nanogenerator (T-NG) devices under a 30-N applied load. **(a)** Peak-to-peak voltage response and power density of the P-NG device as a function of load resistance. **(b)** Peak-to-peak voltage response and power density of the T-NG device as a function of load resistance.

This high output was due to the increased inherent capacitance of the device and the contribution of induced surface charges on the two active layers (Al foil, PDMS), as well as to the variation in the piezoelectric dipoles in the 0.3BCT-0.7BST NPs [32, 33, 36]. The induced surface charge of a composite layer approximated as

$$\boldsymbol{\sigma_{ind}} = (\mathbf{1} - \frac{\mathbf{1}}{\boldsymbol{k}})\boldsymbol{\sigma} \qquad \text{(E7.2.4)}$$

Where $\boldsymbol{\sigma_{ind}}$ is the induced surface charge density, $\boldsymbol{k}$ is the dielectric constant of the material, and $\boldsymbol{\sigma}$ is the free surface charge density. Tuning of the piezoelectric properties of BTO (by the substitution of foreign ions such as Ca^{2+} and Sn^{4+}) facilitates high energy conversion. A strong piezoelectric contribution depends on the creation of dielectric anisotropy, i.e., via

crystallographic orientation of the spontaneous polarization of the material having MPB (i.e., multiphase transition point) [34]. The longitudinal d_{33} concerning the polar axis for the tetragonal crystal structure of BTO ceramics (or single crystals) represented as [37]

$$\boldsymbol{d_{33} = cos\theta[sin^2\theta(d_{15} + d_{31}) + cos^2\theta d_{33}]} \qquad \text{(E7.2.5)}$$

Where θ is the angle to the polar axis, $\boldsymbol{d_{15}}$ is the shear coefficient, and $\boldsymbol{d_{31}}$ is the transverse piezoelectric coefficient. **Figure 7.2.7f(i)** shows the equivalent circuit model for the P-NG mode having one capacitor in which the internal resistance of the material is in series connection with the generated piezoelectric potential and load resistor. **Figure 7.2.7f(ii)** shows the equivalent circuit of a conductor–dielectric T-NG device (contact–separation) having inherent impedance is resulting from the inherent capacitance of the device because T-NGs are high-impedance charge sources. The internal resistance of T-NG is not included in the equivalent circuit because it depends on the critical distance between the contacting active layers. The H-NG equivalent circuit (**Figure 7.2.7f(iii))** describes that the generated electric potential between the electrodes is in parallel connection with the variable internal resistance and the charge accumulation variable capacitor (via metal surface (Q_m), and the piezoelectric composite surface (Q_{pc})). Figure 7.2.14a shows the electrical response of the H-NG device upon various accelerations of 1, 5, and 15 m/s^2 of shaft mass. Increasing the acceleration (from 1 to 5 to 15 m/s^2) increased the mechanical load (from 2 to 10 to 30 N) acting on the H-NG device. The load dependent output response of H-NG (contact-separation ≈2.5 cm) has the output differences are lies in between (7 V, 90 μA). Figure 7.2.15(a-c) shows the single peak output analysis of P-NG, T-NG and H-NG output responses during the press/release conditions. It demonstrates that the output of H-NG is the internal

multiplication process of piezoelectric/triboelectric functional properties of polymer composite to the active metal layers [38].

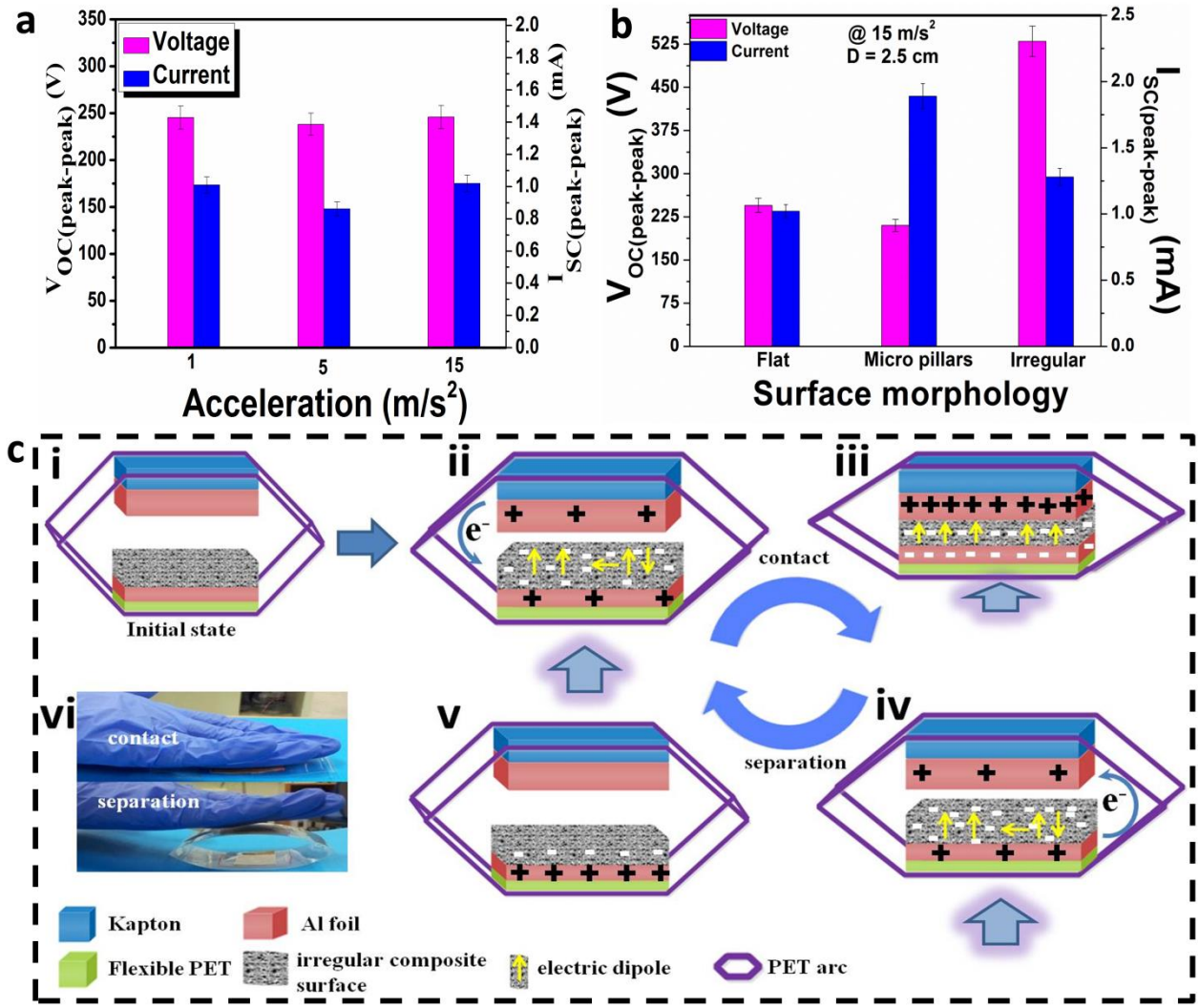

Figure 7.2.14(a, b) Electrical response of the composite surface-based H-NG device for different linear motor shaft accelerations and composite surface morphologies. (**c**) Schematic working mechanism of the H-NG device. Photographs were taken during manual contact and separation.

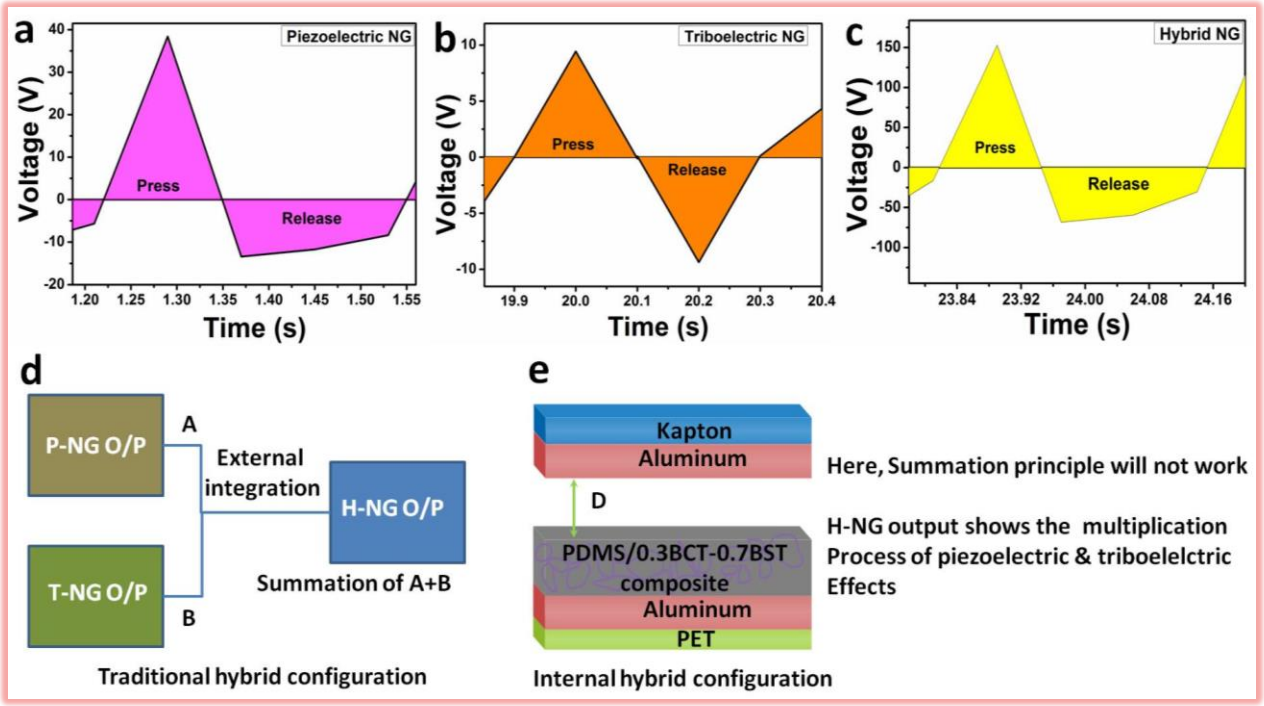

Figure 7.2.15(a-c) The magnified electrical response of all modes of nanogenerator during the press and release conditions of mechanical load (30 N). **(d)** Schematic model of external integration of piezoelectric nanogenerator (P-NG), triboelectric nanogenerator (T-NG) and the hybrid nanogenerator output with the summation principle. **(e)** Internal integration of H-NG using the multifunctional composite film along with the contact-separation distance mechanism (output is based multiplication process of intrinsic properties of individual materials, principle effects).

7.2.3.4 Effect of surface modification on the composite film H-NG

Highly efficient energy conversion depends on many factors such as rational device design [24], the use of high-performance nanostructured materials [16], environmental conditions (humidity, temperature), and the type of harvesting mode [8]. Here, the H-NG mode with a flat composite surface generated a high instantaneous power density that was ≤333 W/m^2 (P_A = (V x I)/A) that of individual modes. Furthermore, we found that the instantaneous power density of the H-NG could be increased above 333 W/m^2 by varying the composite surface morphology from flat to having periodic micropillars or an irregular network. The H-NG performance was evaluated by fabricating the micropillar/irregular morphologies based devices with fixed

dimensions (3 × 2.5 cm^2) and contact–separation distance (25 mm) between the active layers. Interestingly, H-NGs (micropillar, irregular) shows good electric responses such as (210 V, 1.89 mA), (530 V, 1.288 mA) compared to the H-NG (flat) device response (245 V, 1.02 mA) as shown **in Figure 7.2.14b**. Micropillars based H-NG generates high current compared to other two morphologies, may be due to the long-term retention capability of charges on its surfaces and each pillar surface may be acting as an individual charge boosting sites during the press/release conditions [39, 40]. Whereas in other surface morphologies based H-NGs, this effect is a somewhat considerably less, generates the lower current than the surface of the micropillar. It indicates a surface morphology-dependent electrical response of the H-NG device. The working mechanism of the H-NG is analogous to that of the conductor–dielectric layer-based [17] T-NG with an additional contribution from the piezoelectric behavior of the 0.3BCT-0.7BST NPs. The detailed mechanism of the H-NG device and the charge transfer process between the Al layer (top electrode), 0.3BCT-0.7BST/PDMS composite layer, and the bottom Al electrode depicted in the schematic diagram of **Figure 7.2.14c**. The working mechanism depends on the initial, contact–separation, and equilibrium states. During the initial state, the generated electrical potential is zero due to the absence of a friction effect between the active layers. Here, a small induced surface charges (σ_{piezo}) on the electrically poled composite (but not transferred) stemming from the piezoelectric NPs due to the small bending effect attained by the external PET arc structure shown in the inset of **Figure 7.2.14c(i)).** During the contact state, charge transfer occurs between the layers so that the composite layer gains electrons from the Al foil, leaving positive triboelectric charges on the top Al foil ($+\sigma_{tribo}$). Concurrently, minor positively induced surface charges ($+\sigma_{piezo}$) are present on the composite due to the electric dipole orientation (by a force effect) (**Figure 7.2.14c(ii, iii)**). During the separation state (force removal

state), the friction between the top Al foil and the composite layer is negligible. The generated electric potential between the electrodes causes the electrons to move from the bottom Al electrode to the top Al foil through the external load (**Figure 7.2.14c(iv)**). Then, the screened positive triboelectric charges on the top Al foil disappear, but the negative charges remain on the composite layer, which leads to the initial state of the H-NG (**Figure 7.2.14c(v)**). This contact–separation cycle of the H-NG device (Figure 7.2.14c happens periodically, thereby maximizing the induced surface charges on both active layers by driving electrons back and forth between the electrodes. The electric potential between the active surfaces calculated as follows: [41]

$$\boldsymbol{V_+ - V_- = \int_+^- \vec{E}.\overrightarrow{dx}} \qquad \text{(E7.2.6)}$$

Where $\vec{\boldsymbol{E}}$ and $\overrightarrow{\boldsymbol{dx}}$ are the electric field and finite change in the surface area. The electric field between two electrodes can be approximated using the induced SCD (σ_{ind}) in the composite and the free charge density (σ). The induced surface charge density will directly affect the total capacitance of the H-NG device. The estimated total variable capacitance ($C_T(t)$) of the device evaluated as [41]

$$\frac{\mathbf{1}}{\boldsymbol{C_T(t)}} = \frac{\mathbf{1}}{\boldsymbol{C_{composite}(t)}} + \frac{\mathbf{1}}{\boldsymbol{C_{air}(t)}} \qquad \text{(E7.2.7)}$$

$$\boldsymbol{C_{air}(t) = \frac{\varepsilon A}{d(t)} = 0}$$

When $\boldsymbol{d(t) = D = 0}$ (contact state)

Here, the distance (D) between the active layers (conductor–piezoelectric composite) of the H-NG is another crucial factor determining efficient energy conversion and $\boldsymbol{C_{composite}}$ is the capacitance of the composite sheet.

7.2.3.5 Reproducibility test

To understand the percentage of error information in the present work, we fabricated the new devices particularly composite P-NG, and H-NG devices with various surface morphologies (flat, micro pillars and irregular). The difference between the present device electrical outputs

and the electrical response of old devices is very less as shown in **Figure 7.2.16 (a-d)**. Similar kind of the current responses were observed and the corresponding results were shown in **Figure 7.2.17 (a-d)**. The percentage of error or deviation in outputs is lies below 5%. All these results clearly suggest that the proposed device outputs are highly reproducible suggesting that the devices are potential candidates to drive the low power consumed electronic devices.

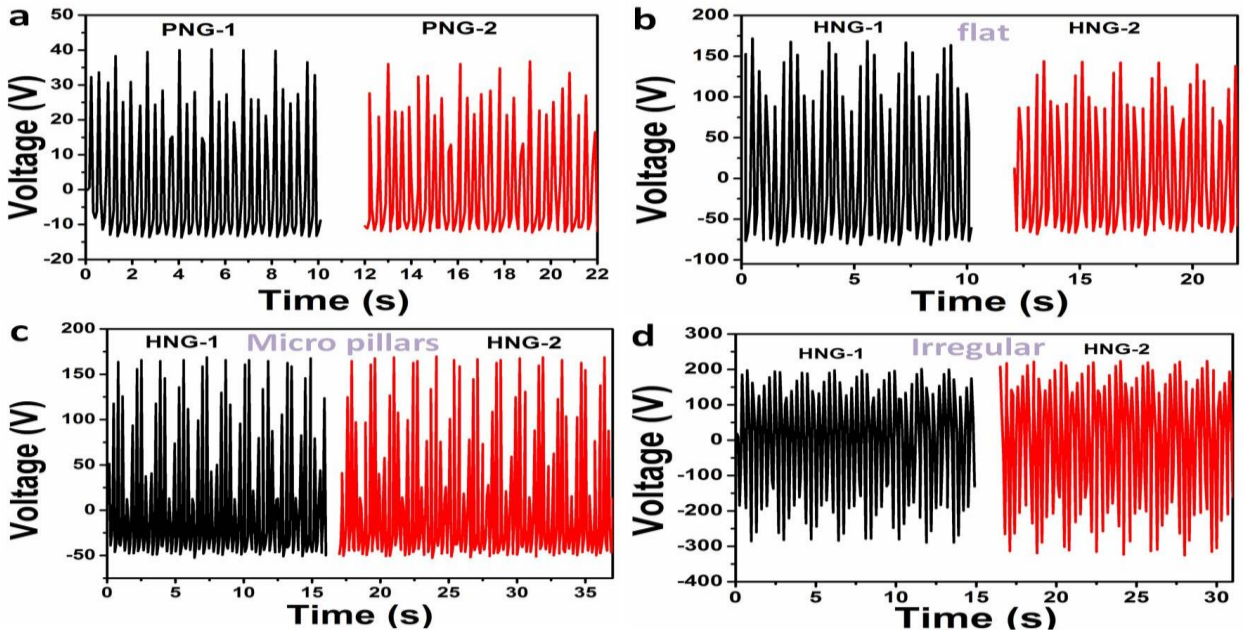

Figure 7.2.16 (a-d) Reproducibility analysis of P-NG, H-NG with various surface morphologies upon 30 N mechanical loading. Percentage of output voltage deviation between two devices is less than 5%.

7.2.3.6 Effect of the contact–separation distance, charge of the H-NG

Devices have contact–separation distances of 10, 15, and 25 mm with an irregular composite surface were fabricated to better understand the contact–separation distance effect on the performance of the H-NG device (**Figure 7.2.18a**). The maximum electrical response was observed for the H-NG device with a 15-mm distance, which confirmed that this was the optimal working contact–separation distance (**Figure 7.2.18b**). The estimated instantaneous energy conversion efficiency (ECE) was 23% for the H-NG device with a 25-mm distance under a 2-N

load. This instantaneous ECE was improved to 86% by reducing the contact–separation distance from 25 to 15 mm. **Figure 5c** shows the results and confirms that the electrical response came from the H-NG device and did not result from any external sources.

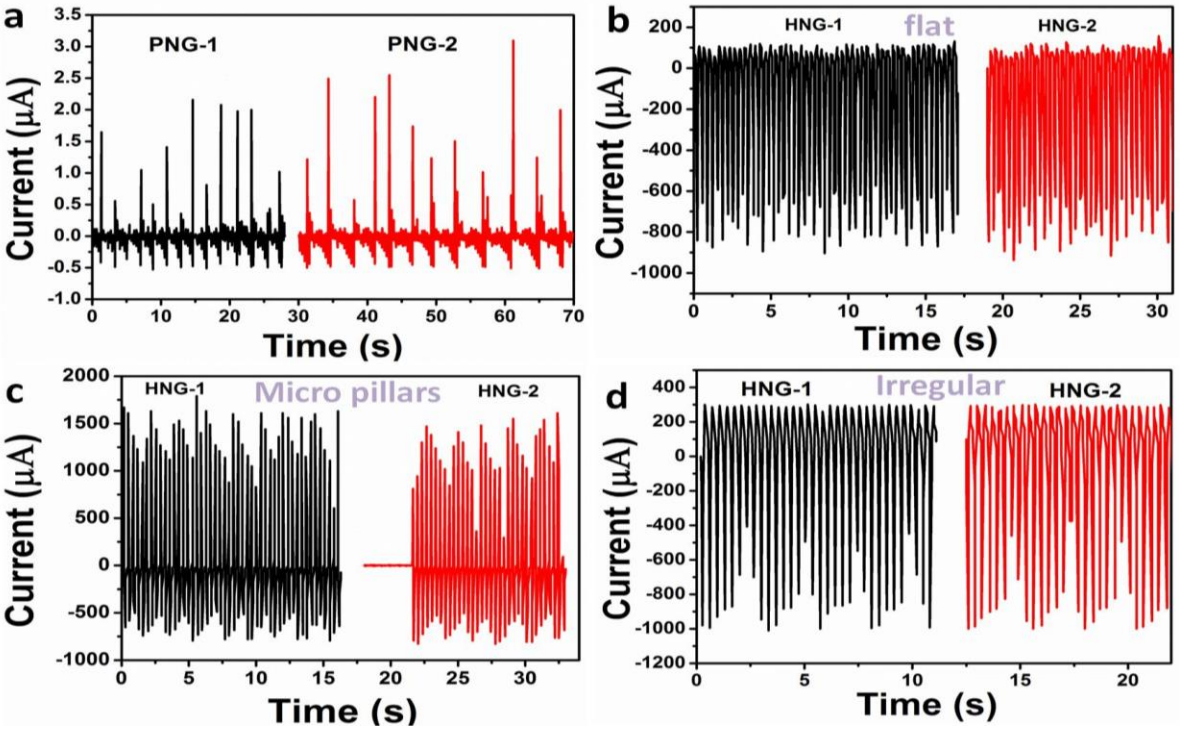

Figure 7.2.17 (a-d) Reproducibility analysis of P-NG, H-NG with various surface morphologies upon 30 N mechanical loading. Percentage of output current deviation between two devices is less than 5%.

Figure 7.2.18c shows higher negative amplitude during press compared to the positive peak amplitude during release condition (in reverse connection). This amplitude difference is due to the interaction between the polymer composite-metal layer, and the charge transfer process is slow due to the various localized surface states in the composite material, slowly deform at the time of contact [38, 42, 43]. **Figure 7.2.18 (d, e)** shows the charge accumulation behavior of the electrodes and the stored electrical potential in a commercial capacitor. A linear charge accumulation response was observed for the 0.22-μF capacitor connected in parallel with the H-NG via a rectifier circuit under various accelerations of the shaft mass. A four-fold increase of

stored charge (1.3 μC) observed for the 0.22-μF case with 15 m/s^2, which compares with a value of 0.3 μC for the same capacitor under low acceleration (1 m/s^2) during a 6 s time interval (inset of **Figure 7.2.18d**). This behavior was due to multiple contact–separations of the active layers under high acceleration of the linear motor shaft.

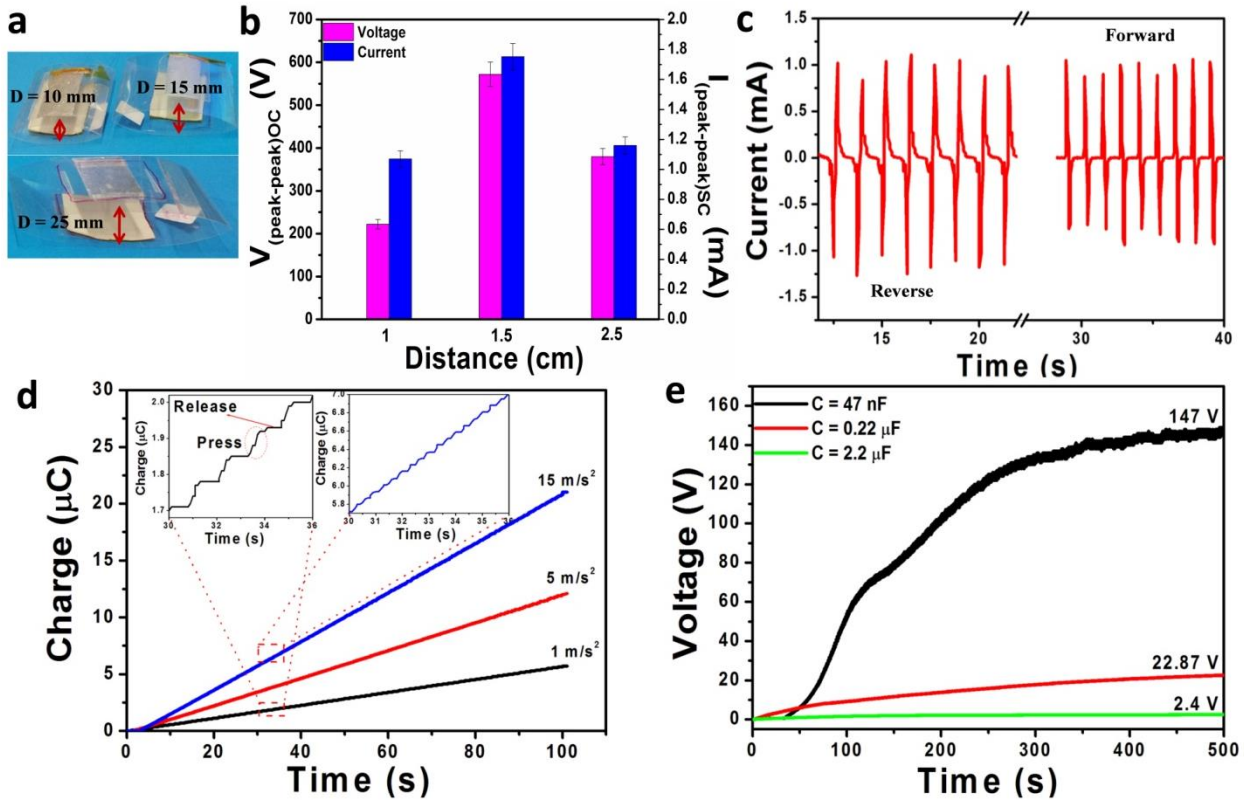

Figure 7.2.18 (a) Photographs of H-NG devices (irregular surface) with different contact–separation distances (10, 15, and 25 mm). **(b)** Peak-to-peak V_{OC} and I_{SC} results for H-NGs under 1 m/s^2 of shaft acceleration. **(c)** Polarity test results of the H-NG device under the application of biomechanical hand force. (**d**) Charge analysis of a commercial capacitor (0.22 μF) using the H-NG device (D = 25 mm) as a function of shaft acceleration. **(e)** Charging behavior of different capacitors (47 nF, 0.22 μF, and 2.2 μF) with the H-NG device upon loading with 15 m/s^2 of shaft acceleration.

Figure 7.2.18e shows the storage of the electrical potential across various load capacitors of the H-NG device under 15 m/s^2 of input acceleration. Over the last decade, to explore the working mechanism of T-NG, H-NG devices, various parameters are considered such as the thickness of layers, the distance between layers, the growth of micro/nanostructures on active

layers. Many device designs such as contact-separation [2], sliding [44], rolling [45], single electrode [46] are tested in various environmental conditions [47], respectively. Nevertheless, the working mechanisms are still not completely understood, and power density is only moderate for simple device designs. The present work experimentally determined the optimal working distance for a proposed device design, polymer *vs.* piezoelectric NPs weight ratio, composite surface morphology (flat, micropillars, irregular network), and high-performance energy harvesting modes from P-NG, T-NG, and H-NGs. The H-NG working mechanism was explained using a simple handmade device design (arc-shaped, BWS), which displayed high current density. The H-NG (D = 15 mm) with an irregular composite surface had an excellent electrical response; extensive additional testing for stability, power density, the effect of acceleration of shaft mass, charging, and development of a BWS multi-unit H-NG were carried out with this H-NG device.

Figure 7.2.19 (a, b) shows the absence of change in the electrical output (V_{OC}, I_{SC}) of the H-NG device during 1200 s of cyclic loading with 1 m/s^2 acceleration acting on the device. The results confirmed the excellent stability and suitability for real-time applications. The inset shows the magnified electrical response with good periodic peak variation with respect to the contact–separation of the active layers under load. **Figure 7.2.20** shows the generated charge quantity during press/release conditions. In reverse connection, during the press condition, the H-NG device generates negative peak current and the corresponding calculated charge quantity [48, 49] is 167.83 μC with the peak period of 0.5 s (**charge density ≈0.22 C/m^2**). During the release condition, the H-NG device generates positive peak current, and the charge quantity is 225.13 μC with the peak period of 0.9 s (**charge density 0.3 C/m^2**), respectively. Here, the charge transfer and the peak time width play a predominant role which purely depends on the intrinsic properties

of metal-dielectric (or piezoelectric/ferroelectric) layers of H-NG device. **Figure 7.2.19c** shows the acceleration-dependent electrical response of an H-NG device (D = 15 mm) indicates that the output differences are lies in between (61 V, 127 μA), respectively.

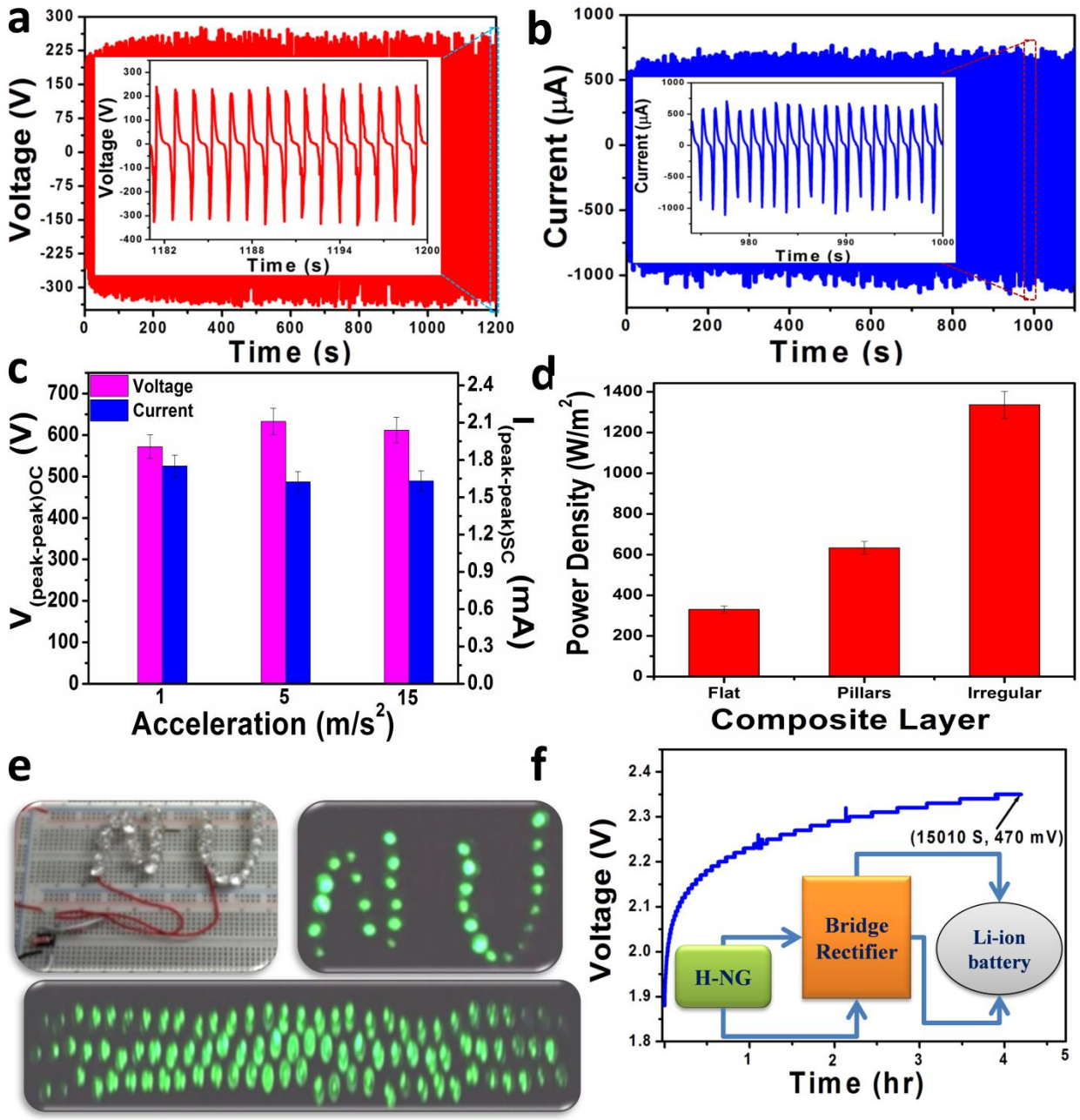

Figure 7.2.19 (a, b) Stability test results of the H-NG (D = 15 mm) with an irregular surface upon 1 m/s^2 periodic acceleration of the shaft over 1,200 s. The inset shows magnified V_{OC} and I_{SC} results of the H-NG device that indicates no degradation in output. **(c)** Peak-to-peak V_{OC} and

I_{SC} results of the H-NG device as a function of acceleration. **(d)** Comparison of power densities of H-NGs having different composite surface morphologies upon 1 m/s^2 acceleration of the linear motor. **(e)** Powering of the "NU" word and 100 green LEDs connected in series using the H-NG device output. (**f**) Charging analysis of Li-ion battery using H-NG output *via* rectifier circuit as shown in inset figure. It stores the output voltage of 470 mV after 15,010 s under 1 m/s^2 of load (i.e., 2 N).

The composite surface morphology effect on the power density of the H-NG device (3 × 2.5 cm^2, contact-separation distance ≈15 mm) estimated by analyzing the obtained outputs of as-fabricated H-NGs with different surface morphologies such as flat, micropillars, and irregular surfaces. **Figure 7.2.19d** compares the power density of the various H-NG devices when accelerated at 1 m/s^2 of shaft mass. The power density increased as the morphology changed from flat (333 W/m^2) to micropillars (632 W/m^2) and maximized with the irregular surface (1,336 W/m^2). The output of the fabricated single arc-shaped H-NG device (with an irregular surface) compared with published data for an H-NG device [50] (both external and internal modes) in **Table 7.2.1**; the results demonstrate the superior output performance of the arc-shaped H-NG device. The hybrid output successfully illuminated or powered-up 100 commercial green LEDs connected in series, as well as green LEDs arranged as the "NU" word (**Figure 7.2.19e**). **Figure 7.2.19f** analyzes the charging behavior of a commercial Li-ion battery (capacity ≈3.7 V) using the H-NG output. Initially, the Li-ion battery was discharged (3.7 to 1.875 V) by connecting to the "NANO" word using a seven-segment display over 72 continuous hours. Then, the discharged Li-ion battery was connected in parallel to the H-NG device (under 1 m/s^2 of load) using a full-wave bridge rectifier (inset of **Figure 7.2.19f**) and charged to 470 mV over 15,010 s.

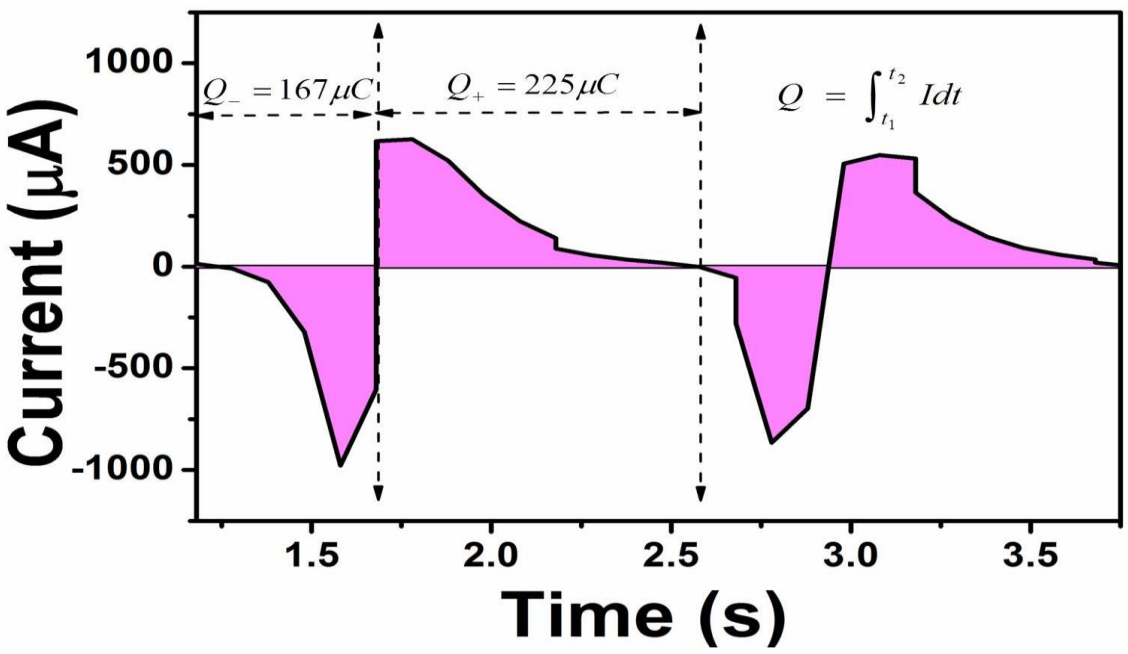

Figure 7.2.20 Evaluation of charge quantity per negative/positive cycles of H-NG device upon the biomechanical hand force.

7.2.3.7 Butterfly wing structure-type multi-unit H-NGs

A single H-NG device (with a separation distance of 15 mm) under 1 m/s^2 acceleration of shaft load (2 N) generated a power density of 1336 W/m^2. This result motivated us to fabricate a novel, simple multi-unit (four) H-NG having a BWS based on flexible PET arcs. The detailed fabrication protocol of the BWS multi-unit H-NGs depicted in the experimental section. Its output current density (J_{SC}) was measured using the mechanical force created by a linear motor at an acceleration of 1 m/s^2. **Figure 7.2.21(a, b)** shows the operating states and the corresponding digital images of the BWS multi-unit H-NG devices. The inset of **Figure 7.2.21a** shows a schematic diagram of the butterfly wings. For the single H-NG device (a1), the achieved average current density of 602 mA/m^2 upon 1 m/s^2 of the load is much higher than many published reports for T-NG and H-NG devices.

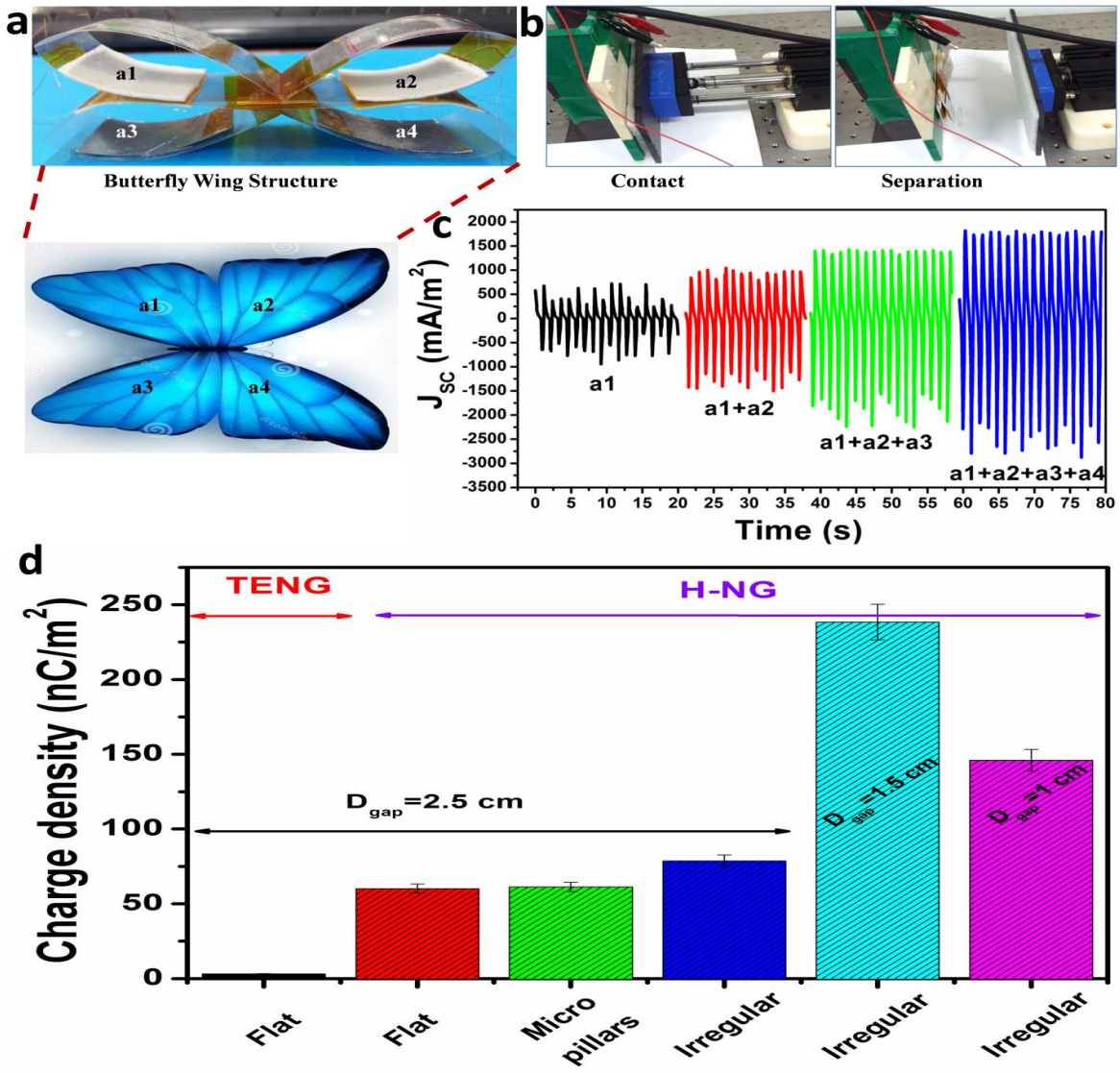

Figure 7.2.21 (a) Photograph of the butterfly wing structure (BWS) showing the four H-NG devices (a1, a2 a3 a4). **(b)** Contact–separation conditions of the BWS using a linear motor. **(c)** Output current density of individual H-NG (a1) and multi-unit H-NGs connected in parallel under constant acceleration of 1 m/s^2 by the linear motor (i.e., 2 N). **(d)** Surface charge density (SCD) of the composite layer (PDMS/0.3BCT-0.7BST NPs) in T-NG and H-NGs with various surface modifications and contact–separation distances under the acceleration of 15 m/s^2 of load (i.e., 30 N).

Table 7.2.1: Comparison of as-fabricated H-NG output with the previously reported piezoelectric-triboelectric H-NG outputs

Hybrid Device Type	Device Shape	Type of Integration	Active Materials	Device Area	Applied Force	Voltage (V)	Current	Power Density	Application/ Powering	Year of Publication/ Ref. No
P-T	r-shaped	External	PVDF PDMS Aluminum	*L*= 4 cm *T*≈100 µm	VA@1 V f_{exe} ≈5 Hz	328	-	-	LEDs/LCD display	2013/22
P-T	3D-fiber shaped	External	ZnO NRs PDMS Nylon film	108 mm^2	ME @ f_{exe} ≈2 Hz	-	300 nA	≤50 mW/m^2	Self-powered pressure sensor	2014/24
P-T	Arc-shaped	External	PVDF PTFE Gold	7x3 cm^2	0.2 N	370	12 µA/ cm^2	4.44 mW/cm^2	600 LEDs	2015/23
P-T	D-shaped	External	PVDF Silicone rubber Aluminum	4x5 cm^2	5 N	25.8	8.82 µA	-	Self-powered vibration sensor	2017/30
P-T	Rectangle	Internal	PDMS/BTO NPs Aluminum	2.25 cm^2x 0.2 cm	ME@1Hz	60	1 µA	97.41 mW/m^2	Plug & play mobile power source	2015/25
P-T	Cantilever-resonator	Internal	PDMS/BTO Copper ITO/PET	1x 3 cm^2	ME@ 20 Hz	5.5	-	-	-	2016/26
P-T	Circular	Internal	PVDF/BTO NPs-MWCNT Aluminum	*Ø*≈3.5 cm, *T*≈1.5 mm	8±0.5 N	48.46	1.22 mA/m^2	29.27 mW/m^2	-	2017/31
P-T	Arc-shaped	Internal	PDMS/0.3BCT-0.7BST Aluminum	3x2.5 cm^2	2 N	572	1.752 mA	1336 W/m^2	100 green LEDs, 'NU' word	**This work**
P-T	BWS type multi-units	Internal	PDMS/0.3BCT-0.7BST Aluminum	30 cm^2	2 N	-	2500 mA/m^2	-	Self-powered air pressure sensor	**This work**

P: Piezoelectric**, T:** Triboelectric, **BWS**: butterfly wing structure, **ME**: Motor excitation, **VA**: vibrator amplitude, **f_{exe}**: Excitation frequency, ***Ø***: Diameter, *T*: thickness, **NPs**: Nanoparticles, **NRs**: Nanorods, **PVDF**: Polyvinylidene fluoride, **PTFE**: Polytetrafluoroethylene, **PDMS**: Polydimethylsiloxane, **BTO**: $BaTiO_3$, **MWCNT**: Multi-walled carbon nanotubes, **0.3BCT-0.7BST**: $0.3Ba_{0.7}Ca_{0.3}TiO_3$-$0.7BaSn_{0.12}Ti_{0.88}O_3$

The average current densities generated were 1,186 mA/m^2, 1,753.6 mA/m^2 and 2,391.7 mA/m^2 for parallel connection configurations between H-NG devices of a1+a2, a1+a2+a3, and a1+a2+a3+a4, respectively (**Figure 7.2.21c**). The high current density of the H-NG device (with the irregular surface) resulted from the acquisition of a large SCD. It depends on the relative permittivity of the composite, the distance between the active layers, and the surface modification of the composite layer (i.e., flat, micropillars, or an irregular network). The induced SCD (σ) of the as-prepared composite surface quantitatively determined for all H-NG devices with different morphologies and distances (D = 10, 15, and 25 mm), respectively. **Figure 7.2.21d** shows the evaluated SCD values. The induced SCD of composite layer was calculated using the permittivity of free space ($\varepsilon_o = 8.8541\times10^{-12}$ F/m) and distance as follows: [40]

$$\sigma = \frac{V_{OC} \times \varepsilon_0}{D} \qquad \text{(E7.2.8)}$$

The SCD of the flat H-NG device (D = 25 mm) was 60.207 nC/m^2, which is much higher than that for the pure PDMS T-NG (3.1984 nC/m^2) under an acceleration of 15 m/s^2 of the linear motor (load). In this case, the relative permittivity of the composite and the weight percentage (f) of the piezoelectric NPs (10 wt %) are essential to achieving an σ that is higher than those of the individual materials (PDMS, ε_{pdms} ≈3; 0.3BCT-0.7BST NPs, ε_{piezo} ≈3800).

The surface charge density of the H-NG device (D= 25mm) with various composite surfaces are analyzed. The irregular surface-based H-NG device generated an induced SCD on the composite surface is (78.67 nC/m^2) higher than that of the flat (60.207 nC/m^2) and micropillar (61.27 nC/m^2)-based H-NG devices. The irregular surface morphology with micropores on the composite surface reduced the thickness and increased the contact surface area. The effect of the contact–separation distance (10, 15, and 25 mm) on the induced SCD of the H-

NG (irregular surface) was also analyzed (**Figure 7.2.21d**). The H-NG device (15 mm) generated a higher induced SCD (238.42 nC/m^2) of the composite than the H-NG (25 mm) (78.67 nC/m^2). The maximum induced SCD (σ_{max}) of an H-NG device can be calculated by treating the device as a flat capacitor, as follows: [39, 40]

$$\sigma_{\max} = \frac{\sigma D \varepsilon_T \varepsilon_{Al}}{d_1 \varepsilon_{Al} + D \varepsilon_T \varepsilon_{Al} + d_2 \varepsilon_T} \qquad \text{(E7.2.9)}$$

Where ε_T and ε_{Al} are the relative permittivities of the composite and Al layer, d_1 and d_2 are the thicknesses of the Al film and composite layer (irregular surface), respectively, and D is the gap between the two contact layers. The maximum induced SCD ($\sigma_{\max}$) of the H-NG devices (10, 15, and 25 mm distances) calculated using Equation (E7.2.9) ranged from 0.96 to 0.98 C/m^2. Experimentally evaluated charge density of H-NG (irregular surface) is 0.3 C/m^2 lesser than the theoretical value (0.98 C/m^2) of H-NG. It suggests that the still there is an unknown parameter is available to reach the theoretical SCD value. The high current density of the BWS multi-unit H-NG resulted from the cumulative effect of the induced SCD of four H-NGs. The high output of the H-NG, BWS multi-unit H-NG is a combination of piezoelectric and triboelectric effects. At the same, the output depends on the optimal weight ratio of the nanoparticles in the polymer, the improvement in ε_{eff} of composite layer, the irregular surface morphology with micropores, the optimum contact–separation distance between the two active layers, the effective contact surface area, and the thickness of the composite film.

7.2.3.8 Self-powered air pressure sensor using BWS multi-unit H-NG

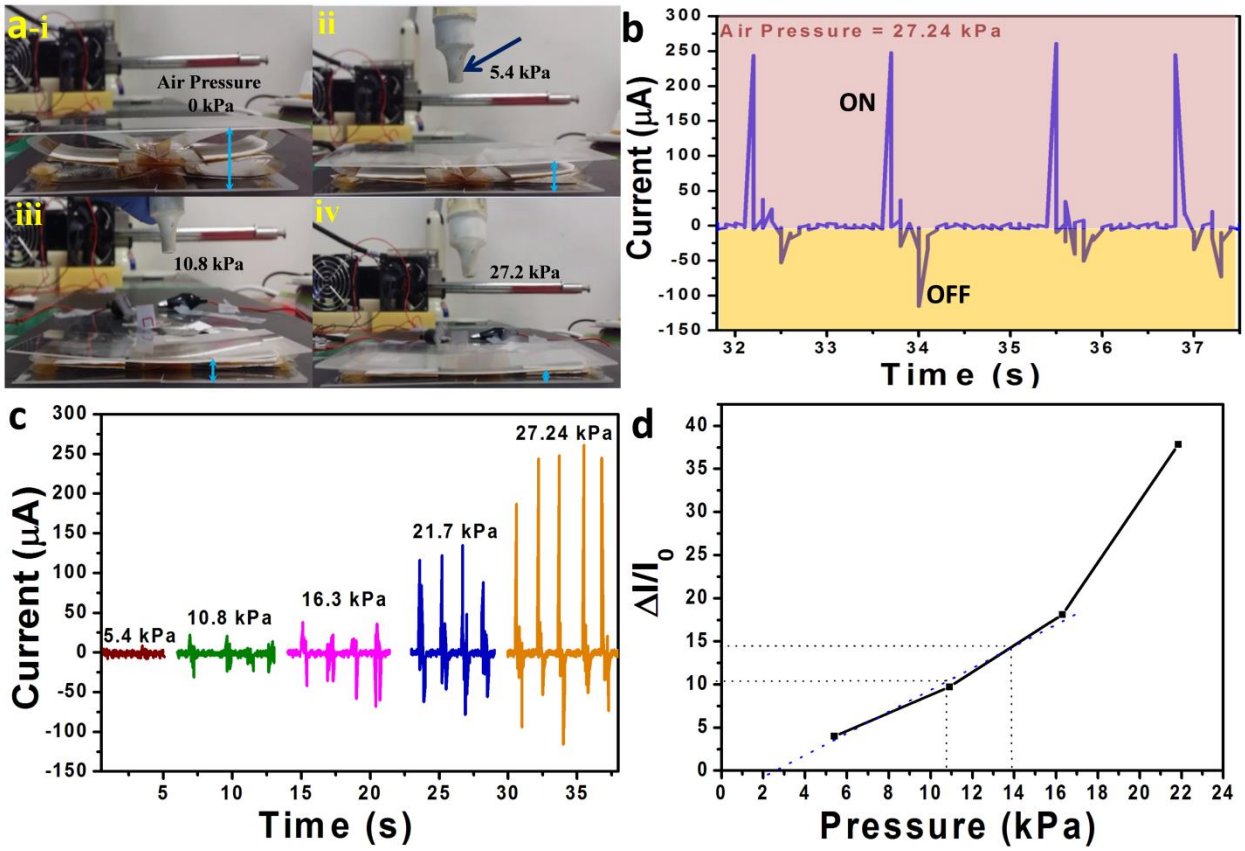

Figure 7.2.22 (a) Photographs of a self-powered air pressure sensor using the BWS multi-unit H-NG under various air pressure conditions. **(b)** I_{SC} of the BWS multi-unit H-NG at high air pressure (27.24 kPa) during periodic ON and OFF states. **(c)** I_{SC} of the BWS multi-unit H-NG for various air pressures ranging from 5.4 to 27.24 kPa. (**d**) Relative current change for the BWS multi-unit H-NG as a function of external air pressure.

The BWS multi-unit H-NG could be used not only as a stand-alone, independent power supply but also as a self-powered air pressure sensor for real-time monitoring applications. An air pressure of 5.4–27.24 kPa was applied to the BWS multi-unit H-NG at 2 cm from the top surface of the device (**Figure 7.2.22a**). Two transparent, flexible flat PET sheets were attached to the top and bottom of the wing structure using double-sided adhesive tape; this tape protected the wing from physical damage and provided proper motions to the wing. **Figure 7.2.22b** shows the I_{SC} of the BWS multi-unit H-NG when high air pressure (27.24 kPa) was applied perpendicularly

to the device with periodic ON/OFF conditions. **Figure 7.2.22a-i** shows that there is no interaction between the wings, resulting in zero output response. Under low air pressure (5.4 kPa), only a minimal output observed across the output terminals due to a weak interaction between the wings as shown in **Figure 7.2.22a–ii**. When medium air pressure (10.8 kPa) was applied, the bottom two wings (two H-NGs) contacted gently (**Figure 7.2.22a–iii**) during the stress ON condition, which generated a positive output current (<20 μA) across the terminals. An air pressure of 10.8–27.24 kPa produced a more significant output current that varied from 20 to 270 μA (positive peak side) (**Figure 7.2.22c**). Here, the movements of the BWS multi-unit H-NGs layers closely resembled the natural butterfly flapping wing motion (up and down). The relative change of current response of the BWS multi-unit H-NG pressure sensor as a function of applied pressure is plotted in **Figure 7.2.22d**. The sensitivity of a pressure sensor can be calculated using the following equation:

$$\boldsymbol{S = \frac{\delta(^{\Delta I}/_{I_0})}{\delta P}} \qquad \text{(E7.2.10)}$$

$$\boldsymbol{\Delta I = I - I_0} \qquad \text{(E7.2.11)}$$

Where *P*, I are the applied pressure, and the obtained current when the force applied to the device and I_0 is the current under the base pressure. The calculated sensitivity of the air pressure sensor in the linear region was 1.286 kPa^{-1}; at high pressures (>20 kPa), the pressure sensor generated a nonlinear high output (**Figure 7.2.22(c, d)**) that was nonlinear. The possible low air pressure limit of 2–3 kPa was estimated by extrapolation (**Figure 7.2.22d**). All of these results demonstrated that a single H-NG or BWS multi-unit H-NG device could function as a stand-alone power source to drive LEDs or liquid crystal displays (LCDs), charge commercial Li-ion cells, or work in self-powered monitoring devices.

7.2.4 Conclusions

In summary, a BWS multi-unit H-NG device (having a contact–separation distance of 15 mm) with high output current density (2,500 mA/m^2) was developed using a scalable synthesis of a microporous irregular composite surface. A high electrical response resulted from the generation of a high SCD on the H-NGs, which in turn depended on the multifunctional properties of the NP fillers in a PDMS matrix, surface modification, and the distance between the layers. Compared with the P-NG and T-NG modes, the arc-shaped H-NG mode had a large electrical output due to the contribution of piezoelectric and triboelectric effects. The power density of a single arc-shaped H-NG with an irregular surface was four-times higher (1336 W/m^2) and that with a micropillar surface was two-timed more (632 W/m^2) that of the H-NG having a flat surface (333 W/m^2). The H-NG parameters are evaluated such as charge accumulation, charging capability (using a commercial Li-ion coin cell and capacitor), the acceleration dependence of shaft mass, the ability to power-up 100 green LEDs, and to light up the "NU" word using LEDs. Other than these, studied the effective relative permittivity, the d_{33} coefficients as a function of the weight fraction of NPs in the PDMS matrix. A single H-NG or BWS multi-unit H-NG device can function as a stand-alone power source or as a self-powered sensor for real-time monitoring applications. This work will have a significant impact on the development of next-generation hybrid devices as high-power, large-scale independent power sources.

7.2.5 References

1. Park, K. I.; Son, J. H.; Hwang, G. T.; Jeong, C. K.; Ryu, J.; Koo, M.; Choi, I.; Lee, S. H.; Byun, M.; Wang, Z. L.; Lee, K. J. *Adv. Mater*. **2014**, 26, 2514–2520.
2. Lin, Z. H; Xie, Y; Yang, Y; Wang, S; Zhu, G; Wang, Z. L. *ACS Nano*, **2013**, 7, 4554.
3. Bowen, C. R.; Taylor, J.; LeBoulbar, E.; Zabek, D.; Chauhan, A.; Vaish, R. ***Energy Environ. Sci*. 2014**, **7**, 3836-3856.
4. Lee, B. S.; Park, B.; Yang, H. S.; Han, J. W.; Choong, C.; Bae, J.; Lee, K.; Yu, W. R.; Jeong, U.; Chung, U. I.; Park, J. J.; Kim, O. *ACS Appl. Mater. Interfaces*. **2014**, 6, 3520−3527.
5. Cha, S. N.; Kim, S. M.; Kim, H. J.; Ku, J. Y.; Sohn, J. I.; Park, Y. J.; Song, B. J.; Jung, M. H.; Lee, E. K.; Choi, B. L.; Park, J. J.; Wang, Z. L.; Kim, J. M.; Kim, K. *Nano Letters*, **2011**, 11, 5142-5147.
6. W. Suk Jung, M. J. Lee, S. H. Baek, I. K. Jung, S. J. Yoon, C. Y. Kang Nano Energy. **2016**, 22, 514-523.
7. Saravanakumar, B.; Thiyagarajan, K.; Nagamalleswara Rao, A.; SoYoon, S.; Taehyun, K.; Lin, Z. H.; Kim, S. J. *Carbon*. **2015**, 84, 56–65.
8. Gu, L.; Cui, N.; Cheng, L.; Xu, Q.; Bai, S.; Yuan, M.; Wu, W.; Liu, J.; Zhao, Y.; Ma, F.; Qin, Y.; Wang, Z. L. *Nano Lett*. **2013**, 13, 91−94.
9. Aneesh, K.; Sodano, H. A. Nat. Commun. **2013**, 4, 1-10.
10. Stassia, S.; Caudab, V.; Ottonea, C.; Chiodonib, A.; Pirri, C. F.; Canavese, G. *Nano Energy*. **2015**, 13, 474–481.
11. Nagamalleswara Rao, A.; Saravanakumar, B.; Sang Jae, K. *ACS Appl. Mater. Interfaces*. **2015**, *7*, 9831–9840.
12. Nagamalleswara Rao, A.; Sophia, S.; Arunkumar, C.; B. Saravanakumar, Gae Myoung L.; Ji Hyun J.; Sang Jae, K. *Energy*, **2016**, 118, 1146-1155.
13. Nagamalleswara Rao, A.; Sophia S.; Arunkumar C.; Balasubramaniam S.; Ji Hyun J.; Sang-Jae K.; Compos. Sci. Technol. **2017**, 142, 65-78.
14. Nagamalleswara Rao, A.; Arunkumar C.; Venkateswaran V.; Yuvasree P.; Sophia S.; Ji Hyun J.; Sang-Jae K.; *ACS Sustainable Chem. Eng.*, **2017**, *5* (6), 4730–4738.
15. Wang, S.; Xie, Y.; Niu, S.; Lin, L.; Liu, C.; Zhou, Y. S.; Wang, Z. L. *Adv. Mater*. **2014**, 26, 6720–6728.

16. Chen, J.; Guo, H.; He, X.; Liu, G.; Xi, Y.; Shi, H.; Hu, C. *ACS Appl. Mater. Interfaces.* **2016**, 8, 736–744.
17. Lee, K. Y.; Chun, J.; Lee, J. H.; Kim, K. N.; Kang, N, R.; Kim, J. Y.; Kim, M. H.; Shin, K. S.; Gupta, M. K.; Baik, J. M.; Kim, S. W. *Adv. Mater*. **2014**, 26, 5037–5042.
18. Zhou, Y. S.; Wang, S.; Yang, Y.; Zhu, G.; Niu, S.; Lin, Z. H.; Liu, Y.; Wang, Z. L. *Nano Lett*. **2014**, 14, 1567−1572.
19. Xiaona, X.; Jie, C.; Guanlin, L.; Muhammad, S.J.; Xue, W.; Chenguo, H. Carbon, **2017**, 111, 569-576.
20. Xiaona, X.; Jie, C.; Hengyu, G.; Guanlin, L.; Dapeng, W.; Yi, X.; Xue, W.; Chenguo, H. Nano Res. 2017, 10, 320-330.
21. Zi, Y.; Lin, L.; Wang, J.; Wang, S.; Chen, J.; Fan, X.; Yang, P.K.; Yi, F.; Wang, Z. L. *Adv. Mater*. **2015**, 27, 2340-2347.
22. Han, M.; Zhang, X. S.; Meng, B.; Liu, W.; Tang, W.; Sun, X.; Wang, W.; Zhang, H.; *ACS Nano.* **2013**, *7*, 8554–8560.
23. Jung, W. S.; Kang, M. G.; Moon, H. G.; Baek, S. H.; Yoon, S. J.; Wang, Z. L.; Kim, S. W.; Kang, C. Y. *Sci. Rep*. **2015**, 5, 1-6.
24. Li, X.; Lin, Z. H.; Cheng, G.; Wen, X.; Liu, Y.; Niu, S.; Wang, Z. L. *ACS Nano*, **2014**, *8*, 10674–10681.
25. Shi, B.; Zheng, Q.; Jiang, W.; Yan, L.; Wang, X.; Liu, H.; Yao, Y.; Li, Z.; Wang, Z. L. *Adv. Mater*. **2015**, 28, 846–852.
26. Suo, G.; Yu, Y.; Zhang, Z.; Wang, S.; Zhao, P.; Li, J.; Wang, X. *ACS Appl. Mater. Interfaces*, **2016**, 8, 34335-34341.
27. Ko, Y. J.; Kim, D. Y.; Won, S. S.; Ahn, C.W.; Kim, I. W.; Kingon, A. I.; Kim, S. H.; Ko, J. H.; Jung, J. H. *ACS Appl. Mater. Interfaces*, **2016**, 8, 6504–6511.
28. Lee, J. H.; Lee, K. Y.; Gupta, M. K.; Kim, T. Y.; Lee, D. Y.; Oh, J.; Ryu, C.; Yoo, W. J.; Kang, C. Y.; Yoon, S. J.; Yoo, J. B.; Kim, S. W. *Adv. Mater*. **2014**, 26, 765–769.
29. Wang, S.; Wang, Z. L.; Yang, Y. *Adv. Mater*. **2016**, 28, 2881-2887.
30. Zhu, J.; Hou, X.; Niu, X.; Guo, X.; Zhang, J.; He, J.; Guo, T.; Chou, X.; Xue, C.; Zhang, W.; Sens. Actuator A-Phys. **2017**, 263, 317-325.
31. Yang X.; Daoud, W.A. **J. Mater. Chem. A**, **2017**, **5**, 9113-9121.

32. Wanchul, S.; Hong-Joon, Y.; Tae Yun, K.; Hanjun, R.; Jihye, K.; Ju-Hyuck, L.; Jeong Hwan, L.; Sanghyun, K.; Yun Kwon, P.; Young Jun, P.; Sang-Woo, K. Adv. Energy Mater. 2016, 7, 1600988-93.
33. Jie, W.; Changsheng, W.; Yejing, D.; Zhihao, Z.; Aurelia, W.; Tiejun, Z.; Wang, Z. L.; Nat. Commun. **2017**, 8, 1-8.
34. Xue, D.; Zhou, Y.; Bao, H.; Gao, J.; Zhou, C. *Appl. Phys. Lett*. **2011**, 99, 122901-3.
35. Liu, W.; Ren, X. *Phys. Rev. Lett*. **2009**, 103, 257602-257605.
36. Peng, B.; Guang, Z.; Yu Sheng, Z.; Sihong, W.; Jusheng, M.; Gong, Z.; Wang, Z. L. Nano Res. **2014**, 7, 990-997.
37. Nye, J. F. Physical Properties of Crystals. Clarendon Press, Oxford, **1957**.
38. Bartosz, A. G.; Marcin, F.; Jason A. W. J. Phys. Chem. B **2005**, 109, 20511-20515.
39. Parvez Mahmud, M. A.; Jae Jong, L.; Gee Hong, K.; Hyung Jun, L.; Kee-Bong, Choi. Eng. **2016**, 159, 102–107.
40. Chun, J.; Kim, J. W.; Jung, W. S.; Kang, C.Y.; Kim, S. W.; Wang, Z. L.; Baik, J. M. *Energy Environ. Sci.* 2015, 8, 3006-3012.
41. Taghavi, M.; Beccai, L. NanoEnergy, **2015**, 18, 283–292.
42. Lowell, J.; Rose-Innes, A.C. Contact electrification, Adv. Phys. 1980, 29, 947-1023.
43. Dawes, D. K., Static Electrification, IOP Conference Series, 1967, No. 4, 29.
44. Niu, S.; Liu, Y.; Wang, S.; Lin, L.; Zhou, Y. S.; Hu, Y.; Wang, Z. L. *Adv. Mater*. **2013**, 25, 6184–6193.
45. Zhu, G.; Chen, J.; Zhang, T.; Jing, Q.; Wang, Z. L. Nat. Commun. **2013**, 5, 1-9.
46. Arunkumar, C.; Nagamalleswara Rao, A.; Saravanakumar, B.; Sophia, S.; Kim, S. J. *ACS Appl. Mater. Interfaces*. **2016**, 8, 9692-9699.
47. Nguyen, V.; Zhu, R.; Yang, R. *NanoEnergy*. 2015, 14, 49–61.
48. Wei, T.; Tao, J.; Feng Ru, F.; Ai Fang, Y.; Chi, Z.; Xia, C.; Wang, Z. L Adv. Funct. Mater. **2015**, *25*, 3718–3725.
49. Guang, Z.; Zong-Hong, L.; Qingshan, J.; Peng, B.; Caofeng, P.; Ya, Y.; Yusheng, Z.; Wang, Z.L. Nano Lett. **2013**, 13, 847−853.
50. Subash Cherumannil Karumuthil, Sreenidhi Prabha Rajeev, Soney Varghese, Nano Energy 40 (2017) 487–494.

CHAPTER-VIII

Summary and future work

8.1 Summary

This chapter describes the overall view of thesis work, conclusions and possible future directions in this research area. The thesis mainly focused on the development of the various self-powered sensors (removal of external battery source, additional components) to monitor the physical/optical/chemical stimuli using the innovative hybrid piezoelectric structure nanogenerators. For this, we proposed the innovative, cost-effective composite fabrication methods for achieving the efficient, flexible hybrid piezoelectric structures and its corresponding nanogenerators. The research work presented in this thesis shown the following contributions in the field of composite technology, piezoelectric nanogenerators and the self-powered sensors.

- First two chapters describe worldwide energy crisis issues, the effect of continuous usage of traditional energy harvesting technologies, problem statement of the present thesis work and materials/instruments used to perform the proposed research work. Also described the working principles of the PNG, TENG devices to harness the waste mechanical energy in the environment and explained the role of the types of existing piezoelectric materials for energy harvesting. Further, briefly explained about the fabrication of piezoelectric nanogenerator, modes of the self-powered sensors/systems and its electrical response measuring instruments.
- The radial growth of TiO_2 (nanoneedles + nanoparticles), $BaTiO_3$ (nanorods + nanoparticles) on the flexible human hair-sized metal Ti-wire [($Ø$) ≈100 μm, (L) ≤6 cm] using the chemical oxidation modification method followed by hydrothermal technique was reported in the Chapter-3. A Raman pattern of grown TiO_2 NSs are in anatase phase,

and the conversion of TiO_2 to BTO NSs is in tetragonal crystalline phase. XPS analysis confirms the existence of titanium (Ti) is 4+, barium (Ba) is 2+ and conversion of TiO_2 NSs into BTO NSs creates internal stresses of TiO_6 octahedron in BTO lattice. The internal pressures of TiO_6 octahedron in BTO lattice observed by the slight peak shift of Ti 2p and O 1s peak positions. The FW-PNG device generates peak-to-peak I_{SC}, V_{OC} is ≈600 nA, ≈7 V, and area power density is ≈ 22.5 μW/cm^2 at 10 MΩ upon 2 N load. This type of FW-PNGs occupies less area, more convenient to place on any contour mechanical surfaces, and excellent portability/wearability, respectively. All the results suggest that flexible BTO NSs/Ti-wire, TiO_2 NSs/Ti-wire, and FW-PNGs are potential candidates for developing micro/nanodevices on mechanical contour structures, wire-based self-powered sensors, and flexible energy harvesters. In the present successfully implemented the self-powered wire type UV sensor was demonstrated using the parallel connection between the wire type piezoelectric nanogenerator, and wire type UV sensor.

- **Chapter-4** describes the two types of planar piezoelectric composites such as PVDF/BTZO-nanocubes, PDMS/BTO-nanocubes using the solution casting technique. High crystalline $BaTi_{(1-x)}Zr_xO_3$ (x = 0, 0.05, 0.1, 0.15, and 0.2) nanocubes synthesized using a molten-salt process. The BTZO/PVDF flexible nanogenerator exhibits a high output response (11.9 V, 1.35 μA) compared to the BTO/PVDF nanogenerator output of (7.99 V, 1.01 μA) constant load (11 N). Demonstrated PNG as a self-powered fluid velocity sensor to measure different water velocities at an outlet pipe. Composite PNG has dual functionality (harnessing energy + sensing). The second composite film based nanogenerator was tested under biomechanical force conditions and the generated electrical output is used to light up the low power consumed light emitting devices.

- For the first time, ionotropic gelation approach was implemented in the energy harvesting sector and the process is eco-friendly, cost-effective (**Chapter-5**). It offers to develop the innovative piezoelectric composite structures such as spherical beads, linear worms and wavy-pattern worm structures. All these structures were used to fabricate the nanogenerators such as piezoelectric, triboelectric and hybrid devices to analyze the energy harvesting capability and its usefulness as a self-sustaining power sources. CBNG device generates (82 V, 227 μA) upon low mechanical pressure 1.70 kPa. Piezoelectric-tribolelectric hybrid nanogenerator work as self-powered flexion sensor to classify and measure the individual/combined finger flexion/extension movements. The **second section** describes the Length dependant piezoelectric response of linear composite worms was analyzed. Commercial LEDs, LCD powered by the aligned WPNGs. The WPNG output voltage increased by up to 1.5 times, when the length of the worm increased from 1.5 to 3.5 cm. Similarly, the output voltages increased about five-fold for a worm length of 2.5 cm (diameter = 550 μm) when the cyclic frequency of the mechanical load changed from 3 to 20 Hz. The **third section** proposed single CWPW device has greater peak-peak $V_{OC} \approx 21.12$ V and $I_{SC} \approx 2.53$ μA (L = 1.95 cm, D = 0.055 cm) as compared to the single nanowire/micro belts. This is due to the crystallographic orientation of BTO lattice, lowering dielectric constant, internal stress of TiO_6 octahedron in BTO lattice and may be due to the acceptance of large mechanical force. We also found that, CWPW structures enable high piezoelectric potential generation and tuneable piezoelectricity by increasing the number of crests for wavy patterns, weight ratio of piezoelectric nanoparticles, electric polling and mechanical force. Next, we demonstrated the CLW as pH sensor under solutions with different pH values (alkaline value: 12-8) and

self powered concept was realized by considering the CWPW device as power source unit. The pH solution dependent conductivity of CLW by metal (M)-semiconductor (S)-metal (M) interface is well matched with the electrical response of self-powered pH sensor.

- **Chapter-6** describes the enhancement of electroactive-β phase of the PVDF polymer by applying the high tip amplitude of the probe sonicator. Also the β-phase content of PVDF improved and stabilizes up to ≈91.75 % by the substitution of sheet type AC fillers in PVDF matrix solution with 30 V/V %. The formation mechanism of β-phase PVDF, energy harvesting capability of the composite nanogenerator was investigated and successfully utilized to monitor the various accelerations of the linear motor shaft load. Here, C-NG generates the instantaneous power density of ≈63.07 mW/m^2. C-NG device itself can act as a self-powered acceleration sensor and the output voltage shows linear behavior between the input accelerations 0.5 to 5 m/s^2 of shaft load.
- **Chapter-7** reports the innovative cost-effective groove technique to fabricate the adoptable/flexible hemispherical composite strips. Also developed the flexible energy harvesting glove to harness the biomechanical energy and demonstrated the self-powered muscle monitoring system using the multiple hemispherical composite strip based devices. HS-CSPNG can generate the maximum amount of output voltage/current are 130 V, 800 nA and switching polarity test of current confirming that the generated electrical response is from the device, not from any other sources. The **second part** in this chapter describes the efficient approach to generate the maximum amount of electrical energy by combining the piezoelectric and triboelectric properties in single composite structure. Also designed the arc-shaped hybrid nanogenerator and investigated

the electrical response by modulating the contact-separation distance between the layers, changing the surface morphology of the composite films. It generates a high amount of power density ≈1336 W/m^2. Finally, developed the butterfly wing structure type multi-unit hybrid nanogenerator and tested to monitor the various amounts of air-pressures. The $V_{OC(P-P)}$ = 572 V and $I_{SC(P-P)}$ = 1.752 mA for the irregular surface-based H-NG is higher when compared with The $V_{OC(P-P)}$ = 53 V and $I_{SC(P-P)}$ = 2.366 μA for P-NG. The power density of a single H-NG with an irregular surface was four-times higher, and that of the micro-pillared surface was double that of the H-NG with a flat surface (333 W/m2). A BWS multi-unit H-NG device (contact-separation distance = 15mm) generates a high output current density 2500 mA/m^2 using the microporous irregular composite surface.

The overview the thesis's research works describes the lead-free piezoelectric $BaTiO_3$ and its co-doped nanostructures along with the polymer support can be possible generate the innovative hybrid structures to improve the instantaneous power density of the PNG and H-NGs as shown in **Figure 8.1**. The flexible hybrid piezoelectric structures performance depends on the weight ratio of nanoparticles in polymer matrix, thickness of the film, external poling process and the applied perpendicular mechanical force. The synergistic (piezoelectric-triboelectric) effect at the material design level or at the device design level will enhance the generated power density of the device. All these hybrid piezoelectric structures and its nanogenerators are potential candidate to develop the self-powered sensors/systems to monitor/glow the physical/optical/chemical stimuli/LEDS'LCDs.

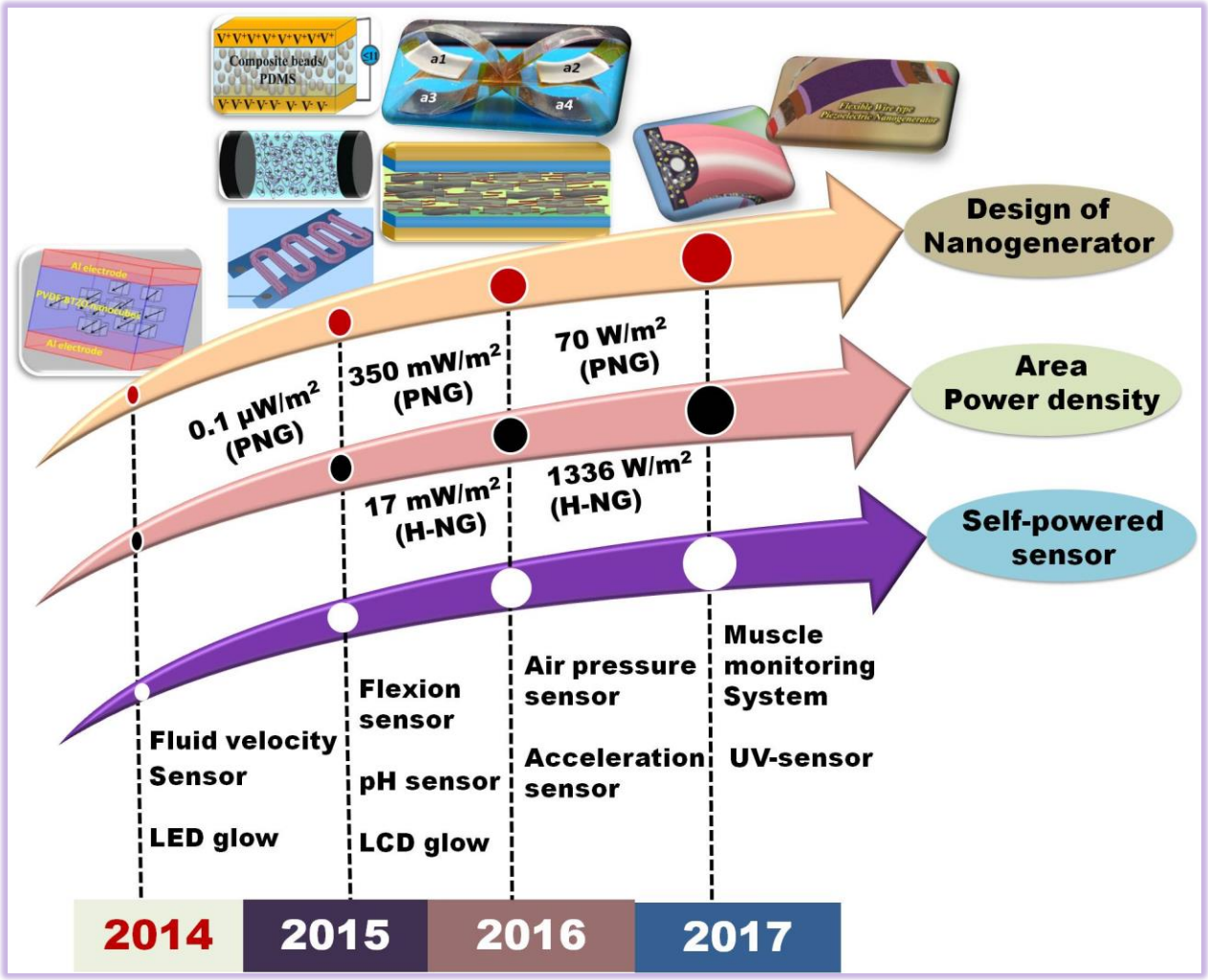

Figure 8.1 The final overview of this thesis

8.2 Suggestions for the future work

Over the decade continuous progress happen on the development and improvement of instantaneous power density of the nanogenerators. Only one or two flexible piezoelectric nanogenerator designs are commercialized and still needs to be improved by understand the growth of perovksite nanostructures on flexible substrates. Highly adoptable and stretchable piezoelectric nanostructure arrays needs to be developed in future for developing the next

generation smart sensors, and energy harvesting units. Based on the thesis content, the following recommendations were suggested for the future.

1. Contrary to traditional planar piezoelectric-triboelelctric H-NGs, innovative internal integration of the H-NG device designs and its underlying intrinsic working mechanisms needs to be explored with the justified theoretical equations.
2. The self-powered sensors performance needs to be improved and at the same time the device area needs to be reduced for better commercialization of the product.
3. The power management circuits, establishment of long range wireless communication protocols needs to be implemented along with the piezoelectric and triboelectric nanogenerators.

Appendix A: List of Publications

1. **Nagamalleswara Rao Alluri**, Arunkumar Chandrasekhar, Sang-Jae Kim, **Biomimetic multiunit piezo-triboelectric hybrid nanogenerator for high power output, ACS Sustainable Chemistry and Engineering**, 2018.
   DOI: 10.1021/acssuschemeng.7b03337 **I.F =5.9**
2. **Nagamalleswara Rao Alluri**, V. Vivekananthan, C. Arunkumar, S. J. Kim, "Adapatable Piezoelectric Hemispherical Composite Strips using Scalable Groove Technique for Self-powered Muscle Monitoring System", **Nanoscale**, 2017.
   DOI: 10.1039/C7NR06674K,
   [Selected as an inside front cover page] **I.F =7.37**

3. **Nagamalleswara Rao Alluri,** Yuvasree Purusothaman, Arunkumar Chandrasekhar, Sang-Jae Kim, "In-situ radial growth of $BaTiO_3/TiO_2$ nanostructures on human hair sized single Ti-wire based battery-free UV sensor", **Chemical Engineering Journal, 2017.** https://doi.org/10.1016/j.cej.2017.11.149 **I.F =6.2**

4. **Nagamalleswara Rao Alluri**, C. Arunkumar Chandrasekhar, J.H. Jeong, S. J. Kim, "Enhanced electroactive β-phase of the sonication-process-derived PVDF-activated carbon composite film for efficient energy conversion and a battery-free acceleration sensor", **Journal of Materials Chemistry C**, 2017, 5, 4833-4844. **[Published as a front cover page & Hot article)** **I.F = 5.25**

5. **Nagamalleswara Rao Alluri**, C. Arunkumar Chandrasekhar, V. Vivekananthan, P. Yuvasree, S. Sophia, J. H. Jeong, S. J. Kim, "Scavenging Biomechanical Energy using High-performance Flexible $BaTiO_3$ Nanocube/PDMS Composite Films"**, ACS Sustainable Chemistry and Engineering ,** 2017, 5, 4730-4738. **I.F = 5.951**

6. **Nagamalleswara Rao Alluri**, S. Sophia, C. Arunkumar, B. Saravanakumar, J. H. Jeong, S. J. Kim, "Piezoelectric $BaTiO_3$/alginate spherical composite beads for energy harvesting and self-powered wearable flexion sensor", **Composite Science and Technology,** 2017**,** 142, 65-78. **I.F = 4.873**

7. **Nagamalleswara Rao Alluri**, S. Sophia, C. Arunkumar, B. Saravanakumar, G. M. Lee, J. H. Jeong, S. J. Kim, "Worm structure piezoelectric energy harvester using ionotropic gelation of barium titanate-calcium alginate composite", **Energy, 2017**, 118, 1146-1155. **I.F = 4.52**

8. **Nagamalleswara Rao Alluri**, S. Sophia, C. Arunkumar, B. Saravanakumar, J. H. Jeong, S. J. Kim, "Self-powered pH sensor using piezoelectric composite worm structures derived by ionotropic gelation approach", **Sensors and Actuators B: Chemical**, 2016, 237, 534-544. **I.F = 5.401**

9. **Nagamalleswara Rao Alluri**, B. Saravanakumar, S. J. Kim, "Flexible, hybrid piezoelectric film ($BaTi_{(1-x)}Zr_xO_3$/PVDF nanogenerator as a self-powered fluid velocity sensor)", **ACS Applied Materials & Interfaces**, 2015, 18, 9831-9840. **I.F = 7.501**

10. P. Yuvasree, **Nagamalleswara Rao Alluri**, C. Arunkumar, V. Vivekananthan, S. J Kim, "Regulation of Charge Carrier Dynamics in ZnO Micro-Architecture Based UV/Visible Photodetector via Photonic-Strain Induced Effects", Small, 2017, DOI: 10.1002/smll.201703044 **I. F = 8.315**

11. V. Vivekananthan, **Nagamalleswara Rao Alluri**, P. Yuvasree, C. Arunkumar, S. J. Kim, "A flexible, planar energy harvesting device for scavenging road side waste mechanical energy via synergistic piezoelectric response of $K_{0.5}Na_{0.5}NbO_3$-$BaTiO_3$/PVDF composite films", **Nanoscale,** 2017, 9, 15122-15130. **I.F = 7.367**

12. S. Sophia, **Nagamalleswara Rao Alluri**, C. Arunkumar, S. J. Kim, "Direct detection of cysteine using functionalized $BaTiO_3$ nanoparticles film based self-powered biosensor", **Biosensors and Bioelectronics,** 2017, 91, 203–210. **I.F = 7.780**

13. C. Arunkumar, **Nagamalleswara Rao Alluri**, M.S.P Sudhakaran, Y. S. Mok, S. J. Kim, "Smart Mobile Pouch as a Biomechanical Energy Harvester towards Self-Powered Smart Wireless Power Transfer Applications", **Nanoscale,** 2017, 9, 9818-9824. **[Published as a front cover page]** **I.F=7.367**

14. P. Yuvasree, **Nagamalleswara Rao Alluri**, C. Arunkumar, S. J. Kim, "Elucidation of the unsymmetrical effect on the piezoelectric and semiconducting properties of Cd-doped 1D-ZnO nanorods", **Journal of Materials Chemistry C**, 2017, 5, 415-426. **I.F = 5.2565**

15. S. Sophia, **Nagamalleswara Rao Alluri**, C. Arunkumar, S. J. Kim, "Unconventional active biosensor made of piezoelectric $BaTiO_3$ nanoparticles foe biomolecule detection",**Sensors and Actuators B: Chemical**, **2017,** 253, 1180-1187. **I.F=5.401**

16. C. Arunkumar, **Nagamalleswara Rao Alluri**, V. Vivekananthan, P. Yuvasree, S. J. Kim, "Sustainable freestanding biomechanical energy harvesting smart back pack as a portable–wearable power source", **Journal of Materials Chemistry C**, **2017**, 5, 1488-1493. **I.F = 5.2565**

17. P. Yuvasree, **Nagamalleswara Rao Alluri**, C. Arunkumar, S. J. Kim, "Harnessing low frequency-based energy using $K_{0.5}Na_{0.5}NbO_3$ (KNN) pigmented piezoelectric paint system", **Journal of Materials Chemistry C**, **2017**, 5, 5501-5508. **I.F = 5.2565**

18. C. Arunkumar, **Nagamalleswara Rao Alluri**, V. Vivekananthan, J. H. Park, S. J. Kim, "Sustainable Biomechanical Energy Scavenger towards Self-Reliant Kids' Interactive Battery-Free Smart Puzzle", **ACS Sustainable Chemistry and Engineering,** 2017, 5, 7310-7316. **I.F = 5.951**

19. C. Arunkumar, **Nagamalleswara Rao Alluri**, B. Saravanakumar, S. Sophia, S. J. Kim, "Microcrystalline cellulose ingrained polydimethylsiloxane triboelectric nanogenerator as a self-powered locomotion detector", **Journal of Materials Chemistry C**, **2017**, 5, 1810-1815. **I.F = 5.2565**

20. S. Sophia, **Nagamalleswara Rao Alluri**, C. Arunkumar, S. J. Kim, "$BaTiO_3$ nanoparticles as biomaterial film for self-powered glucose sensor application", **Sensors and Actuators B: Chemical**, 2016, 234, 395-403. **I.F = 5.401**

21. C. Arunkumar, **Nagamalleswara Rao Alluri**, B. Saravanakumar, S. Sophia, S. J. Kim, "Human interactive triboelectric nanogenerator as a self-powered smart seat", **ACS Applied Materials & Interfaces,** 2016, 8, 9692-9699. **I.F = 7.501**

22. V. Ganesh Kumar, MSP Sudhakaran, **Nagamalleswara Rao Alluri**, K. Karthikeyan, Y. S. Mok, S. J. Kim, "Effective use of an idle carbon-deposited catalyst for energy storage applications", **Journal of Materials Chemistry A**, **2016**, 4, 12571-12582. **I.F = 8.867**

23. B. Saravanakumar, K. Thiyagarajan, **Nagamalleswara Rao Alluri**, S. Y. Shin, K. Taehyun, Z. H. Lin, S. J. Kim, "Fabrication of an eco-friendly composite nanogenerator for self-powered photosensor applications", **Carbon, 2015**, 84, 56-65. **I.F = 6.337**

24. K. Karthikeyan, V. Ganesh Kumar, **Nagamalleswara Rao Alluri**, S. J. Kim, "One-pot hydrothermal synthesis, characterization and electrochemical properties of CuS nanoparticles towards supercapacitor applications", **Materials Research Express, 2014**, 1, 035006. **I.F = 1.068**

List of submitted papers & book chapters

1. Book chapter on “Energy Harvesting” and the chapter title: “Hybrid structures for piezoelectric nanogenerators: Fabrication methods, energy generation and self-powered applications” by **Nagamalleswara Rao Alluri**, Arunkumar Chandrasekhar, Sang-Jae Kim, Edited by: Prof. Reccab Manyala, **ISBN 978-953-51-5992-6**, **IN TECH Open**. [**Under Progress**]

Appendix: B List of Cover Pages

1. Published as a front cover in Journal of Materials Chemistry C (I.F = 5.2)

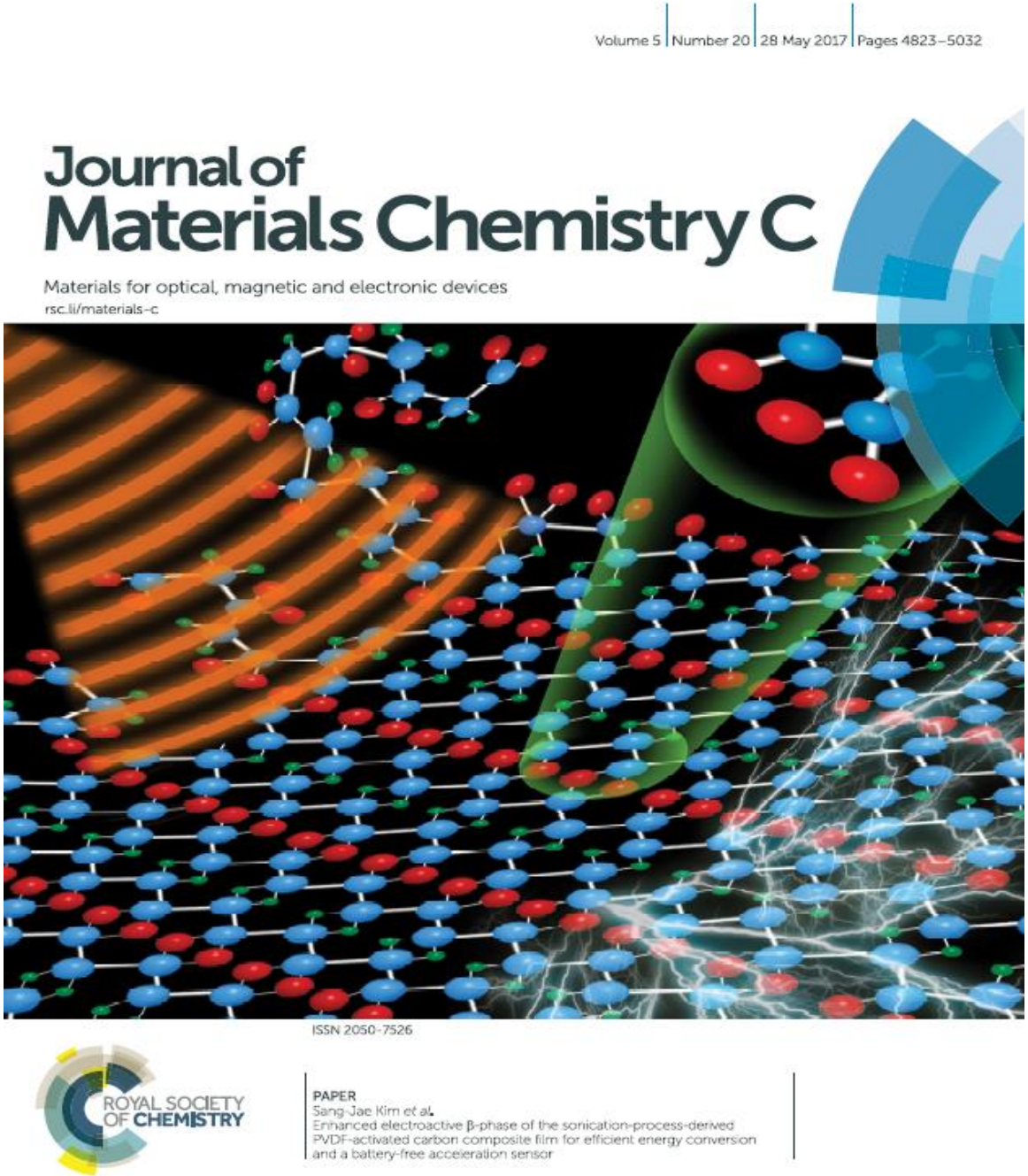

2. Selected as a inside front cover-Nanoscale (I.F 7.37)

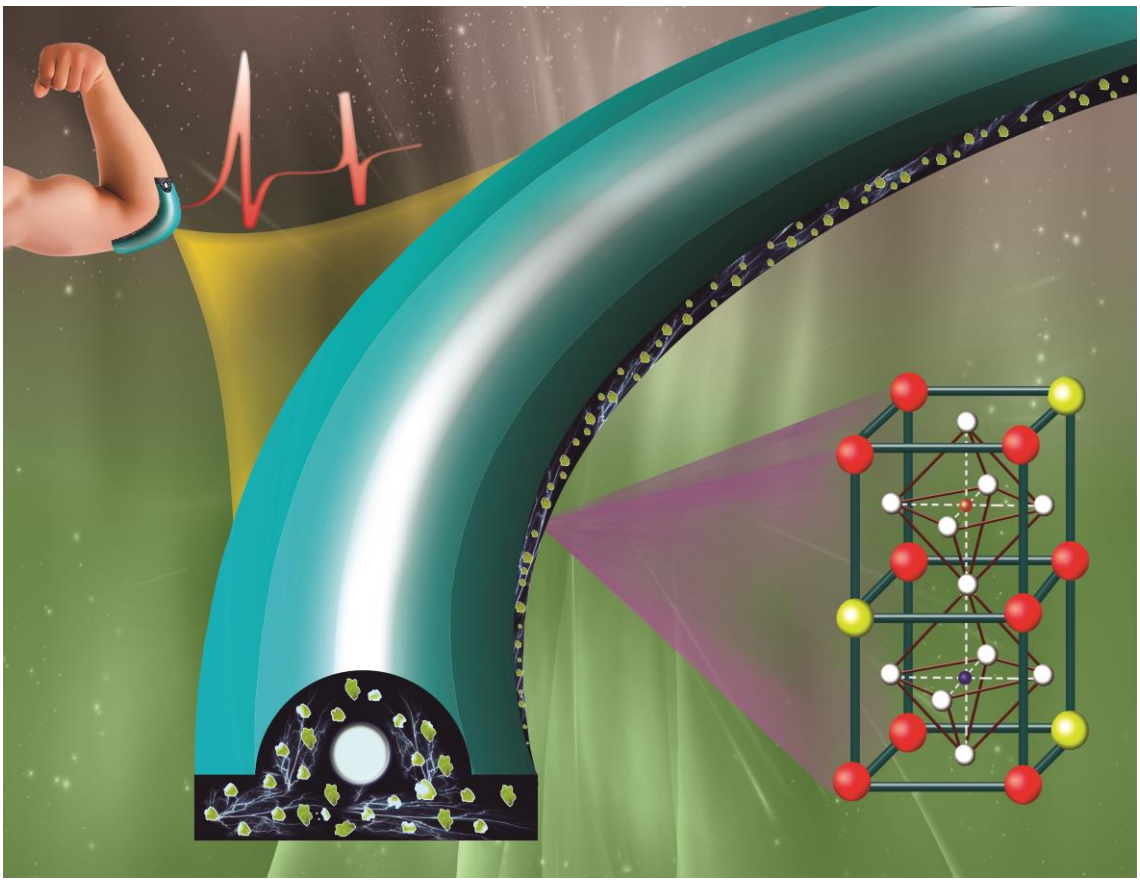

Appendix: C List of Patents

1. **Butterfly wing structure type multiunit Hybrid Nanogenerator with high energy conversion**
   - Piezo Triboelectric Hybrid Nanogenerator for High Power output and Preparation Method of the same**, Korean Patent, Ref. No: DP20160304,** filed on 2016.12.28. [Jointly with Prof. Sang-Jae Kim]

2. **Cost-effective Groove Technique for Hemispherical Composite Strips**
   - Strip type Piezoelectric Composite Preparation Method and Muscle Monitoring System, **Korea Patent, Ref. No: DP20170117** (Final draft filing is Under Process). [Jointly with Prof. Sang-Jae Kim]

3. **Developed Radial Growth of $BaTiO_3$ Nanostructures on Human hair sized Ti-wire**
   - Flexible Piezoelectric Nanogenerator Containing Barium Titanate and Preparation Method of the same, **Korea Patent, Ref. No: DP20170116** (Final draft filing is Under Process). [Jointly with Prof. Sang-Jae Kim]

4. **Method for Manufacturing Titanium-based Optical Sensitive Wire**, **Korea Patent, Ref. No: DP20170136** Final draft filing is Under Process). **[**Jointly with Prof. Sang-Jae Kim]

Appendix D: List of Conference/Symposium Proceedings

Conferences/ Symposiums	Total	Awards
International	42	1 [Oral, First author], 1 [Poster, First author] 4 [Poster, Co-author]
National	11	1 [Oral, First author] 2 [Oral, Co-author]

Selected Conferences/Symposiums

1. **Nagamalleswara Rao Alluri,** ArunKumar Chandrasekhar, Sang-Jae Kim, **"**Boosted Energy Conversion via Piezo-Triboelectric Coupling in Irregular Composite Film for Self-powered Systems, **NENS2017,** Beijing, China, October 21-23, 2017. **[Oral Presentation]**
2. **Nagamalleswara Rao Alluri**, Sophia Selvarajan, Arunkumar Chandrasekhar, Ji Hyun Jeong, Sang-Jae Kim, Hybrid Nanogenerator as a Self-Powered Air Pressure Sensor, **ICAMR-2017**, Hong Kong, Jan 20-22, 2017. [**Awarded as a Best Oral Presentation**]
3. **Nagamalleswara Rao Alluri**, Sophia Selvarajan, Arunkumar Chandrasekhar, Ji Hyun Jeong, Sang-Jae Kim, Beads-Worm microstructures using BTO nanoparticles functionalized by Ca-Alginate biopolymer for Piezoelectric nanogenerators, 14th IUMRS-International Conference on Advanced Materials **(IUMRS-ICAM)**, October 25~ 29, 2015, ICC Jeju, Korea (Oral).
4. **Nagamalleswara Rao Alluri**, Arunkumar Chandrasekhar, Sang-Jae Kim, Composite Piezoelectric Nanogenerator as Self-Powered Acceleration Sensor, Joint symposium of Jeju National University and Nagasaki University on Science and Technology (JSST 2017) 25.05.2017, Jeju Island, Korea. [**Award as a Best Oral presentation**]
5. **Nagamalleswara Rao Alluri**, Sophia Selvarajan, Arunkumar Chandrasekhar, Ji Hyun Jeong, Sang-Jae Kim, BTO/Ca-Alginate Linear Worm based piezoelectric nanogenerator and its self-powered application**,** The 3rd International conference on Advanced Electromaterials **(ICAE),** November, 17~20, 2015, ICC Jeju, Korea (Oral)**.**
6. **Nagamalleswara Rao Alluri**, C. Arunkumar, S. Sophia, Ji Hyun Jeong, Sang Jae Kim, High Performance Piezoelectric-Triboelectric Nanogenerator using Irregular Surface Morphology, **ISPSA-2016**, July 3-7, Jeju Island, Korea (Oral).
7. **Nagamalleswara Rao Alluri**, Balasubramaniam Saravanakumar, Kim Taehyun, Ji Hyun Jeong, Sang-Jae Kim, Nanogenerator as a self-powered flow sensor to measure fluid velocity,

AsiaNANO 2014, October 26 to 29, **[Awarded as a Best Poster Award]**

8. **Nagamalleswara Rao Alluri**, Sophia Selvarajan, Arunkumar Chandrasekhar, Ji Hyun Jeong, Sang-Jae Kim, Chemically synthesized $BaTiO_3$ nanostructures-polymer interfaces for self-powered devices, **MCARE-2017**, Jeju Island, Korea, Feb.20-24, 2017. [**Poster**]
9. **Nagamalleswara Rao Alluri**, Arunkumar Chandrashekar, Sophia Selvarajan, Ji Hyun Jeong, Gae Myoung Lee Sang Jae Kim, Piezoelectric-Triboelectric Hybrid Nanogenerator as a Self-Powered Air Pressure Sensor, **ENGE-2016**, Nov 6 -9, Jeju, South Korea.
10. **Nagamalleswara Rao Alluri,** Arunkumar Chandrashekar, Sophia Selvarajan, Ji Hyun Jeong, Sang Jae Kim, Radial growth of $BaTiO_3$ nanostructures-polymer interfaces for self-powered devices, **MRS-2016 Fall meeting**, Nov 27-Dec 2, Boston, USA.
11. **Nagamalleswara Rao Alluri**, Sophia Selvarajan, Arunkumar Chandrasekhar, Ji Hyun Jeong, Sang-Jae Kim, Piezoelectric Composite Wavy Pattern Worm Nanogenerator for Self-Powered pH Sensor, **NGPT 2016**, Rome, June 15-17, 2016 (Poster).
12. **Nagamalleswara Rao Alluri**, Arunkumar Chandrasekhar, Sang-Jae Kim, Realization of Self-Powered Acceleration Sensor using PVDF Polymer/Activated Carbon Composite Film, **4th ICAE**, Nov. 21~ 24, 2017, Jeju, Korea.
13. **Nagamalleswara Rao Alluri**, Venkateswaran Vivekananthan, Arunkumar Chandrasekhar, Sang-Jae Kim, Enhanced output performance of piezoelectric $BaTiO_3$ Nanocubes/PDMS composite film, **10th ICAMD-2017,** 05 ~ 08, 2017 Jeju, Korea.
14. **Nagamalleswara Rao Alluri**, Balasubramanian Saravanakumar and Sang-Jae Kim, Brick shaped microstructure of $BaZr_{0.05}Ti_{0.95}O_3$ powders by Molten-Salt Method and its Nanogenerator application, **Korean Physical Society Jeju Special Branch**, Academic paper presentations and conferences, poster No: PA-12 2014/8/13 to 14.
15. **Nagamalleswara Rao Alluri**, Sophia Selvarajan, Arunkumar Chandrasekhar, Ji Hyun Jeong, Sang-Jae Kim, Eco-Friendly Hybrid Piezoelectric Structures for Utilization of Wind and Vibration Energy, **KMEMS 2017**, Mar 30 ~ Apr 01, Jeju Island, Korea.
16. **Nagamalleswara Rao Alluri,** Ji Hyun Jeong, Sang-Jae Kim, Eco-Friendly composite nanogenerators for self-powered sensors, **Invited lectures and workshops for the third year (BK21+)** 2016-01-18. [Oral Presentation]
17. Venkateswaran Vivekananthan, **Nagamalleswara Rao Alluri**, Arunkumar Chandrasekhar, Yuvasree Purusothaman, Stuctural and Piezoelectric Analysis of Flexible (1-x)KNN-xBTO/PVDF Composite films for Energy Harvesting Applications. Joint symposium of Jeju National University and Nagasaki University on Science and Technology (**JSST 2017**) 25.05.2017, Jeju Island, Korea. [**Award as a Best Oral presentation**]

18. Arunkumar Chandrasekhar, **Nagamalleswara Rao Alluri**, Venkateswaran Vivekananthan, Sang-Jae Kim, Portable-Wearable Triboelectric Nanogenerators for Self-Powered Systems, **4th ICAE**, Nov. 21~ 24, 2017, Jeju, Korea.
19. Ganesan Kausalya, **Nagamalleswara Rao Alluri**, Kim Pandiarajan Thangavel, Nirmal Prashanth Maria Joseph Raj, Sang-Jae, Flexible, Self-poled ferroelectret polymer composite film based nanogenerator for sustainable power sources, The **10th ICAMD-2017,** 05 ~ 08, 2017 Jeju, Korea.2017 Jeju, Korea.
20. Sophia Selvarajan, **Nagamalleswara Rao Alluri**, Arunkumar Chandrasekhar, Sang-Jae Kim, Multifunctional biosensor for monitoring protein-drug interactions with potential in theranostics, **10th ICAMD-2017,** 05 ~08, 2017 Jeju, Korea. [**Awarded as a best poster**]
21. Ganesan Kausalya, **Nagamalleswara Rao Alluri**, Kim Sang-Jae, Role of Oxidation States on the Nucleation of Poly(vinylidene fluoride) β- Phase for Harnessing Biomechanical Energy, The 4th International Conference on Advanced Electromaterials (ICAE-2017) Nov. 21-24, 2017 Jeju, Korea.
22. C. Arunkumar, **Nagamalleswara Rao Alluri**, Venkateswaran Vivekananthan, Sang-Jae Kim, Multifunctional NE-TENG for Biomechnical Energy Scavenging and Self-Powered Health Monitoring Systems, Joint symposium of Jeju National University and Nagasaki University on Science and Technology (JSST 2017) [**Awarded as a Best Oral Presentation**]
23. Sophia Selvarajan, **Nagamalleswara Rao Alluri**, Arunkumar Chandrasekhar, Sang-Jae Kim, Self-powered biosensor for direct detection of cysteine using functionalized $BaTiO_3$ Nanoparticles, 13th International Conference on Nanotek and Expo, 2016, December 05 to 07, USA. [**Awarded as a Best Poster**]
24. Arunkumar Chandrasekhar, **Nagamalleswara Rao Alluri**, Venkateswaran Vivekananthan, Gaurav Khandelwal, Sang-Jae Kim, Smart Puzzle Toy: A Step towards the Commercialization of Triboelectric Nanogenerator, **10th ICAMD-2017**, Dec 05~08, 2017, Jeju Island, Korea.
25. Arunkumar Chandrasekhar, **Nagamalleswara Rao Alluri**, Sudhakaran M. S. P, Young Sun Mok, Sang-Jae Kim, Human Interactive Smart Mobile Pouch Triboelectric Nanogenerator and its Self-powered Applications, International Conference on Electronic Materials and Nanotechnology for Green Environment **(ENGE 2016)**, Nov 6 -9, Jeju, South Korea **[Awarded as a General Poster**].

Declaration

I **Alluri Nagamalleswara Rao**, hereby declare that the thesis entitled: **"Development of Self-Powered Sensors using Hybrid Piezoelectric Structure Nanogenerators"**, submitted to the **Jeju National University**, in partial fulfillment of the requirement for the award of the **Degree of Doctor of Philosophy in Faculty of Applied Energy Systems, Major in Mechanical Engineering** is a record of original and independent research work done and published by me during the period of March-2014 to Feb 2018 under the supervision, guidance of **Prof. Sang Jae Kim**, Department of Mechatronics Enginnering and the co-supervision from **Prof. Ji Hyun Jeong**, Department of Mechanical Engineering, Jeju National University. This thesis solely based on our publication in reputed journals, and it has not been formed for the award of any other Degree/Diploma/Associateship/Fellowship to any candidate of any University.

Alluri Nagamalleswara Rao